

AD629363

# Technical Report

381

J. L. Allen, et al.

## Phased Array Radar Studies

1 January 1963 to 1 July 1964

31 March 1965

Lincoln Laboratory

CLEARINGHOUSE FOR FEDERAL SCIENTIFIC AND TECHNICAL INFORMATION			
Hardcopy	Microfilm		
34.20	1.75	346	as
ARCHIVE COPY			

coll. 1

The work reported in this document was performed at Lincoln Laboratory,  
a center for research operated by Massachusetts Institute of Technology,  
with the support of the U.S. Air Force under Contract AF 19(628)-500.

This report may be reproduced to satisfy needs of U.S. Government agencies.

Distribution of this document is unlimited.

Non-Lincoln Recipients

PLEASE DO NOT RETURN.

Permission is given to destroy this document  
when it is no longer needed.

MASSACHUSETTS INSTITUTE OF TECHNOLOGY  
LINCOLN LABORATORY

PHASED ARRAY RADAR STUDIES  
1 JANUARY 1963 TO 1 JULY 1964

J. L. ALLEN	S. D. EWING
D. M. BERNELLA	W. J. INCE
F. BETTS	T. B. LEWIS
L. CARTLEDGE	H. J. PRATT, JR.
W. P. DELANEY	M. SIEGEL
B. L. DIAMOND	E. STERN
J. DiBARTOLO	D. H. TEMME

Group 44

TECHNICAL REPORT 381

31 MARCH 1965

LEXINGTON

MASSACHUSETTS

## ABSTRACT

This is the fourth in the series of reports describing the work of a general research nature carried out by the Lincoln Laboratory Array Radars Group during the period 1 January 1963 to 1 July 1964. Effort prior to this time is covered in Lincoln Laboratory Technical Reports 228, 236, and 299. We have also issued one report of a general tutorial nature on the subject of large-array antennas, Lincoln Laboratory Technical Report 323.

The effort reported is directed toward an investigation of components, techniques, and fundamental theoretical limitations of arrays, primarily for high-power radar applications. The emphasis is on those applications which place the most stringent demands on the radar for resolution of very small targets from backgrounds of extensive and relatively large clutter (arrays with capability for high power, broad bandwidth, and narrow beamwidth).

Part I deals with the concluding activities on the 900-Mcps test array, emphasizing the configuration of the transmitting array and our experiences with it. This is a transmitter-per-element array that uses tetrode tubes at a power level of approximately 6 kw peak and 60 watts average per element.

Part II is devoted to work on an S-band subarray transmitter configured around the use of high-power helical phase shifters. The major emphasis during the period has been upon the development of the phase shifters and upon the time-delay units to be used, one per each subarray. Some work on increasing the dynamic range of tunnel-diode amplifiers at microwave frequencies is also reported in this section, along with miscellaneous support activities for the subarray development.

Part III deals with studies of antennas and beam-forming systems. The first thorough analytical analysis of the so-called Blass multiple-beam matrix is presented indicating performance bounds as a function of the desired bandwidth and array size. The effect of multiple feeds on the patterns of optical multiple-beam systems, such as a Luneburg lens fed with multiple closely spaced feeds, is analyzed; it is pointed out that prior studies of mutual-coupling effects in flat arrays are directly applicable to the problem of producing satisfactory beam shapes from such antennas. Work on a better understanding of the basic effects of mutual coupling in large arrays continues with both analytical and experimental studies. A new and more extensive program for the computation of mutual effects in dipole arrays is described which can handle dipoles of arbitrary lengths less than or equal to one-half wavelength, with or without ground plane. The results for impedance variation as a function of scan angle and element gain function shape are given for central and edge elements in arrays of various sizes, for dipoles with and without a ground plane. Direct measurements of the impedance variation of dipoles above a ground plane made on a small test array are also discussed. A comparison of these results with the computer predictions shows excellent agreement between theory and experiment.

Accepted for the Air Force  
Stanley J. Wisniewski  
Lt Colonel, USAF  
Chief, Lincoln Laboratory Office



## TABLE OF CONTENTS

Abstract	iii
PROJECT AND REPORT ORGANIZATION	
I. Introduction	1
II. Project Philosophy	1
III. Report Contents and Organization	2
PART I	
900-Mcps TEST ARRAY	
CHAPTER 1 - TEST TRANSMITTING ARRAY	5
Summary	5
A. Introduction	5
B. Test-Array Layout	5
C. Initial Setup of Transmitter Module	9
D. Performance of Transmitter Components	9
E. Performance of Unit Module	15
F. Performance of 16-Element Array Monitor System	15
G. Performance of Transmitting Array	17
H. RF Cabling	29
I. 900-Mcps Array Cooling System	29
J. Conclusions	33
CHAPTER 2 - MISCELLANEOUS SUPPORT FACILITIES	35
Summary	35
A. Solid-State Video Driver	35
B. High-Voltage Modulator and Power Supply for Testing Phased Array High-Power Tubes	37
C. 900-Mcps Receiving Array Experience	39
PART II	
"SUBARRAYED" ARRAY RADAR	
Summary	41
CHAPTER 1 - SUBARRAY CONFIGURATION AND SPECIFICATIONS	41
CHAPTER 2 - ANTENNAS	45
CHAPTER 3 - HIGH-POWER PHASERS	47
Summary	47
A. Introduction	47
B. Present Design Goals for High-Power Phasers	47
C. Diode Phasers	48

Part II, Chapter 3 (Continued)

D. State-of-the-Art Survey of Ferrite Phasers	52
E. Status and Estimates of Phasers Meeting Design Goals	68
F. Acknowledgments	70
CHAPTER 4 - RF POWER DISTRIBUTION AND CIRCULATOR	71
Summary	71
CHAPTER 5 - TRANSMITTER AMPLIFIERS	75
Summary	75
A. Introduction	75
B. Amplifier Requirements	75
C. Existing Tubes and Development Possibilities	77
D. Modulators	79
E. High-Power S-Band Test Sources	80
CHAPTER 6 - MISCELLANEOUS COMPONENTS	81
A. Duplexers	81
B. Input Circulator	81
CHAPTER 7 - RECEIVER PREAMPLIFIERS	83
Summary	83
A. Introduction	83
B. Design Goals for Subarray Preamplifier	83
C. Tunnel-Diode Amplifiers	84
D. Development of Improved Tunnel-Diode Amplifier Having Extended Dynamic Range	85
E. Continuing Configuration Studies	88
F. Microwave Transistor Amplifiers	89
G. Phase-Stability Test on 900-Mcps Receivers	96
CHAPTER 8 - TIME DELAYS	103
Summary	103
A. Introduction	103
B. Present Design Goals for Time Delays	103
C. Configurations	104
D. Measurements	107
E. Time-Delay Hardware	116
CHAPTER 9 - S-BAND SUBARRAY PATTERN RANGE	155

PART III

ANTENNAS AND BEAM-FORMING STUDIES

CHAPTER 1 - RF BEAM-FORMING TECHNIQUES	157
Summary	157
A. Introduction	157

Part III, Chapter 1 (Continued)

B. Basic Configuration	158
C. Matrix Design Procedure	164
D. Computed Results	170

CHAPTER 2 - EFFECTS OF MUTUAL COUPLING ON PATTERNS OF MULTIPLE BEAM OPTICAL-TYPE ANTENNAS	223
--	-----

Summary	223
A. Introduction	223
B. Analysis	224
C. Gain and Directivity of System	226
D. Use of Lens for Simultaneous Reception of Multiple Beams	230
E. Conclusions and Suggestions for Further Work	232

CHAPTER 3 - THEORETICAL INVESTIGATION OF MUTUAL COUPLING EFFECTS	239
---	-----

Summary	239
A. Introduction	239
B. Mathematical Description of Mutual Coupling Effects	241
C. Computational Programs	261
D. Comparison of Computed Results with Known Results for Infinite Arrays	266
E. Summary and Discussion of Computed Results	270
F. Conclusions and Observations	274

CHAPTER 4 - EXPERIMENTAL MUTUAL COUPLING PROGRAM	299
--	-----

Summary	299
A. Introduction	299
B. Description of Experimental System	301
C. Results and Comparison of Data with Computed Data	302

APPENDIX A -- Rigorous Derivation of Aperture Illumination Relationship	319
--	-----

APPENDIX B	323
------------	-----

# PHASED ARRAY RADAR STUDIES

1 January 1963 to 1 July 1964

## PROJECT AND REPORT ORGANIZATION

J. L. Allen

### I. INTRODUCTION

Lincoln Laboratory has been active in array antennas and array radar systems since the mid-1950's. This is the fourth in a series of progress reports by one group engaged in this activity. The group whose work is reported herein has been pursuing a comprehensive program of research and development in the techniques, components, and understanding of large-array systems since early 1959. This work was begun and carried out as part of the program of the Special Radars Group until July of 1963 at which time a new group, Array Radars (Group 44), was organized.

This report, like the earlier ones, describes all work performed during the stated period, as well as work still in progress. The work is reported in considerable detail; each section is written by the engineer directly responsible for the investigation. The bulk of the report is intended primarily for other workers in the field of large arrays, but each major division of the report starts with a brief summary of the work for the more casual reader. Although we have tried to hold cross referencing to a minimum, inevitably there are numerous references to previous reports in this series, cited for brevity simply as TR-228, TR-236, and TR-299.\*

### II. PROJECT PHILOSOPHY

This project was conceived in the early days of the current interest in large-array radar systems and was founded upon the philosophy that such complex and redundant systems not only justify but also demand intensive research and development into the components required for such systems, as well as into the techniques for reducing and simplifying the numbers of such components. In order to guide this work realistically, significant effort has been devoted to studies of systems applications of arrays and the fundamentals of large-array antennas.

It has become clear that of the numerous array configurations known, the combined desires for simplicity, reliability, and effectiveness point to certain guidelines about the general class

---

\* J. L. Allen, et al., "Phased Array Radar Studies, 1 July 1959 to 1 July 1960," Technical Report 228, Lincoln Laboratory, M.I.T. (12 August 1960), DDC 249470, H-335.

J. L. Allen, et al., "Phased Array Radar Studies, 1 July 1960 to 1 July 1961," Technical Report 236, Lincoln Laboratory, M.I.T. (13 November 1961), DDC 271724, H-474.

J. L. Allen, et al., "Phased Array Radar Studies, 1 July 1961 to 1 January 1963," Technical Report 299, Lincoln Laboratory, M.I.T. (20 February 1963), DDC 417572.

of configurations of most interest for high-performance radar systems. A principal virtue of arrays is their capacity to resolve a complex, dynamic target situation. Realizing this potential of arrays leads almost invariably to the consideration of microwave frequencies (approximately L- through X-bands) and electrically large antennas for both transmitting and receiving. At such frequencies, economics, reliability, and packaging constraints dictate against the use of a transmitting tube per element in a transmitting array and leads one to consider the so-called "subarrayed" approach to transmitters in which the only elements common to each antenna are a phase shifter and (perhaps) its associated driver. Numbers of elements are grouped together to be fed from a common transmitting source, with the number to be grouped depending in theory on bandwidth considerations and in practice also upon the optimum distribution of power sources throughout the array. The receiving systems for such configurations seem also to have a common denominator -- the need for forming multiple simultaneous beams. This requirement arises because of the combined needs of high resolution and reasonably high rates of volume coverage.

Consistent with this philosophy, then, we have seen over the past years a more defined channeling of the activities of this group into areas which support this system philosophy. The bulk of the present report is devoted to the problems of high-powered, low-loss phase shifters operating directly at microwave frequencies, time-delay units for broad-band steering of electrically small subarrays, means for essentially lossless formation of multiple simultaneous beams and receiving arrays, and such supporting studies that we feel to be of a critical nature (e.g., the effects of mutual coupling on the choice of antennas and array configurations). No pretense is made that the resulting coverage is all inclusive; for example, we are doing no work in the critical area of power sources for arrays because of the limitations which prohibit our entry into this expensive, high-risk business. Perhaps an even greater shortcoming is the lack of any effort in the group toward the control and processing of arrays. Our interests are essentially in the microwave end of the spectrum, and we are working very diligently to help realize arrays capable of generating information at an almost unbelievable rate. Logic would suggest that we investigate the sort of information the arrays should generate and what should be done with that information. However, we have been unsuccessful at finding or cultivating people with the unusual blend of talents it takes to successfully launch and conduct such an investigation.

In addition to our own internal work, we recognize the obligation of the group to interact with and support the activities in arrays in other government agencies and to be of assistance, where possible, to industrial contractors working in this field. To this end we have devoted several thousand man-hours to consulting for government or industry. We also attempt to disseminate our work widely through the means of formal technical reports such as this, occasional shorter, more timely reports, journal articles, and both formal and informal verbal presentations. We welcome visitors to discuss our activities, and only request that they be familiar with our previous reports.

### III. REPORT CONTENTS AND ORGANIZATION

As stated in the Introduction, this is a progress report. It describes work both completed and in progress during the reporting period. We have attempted to discuss all significant work in detail, including projects which were unsuccessful, when the lack of success would be meaningful to other workers in the field.

Since responsibility for various facets of the project has been undertaken by individual engineers, the report has been written by the people directly concerned, with a minimum of alterations on the part of the editors. To promote further direct interchange of ideas on the topics discussed, the authors of individual sections have been indicated in the appropriate places. Where no name appears on the section, the author last named is also the author of that section.

The report is divided into three parts. Part I deals with the concluding activities of our 900-Mcps test array work. Part II is devoted to new work in subarrayed transmitting arrays and associated components. Part III deals with studies in multiple-beam-forming systems and supporting studies in mutual-coupling effects.

# PART I 900-Mcps TEST ARRAY

## CHAPTER 1 TEST TRANSMITTING ARRAY

### SUMMARY

Most of the effort during the reporting period concentrated on implementing the transmitter array and coordinating the entire receiver, transmitter, and supporting equipment into a working array radar system.

A block diagram of the implemented system is shown together with pictures of the actual setup and a brief description of its function. Component difficulties and the methods used to eliminate them are discussed, as are the initial setup and performance of the modules.

The usefulness of the monitor system is examined, and the successful performance of the over-all system is illustrated through the presentation of antenna patterns for various beam positions. The design and performance of the water-cooling system are discussed, and finally, a brief description of a high-power tube test facility is presented.

### A. INTRODUCTION

J. DiBartolo

Various concepts, some quite complex, have been proposed for implementing electronic array systems. Lincoln Laboratory's array project has moved toward simple system designs. These designs are characterized by most, if not all, of the following: (1) Phase shifting or other steering is done at the highest power level that the state of the art permits and at the signal frequency. (2) Insofar as possible, all electronics associated with a single element or group of elements are located in a single replaceable package. (3) Both the electronic package and the fixed cabling in the array have long-term stability in phase and amplitude so that retuning or other adjustment of the electronics package is not necessary, either in the array or after long periods of storage. (4) The electronic packages are so nearly identical and the array cabling is accurate enough so that any package can be used anywhere in the array without retuning or other readjustments.

The realization of such a system depends upon the availability of suitable components. In particular, passive components like cabling, phase shifters, and power dividers of excellent quality and unusual uniformity are essential. A 16-element linear transmitting array was built by Lincoln Laboratory to determine (and solve if possible) some of the problems associated with this design philosophy.

### B. TEST-ARRAY LAYOUT

J. DiBartolo

A block diagram of the test-array system is shown in Fig. I-1. The major parts that make up the system are: the preprogrammed beam-forming computer, the signal processor and display, a centralized control panel, RF generator and driver amplifiers, DC supplies, high-power video driver, 16 transmitters, and 16 receivers. All these units are interlocked and sequentially controlled to avoid damage which could be caused by applying some voltages prematurely during the turn-on time or in default of other voltages while the array is in operation.

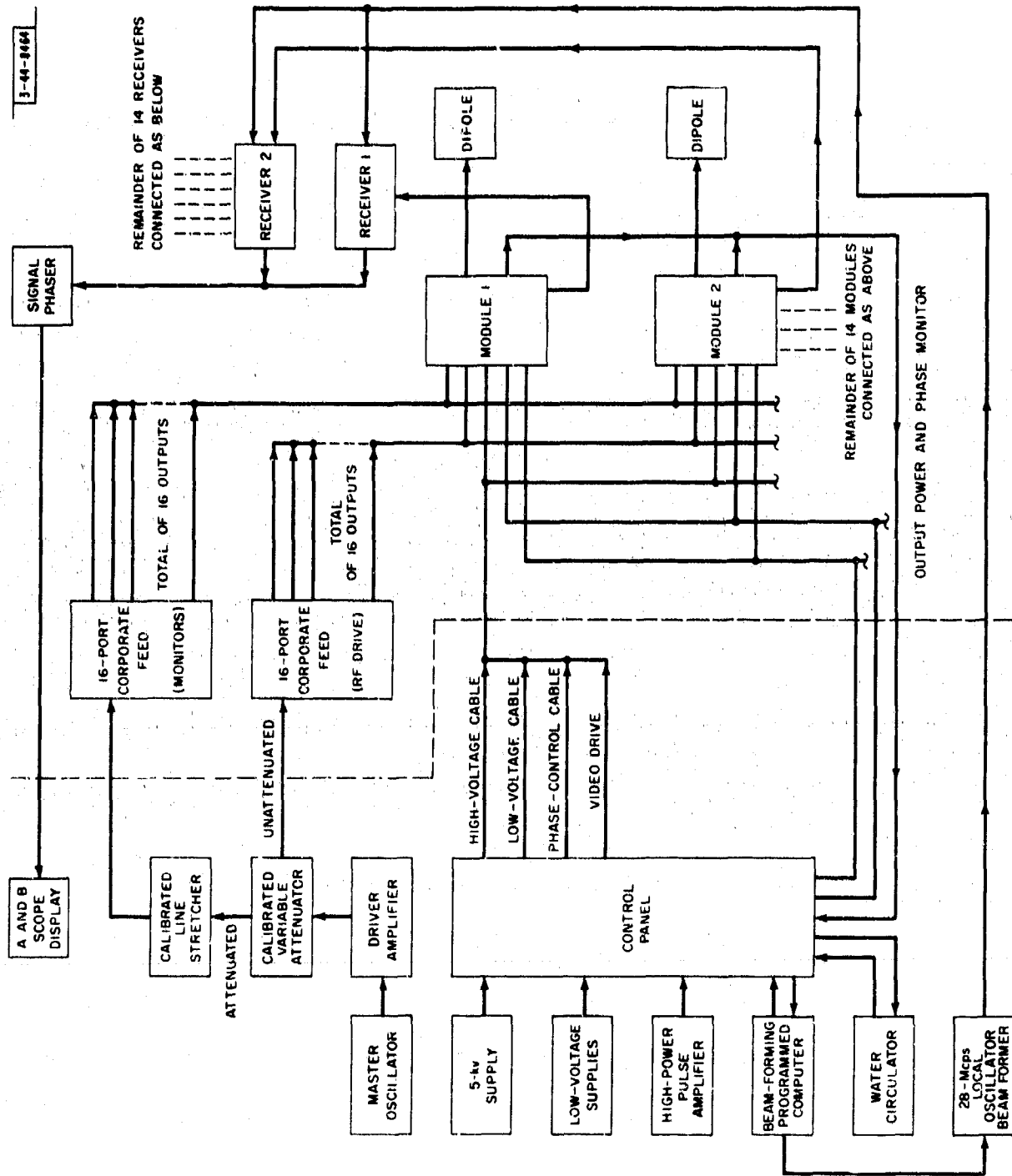


Fig. 1-1. Block diagram of phased array system and block distribution.



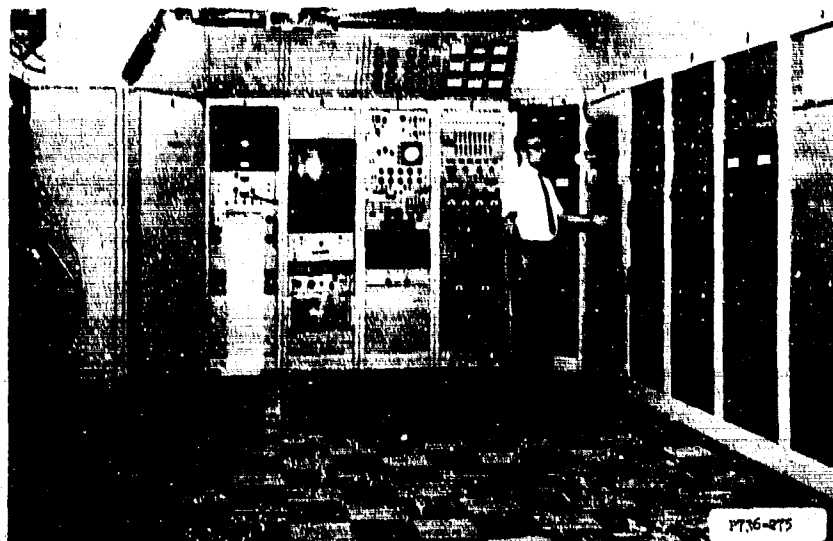


Fig. I-2. Phased array control room.

Some of these major components are located in the racks lettered E through R of the control room (see Fig. I-2); others are located in the antenna pedestal.

The computer enclosed in rack E is capable of forming new beams in a few microseconds and can be operated in at least three modes: (1) the automatic sequential mode, (2) the manual sequential mode, and (3) the transmitter-phase test mode. In the automatic sequential mode, all the preprogrammed beams are formed sequentially. This is the normal scanning mode of the array whereby beams are pointed up to  $\pm 45$  degrees of boresight. Within this mode we can use a seven-position switch to set the scanning speed of the beams by varying the radar hits per beam-position step. In this way the position of each beam is fixed for some binary number of "hits" between 1 and 64.

The manual sequential mode which is used to form fixed beams facilitates the recording of antenna patterns for all beam positions. Finally, the transmitter-phase test mode is used not only to make measurements of all transmitter-phase shifters in their respective operating positions, but also to check the initial over-all electrical length of each transmitter channel.

The computer\* supplies all the timing signals for the system and for the receiver; it supplies RF beam forming, IF beam forming, and information for monopulse. The computer's performance has been trouble-free.

The phase-shifting apparatus for the 28-Mcps local oscillator is found in rack F. This is used to form IF beams and was described in TR-228.<sup>†</sup> Racks G, H, and J contain the antenna pattern recorder, the B-scope display, part of the receiver's amplitude and phase test gear, and part of the receiver and the A-scope. Rack L holds the RF (900-Mcps) driver for the entire array. It consists of two modules identical to the 16 which form the transmitter system. One module is in operation, while the other is held as a spare. Racks M and N house the array's high-voltage regulator and the RF driver power supply, respectively.

\* The computer was designed by Harvey Greenburger.

<sup>†</sup> TR-228, pp. 81-101.

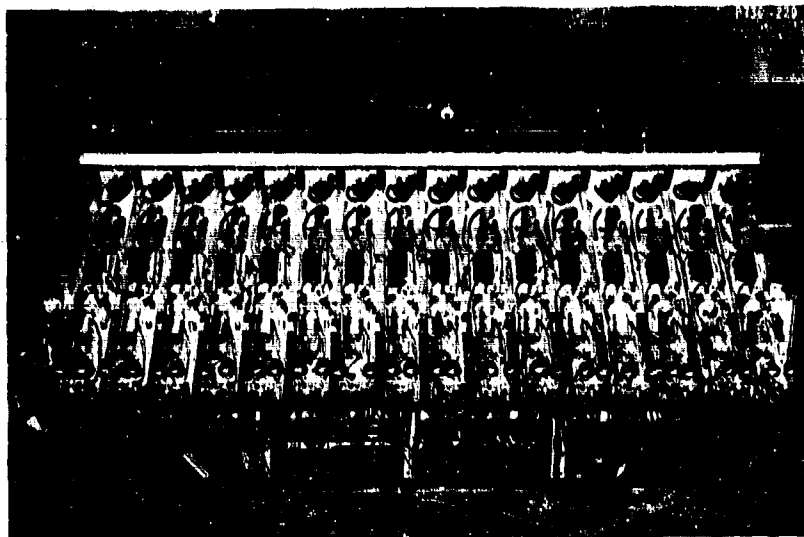


**Fig. I-3. Sixteen transmitters shown mounted on a rotating pedestal. An associated receiver is mounted under each transmitter.**

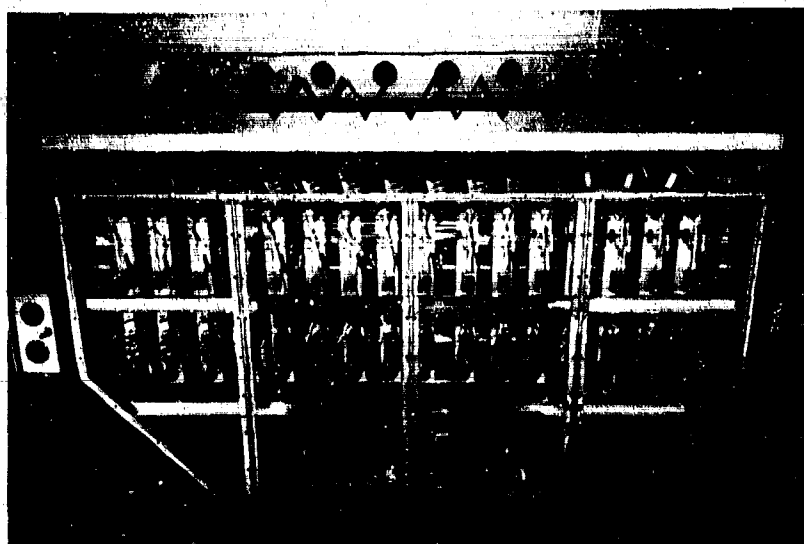


**Fig. I-4. Sixteen receivers shown mounted on a rotating pedestal (1960 vintage).**

The hard-tube high-power video driver which fed the entire array and the new solid-state high-power video driver which replaced it (described in Ch. 2, Sec. A) are located in racks P and R, respectively. The 16 transmitters are mounted on a pedestal capable of 370-degree rotation which is shown in Fig. I-3; the 16 receivers\* are mounted on the same pedestal below the 16 transmitter modules, as shown in Fig. I-4 (transmitter not shown).

The wiring of the entire system has been completed and debugged, and the system is now operating as a linear, phased array radar.

### C. INITIAL SETUP OF TRANSMITTER MODULE

J. DiBartolo

The transmitter modules are set to a standard power output and electrical length before they are plugged into the array. The setup used to make these initial adjustments is shown in Fig. I-5. Figure I-6 is a diagram of the "test harness" which is essentially a microwave comparison bridge with the active module in one leg and a calibrated attenuator and a calibrated trombone line in the other.

Signals from the two legs are compared in a 4-port coupler. The detector is part of the performance-monitoring system in the module (described in detail in TR-299). When a bridge such as this is operated near a null, amplitude and phase errors are essentially orthogonal (for a narrow-band signal at least) and it is possible to resolve amplitude and phase errors.

Two controls were included in each transmitter module during the initial design: (1) a line stretcher to adjust the module's electrical length, and (2) a potentiometer in the modulator circuit to adjust the output power level.

It has been observed in the test bench that the line stretchers could have been eliminated since the module-to-module phase errors are always within a range which permits trimming by the cavity tuning adjustments without affecting the output power. The potentiometer in the modulator screen circuit has been much more useful. It regulates the magnitude of the DC voltage on the screen grid of the modulator tube, thereby setting the amplitude of the video pulses which drive the RF amplifiers, compensating for differences in power gain.

The performance of each bit of the digital phase shifter is also checked while the module is on the test bench. This is done by back biasing the proper pair of diodes, using the manual controls shown at the bottom of Fig. I-6; the accuracy of the incremental delay introduced by the phase shifter is checked by reading the equivalent displacement from the calibrated line stretcher.

This setup has been very useful in the debugging process. A similar setup has been used to make phase and amplitude stability measurements during the actual operation of all 16 transmitters in the test array (see Sec. F of this chapter).

### D. PERFORMANCE OF TRANSMITTER COMPONENTS

J. DiBartolo

The major components in a transmitter module are (1) a 4-bit digital phase shifter, (2) two cavity amplifiers, (3) a video modulator, and (4) a multifunction "duplexer board." Since these components have been discussed in TR-299, the comments in this section will be limited to their performance and to some modifications which were found to be necessary.

---

\* For a complete description of these receivers, see TR-228.

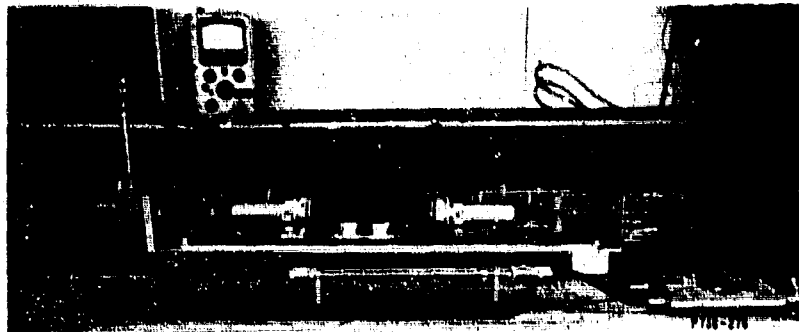


Fig. 1-5. Test bench set up to trouble-shoot and make final adjustments on transmitter modules.

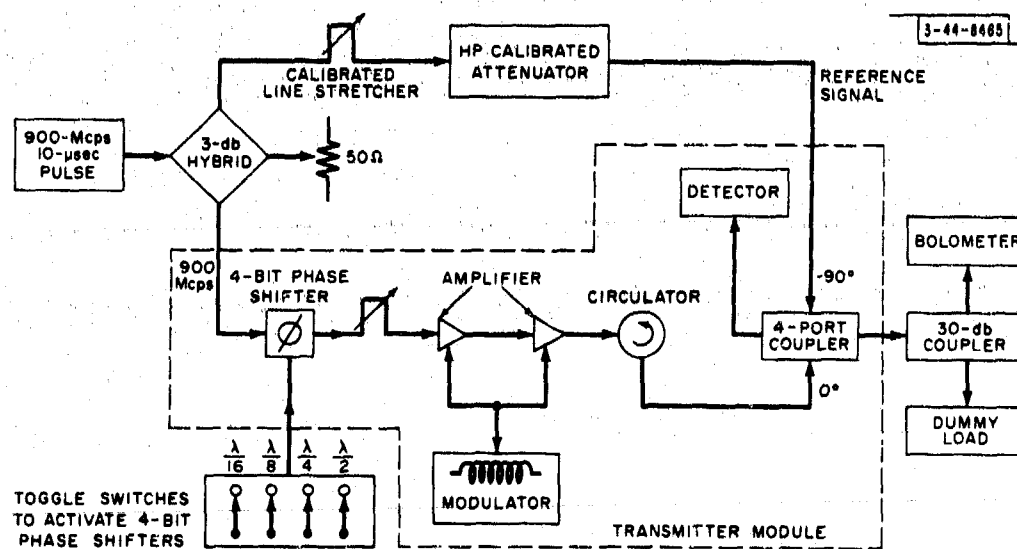


Fig. 1-6. Block diagram of test bench and monitor system. Toggle switches (lower left corner) are manually controlled to check performance of 4-bit phase shifter.

## 1. Phase Shifters

The electrical design of the phase shifter has proved satisfactory on the basis of individual performance checks and antenna patterns obtained at the various beam positions with these phase shifters installed. Although some difficulties were encountered, they were eliminated. Excessive phase drift was traced to the geometry of the capacitors that were used to trim the lines. These were replaced with JFD-SC131 variable piston capacitors mounted in an aluminum block as shown in Fig. I-7. The new capacitors provided better stability, higher accuracy, and greater ease of adjustment of the line length than the previous design (see TR-299).

A second problem arose from the high-level video pulse generated within the module. Cables to and from the phase shifters had been carefully shielded except for about  $\frac{1}{2}$  inch at the point of contact in the bias terminal of the phase shifter. This point is well by-passed for RF, but not well enough to avoid video interference. As a quick solution, 0.01- $\mu$ f capacitors (also shown in Fig. I-7) were added at these points. Unfortunately, these capacitors limit the beam steering speed. Adequate shielding, a more desirable solution which would allow high-speed steering, is planned in future designs.

It would also be desirable to strengthen the structure of the phase shifter mechanically by mounting two aluminum plates, about  $\frac{1}{8}$ -inch thick, on each side to eliminate changes which are caused by mechanical stress from either handling or large temperature variations. Maximum dependability could thus be assured, although we do not plan to make these changes.

Finally, the phase-shifter drivers described in TR-299 have been modified. Transistors such as RCA 2N3440 are now available and reasonably priced. These transistors have  $V_{CBO} = 300$  volts;  $I_{C_{max}} = 0.5$  amp, and  $P_D = 5$  watts. By using the 2N3440, we have eliminated the instability caused by the erratic performance of the four-layer diode and have reduced the cost of the driver. The modified version of the driver is shown in Fig. I-8.

## 2. RF Amplifiers

The RF cavities were originally designed to handle power up to 5 kw but, as noted in TR-299, the output power could be increased to 10 kw by applying higher plate and screen voltages. To reach these levels, the plate blockers on these cavities had to be modified to eliminate arcing which, reflected into the modulator, would explode the small resistors used in the modulator plate circuits. In the original cavity design shown in Fig. I-9(a), the outer disk was at high-voltage potential and was attached to the body with metal bolts insulated by a washer. In the new version shown in Fig. I-9(b), another metal plate of a larger diameter has been placed over the high-voltage plate which is insulated from it by a four-inch mica disk. This new plate is held at ground potential by the metal bolts which attach it to the cavity's body. However, the bolts no longer go through the high-voltage insulator. This modification not only eliminated the corona problem, but also made the operation of tuning the cavities much safer. Moreover, because more mica was needed with this modification, we used less expensive synthetic mica.

In one experiment, epoxy-bonded India mica disks were used. (Epoxy-bonded mica is significantly cheaper than ruby mica.) After several months of operation at 3.5 kv, these insulators were examined and no trace of corona was found. They have also been operated at 5 kv without any sign of degradation.

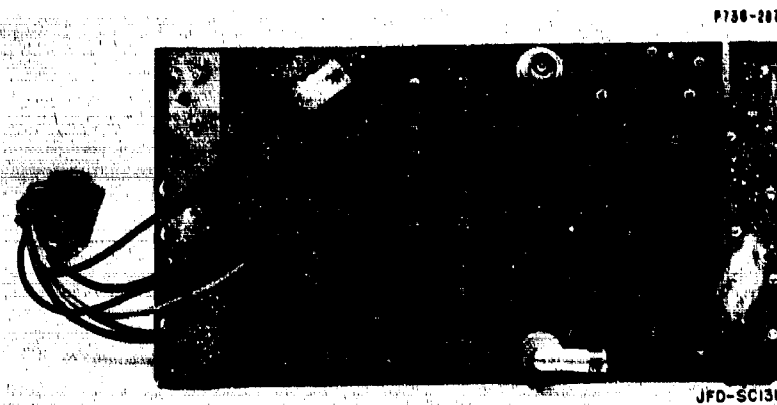


Fig. I-7. Four-bit phase shifter. Disk capacitors ( $0.01 \mu\text{f}$ ) have been added to eliminate video interference. Addition of JFD-SC131 variable capacitors provides better mechanical stability and more sensitivity to balance the lines.

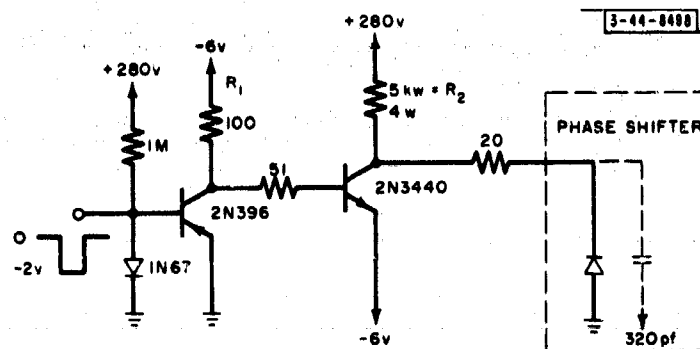
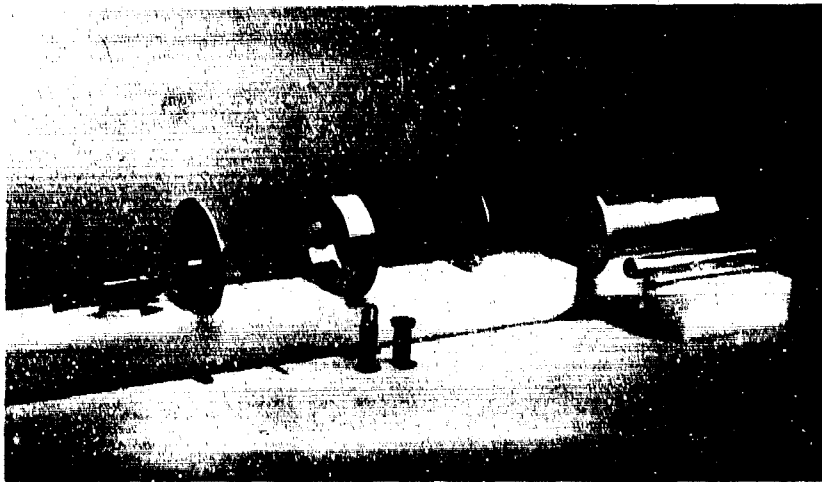


Fig. I-8. Modified phase-shifter driver using high-voltage transistor.



(a)



P736-283

(b)

Fig. 1-9. (a) Initial version of RF cavity. (b) Modified version of RF cavity. Metal plate (1) and DC blocker (2) are new additions. Mounting holes have been eliminated from plate (3). These modifications prevent corona formation.

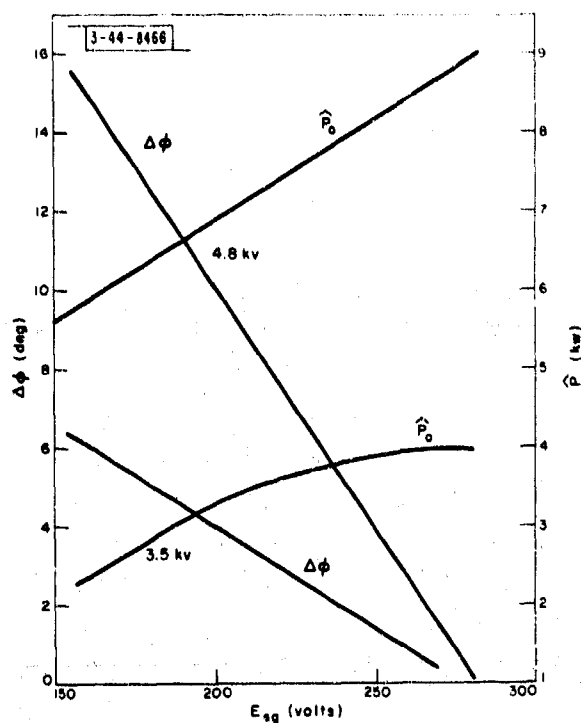


Fig. I-10. Effect of modulator screen voltage control.

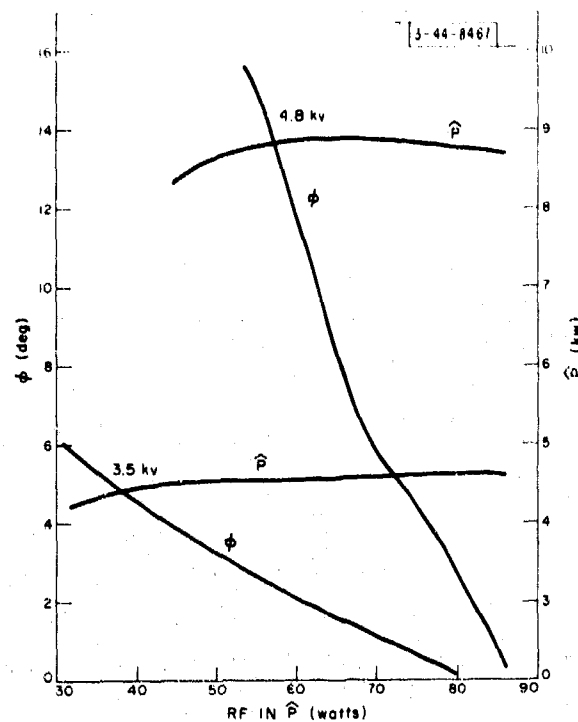


Fig. I-11. Module phase and amplitude compression curves.

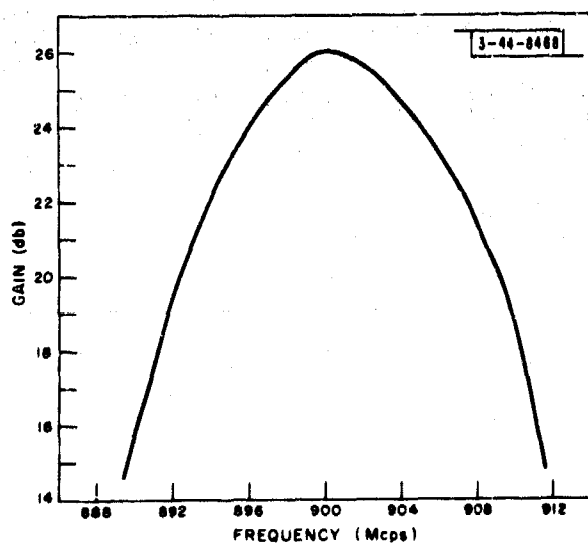


Fig. I-12. Transmitter module frequency response obtained by using an AIL power oscillator as the RF source.



### 3. Modulators

When the output power of the RF cavities was increased by increasing the modulator's plate voltage to 5 kv, the addition of a clamping diode was necessary to avoid arcing due to high-voltage back swing. The clamping was done in the low-voltage transformer secondary tap that feeds the screen grid of the RF tubes to avoid using costly high-voltage diodes. This change, together with the modification of the RF cavities, eliminated what had earlier appeared to be modulator instabilities.

### 4. Monitor-Duplexer Boards

The monitor-duplexer boards have performed well in all functions. No adverse effects were noticed even at outputs of 10 kw. However, it is mandatory that proper bias be applied to the diodes during transmitting time since these diodes can be permanently damaged or destroyed by applying high power to them in the unbiased conditions.

## E. PERFORMANCE OF UNIT MODULE

J. DiBartolo

The phased array transmitter has been in operation for over six months. Data obtained while operating several of these unit modules on a special test bench show that they are more than adequately stable to meet phased array requirements.

It was pointed out earlier that the power gain of each module can be controlled by varying the screen grid voltage of the modulator tubes. This is demonstrated in Fig. I-10. The absolute phase changes only a few degrees when the output power is lowered by almost 2 db. This fact, together with the good long-term stability of these amplifiers, could be used to simplify the performance-monitoring system of a large working array. Satisfactory performance could be indicated with confidence by a simple output amplitude measurement and a check of the phase-shifter diode currents.

The modules maintain constant output power and good phase stability even with varying input RF power. This is demonstrated in Fig. I-11 which shows that the RF output changed 1 db and the absolute phase changed only eight degrees for a 6-db change at the input. Hence, the performance of these units can be optimized by driving them to the saturation level. This would tend to reduce output variations caused by nonuniform insertion loss of the corporate feed and of the phase shifters as the various bits are switched.

The small signal gain and bandwidth of a typical transmitter module are shown in Fig. I-12. The gain is 26 db and the bandwidth is 10 Mcps (with the two stages synchronously tuned). These were measured using an Airborne Instruments Laboratory (AIL) power oscillator at 2 watts peak as a driver. The module was operating in its normal mode and tuned to give maximum output at 900 Mcps.

## F. PERFORMANCE OF 16-ELEMENT ARRAY MONITOR SYSTEM

J. DiBartolo

To check the performance-monitoring system described in TR-299,\* the operation of modules in the phased array system is evaluated through the monitor system depicted in Fig. I-13. Sixteen test points are available at the control room; one for each module. During the setup

---

\* TR-299, pp. 123-129.

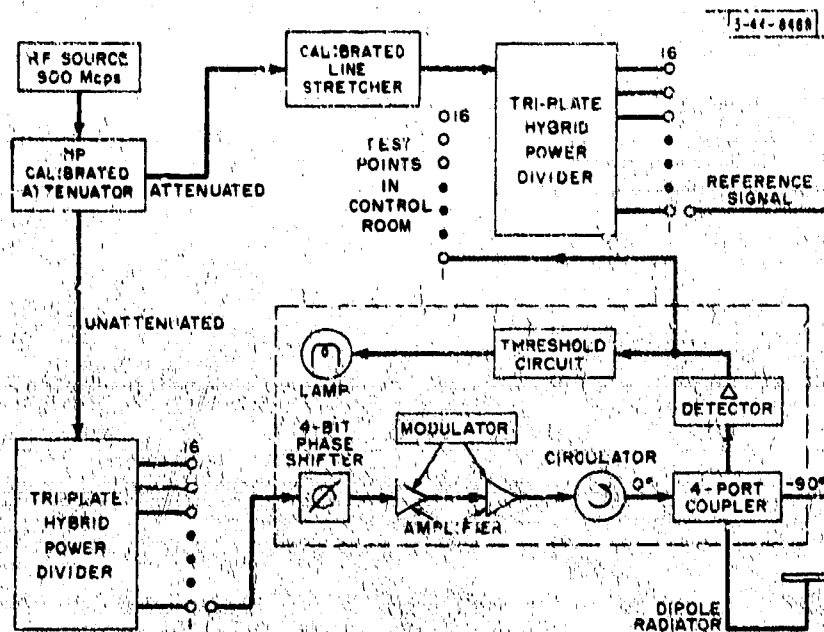


Fig. 1-13. Monitor system for 16-element array. The signal at difference port of the 4-port hybrids is monitored to evaluate the working condition of each module and to give a visual alarm when it is no longer performing satisfactorily.

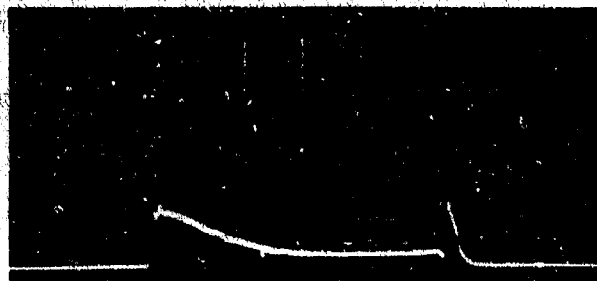


Fig. 1-14. Typical null observed at a test point of the monitor system. It indicates phase coherence and amplitude stability for a transmitter module.

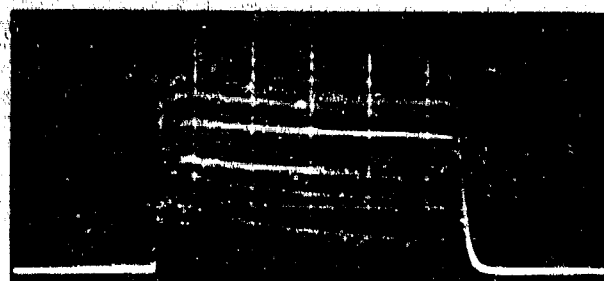


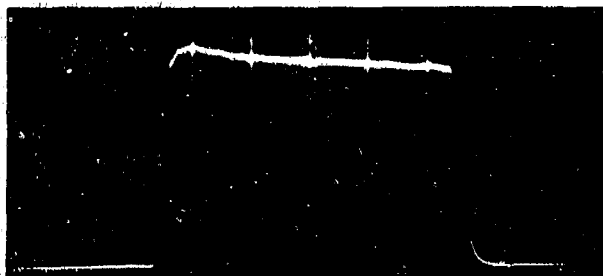
Fig. 1-15. Amplitude variations observed at same test point as Fig. 1-14. They correspond to phase changes necessary to scan the beam.

procedure on the test bench, the stability of each module is observed and the monitor circuit is adjusted to turn on a light in the control room for module errors equivalent to a 20-degree phase error.

A typical null, as observed at a test point when complete phase coherence exists and the computer is set in the transmitter test mode, is shown in Fig. I-14. However, when the computer is set to the automatic scan mode, discrete amplitude differences result from different phase-shifter settings (Fig. I-15). The bottom line shows the null which occurs when the beam goes through broadside; the rest of the lines show other phase differences due to the sequential formation of off-boresight beams.

-44-8472

Fig. I-16. Amplitude of pulse indicates 22.5 degrees of phase error (viewed at same test point as Figs. 14 and 15). Scope sensitivity is 20 mv/cm.



The threshold circuit includes a "broadside gate" and is only active at broadside. In order to utilize more fully the versatility of the monitor system, corresponding bits of every phase shifter can be energized simultaneously by a common control. In this way one can check the absolute phase of any bit while the system is operating in the transmitter-phase test mode. For example, Fig. I-16 is a check of bit No. 1 (equal to  $22\frac{1}{2}$  electrical degrees) for the phase shifter of channel 16. The sensitivity of the oscilloscope is 20 mv/cm which is quite adequate to make measurements to within a few electrical degrees.

## G. PERFORMANCE OF TRANSMITTING ARRAY

J. DiBartolo

The performance of the phased array system is estimated by evaluating its antenna patterns. The 16 transmitters are mounted on an azimuth pedestal located in the penthouse of Building C, and the pattern test receiver is situated some 1700 feet away as shown in Fig. I-17. This test receiver (see block diagram, Fig. I-18) was designed to produce a voltage at the frequency of 1 kcps, proportional to the RF power intercepted by the receiving dipole. Then the 1-kcps output voltage is sent back, through a telephone pair, to the antenna pattern recorder which is also situated in Building C. Utilizing this setup, antenna patterns are taken of the test array transmitter.

Figure I-19(a-e) shows various beam positions obtained by using the 4-bit digital phase shifters when the complete transmitter system was operated. The worse case in this series of patterns [Fig. I-19(e)] was that in which the sidelobe reached the point -11 db (theoretical value of first sidelobe for a uniform array is approximately -13 db). The theoretical angular position that each beam should occupy can be calculated by the expression

$$\theta = \arcsin\left(\frac{B}{0.58n}\right)$$

where

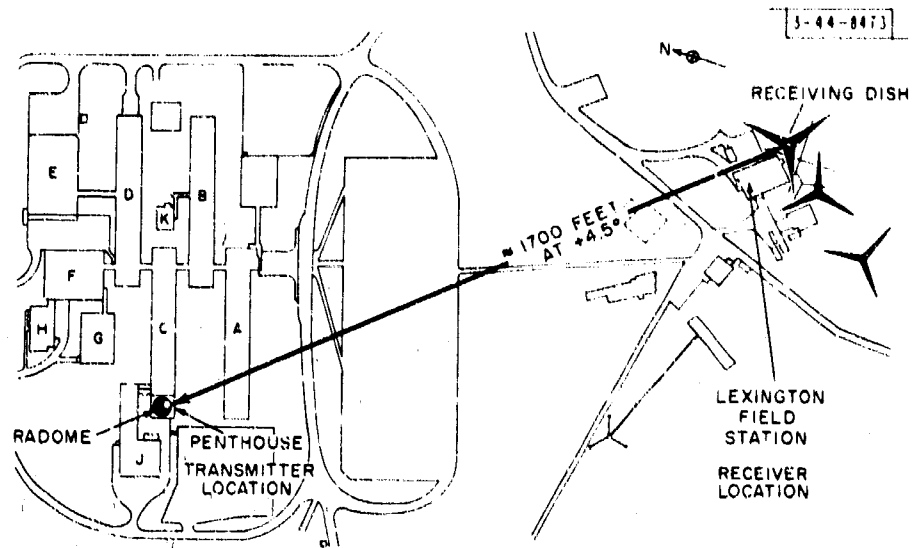


Fig. 1-17. Location of transmitting array test facility and pattern test receiver.

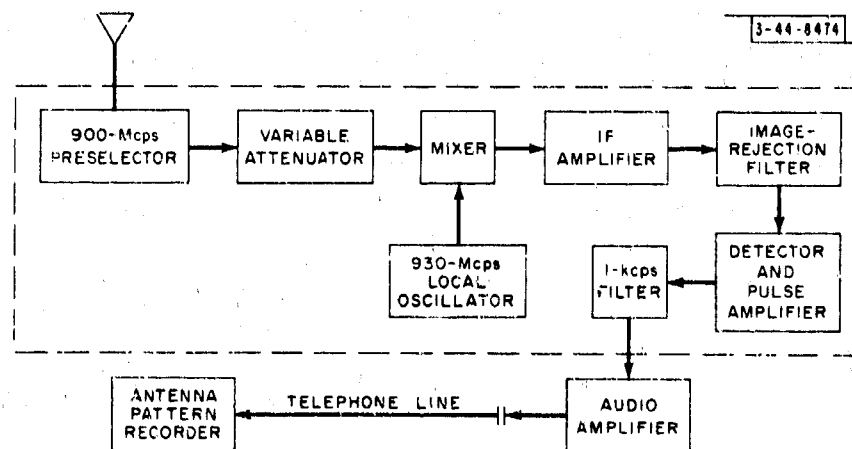
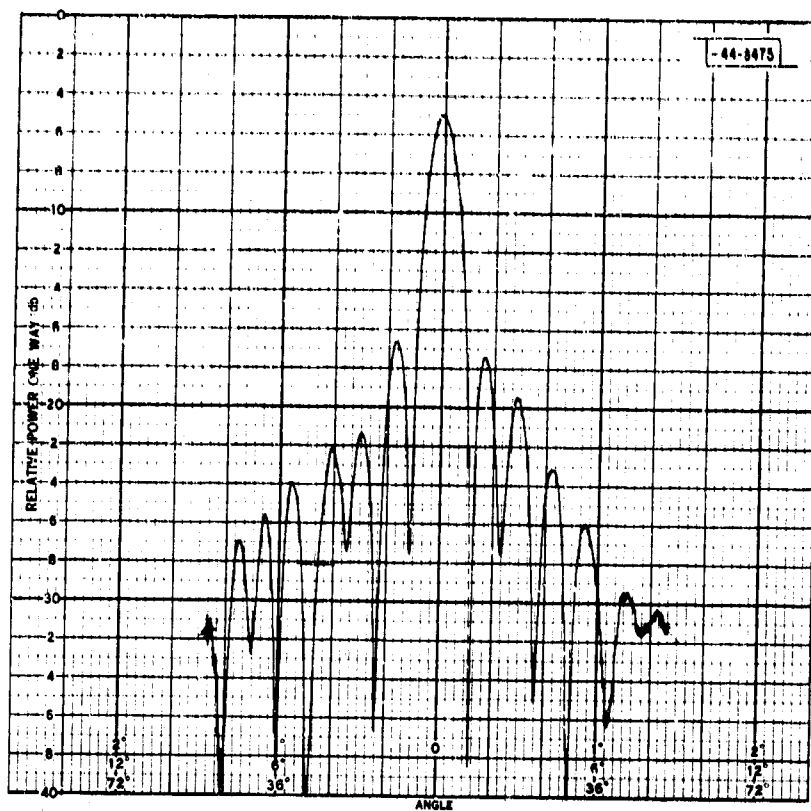


Fig. 1-18. Pattern test receiver block diagram. A 1-kcps output voltage, proportional to signal power intercepted by receiver's dipole, is sent back to Building C where antenna pattern recorder is located.

(a) Boresight beam.



(b) Beam 4 left.

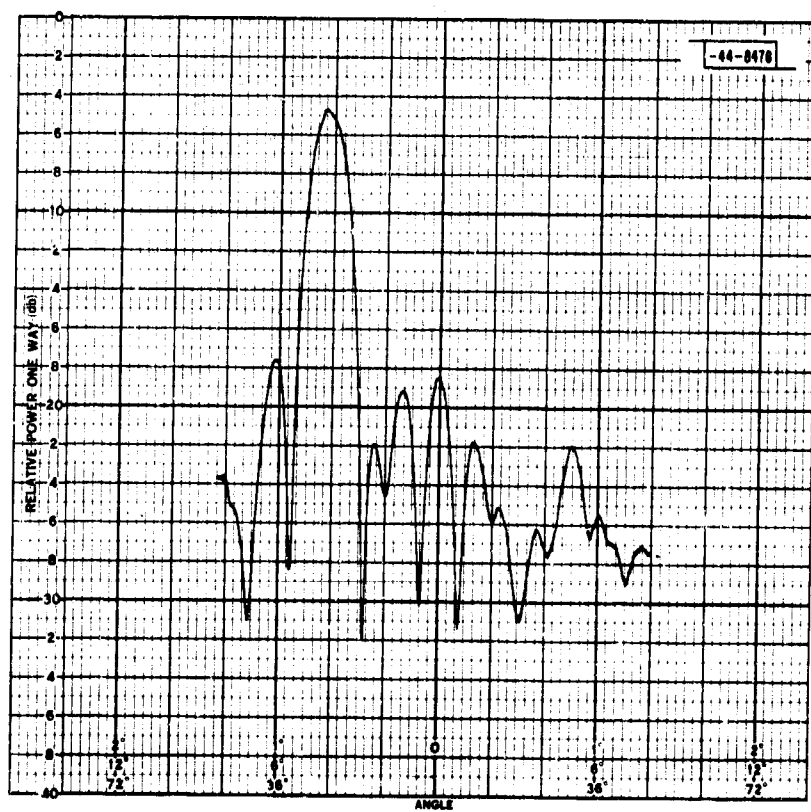
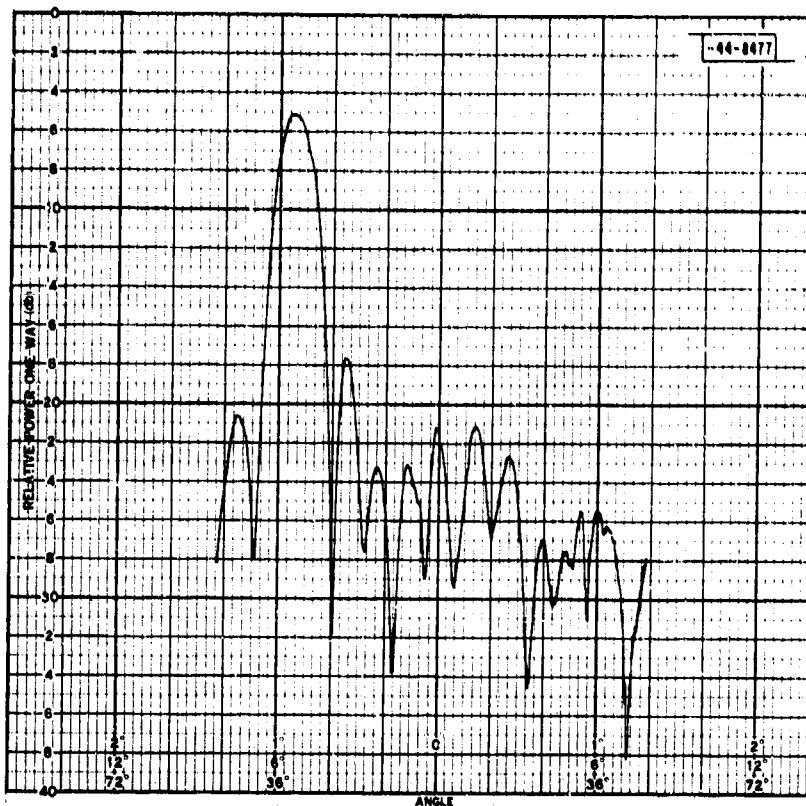
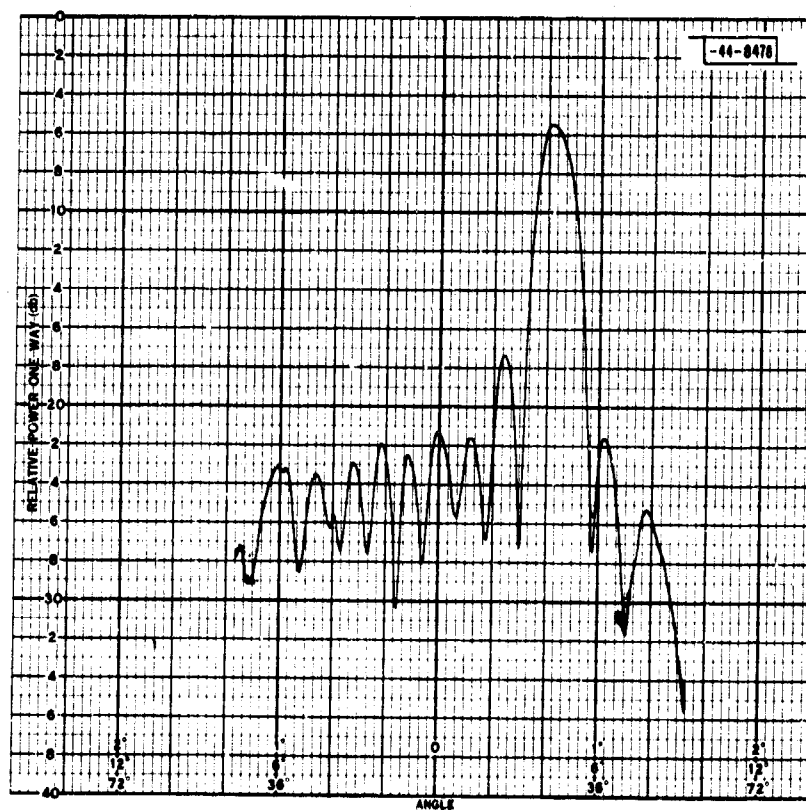


Fig. 1-19(a-f). Measured pattern (complete transmitter).



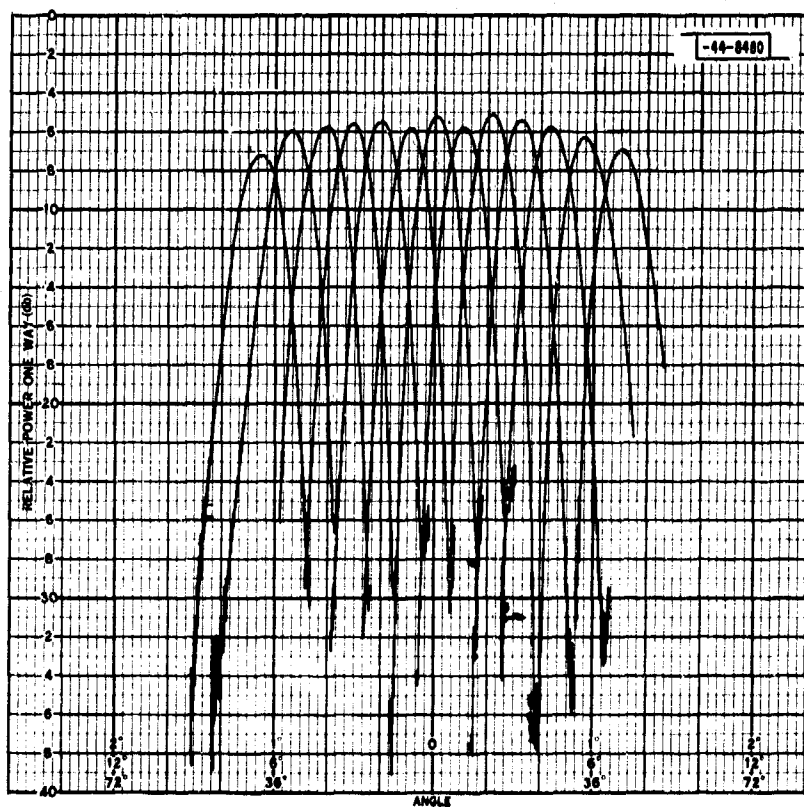
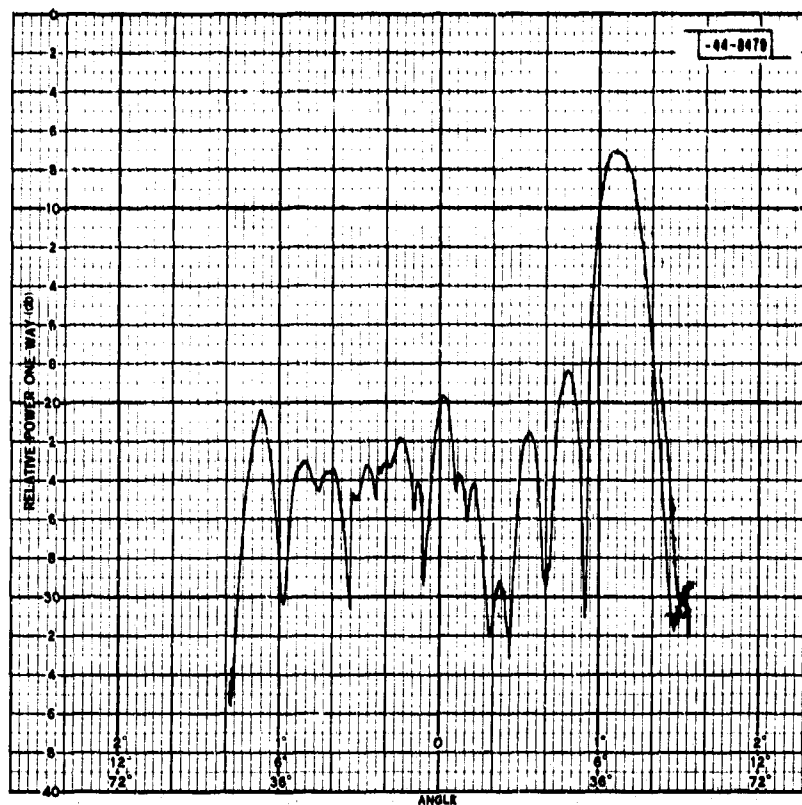
(c) Beam 5 left.



(d) Beam 4 right.

Fig. I-19. Continued.

(e) Beam 6 right.



(f) Main lobes for 13 beams – 6 left, 6 right, and boresight beam.

Fig. 1-19. Continued.

$\theta$  = angle of beam

B = number of beam being investigated (assuming we move one full beam every time)

n = number of dipoles used (in this case 16)

0.58 = distance in wavelengths between any two adjacent dipoles.

It can be seen from Fig. I-19(f), where the main lobe of each obtainable beam is presented, that each beam is in its correct position except beam 6 right which makes an angle of about 42 degrees - it should be 40.2 degrees. The cause for this error has not been investigated yet.

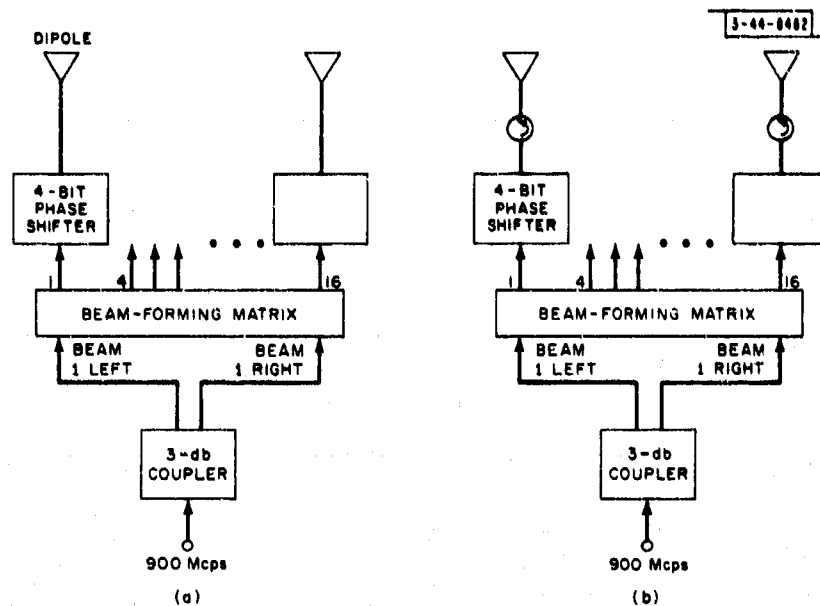


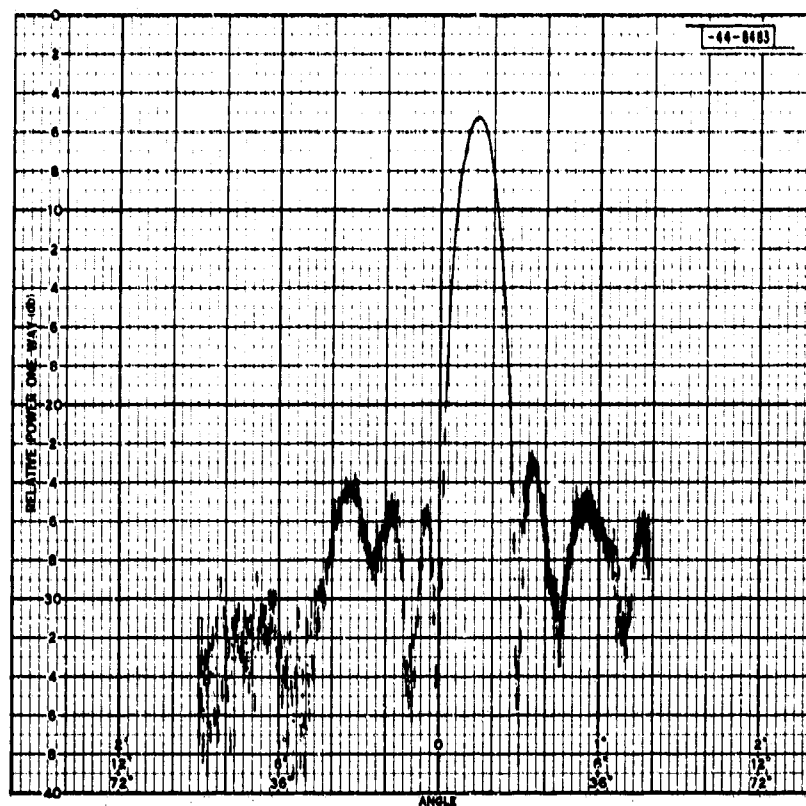
Fig. I-20(a-b). Transmitter setup. Cosine tapered voltage fed to 4-bit phase shifter to demonstrate system errors.

To obtain a better estimate of the degree of pattern control limitations inherent in the phasing technique alone, antenna patterns were also taken with the amplifiers by-passed using a cosine taper in the aperture, obtained by adding the beams 1 left and 1 right, from a Butler beam-forming matrix. The transmitter setup is depicted in Fig. I-20(a) and the patterns of the resulting beams are shown in Fig. I-21(a-e). The worst condition is that of Fig. I-21(e) where the sidelobes approached -16 db (theoretical value of first sidelobe for a 16-element array with cosine taper = -23 db). To assess the extent to which reflections from the antennas back through the phase shifters are significant, circulators were introduced between the phase shifters and the dipoles as shown in Fig. I-20(b). The sidelobes were reduced by the circulators by an average of 2 db. The reduction was more-or-less uniform in space since the well-defined "reflection lobes" that could be produced by identical multiple reflectors through the phasers\* were not found. The sidelobes are higher when the circulators are not used. This can be seen by comparing the patterns of Fig. I-21(a-e) with those of Fig. I-22(a-e). The latter have sidelobes which are 20 db down from the main lobe.

\* See, for example, J.L. Allen, "The Theory of Array Antennas (with Emphasis on Radar Applications)," Technical Report 323, Lincoln Laboratory, M.I.T. (25 July 1963), p. 76, DDC 422945, H-563.



(a) Beam 1 right.



(b) Beam 5 right.

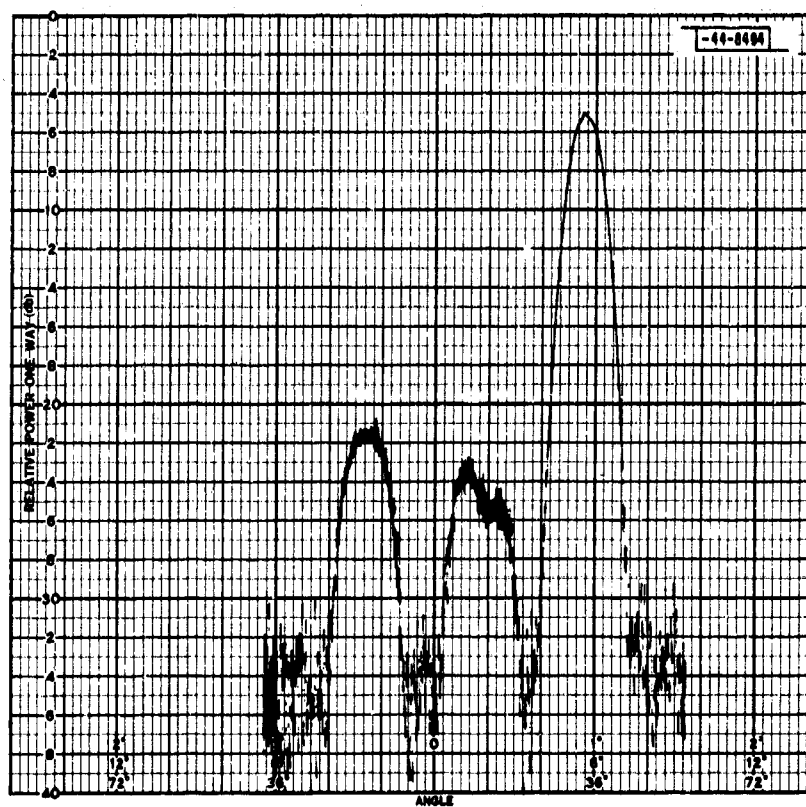
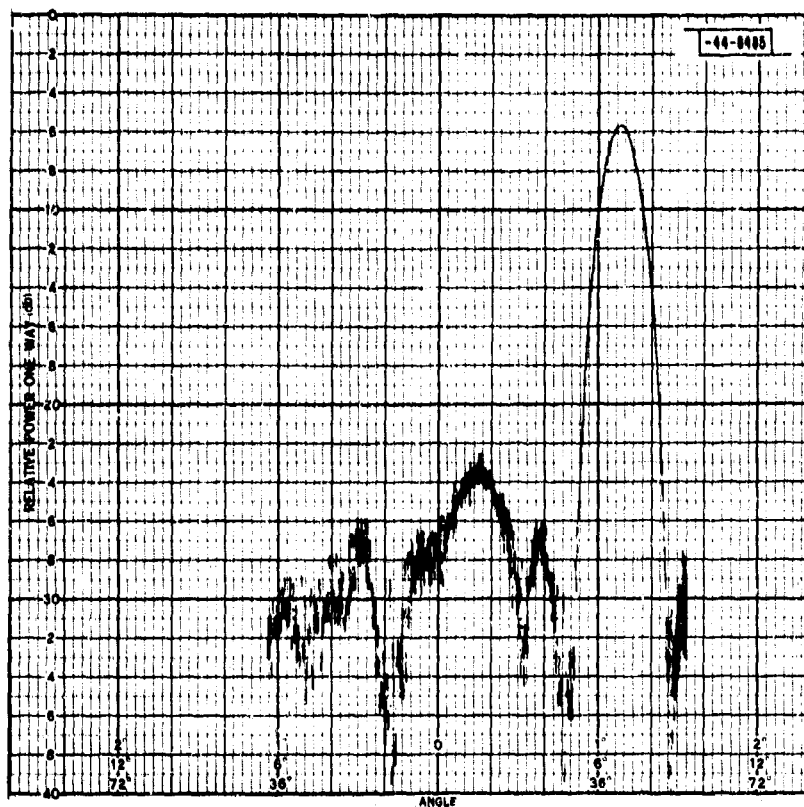


Fig. I-21(a-e). Measured pattern (cosine illumination without circulators).



(c) Beam 7 right.

(d) Beam 4 left.

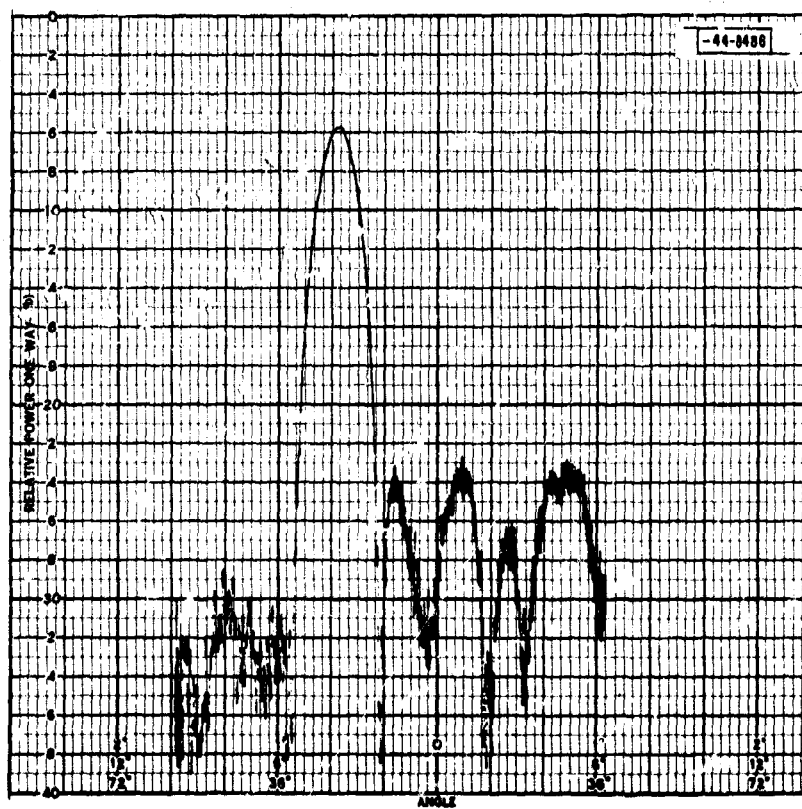
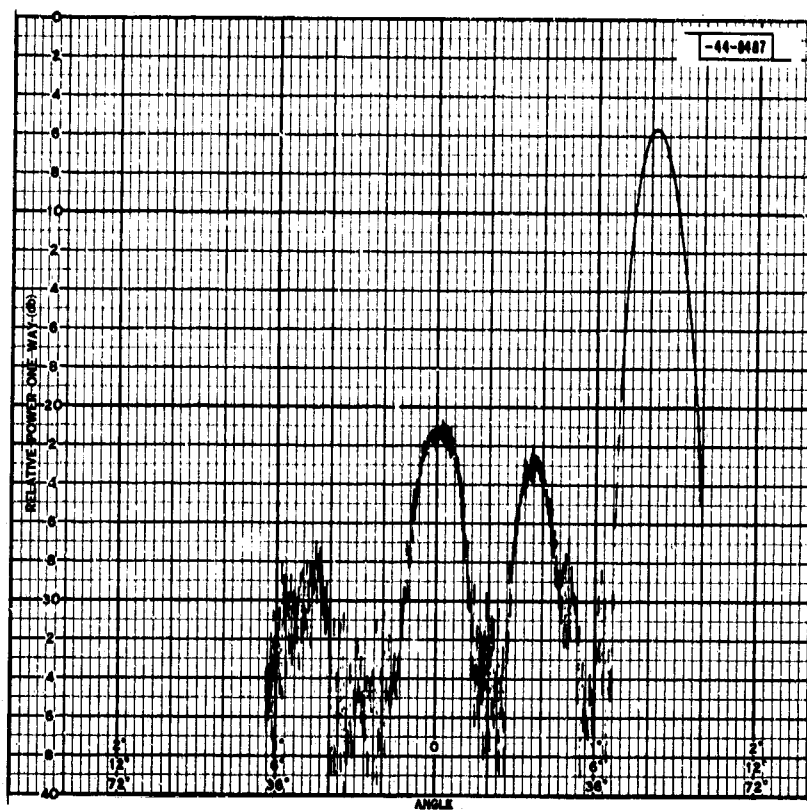
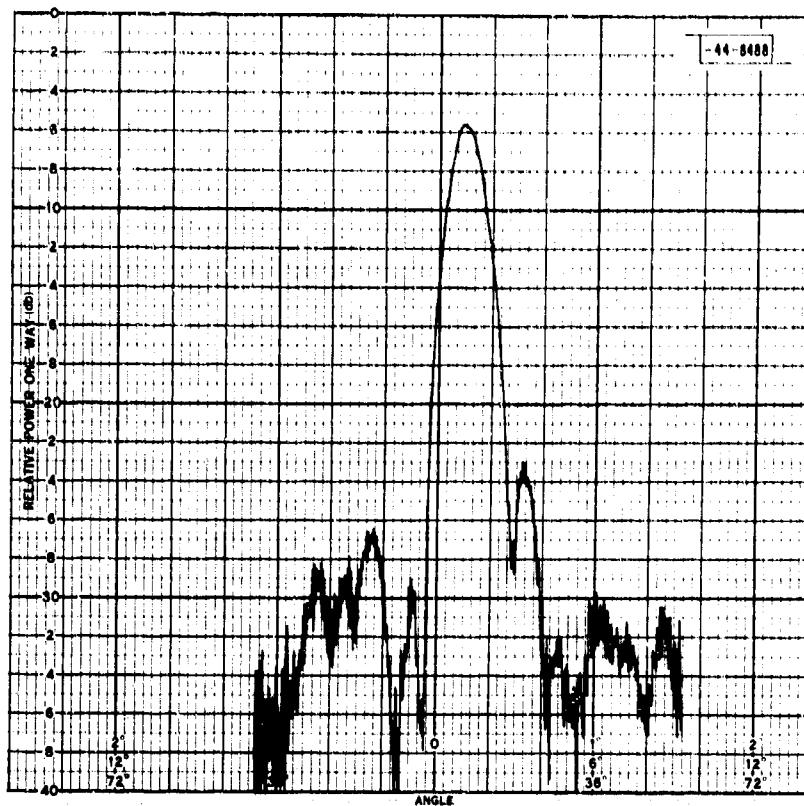


Fig. I-21. Continued.

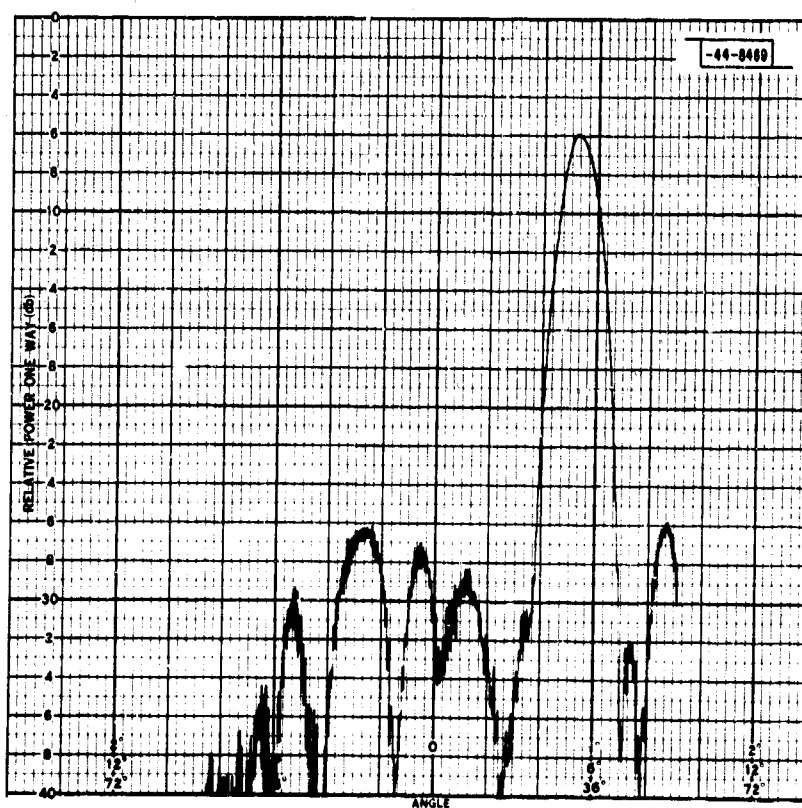


(e) Beam 8 right.

Fig. I-21. Continued.



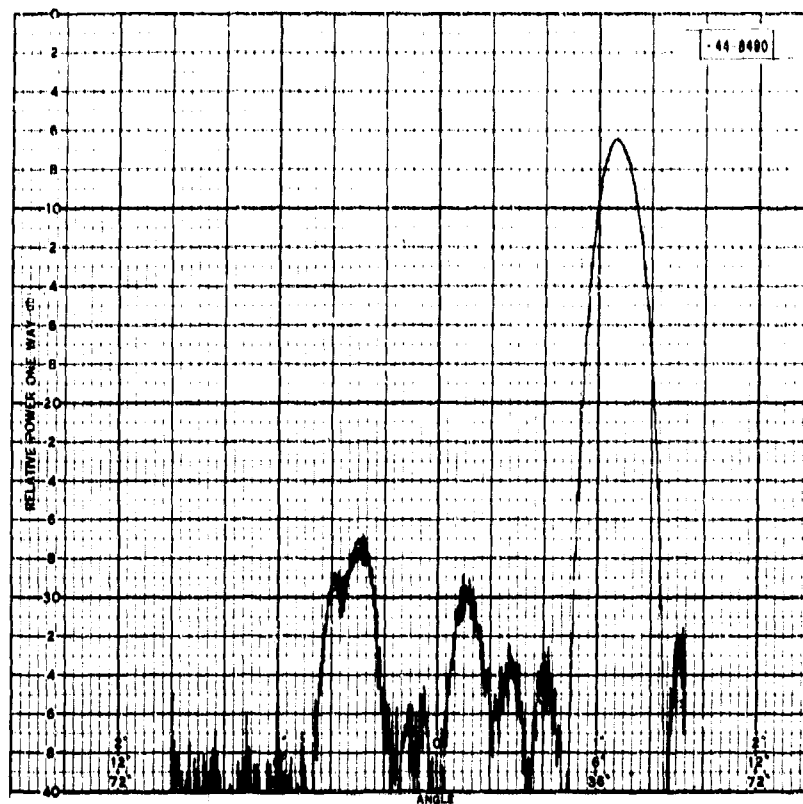
(a) Beam 1 right.



(b) Beam 5 right.

Fig. I-22(a-e). Measured pattern (cosine illumination with circulators).

(c) Beam 7 right.



(d) Beam 4 left.

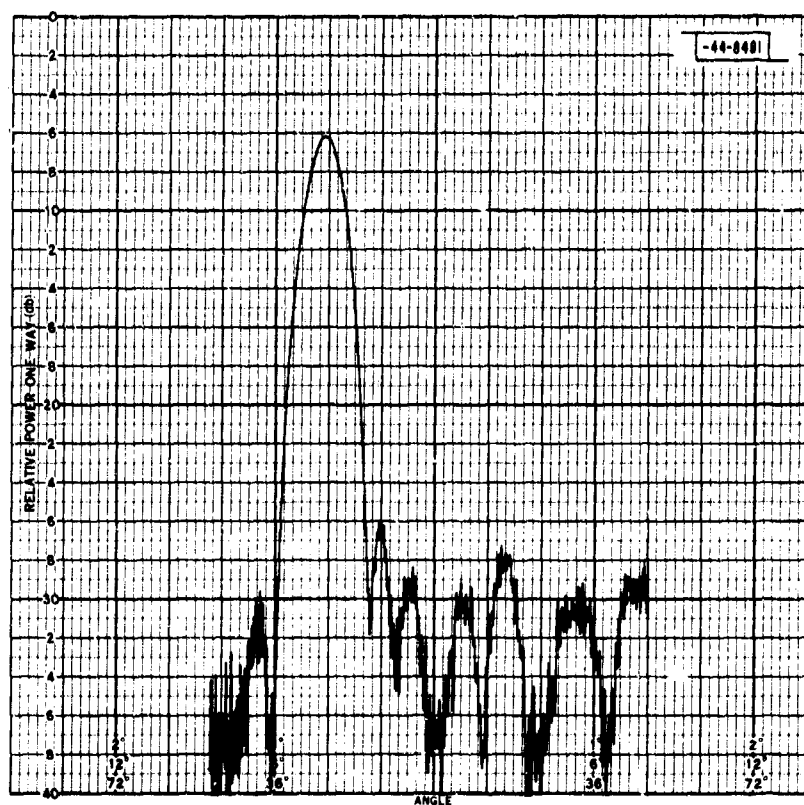
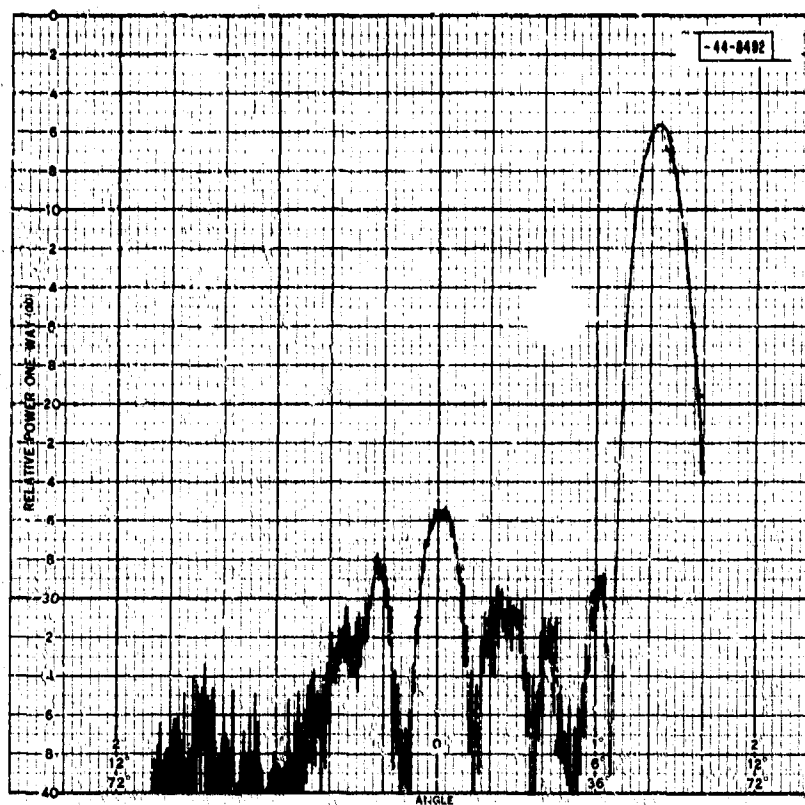


Fig. I-22. Continued.



(e) Beam 8 right.

Fig. I-22. Continued.

It is clear that the operation of a phased array depends upon the existence of at least one RF feed network which can be relied upon to produce an RF output of adequately well-known phase for each active element. This feed network can be used to distribute a reference signal with which the array output signals are compared or, if the electronic components are stable enough, the precision feed can be used as the RF power distribution network. In either case, phase errors caused by discrepancies in the feed network should be held to a very few degrees. The design and construction of this feed network is a significant part of the over-all array problem.

The 900-Mcps transmitting array was originally designed with two corporate feed networks. The power division was accomplished in 16-way printed corporate feeds made up of hybrid ring power dividers. The distribution from these printed circuit feeds to the modules was accomplished with lengths of braided coaxial cable (RG-9 for the high-power feed and RG-223 for the lower powered monitor reference feed). These cables were cut to length very carefully. Cable lengths were adjusted to correct for phase errors in the printed circuit feeds at the operating frequency.\* These cables, in particular the smaller cables, proved to be too unstable and were replaced with  $\frac{1}{4}$ -inch foam dielectric semi-rigid coaxial cables.

Although some "stable" braided cables have been developed for certain applications, it was decided that semi-rigid cables would be used for future RF cabling in array applications at Lincoln Laboratory for the following reasons:

- (1) Mechanical stability: Semi-rigid cables are stronger and less likely to be stretched or otherwise deformed by handling.
- (2) Better shielding: This is particularly important when cables carrying low-level monitoring signals must be routed next to high-level signal sources.
- (3) Less loss: For a given diameter, semi-rigid cables have significantly less attenuation than solid dielectric braided cables.
- (4) Uniformity: Properly handled semi-rigid cables have fewer reflection-causing discontinuities, and, therefore, significantly lower VSWR's than braided cables. (This factor becomes more and more significant as the operating frequency increases.)
- (5) Convenience: With the help of a few simple tools, semi-rigid cables can be cut to exact lengths and fabricated as easily as flexible braided cables.

The commercially available connectors designed for use on semi-rigid cables are generally designed for field installation. As might be suspected, they are not ideal for use in an array radar for at least two reasons. First, in order to hold the connector body to the cable sheath firmly enough, it seems to be necessary to make the clamp quite large, and the connectors are therefore larger than convenient. Second, the impedance match of most commercial connectors is not so good as desired. In view of these deficiencies and for other reasons, a program to design connectors for semi-rigid cables which are ideally suited for use in arrays is underway (see Part II, Ch. 8, Sec. E-3-c).

## I. 900-Mcps ARRAY COOLING SYSTEM

L. Cartledge

The power densities involved in the 900-Mcps transmitter modules, although not so high as might be desired for some applications, are high enough to make liquid cooling advisable. Consequently, the modules are designed so that almost all the heat generated is removed by cooling

\* See TR-299, p. 113.

water. Direct water cooling is employed at the anodes of the RF tubes, whereas various forms of indirect water cooling are used to cool the remaining heat generators within the module. Simple inexpensive devices are used to regulate the water flow through each module and to provide for quick disconnects and interlocks. Use of coolant flow higher than the minimum necessary provides very good stability.

A single heat exchanger, with pump and purifying loop, serves both the array and the various high-power test facilities operated by the phased array group. This setup circulates filtered deionized water at a temperature of  $90^{\circ} \pm 3^{\circ}\text{F}$  and at a differential pressure of  $15 \pm 1$  psi (maximum system pressure, 20 psig). Cooling-water supply and return manifolds are provided with quick disconnect fittings, and the differential pressure is regulated so that various cooling loads can be connected in parallel or disconnected without interrupting the operation of the other loads. The 16-element transmitting array contains smaller cooling-water supply and return manifolds which are connected to the central manifolds through lengths of garden hose.

Figure I-23 is a schematic of the 900-Mcps array water cooling system. As this figure shows, the components within a module are arranged in "series," whereas the modules are arranged in "parallel" between the manifolds. The various parts are discussed in more detail in the following paragraphs.

The flow regulator is a neoprene washer containing an orifice which adjusts itself automatically and is capable of regulating the flow to within a few percent of a nominal value over a wide range of differential pressures. This item is typical of a line of inexpensive stock items which are widely used in industrial plumbing installations. Use of such an automatic regulator in each module greatly simplifies the design of the cooling-water distribution system since no special balancing provisions are needed. Individual modules can be removed without changing the rate of coolant flow through adjacent modules.

The module chassis or "keel" is a  $\frac{1}{2}$ -inch-thick piece of aluminum which forms a "cold plate" for most of the miscellaneous heat sources in the module. It has a coolant tube running almost its entire length which provides 42 square inches of interface between the aluminum and the cooling water. After buildup of an oxide film between the aluminum and the water, the metal-to-water heat exchange would occur at an estimated thermal conductance of 30 watts/ $^{\circ}\text{F}$ . This keel provides a heat sink for the amplifier cavities, the circulator, several relays and resistors, and in part, for the modulator sub-chassis.

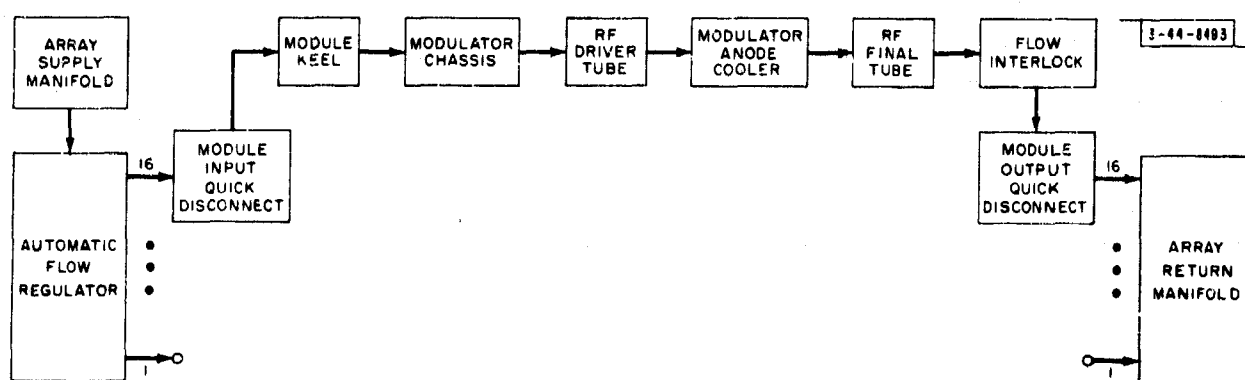


Fig. I-23. Schematic of water flow.



The modulator sub-chassis is thermally connected to the main keel by two pieces of aluminum which provide an estimated heat conductance of about 10 watts/°F. In addition, it is brazed to a water-carrying tube which provides an estimated 6 watts/°F. This sub-chassis provides the heat sink for the heat conducting tube shield around the two 3E29 tubes in the modulator and for the pulse transformer and some miscellaneous resistors.

Both RF tubes are directly water cooled. A water jacket, which is discussed in detail in TR-236, is supplied around the external anode of each tube.

The 3E29 tubes, two of which are used in each module, are designed for radiation cooling. Heat radiated upward from these tubes was producing a hot spot on the module cover and overheating the small parasitic suppression resistors which are in series with each anode. The expense of redesigning the modulator around one of the water-cooled tubes which have recently become available did not seem to be justified. Hence, a cold plate was designed to absorb the radiated heat and provide some conduction cooling through boron-nitride washers. This assembly is shown in Fig. I-24. The thermal conductance between the plate and the cooling water is estimated at about  $4\frac{1}{2}$  watts/°F. Neither the thermal conductance between the anode connections and the cold plate nor the radiant heat transfer between the tube anodes and the cold plate was estimated. However, addition of the cold plate lowered the anode seal and bulb temperatures of the tubes by some 150°F, eliminated the hot spot on the module case and, incidentally, eliminated a VHF parasitic oscillation which had been undetected in some of the modulators.

The water interlock switch described in TR-236 has been replaced with a commercial item which uses a moving magnetic element in the water stream combined with a sealed magnetic reed switch.

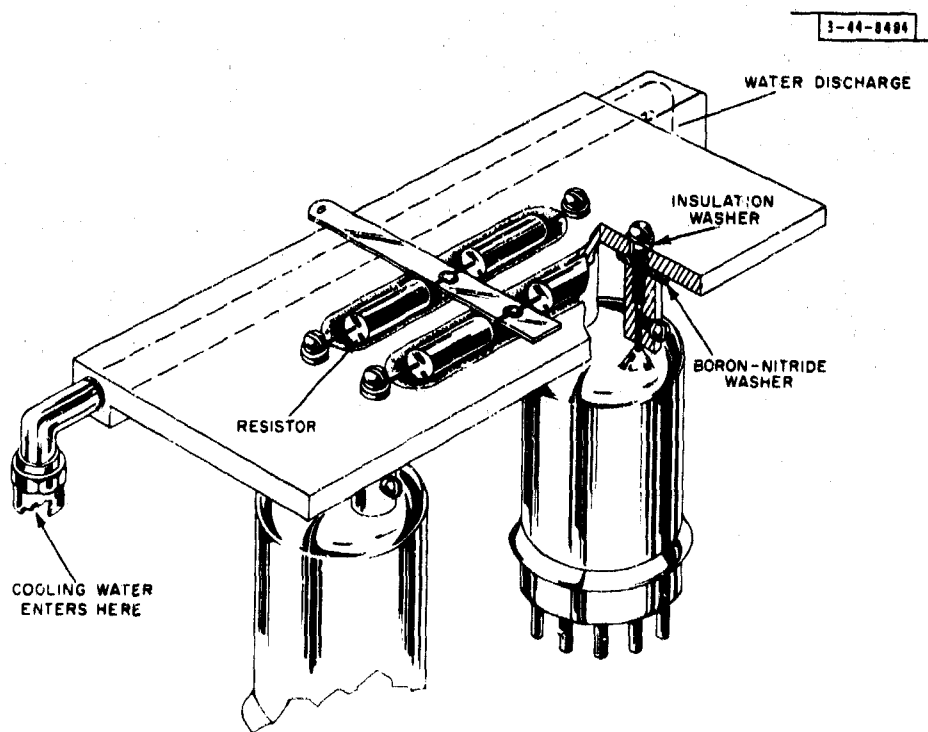


Fig. I-24. Anode heat sink.

The quick disconnect fittings are of the standard brass two-way shut-off type. In some three years of operation of various cooling-water systems, no trouble has been caused by these quick disconnects.

Similarly, interconnections between the various metal parts in the cooling-water stream are made with flexible plastic tubing ( $\frac{1}{4}$  inch TYGON) and commercial compression fittings (Imperial-Eastman Poly-Flo series). Again, in more than two years of operation, we have had no trouble from any of the several hundred of these tubing fittings which are operating at gauge pressures up to 20 psi. (We have had leaks caused by older ridged hose stems, however.)

The cooling system performance has been satisfactory and largely trouble free. The water circulation system has now been running 24 hours a day and seven days a week for more than two years. It is left unattended except during normal working hours. RF tubes which leaked water because the water jackets were not soldered onto the tubes properly were an important cause of trouble. These tubes were replaced by the manufacturer. In addition, RF tubes which had water jackets cemented on them at Lincoln Laboratory have leaked in some cases.

A test was made in order to check the effectiveness of the module cooling in a simulated planar array environment. A module was set up on the test bench with the top and both sides insulated with two inches of light plastic foam. The module was allowed to stabilize at the water temperature (90°F). Then, differential water temperature, RF output power, and electrical length were monitored as the module was turned on and operated. The changes in electrical length are shown graphically in Fig. I-25. RF power did not vary significantly.

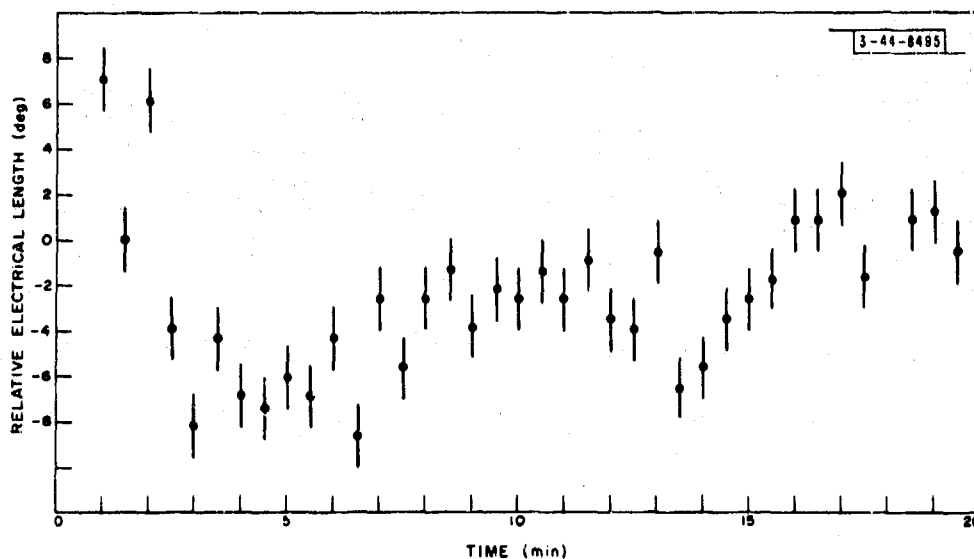


Fig. I-25. Electrical length of module vs time from cold start.

These results indicate that this type of cooling allows very short warm-up times. Note that the electrical length of the module never deviates from its final value by more than 9 degrees. Full output power is produced immediately when the plate voltage is applied. The module is "on the air" one minute after the heater voltage is turned on (this time is dictated by the tube manufacturer's heater operation recommendations). In essence, the time required for the element to stabilize after it is turned on is very short. If the element-to-element variation limits the differential phase excursions, one could visualize an array which was in a standby

condition with the filaments turned off and could be operational literally on a minute's notice. Use of quick heating tubes might reduce this time to a few seconds.

Prior to the start of the test outlined above, the module case was marked with temperature sensitive paints. After the test the plastic foam insulation was removed and the paint was examined in an attempt to locate any hot spots on the case. The case temperature was above 100°F over a few small areas but was less than 150°F everywhere.

The test was run at a water flow rate of 600 cc/min. At this flow rate and at 15-psi pressure drop, the work done in pumping water through a module is 2740 ft-lb/hr (1.03 watts). The modules in the array receive  $\frac{1}{4}$  gpm since the smallest stock flow regulator available is the  $\frac{1}{4}$ -gpm size (the cost of designing a special item did not seem to be justified in view of the small number of modules involved). It should be noted that most of the 15-psi drop is due to the flow regulator and fittings outside the module. The pressure drop through a module alone without the regulator is less than 4 psi at a 600-cc/min flow.

## J. CONCLUSIONS

J. DiBartolo

The test array has been a useful tool in testing the reliability and behavior of 900-Mcps components. These components, which have been designed for phased array use, have been integrated into a system that has been operational for more than six months.

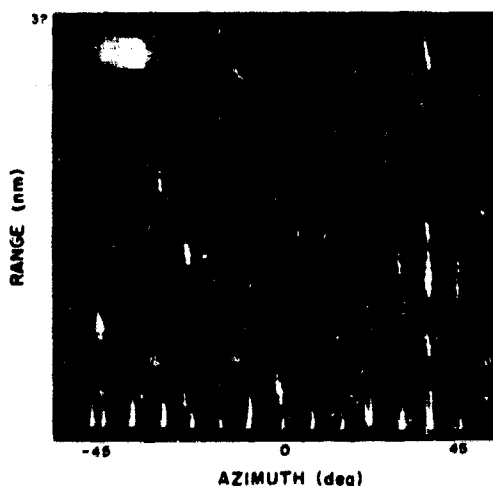
In general, the operation of the array has been limited to regular working hours although, at various times, it has been left running unattended overnight. Virtually no breakdown of components has been experienced throughout this period.

It recently became evident that the RF output power of some modules had diminished enough to warrant taking them out of the array. This situation was remedied by changing the RF tubes. These tubes, however, have had at least 8000 filament hours.

The working average power has been limited to 60 watts/module. This results in an average power density of 150 watts/ft<sup>2</sup> (at the face of a hypothetical planar array). It was obtained with unusual simplicity for an active element array. Only four tubes are used in each module, two in the modulator and two tetrodes as the RF power amplifiers. It has been demonstrated that these modules can be safely plugged in and taken out of a working array when the recommended cable connecting sequence is followed. This makes it possible to service any defective module while maintaining the system operational.

The entire system is being operated as a radar, and targets have been tracked as far out as 50 miles. Figure I-26 is a photograph of the B-scope and indicates the simultaneous display

Fig. I-26. B-scope display of eight targets.



of eight different targets which are shown as white dots. The abscissa represents the over-all scan angle of the array, equal to  $\pm 42$  degrees, and the ordinate represents the range. The target shown in the upper right-hand corner is 32 miles away and about 30 degrees from boresight.

It is safe to conclude that the RF components developed during the phased array study are being used successfully in their present configuration. It has been demonstrated, with the help of the monitor system and by taking periodic antenna patterns, that both the short-term and the long-term stability of the system are good. Furthermore, it is believed that components designed with the same ruggedness, using gridded tubes and water cooling, would be adequate for a large modest bandwidth phased array system operated at L-band or lower frequencies.

## CHAPTER 2

### MISCELLANEOUS SUPPORT FACILITIES

#### SUMMARY

This chapter describes two units which, although not part of the array, were required as part of the array program. The chapter also presents a brief summary of our experience with the 900-Mcps receiving array components. The first component is a solid-state video driver which is capable of driving thirty-two 3E29 tubes in parallel; the second is a high-voltage supply and modulator which was set up to test an experimental phased array tube.

#### A. SOLID-STATE VIDEO DRIVER

M. Siegel

During the course of debugging the array system, it was determined that the droop in the video drive pulse was sufficient so that satisfactory nulls could not be obtained on the monitoring system. It was decided that the vacuum-tube driver which was used to generate the video drive for the array modulators be replaced with a solid-state driver. Since solid-state devices by their very nature are current devices with low internal impedance, in general, they are able to work into a much lower impedance than vacuum tubes. Therefore, a solid-state driver would be able to supply a better pulse into the positive grids of the modulators in the array than the existing vacuum-tube driver. As a result, the output RF pulse would have a flatter top, and better amplitude comparison measurements between different array modules could then be made.

The equivalent grid circuit during the pulse for each modulator in the array is shown in Fig. I-27. Also shown is the equivalent load impedance presented by 16 modulators in parallel.

The solid-state driver that was designed and built consists basically of a line-type modulator which uses a pair of silicon-controlled rectifiers (SCR's) as a discharge switch and a second pair of SCR's as a recharge (resonant) switch. The recharge switch is necessary in order to allow the modulator to deliver the required power at a high pulse repetition frequency (prf).

A transistor timing and driver unit controls the timing triggers to the charge and discharge SCR pairs, allows each pair of switches sufficient time to recover and the delay line sufficient time to recharge, and provides the proper drive pulses to the gates of the SCR's.

Protection is provided by overload relays and a transistor-diode gating circuit. The latter, shown in Fig. I-28, was added when it was found that spurious triggers were generated in the trigger source (the computer) whenever any of the following was done: (1) the mode of operation of the array was changed, (2) the prf was reduced, or (3) various test and monitor functions were performed. These spurious triggers caused the SCR's to malfunction and overload. The protective gating circuitry disables the solid-state driver's trigger circuitry during the interpulse period and thus prevents these overloads.

Difficulty is normally encountered in using a line-type modulator to drive the grids of power tubes. Since the grids are normally biased off by a large negative voltage during the quiescent period, the modulator load is quite high — effectively an open circuit. When the grids are in the positive conducting region however, the impedance becomes extremely low (a few hundred ohms per tube, or tens of ohms for many paralleled tubes). Matching problems occur between a line-type modulator and a varying load. The especially difficult part is the adjustment of the delay-line impedance such that sufficient power will be efficiently transferred from the delay line to the grids of the tubes, at the same time ensuring that the modulator switch will be provided at the end of the pulse with a slightly negative voltage for a sufficient period of time to allow it to

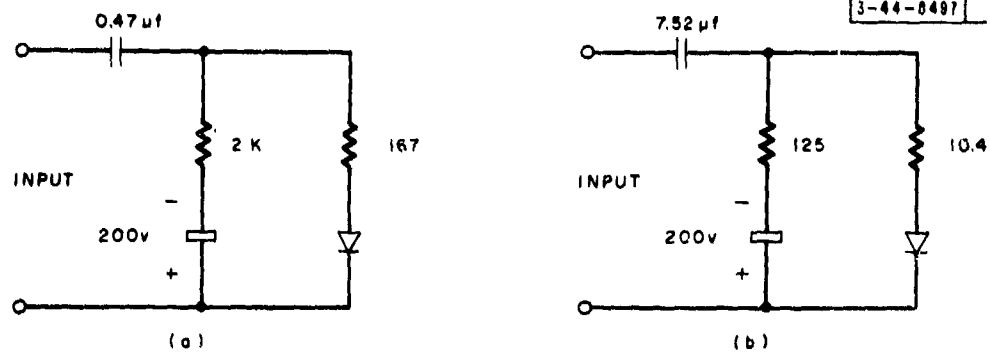


Fig. I-27. (a) Modulator grid circuit. (b) 16 parallel modulator grids.

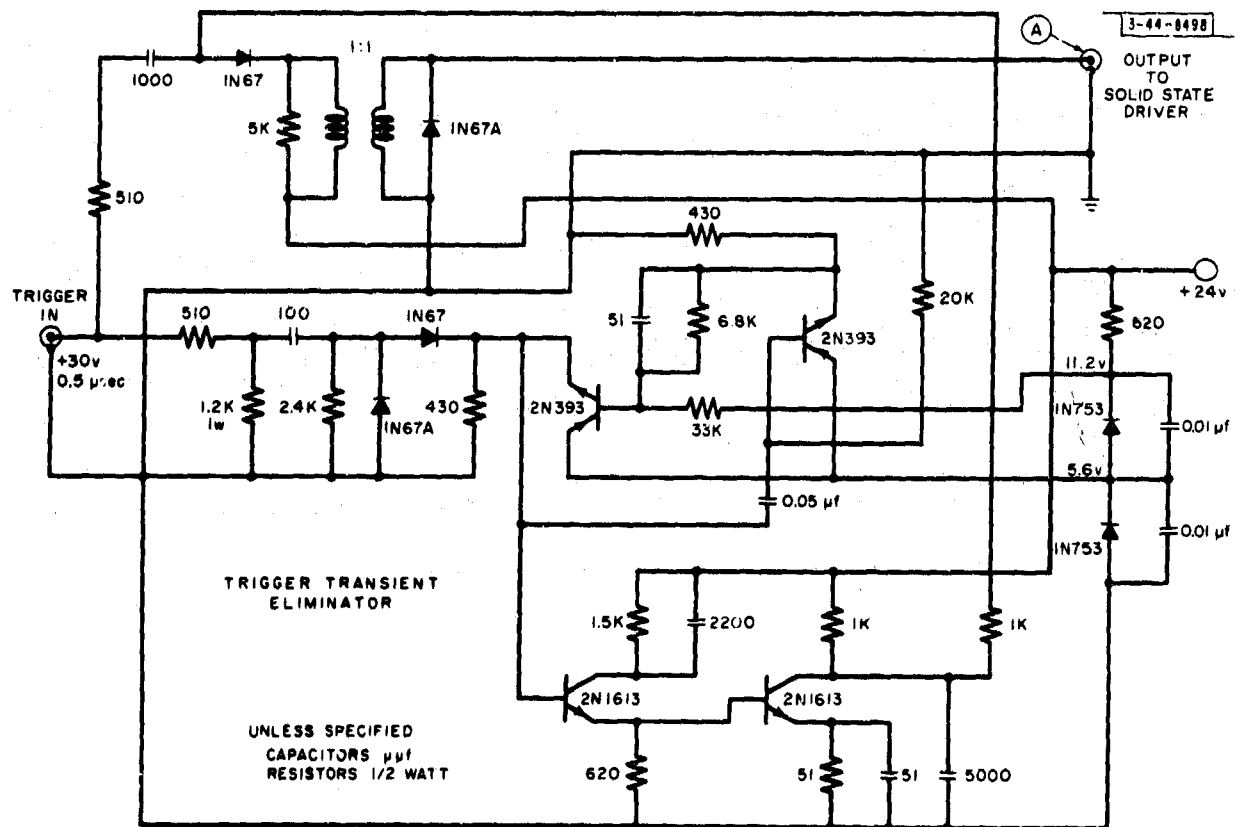
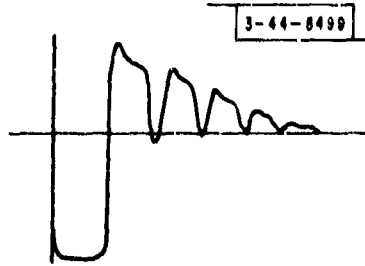


Fig. I-28. Trigger gating circuit.

Fig. I-29. Typical voltage pulse tails on a biased-diode load.



turn off and recover. This common problem occurs whenever a delay-line modulator works into a biased-diode load; typical pulse reflections occur as shown in Fig. I-29.\*

Normally, at low prf's, these repeating pulses do not cause problems since sufficient time exists for the switch or thyatron to recover before the charge period begins. With higher prf's however, considerable difficulty occurs, especially when a delay-line recharging switch is used. The potential danger of the discharge switch still conducting when the recharging switch fires (thus literally shorting the power supply to ground) forces the use of a "waster load." This load acts in parallel with the regular load to provide a better match for the pulse-forming network, thus reducing to a considerable extent the multiple reflections. Approximately 25 to 30 percent of the grid drive power is wasted in this load.

The solid-state driver (Fig. I-30) produces up to +300 volts (continuously variable) into a 10-ohm load at a pulse width of 18  $\mu$ sec, a prf of 1000 pps or less (continuously variable). Rise and fall times are approximately 1  $\mu$ sec each when working into the driver load and 100 feet of coaxial cable. Since no output pulse transformer is used, the video pulse width can be easily varied by changing delay lines.

Results with this solid-state driver indicate a large improvement in pulse top flatness over the previous vacuum-tube pulse-transformer driver.

#### **B. HIGH-VOLTAGE MODULATOR AND POWER SUPPLY FOR TESTING PHASED ARRAY HIGH-POWER TUBES**

M. Siegel

A high-voltage test stand was assembled in order to examine the performance of the 100-kw peak 1-kw average Watkins-Johnson traveling-wave tube that was being developed for phased array use.<sup>†</sup> This tube will need to be operated up to 30 kv with its cathode grounded, and will have a peak beam current of approximately 15 amp.

Available in the Laboratory as surplus was a 35-kv 6-amp peak hard-tube modulator with power supply which uses 5 Eimac 4PR250C tetrodes in parallel as switch tubes. This power supply and modulator, with some modification, could be made capable of supplying the required peak power but not the average power. For the purpose of testing many parameters of the phased array tube however, the prf could be lowered until the power supply and modulator were able to deliver the correct peak power at a reduced average power.

The major difficulty was that the power supply was a negative supply, and the modulator produced negative pulses. The tube to be tested required a positive supply and positive pulses. Since the high operating voltages and large pulse widths prohibited the use of a pulse transformer, it was decided to attempt to reverse the polarity of the power supply and output pulses.

\* G. N. Glasoe and J. V. Lebacqz, eds., Pulse Generators, Radiation Laboratory Series, M. I. T. (McGraw-Hill, New York, 1948), Vol. 5.

† J. W. Sedin and K. W. Slocum, paper presented at the IRE Electronic Devices Meeting, Washington, D. C. (25-27 October 1962). For specification, see TR-236, p. 105.





The power supply rectifier tubes and their filament transformers were remounted and re-wired so that it is now possible to change the supply from positive to negative output, or vice versa, by changing two leads which are accessible from hand openings in the oil tank enclosing the supply. Potential corona problems caused by air trapped in the oil were eliminated by repeated pressure cycling in an altitude chamber. The supply was tested under full voltage and performed well with reverse polarity conditions.

The reversing of the modulator switch tubes posed a problem. With a negative output pulse, the triggering circuitry, the switch-tube-grid biasing circuitry, the screen voltage circuitry, and the isolating transformer are all located on the power supply side of the switch tubes and therefore do not load (especially capacitively) the output pulse. When positive pulse outputs are used, all these components are on the output side of the switch tubes and therefore load the output pulse (they literally "ride up and down" with the output pulse). This problem was solved by carefully spacing all components, minimizing the stray capacitance, and using low-capacity power transformers and trigger transformers to couple to the floating circuitry.

The existing pulse driver for the switch tube grids had been designed to obtain 6 amp of switch tube current, whereas 15 amp of switch tube current was needed for the tests. A solid-state pulse driver using SCR's was designed and built which was capable of driving the parallel grids from a bias of -500 volts well into the positive grid region, sufficient to produce 15 to 20 amp of pulse current from the switch tubes.

Additional energy storage was provided for the modulator, and the modulator and controls were separated from the power supply. The power supply was placed in a caged storage area and is now remotely controlled from the test location. Additional x-ray shielding was provided; the crow bar circuitry was modified, tested, and proved completely satisfactory.

Tests of the completed unit were then conducted. At approximately 30 kv and 15 amp at a low prf, 20- $\mu$ sec positive pulses were produced. The pulse shape was reasonably flat (droop  $\leq 5$  percent) and rise and fall times were 1 to 2  $\mu$ sec when pulsing an RC synthesized load.

### C. 900-Mcps RECEIVING ARRAY EXPERIENCE

J. DiBartolo

The receiver of the experimental phased array radar consists of 16 identical channels. Each channel comprises an electron-beam parametric amplifier (designed by Zenith Radio Corporation), a crystal mixer, a wide-band IF amplifier, and a 2-Mcps phase shifter. Information about these components can be found in TR-228, TR-236, and TR-299.

A special Lincoln Laboratory report\* has been compiled to give detailed information about the electron-beam parametric amplifiers (EBPA's). The useful life of these EBPA's was anticipated in that report to be in excess of 2500 hours. At the time of the present writing, these amplifiers have actually accumulated over 8000 hours each, and just one of the original tubes has failed.

It should be pointed out that, although the same antenna is used for both the transmitter and its associated receiver, the EBPA's have not been exposed to heavy RF loading. A diode duplexer

---

\* J. H. Teele, "Operational Characteristics of 16 Electron-Beam Parametric Amplifiers in a 900 Mcps Phased Array," Group Report 41G-1, Lincoln Laboratory, M.I.T. (6 August 1962), DDC 288223, H-444.

used with each transmitter module has provided receiver protection greater than 60 db during the transmit time (the operational peak power of each transmitter module is 6 kw). Some intermittent instability was discovered in two EBPA's after 5000 hours of operation, but this instability was traced to a faulty balun.

The receiver as a whole has performed very well. No breakdown has been experienced in any of the 16 wide-band IF amplifiers; however, two bad transistors were found in a 2-Mcps phase-shifter unit. These units have been in operation for over 10,000 hours.

## PART II

### "SUBARRAYED" ARRAY RADAR

#### SUMMARY

D. H. Temme

This part of the report describes a "subarrayed" time-delayed array radar configuration that should permit significant cost reduction predicated on the availability of cheap "high-power" phasers (10-kw peak, 150-watt average). The high-power phasers are placed behind each of several radiating elements which are subarrayed and driven by a convenient size power source. The subarrays are phased by a single time delay per subarray to permit large signal bandwidth array operation. The addition of duplexers and receivers permits the inclusion of a receive mode in the subarray. After an introductory description of the subarray, a specific experimental S-band subarray is presented. Because of limited manpower and funds, only some of the significant components necessary to demonstrate the feasibility of the subarray concept are being developed. However, the requirements for all the subarray components are outlined and, in a number of cases, the general development status of such components is discussed. Detailed data on a number of components are given.

#### CHAPTER 1

##### SUBARRAY CONFIGURATION AND SPECIFICATIONS

L. Cartledge

Phased array radars built in the past have used steering systems which were characterized by rather low-power-handling capability and rather high losses. These characteristics have imposed the requirement that a power amplifier, and usually a receiving amplifier, be associated with each radiating element. The recent development of high-power, low-loss phasers\* allows the designer of a phased array freedom to select the number of transmitting and receiving amplifiers. The number of amplifiers can be selected by considering efficiency, reliability and cost alone.

A constraint on the number of active devices reappears when large arrays must be designed for wide bandwidths. It is well known that large arrays must employ "true time-delay steering" in order to handle large bandwidth signals.<sup>†</sup> Power-handling capabilities of existing and projected true time-delay steering devices fall short of the levels desired for driving the radiating elements. Losses in these devices are high; hence, both transmitting and receiving amplifiers must be inserted between the time-delay steering devices and the radiators. Further, true time-delay steering devices for large arrays tend to be large, costly and complex. For these and other reasons, it is desirable to reduce the number of time-delay steering elements which must be used.

The scheme of dividing the array into multi-element subarrays suggests itself. Each radiator in the subarray is steered by a high-power, low-loss phaser; hence, the subarray can be considered to be a large steerable "element" (see Figs. II-1 and II-2). The subarray, then, is driven by a time-delay steering element and appropriate electronics. The antenna can be

\* H. A. Hair, "Development of Helical Phase-Shifters," Final Report under Subcontract No. 250, Electronics Laboratory, General Electric Company, Syracuse, N. Y. (December 1964).

† See J. R. Sklar in TR-236, pp. 243-253.

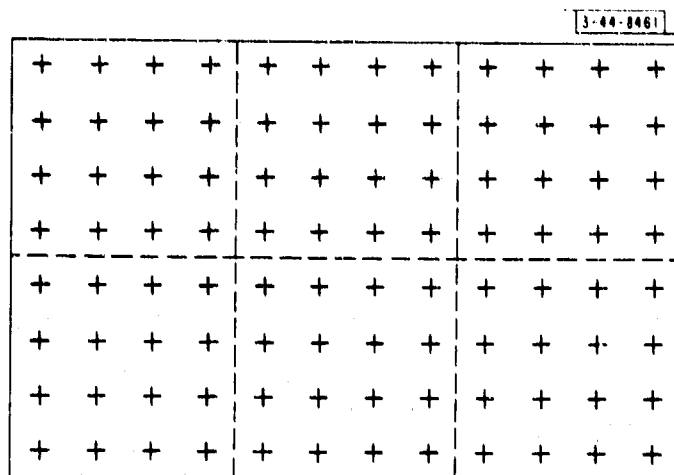


Fig. II-1. Plan of a 96-element ( $8 \times 12$ ) array made up of 6 subarrays each having 16 elements (radiating elements indicated by crosses; sub-array boundaries outlined by dashed lines).

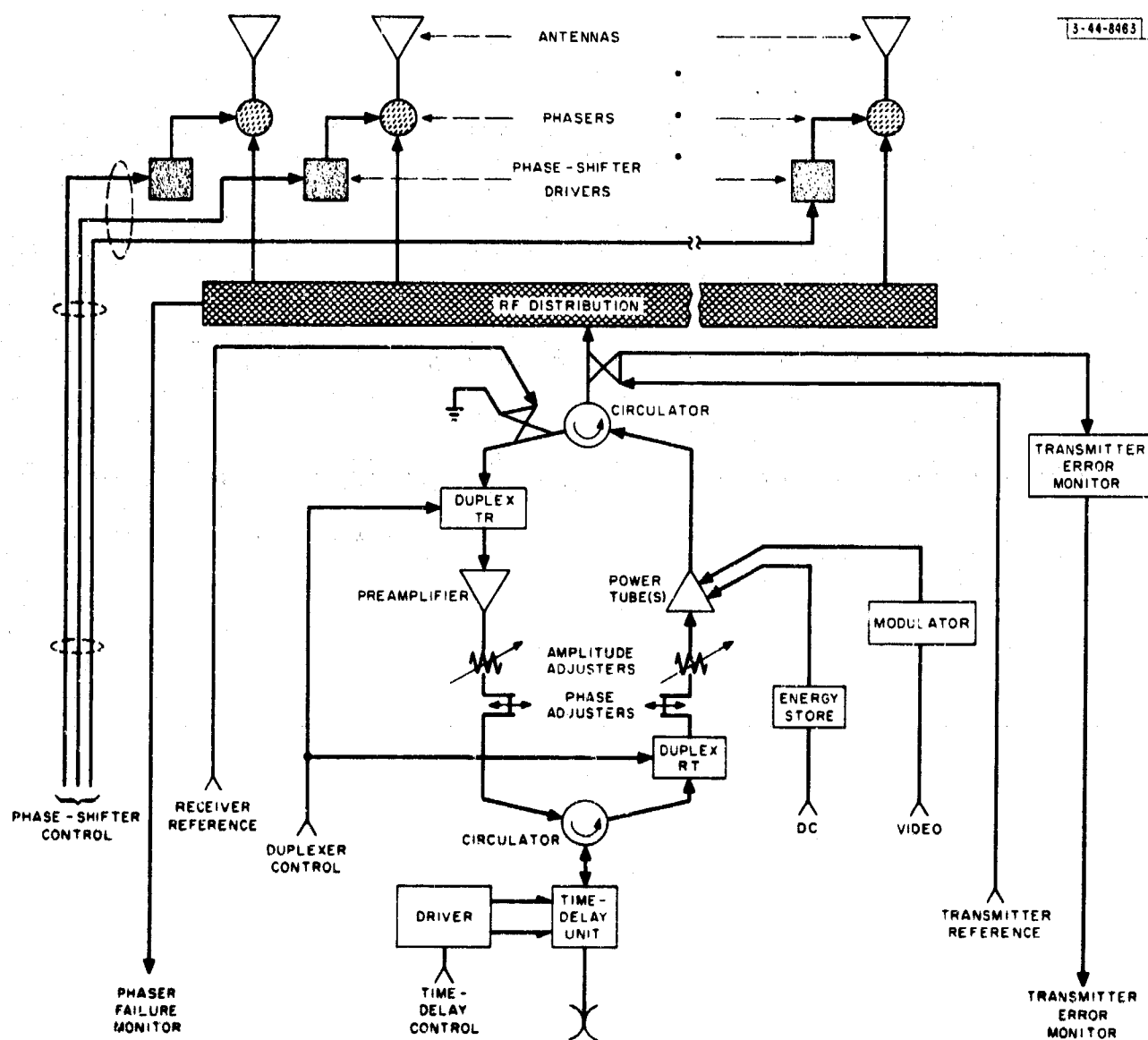


Fig. II-2. Block diagram of subarray.

designed so that the nulls of the subarray pattern suppress the grating lobes of the array pattern to a useful degree.

Constraints on the subarray size (number of radiating elements in the subarray) are related to the bandwidth, to how the array is to be used, and to the required grating lobe suppression. The maximum allowable size of the subarray ranges from about 10 to about 100 elements.

Each subarray can be considered as being an element in applying familiar relationships between the number of elements and such things as rms phase and amplitude errors, sidelobe probabilities, and directivity.\*

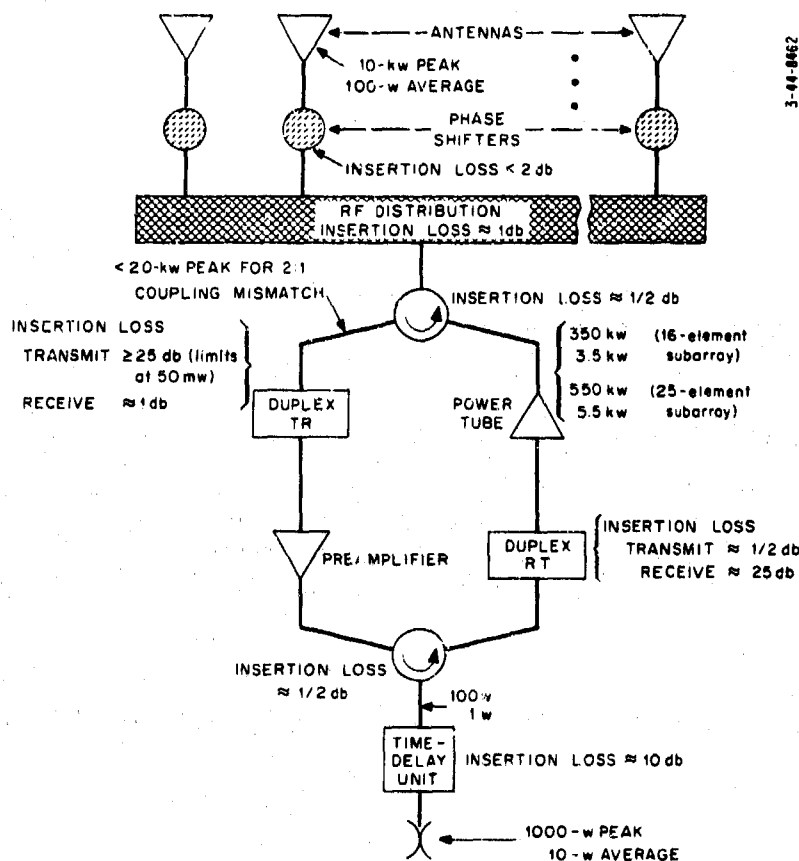


Fig. II-3. Simplified block diagram of subarray showing assumed insertion losses.

As a continuation of our study of array radar components and techniques, we have undertaken the development of the necessary components, and the fabrication and testing of a 16-element subarray (shown in block diagram form in Fig. II-2). Some of its specifications are:

Frequency	2700 to 3000 Mcps
Antenna spacing	0.58 wavelength at 3000 Mcps (principal planes)
Power radiated per element	10-kw peak; > 100-watt average
Pulse widths	0.1 to 10 $\mu$ sec
Beam steering speed	2 $\mu$ sec

Some of the implications of these requirements are depicted in Fig. II-3. The largest gaps

\* See J. L. Allen in TR-236, pp. 259-279.

between state-of-the-art components and those required for this subarray lie in the areas of power amplifiers, high-power circulators, and time-delay units.

The most expensive of these to remedy, in terms of both time and money, appears to be the transmitting tube. No tube with electrical specifications close to those outlined here exists, let alone one physically configured for packaging in a physically small subarray. Hence, in order to test a breadboard subarray in as short a time as possible, and with limited funds, we decided to use the commercially available tube most nearly meeting the above requirements. This appears to be the VA-136, which is rated at 100-kw peak and 5-percent duty at S-band.

The status of the development of the other components is covered in this part of the report.

## CHAPTER 2

### ANTENNAS

J. L. Allen

For initial development, the antennas used will be circular ridged waveguide horns excited by crossed loop couplings. These antennas were designed by and purchased from Hughes Aircraft Co., Fullerton, Calif. Detailed testing of these units will be carried out later on L-band scale models as part of the mutual coupling experimental studies (see Part III, Ch. 4).

Consideration is also being given to simpler element types such as open rectangular waveguides, but an intelligent decision awaits the outcome of the mutual coupling studies.

## CHAPTER 3

### HIGH-POWER PHASERS

#### SUMMARY

A more complete set of design goals for high-power phasers for array radar application has been formulated. Although most of this chapter pertains to ferrite phasers, some work on diode reliability and improved couplers for diode phasers is reported.

A summary and status report of the presently known major design considerations and probable limitations of ferrite phasers is given. A brief comparison of diode and ferrite phasers has been made. A separate detailed final report on the development of a helical ferrite phaser\* for the experimental S-band subarray has been prepared by General Electric for distribution.

#### A. INTRODUCTION

During this reporting period, considerable progress in the state of the art has been made in the realization of phasers at the intermediate power levels (10-kw peak, 100-watt average). More detail design goals have been formulated. Our previous parallel efforts in diode and ferrite phasers have been shifted toward ferrite phasers as new developments overcame early ferrite phaser limitations. Present efforts continue to attempt to define capabilities and limitations of ferrite phasers in the L- through X-frequency bands.

#### B. PRESENT DESIGN GOALS FOR HIGH-POWER PHASERS

F. Betts and D. H. Temme

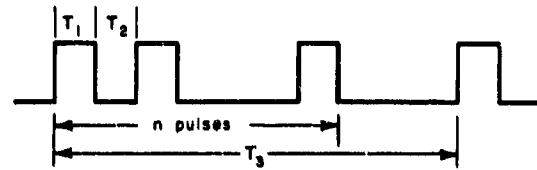
Present design goals have not changed substantially from those first listed in TR-236. They have been expanded and detailed as follows.

Frequency	L- through X-bands
Bandwidth	10 percent
Characteristic impedance	50 ohms
Phase	360° in $2^4$ steps
Size	Transverse dimensions $< \frac{1}{2}\lambda$ at upper-band edge
RF power	20-kw peak; 150-watt average into matched load
Switching speed	Any new phase setting shall be attained in $\leq 3 \mu\text{sec}$
Switching power	$\leq 10$ watts "raw" input power per driver unit
Insertion loss	$< 1.5$ db
Match	Adequate to meet phase and loss tolerances below
Insertion loss tolerance	$\leq 0.4$ -db total excursion vs phase setting
Phase tolerance	$\leq 6^\circ$ deviation from nominal value. <u>Note:</u> this tolerance is to be maintained in the presence of source mismatch $\leq 1.2/1$ and load mismatch $\leq 2.5/1$ .

\*See H. A. Hair as cited in Part II, Ch. I, p. 41.



Typical waveform



$T_1 = 0.1$  to  $75 \mu\text{sec}$ ;  $T_2$  (min) =  $0.5$  to  $2.0 \mu\text{sec}$ ;  $nT_1 \leq 75 \mu\text{sec}$ ;  $T_3 = 3 \text{ msec}$ ;  $n \leq 75$ .

Waveform distortion

For an input pulse having 10-nsec rise time and 100-nsec duration, the output rise and fall times shall be  $\leq 15 \text{ nsec}$ .

Temperature

Above specifications shall be met within the ambient temperature range  $20^\circ$  to  $30^\circ\text{C}$ . Cooling water ( $\pm 1^\circ\text{C}$ ) available.

Unit-to-unit reproducibility

Units shall track one another in phase for all phase settings and differences in delay to  $\leq 4^\circ$  within a 10-percent band; units shall track one another in insertion loss to  $\leq 0.4 \text{ db}$  within a 10-percent band.

Reliability

Life,  $\geq 100,000$  hours

Cost of phaser with driver

Reducible to \$150 in lots of 10,000 units, tooling costs not included.

Driver

A driver shall be furnished, capable of receiving digital control words at  $\sim 3\text{-mw}$  signal level and having suitable termination (e.g., 100 ohms) for the logic signal. Driver output shall be capable of switching the phaser during the interpulse intervals in an RF waveform, such as that specified above.

Although the present state of the art in diode and ferrite phasers is approaching these goals, they have not yet been met. However, it is anticipated that they can be met within the next two years; reasons for such expectations are included in the following phaser discussions.

### C. DIODE PHASERS

F. Betts

It has already been stated that parallel work on diode and ferrite phasers was shifted to ferrite phasers. Reasons for the shift follow the ferrite phaser discussion. Some work that does relate to diode phasers, performed at the beginning of the report period, follows.

#### 1. Improved 3-db Couplers

Diode phasers constructed for the 900-Mcps array (see Part II, Ch. 1 of this report and TR-299) are hybrid types. Improvement in the 3-db coupler was discussed in TR-299 and was considered feasible with the higher tolerance Tellite material that had just become available. Improved 3-db couplers with a 1300-Mcps center were built under a development contract to Rantec. Six boards, each containing four cascaded 3-db traveling-wave couplers, were compared from 1200 to 1400 Mcps with a microwave comparison bridge (described in Ch. 8, Sec. D-2-b below). The units phase tracked within a few tenths of a degree; insertion loss of the units appeared

identical, each measuring 0.25 db. This demonstrates that high-quality couplers can be built for the hybrid-type diode phasers.

## 2. Diode Reliability

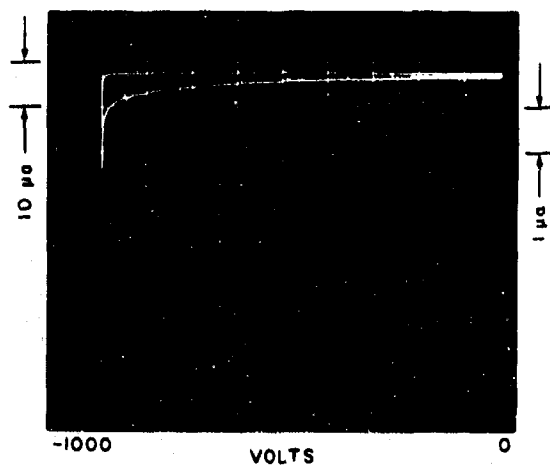
### a. Exploratory Stress Tests

The very large number of diodes used in many proposed phased array configurations indicates that a very high reliability for a single diode must be attained in order to keep the replacement rate at a reasonable level. For a phased array using a few tens of thousands of diodes, one can see that a mean time to failure of upward of  $10^5$  hours is necessary to keep the replacement rate within reason. While failure rates and mechanisms have been studied quite intensively for other solid state components, at the beginning of this reporting period microwave switching diodes had not been studied to any extent. Therefore, it was decided to undertake some very limited experiments which, it was hoped, would indicate the most immediate directions that larger scale testing should take. Following the first of these tests, a contract was awarded to Microwave Associates to make further studies on a larger number of diodes. Results of these tests are summarized in the following paragraphs.

In the first test, 15 mesa PIN diodes in three groups of five were maintained in an oven at  $100^\circ\text{C}$  for one week. Group A was operated forward-biased with about 400-mw dissipation, Group B with 300-volt reverse bias, and Group C with 600-volt reverse bias. Initially, all diodes had leakage currents under  $0.5\ \mu\text{A}$  at 600 volts and room temperature. The reverse breakdown voltage of the diodes ranged from about 675 to over 800 volts, though these data were not recorded. At the completion of the test, when the leakage current was again measured at room temperature, many of the diodes were observed to have experienced drastic changes in leakage. All units in Group A, one unit in Group B, and three units in Group C experienced such changes. While the 400-mw dissipation in Group A certainly caused appreciable rise in the junction temperature, these data suggest that forward bias is a significant stress and that high reverse bias (near breakdown) is a more severe stress than lower bias. The 100-kcps capacitance data, showing mean capacity changes of 56, 45 and 55 percent for Groups A, B and C, respectively, were not judged significant due to the large in-group variance.

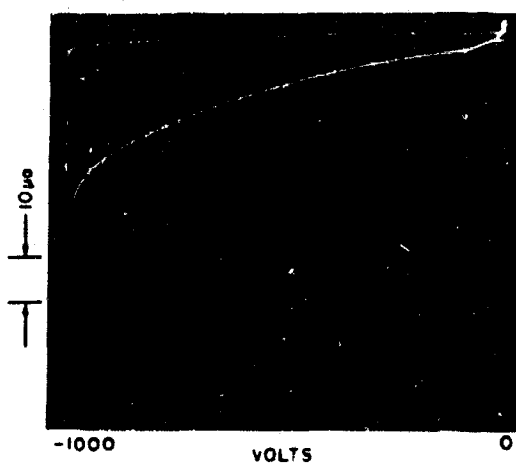
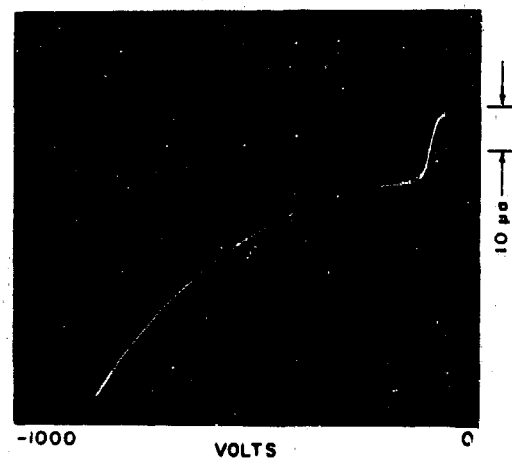
A second test lasting about 8 weeks was run with slightly altered test conditions. Diodes in Group A were subjected to a bias alternating at a 60-cps rate between 50-ma forward bias and 500-volt reverse bias. Groups B and C were operated at 250 and 500 volts, respectively. Again, the oven temperature was  $100^\circ\text{C}$ . Breakdown voltages for these diodes were in the range 750 to 975 volts. At the end of the test, three units in Group A, one unit in Group B, and no units in Group C had shown drastic changes in bias. Speaking only of the remaining units, the leakage at 500 volts, which had been initially of the order of tenths of microamperes, was of the order of a few microamperes at the end of the test. The 100-kcps capacitance data were again considered inconclusive due to large in-group variations.

Diodes in the second test were part of a much later production run and differed in junction area and package from the earlier units. Breakdown voltages were somewhat higher, as noted. The size of the groups is too small to make really meaningful comparisons with corresponding groups in the previous experiment, or between Groups B and C in this experiment. However, from the second experiment it appears that something in the alternating bias group (Group A) caused this to be a more severe stress. Also, one is tempted to conclude, by comparing data



(a) Before test. Upper trace:  $10\mu\text{A}/\text{div.}$ ; lower trace:  $1\mu\text{A}/\text{div.}$

(b) After 24 hours at 100-percent relative humidity.



(c) After being "dried out" for 12 hours at  $100^{\circ}\text{C}$ .

Fig. II-4. Diode P3053 in humidity tests.

from Groups B and C between the two experiments, that the diodes in the second test were superior to those in the first.

Summarizing then, these experiments suggest that operation at elevated temperatures with electrical bias may constitute an appreciable stress on the diode, producing considerable deterioration in a relatively short time. Also, forward or alternating biasing might be more severe than moderate reverse biasing. The sample size and variability of data within groups are such that these results can really only suggest hypotheses for further testing. Considering each test as a whole, there is some indication that the later diodes were superior to the earlier ones, and that performance may be further improved in future tests.

#### b. Hermeticity Tests

Welds closing the cases of the later diodes (earlier diodes had brazed seals) sometimes broke, allowing the top of the package to come off. Examination of several units indicated that many packages, though having mechanical integrity, did not appear to be sealed. When several of these diodes were placed in a 100-percent relative humidity atmosphere for 24 hours, their leakage increased and the general shape of the reverse characteristic [as shown on a curve tracer in Figs II-4(a-c) and II-5(a) and (b)] changed considerably. Though the surface of the mesa was coated with a protective material, the drastic change in the appearance of the curve was taken as an indication that effects on the surface of the semiconductor were being observed. Storage at 100°C in an oven for 24 hours returned two of the units to roughly their original reverse characteristics, but two remained considerably altered.

Results of this experiment suggest that, at least for the diodes of this lot, the life of the diodes could be adversely affected by constituents of the environmental atmosphere unless care is taken to ensure that the cases are hermetically sealed.

#### c. Life Testing

To obtain information on a larger sample of diodes, Microwave Associates was contracted to perform temperature storage tests. The experiment is reported in detail in "Reliability Test Report on MA 4248 PIN Diodes for Phase Shifting in Array Antennas with Planar and Mesa

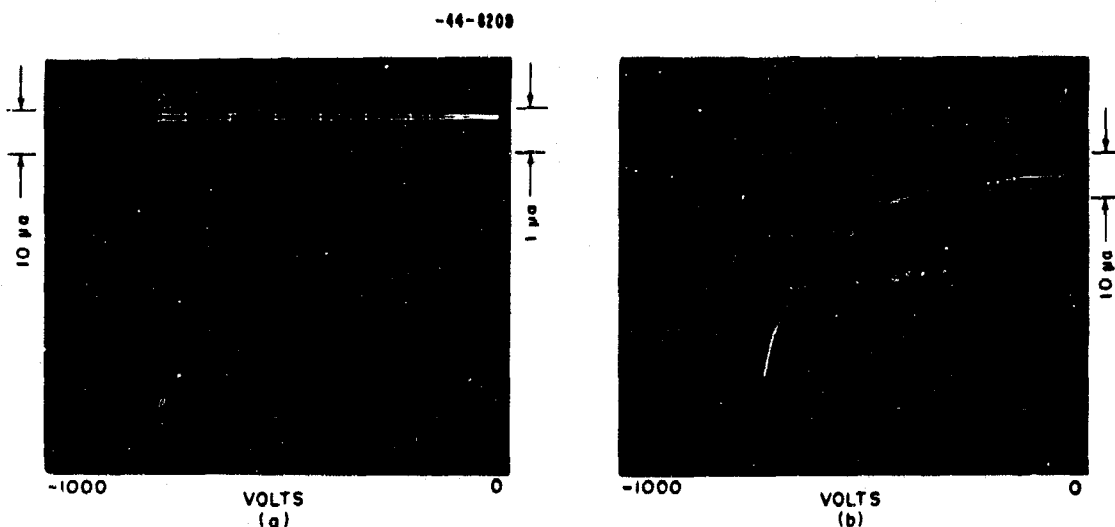


Fig. II-5. (a) Diode P3058 before test; (b) after 24 hours at 100-percent relative humidity. At the end of the "drying out" period, this diode was found to have extremely high leakage.

Construction," by Microwave Associates (17 June 1964). The results will be summarized here.

During the time that diodes were being prepared for the test, preparation of planar PIN diodes progressed to the point where it appeared reasonable to include them in the test. Accordingly, 40 mesa diodes and 60 planar diodes were put on test, being divided into groups and stored as follows: mesa diodes at 110°, 140°, 180° and 225°C; planar diodes at 110°, 150°, 185° and 225°C. The duration of the test was 1316 hours. A diode was considered to have failed when its leakage current at 25°C exceeded 1.0  $\mu$ A at 500-volt bias.

Results showed that the diodes used in the test fall far short of the reliability goals mentioned earlier. There were substantial numbers of early failures which could presumably be weeded out of future batches by a burn-in period. Failure rate estimates showed rapid decline as the test continued. Even so, a number of diodes failed during the latter part of the test (leakage exceeding 1.0  $\mu$ A at 500 volts, 25°C).

The percent failure data did not show planar units to be markedly superior to mesa diodes. However, the planar diodes tested were among the first successful production and had somewhat lower breakdown voltage than the mesa diodes. The very wide spread in leakage current from unit to unit of planar diodes suggests that tests with a more uniform sample from later production will show the expected superiority of planar diodes.

Of interest in microwave applications, the capacitance at 900 Mcps (25°C, 50-volt bias) shows changes of the order of 10 percent for some diodes, both mesa and planar, with a trend toward capacity increase. The planar diodes appear to show less change than the mesa diodes. The 1-Mcps capacitance data show substantially less variation for the planar diodes. While not affecting microwave behavior, the low-frequency capacitance data are indicative of "something happening" in the diodes.

In summary, this test shows the need for substantial and continued effort in order to achieve diodes sufficiently reliable for use in very large numbers in phased arrays. Additional testing to determine the effect of DC bias and RF operation is also clearly necessary.

#### d. Conclusions

The reliability of microwave switching diodes, as indicated by these several tests, is far from the stated goals for phased array applications. However, the testing procedures used cannot be considered to yield definitive results. Additional testing is being carried out by Microwave Associates under a Navy contract aimed at testing under more realistic electrical stresses and gaining further experience with planar diodes. The latter objective is very important, as high-voltage planar switching diode experience is quite limited so far, and very substantial improvements can be expected as techniques improve. The increase in reliability of transistors and computing diodes has shown the tremendous progress that can be expected in the future if the appropriate effort is expended.

### D. STATE-OF-THE-ART SURVEY OF FERRITE PHASERS

#### 1. Introduction

This section is a brief survey of the digital remanent (latching) ferrite phaser state of the art. A summary and status report of the presently known major design considerations and limitations is given. The capability of present techniques\*† to meet the phaser design goals outlined

\*See H. A. Hair as cited in Part II, Ch. 1, p. 41.

†L. Levey and L. Silber, 1960 IRE WESCON Convention Record, Part 1, pp. 11-20.

in Part II, Ch. 3-B is examined. The first reference is a final report prepared by General Electric for Lincoln Laboratory. It details the development of the helical phaser which will be used in the S-band subarray. The other reference, which is readily available, describes a waveguide ferrite phaser. Finally, a brief comparison of diode and ferrite phasers is given.

The shortcomings of early ferrite phasers were their low average power capability, slow speed of response for reasonable control power, and their phase-temperature sensitivity. The principal embodiments of remanent ferrite phasers without these undesirable features are shown in Figs. II-6(a) and (b). Both devices depend on the fact that the transmission propagation constant in turn depends on the direction of magnetization of the ferrite placed in circular polarization regions of the transmission structure, thus providing differential phase shift. In the waveguide type, the ferrite is in the circular polarization region of the guide. In the helical type, the electrical length of a turn is an odd multiple of a quarter wavelength, thus giving rise to a region between the turns where the RF magnetic field is spatially orthogonal and properly time phased for circular polarization.

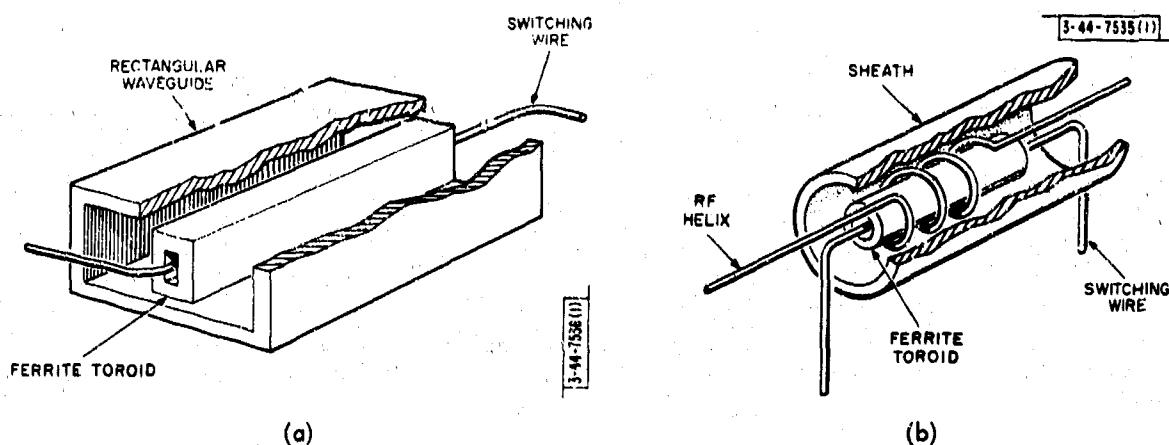


Fig. II-6. Two remanent ferrite phaser configurations: (a) waveguide type; (b) helical type.

In both types of devices, the ferrite is a closed path magnetic structure (toroid) made with square-loop microwave ferrite material. It is switched between the two remanent states of magnetization required for microwave operation by a current pulse, as in magnetic memory core operation. The size of the toroids in these structures is such that switching energies required for about 1- $\mu$ sec speeds is typically less than 100 microjoules. Thus, these devices overcome the deficiency in switching speed and control power of the early ferrite phasers.

One way the phase-temperature sensitivity of early phasers is overcome in the remanent phasers is through the control of the flux switched into the microwave ferrite prior to each transmission or reception. The differential phase is related to the differential flux of the two remanent states, thus a dynamic phase-temperature stability is achieved. Flux control techniques are examined later, after first discussing present knowledge of microwave characteristics of ferrite materials operated at remanence and the effectiveness of various ferrite configurations.

## 2. Microwave Characteristics of Ferrite Materials Operated at Remanence

Until recently, the ferrite in most microwave ferrite devices was placed in an external magnetic field. The pertinent material characteristic usually given for such application is incomplete for remanent devices. We begin with a discussion of other important material characteristics with the hysteresis-loop characteristic.

#### a. Hysteresis-Loop Characteristic

Propagation constant in both the helical and waveguide phasers is proportional to the remanent magnetization of the ferrite. Therefore, the squareness of the hysteresis loop of the ferrite material is one important quality factor of a ferrite material to be used in a remanent ferrite device. Squareness, for this discussion, is arbitrarily defined as the ratio of the remanent magnetization to the magnetization at a driving field five times the coercive force. A driving field of this magnitude or greater is generally adequate to produce a constant value of remanent magnetization. Surveys\*†‡ show that the squareness of garnets ranges from 0.5 to 0.8, and that of the magnesium-manganese ferrites ranges from 0.7 to 0.9. The coercive force for most of the materials is between 1 and 2 oe.

Very recently, Green§ and others have called attention to the fact that the remanence ratio, defined as the remanent magnetization to the saturation magnetization, is lower than the squareness ratio by about 10 percent. It takes fields of about 1000 oe to approach saturation; the moment is still increasing slightly at fields of  $10^5$  oe. The important point is that a constant value of remanence is reached when the switching field is greater than a few times the coercive field. This is a characteristic common to both computer and microwave ferrites.

The question arises whether loop squareness (remanence) and good microwave properties in a ferrite are incompatible. To the best of our knowledge, no good reason why they must be is known. In fact, it is probably reasonable to expect that the squareness of some microwave materials can be significantly improved as the knowledge of both computer and microwave ferrites is brought to bear on the problem.

Another important question is what is the tolerance of the remanent magnetization of the ferrite materials. This is the proverbial question of the tolerance of the saturation moment, since the remanent ratio is thought to be constant for a given material. Ferrite material manufacturers have been constantly improving the tolerance on saturation magnetization to the present typical value of  $\pm 5$  percent. Since this tolerance contributes directly to the phase tolerance of the phaser, it may often be inadequate and some form of phase trimming must be provided in the phaser.

Another important ferrite material tolerance, although not related to the hysteresis loop, is the variation in the dielectric constant which affects the value of propagation constant. The present tolerances are about  $\pm 5$  percent; thus, the method of phase trimming must accommodate this variation.

It is important to measure the remanent magnetization vs temperature directly; it cannot be inferred from the saturation magnetization-vs-temperature curve (the curve of remanent magnetization vs temperature frequently does not have a similar shape).

Finally, some ferrite materials are quite magnetostrictive; that is, the shape of the hysteresis loop changes significantly with small applied pressure to the toroid. The garnets and nickel ferrites are strongly magnetostrictive; in contrast, the magnesium-manganese ferrites

---

\*See H.A. Hair as cited in Part II, Ch. 1, p. 41.

†J.A. Weiss, "Hysteresis Properties of Microwave Ferrites and Ferromagnetic Garnets," Interim Report under Subcontract No. 302, Worcester Polytechnic Institute, Worcester, Mass. (August 1964).

‡Trans-Tech Incorporated, Gaithersburg, Md., July 1964 Catalog.

§J. Green, private communication.

are only weakly magnetostrictive. This magnetostrictive characteristic of the ferrite material must be kept in mind when dealing with the design of the toroid mount.

Presently, it appears that the loop properties of the ferrite are not the most limiting characteristics for remanent phasers. However, it remains an area for significant improvement.

#### b. High-Power Effects

An increase in insertion loss occurs in both types of phasers when the RF power level exceeds a certain threshold. Figure II-7 is a typical plot of the observed threshold of a helical phaser vs  $\omega_{ms}/\omega$ , the ratio of the ferrite material resonance frequency to the operating frequency. A similar plot for the waveguide ferrite phaser resulted when data obtained from Westinghouse were plotted. Killick\* obtained a similar curve by partially filling a coax line with ferrite toroids. Hair† ascribes the nonlinear effect to frequency down-conversion‡; more experimental work is necessary to verify this hypothesis. The data, however, clearly suggest that the threshold power will increase for remanent devices as the operating point is moved away from resonance ( $\gamma 4\pi M_s$ ) in below-resonance operation. An  $\omega_{ms}/\omega$  ratio of about 0.5 is usually required for the 10-kw peak-power level. Thus, a trade-off exists between the figure of merit (phase shift/db of loss) of the phaser and the peak-power-handling capability. A larger  $\omega_{ms}/\omega$  ratio (a larger magnetization – large phase shift per unit length of ferrite material) than 0.5 gives a larger figure of merit, but a lower peak power handling capability.

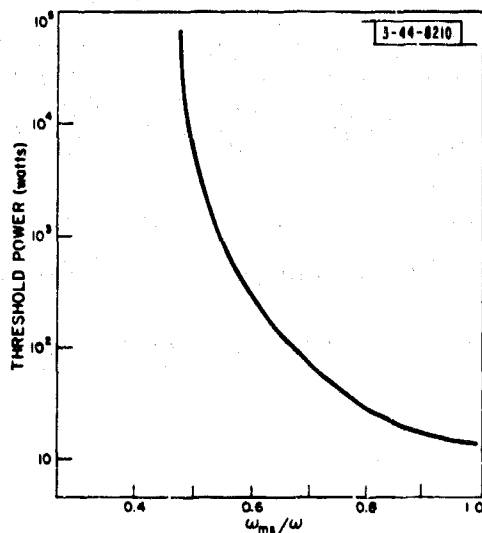


Fig. II-7. Typical threshold curve.

Whether an improvement in the power-handling capability of ferrite material can be expected is not clear and probably awaits a better detailed understanding of the effect.

#### c. Magnetic Loss

An attempt§ has been made to assess the variation in magnetic loss that can be expected with different ferrite materials in a phaser. A circumferentially magnetized toroid in the remanent

\*E. Killick, "Problems of Materials for High Power Ferrite Phase Shifters for Aerial Scanning," RADC Electronic Scanned Array Symposium Proceedings, RADC-TDR-64-225, Vol. I (July 1964), p. 224.

†See H. A. Hair as cited in Part II, Ch. I, p. 41.

‡E. Schlomann, *et al.*, J. Appl. Phys. **31**, 3945S (1960).

§H. A. Hair, *op. cit.*, p. 58.



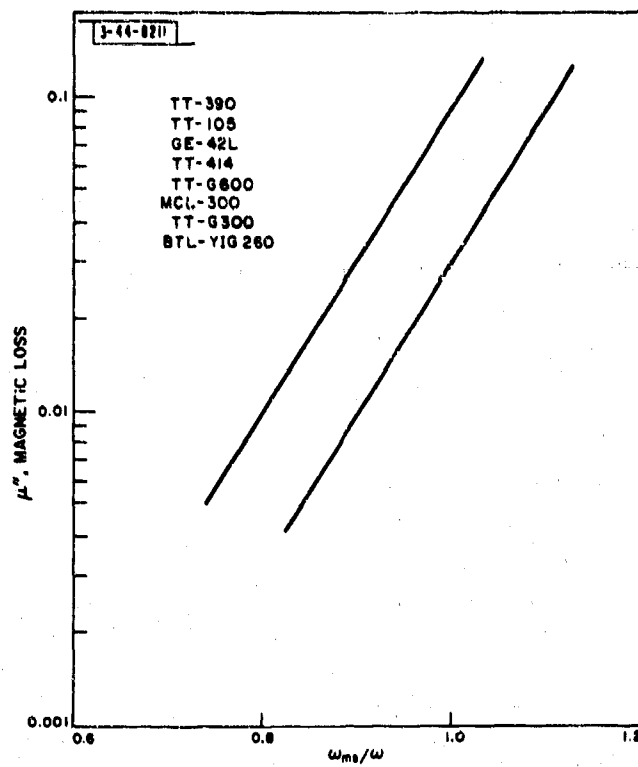
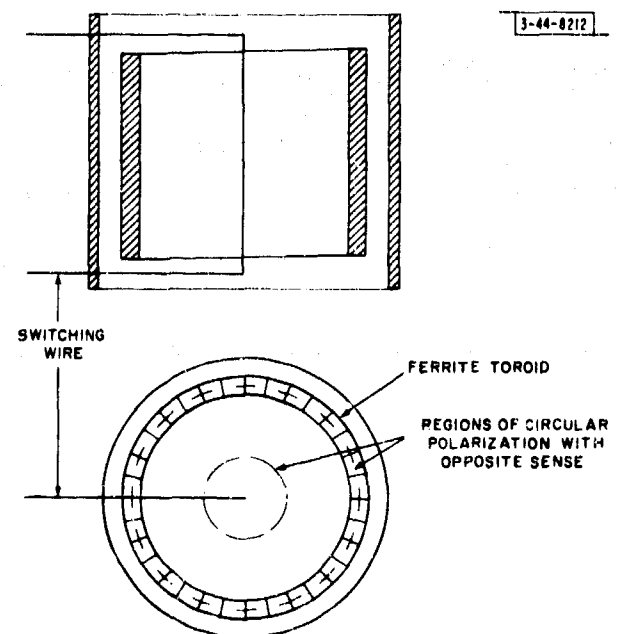


Fig. II-8. Magnetic loss measurements.

Fig. II-9. Circular  $TE_{01}$  configuration.



state that completely fills the coax line was placed against a short-circuit termination of a coaxial slotted line. The distance  $\Delta d$  between the 3-db points of the standing-wave null is related to the magnetic loss  $\mu''$  by  $\mu'' = \Delta d/2\ell$ , where  $\ell$  is the toroid length which is kept small compared to a wavelength in the ferrite. In the frequency range of interest, the loss appears to approximate an exponential relationship. Most ferrites exhibit similar characteristics when the loss is plotted against  $\omega_{ms}/\omega$ , the ratio of the ferrite resonance frequency to the frequency. Figure II-8 shows a plot of boundary curves for the materials listed on the graph. No attempt has been made to refine these measurements or to study some of the material that fell outside the boundaries. The emphasis so far has been directed toward S-band high-power phasers where  $\omega_{ms}/\omega$  is sufficiently low for high-power reasons so  $\mu''$  is not the most significant factor.

Whether the method is a good way to evaluate ferrite materials for receive (low-power) phaser is not known. In this case, peak-power effects do not occur and the optimum ratio of  $\omega_{ms}/\omega$  is determined by the point where the increase in magnetic loss exceeds the gain in phase shift, namely, the largest figure of merit vs  $\omega_{ms}/\omega$ .

### 3. Phaser Configurations

The ideal structure would (a) have a circularly polarized RF magnetic field throughout the ferrite, (b) have a uniform field intensity throughout the ferrite, and (c) permit establishing the appropriate magnitude of the field intensity in ferrite region for the maximum RF power to be transmitted through the phaser. Neither of the structures shown in Figs. II-6(a) and (b) have these properties, nor is it likely that one will be found. However, there may be configurations that approach the ideal more closely; some work on this subject has been done and is outlined below.

A circular waveguide  $TE_{01}$  mode field configuration (Fig. II-9) is attractive since the ferrite can be entirely in a region of circular polarization and switching wires can be introduced without RF coupling. The transducer problems, i.e., bulkiness, match, bandwidth and mode purity, were sufficiently severe that efforts to investigate such a structure never proceeded beyond the exploratory state.

The extent to which the RF magnetic field in the waveguide structure [Fig. II-6(a)] can be more effectively shaped for a higher figure of merit by dielectric loading\* is an open question. In some high-power phaser applications, a dielectric slab located in the center of the waveguide with a ferrite toroid on each side may be a good way to control the RF magnetic-field intensity in the ferrite to avoid high-power nonlinear effects in the ferrite. This method will require a longer phaser for a given phase shift. The loss of the phaser will increase with length, and the figure of merit will decrease. A computer program is being written to assist in the numerical computations of the fields, phase shift, and loss by solving the boundary value problem of ferrite slabs in a waveguide. It is hoped that this will permit selecting optimum waveguide configurations.

For L- and S-band frequencies, the simple waveguide structure is inadequate because of size. A reduced height, dielectric loaded waveguide structure may be attractive. So far, only the helical phaser is a practical ferrite phaser for the L- and S-band frequencies. Its geometry provides a long ferrite-field interaction length for a reasonably long toroid which can be switched

\*L. Levey and L. Silber, "A Fast-Switching X-band Circulator Utilizing Ferrite Toroids," 1960 IRE WESCON Convention Record, Part 1, pp. 11-20.

with a moderate amount of energy. The geometry also permits handling high peak powers by decoupling the ferrite from the transmission line by increasing the spacing between the ferrite and the helix. The figure of merit for the high-power case is mainly determined by the copper loss of the helix. For example, in an S-band 10-kw helical phaser, the helix loss is about 0.8 db of the total 1.2-db loss. It seems clear that some sort of non-TEM structure will be required to obtain a significantly higher figure of merit for an S-band phaser.

In summary, one can probably expect that the peak-power requirement will dictate the phaser configuration. New ferrite materials with better high-power characteristics will probably only alleviate, but not eliminate, the problem.

#### 4. Phase-Temperature Sensitivity

This, of course, is essentially a problem of stabilizing the effective magnetic moment with changes in temperature. There are several possible methods for accomplishing this end.

The first obvious solution is to find a material with a temperature-stable moment. Over the typical operating temperature ranges, the variation of the moment of high Curie temperature ( $>300^{\circ}\text{C}$ ) materials is probably not significant. Usually, their moment (greater than 1500 gauss) restricts their use to X-band frequencies.

Another possible solution to the phase-temperature sensitivity problem is the use of temperature-compensated garnets.\* Loss of these materials, however, at L- and S-bands has been high to date.

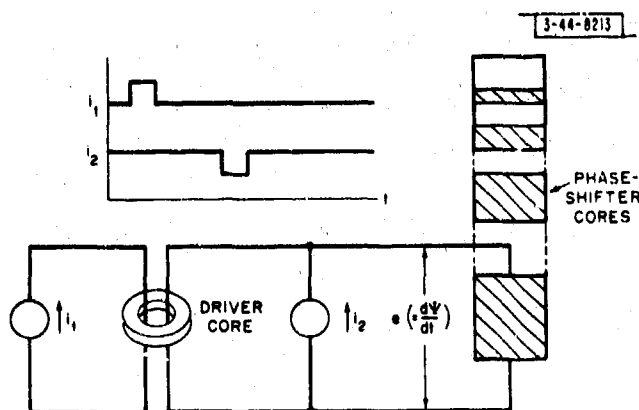


Fig. II-10. An individual bit flux transfer circuit.

The best solution, so far, for phase stabilizing a phaser with a material having an unsatisfactory phase-temperature characteristic, is a flux drive method described by Hair.† An ordinary pulse generator and a ferrite toroid constitute a flux driver (Fig. II-10). The current pulser  $i_2$  resets both the microwave and driver cores to the reference state. To change the phase, the driver core is switched by the flux transfer pulse  $i_1$ ; the output voltage  $e (= d\psi/dt)$ , on the secondary of the driver core also appears across the microwave core. Faraday law says the rate of flux change must be the same in both cores. Therefore, a defined flux change  $\Delta\psi = \int e dt$ ,

$$\Delta\psi = \int \frac{d\psi}{dt} dt = \int e dt,$$

twice the remanent flux of the driver core, is transferred during the switching of the driver core to the microwave core. The driver core is a ferrite with good squareness and a high Curie

\* G. Harrison and L. Hodges, Jr., *Microwave J.* 4, No. 6, 5<sup>th</sup> (June 1961).

† See H. A. Hair as cited in Part II, Ch. 1, p. 41.

temperature. Its position is external to the phaser and thus it can easily be cooled. Hence, the  $\Delta\psi$  switched out of the driver core is essentially constant over a wide range of operating conditions and, likewise, the related differential phase remains essentially constant. The method is adequate to stabilize the phase of an S-band phaser to a few degrees while the average power varies from 0 to 400 watts, corresponding to a ferrite temperature variation of about 20°C. The flux drive method provides only a dynamic temperature stability, since the flux level will change as the temperature changes; thus, the microwave toroid must be reset as the temperature changes. In practice, this probably means setting the toroid just before transmission or reception. Practical constraints and limitations of this method are discussed in more detail by Hair.\*

There are some additional factors of a conceptual nature that may be of interest concerning flux drive. This mode of operation essentially is a change of the usual current constraint in the switching circuit to a volt-time integral constraint. The switching circuit must supply the hysteresis loss of the toroid which changes with temperature. When the toroid is switched by a defined  $\Delta\psi = \int e \, dt$ , the current adjusts with temperature to supply the required hysteresis loss.

Is the driver toroid the best  $\int e \, dt$  generator? The common pulse generator does not qualify because its source impedance is not low with respect to the dynamic impedance of the microwave toroid, which is typically in the 1-ohm region. The tolerable source impedance of the generator is determined by the change of microwave toroid impedance with temperature. A tentative qualitative argument is advanced concerning the variation of the impedance of such a toroid with temperature, since the subject has not been fully investigated to the best of our knowledge.

Switching characteristics of a toroid, useful in computer applications, are well known.† The toroid is switched with a current pulse, and the switching speed  $\tau$  is related to the driving field  $H$  by  $\tau^{-1} = S(H - H_0)$ , where  $S$  is a constant of the material, and  $H_0$  is the abscissa intercept of a plot of the experimental data of  $\tau^{-1}$  vs  $H$ .  $H_0$  is very nearly equal to the coercive force  $H_c$ . If the toroid is switched in about 1  $\mu$ sec, the driving field  $H$  is typically three to four times  $H_c$ . Similar values would be expected when the drive is an  $E\Delta t$  source, and this has been observed. When the temperature of the toroid changes,  $H_0$  decreases and, for a constant drive  $H$ , the switching speed increases. For the operating temperature range of toroids in phasers,  $H_0$  may decrease to 50 percent of its room-temperature value. When the microwave toroid is driven by an  $E\Delta t$  source, the switching time will remain essentially constant since the same amount of flux,  $\Delta\psi = E\Delta t$ , must still be switched. Thus,  $H$  must drop from about 3 to 2.5  $H_0$ , or about 20 percent. Values of this order have been observed; thus, the  $\int e \, dt$  generator must be able to cope with toroid impedance changes of this order.

An ordinary pulse generator with its output constrained by a Zener diode may qualify as an  $E\Delta t$  generator with a sufficiently low source impedance. If so, then the phase of a phaser with only one microwave toroid could be varied by programming the pulse length of the  $E\Delta t$  generator. The reduction in the number of switching wires and spacers in the phaser would reduce the insertion loss. This scheme is being investigated.

\*See H. A. Hair as cited in Part II, Ch. I, p. 41.

†N. Menyuk and J. Goodenough, J. Appl. Phys. 26, 8 (1955).

‡R. H. Tancrell and R. E. McMahon, "Studies in Partial Switching of Ferrite Cores," Technical Report 210, Lincoln Laboratory, M. I. T. (21 September 1959), DDC 227928.

In summary, the concept of flux control in the microwave toroid of a phaser prescribes a method of phase-temperature stability. The use of an auxiliary driver toroid is a proven method of implementing the concept. It can be expected that other methods will be devised that may be advantageous for certain applications.

## 5. Driver Considerations

L. Cartledge

### a. Phaser Switching Energy

Square-loop ferrite cores of the type used in the phase shifters under discussion can be characterized by a volt-time product for a specific temperature which remains invariant for a particular core. This volt-time product,  $\int e \, dt$ , is another way of expressing the total magnetization of the core. The volt-time product associated with switching the core is linearly related to twice the saturated magnetization of the core multiplied by its cross-section area.

It is generally accepted that the switching speed of a square-loop ferrite core is inversely related to the so-called driving force ( $H - H_0$ ), where  $H$  is the instantaneous magnetizing force, and  $H_0$  is the coercive force for the particular core under observation. In the case of radially very thin toroidal cores driven by a straight wire along the axis,  $H$  is related to the driving current by a constant multiplier. In the case of thicker toroids or asymmetrically driven cores, the relationship between  $I$  and  $H$  becomes a function of the geometry. In these latter cases, the actual driving function is not constant through the core and may be difficult to compute.

In any case, however, the energy put into the core in switching it from one remanent state to another can be expressed as

$$E = \int_0^T e \, dt$$

In the case where the drive is a step of current, this becomes simply

$$E = I \int_0^T e \, dt$$

Since the volt-time integral is constant and faster switching is obtained by increasing  $I$ , it is clear that faster switching is obtained at the expense of putting more energy into the ferrite.

In the "square-loop" ferrites which are useful in latching phase shifters, only a few percent of the energy delivered to the core is stored and returned to the circuit via the reversible flux changes. Some 80 to 90 percent of the switching energy is dissipated in the ferrite as heat. In a typical half-wave bit of an S-band helical phase shifter, the volt-time product is on the order of 6-volt microseconds and switching in a microsecond can be produced by applying a current step on the order of 4 amp; hence, a single reversal in 1  $\mu$ sec deposits about 200 ergs of energy in the ferrite. A single reversal which took place in a tenth of a microsecond would deposit more than 600 ergs in the ferrite.

By comparison, a good ferrite material may introduce 0.15-db insertion loss in a 180° bit. Thus, if the applied RF power is a rectangular pulse, 100 nsec long with a peak power of 10 kw, the energy deposited in the ferrite by RF losses would amount to some 350 ergs. Consequently, the energy lost in beam steering can contribute significantly to the average power limitation if the radar must be capable of transmitting short single pulses of high energy, or of interlacing the transmission of pulse trains in different directions. This situation is aggravated if the array

is duplexed and the phase shifters must all be switched a second time for receiving. It is aggravated still further in those cases where the phase shifters must be reset to zero before being set to the next position.

Of the several flux transfer drive circuits proposed,\* the one depicted in Fig. II-11 seems to offer the greatest flexibility and speed and will probably be used in the subarray. This arrangement involves four driver cores and eight bipolar drivers per four-bit phase shifter. The arrangements using fewer parts seem to do so at a penalty in either speed or efficiency, or both. Note that the pulser must supply the energy lost in switching both cores and the  $I^2R$  losses as well.

Analysis of the currents and voltages in the circuit is made difficult by the two nonlinear ferrite cores involved. It can be seen, however, that the current through the phase-shifter core subtracts from the driving current in the driver core. Hence, the pulser must supply a peak current that corresponds to the sum of the driving forces of the two cores.

While the calculation of the currents and voltages in the two loops of the flux drive circuit would involve numerical methods and a digital computer, it is relatively easy to breadboard the circuit and observe the currents and voltages. This was done using a 90° S-band phase-shifter core in the circuit shown in Fig. II-12. Some typical results, which were obtained using TT-390 as the driving core, are shown in Figs. II-13(a-d). The applied pulse has a rise time on the order of 0.8  $\mu$ sec to simulate the transistor driver which will be used in the subarray.

Note that, if the phase shifter is to be used for both transmitting and receiving, the two video drivers must be capable of supplying both negative and positive pulses. If, however, the phase shifter is to be used only for transmitting or only for receiving, each driver need only supply pulses of one polarity.

#### b. Switching Speed as a Function of System Parameters

The radar system designer must select the beam-steering speed that represents the optimum trade-off between the increased transmitter efficiency, which can sometimes be had for faster beam-steering speeds, and the cost of the beam-steering system, which increases with increasing steering speed. Detailed knowledge of the system configuration, mode of operation and waveforms is a prerequisite to exact optimization of the steering speed. Lacking a well-defined system, we can only indicate the points where the effect of steering speed on the overall system changes.

There is, for instance, a minimum obtainable beam-steering time which is of the order of the "buildup time" of the array. It is theoretically possible to start the transmission or reception of a pulse on one side of the array before the trailing edge of the previous pulse has cleared the opposite side. To do so, however, would involve real time "steering" of the steering commands to the phasers, hence a great increase in the complexity and cost of the beam-steering system. The buildup time varies with the array dimensions and the beam-pointing angle from zero to values in excess of 100 nsec.

We note another break point, in transmitting arrays at least, when the steering time of the phase shifters is longer than the combined rise and decay times of the transmitter modulators. The minimum obtainable time between transmission of pulses in different directions is the beam-steering speed. If the electron beams in the transmitting tubes cannot be turned completely off

\*See H. A. Hair as cited in Part II, Ch. I, p. 41.

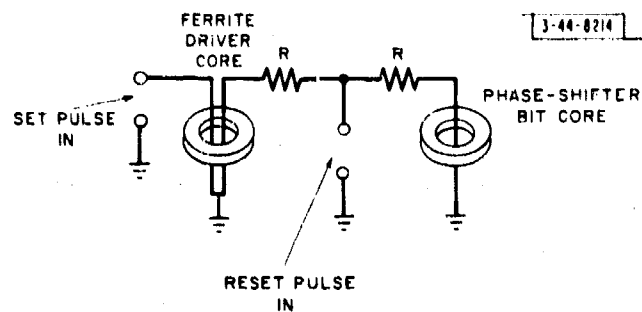


Fig. II-11. Schematic of phase-shifter bit drive.

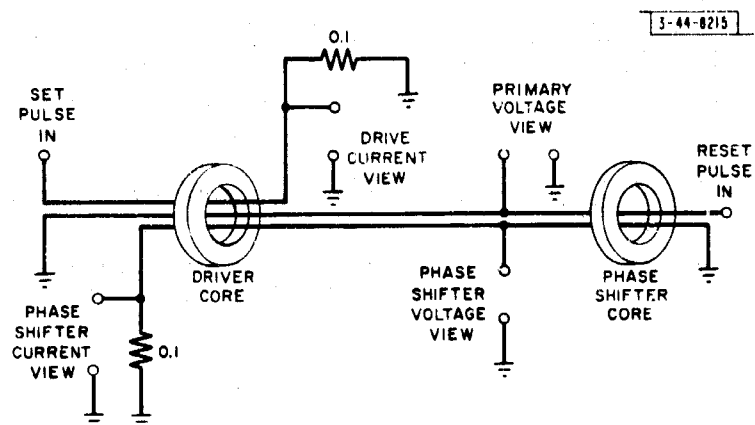


Fig. II-12. Flux drive waveform viewing setup.

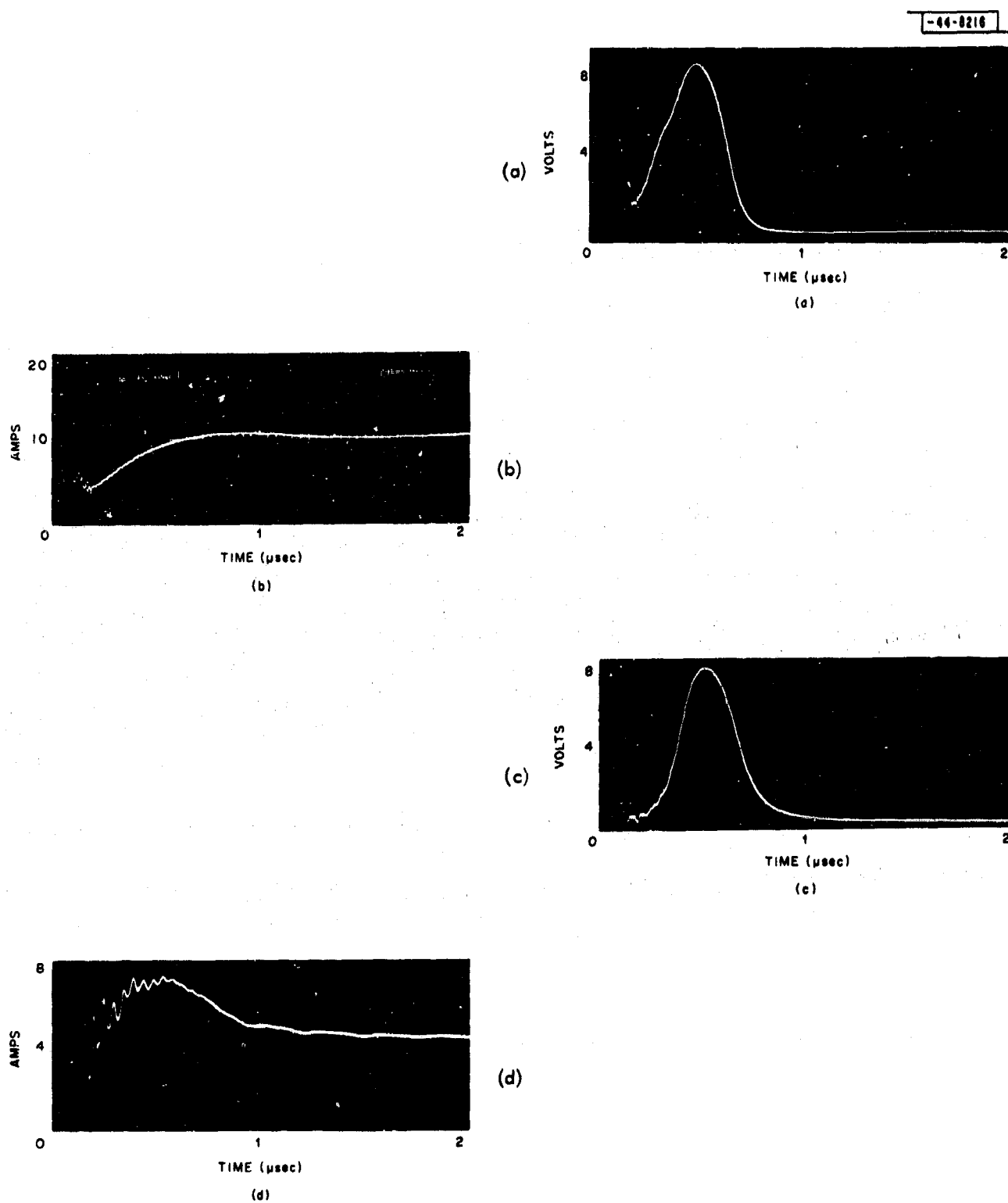


Fig. II-13. Waveforms observed using circuit of Fig. II-11. (a) Primary voltage, (b) primary current, (c) phase-shifter voltage, and (d) phase-shifter current.



in the time between pulses, then decreasing the time between pulses will result in increased efficiency in the transmitters. If, on the other hand, the minimum time between pulses, as set by the phaser steering speed, is longer than the combined rise and fall times of the transmitter modulator, then no penalty in efficiency will be incurred by increasing the time between pulses (i.e., reducing the beam-steering speed).

Thus, if the array is transmitting interleaved bursts of very short pulses in different directions, and if we are in the region between the minimum beam-steering time and one equal to the rise and fall times of the modulators, there is a trade-off available between beam-steering speed and transmitter efficiency. Efficiency can be gained only by speeding up the beam steering when the time between pulses, as set by the beam-steering speed, is less than the combined rise and fall times of the modulator.

Presently available high-power tubes can be turned on or off in times on the order of  $\frac{1}{2}$   $\mu$ sec. Hence, steering times of less than a microsecond are prerequisite to increased efficiency in short pulse burst modes. Tubes now being developed will probably permit much faster modulation, which will lead to higher efficiencies more nearly independent of beam-steering speeds.

Another point of interest is that at which the beam-steering time becomes so long that it adds significantly to the minimum range of the radar. This is probably not a problem area since the phasers discussed in this report can be switched in a few microseconds. However, these minimum range considerations do become a limitation in systems using reciprocal analog phase shifters or switched circulators where beam-steering speeds may be on the order of 100  $\mu$ sec.

Obviously, the steering speeds that can be obtained will be limited by the semiconductor devices used in the phase-shifter drivers. Readily available devices which are relatively inexpensive can provide switching speeds on the order of a microsecond.

#### c. Subarray Control Logic

Each subarray contains sixteen elements; each element contains a four-bit phase shifter, and corresponding phase shifters in every subarray are set to the same phase shift. Hence, to move the beam to a new position it is necessary to calculate a four-binary-bit command for each of sixteen phase shifters and send the resultant 64-bit binary word to every subarray in the array.

The number of 64-bit binary words defined is on the order of  $10^{19}$ . However, the number of usable beam positions which can be resolved by a 16-element subarray made of 4-bit phase shifters is on the order of 4000.

Since the beam position is determined only by the relative differences in phase delay between the various elements in the subarray, adding an identical delay to every element does not change the beam-pointing angle; e.g., if all phase shifters in the subarray are set to zero delay, the subarray will be a broadside beam. Similarly, if all phase shifters are set to  $\frac{1}{2}$  wavelength delay, or  $\frac{1}{4}$  wavelength or any other increment so long as all the phase shifters are set to the same number, a broadside beam will result. In the same manner, equal constants can be added to each phase shifter at any beam position without disturbing the beam-pointing angle. Thus, there are sixteen control words available for each resolvable pointing angle of the subarray. The number of switchings involved in going from one beam position to another can be minimized by selecting, from the two groups of sixteen words, the two words which have the smallest Hamming distance from each other, i.e., by selecting the pair which have the smallest number of unlike bits in corresponding positions.

If the beam-pointing angles which follow each other in time are picked at random, minimizing the number of switchings in steering to  $n$  different beam positions involves calculating and storing  $(16)^n$  sequences of  $n$  numbers and selecting the one whose sum is smallest. This is probably a prohibitive amount of calculation for all but the very shortest sequences. Use of simpler algorithms may provide significant relief in some cases.

#### d. Pulse Driver for Ferrite Phase Shifters

J. DiBartolo

Transistors are available which have rise times of tenths of microseconds, yet are capable of delivering peak currents of up to 10 amp.

In an effort to obtain preliminary information about the behavior of ferrite phase shifters, a driver was implemented as shown in Fig. II-14. Two different type transistors were used to drive the ferrite from one saturated condition to the other, and the related currents are shown in Fig. II-15 where it can be seen that the ferrite core begins to saturate after 0.2  $\mu$ sec with 3 amp of current, and reaches full saturation after almost 1  $\mu$ sec. These waveforms were obtained from driving a 180° bit, S-band ferrite phase shifter.

For obvious economical reasons, one type transistor could be used to switch the core both ways; however, two separate windings would be needed, situated in opposite sense as shown in Fig. II-16. In either case, we recommend driving the transistor well into saturation so that it will provide clamping during turn-on time to eliminate the ringing which is normally present (for an underdamped case) due to stray inductance and capacitance.

More samples of the microwave core to be used in the phase shifter are now available; therefore, a more direct approach will be taken to determine the type driver which will give the best differential phase stability at a reasonable price.

#### e. Pulse Driver for Diode Phase Shifters

Since diode phase shifters are contenders as well as ferrite phase shifters, an equal consideration was given to building drivers for them. When a negative pulse is present at the input of the driver shown in Fig. II-17, both transistors are biased on and the phase-shifter diode is consequently turned on for the duration of the pulse. After the pulse is over, the collector of the output transistor must immediately rise to the full B+ voltage to back-bias the phase shifter. Assuming the transistors recover immediately, it takes 3  $\mu$ sec to bring the back-bias to +280 volts as determined by  $R_2$  and the capacitor C (C is the combination of the stray capacitance, the transistor capacitance and the diode capacitance). However, recovery time can be reduced to 0.3  $\mu$ sec by using the circuit shown in Fig. II-18, where an input pulse turns on  $T_1$  which turns on  $T_2$  and  $T_3$ .  $T_2$  biases on the phase-shifter diode while  $T_3$  turns off  $T_4$ . When the input pulse goes back to zero,  $T_1$  goes off and shuts off  $T_2$  and  $T_3$ . However,  $T_4$  turns on and charges C through its low output impedance, thus reducing the charge time.

As a third choice, one should consider using "gate turn-off" silicon controlled rectifiers (GTO's) as phase-shifter diode drivers. Reportedly, commercial GTO's are available which can control currents up to 10 amp. They have turn-off times of 1  $\mu$ sec and turn-off gains ( $\beta_{off}$ ) of almost 30. Thus, only about 1/30th the current flowing through the device is needed to turn it off. Furthermore, the GTO's can withstand several hundred volts in the anode.

Fundamentally, the price it costs to implement a transistor driver for each bit of a diode phase shifter is lower for low-power phase shifters but, as more diodes per bit are needed to handle the higher power cases, this condition reverses and it becomes cheaper to build drivers

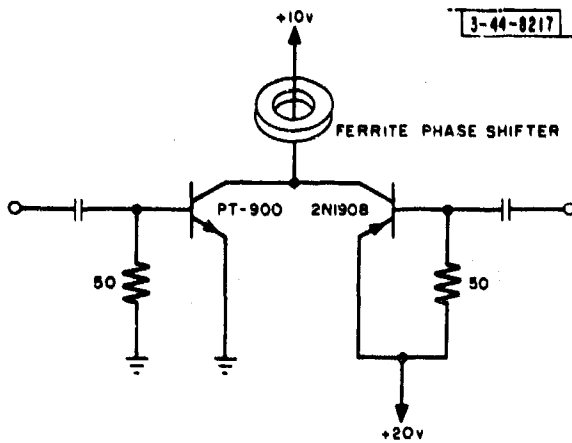


Fig. II-14. Basic configuration used to drive phase shifter.

Fig. II-15. Set and reset currents for a 180° bit of an S-band phase shifter. Calibration is 1  $\mu$ sec/cm for the ordinate and 4 amp/cm for the abscissa.

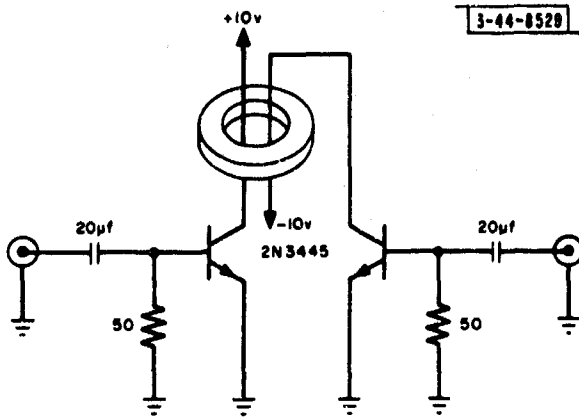
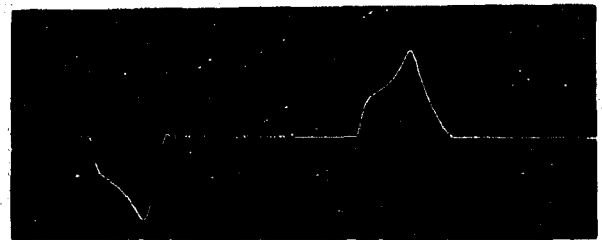


Fig. II-16. Configuration used to utilize two identical transistors.

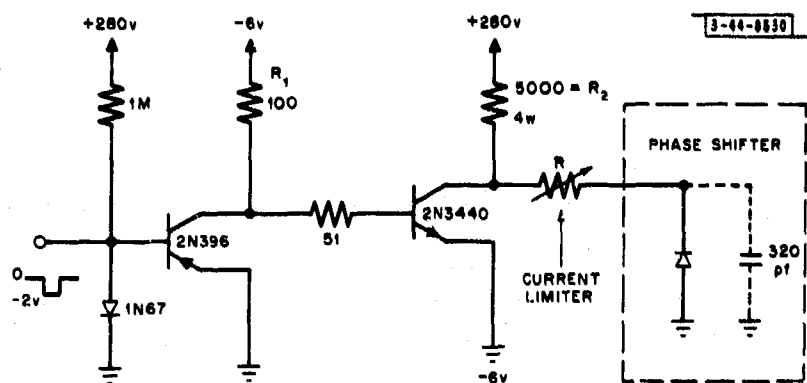


Fig. II-17. Driver for diode phase shifter.

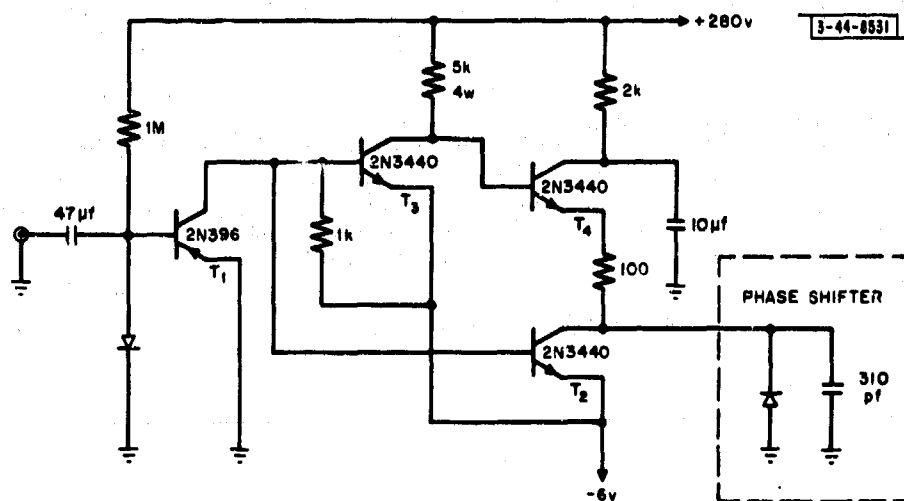


Fig. II-18. Suggested diode phase-shifter driver to improve recovery time.

for ferrite phase shifters. However, if one used GTO's for the higher power case, one can find a balance between the cost of ferrite and diode phase-shifter drivers.

#### E. STATUS AND ESTIMATES OF PHASERS MEETING DESIGN GOALS

As a concluding section in this chapter, an attempt will be made to compare the present development status of diode and remanent ferrite high-power phasers, and to estimate the difficulty in meeting the high-power phaser design goals given at the beginning of the chapter.

A number of parameters of these devices are interrelated; some are not well defined. Table II-1 suggests some key comparisons. Except for the reliability and cost figures, the values listed have been singularly demonstrated and have been chosen since they are similar to those listed in the design goals. The following discussion attempts to clarify the table.

In principle, both diode and ferrite phasers can be designed to handle any peak power. In both cases, the interacting element is decoupled to the degree required, from the transmission line. The interaction length increases with power and the attendant losses decrease the figure of merit (differential phase/db loss). This is graphically depicted in the plot of the figure of merit vs peak-power level in Fig. II-19. The position of a phaser on such a plot and its cost will probably be the best indication of its competitive position with respect to other phasers.

TABLE II-1 SOME KEY COMPARISONS - JUNE 1964			
	Diodes		Ferrites
	1.3 Gcps	3.0 Gcps	
Peak power	16 kw	15 kw	20 kw L- through X-bands
Pulse length (estimated)	200 $\mu$ sec/single pulse	150 $\mu$ sec/single pulse	Set by average power
Average power			
Estimated	1 kw	600 watts	750 watts
Tested	16 watts	15 watts	300 watts (3.0 Gcps)    50 watts (5.6 Gcps)
Figure of merit	240	200	200 (3.0 Gcps)    350 (5.6 Gcps)
Switching speed	1.0 $\mu$ sec		2 $\mu$ sec
Raw driver power	3 watts		$2 \times 10^{-3}$ f (cps) watts
Reliability	Set by diode		Set by driver
Estimated MTBF	$>10^4$ hr		$>>10^4$ hr
Estimated cost/unit in lots of 10,000 ex- cluding tooling cost			
Phaser	\$250		\$150
Driver	\$100		\$100

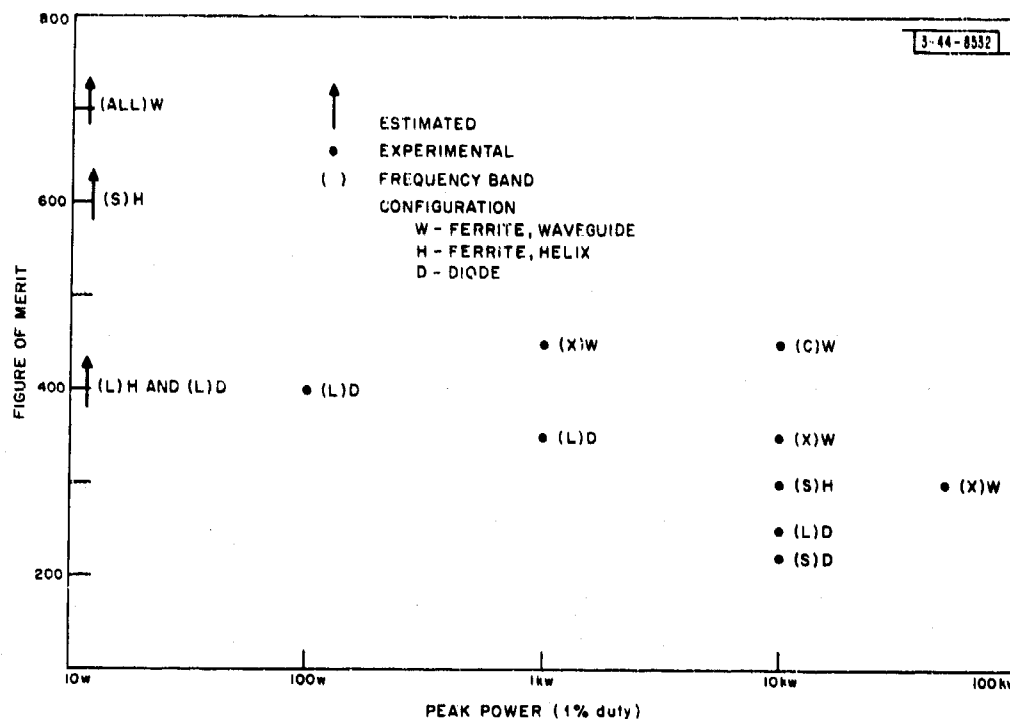


Fig. 11-19. Phaser figure of merit vs peak-power-handling capability (November 1964).

Diode phaser peak-power limits for a given number of diodes have been quite well defined in terms of diode operating parameters.\*† Reliable diode operating parameters are not well defined, but should be forthcoming from diode reliability tests under way at Microwave Associates (see Sec. B-2 of this chapter). The power-handling capability of the individual diode determines the number of diodes required in a high-power diode phaser. The insertion loss is roughly proportional to the number of diodes. Presently, transmission structure losses are roughly equal to the diode loss. Thus, an increase in the figure of merit for a high-power diode phaser will depend upon increasing the individual diode power-handling capability and cutoff frequency, and decreasing the transmission structure losses. A factor of two improvement seems likely, but not a factor of six.

The figure of merit of diode devices would vary inversely with frequency if only the diode loss were significant. Since the transmission structural loss is significant, the change in figure of merit with frequency does not change as rapidly. Bearing the above factors in mind, and noting present diode phaser performance figures, it does not seem likely that diode phasers will meet the design goals outlined in Sec. A of this chapter for C- and X-band frequencies on the basis of loss for the 20-kw level.

Remanent ferrite phasers can presently meet the peak-power and insertion-loss design goals for the S- through X-band frequency ranges. Ferrite materials for L-band will have to be improved to meet design goals at L-band. Present knowledge about ferrite materials is sufficiently limited to make it difficult to venture a good guess whether ferrite material improvements will significantly improve L-band high-power ferrite phaser performance.

\*M. Hines, Proc. IEEE 52, No. 6, 697 (1964).

†J. White, 1964 PTGMIT Symposium, pp. 181-185.

The switching speeds listed in Table II-1 are not fundamental limits but indicate a likely value for reasonable semiconductor driver complexity and control logic. Switching speeds significantly below 1  $\mu$ sec require time-delayed propagation of control signals and more-expensive drivers. The switching energy per switching of remanent ferrite phaser is about 100 microjoules for 2- $\mu$ sec switching speed; thus, the raw driver power is repetition-rate dependent as listed. For the diodes, if one assumes that half the diodes are forward biased at a value of 200 ma all the time, the raw power dissipated by a 32-diode phaser required for the 20-kw level is about 3 watts. Rough estimates of the semiconductor driver complexity and cost are not significantly different. Thus, the conclusion is that driver and switching-speed considerations for the diode and ferrite phasers are not sufficiently different to be a significant factor in the choice between the two types of phasers.

The reliability figures listed in Table II-1 are essentially an estimate made after studying available data and the problem. Properly designed ferrite phasers should be inherently reliable; ferrites are chemically homogeneous. When a transient overload occurs, the ferrite phaser will heat up, but will immediately recover after overload if RF breakdown does not occur during the overload. In contrast, the diodes in a diode phaser generally will burn out or suffer irreversible damage in a transient overload. Reliability testing of microwave-switching diodes has not progressed sufficiently to determine good mean-time-between-failure figures for the diode phaser.

The semiconductor driver will determine the reliability of the ferrite phaser-driver combination. The estimates listed in Table II-1 reflect the view that the diode phaser will determine the reliability of the diode phaser-driver combination. All that can really be stated at this time is that phaser-driver characteristics urgently require careful study and effort.

Cost estimates in Table II-1 were arrived at by considering the number and kinds of piece parts in these devices. The ferrites may have a cost advantage unless the production price of a high-power microwave-switching diode decreases to about one dollar.

There appears to be no significant difference between the two types of phasers with respect to size, phase and amplitude tolerances, bandwidth, and reproducibility.

## **F. ACKNOWLEDGMENTS**

The authors wish to thank J. A. Weiss, Dr. A. Uhlir of Microwave Associates, Inc., H. A. Hair of General Electric Company, E. Stern of Microwave Chemicals Laboratory, Inc. and J. Kempic of Westinghouse Electric Corporation for their many helpful discussions.

## CHAPTER 4 RF POWER DISTRIBUTION AND CIRCULATOR

D. H. Temme

### SUMMARY

This chapter lists the requirements as presently known for the RF power distribution and circulator network. Several power dividers are discussed in terms of electrical performance and packaging size. Some incomplete test data are given on the three-port waveguide circulator to be used initially in the S-band subarray.

The RF power distribution network for a subarray should (a) distribute the input power to the  $n^2$  outputs ( $n$  elements per side) with equal phase and amplitude, (b) provide a good match to the power amplifier, and (c) have a cross section less than  $n\lambda/2$  on a side. This chapter describes the distribution network for the experimental S-band subarray, and some initial results of incomplete studies of the problem.

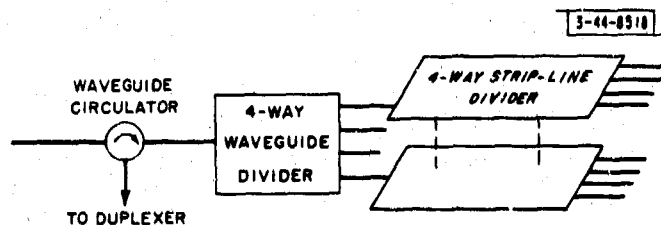


Fig. II-20. S-band RF distribution network.

Figure II-20 is a block diagram of the distribution network for the S-band subarray. The last two stages of power division use plastic strip-line devices for space reasons, since waveguide devices with good isolation between the output ports are very difficult to package in  $n\lambda/2$  by  $n\lambda/2$  space. The first 4-way power division occurs in a waveguide divider since it can readily handle the peak power. A three-port waveguide circulator provides a match for the power amplifier and routes the received energy, if the subarray performs both the transmit and receive functions. In the following discussion, some of the known limitations and advantages of different power dividers are discussed, after first describing some unknown characteristics of the load.

The match of a planar array antenna varies considerably with scan angle. The VSWR range to be expected is from about 1.0 to 2.5. If a reciprocal phaser is used behind each antenna, the power divider must have good isolation between output ports to insure that the incident wave at the output ports is equal in phase and amplitude. If a nonreciprocal ferrite phaser is used, the isolation requirement of the power divider may be relaxed; i.e., if the reflection coefficient of each antenna is the same, the reflection coefficient at the input of all the nonreciprocal phasers is the same, since the round trip phase through a nonreciprocal phaser is a constant for all phaser settings. Thus, all the reflected energy sums at the input port of the power divider, and this energy can be dumped in a single load by the circulator. The question, of course, is how



good is the assumption of identical reflection coefficients of an array antenna. What happens at the edge elements? What deviations in reflection coefficient occur when an array is excited with a stepped phase front resulting from the use of digital phasers? While the means to answer these questions are now at hand for at least one type antenna element in the computer program described in Part III, a detailed investigation has not yet been made.

The initial strip-line dividers will use "rat-race" hybrid rings, which are simple but have undesirable phase and amplitude characteristics. The amplitude characteristic is given by Reed and Wheeler\* who indicated that the amplitude unbalance between the two output ports of a  $1.5\lambda$  rat-race hybrid ring is 0.14 db for a 12-percent band. Carrying along the phase terms for the computation gives a phase unbalance of  $3.8^\circ$  for the 12-percent band. These values increase  $n$  times in an  $n$ -level divider to unacceptable values.

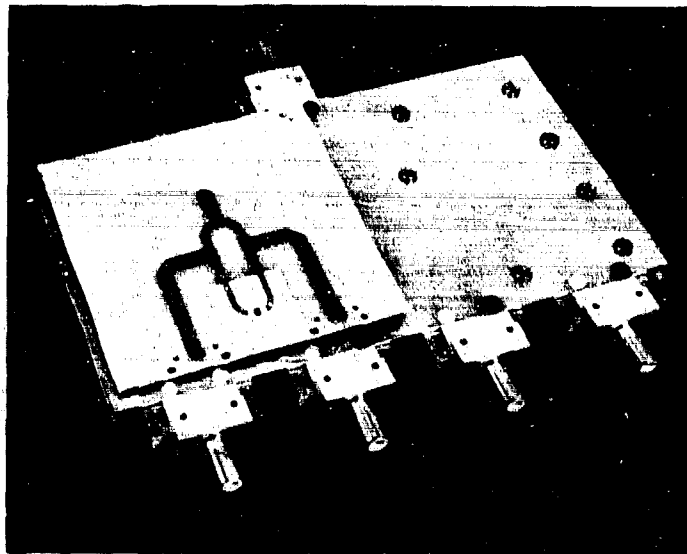


Fig. II-21. TEM power divider.

A TEM power divider equally simple to construct is a ring hybrid with a series termination.<sup>†‡</sup> Figure II-21 is a photograph of such a divider which has equal phase and amplitude characteristics because of its symmetrical construction. The problem with this divider is making the series termination capable of absorbing the high power that might result from, for example, failure of an antenna or phaser. It is desirable that the termination be made as long as possible to improve its power-handling capability. The electrical length of the termination can be accommodated in the configuration shown in Fig. II-21. All that is required is that the termination branch be effectively a wavelength long between the output ports, and that the frequency sensitivity of this configuration be not significantly greater than the configuration described by Dent,<sup>‡</sup> where a short resistor directly connects the output ports. In one case, the frequency sensitivity is controlled by the combination of a  $\lambda/4$  dividing branch and a "zero" length resistive branch; in the other

\*J. Reed and G. J. Wheeler, Trans. IRE, PGMTT MTT-4, 246 (October 1956).

†W. Tyrell, Proc. IRE 35, 1294 (1947).

‡J. Dent, Electronic Design 8, No. 8, 52 (31 August 1960).

case, by the  $\lambda/4$  dividing branch and the  $\lambda/2$  branch to the termination. In each case, the frequency sensitivity is essentially determined by a  $\lambda/4$  frequency sensitivity and can give isolations in excess of 25 db for a 10-percent bandwidth.

The length of the termination cannot be very long, however, before the insertion loss is significantly affected. When the electrical length of the resistor is  $20^\circ$ , the added insertion loss is about 0.05 db. Even a resistor of this length has significant average-power capability if the resistor is a metal film evaporated on a beryllia block thermally connected to the ground plane. When the ground plane was held to  $30^\circ\text{C}$  with a water-carrying copper tube attached, 20 watts was easily achieved. The limiting factor is the voltage breakdown of the resistor, which is about 3 volts/mil or about 500 volts. If impedance transformers are used in the termination branch, the termination can be reduced to 50 ohms from the nominal value of 100 ohms without significant bandwidth reduction, giving a peak power in the termination of about 2.5 kw. This has been considered marginal for our subarray application. If one resorts to additional construction complexity, a compact TEM structure with acceptable "equal amplitude-phase" characteristics can be built. For instance, one might bring out the series termination with a wide band balun,\* but such possibilities have not been investigated.

The waveguide divider for the S-band array is being fabricated by Microwave Development Laboratories. An in-line waveguide-to-coax adapter, similar in type to one described by Wheeler,† is used. The length of the waveguide divider plus transitions is about 18 inches. It was decided not to compact the package to the ultimate degree at this time.

The waveguide circulator is an Airtron Model F315F (335775) with an improved high-power ferrite. The nonlinear threshold for this ferrite occurs above 300 kw. The average power-handling capability will not be determined until the power source for the subarray is available (see Part II, Ch. 3, Sec. C-5-c). It is expected to be marginal, if not inadequate. This limitation can be circumvented by using multiple circulators (for example, one at each output of the waveguide divider). This, of course, is a less-desirable solution.

In conclusion, the RF distribution network study has not been completed. The initial S-band subarray tests will be conducted with a less-than-optimum network, but will not significantly affect test results.

---

\* V. J. Albanese and W. P. Peyser, Trans. IRE, PGMTT MTT-6, 369 (October 1958).

† G. J. Wheeler, Proc. IRE Natl. Conv. Vol. 5, Part 1, 182 (1957).

## CHAPTER 5

### TRANSMITTER AMPLIFIERS

#### SUMMARY

This chapter contains a brief discussion of the physical and electrical requirements that the subarray transmitter amplifiers must meet. The state of the art of the microwave tube, as related to S-band subarrays, is discussed.

#### A. INTRODUCTION

L. Cartledge

As has been noted in Part II, Ch. 1, one or more transmitter amplifiers must be used between the delay-shifter output and the phase-shifter inputs in the subarray. No development of such an amplifier is being conducted by Lincoln Laboratory. Limitations in manpower and funding permit us to study only the requirements for the power amplifier and to observe the developments of others.

The electrical and mechanical requirements which these amplifiers must meet are dictated in part by system requirements and in part by the capabilities of other components in the subarray. These requirements are discussed in Sec. B below. A cursory survey of available tubes indicates that some development will precede the appearance of the tube that is well suited to this use. This survey is outlined in Sec. C of this chapter.

#### B. AMPLIFIER REQUIREMENTS

Power:- The peak power required is determined by the product of the number of elements which the amplifier must drive and the peak power per element. Our S-band component development has been centered around a value of 10-kw peak per element, and subarray sizes from 16 to 64 elements. After allowing for some losses, the peak power required per subarray might then be on the order of 250 kw to 1 Mw. Nothing restricts us to a single amplifier per subarray; however, our experience has been that, within a given type tube, best economy is obtained by using the largest size possible.

Duty cycles of 1 or 2 percent seem to be reasonable.

Gain:- Gains as high as 40db or so may be required, depending upon the delay-shifter development and upon the peak-power output of the amplifier. Amplifiers may consist of more than one stage; however, unless otherwise noted, all other requirements must be regarded as applying to the complete amplifier rather than to a single stage.

Bandwidth:- The amplifier must meet all other listed requirements over a bandwidth which is wider than the desired system signal bandwidth. This is because the amplifier is one of many components in cascade. Applications for arrays with 10-percent bandwidth have been discussed seriously.

Phase and Amplitude Stability:- The standard deviation of the absolute value of the complex difference between the actual RF output current and the desired output current, when averaged over a large number of amplifiers operating in an array, must be less than some number set by a "system error budget." This error budget, in turn, is set by the desired sidelobe performance of the array. The amplitude of this rms error will usually be in the neighborhood of 10 percent of the desired output voltage.

Evolution of economically feasible means to insure that this requirement is being met would seem to be an important part of the tube development effort.

Size, Shape, etc.:- It is desirable that the cross section of the electronics behind an array radar aperture, at about the same size as the aperture itself, be maintained. This leads to an objective that the amplifier fit through a square hole which has sides given by the relation

$$S = \lambda \sqrt{\frac{\hat{P}_a}{\hat{P}_e} D_x D_y}$$

where

$S$  = length of one side of the amplifier pigeonhole

$\lambda$  = shortest wavelength in the same units as  $S$

$\hat{P}_a$  = amplifier peak-power output

$\hat{P}_e$  = peak power required per element

$D_x, D_y$  = element spacings (in wavelengths at the highest frequency in two orthogonal principal planes, assuming a rectangular grid)

At S-band and 10 kw per element, this leads to pigeonholes which are about  $\sqrt{2\hat{P}_a}$  cm on a side.

This cross-section restriction is the most important size restriction on the amplifiers. It must be applied to the interconnecting cables and other support hardware as well as to the actual amplifying device. There is little restriction on the length of the amplifiers so long as they can be replaced readily.

Life:- End of life can be defined as that time when the absolute value of the vector difference between the actual output current and the desired output current exceeds some value. This value can be expressed as some multiple of the standard deviation error which is allowed by the system error budget. Exactly how many standard deviations will be allowable is a function of both the system requirements and the history of the particular tube type. Values on the order of two or three standard deviations seem reasonable.

The average life required is a function of the system usage. Clearly, surveillance radars and other systems which must be on the air continuously require very long tube lives in order that tube replacement costs be held to a reasonable value. In radars which are used for short periods of time, and are in a stand-by or off condition most of the time, long life may not be so important as "graceful" turn-on characteristics. Tube lifetimes of a few thousand hours seem reasonable for the latter case, while continuous-duty systems would seem to require average tube lifetimes on the order of 20,000 hours or so to be economically desirable.

Signal Waveforms:- Optimum use of the array radar often involves transmission of bursts of short pulses. Bursts of up to 50 pulses, having pulse lengths of less than 0.1  $\mu$ sec and spacings down to a few microseconds, have been proposed. Hence, tubes which operate at this type duty will be required. This requirement complicates the modulator design problem.\*

Desirable Characteristics:- Low operating voltages are desirable. [Very high operating voltages pose a number of problems: e.g., insulation, x-ray shielding, large cables for distribution, etc.] Hence, if all other things about types were equal, a type with significantly lower operating voltage would be preferred.

\* For a detailed discussion of this problem, see M. Siegel in TR-299, p. 191.

Similarly, other desirable characteristics are: light weight, no external magnetic field requirement, and a high-gain modulating element with low stray capacitance.

Interactions: - Amplifiers must be well shielded enough that no harmful interactions occur when they are operated in proximity to each other. The center-to-center spacing will correspond to the size of the pigeonholes outlined earlier.

### C. EXISTING TUBES AND DEVELOPMENT POSSIBILITIES

"O"-Type Beam Tubes: - This class consists of traveling-wave tubes, klystrons and some hybrid combinations of the two. Varian catalogs list a TWT (VA-136) which they claim will produce at least 100 kw at 0.05 duty over a 400-Mcps band at S-band. This tube requires a solenoid and operates at 36 kv; it can be obtained with a modulating anode ( $\mu = 1$ ), and has a gain of 30 db. Installed in its solenoid, this tube occupies a space some 36 in. long and 12 in. square, and weighs more than 60 lb. The solenoid weighs approximately 200 lb.

Hughes Microwave Tube Division has made PPM focused tubes which produce more than 250-kw peak power over a 500-Mcps band at S-band. These tubes operate at beam voltages higher than 55 kv. Typically, they are 31 in. long and approximately 6 in. in diameter. These tubes have been limited in duty-cycle capability to something less than 1 percent.

Varian lists a VA-125 which, according to their catalog, can produce 2-Mw peak power at 0.002 duty over a 300-Mcps band at 2750 Mcps. This tube runs in a solenoid and is cathode modulated at a beam voltage of 120 kv. It is  $43\frac{1}{2}$  in. long and weighs 120 lb. exclusive of its solenoid.

Under development at Litton is an electrostatically focused klystron aimed at producing 250-kw peak at 2-percent duty over about 7-percent bandwidth at S-band. This tube will be cathode modulated at a beam voltage of 50 kv. The probability of meeting most of these objectives seems high. Because the tube is electrostatically focused, it should be much lighter and smaller than magnetically focused tubes with the same ratings.

From the above it is clear that O-type tubes capable of the power, bandwidth and gain desired are entirely feasible. Meeting all these within the size restrictions may not be so easy, and the O-type tubes are the least-stable class under consideration. Hence, meeting the stability requirements with O-type tubes would require better power supply regulation than with other types.

Further, development of a TWT to produce 250-kw peak power at voltages below 40 kv represents more than just extrapolation from existing devices. The beam voltage of a TWT can be estimated from the relation:

$$E = \left[ \frac{\hat{P}}{K\eta} \right]^{2/5}$$

where

$\hat{P}$  = peak-power output in watts

$K$  = beam perveance in perva

$\eta$  = beam efficiency (with the collector and circuit at the same voltage)

Most present-day TWT's operate at efficiencies of less than 25 percent and at perveances of less than 2 micropervs. Development of an S-band tube to meet the other requirements and to run

at 3 micropervs and 25-percent efficiency would be a major undertaking. Accurately predicting a schedule for such a job would be extremely difficult.

Similarly, a low-level modulating element for TWT's with this much peak and average power seems to be outside the present state of the art. Some work sponsored by the U. S. Army is in progress at Sylvania Electric Products, Microwave Device Division; however, it is a rather low-level effort.

"M"-Type Beam Tubes:— As a class, M-type amplifiers are a relatively new development, and are not so well understood as O-type devices. M-type tubes seem to offer somewhat better phase stability with respect to applied voltage than that obtainable from O-types at the same power levels. Further, M-types usually operate at significantly lower voltages than O-type devices at the same power levels. On the other hand, M-type tubes usually require stronger and more accurate magnetic fields than equivalent O-types.

The best known M-type amplifying device is the re-entrant-beam backward-wave "amplitron" pioneered by Raytheon Manufacturing Company. S-band amplitrons, which will provide 200-Mcps bandwidth at higher peak and average powers than we require, are in production (e.g., QKS-622). They are efficient, can be run with cold cathodes, and are reasonably small, although it is not clear that existing types could meet our size and shape requirements without some modification. They operate with lower voltages than O-type tubes for a given power.

Amplitrons are essentially constant-current devices. Hence, if broad-band operation is desired the amplitrons must be operated from a current source, as the voltage across them varies as a function of the signal frequency.

A more disturbing disadvantage is the fact that the amplitron behaves very much like a locked oscillator. In normal usage, the RF drive must overlap the video drive or spurious outputs and possible destruction of the tube result. These characteristics make satisfactory operation at very short pulsewidths very difficult to achieve.

A second M-type device is the re-entrant-beam forward-wave amplifier. This device has been pioneered by SFD Laboratories, now a subsidiary of Varian Associates. Cold cathode types, which are operated with DC voltage applied to the cathode, turned on by the incident RF signal and turned off by relatively low energy video pulse, have been operated in the laboratory from L- through X-bands with the exception of S-band. At S-band, the peak and average powers we require do not seem to present much of a problem. The tubes can be made quite small, although packaging the tube and associated magnet in pigeonholes as small as we require might well entail considerable difficulty.

Short pulse operation of these tubes is possible. When using the input RF to turn on the tube, the pulse rise time is limited to values longer than about 10 or 15 nsec. This limitation is met because the buildup of re-entrant electron beam through secondary emission takes several "laps." The video turn-off time is limited only by the rise time of the video pulse. Some care must be taken in system designs using these tubes in short pulse applications to insure that the video turn-off pulse and the end of the RF driving pulse are synchronized. Several kilowatts of RF power are required to start the secondary emission process.

Non-re-entrant forward-wave injected-beam M-type amplifiers have been developed in France by CSF, and later in this country by Raytheon and Litton. CSF is producing these tubes (called TPOM's) at the 1-Mw peak-power level at L-band. Litton has made various low-power models of this type. There is reason to believe that an S-band tube of this type could be developed to meet our requirements.

The latest variety of M-type tube to appear is the distributed emission non-re-entrant-beam forward-wave amplifier developed by Litton and named DEMATRON. This tube is operated with a cold cathode and DC plate voltage applied, and the electron beam is both turned on and off by the RF input power using a secondary emission process. The beam is non-re-entrant, and the electrons are collected at the downstream end of the interaction space. Laboratory tubes have operated at 50-kw peak at X-band, and at higher power at S-band. This is a relatively new device, but there is reason to believe that a device to meet our specifications could be built. If so, it would be desirable because of the ideal RF pulsing characteristics and because it would operate at relatively low voltage. These tubes are limited to relatively low gain because the secondary emission process requires several kilowatts of RF power input.

Gridded Tubes:- RCA has developed a class of integral cavity triodes, called "Coaxitrons" because of their coaxial geometry. These tubes have been built from VHF up through 900 Mcps (producing up to 1-Mw peak at 900 Mcps). VHF and UHF tubes are now catalog items.

Triodes have a number of features that make them very desirable for use in array transmitters. They are much smaller and lighter than tubes which require magnetic fields, their phase stability is outstanding, and they operate at relatively low plate voltages and high efficiency. The possibility of developing Coaxitrons or something similar for use in at least the low-power stages of the subarray amplifier should be investigated.

#### D. MODULATORS

M. Siegel

In a previous report,\* it was shown that the over-all efficiency of a transmitter can become very poor (as low as 5 or 10 percent) when short pulses or pulse bursts are required. The two major sources of video energy loss in short pulse applications are: (1) energy wasted in charging and discharging circuit and tube stray capacitance, and (2) energy wasted in the transmitter tube during the rise and fall periods of the video pulse. Typically, to produce 0.1- $\mu$ sec pulses using plate modulation or low mu grid modulation (modulating anodes) with "O"-type beam tubes (klystrons or TWT's), over-all efficiencies of 5 to 10 percent are to be expected. Whereas, if "M"-type beam tubes are used, over-all efficiencies of 10 to 15 percent are to be expected (even though some M-type devices have DC to RF conversion efficiencies of up to 70 percent).

To maximize efficiency, conclusions drawn from this report were: (1) stray capacitance associated with cathode-to-anode and cathode-to-grid circuits should be minimized; and (2) grid modulation with the highest mu obtainable should be used when possible.

Another possibility exists when providing modulation for pulse bursts. Instead of providing individual video modulation for each narrow pulse within the burst, video envelope modulation embracing the entire burst is provided, while the individual narrow pulses within the burst are generated by gating the RF drive to the power amplifier. This eliminates the wasting of considerable energy in the charge and discharge of the power tube and its associated capacitance, but considerable video energy can be wasted in between the individual narrow pulses unless special effort is made to design a power tube that has very low beam current when the RF drive is removed. An additional problem with envelope modulation is that considerable limitations are placed on the design of the pulse burst if reasonable over-all efficiencies are to be had.

---

\* See TR-299, pp. 191-204.

It presently appears that the optimum modulation scheme will be available (in the near future) within certain M-type tubes where DC beam voltage is continuously applied between anode and cathode, and the RF drive gates the beam current both on and off.

One further comment is perhaps in order with regard to the interrelationship between the modulator and the fault protection. Adequate fault protection becomes a serious problem when phased array transmitters are considered. Very often the modulator can be designed to also serve as a fault protection or fault limiting device, to protect the tube or the system in case of failure. Systems which allow DC high voltage to be continuously applied to the transmitter tube will require careful consideration with regard to energy storage, fault protection and isolation.

#### **E. HIGH-POWER S-BAND TEST SOURCES**

L. Cartledge

In order to demonstrate that the peak- and average-power capabilities required of the various components and of the assembled subarray have been met, a high-power RF source will be required. To meet this requirement, we have ordered a VA-136 traveling-wave tube which is rated at 100-kw peak at 5-percent duty. High-voltage DC and modulating voltage for the VA-136 will be supplied by a transmitter that was declared surplus on another Lincoln Laboratory program. This source does not meet all the subarray parameters, but it is the best compromise we could make using available tubes.

RF drive for the VA-136 will be supplied by a pulsed triode oscillator. This oscillator can also be operated, at lower duty cycles, at peak-power levels up to 10 kw. It will be used in this mode for testing peak-power capabilities of individual components.



**CHAPTER 6**  
**MISCELLANEOUS COMPONENTS**  
D. H. Temme

**A. DUPLEXERS**

Because of limited manpower and funds, it was decided not to allocate effort toward duplexer design since it has not been considered as important a problem as others discussed. Several solutions are possible: diode duplexers, switching 4-port circulators utilizing 90° differential ferrite phasers and hybrids, etc. The relative merits of the various solutions have not been studied.

**B. INPUT CIRCULATOR**

There are a number of existing commercial circulators suitable for the input circulator. They must have low insertion loss ( $< \frac{1}{2}$  db) and good isolation ( $> 20$  db) over a 15-percent bandwidth. The units must track in amplitude ( $< 0.2$  db) and phase ( $< 2^\circ$ ) over the 10-percent band and a 10° differential ambient temperature.

## CHAPTER 7

### RECEIVER PREAMPLIFIERS

#### SUMMARY

W. J. Ince

In this chapter, the requirements of a subarray preamplifier are discussed. For this application, tunnel-diode and transistor amplifiers have been investigated. Experimental results are discussed which demonstrate that the tunnel diodes usually used in microwave amplifiers, having a negative resistance in the range 50 to 100 ohms, are not suitable. A technique utilizing high peak current tunnel diodes in cascaded amplifiers, which enables the dynamic range to be improved by about 20 db, is described. Results of a long-term stability test on a number of tunnel-diode amplifiers, utilizing conventional diodes, are presented.

The development of an L-band transistor amplifier is also described. A 4-stage strip transmission line version having about 20-db gain and 6-db noise figure has been designed. Coaxial transistor circuit configurations have also been investigated, and the results are given.

#### A. INTRODUCTION

In the choice of a suitable low-noise preamplifier for the subarray, there are two main problems to consider in addition to those encountered in the scheme which utilizes one preamplifier per receiving antenna element.

##### 1. Increased System Loss

Digital time delays have inherently more loss than digital phase shifters. If we consider a phased array and a time-delayed array, both having diameters of roughly 100 wavelengths and having the same degree of control on beam positioning, the beam-steering losses would differ by about 10 db. Hence, the preamplifier should have more gain in the case of the time-delayed array than for the phased array situation. The appropriate amount of gain required depends, of course, on the particular radar configuration used and the operational requirements which must be met. However, a minimum gain of 20 to 25 db for the subarray preamplifier seems a reasonable value.

Since the loss in the duplexer, power summing-divider network, and phaser between the antenna and the preamplifier increases the equivalent receiver noise temperature, it does not appear worthwhile to expend much effort to obtain a preamplifier noise figure less than about 6 db.

##### 2. Dynamic Range

The power summing-divider network increases the signal input to the preamplifier by a factor of 16. This fact, in addition to the increased gain, makes the dynamic range requirement accordingly greater.

#### B. DESIGN GOALS FOR SUBARRAY PREAMPLIFIER

The objective parameters for a subarray preamplifier are:

Frequency	L- through X-bands
Gain	20-db minimum
Bandwidth	15 percent (at 1.5-db gain compression)
Noise figure	<6 db
Saturated output power (at 1-db compression)	$\geq -10$ dbm
Input match	<2:1
Output match	<1.3:1
Stability	Unconditional for all input and output matches
RF overload	50 mw CW
Size	Maximum transverse dimension < $1.7\lambda$
Amplitude tracking	$\pm \frac{1}{2}$ db over 10-percent bandwidth
Phase tracking	$\pm 3^\circ$ over 10-percent bandwidth
Reliability	>100,000 hours

The basic assumption has been made that only a solid state device will be suitable as a pre-amplifier. For the usual reasons of low cost and simplicity, the ultimate selection considered is between the tunnel diode and the transistor. We are studying both these devices in an attempt to develop suitable amplifiers to cover the frequency range L- through X-bands.

### C. TUNNEL-DIODE AMPLIFIERS

The outcome of earlier work, reported in TR-299, indicated it was possible to construct relatively inexpensive and stable tunnel-diode amplifiers. Such devices are now commercially available over the entire frequency range L- through X-bands. However, the dynamic range of a typical tunnel-diode amplifier is limited. Since this parameter is of fundamental importance in array applications, an investigation of the effects of dynamic limitations on amplifier performance has been made. The amplifier used for this investigation was one based upon a design described in detail in TR-299. This amplifier utilizes a germanium diode (MicroState type MS-1047) having a minimum negative resistance of 60 ohms. Figure II-22 shows a pen recording of the

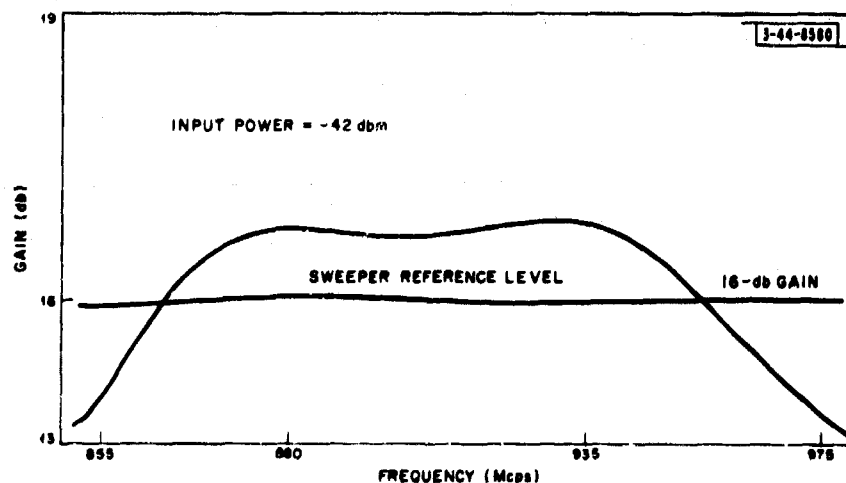


Fig. II-22. Wide-band tunnel-diode amplifier gain vs frequency response.

swept frequency response of the amplifier and, for reference, the relative power output response of the sweeper. Figure II-23 gives the amplifier noise figure as a function of frequency, and Fig. II-24 shows three point-by-point gain plots of the same amplifier vs input power. The curves were taken at the center frequency and approximately at the 3-db points. It can be seen that the 1-db saturation point occurs for a higher output power at the 3-db frequencies than at the center frequency, where the gain is larger. In fact, the dynamic range of a tunnel-diode amplifier can be improved by replacing it with two amplifiers in cascade, each having half the gain of the original amplifier.

Figure II-25 shows the relative insertion phase (modulo  $2\pi$ ) through the amplifier vs frequency. It is important that all preamplifiers track in phase under all operating conditions. Figure II-26 illustrates what happens as the input power to the amplifier is increased. There is a change in insertion phase, which is not the same at all frequencies but increases toward the band edges. For large target returns, this phase modulation could cause large errors in pointing accuracy or cause considerable distortion of the beam. It is possible that some form of sensitivity time control or AGC would alleviate this problem, but the radar would still be vulnerable to random jamming.

Figure II-27 shows the variation of preamplifier gain vs tunnel-diode bias, which is often used as a method of gain control. However, Fig. II-28 indicates that there is a corresponding change in insertion phase, which makes the method unworkable for STC or AGC. A possible solution would be to use equal-length stepped attenuators placed in front of every preamplifier, although such additions begin to detract from the main advantage of tunnel diodes, namely their simplicity.

Intermodulation (IM) distortion is also a sensitive function of the signal level. The relative level of the first-order IM product (i.e.,  $2f_1 - f_2$ ) was measured when two equal amplitude in-band signals were injected into the amplifier. The results were as follows.

Input Level (db)	Gain of Amplifier at $f_1$ (db)	Gain of Amplifier at $f_2$ (db)	IM Distortion Level Relative to Output Level at $f_1$ (db)
-45	18	17.1	-22
-50	19	17.8	-29
-55	19.5	18	-40

IM distortion is undesirable because it gives rise to spurious targets.

#### D. DEVELOPMENT OF IMPROVED TUNNEL-DIODE AMPLIFIER HAVING EXTENDED DYNAMIC RANGE

It is clear that for the tunnel-diode amplifier to provide an acceptable level of performance, at least an order of magnitude improvement in dynamic range is required. Lincoln Laboratory is sponsoring, under subcontract, work by RCA Microwave Tube Operations Department to develop such an amplifier with the objective of obtaining a 1-db saturation output level of -10 dbm. The theory and description of the proposed technique have been described by Steinhoff and Sterzer.\* Salient features of the design are:

\* R. Steinhoff and F. Sterzer, RCA Review 25, No.1, 54 (March 1964).

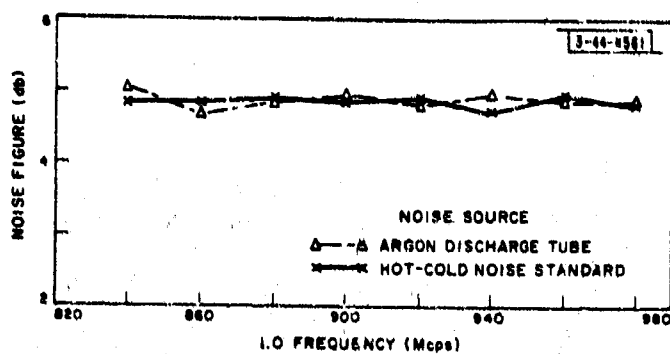


Fig. II-23. Noise figure of wide-band tunnel-diode amplifier.

Fig. II-24. Wide-band tunnel-diode amplifier No. 1, gain vs input level.

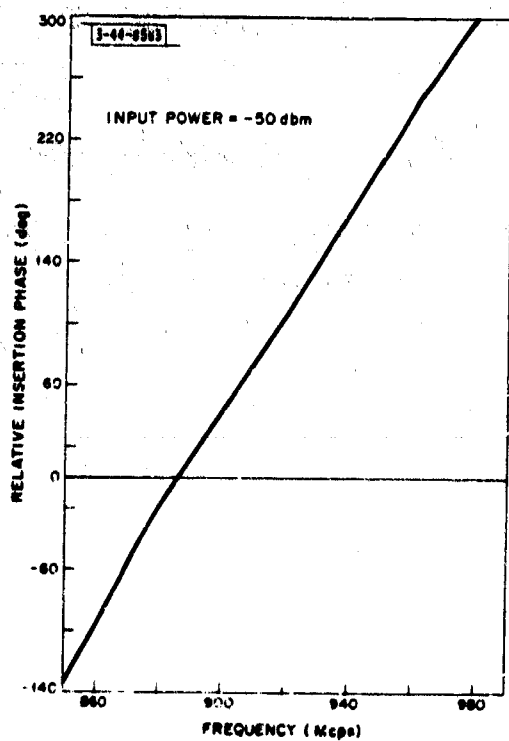
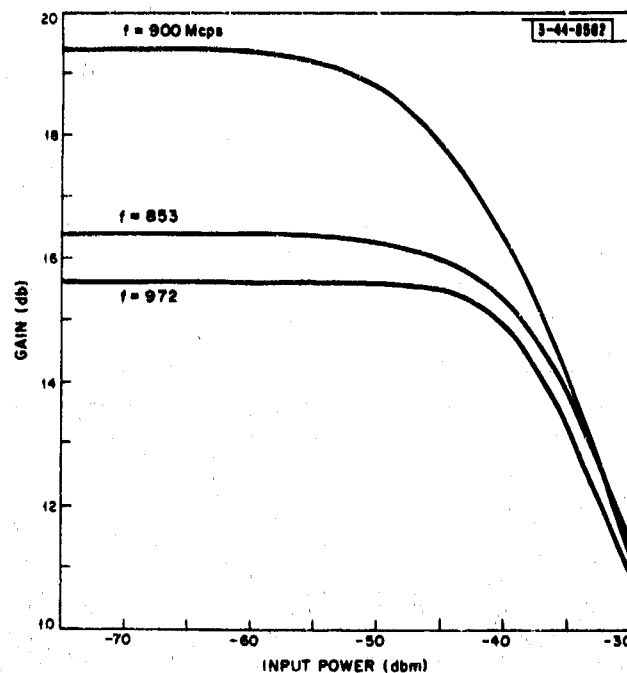


Fig. II-25. Relative Insertion phase vs frequency of tunnel-diode amplifier.

Fig. II-26. Relative phase vs input level of wide-band tunnel-diode amplifier No. 1.

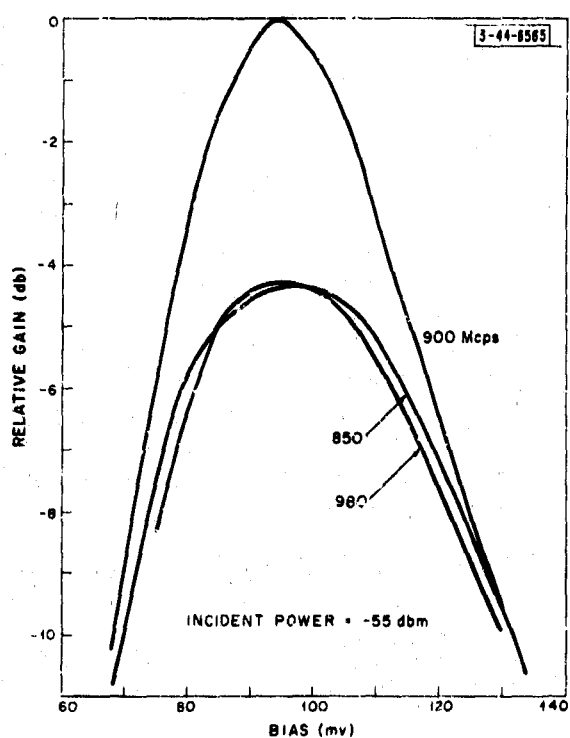
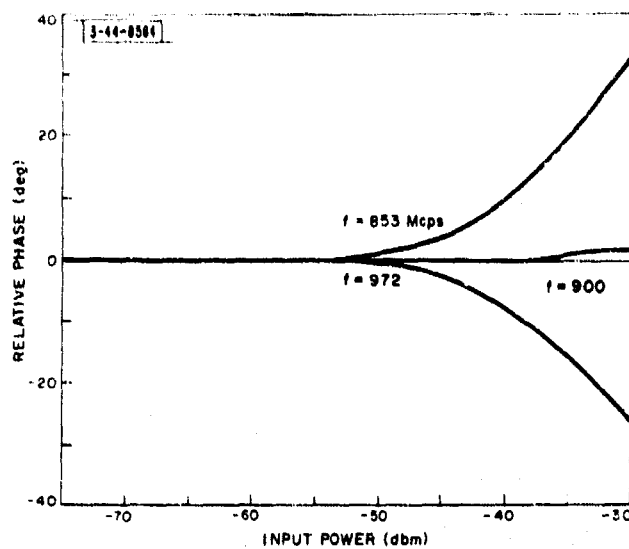
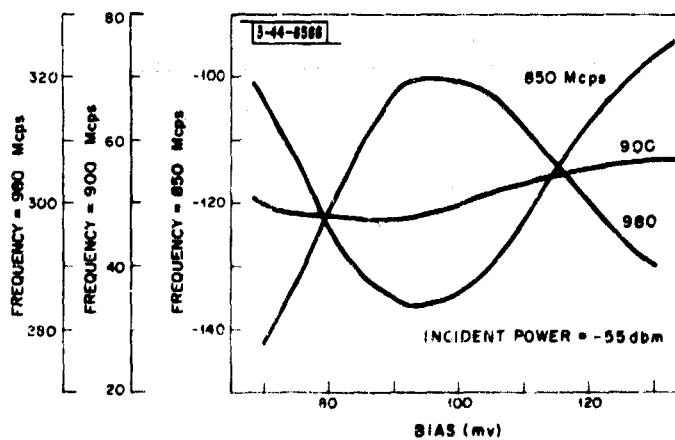


Fig. II-27. Variation of gain vs tunnel-diode bias.

Fig. II-28. Variations of phase shift (in degrees) with bias.



- (1) Use of two relatively low gain cascaded amplifiers instead of a single amplifier having relatively high gain.
- (2) Use of a germanium diode in the first stage and a gallium-arsenide diode in the output stage.
- (3) Use of high peak current diodes.

Theory predicts that there is approximately 15-db difference between the saturation level of a single germanium tunnel-diode amplifier having 20-db gain and a two-stage amplifier using a germanium diode in the first stage and a gallium-arsenide diode in the second, each stage having 10-db gain. An additional advantage of this combination is that the noise figure is only 0.1 db higher than the single high-gain germanium amplifier.

Further improvement in raising the saturation level can be made by use of high peak current diodes. It is estimated that the output stage should have a peak current of 20 ma to obtain a 1-db saturated output level of -10 dbm. Already, a saturation level of -15 dbm has been obtained with a 6-ma peak current gallium-arsenide unit.

A major disadvantage of high peak current diodes is the low impedance level of the diode. The negative resistance of a gallium-arsenide diode is approximately given by  $R_{\min} = 0.22/I_P$ . In practice, it is very difficult to prevent the diode from oscillating if  $L_d > R_{\min} C_d$ , where  $L_d$  is the package inductance, and  $C_d$  is the junction capacitance. Hence, the use of diodes with very low inductance\* is of major significance in the RCA amplifier design.

It is well known that gallium-arsenide tunnel diodes deteriorate when driven past the valley voltage. However, life testing at RCA indicates that degradation may not be significant when the diode is biased solely in the negative resistance region. Fortunately, the two-stage circuit is self-protecting, since the first-stage germanium diode saturates first and limits the power incident on the second stage.

Amplifier development is being performed at S-band although, in principle, the technique should be applicable at higher frequencies.

## E. CONTINUING CONFIGURATION STUDIES

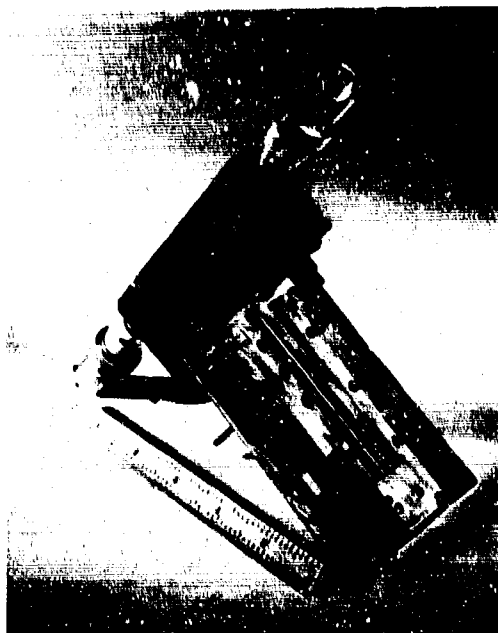
Some experimental work is continuing in order to establish reliable hardware techniques over the entire L- to X-band spectrum. The basic L-band design previously mentioned has been translated to S-band. Three important differences are (1) use of slab line instead of strip line, (2) elimination of the standard connector on the circulator, and (3) use of a five-port circulator.

The amplifier is shown in Fig. II-29. The TNC connector on the amplifier port of the circulator has been removed, and the slab-line rod center conductor mates directly to the strip center conductor of the circulator. The center conductor is terminated in a 50-ohm series rod resistor for stabilizing purposes. The diode is shunt mounted, utilizing a low-inductance symmetrical connection to the ground planes described by F. Betts.† The diode is shunt tuned by a quarter-wave open-circuited stub placed a short distance from the diode. The stub also serves the function of shorting out the resistor in the amplifier passband. There are two additional tuners: the first is situated close to the circulator in order to match out the residual VSWR; the second, which is a rotating vane, provides capacitive loading. Rotation of the vane adjusts the position of the tuning with respect to the diode. The magnitude of the susceptance can be altered by varying the spacing between the vane and the center conductor. Residual matching of

\* Developed under Signal Corps Contract No. DA36-039-SC-90773.

† See Part II, Ch. 3, Sec. B-2.

Fig. II-29. S-band tunnel-diode amplifier utilizing slab-line construction.



the diode to the slab line, in order to establish the gain, has been accomplished by introducing a step in the diameter of the center conductor near the diode.

Bias is applied through a high-impedance choke, which makes connection to the center conductor at a low-impedance point. The point of connection is the junction formed by the center conductor and the shunt stub. DC isolation between the circulator and the diode exists in the form of a 2-mil mylar sleeve, which has low RF impedance, inside the center conductor.

With this circuit, 15-db gain was achieved over a 12-percent 1-db bandwidth, with a center frequency of 2.85 Gcps.

## F. MICROWAVE TRANSISTOR AMPLIFIERS

J. DiBartolo and W. J. Ince

Transistors are now available for low-noise amplifier applications in the lower microwave frequency range. Transistors offer the prospect of lower cost, since circulators are not required, and considerably larger dynamic range than the tunnel-diode amplifier. Furthermore, transistor circuits are less liable to instabilities and the design is less sensitive to parameter fluctuations.

Largely because of transistor package constraints at the time, two configurations were studied: the first utilized transistors in coaxial packages, mounted in coaxial cavities; the second utilized strip transmission line techniques in conjunction with transistors in the flat TO-51 micromesa package. Circuits were designed to operate in the low L-band region because of the high frequency limitations of the transistors that were available at the time.

None of the transistors used were able to provide 20-db gain in a single stage with the objective 10-percent bandwidth. Hence, because of the difficulty of cascading several coaxial amplifiers and, at the same time of achieving an inexpensive, compact design, the coaxial version was not pursued beyond a single stage.

### 1. Coaxial Transistor Amplifier

The coaxial cavity shown in Figs. II-30(a) and (b) was designed to demonstrate the feasibility of obtaining power gain from a coaxial-type transistor in the 600-Mcps to 1.2-kMcps regions.



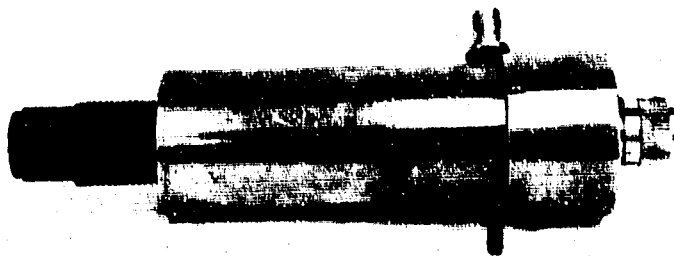


Fig. II-30(a). 900-Mcps cavity used in conjunction with coaxial transistor (Philco MADT T-2351).

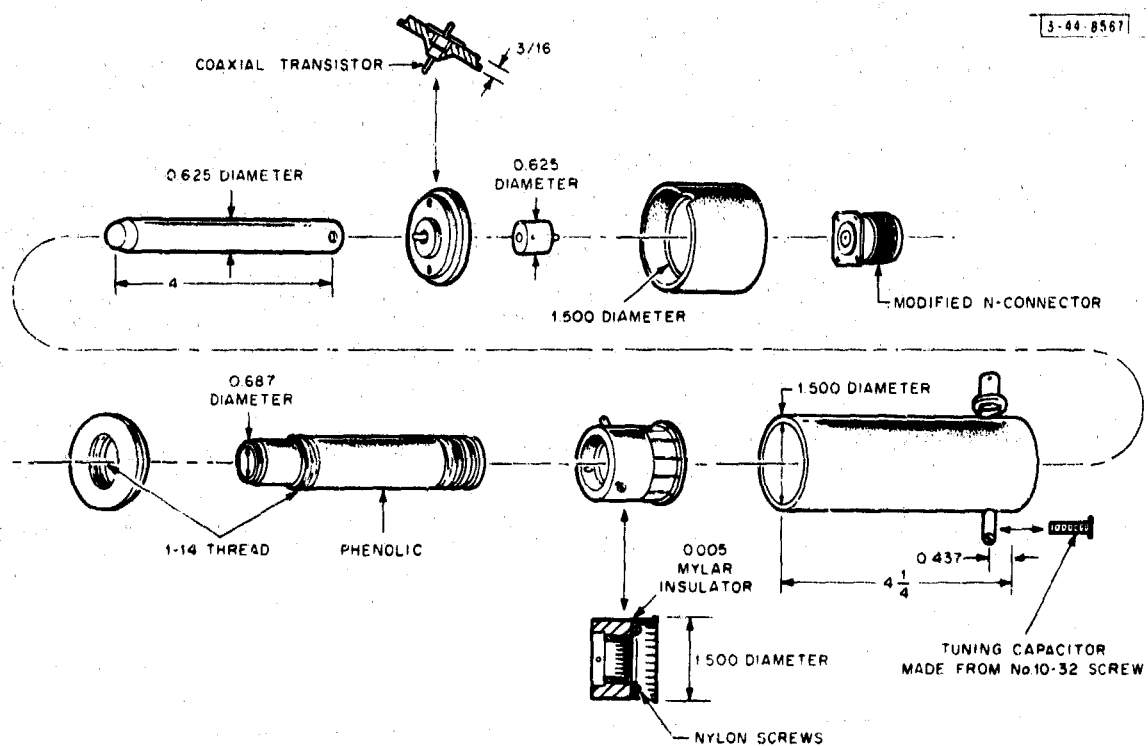


Fig. II-30(b). Exploded view of coaxial cavity.

The coaxial transistor used is a germanium MADT T-2351 made by Philco, and it has a theoretical maximum frequency of oscillation up to 5 kMcps. However, the package of the transistor imposes frequency limitations far below 5 kMcps.

The transistor is operated in a grounded base configuration with 2-ma emitter current and 17 volts of collector biasing voltage to assure optimum power gain plus good phase and amplitude stability. A check of the transistor's input and output impedances as a function of emitter bias current and collector voltage indicates they are more stable at this operating point. In fact, power supply voltages can be varied  $\pm 15$  percent without noticeably affecting the transistor's parameters. These parallel equivalent input and output impedances, obtained at the optimum bias point, for the frequency range 200 to 1200 Mcps are depicted in Figs. II-31(a) and (b), respectively.

The coaxial cavity used in conjunction with this transistor is basically a quarter-wavelength resonator short-circuited at the far end. Its impedance, at the frequency of resonance, is fixed to be equal in magnitude and opposite in sign to the transistor's reactance which shunts it, and is determined by the familiar equation

$$Z_{in} = jZ_0 \tan \beta l$$

where  $Z_0$  is the characteristic impedance of the line [as determined by the expression  $Z_0 = 138 \log(D/\delta)$ ],  $D$  is the inside diameter of the outer conductor and  $\delta$  is the outside diameter of the inner conductor of the cavity,  $l$  is its length, and  $\beta$  is the phase constant ( $\beta = 2\pi/\lambda$ ).

The cavity was first tuned to 900 Mcps, and the input and output impedances of the amplifier were matched to 50 ohms using a double stub tuner for the former and an adjustable capacitor probe for the latter. The adjustable capacitor probe is located at the high-impedance end of the cavity. This amplifier has 8-db gain and 30-Mcps bandwidth, and its swept frequency response is shown in Fig. II-32. Finally, the cavity was tuned from 600 to 1200 Mcps in various steps. The frequency of resonance was changed by use of the movable short-circuiting plunger which changes the length of the resonator, and a trimmer capacitor also located at the high-impedance end of the cavity. The compound plot of its gain, as a function of frequency, was plotted and is shown in Fig. II-33. It is clear that the gain follows closely the roll-off of beta.

The noise figure was also measured with the amplifier tuned for maximum power at 900 Mcps, and was found to be 11 db. Of course, such a high noise figure reduces the usefulness of this particular coaxial transistor as a preamplifier. Since other high-frequency transistors were available in a package more adaptable to strip transmission line, the investigation of small-signal coaxial amplifiers was not pursued further.

## 2. Strip Transmission Line Amplifier

Transistors used in the circuit designs were all Texas Instruments type TIX-2000, an experimental p-n-p epitaxial diffused-base mesa germanium transistor which has since been superseded by the 2N2999.

The performance of TIX-2000 was studied in both common-emitter and common-base configurations. We found that a single untuned common-emitter stage could amplify. The gain decreased with an increase in frequency, as shown in Fig. II-34, and was  $4\frac{1}{2}$  db at 1 Gcps when connected to a 50-ohm load and driven from a 50-ohm source. Gain was a maximum for a particular value of emitter current, between 2.5 and 5 ma, depending on the transistor. The collector voltage was set at -7 volts.

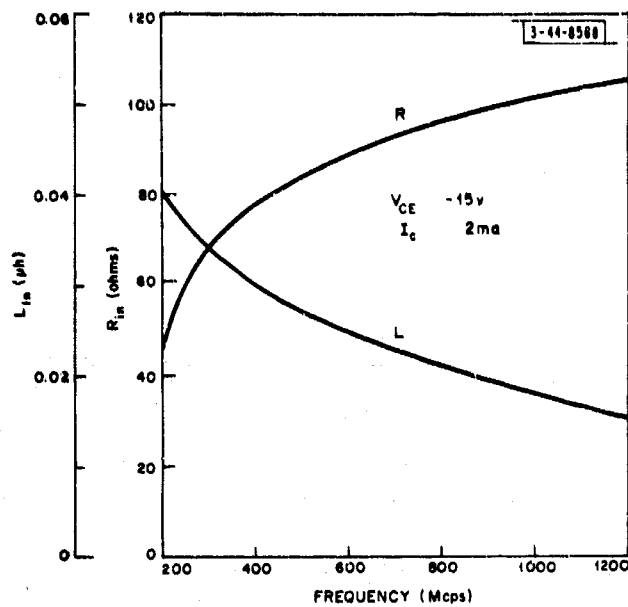


Fig. II-31(a). Parallel equivalent input impedance (with Philco MADT T-2351 transistor).

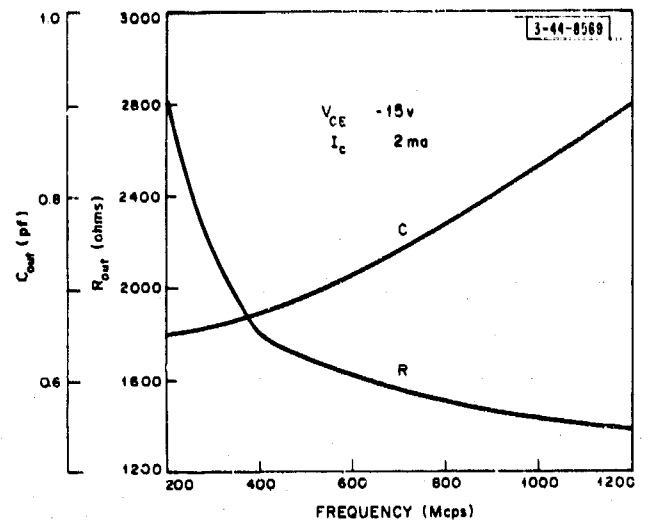


Fig. II-31(b). Parallel equivalent output impedance (with Philco MADT T-2351 transistor).

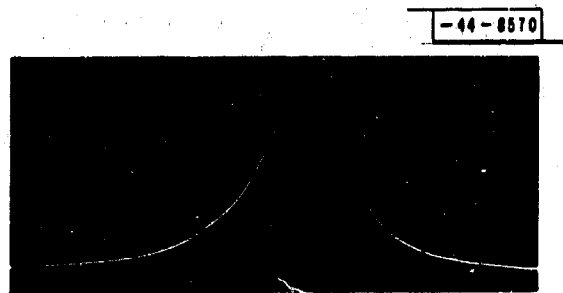


Fig. II-32. Coaxial cavity amplifier tuned at 900 Mcps (gain: 8 db; bandwidth: 30 Mcps).

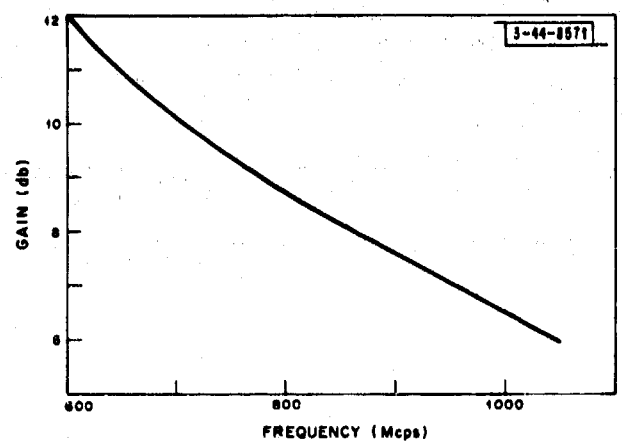


Fig. II-33. Tunable gain of coaxial cavity (with Philco MADT T-2351 transistor).

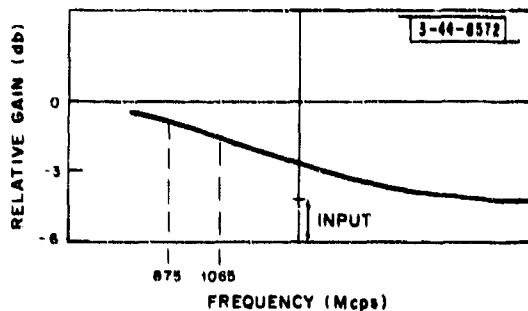


Fig. II-34. Untuned single-stage transistor amplifier gain vs frequency response in common-emitter configuration.

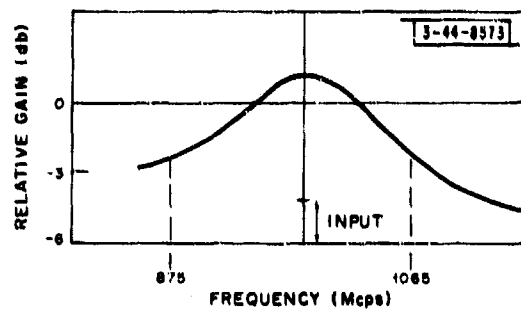


Fig. II-35. Single-stage transistor amplifier gain vs frequency response in common-emitter configuration with tuned collector.

The collector capacitance was tuned with a shunt inductor, in the form of a shorted transmission line whose length was less than  $\lambda/4$ . Output was taken from a variable tap point along the stub. Maintaining the previous conditions of bias, 6-db gain was obtained at 950 Mcps, with 200-Mcps (3-db) bandwidth (see Fig. II-35). The reverse gain was not greater than -15 db over the band. It was possible to match the input and output impedances to 50 ohms by the addition of simple quarter-wave matching transformers.

Connected in common-base configuration, a single stage with tuned collector had about the same value of gain but only about one-fifth the bandwidth.

Two-, three-, or four-stage amplifiers were successively built. Since microstrip construction was used, it was relatively easy to optimize the cascading procedure. All stages were identical common-emitter configurations. Starting with the two-stage amplifier, the output tap point and the distance between the transistors were varied until the gain was maximized; the third and fourth stages were added in a similar manner. The four-stage amplifier schematic is shown in Fig. II-36, and the actual amplifier is shown in Fig. II-37. Bias conditions for each transistor could be adjusted individually for the purpose of maximizing the gain. Diodes  $D_1$  through  $D_4$  were small-signal germanium units (type 1N34) specially selected to have small forward voltage drop in the conducting state. Their function was to protect the transistors, which have a reverse breakdown rating of  $\frac{1}{2}$  volt, from accidental reverse bias. The microwave and bias parts of the circuit were fairly independent of each other, since the former were constructed with distributed components, and the latter with lumped components. DC blocks ( $C_1$  through  $C_8$ ) required in the circuit were etched from 2-mil copper-clad KEL-F Dielectric, and were about 30 pf in value. The microstrip board was  $\frac{1}{8}$ -inch copper clad teflon fiberglass. Etched lines were all of 50-ohm impedance level.

Figure II-38 shows the amplifier gain vs frequency characteristic. The 3-db bandwidth is well in excess of 10 percent. In addition, the reverse gain over this band was less than -30 db. Some instability was observed when the amplifier was connected to a highly mismatched load. The instability was evidently due to the fact that the amplifier gain increased at low frequency, as shown in Fig. II-38. As the frequency is lowered, the transistor parameter  $|h_{fe}|$  increases at a rate of 6 db per octave. Thus, care must be exercised in preventing the increased gain of the transistors from causing low-frequency oscillations.

Use of quarter-wave transformers enabled the input and output VSWR to be held to about 1.5:1 over the entire bandwidth.

Variation of gain with signal level is plotted in Fig. II-39. The 1-db saturation level is about +2-dbm output.

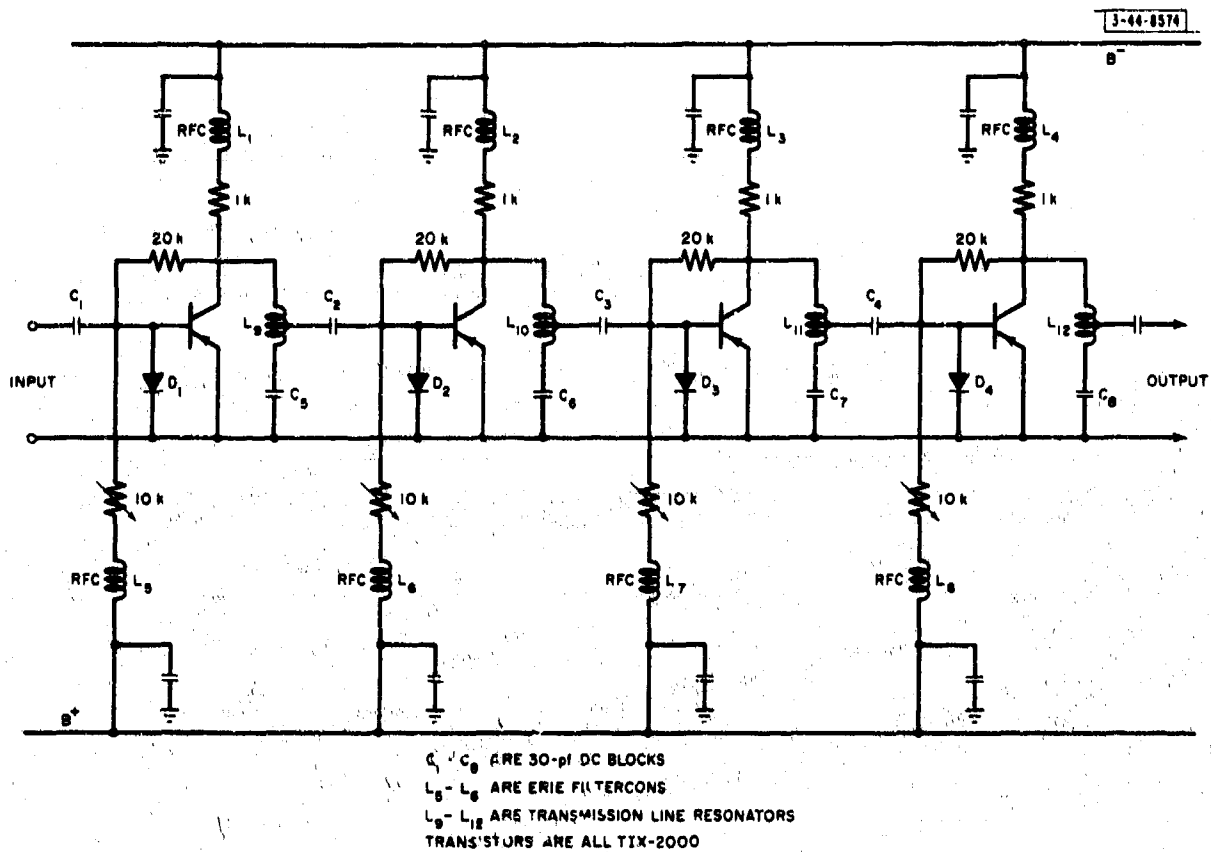


Fig. II-36. Four-stage transistor L-band amplifier.

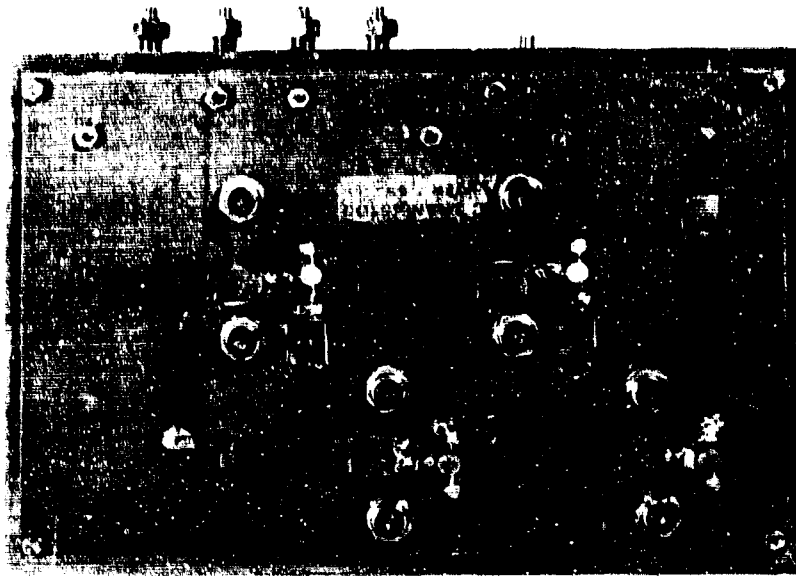


Fig. II-37. Four-stage L-band transistor amplifier.

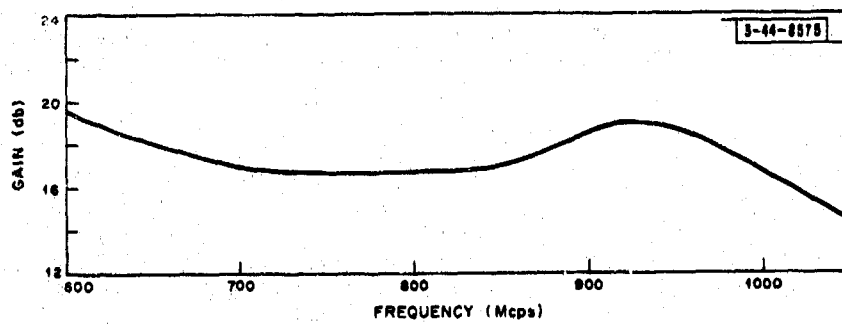


Fig. II-38. Four-stage transistor amplifier frequency response.

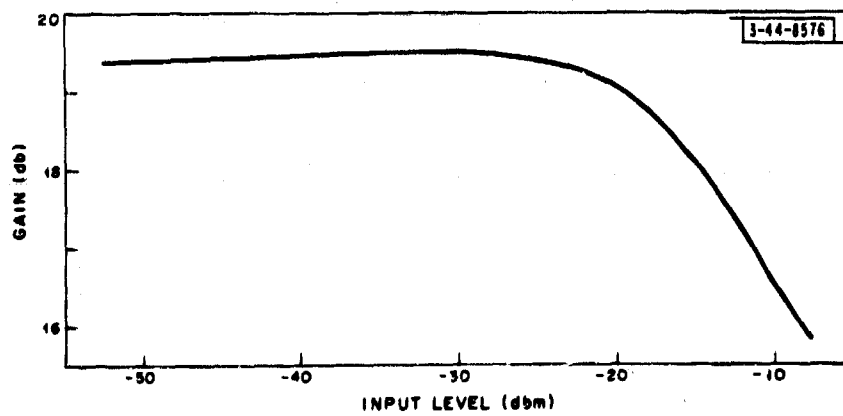


Fig. II-39. Four-stage transistor amplifier saturation characteristics.

An amplifier noise figure of about 8 db was obtained with initial samples of the TIX-2000 transistor. Later consignments led to considerable improvement in this figure. Figure II-40 shows the noise figure of the amplifier as a function of frequency, obtained with the improved type transistor.

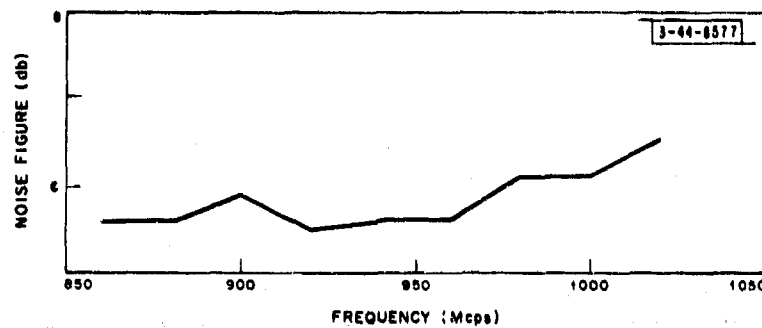


Fig. II-40. Four-stage transistor amplifier noise figure vs frequency.

Based on our results, we conclude that transistor amplifiers are preferable to tunnel-diode amplifiers up to about 1 Gcps at the present state of the art.

#### G. PHASE-STABILITY TEST ON 900-Mcps RECEIVERS

W. J. Ince

Long-term phase-stability information has been obtained on eight tunnel-diode receivers. Figure II-41 is a block diagram of the receiver and test circuit.

Each receiver assembly consists of a tunnel-diode amplifier, balanced mixer, and a mixer harmonic (low-pass) rejection filter. The tunnel-diode amplifier design (described in detail in TR-299) consists of a single shunt-tuned diode coupled to a four-port circulator. The nominal characteristics of the amplifiers are:

Gain	17 db
Bandwidth	40 to 45 Mcps
Center frequency	900 Mcps
Noise figure	4 to 4½ db

Diodes were carefully selected to provide roughly equal gain, although the gains of the eight amplifiers were equalized by adjusting the diode DC bias current.

The mixers, which were obtained from Sage Laboratories, are of a balanced configuration utilizing coaxial hybrids to obtain high LO isolation while maintaining a good match within the passband. It had previously been established that LO feedback into the output port of the circulator can cause serious gain degradation of a tunnel-diode amplifier. Consequently, a low-pass strip transmission line filter was inserted between each amplifier and mixer. The cutoff frequency of the filter design is about 1400 Mcps.

The test equipment, which is fully automatic, was designed by S. Spoerri (see TR-236). The test signal and local-oscillator power, at frequencies 900 and 870 Mcps, respectively, are supplied by a coherent frequency synthesizer. The fundamental source, which drives the synthesizer, is a 1-Mcps crystal-controlled oscillator, with a long-term stability of 1 part in  $10^8$ . The test signal is routed to the TD amplifiers via a 16-way hybrid corporate feed. A similar corporate feed is used for LO distribution purposes. The signal at the inputs to the tunnel-diode

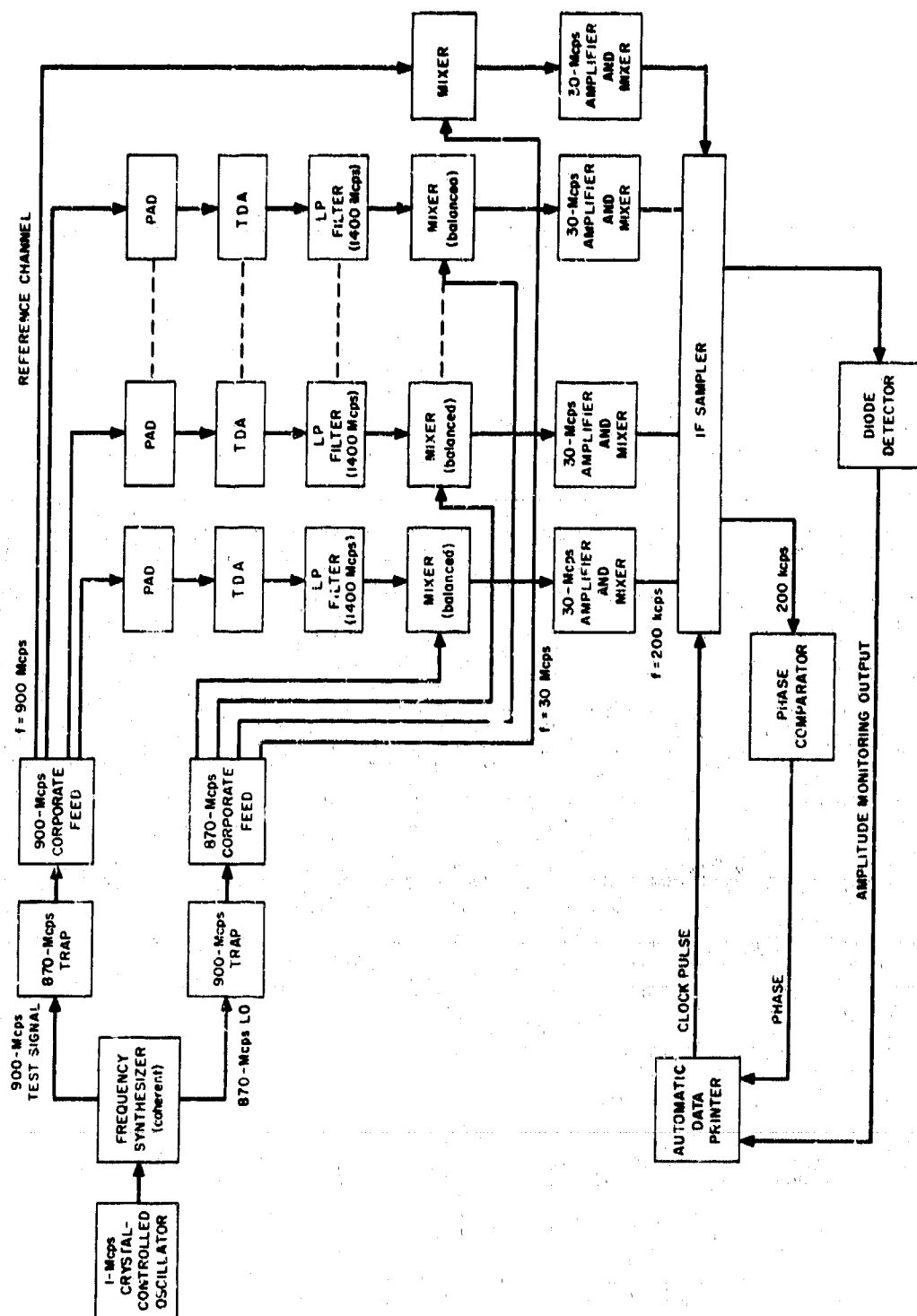


Fig. 11-41. Block diagram of tunnel-diode phase and amplitude test circuit.



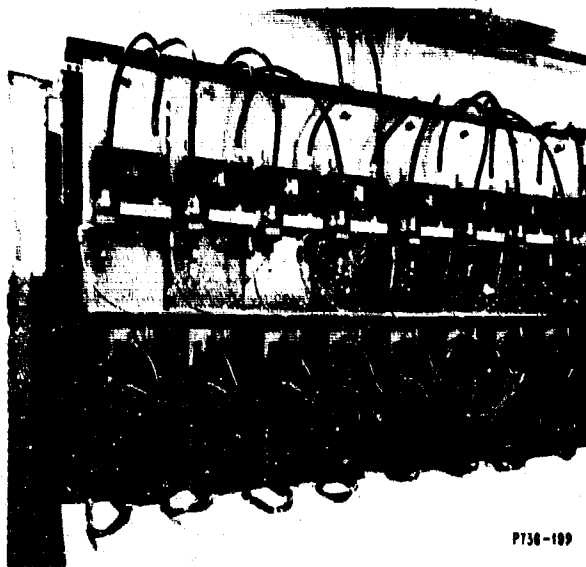
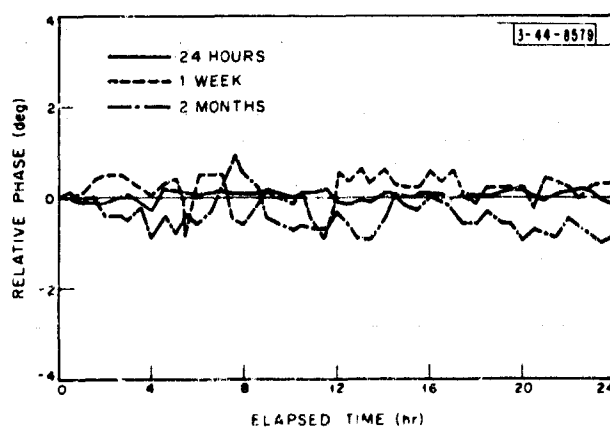
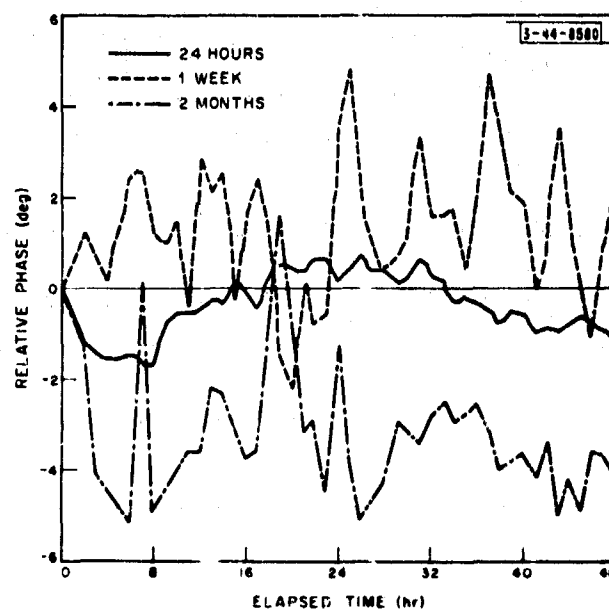


Fig. II-42. Tunnel-diode amplifiers mounted in test rack for long-term stability test.



(a) Amplifier 1.



(b) Amplifier 2.

Fig. II-43(a-h). Amplifier phase stability vs time.

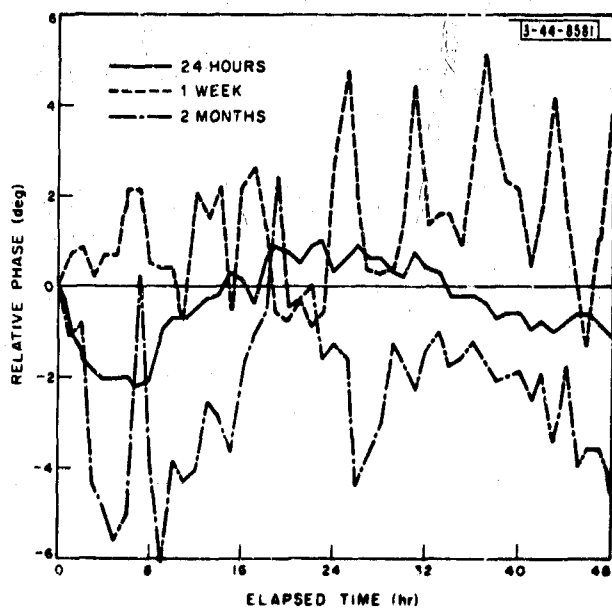
amplifiers is padded down to  $-60$  dbm in order to be well below the saturation level (approximately  $-45$ -dbm input). The LO level is set to be about 1.5 mw at the mixers. In order to reduce cross coupling, which is appreciable, 900- and 870-Mcps traps are inserted before the LO and test signal corporate feeds, respectively.

Following preamplification and conversion to the 30-Mcps intermediate frequency, there is additional amplification and further frequency conversion to 200kcps. The eight channels are examined sequentially by the IF sampler. Phase comparison is performed at the IF frequency of 200kcps; amplitude monitoring is performed by a diode detector; and test results are recorded by the automatic data printer (ADP). It takes about 30 sec for the test sequence to be completed.

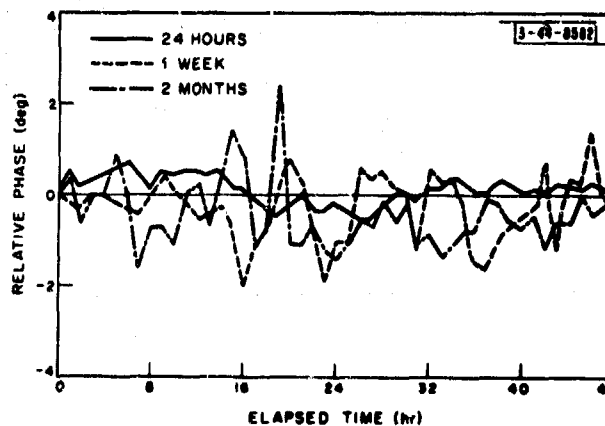
The interval between tests is controlled by a clock in the ADP, and can be preset to any desired value. In this series, the interval was mainly set at half an hour. The amplifiers were switched on and were maintained with RF and DC power applied for a total period of 2976 hours. In addition to the eight channels, the 870- and 900-Mcps output power levels from the frequency synthesizer were continuously monitored.

The circuits under test and all the test equipment, with the exception of the frequency synthesizer and the ADP, were located in an air-conditioned RF shielded enclosure. The amplifiers, mounted and ready for testing, are shown in Fig. II-42.

Results of the tests are shown in Figs. II-43(a) through (h). Data are plotted for three different time intervals: 24 hours, 1 week, and 2 months. It can be seen that the maximum peak phase deviation of the worst channel is under  $10^\circ$ . During the test period, the level of the signal power provided by the frequency synthesizer varied by as much as 4 db, as shown in Fig. II-44. However, the signal level is low enough for the phase modulation, caused by the variation in signal level, to be very small (cf., Fig. II-26).

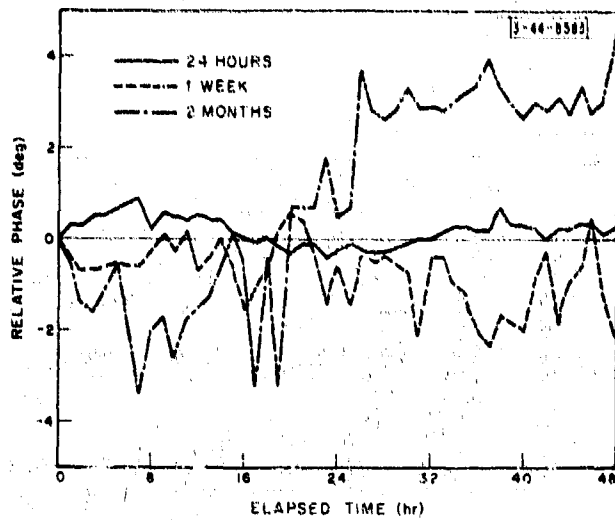


(c) Amplifier 3.

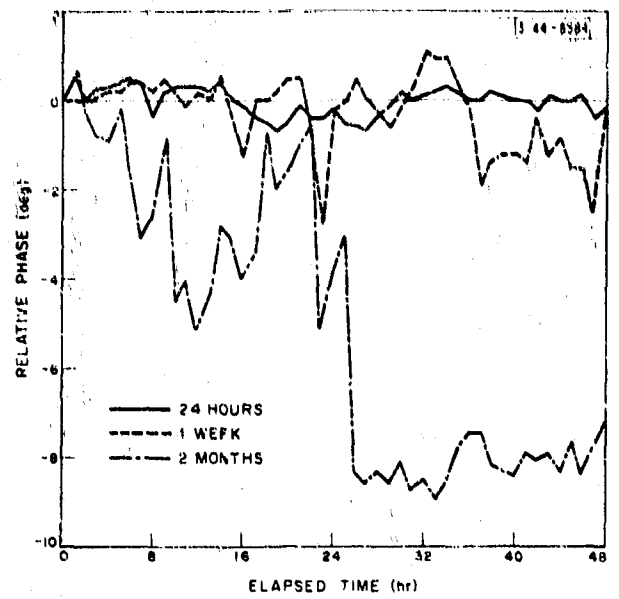


(d) Amplifier 4.

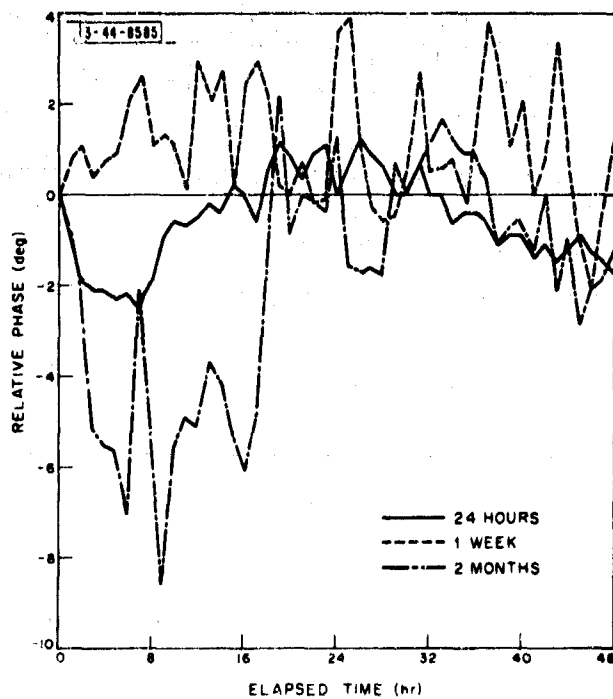
Fig. II-43. Continued.



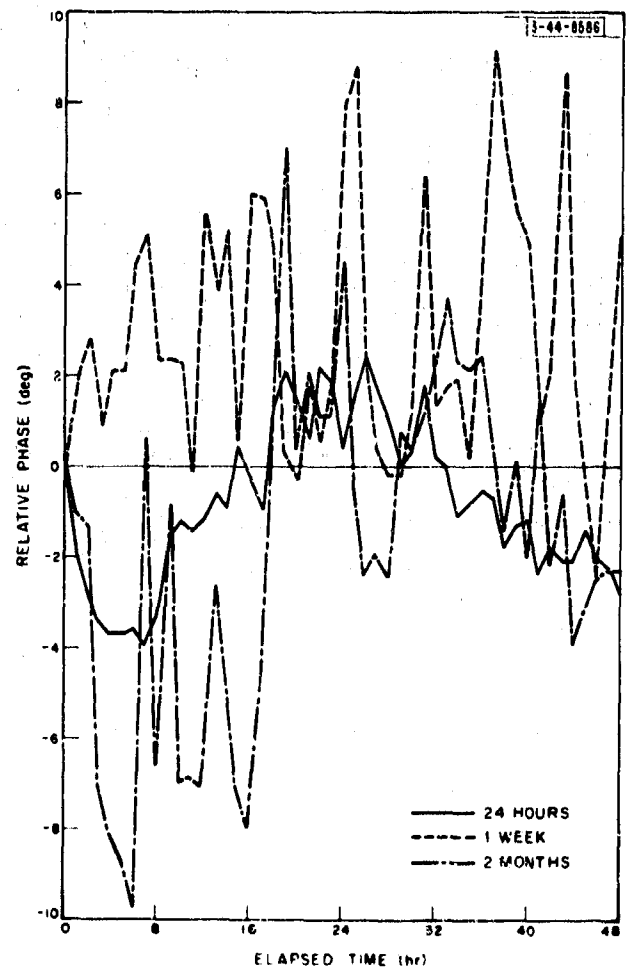
(e) Amplifier 5.



(f) Amplifier 6.



(g) Amplifier 7.



(h) Amplifier 8.

Fig. II-43. Continued.

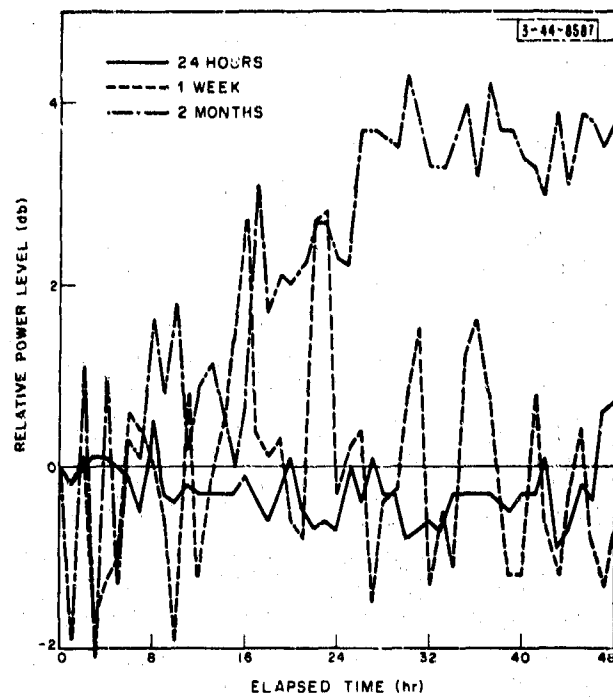


Fig. II-44. Amplitude stability of 900-Mcps signal.

## CHAPTER 8

### TIME DELAYS

#### SUMMARY

General design goals for time delays for subarray application have been formulated. Initial experimental efforts are being conducted at S-band, but the techniques chosen are expected to be equally applicable at C-band.

Various circuit configurations employing switches to insert different lengths of transmission line are compared. Present experimental designs use diode switches. Attention is being directed toward solutions to the problems of temperature instability, multiple reflections, and leakages that degrade delay characteristics. A survey of transmission lines with suitable temperature stability, packaging and loss characteristics has been made. Special efforts to improve connectors, transitions, and turns to control multiple reflection are described. Special attention has also been given to impedance match, and phase- and amplitude-tracking measurements as described. Suitable switches for high-power delay will be considered later in the program.

#### A. INTRODUCTION

The time delays for a time-delayed array radar with a fractional-degree beamwidth must be about 100 wavelengths long with a smallest delay variation a fraction of a wavelength. Thus, the delay tolerances are a fraction of 1 percent. This dictates that the transmission media be especially temperature stable, i.e., approaching metal-air structures.

Time-delayed array systems are implicitly broad signal bandwidth systems. Since phase modulations within a channel due to multiple reflections cannot be "trimmed out" over a broad band, reflections must be reduced to a minimum. A similar argument applies to unwanted signal leakage paths. These factors create a major design challenge in time-delay construction while coping with cost and size problems.

The work reported here differs from previous work in at least two significant respects: a higher frequency (S-band) is used, and essentially metal-air structures are used to achieve temperature stability.

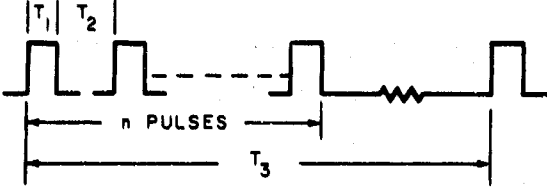
Detailed design goals have been established; a few choices of various circuit configuration have been made as well as a survey of presently available transmission media and materials. The initial work on switches has essentially been completed, and the assembly of a complete delay is under way. The discussion begins with a tabulation of design goals for the time delay.

#### B. PRESENT DESIGN GOALS FOR TIME DELAYS

D. H. Temme and F. Betts

Design goals similar to those for the high-power phaser, but with appropriate changes and additions, have been formulated as follows.

Frequencies of interest	L- through X-bands (principal effort presently at S-band)
Bandwidth	10 percent
Characteristic impedance	50 ohms
Differential delay	About $128\lambda$ in about $2^{12}$ steps
Size	Transverse dimensions $< 2\lambda$ at upper-band edge

RF power out	1-kw peak; 10-watt average
Switching speed	Any new delay setting shall be attained in $\leq 1 \mu\text{sec}$
Switching power	$\leq 10$ watts "raw" input power per bit driver
Insertion loss	$\leq 10$ db
Match	Adequate to meet phase and loss tolerances below
Insertion loss tolerance	$\leq 0.5$ -db total excursion vs delay setting
Delay tolerance	$\leq 5^\circ$ deviation from nominal value
Typical waveform	 <p><math>T_1 = 0.1</math> to <math>75 \mu\text{sec}</math>; <math>T_2</math> (min) = <math>0.5</math> to <math>2.0 \mu\text{sec}</math>; <math>nT_1 \leq 75 \mu\text{sec}</math>; <math>T_3 = 3 \text{ msec}</math></p>
Phase modulation during pulse, due to time-delay unit	$\leq 5^\circ$
Spurious signals before and after pulse, due to unit	$> 40$ db down
Waveform distortion	For an input pulse having 10-nsec rise and fall times and 100-nsec duration, the output rise and fall times shall be $\leq 15$ nsec.
Temperature	Above specifications shall be met within the ambient temperature range $20^\circ$ to $30^\circ\text{C}$ . Cooling water ( $\pm 1^\circ\text{C}$ ) available.
Unit-to-unit reproducibility	Units shall track one another in phase for all delay settings and differences in delay to $\leq 5^\circ$ within a 10-percent band; units shall track one another in insertion loss to $\leq 0.5$ db within a 10-percent band.
Reliability	Life, $\geq 10,000$ hours
Cost	Reducible to \$2000 in lots of 10,000 units, tooling costs not included.
Driver	A driver shall be furnished, capable of receiving digital control words at $\sim 3$ -mw signal level and having suitable termination (e.g., 100 ohms) for the logic signal. Driver output shall be capable of switching the time-delay unit during the interpulse intervals in an RF waveform, such as that specified above.

### C. CONFIGURATIONS

Discretely stepped, electronically switched microwave line stretchers for time delays have been chosen because of their inherent compatibility with digital-control systems and their

expected stability. In order to keep losses low, only configurations using switches to insert various lengths of transmission have been considered. The choice between possible switch configurations has primarily been influenced by the phase effects of signal reflections and leakages which are generally more significant in time delays than in short phasers. These phase effects produce deviations from linear phase with frequency. While it is not necessary for the entire delay to have a linear phase with frequency characteristic, the sections of transmission line providing the differential delay should have a linear (as possible) phase vs frequency characteristic. The prime requirement on the routing switch is that the two paths have essentially identical transfer functions and a good match over the desired bandwidth. When the ferrite switch is nonreciprocal, the effect of multiple reflections in such ferrite-switch configurations is different from diode-switch configurations. This section discusses the effects of reflections and leakages in various switch configurations, including both reciprocal and nonreciprocal switches, and concludes with reasons for our choice of a particular configuration.

The effects of reflections and leakage are described with reference to the configurations shown in Figs. II-45(a-e) (only one bit of a cascaded chain of bits is shown).

### 1. Reflections

The possible effect of single reflections is considered first with reference to a hybrid with diode switches type time-delay configuration [Fig. II-45(a)]. Assume the diodes are reverse-biased (transmission state) and the diode assembly has a 1.1 match (the reflection is 26 db down). The reflection signal phase modulates the main signal which is reflected from the short circuit. Phase of the reflection relative to the main signal changes by  $2\pi$  when the product of the percentage bandwidth ( $\Delta f/f$ ) and the length of the delay ( $n\lambda$ ) are equal to  $2\pi$ . The magnitude of the phase modulation ( $\Delta\theta$ ) is approximately  $\tan^{-1}(V_-/V_+)$  (the ratio of reflected to incident signal voltage). For the 1.1 match cited, it is about  $4^\circ$ . Similar phase modulation occurs for the circulator arm in Fig. II-45(d). Such phase modulations [ $\Delta\theta = \tan^{-1}(V_-/V_+)$ ] due to SINGLE REFLECTIONS occur in all time-delay configurations containing high standing waves.

The effect of two mismatches on the phase of a transmitted signal through a transmission line with two susceptances is readily analyzed by signal flow techniques [see Figs. II-46(a) and (b)]. The ratio of the incident voltage  $V_1^+$  at port 1 and the load voltage  $V_2 = V_2^+ + V_2^-$  at port 2 is

$$\frac{V_2}{V_1^+} = \frac{(1 + \Gamma_1)(1 + \Gamma_2)\alpha e^{-j\theta}}{1 - \alpha^2 \Gamma_1 \Gamma_2 e^{-j2\theta}} \quad (1)$$

where  $\Gamma_1$ ,  $\Gamma_2$  are the reflection coefficients corresponding to mismatch susceptances  $B_1$ ,  $B_2$  when followed with a match termination, and  $\alpha$  is the attenuation of the line. The expression contains two types phase variation from linear phase ( $e^{-j\theta}$ ). The  $1 + \Gamma$  factor varies slowly with frequency for reasonable matches (Fig. II-47) so that it can be regarded as a bias error and can be "trimmed out." The expression in the denominator is a phase modulation due to multiple (two) reflections. The phase of the multiple reflection relative to the main signal changes by  $2\pi$  when  $(\Delta f/2f)n\lambda = 2\pi$  and the magnitude (Fig. II-48) is

$$\Delta\theta = \tan^{-1}|\Gamma_1 \Gamma_2|$$

For two 1.1 mismatches in lossless line,  $\Delta\theta$  is about  $0.1^\circ$ .

Extension of this analysis to  $n$  shunt and equal discontinuities with equal line lengths between the discontinuities gives

$$\Delta\theta_{\max} = n(n-1) \tan^{-1} |\Gamma|^2.$$

Thus it becomes apparent that the phase deviation from linear phase can be significant for a long switchable delay which will contain many mismatches IF the individual mismatches are not kept small.

## 2. Leakages

There are several ways that the signal may leak from the desired path, and then leak back to the desired path and produce a phase modulation. In Fig. II-45(a), the leakage signal due to finite hybrid isolation modulates the main signal. Even an excellent hybrid isolation of 36 db can cause phase modulations of  $1^\circ$ .

The finite isolation of switches poses similar problems. The isolation of two identical cascaded switches [Fig. II-45(b)] may vary from the isolation of one switch plus 6 db to twice the isolation of one switch plus 6 db. The lower value occurs when the switch is separated by a resonant line length (effective  $\lambda/2$ ). Switch isolations of 30 db permit phase error in excess of  $1^\circ$ . However, placing a third switch  $\lambda/4$  from one of the other switches prevents this "resonance."

The effect of finite isolation of the circulator in Fig. II-45(c) is similar to the hybrid case in Fig. II-45(a).

In the routing three-port circulator configuration [Fig. II-45(d)], the leakage causes a ring resonance when the path length FEDCF is a multiple of a wavelength. Assume the main signal path is ACDB. A leakage signal down in level by the isolation of the input circulator leaks via AF into and circulates in the ring path FEDCF. This circulating signal in the ring grows until the leakages from the ring via CA and EB (leakage paths through the circulators) and the losses in the ring equal the input leakage power via path AF; that is, in steady state the power leaking into the ring must equal the ring losses plus the power leaking out of the ring. For identical circulators and no losses, the ring resonance level is 3 db less than the main signal, and the leakage signal from the ring resonance modulates the main signal at 3 db less than the isolation of one circulator. The routing four-port switching circulator configuration, shown in Fig. II-45(e), prevents a ring resonance by routing signal leakages into a termination.

In summary, the effects of leakages are generally greater in configurations containing high standing waves. Signal leakage via undesired paths can cause significant phase deviations. These effects can be reduced to desired levels with additional elements and circuit complexity.

## 3. Reciprocal and Nonreciprocal Switches

The difference in time-delay characteristics when using reciprocal or nonreciprocal switches is discussed with reference to Fig. II-49(a-b). Figure II-49(a) shows an intermediate bit of the delay between the rest of the delay represented by network boxes A and B; Fig. II-49(b) shows a general signal flow graph. Networks A and B are represented by a scatter diagram, and an ideal circulator is assumed for this discussion, i.e.,  $\theta_F$  is the electrical path length AB for the circulator state shown,  $\theta_B = \text{BCDCA}$ . The transfer function is



$$T(\omega) = \frac{S_{21}^a S_{21}^b e^{-j\theta_F}}{1 - S_{22}^a S_{11}^b e^{-j(\theta_F + \theta_B)}}$$

$$= T_1(\omega) e^{-j\theta_F}$$

$T_1(\omega)$  is the same for both states of the intermediate bit since the  $\theta_F$  and  $\theta_B$  values interchange when the circulator is switched. Therefore, adjacent channels in opposite states track with the desired  $e^{-j\theta}$  (linear phase vs frequency) difference even with poorly matched networks A and B. If the circulator bit is replaced with the analogous diode-hybrid bit [Fig. II-45(a)], tracking with the desired  $e^{-j\theta}$  does not occur since  $\theta_F = \theta_B$  and the denominator of  $T(\omega)$  is different in the two states.

In Secs. C-1 and C-2 above, reasons were given for preferring the bit configuration of Fig. II-45(e) over that of Fig. II-45(c). The nonreciprocal phase consideration given in the preceding paragraph does not alter those conclusions; thus, Fig. II-45(e) is the preferred bit configuration of the configurations with nonreciprocal phase characteristics. In summary, non-reciprocal switch configurations should track better than reciprocal switch configurations IF the two type switches are similar in quality.

As stated in the beginning of Sec. C in this chapter, diode switches were chosen because the development of adequate quality diode switches seemed more readily in hand (see Part II, Ch. 8, Sec. E-4). The configuration in Fig. II-45(b) was considered to be well suited to cope with reflection and leakage problems. A parallel effort to develop suitable ferrite switches is under way, and progress to date has been reported by J. Weiss.\*

#### D. MEASUREMENTS

We pointed out in the beginning of this chapter that delay tolerances for the time delay are a fraction of 1 percent. Cumulative errors should be kept within this tolerance; thus, individual errors must be very small. From a design viewpoint, it is desirable to measure the individual errors while attempting to reduce them. For example, the ability to measure low VSWR is obviously desirable because of the importance of matches cited in Sec. C of this chapter. At the beginning of the time-delay effort, commercial equipment was not available to readily measure a VSWR below 1.04 at S-band.

We decided to spend considerable effort to be able to measure and correct small reflections, confident that if the acquired capability exceeded that required for the construction of time delays when good nonreciprocal switches became available, the benefits of good matching techniques to other areas warranted the effort.

This discussion of measurements consists of two main categories: namely, VSWR and transfer function comparisons. The VSWR discussion includes both frequency- and time-domain methods. The improved time-domain reflectometry equipment that became available during the latter half of this reporting period has proved to be invaluable and is described in detail.

---

\* J.A. Weiss, IEEE Trans. Microwave Theory Tech. MTT-13, 38 (1965).

## 1. VSWR

### a. Frequency Domain

The slotted line still is the best device for accurate VSWR measurements due to susceptances. The art has considerably been improved by Sanderson\* and his colleagues. The VSWR substitution method described by Sanderson references impedance measurements to the impedance of an air line whose accuracy is only limited by mechanical tolerances. Use of this method with a precision GR 900 slotted line, obtained toward the end of the reporting period, proved to be of great value. Slotted-line measurements are spot frequency measurements and time consuming. Fortunately, improved swept frequency reflectometry has recently become possible, so slotted-line measurements were mainly used as checks on other methods.

A swept frequency domain reflectometer (FDR) is limited by the directivity of the directional coupler. It has been found that the recently introduced Merrimac coaxial magic tee with minor modifications can be used as a directional coupler with a directivity better than 32 db (residual VSWR < 1.05) at S-band (2 to 4 Gcps), and 28 db (residual VSWR < 1.08) at C-band (4 to 8 Gcps). High-quality loads are, of course, required. The GR 900 termination with a GR 900-N adapter was used to obtain the cited results. The minor modification to the tee consisted of making the pin spacings of the connectors on ports 1 and 2 of the tee identical (see connector discussion in Part II, Ch. 8, Sec. E-2). Ports 1 and 2 are the bridge arms of the tee for the unknown and the comparative matched termination. The brass outer shell was also replaced with a stainless-steel shell to reduce wear which changes the pin spacing.

A reflectometer substitution method similar to the VSWR substitution method used by Sanderson\* was used to observe VSWR below 1.05 [see Fig. II-50(a-d)]. A section of air line, fixed to hold a transition to be tested, is placed on the reflectometer coupler and terminated. For this setup, a voltage vector diagram [as shown in Fig. II-50(b)] exists at each frequency.  $\Gamma_m$  is the measured reflected voltage when the incident voltage has unit amplitude.  $\Gamma_m$  is also the vector sum of the leakage and reflected voltages in the coupler, and the reflected voltages from the connectors on the air line and the load.  $\Gamma_D$  represents the leakage voltages (or coupling imperfections).  $\Gamma_{B_1}$  is the reflection from an equivalent susceptance†  $B_1$  that has the same effect as all the susceptances in the output connector of the coupler and the input connector of the air line.  $\Gamma_{B_2}$  is the reflected voltage from the equivalent susceptance  $B_2$  representing the susceptance of the output connector of the air line and the load. This vector diagram does not include the effect of multiple reflections, which is small for small mismatches.

Now suppose a section of air line is replaced with a test section (i.e., a connector pair). Let  $B_t$  be the equivalent susceptance of the test section and  $\Gamma_t$  the associated reflection coefficient. The vector diagram [Fig. II-50(b)] becomes Fig. II-50(c); now  $\Gamma_M$  is the measured reflected voltage. Since phase information is not available in the simple reflectometer setup, the exact value of  $\Gamma_t$  cannot be deduced. Two obvious outer limits exist, namely  $|\Gamma_M| = |\Gamma_m| \pm |\Gamma_t|$ . Since the transitions for this type investigation are meant to be wide band, a qualitative picture of the match over a sweep oscillator bandwidth is seen in the typical presentation of a reflectometer set-up [Fig. II-50(d)]: namely, reflected power vs frequency. The difference between the two curves establishes a lower bound on the match. When the display is calibrated in terms of VSWR, the minimum value for the match of the transition is

\* A. E. Sanderson, Trans. IRE, PGMTT MTT-9, 524 (1961).

† H. V. Shurmer, Proc. IEE 105C, 177 (March 1958).

$$\Gamma_t = |\Gamma_M - \Gamma_m|$$

$$\approx \frac{1}{2} |S_M - S_m|$$

or

$$S_t = 1 + |S_M - S_m|$$

When the two curves superimpose, one is assured of an excellent match.

The chief value of this method is spotting joint resonances and determining quickly where to look with a slotted line. It is also a good method to "production check" low VSWR components.

#### b. Time Domain Reflectometry

F. Betts

Time domain reflectometry (TDR) is a technique that has not been widely used in the past. It will be shown that newly developed test equipment makes possible considerable application to the development and evaluation of microwave transmission systems. First, a brief discussion of the theory necessary to make and interpret TDR measurements is presented. Then, an operating TDR system and the type measurement results that are attainable are described. Some limitations on system usefulness are mentioned. Last, several applications of TDR are shown where results were readily obtained which would have been difficult or impossible to obtain with other techniques.

##### (1) Theory and Practice of TDR

Much of the difficulty of developing microwave transmission systems and components lies in determining from VSWR or impedance measurements just what is happening at various points in the system. TDR, a radar-like technique, utilizes the reflections from a very fast rise voltage step, thus separating the reflections in the time domain.

While not a new technique,<sup>\*†</sup> TDR has only recently become of great value in developing and evaluating low VSWR microwave transmission systems. The recent introduction of tunnel-diode pulse generators and high-sensitivity feedthrough sampling oscilloscopes makes TDR useful at least through 8 Gcps in slab, strip and coaxial systems with VSWR's of less than 1.1. The resolution is such that connectors, bead supports, transitions, etc., may readily be studied.

The equipment configuration for TDR measurements is shown in Fig. II-51. A voltage step waveform is launched down the transmission system, arriving first at the oscilloscope and subsequently at the interconnections and at the system under test. Reflections occur at any discontinuities in the system and return to the oscilloscope where they are seen as "riding" on top of the incident step. Since the reflections pass on through, the pulse generator must be a good match to prevent confusing multiple reflections.

What theory is necessary to interpret TDR measurements has been thoroughly presented elsewhere<sup>\*</sup> and is only briefly outlined here, omitting, among other things, analytical consideration of the shape of reflection waveforms. The effect of nonzero rise time of the incident step is considered here.

<sup>\*</sup> "Time Domain Reflectometry," Hewlett-Packard Co. Application Note 62.

<sup>†</sup> H. Halverson, *Electronics* 34, No. 26, 86 (30 June 1961).

## (2) Pure Resistance Lossless Line

Figure II-52(a) shows the idealized waveform of reflection from a resistive termination of other than 50 ohms (since the commercial equipment has 50-ohm characteristic impedance, this value is assumed to be a "match" in what follows). Two features are apparent. The echo follows the incident step by a delay

$$\Delta t = t_1 - t_0 = \frac{2l_1}{c_1}$$

where  $l_1$  is the length of line from the oscilloscope to the termination, and  $c_1$  is the velocity of propagation in that line. Thus, where the transmission medium has known uniform velocity of propagation, the position of reflection-causing discontinuities can be determined. Also, the amplitude of the reflection is

$$\Delta E = E_1 - E_0 = \Gamma E_0$$

$$\Gamma = \frac{\Delta E}{E_0} \quad (2)$$

where  $\Gamma$  is, as usual, found from

$$\Gamma = \frac{Z_L - Z_0}{Z_L + Z_0} \quad (3)$$

In low VSWR systems, the impedance error  $Z_L - Z_0$  is a convenient quantity to discuss and can be seen to be given by

$$Z_L - Z_0 = \frac{2Z_0 \Gamma}{1 - \Gamma}$$

For 50-ohm systems and impedance errors of a few ohms, the error is given to within a few percent by

$$\Delta Z = Z_L - 50 = 100 \frac{\Delta E}{E_0}$$

Thus, the oscilloscope can be calibrated directly in  $\Delta Z$ , as  $E_0$  is usually fixed.

It can be shown that a section of line with impedance  $Z_L$  and length greater than the resolution of the system [see Sec. (7) below, on the effects of nonzero rise time] produces a reflection whose amplitude is equal to that of a resistance of the same value. The duration of the reflection [Fig. II-52(b)] is determined by the length of the line. Where several dissimilar impedance lines are cascaded as in Fig. II-53, only for the first section is Eq. (3) exact. The voltage  $E_1$  in line section 1 is of amplitude  $E_0(1 + \Gamma_1)$  and, consequently, the reflection at line 2 is of amplitude  $E_{r2}$  (Fig. II-54) given by

$$E_{r2} = E_1 \Gamma_2 = E_0(1 + \Gamma_1) \Gamma_2$$

The reflected signal seen on the oscilloscope has been further changed in amplitude, as part of  $E_{r1}$  is again reflected at the junction of lines 1 and 2. For low VSWR systems, however (say  $Z - 50 \leq 5$ ), it can easily be shown that to within a few percent, for line section  $k$ ,

$$\Delta Z_k = Z_k - Z_0 = 2Z_0 \frac{k}{E_0}$$

making the previous calibration applicable.

It should be noted that multiple reflections from large discontinuities not only affect the impedance calibration but are seen at improper times, confusing measurements. Therefore, one should begin reducing reflections at the system input. An additional reason for doing this will appear in Sec. (7) below.

Thus TDR permits, for low-reflection lossless systems, an extremely quick and simple method of determining characteristic impedance at any point in the system. For a single large discontinuity in characteristic impedance, simple calculations from Eqs. (2) and (3) are needed for accurate results.

### (3) Shunt Capacity

Since the physical constraint of finite power in the traveling wave prevents instantaneous change of voltage (stored energy) across a shunt capacitor, the perfect step must initially be totally reflected with change of sign, the reflection decreasing exponentially as the capacitor charges [Fig. II-55(a-b)].\* The value of capacitance is determined from the exponential charging time constant and knowledge of the characteristic impedance. For small capacity values, the step rise time must be taken into account; this is discussed in Sec. (7) below.

### (4) Series Inductance\*

Again, the finite power constraint prevents instantaneous change in current in the inductance, and the step is initially totally reflected without change in sign. The reflection decreases exponentially as shown in Fig. II-56(a-b). The case where  $L/Z_0$  is not large compared to the step rise time is discussed in Sec. (7) below.

### (5) Series Capacitor\*

This case is shown in Fig. II-57(a-b), again for a perfect step. Here there is no initial reflection, the reflected signal rising exponentially showing the changing of the capacitor.

### (6) Effect of Attenuation

Transmission systems in which series losses predominate reflect a voltage wave with an exponential rise, while those with predominant shunt losses show a response that falls exponentially. As explained elsewhere,\* it is difficult to determine actual cable loss from such measurements but the magnitude of the slope can be useful in loss comparisons. There is, of course, the highly detrimental effect that this slope has upon the ability to measure characteristic impedance, or even compare impedances at different points in a lossy system. Step changes in impedance, however, can still be determined and it is sometimes possible to insert a lossless 50-ohm section in the system for comparison. For small shunt  $C$  and series  $L$ , the measurement accuracy is not affected.

### (7) Nonzero Step Rise Time\*

The most obvious effect of nonzero step rise time is to cause the reflections from adjacent discontinuities to merge, making it impossible to obtain accurate quantitative information on any of the discontinuities. The seriousness of the interference depends on their relative

---

\* Considered in detail in "Time Domain Reflectometry," Hewlett-Packard Co. Application Note 62.

magnitudes and the accuracy of measurement required. If, imitating radar usages, we define the resolution as  $\Delta x$ , and the step rise time as  $t_r$ , then

$$\Delta x = \frac{1}{2} c t_r$$

This distance is about 1.5 cm for present-day TDRs; thus, the reflections from a shunt  $C$  and a series  $L$  less than, say, 1 cm apart can be made to cancel on TDR. At 3 Gcps in air,  $1 \text{ cm} = 0.1\lambda = 36^\circ$  and the cancellation obviously would not be good. Thus, an accurate knowledge of the mechanical details of the structure being tested is very helpful. One can also locate discontinuities more accurately by intentionally introducing reflections with a small probe.

The second effect of nonzero rise time is that, for small  $L$  and  $C$  ( $Z_0 C$  or  $L/Z_0$  of the order of  $t_r$ ), the reflection is not the full height of the step. Equations are obtained\* which relate actual reflection amplitudes to the parameter values and system rise time. These are given here, and again in Fig. II-58(a-b) where the shape of such reflections is suggested

$$L = \frac{2Z_0}{m} e_{\max}$$

$$C = \frac{2}{mZ_0} e_{\max}$$

where  $m$  is  $dv/dt|_{\max}$  for the system step response. It should be pointed out that lossy lines increase the rise time of the step so that, ideally, one should first introduce a short at the location of interest and obtain  $m$  by measuring the rise time of the reflection from the short.

#### c. A Laboratory TDR System

In this section a laboratory TDR system is described, and some of its capabilities and limitations are considered.

Figure II-51 has shown the equipment as it is set up for TDR measurements. The Hewlett-Packard HP213B pulser is a tunnel-diode unit generating a long pulse with extremely fast rise. The sampling oscilloscope is an HP185B with 188A dual-trace plug-in. The specifications of this plug-in are also listed in Fig. II-51. The generator is mounted right at the scope to minimize reflection-causing interconnections. A low-loss cable about 30 inches long serves mainly to insure that reflections are observed superimposed on the flat top of the pulse after all overshoot, etc., have died out.

An X-Y recorder, always a useful adjunct to a sampling oscilloscope, greatly increases the utility of the system since it is capable of showing much more detail than the CRT display. But, perhaps even more important, the narrow bandwidth of the pen servos produces appreciable extra smoothing, increasing the over-all sensitivity. It can be seen by comparing CRT photos and pen recordings that the recorder improves the sensitivity probably by 10 db or more.

Figure II-59 shows the leading edge of the incident step, as seen with a good 50-ohm termination on the system. The pulse amplitude is 230 mv, the 10- to 90-percent rise time is 0.097 nsec, and the initial overshoot is 7.6 percent. The maximum rate of rise of voltage, a value necessary for  $L$  and  $C$  determination, is  $1.91 \times 10^9$  volts/sec. The top of the pulse becomes

\* "Time Domain Reflectometry," Hewlett-Packard Co. Application Note 62.

very flat for more than 30 nsec, and is quite useful for about 100 nsec. Figure II-60 shows the reflections from the open end of a 30-cm air line. Here, and particularly in the scope photo of Fig. II-61, one sees a reflection first from the sampling circuits in the scope and then from the open end. As this reflection is down only by about a factor of 6.8 from the incident pulse, one can see that to make accurate measurements of small reflections, no large reflections should exist anywhere in the system. To determine whether any observed reflection is spurious, a useful technique is to reverse the test structure, turning it end for end, and compare records.

To indicate the sensitivity of TDR measurements, a transmission structure was made having a screw for adding shunt capacity. The added capacity was measured on a bridge and compared with that calculated from TDR data. Results which show reasonable agreement are given in Fig. II-62. Since TDR has been used mainly to locate and reduce such discontinuities, no more careful checks of accuracy have been made. A shunt capacity of 0.04 pf in a matched 50-ohm system causes a VSWR at 3 Gcps of about 1.04:1. In Fig. II-62 the reflection from the capacitance is far from "just distinguishable," indicating considerably more sensitivity.

In practice, the full sensitivity of the system cannot always be utilized for the following reason. Referring to the discussion of reflections from different characteristic impedances, one can show that a characteristic impedance error of 1 ohm produces a reflection of 2.3 mv. (The corresponding VSWR at all frequencies is about 1.02:1.) Thus, particularly at transitions (slab line to strip line, for instance) or changes in dielectric constant, characteristic impedance changes can mask small reactance effects on the TDR display.

A few other precautions help avoid errors in TDR measurements. Series reactance shunted by a small capacity (as in the case of a partially mated connector) can cause prolonged ringing.\* Large reflections ahead of those under study should be removed first; one may test for such spurious reflections by reversing the test structure. Also, the incident pulse has a long slow rise before the tunnel diode fires (Fig. II-59) which makes it inadvisable to work near shorts or opens. As pointed out in Sec. b-(7) above, because of the limited resolution of the TDR systems, large capacitive or inductive discontinuities must be compensated with great care as their electrical separation at high frequencies may be quite large even though their reflections on TDR merge and cancel.

While TDR has up to now been used chiefly for systems operating at or below 3 Gcps, the foregoing indicates that with present equipment it should be a useful technique, at least through 8 Gcps.

#### d. Some Applications of TDR to Time-Delay Problems

In certain applications, TDR has tremendously reduced the labor in such tasks as connector development and modifying of complex structures for good match. TDR also permits identifying defects that would otherwise be virtually unlocatable. A few applications have been chosen to illustrate this great utility.

When the time-delay unit design problem suggested the use of cable as a microwave delay line, two commercial cables and a strip transmission line with styrofoam dielectric were tested. The strip line is described in Part II, Ch. 7, Sec. F-2 of this report. Figures II-63 through II-65, all to the same horizontal and vertical scales, reveal at once significant characteristics of the lines tested.

\* See Fig. 17 in "Time Domain Reflectometry," Hewlett-Packard Co. Application Note 62.

Referring to Fig. II-63, the trace for RG9 cable labeled "termination" establishes the 50-ohm level and shows that there is considerable curvature of the top of the incident step at this point. (An extra 50 cm of air line was then inserted ahead of the cable to secure operation on the flat portion of the pulse, as shown in Fig. II-64.) The impedance differs considerably from 50 ohms (note calibration at right edge of Fig. II-64), fluctuating with a period of about 0.75 nsec around an average of about 49.2 ohms.\* Interestingly enough, FDR (frequency domain reflectometry) showed large VSWR at certain frequencies.

Figure II-64 clearly shows that the "Spiroline" cable tested was far more uniform in characteristic impedance than was RG9. The slight rise of the trace also indicates a small amount of series loss. Characteristic impedance is about 50.8 ohms. At the left edge of Fig. II-64 a large reflection from the commercial cable connector can be seen. The amplitude of 3.3 mv indicates a capacity deficit of

$$C = \frac{2}{mZ_0} e_{\max} = \frac{2 \times 3.3 \times 10^{-3}}{1.91 \times 10^9 \times 50} = 0.069 \text{ pf}$$

In a 50-ohm system, this would correspond to a VSWR at 3 Gcps of

$$\text{VSWR} \approx 1 + 2|\Gamma| \approx 1 + 2 \left| \frac{Y_c}{2Y_0} \right| = 1 + 2 \frac{6.28 \times 3 \times 10^9 \times 0.069 \times 10^{-12}}{2 \times 0.02} = 1.065$$

Figure II-65 shows the results for the strip transmission line with foam dielectric. The rapidly rising trace is indicative of the losses of the beryllium-copper strip conductor, which has appreciably higher resistivity than copper. A periodicity is evident, together with several large fluctuations believed to be due to distortion of the ground planes caused by screw holes, etc., during the fabrication of the line. The large peaks at the right of Fig. II-65 were found (by probing with a capacitive probe) to be: first, a transition from strip conductor to slab line; and second, the type N connector on the assembly. The left edge of the trace shows the line impedance quite close to 50 ohms.

Figure II-66 shows the TDR records obtained while testing a special connector made up for Foamflex line; the impedance error of the line is immediately apparent. The large dip indicating excess shunt capacity was found to correspond to one end of the extruded aluminum cable sheath. However, the two traces made by reversing the piece of cable in the connectors, keeping the same connector on the input end, showed clearly that the fault is in the cable, an examination of which showed a pronounced burr where the cable jacket was cut. With the burr removed, the capacitive dip vanished. FDR measurements verified that the line plus cables gave low VSWR.

Figure II-67 is a photograph of a section of foam-supported strip transmission line made up to show how a complex structure can be quickly "cleaned up" with TDR. Note that the coaxial connectors have a transition to slab line of which there is about one inch. The transition to strip line is a 0.025-inch slot in the slab conductor into which the strip is soldered. In Fig. II-68, the two traces were obtained by reversing the whole structure so that alternate ends served as inputs. Note the similarity of the traces. It is evident that the slab-strip transitions have an excess of shunt capacity. Estimating  $e_{\max}$  as 0.4 mv

\* The cable manufacturer suggested that this might be due to oscillatory behavior in the diameter control servo in the jacket extruder.



$$C = \frac{2 \times 0.4 \times 10^{-3}}{1.91 \times 10^9 \times 50} = 0.0084 \text{ pf}$$

The resulting VSWR would be 1.008 at 3 Gcps. The connectors show a deficiency of capacity of about 0.02 pf, which would be a VSWR of 1.02 each at 3 Gcps and 1.03 each at 4 Gcps. The FDR record of Fig. II-70(a) is not inconsistent with these values. However, the residual VSWR of the FDR setup cannot be guaranteed to be much less than 1.05, producing considerable indeterminacy in the measurement.

Next the transitions were modified, as sketched on Fig. II-69, and capacity was added to appropriate places in the connectors by applying small dabs of vaseline and observing the effect on the TDR display. The traces of Fig. II-69 were readily attained, showing considerable improvement. Figure II-70(b) shows that substantial improvement was made in the FDR record as well. The magnitude of FDR system residual VSWR makes any comparison of numbers rather meaningless. A few slotted-line measurements, all under 1.03 VSWR, were made between 2.5 and 3.5 Gcps. These data show clearly that TDR is a highly useful tool for obtaining improvements in complex devices. These improvements would be very difficult to achieve with FDR or slotted-line measurements alone.

## 2. Phase and Amplitude Tracking Measurements

D. H. Temme

### a. S-Band

It has already been stated in Sec. C of this chapter, as well as in Sec. B, that the delays in an array should track within specified limits in both amplitude and phase for all delay settings and differences in delay. Furthermore, limits on waveform distortion, phase modulation in the pulse, and spurious signals caused by the unit were given. These items can all be checked with a suitable form of the well-known microwave comparison bridge. Figure II-71 shows an assembly of components used at S-band. Identical components are used in both sides of the bridge to keep the transfer functions identical in both paths. The bridge itself, without devices to be compared, has a signal input-detector port ratio of  $\leq 31$  db from 2.2 to 3.8 Gcps. This corresponds to a pure phase difference of  $5^\circ$ , or pure amplitude difference of 0.5 db. Whether the unbalance is a phase or an amplitude difference, or some combination, can be readily resolved by observing whether a line stretcher or attenuator adjustment, or both, effects a balance. This is a consequence of the fact that, near balance, the difference signal can be resolved into an orthogonal amplitude and phase difference component. Because of the orthogonality condition and the fact that, near balance, a  $1^\circ$  phase difference is about equivalent to a 0.1-db amplitude difference, the magnitude of the bridge unbalance will always be given as an equivalent phase unbalance in the following discussion.

The unbalance of the bridge itself reduces to about  $3^\circ$  over a 10-percent band. A comparison to less than  $1^\circ$  can be made between two devices when a third device is kept as a reference in one arm while making recordings of the unbalance of each of the other two devices against the reference, and noting the difference between the two recordings. To resolve the possible ambiguity of leading or lagging phase, the bridge is kept unbalanced for the entire record.

Some particular characteristics of the components in the bridge led to their selection. The Merrimac magic tee was selected for its wide-band performance and good isolation characteristics. The GR 10-cm line stretcher was selected for its good match; however, the 874 connector had to be changed to an N connector (parts are available from GR), because the 874 connection was not sufficiently stable at S-band. A small-diameter semi-rigid cable was used

rather than cable with a braided outer shield, since the latter are not phase stable. The Weinschel 953 resistive sleeve variable attenuator is essentially phase-shiftless with change in value. The setting is kept at high values where the match is better than it is at low values. The increased sensitivity of the tunnel detector over a crystal detector easily permits measurements of bridge unbalance of  $0.1^\circ$  with an input level of 1 mw. This sensitivity is only achieved by matching the tunnel-detector video impedance to the input impedance of an oscilloscope with an audio transformer. It is frequently necessary to suppress ground loop currents with an inside-outside low-frequency block like the Weinschel 936N noise suppressor.

#### b. L-Band

At the beginning of this reporting period, L-band Merrimac magic tees and Weinschel resistive sleeve attenuators were not available. During this period, a bridge similar to that shown in Fig. II-71 was used. Rantec Model CA-342,  $90^\circ$ , 3-db hybrids that have excellent isolation (and thus, an excellent  $90^\circ$  phase difference between output ports) were used. The variation of coupling with frequency of the  $90^\circ$  hybrid was compensated with an electronic programmed PIN diode attenuator over a 10-percent band. The attenuator consisted of a diode mounted in series with the line with the required DC bias network. Attenuation of the diode was varied by a DC current and was phase-shiftless over about a  $\frac{1}{2}$ -db range. Diode current variation was provided by a function generator which converted the video ramp output of the sweep oscillator into the appropriate current waveform for the diode. Only one attenuator was programmed to compensate the variation of the coupling of the  $90^\circ$  hybrid; the bias of the other was set to equalize the amplitude of the signals in the two arms at the center frequency.

Performance of this L-band bridge over a 10-percent band was similar to the results cited above for the S-band bridge. The L-band bridge with diode attenuators is now obsolete with the availability of L-band Merrimac magic tees and L-band resistive sleeve attenuators. However, it does illustrate the improved microwave comparison bridge performance that can be obtained with programmed PIN diode attenuators (varactor diode phasers should be included) when the additional complexity is warranted.

Performance of the microwave transfer function comparison bridge is illustrated with results obtained while comparing five printed circuit boards (each containing four cascaded couplers) with a sixth printed circuit board as a reference (see Part II, Ch. 3, Sec. C). Figure II-72 shows an oscilloscopic record of three unipolar unbalanced traces of the bridge. The center trace is used as a reference, and the two adjacent traces were obtained by varying the line stretcher to provide calibration traces removed  $\frac{1}{2}^\circ$  from the reference trace. Figure II-73 shows the traces obtained when the five printed circuit coupler boards were compared with a sixth as a reference. Line-stretcher adjustments were made before each trace was recorded to equalize the insertion phase of the five boards at the center frequency. Spread in the value of insertion phase at the center of the band was about  $1^\circ$ . The record shows the boards track within a few tenths of a degree except near the end of the band.

### E. TIME-DELAY HARDWARE

This last section of Ch. 8 discusses time-delay hardware investigations and developments. A survey of transmission media and materials presently available and judged worthy of consideration has been completed. Since it is important to be able to wrap up long lengths of transmission line in a compact form, turns and bends in the line are required. To obtain low VSWR

turns, appropriate strip-line mitres were determined for several strip lines with different kinds of dielectric.

It was clear early in the time-delay development program that connector mismatches would impair both the performance of various parts of the delay and efforts to evaluate individual mismatches. Considerable progress has been made on improving connectors and transitions for time delays and for other subarray needs as well. Since all connector development has been interrelated, this work will be reported in a forthcoming technical note.

Development of a diode switch assembly to be used for initial time-delay studies has been essentially completed. After the reproducibility of the assemblies has been established, the complete assembly of a time delay will commence.

## 1. Transmission Media

W. J. Ince

### a. General Requirements

A suitable transmission medium for long delays should have very small loss, be highly stable, preferably nondispersive, and be capable of adaptation to high-density packaging. The time-delay medium should not present mechanical problems in fabrication of the time delay which could increase assembly costs. Furthermore, the medium should be stable, should not deteriorate with time, and should not exhibit hysteresis effects with changes in environmental conditions. A power-handling capability of 10 kw is expected to be well within capability of the transmission media considered.

The important requirements will be discussed in detail.

#### (1) Dispersion

Where possible, it is preferable to use TEM structures, which are nondispersive. However, they have appreciable loss, particularly at the higher microwave frequencies where waveguide is preferable from loss considerations alone. Unfortunately, waveguide is dispersive; hence, phase errors are introduced in the longer delays. For waveguide, the fractional change in electrical length in degrees is related to the fractional change in frequency by the relationship

$$\frac{\delta\varphi}{\varphi} = - \left( \frac{\delta f}{f} \right) \frac{1}{1 - \left( \frac{f_c}{f} \right)^2} \quad \text{where } f_c = \text{cutoff frequency}$$

If waveguide is used to minimize loss, a phase correction must be applied.

#### (2) Loss

In order to meet the design objective of 10-db maximum loss for a 7-bit time delay, the longest delay of  $128\lambda$  should have a loss not exceeding 5 db, since the diode switches have about 0.7 db per bit. This implies that the delay structures should either be air filled or be filled with very low loss material.

#### (3) Phase Stability

Time delay must be mechanically stable. For example, braided cable has poor stability; the insertion phase of even a small length has a tendency to change when flexed. Conversely, rigid or semi-rigid cable is extremely stable, and once installed it is not usually subjected to further bending.

Another example of poor stability is the thermal lag exhibited by certain commercially available irradiated polyolefin dielectrics. These materials exhibit long-term recovery from thermal shock, which could be disastrous in the event of a power failure in conditions of extreme ambient temperatures.

#### (4) Temperature Stability

Time delay must have a small temperature coefficient which, to be consistent with the phase tolerance specification in Sec. b, below, should be no more than about  $10^{-5}/^{\circ}\text{C}$ .

Consider, first, an air-filled time-delay structure in which the temperature coefficient of electrical length is essentially due to the thermal expansion of the metal from which the delay line is constructed. The number of electrical degrees change per degree centigrade change in temperature has been calculated for the largest bit ( $128\lambda$ ), assuming various types of common metals used in the construction of the time delay, and is given in Table II-2.

TABLE II-2 TEMPERATURE STABILITY OF $128\lambda$ BIT FOR VARIOUS MATERIALS		
Material	Average Coefficient of Thermal Expansion $/^{\circ}\text{C}$ ( $\times 10^{-6}$ )	Phase Change $/^{\circ}\text{C}$ (deg)
Copper	16.1	0.74
Aluminum	28.7	1.3
Brass	20.2	0.93
Stainless steel	19.1	0.88
Teflon	99	4.60
Polyethylene	160	7.36

Phase errors due to the metal alone are far from negligible. Addition of a dielectric propagation medium provides an additional complication, since the coefficient of expansion is generally larger than the metal. For instance, the coefficients of expansion of teflon and polyethylene resin are 99 and 160 parts per million per degree centigrade, respectively. The composite temperature coefficient of the structure depends on whether the dielectric can expand or is constrained by the metal. It is possible to trade off the differential expansions of metal and dielectric and to obtain phase compensation over a limited temperature range.

There is evidence that dielectric-filled coaxial cables exhibit thermal hysteresis effects.\* Despite the substantial advantage of the size reduction obtained by use of dielectric-filled structures, our policy has been to minimize the quantity of dielectric used in the time delay in order to avoid this effect and, simultaneously, to reduce the attenuation.

\*A.M. Kushner, "Discussion of Phase Stability of Coaxial Cables," Internal memo, Times Wire and Cable Division, The International Silver Company, Wallingford, Conn. (1 May 1962).

#### (5) Size

The time-delay unit is required to fit within a cross section equivalent to  $4 \times 4$  antenna elements. Thus, the long sections of time delay must be amenable to coiling or snaking up into a high-density package without incurring serious deterioration in electrical performance. This problem will be dealt with in more detail in Sec. E-2 of this chapter.

#### (6) Match

In order to obtain a time delay with low VSWR, the delay medium must be extremely uniform. For long delays with a number of discontinuities, it is possible to find many frequencies across the band where the multiple internal reflections add in phase, causing high VSWR. Rigid or semi-rigid cables are generally much more uniform than braided cables. Also, we have found that long runs in strip transmission lines can be made with good uniformity.

A second consideration is one of connector mismatch. It is obviously desirable to avoid as many transitions as possible within the time-delay assembly. From this point of view, fabrication of the time delay by interconnection of switches with appropriate lengths of coiled-up coaxial cable would not seem desirable. Instead, an attempt has been made to integrate the individual parts by using similar configurations. The approach finally adopted was to construct both switches and delay lines in sandwich-type transmission line.

#### b. Configurations

##### (1) Summary of Results

Table II-3 summarizes the types of delay media that were considered, their important advantages and disadvantages, and it indicates whether or not their properties were suitable. The results of a temperature-stability experiment helped shorten the list of possible alternatives to a choice between one of the semi-rigid coaxial lines, or a sandwich line that is foam filled or only partially filled with dielectric for purposes of center conductor support. Moreover, the sandwich-line versions were considered preferable to coaxial-line versions for reason of compatibility with the switch designs. Much of the early delay-line construction was in slab line, but this was finally rejected because of the difficulty in maintaining the high degree of uniformity required. The final choice between an air-filled strip transmission line with the center conductor etched on thin dielectric sheet, and a dielectric foam-filled line, was made in favor of the latter. Both are illustrated in Figs. II-74(a) and (b). Experience has shown that the foam-filled line can be constructed with a high degree of uniformity and has low loss. The air-filled type requires that accurate registration be maintained and has somewhat higher loss.

##### (2) Temperature-Stability and Attenuation Experiments

Six types of transmission lines were tested to determine their changes in electrical length vs temperature. The lines selected and the test results are listed in Table II-4. For purposes of comparison, the transmission line losses have also been listed.

The test circuit shown in Fig. II-75 was used for all lines except the phase-compensated flexible cable which, because of its higher loss, was tested with the circuit of Fig. II-76. Measurements were made at S-band.

As shown in Fig. II-75, the transmission line was open-circuited at one end and driven from the other end by a generator. Voltage at a fixed point, located at a distance  $l$ , was sampled

TABLE II-3 TYPES OF DELAY MEDIA			
Type of Transmission Line	Important Advantage	Important Disadvantage	Suitability
Waveguide	Low loss	Dispersive, bulky	Undesirable
Phase-compensated flexible coaxial cable	Moderate temperature coefficient	Lossy, braided outer conductor	Unacceptable
Semi-rigid coaxial cable, 1/2 inch	Low loss and temperature coefficient	Cannot be integrated into a single package with the switches	Acceptable
Irradiated polyethylene-filled coaxial line	Good uniformity	Poor thermal stability	Unacceptable
Irradiated polyethylene-filled strip transmission line	Good uniformity	Poor thermal stability	Unacceptable
Air-filled strip transmission line with thick center conductor	Low loss	Requires center conductor support, relatively expensive	Unacceptable
Air-filled strip transmission line with center conductor etched on thin dielectric sheet	Low loss	Requires accurate registration	Acceptable
Alumina foam-filled strip transmission line	Low loss	Fragile	Unacceptable
Quartz foam-filled strip transmission line	Low loss	Fragile	Unacceptable
Slab line with bead support	Low loss	Difficult to maintain uniformity	Acceptable
Slab line with foam support	Low loss	Difficult to maintain uniformity	Acceptable
Dielectric foam-filled strip transmission line	Low loss		Preferred

TABLE II-4  
RESULTS OF TRANSMISSION LINE TESTS

Type of Transmission Line Tested	$\Delta l/l$ per °C ( $\times 10^{-5}$ )	Temperature Range of Tests (°C)	Length Tested (ft)	Cable Attenuation at 3 Gcps (db/100 ft)
Phase-compensated flexible coaxial cable	7.7 to 8.7	16 to 46	120	18
Semi-rigid coaxial cable, 1/2-inch Type I	2	-30 to 66	15	5.5
Semi-rigid coaxial cable, 1/2-inch Type II	5	-15 to 79	25	5.5
Irradiated polyethylene-filled strip transmission line, 0.25-inch ground plane spacing	16	-50 to 80	1.35	12
Irradiated polyethylene-filled coaxial line, 0.160-inch o.d.	10	-50 to 80	1.54	19
Polyethylene dielectric foam-filled strip transmission line, 0.25-inch ground plane spacing		-30 to 66	1.35	8

with a probe or T junction. The frequency of the generator was varied until a null was observed at the detector placed in the branch arm. When this condition was obtained, an odd number of quarter wavelengths was contained in the length  $l$ . The temperature of the transmission line, which was in an oven, was changed. When an appropriate period of time had elapsed for the new ambient temperature to stabilize, the frequency of the generator was varied until the null condition was found once more. Hence,

$$\Delta l = l_{t_1} - l_{t_2} = \frac{n(\lambda_1 - \lambda_2)}{4} = \frac{nv}{4} \left( \frac{1}{f_1} - \frac{1}{f_2} \right)$$

where  $v$  is the velocity of propagation in the transmission line, and  $n$  is some odd integer that was easily established by a crude measurement of the line length.

The accuracy of the method rests in the accuracy with which the difference between  $f_1$  and  $f_2$ , both large numbers, can be determined. It was estimated that the experimental error in the measurement of  $\Delta l/l$  was one part in  $10^5$ .

In the case of phase-compensated cable, good nulls could not be obtained because  $Q$  was too low. The phase bridge method of Fig. II-76 was used, which read directly the change in electrical length. This method has accuracy similar to the null-shift method.

Significant thermal hysteresis was exhibited by the irradiated polyethylene-filled structures and, to some extent, the phase-compensated coaxial cable. Figure II-77(a) is a plot of a hysteresis loop observed in an irradiated polyethylene-filled structure. For small excursions the loop is closed. However, for large temperature excursions, dimensional changes take place which at first seem irreversible but, after a long period of time, the structure slowly recovers. For example, a specimen at room temperature ( $25^\circ\text{C}$ ) was cooled to  $-50^\circ\text{C}$  and then brought back to room temperature. After contraction, the specimen did not immediately return to its original length; however, it apparently recovered after three days had elapsed.

Of the transmission lines tested, the dielectric foam-filled transmission line had the lowest temperature coefficient. The attenuation characteristics of various transmission lines are shown in Fig. II-77(b).

## 2. Bends and Turns

M. Siegel

One of the numerous problems associated with building time-delay units for a time-delayed array radar is that of wrapping up long lengths of microwave cable within the relatively small and confined spaces available behind the array face. A specific problem directly associated with closely spaced cable is the choice of a minimum turning radius on the many turns and bends in the delay unit. Therefore, an attempt was made to evaluate the effects of the turns and to optimize the turning radius in the various transmission media that were available. Those media considered were (a) coaxial line, (b) dielectric-filled strip and slab lines, and (c) air- or foam-filled strip or slab lines.

The only coaxial line that was and still is being considered is  $\frac{1}{4}$ -inch-diameter foam-filled cable. (The bending radius in this cable, as a rule of thumb, should be greater than 10 cable diameters in order for the bend to be reflectionless.) The major difficulty associated with solid-dielectric strip line is the serious variation of this line with temperature. Therefore, the major interest (in addition to miniature foam coaxial lines) lies in foam-filled strip line. However, since solid-dielectric strip line and connectors (irradiated polyethylene-filled boards) are so readily available, experiments were conducted both in the irradiated polyethylene-filled medium



and in the foam-filled strip line, examining the reflection from turns. The final delay units are expected to be made in some kind of foam line, since these lines have comparatively low loss and small temperature-variation characteristics.

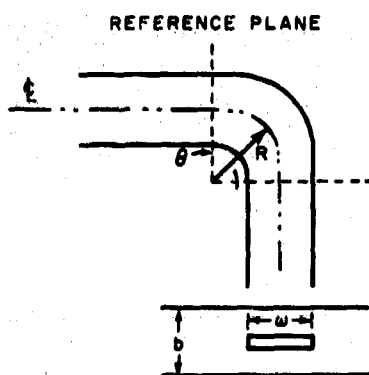
Both round turns of various turning radii and mitred turns of various mitre dimensions were investigated. It should also be mentioned that the primary technique used for experimentally evaluating the various turns was microwave frequency reflectometry, using the substitution method to detect reflections. Later in the investigation, as TDR equipment became available, most of the effort employed this powerful technique.

To attempt to evaluate analytically the minimum turning radius in various media, the literature was consulted. Schelkunoff\* discussed bends in structures guiding waves, and predicts a decrease in characteristic impedance and an increase in mean wave velocity around the bend, for structures whose parallel conductors are bent in a plane perpendicular to the plane of the electric field. However, whether the bend is in the E- or H-plane, one can return the impedance along the turn to its normal value by decreasing the dimensions of the conductors in the plane of the bending, or by increasing the dimensions perpendicular to this plane. In strip or slab line, it is therefore expected that the change in impedance around the turn can be compensated by decreasing the width of the center conductor around the turn.

Expressions are derived, by use of variational techniques, for the variation in impedance and electrical length along a bend in waveguide.† Getsinger‡ obtained equivalent expressions for the impedance change along a bend in strip line by using a dual analog. These results are as follows.

For a thin strip:

$$D = \omega + \frac{2b}{\pi} \ln 2$$

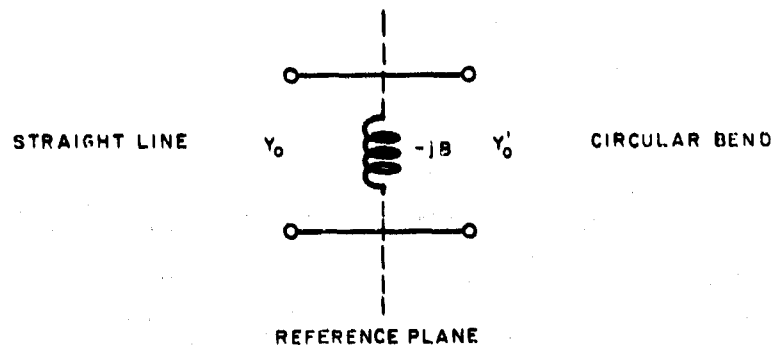


\*S.A. Schelkunoff, Electromagnetic Waves (Van Nostrand, New York, 1956), p.324.

†N. Marcuvitz, Waveguide Handbook, Radiation Laboratory Series, M.I.T. (McGraw-Hill, New York, 1951), Vol. 10.

‡W.J. Getsinger, private communication to D.H. Temme.

Equivalent circuit:



Admittance:

$$\frac{Y_0'}{Y_0} = 1 + \frac{1}{12} \left(\frac{D}{R}\right)^2 \left[ \frac{1}{2} - \frac{1}{5} \left(\frac{2\pi D}{\lambda}\right)^2 \right]$$

Susceptance:

$$\frac{B}{Y_0} = \frac{32}{\pi^7} \left(\frac{2\pi D}{\lambda}\right)^2 \left(\frac{D}{R}\right)^2 \sum_{n=1, 3, 5, \dots}^{\infty} \frac{1}{n^7} \sqrt{1 - \left(\frac{2D}{n\lambda}\right)^2}$$

Electrical length:

$$l = \frac{R\theta}{1 - \frac{1}{12} \left(\frac{D}{R}\right)^2 \left[ -\frac{1}{2} + \frac{1}{5} \left(\frac{2\pi D}{\lambda}\right)^2 \right]}$$

The first group of measurements was made on Tellite board. It should be noted that the magnitude of the VSWR expected from the turns was as low as 1.02. However, the connectors in a Tellite board can have a VSWR as high as 1.2. It was therefore decided that the most reasonable approach to evaluating the bend mismatch would be by means of the substitution method. An alternate approach was considered which consisted of building a slotted line into the transmission media, hence bypassing the masking effect of the connectors (in fact, a slotted line was actually assembled in slab line). However, after considering the many different types of transmission media of interest, plus the realization that very many measurements would be needed to make broad-band measurements, the substitution method was decided upon.

A fundamental precept to the successful use of the substitution method is that nothing else in the experimental structure be allowed to change other than the bend under consideration. Hence, a very rugged Tellite board was built, incorporating mode suppression and allowing the connectors to be permanently attached to the board. It had been found previously that if connectors had to be removed each time the board was disassembled, repeatable results would not be possible. When the board was modified such that it could be disassembled without disturbing the connectors, repeatable results using the swept frequency reflectometer were obtained.

The first experiment was designed to evaluate the effect of turn radius on reflected energy as the radius was made successively smaller. A Tellite board (ground plane spacing = 0.25 inch, center conductor width = 0.200 inch) having two turns was assembled; one turn was made sufficiently large (1.5-inch radius) to be assumed essentially reflectionless, while the other turn was made variable (radii from 1.5 to 0.3 inches in 0.1-inch steps). A unique feature was that the over-all

path length from connector to connector on the board was to be kept approximately constant as the radius was varied, so that reflections due to connector phasing would stay relatively constant throughout the series of measurements. A series of FDR (frequency-domain reflectometry) photographs were taken, one for each turn radius. These data were reduced, and plots of reflected energy vs turn radius at nine different frequencies evenly spaced throughout the band were made. These measurements were made at S-band (2 to 4 kMcps) which enabled a choice to be made of the minimum turn radius possible before reflections from the turn became excessive. From these data, a value of the radius of 0.7 inch was estimated to be the point where reflections would noticeably begin to increase if the radius were further reduced.

Since a turning radius of 0.7 inch was considered too great to use in the time-delay units, it was decided to attempt to compensate the round turns according to Marcuvitz's (modified) technique and to evaluate the magnitude of the reflection from the modified turn. Substituting the constants of the Tellite board being used, and using one of the smaller radii (radius = 0.3 inch; this places parallel center conductors 0.4 inch apart), it was found that the center line would have to be etched 8 mils narrower (4 mils on each side) along the turn to return the impedance along the turn to the normal characteristic impedance. Susceptance at the junction is of the order of  $10^{-6}$  of the characteristic admittance and therefore can be neglected. The electrical length was approximately 4 percent less than the physical length.

Measurements made on this compensated turn, and on turns with slightly different compensations, indicated that while there was considerable improvement over the uncompensated turn of the same radius, objectionable reflections still existed.

A parallel investigation was performed using various mitred corners. Coarse measurements were at first made by means of the substitution method, ascertaining that the proper value of  $a/\omega$  in Tellite strip line was in the region of 1.3 to 1.7 (where  $a$  = length of the diagonal mitre cut, and  $\omega$  = center conductor width).

A series of measurements was subsequently made with  $a/\omega$  varying between 1.3 to 1.7 in 0.2 intervals. After reducing the data into plots of reflected energy vs mitre  $a/\omega$  for nine different frequencies spread throughout S-band, examination showed that very little difference could be noted between mitre turns using  $a/\omega = 1.50$  to  $1.52$  and a reflectionless 1.5-inch radius circular turn. This  $a/\omega$  ratio then appeared optimum for this size Tellite.

The mitred turn was more successful than the compensated circular turn. In addition, measurements made at X-band similar to those made at S-band indicated that the mitred turn was behaving quite well at X-band. Therefore, most of the interest was shifted over to mitred turns. One immediate advantage of a mitred turn is the very close spacing that is possible since the turn is composed of right-angle intersections.

It was necessary at this point to evaluate the magnitude of the reflection from this turn (note that, while the substitution method gives a relative indication that reflections exist, it gives no indication as to their absolute magnitude).

One way to evaluate the magnitude of the reflection from the turn is to cluster a large number of turns periodically spaced in Tellite, which is a sufficiently low-loss media (see Figs. II-78 and II-79); the spacing should be adjusted so that reflections from all the turns would be in phase in the middle of the frequency band. (The frequency is chosen to be at a location where the relative measurements made by the substitution method indicate that a maximum, in reflected energy from the turn, exists.) This large reflection from the phased-up turns would therefore "swamp-out" connector effects and, assuming the effect of  $n$  reflections gives  $n$  times an

individual reflection, the approximate magnitude of the individual reflections could be obtained. This line, referred to as a "snake line," also had interesting properties in that a correspondence exists between reflections (displayed as a function of frequency) from a periodically spaced series of discontinuities, and an antenna pattern from a phased array antenna having periodically spaced antenna elements displayed as a function of spatial angle. Plots of reflected energy vs frequency for the snake line exhibit a  $\sin nx / \sin x$  character (which is the case for a lossless media) similar to spatial patterns for a phased array antenna. In addition, analogous to the array- and element-factor concepts of array antennas, it is probably possible to characterize the nature of the individual reflection from each mitre vs frequency.

Figure II-80 shows a photograph of reflected energy vs frequency for 98 mitred corners ( $a/\omega = 1.52$ ) evenly spaced on a Tellite board over an S-band region. Figure II-81 shows a similar photograph of the same board over an X-band region. These photographs (together with photographs of the individual mitres vs frequency) indicate that the VSWR from each mitre corner was approximately 1.01 at the S-band, and 1.02 at the X-band regions investigated.

Next, it was decided to optimize the mitre corner in foam strip line. This line used a 0.312-inch center conductor, a 0.228-inch ground plane spacing, and a foam having  $\epsilon = 1.04$ .

It had previously been noted that small variations in centering the center conductor between the ground planes would cause considerable reflection. (Typically, for a ground plane spacing of 0.228 inch, an 8-mil variation in centering the line would cause a VSWR of 1.01.) The foam dielectric therefore had to be milled to the proper dimensions and assembled in a rigid sandwich structure, supported by machined bar stock which served both as a support medium and as mode suppression. A rugged foam strip-line board was constructed such that the connectors would not have to be touched when it was desired to disassemble the board. This board was used to examine the reflections (by the substitution method) of mitres having  $a/\omega$  varying from 1.30 to 1.50 in steps of 0.02. Comparing these results to a circular turn of 1.5-inch radius, the optimum mitre (from a minimum reflection point of view) appeared to have  $a/\omega = \sim 1.36$  or 1.38.

As a check on the FDR measurements, time-domain reflectometry (which had recently become available and sufficiently sensitive to be useful) was utilized to evaluate, by means of the substitution method, the optimum mitre in foam strip line. This technique also indicated that the optimum mitre  $a/\omega$  was approximately 1.36 to 1.38. It should be mentioned that the curves indicating the optimum mitre were rather broad; hence, only approximate numbers can be given.

Snake lines were assembled in the foam dielectric similar to those made in Tellite (see Fig. II-82) and indications were that, using a mitre  $a/\omega$  of 1.38, the approximate VSWR per mitre at S-band was 1.01 while at X-band it was 1.02.

As a final check on the reflection from a turn, a foam strip-line board was assembled containing a delay line of 100 wavelengths at S-band involving 34 mitred corners (Fig. II-83). It is expected that delay lines much more compact than this one will finally be built, since the only restriction placed on the spacing is related to mutual coupling between parallel center conductors and not on turning radius, when mitres are used. The only difficulties associated with the 100 wavelength line were found to be related to the making of joints in the center conductor, and mechanical ripples in the ground planes.

Both FDR (Fig. II-84) and TDR measurements that have been made on the above delay line lead to the belief that reflections from turns in large delay lines should be tolerable and manageable.

### 3. Connectors and Interconnections

D. H. Temme

It was clear early in the time-delay development program that efforts to evaluate the match of different types of delay line and switches would be significantly impaired by the mismatch of connectors. Likewise, it appeared that interconnection between the tightly packed components in parts of the subarray with any of the existing connectors would be considerably less than optimum. Some initial investigations suggested (a) that a family of connectors and transitions could be based on the dimension of the N connector, (b) that an improved N connector and associated transitions with good match and mechanical mating with the present N connector was possible, and (c) that a phase stable dielectric push connector with high-power capability could be directly substituted for the improved N connector after initial evaluation of the component with the improved N connector. All connector work is included in a report to be published separately.

### 4. Diode Switches

F. Betts

This section discusses the development of low-power diode switches to be used in the large delay bits of the time delay. Part a sets forth performance considerations, discusses the switch configuration chosen, and relates performance to certain diode and circuit parameters. Part b presents results obtained with one- and two-diode switch assemblies. Part c describes the single-pole double-throw switches and their use to make a time delay along the lines discussed in Sec. C of this chapter.

#### a. Switch Requirements and Performance Considerations

Work reported in Sec. C of this chapter has suggested that diode time-delay units should follow the general configuration of Fig. II-85; hence, development work was aimed toward diode switches of large bandwidth to achieve the switching operations suggested in the figure. A general single-pole double-throw switch is shown in Fig. II-86. For transmission from port 1 to port 2,  $Z_1$  should be larger and  $Z_2$  smaller than  $Z_0$ . For transmission from port 1 to port 3,  $Z_2$  should be larger and  $Z_1$  smaller than  $Z_0$ .

The basic configuration of Fig. II-85 then becomes as shown in Fig. II-87. Thus, for transmission through path 1,  $Z_1$  and  $Z_3$  would be high, and  $Z_2$  and  $Z_4$  would be low.

Section C of this chapter showed that signal leakage through the unused path should be at least 36 db below the transmission through the desired path. If  $l_2$  is the long path for a long delay section, then over even a small bandwidth it will vary in length by at least one-half wavelength.

Two shunt impedances  $Z_s$  separated by a line section  $d$  have a total insertion loss  $L_T$  which is a function of their separation in wavelengths. If the loss  $L$  due to a single diode across the line is

$$L = \left| 1 + \frac{Z_0}{2Z_s} \right|^2$$

it can be shown that, for two diodes, the total loss  $L_T$  is bounded by

$$4L \leq L_T \leq 4L^2$$

The upper bound is obtained when the separation is an odd multiple of  $\lambda/4$ ; the lower bound is obtained when the separation is a multiple of  $\lambda/2$ . Since  $f_2/\lambda$  varies as discussed above, the use of two diodes per delay arm plus the 36-db leakage specification would require

$$10 \log (4L) - 10 \log L + 6 \geq 36$$

or that each diode provide 30 db of isolation. However, if an additional diode is placed  $\lambda_0/4$  from an existing switch (Fig. II-88) in each arm, then the total attenuation is greater than twice the loss (in db) of a single diode. Thus the required isolation per diode is greatly reduced.

The requirement on maximum VSWR obtained is from the results given in Sec. C-1 of this chapter, in which the case of two shunt susceptances separated by a lossless line stretcher was analyzed. From these results it was decided to set a maximum VSWR of 1.1 for each switch assembly as a design goal.

The matter of VSWR of the multi-switch time-delay unit appeared difficult to assess analytically, as the configuration of Fig. II-88 has five shunt elements whose reflections must be taken into account. Accordingly, a simple computer program was written which would compute the input VSWR at many frequencies over a specified band with specified frequency increment. All parameters could be arbitrarily specified. Its use will be discussed in part c, below.

Shunt diode switches have been well described in TR-299 and are only briefly discussed here. The equivalent circuit for the forward-biased case is shown in Fig. II-89. In TR-299, the isolation of this switch\* was shown to be

$$L = \left| 1 + \frac{Z_0}{2Z_1} \right|^2 = \left| 1 + \frac{Z_0}{2[R_s + jX_0(f/f_0 - f_0/f)]} \right|^2$$

The maximum isolation  $L_{\max}$  is

$$L_{\max} = \left( 1 + \frac{Z_0}{2R_s} \right)^2$$

Thus, for large maximum isolation, a diode with low  $R_s$  should be chosen. Actually, the band over which the isolation is greater than some fixed amount  $L_B$  is probably of more interest.

$$L_B \leq \left| 1 + \frac{Z_0}{2(R_s + jX)} \right|^2 \approx \frac{Z_0^2}{4|R_s + jX|^2}$$

If  $L_{\max}$  is 10 db or so larger than  $L_B$ , we can write

$$L_B \leq \left( \frac{Z_0}{2X} \right)^2$$

$$L_B \leq \frac{Z_0}{2X}$$

$$X = X_0 \left( \frac{f}{f_0} - \frac{f_0}{f} \right) \leq \frac{Z_0}{2L_B}$$

---

\* Normally  $R_s \ll X_{LPT}$ .

Now  $X_o = 2\pi L_o f_o$ . Assume  $B_R/2 < 0.1f_o$ . Then, if equality holds at  $f = f_o + (B_R/2)$ , we have nearly

$$\frac{B_R}{f_o} X_o = \frac{Z_o}{2L_B}$$

$$B_R = \frac{Z_o}{4\pi L_{eq} L_b} \quad (4)$$

For large bandwidth, a diode and circuit configuration should be chosen to minimize  $L_{eq}$ . This is an interesting relation in that it indicates that, for fixed  $L_{eq}$ , one should be able to obtain bandwidth  $B$  at any center frequency by changing  $C_s$ .

The equivalent circuit for reverse-biased operation is shown in Fig. II-90. For present switching diodes,

$$\frac{1}{2\pi R_s C_j} \geq 100 \text{ Gcps}$$

Also, if the series resonant frequency of  $C_j$  and  $L_{eq}$  is high, i. e., if

$$\frac{1}{2\pi L_{eq} C_j} \gg f_o$$

then we can neglect the net reactance

$$X_{L_{eq}} - X_{C_{ST}}$$

The simplified equivalent circuit of Fig. II-91 is thus obtained. We then choose

$$X_{L_{PT}} = X_{C_j}$$

Generally, we are interested in the band over which the VSWR caused by such a switch is less than some value  $S_{max}$ . If  $S$  is near unity

$$S = \frac{1 + |\Gamma|}{1 - |\Gamma|} \approx 1 + 2|\Gamma|$$

Now, for an admittance  $Y_s$  in shunt with a matched system of characteristic admittance  $Y_o$

$$\Gamma = \frac{-Y_s}{2Y_o + Y_s}$$

Again, if  $|\Gamma|$  is small,

$$|\Gamma| = \frac{|Y_s|}{2Y_o}$$

Thus, from Fig. II-90,

$$Y_s = j2\pi f_o C_j \left( \frac{f}{f_o} - \frac{f_o}{f} \right)$$

and

$$S_{\max} \geq S = 1 + 2 \frac{|Y_s|}{2Y_o} = 1 + \frac{2\pi f_o C_j \left( \frac{f}{f_o} - \frac{f_o}{f} \right)}{Y_o}$$

$$S_{\max} \leq 1 + \frac{B_o \left( \frac{f}{f_o} - \frac{f_o}{f} \right)}{Y_o}$$

$$B_o \left( \frac{f}{f_o} - \frac{f_o}{f} \right) \geq Y_o (S_{\max} - 1)$$

If equality holds at  $f = f_o + (B_f/2)$ , then for  $B_f/2 < 0.1f_o$  we have nearly

$$\frac{B_f}{f_o} B_o = Y_o (S_{\max} - 1)$$

$$B_f = \frac{Y_o}{2\pi C_j} (S_{\max} - 1) \quad (5)$$

Again it is seen that, for fixed  $C_j$ , the bandwidth is independent of frequency. Of course, the equivalent circuit from which these conclusions were deduced ceases to be valid at higher frequencies.

#### b. Results Obtained with One- and Two-Diode Switch Assemblies

First construction attempts used slab line with the diode mounted between the center conductor and a ground post. End and top views of this construction are shown in Figs. II-92(a) and (b). The value of total circuit inductance for this configuration was determined to be about 0.5 nh for 0.228-inch ground plane spacing. Using Eq. (4), taking  $L_B$  as 20 db and  $Z_o$  as 50 ohms

$$B_R = \frac{50}{4\pi \times 0.5 \times 10^{-9} \times 100} \approx 800 \text{ Mcps}$$

Switches built at 3 and 7 Gcps yielded very close to this value of bandwidth. Turning to Eq. (5) with  $S_{\max} = 1.1$ ,  $Y_o = 0.02$  and  $C_j = 0.8 \text{ pf}$

$$B_f = 398 \text{ Mcps}$$

Bandwidths actually obtained were around 280 Mcps, suggesting an extra circuit capacity of the order of 0.4 pf.

A two-section switch, with two diodes  $\lambda_o/4$  apart, was built in slab line, yielding the performance shown in Figs. II-93(a) and (b). As the VSWR, isolation and insertion loss appeared to meet the requirements for a time-delay unit, a six-diode assembly with connectors for an external delay line was constructed. Though its insertion loss was measured to be less than 0.5 db at 3 Gcps, the severe mechanical problems in making complex slab-line structures prompted investigation of other transmission media. A strip-line switch was made using polystyrene foam to support a copper conductor, etched from 1-oz copper on a 2-mil mylar base. The construction details and a photo of such a switch are given in Figs. II-94(a) and (b) and II-95.



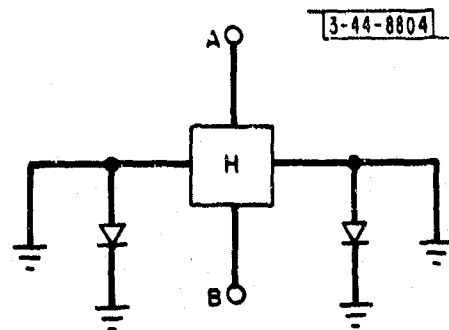
The mechanical characteristics of this type construction yield easy assembly and reliable operation.

As seen in the photograph, the line was narrowed at the diode which gave an  $L_{eq}$  value of about 0.7 nh. Here the "notch" is about one fourth of a line width. Further narrowing did not seem to yield lower values. Though not shown in this picture, tuning screws in the removed ground plane allow compensation for diode-to-diode capacity variation by adding a variable capacity essentially in parallel with the diode. With the exception of slightly narrower bandwidth in the isolation state due to larger  $L_{eq}$ , the performance was similar to that shown in Figs. II-92(a) and (b). However, the insertion loss is somewhat higher possibly due to the use of some beryllium copper in connecting tabs.

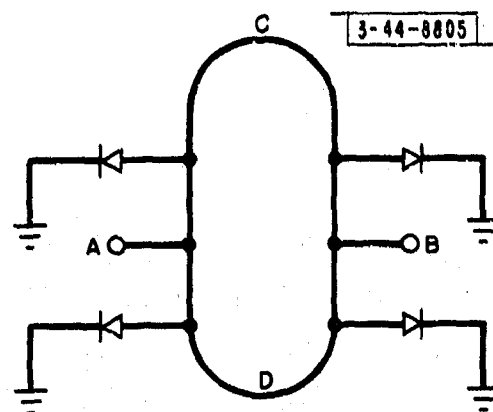
#### c. Six-Diode Time-Delay Assembly

Referring to Fig. II-88, it is seen that each delay unit presents two possible paths having equivalent circuits as shown in Fig. II-96. The leakage path has been neglected. Manual computation of VSWR vs frequency for such a circuit, when behavior over a wide band and several sets of circuit parameters is of interest, seemed very laborious, so a simple computer program was written giving ability to assign all parameters independently. In addition, it was decided to add an extra tuning stub at the input and see if it could be used to improve match. The program proved quite useful and showed that the input VSWR could be easily kept under 1.1 over a 10-percent bandwidth at 3 Gcps.

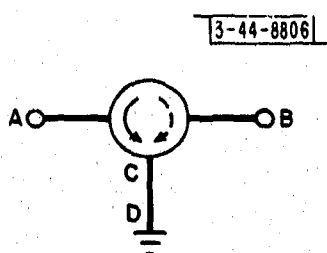
Using the strip conductor foam dielectric construction, development work was begun on a time delay with a very short length delay arm to see what kind of performance could be obtained. The photograph of Fig. II-97 shows the appearance of the completed unit. The layout was arranged so that the switches could later be mounted on the long foam-strip delay boards described in Sec. E-2 of this chapter. Connections to this delay line are to be made from the right side of the circuit. The oscilloscope photograph (Fig. II-98) shows the performance obtained. Though the two paths differ only slightly in length, it was possible to tune them for nearly identical response. The insertion loss was measured as 1.5 db. However, as this device was assembled with several beryllium copper sections and much scotch tape, merely to check the tuning capability, it should be possible to get the insertion loss well under 1 db even without gold plating the copper.



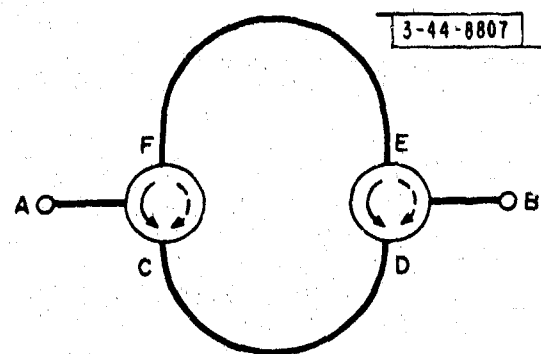
(a) Hybrid.



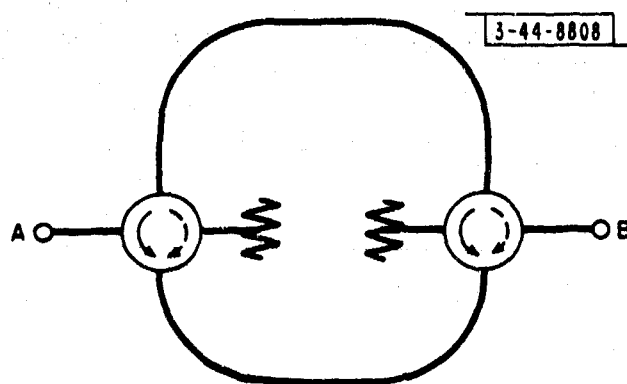
(b) Routing diode switch.



(c) Switching circulator with delay arm.



(d) Routing three-port switching circulator.



(e) Routing four-port switching circulator.

Fig. 11-45. Some time-delay configurations.

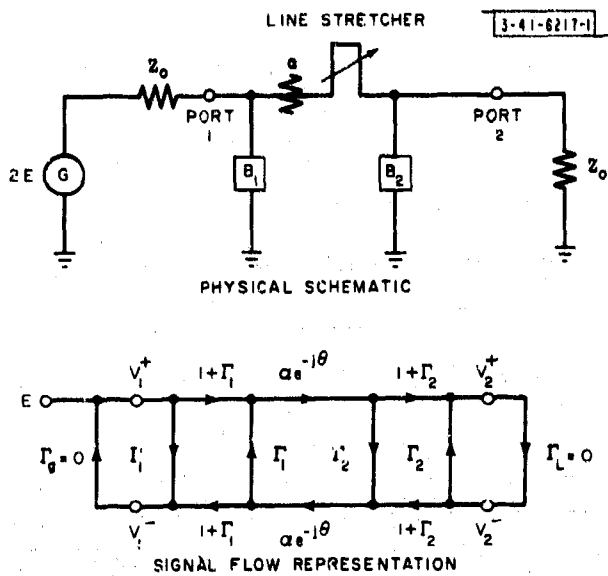


Fig. II-46(a). Effect of mismatches on phase of a transmitted signal.

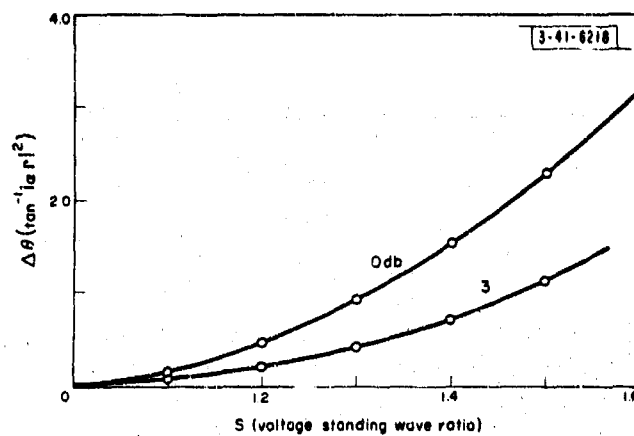


Fig. II-46(b). Phase errors due to mismatches.

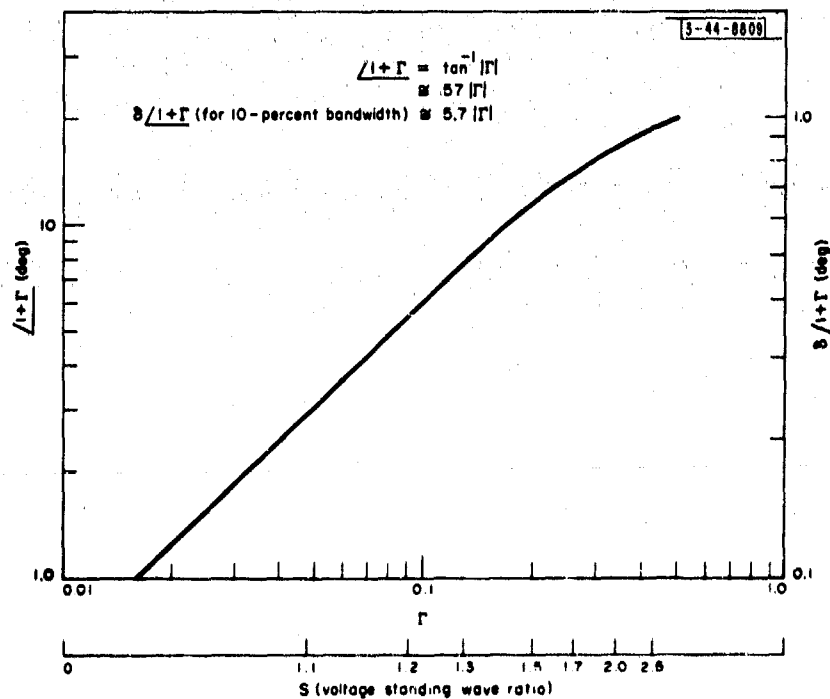


Fig. II-47. Bias errors.

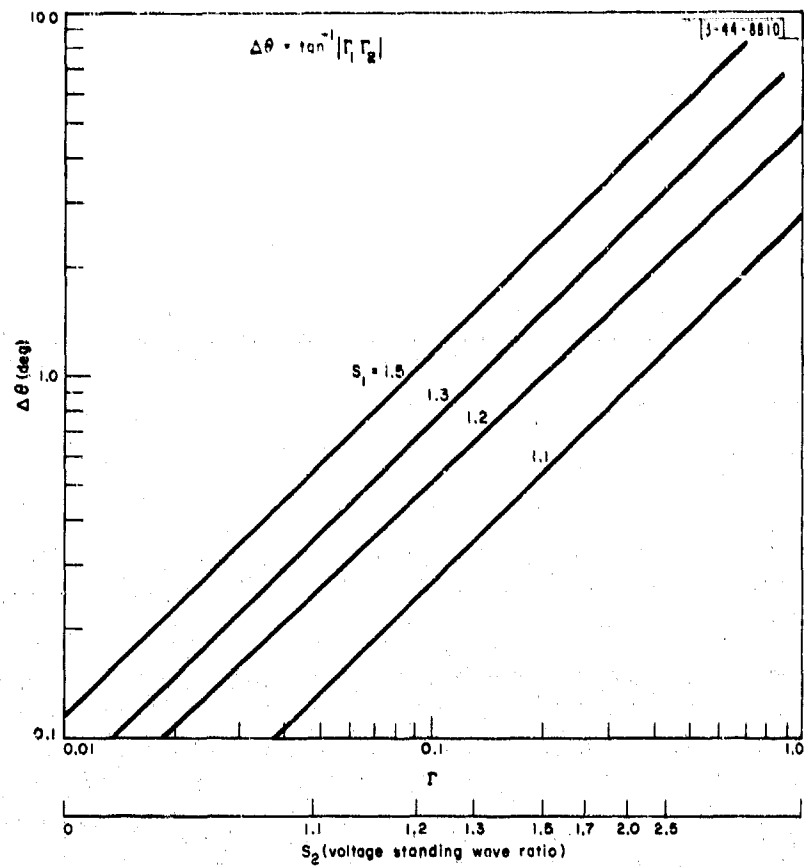


Fig. II-48. Phase errors associated with two susceptances.

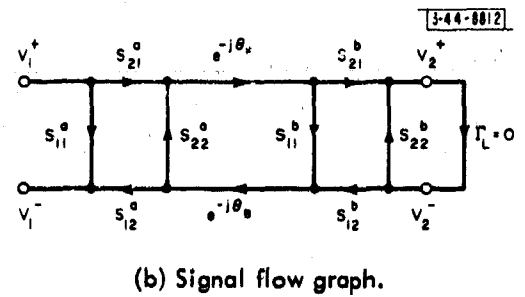
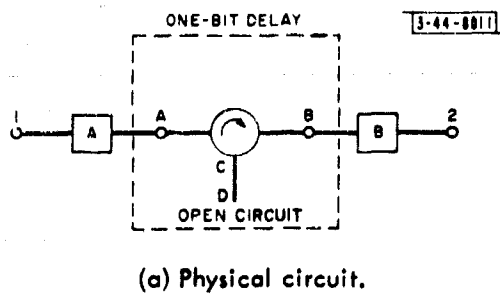
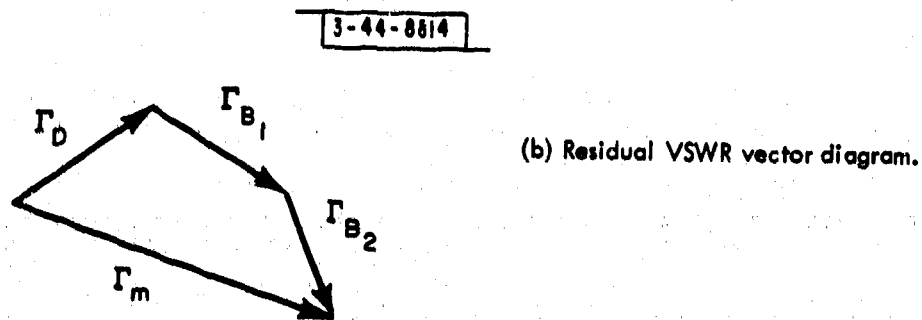
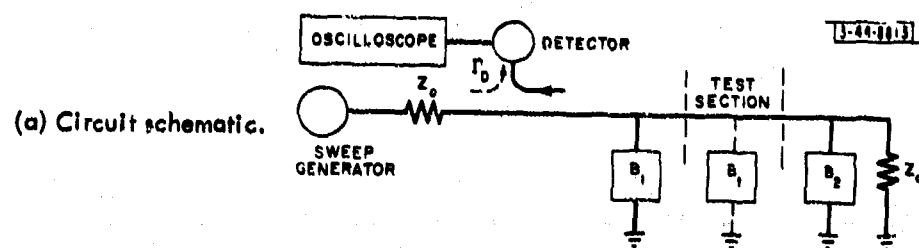


Fig. II-49. Difference in time-delay characteristics using reciprocal or nonreciprocal switches.



(c) Vector diagram with transition.

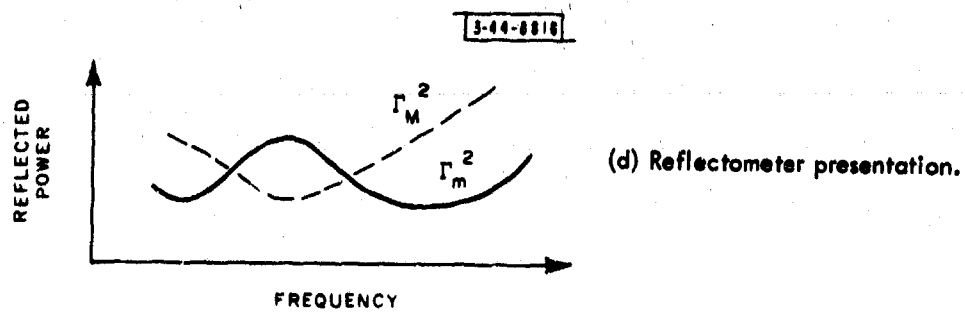
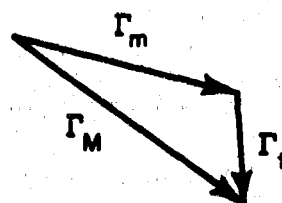


Fig. II-50. Reflectometer substitution method.

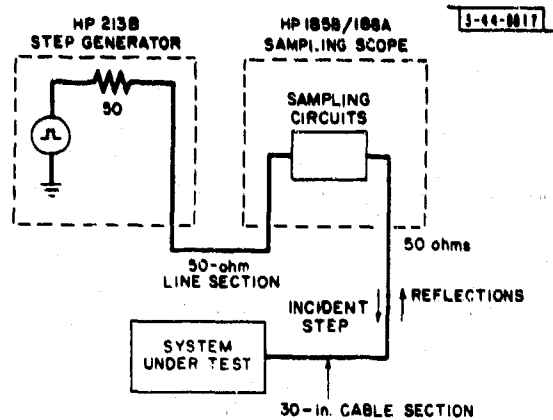


Fig. II-51. Equipment configuration for TDR measurements. The purpose of the 30-inch cable section is explained in Sec. D-1-c of this chapter.

Fig. II-52(a). Idealized reflection from mismatched termination.

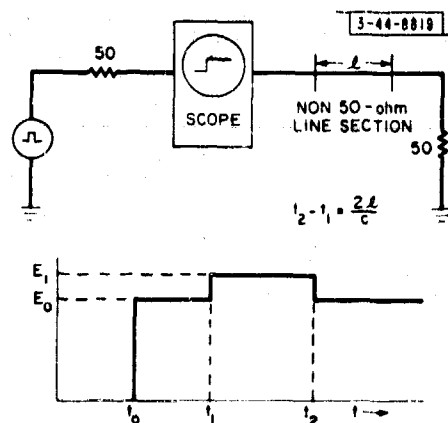
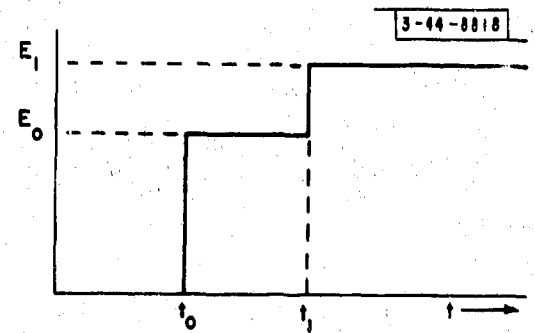


Fig. II-52(b). Reflection from section of non-50-ohm line.

Fig. II-53. Cascade of dissimilar impedance lines.

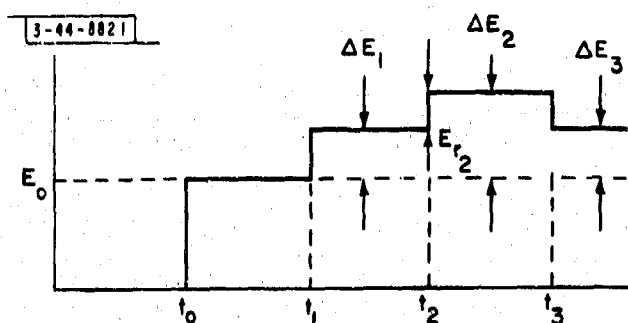
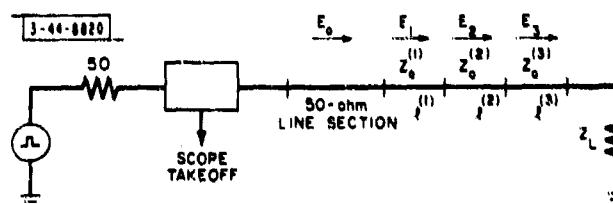
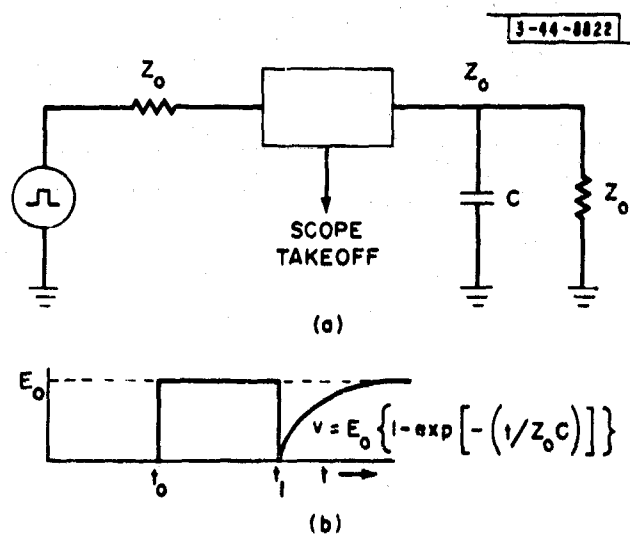
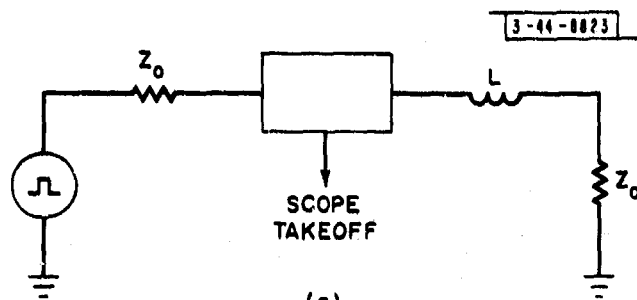


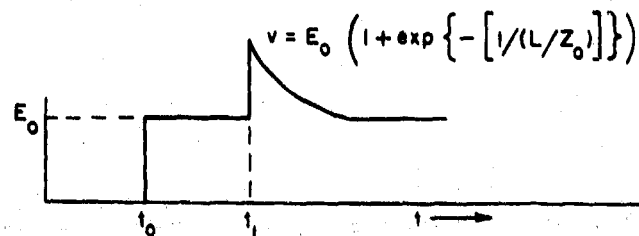
Fig. II-54. Observed reflection from cascaded dissimilar lines.

Fig. II-55. Reflection from shunt capacity, zero rise time step.



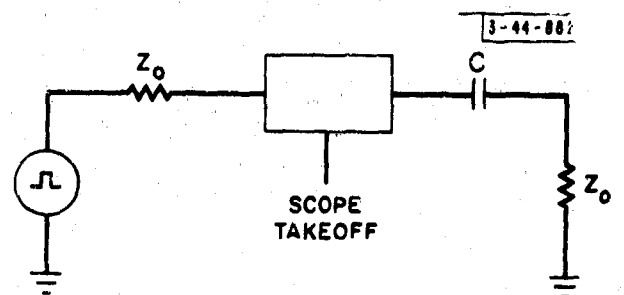


(a)



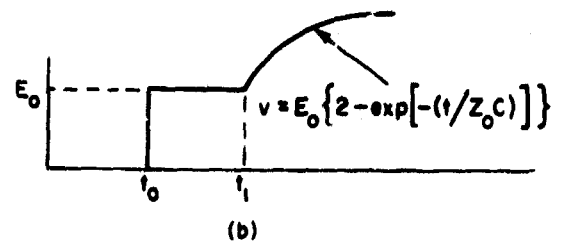
(b)

Fig. II-56. Reflection from series inductance.



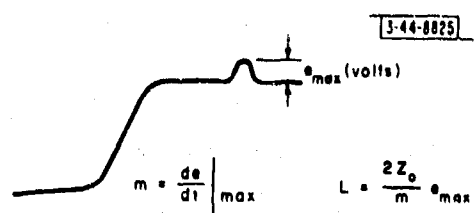
(a)

Fig. II-57. Reflection from series capacitor.

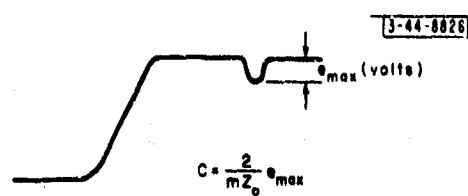


(b)





(a) Reflection from small series inductance.



(b) Reflection from small shunt capacitance.

Fig. II-58. Reflections from L and C showing effect of finite rise-time pulse.

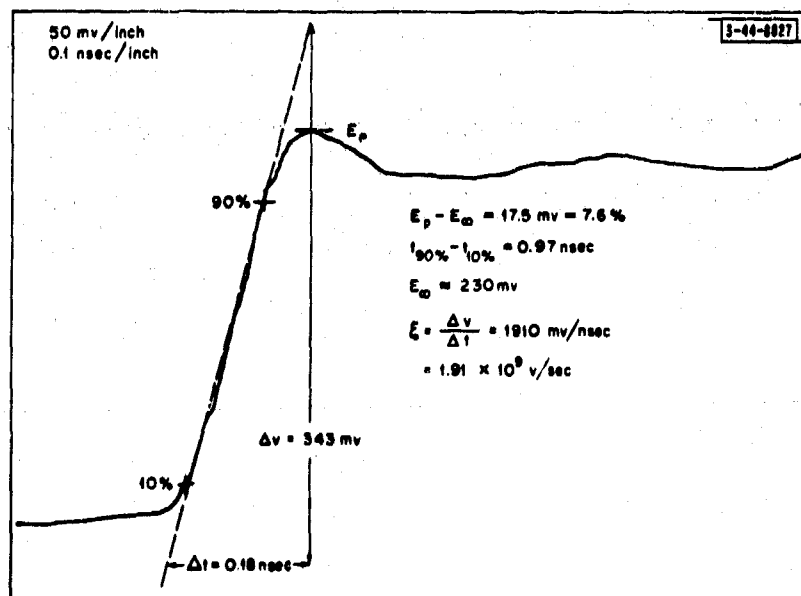


Fig. II-59. HP213B pulser output as viewed on HP185B/188A sampling oscilloscope with X-Y recorder.

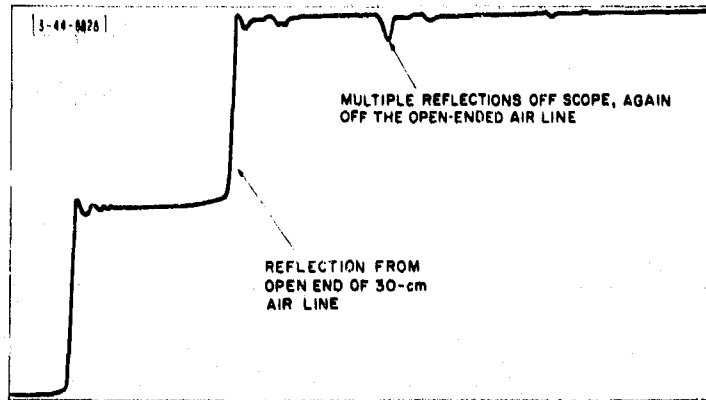


Fig. II-60. Open-circuit response of TDR system showing pulse shape and spurious reflections.

Fig. II-61. Scope photo showing multiple reflections from scope and then from open end. Incident pulse = 230 mv from scope; reflection = 34 mv;  $\Gamma = 0.1477$ .

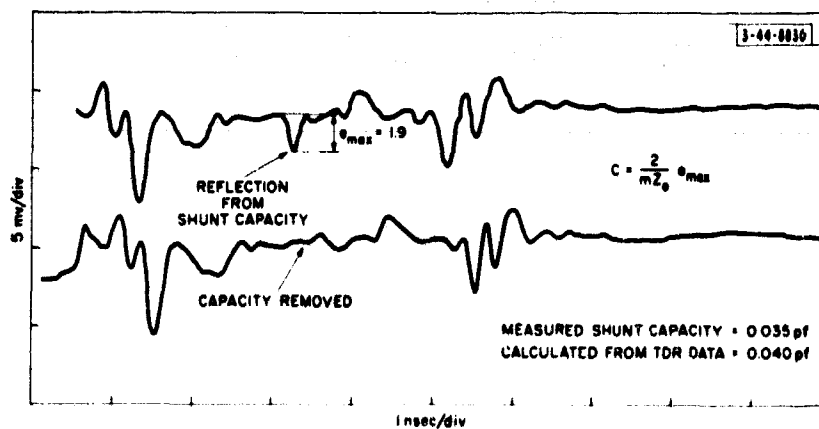
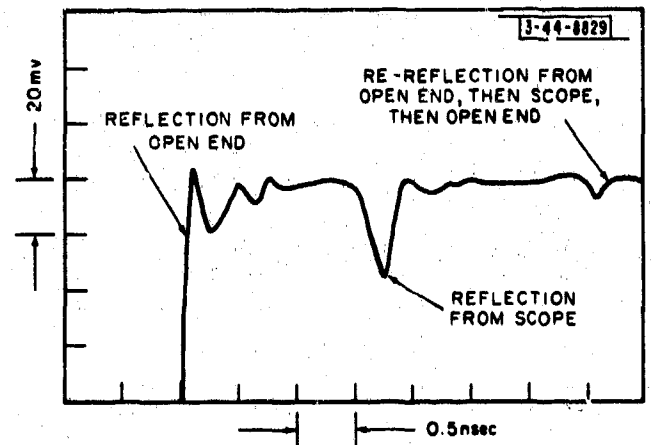


Fig. II-62. Reflections from small shunt capacity.

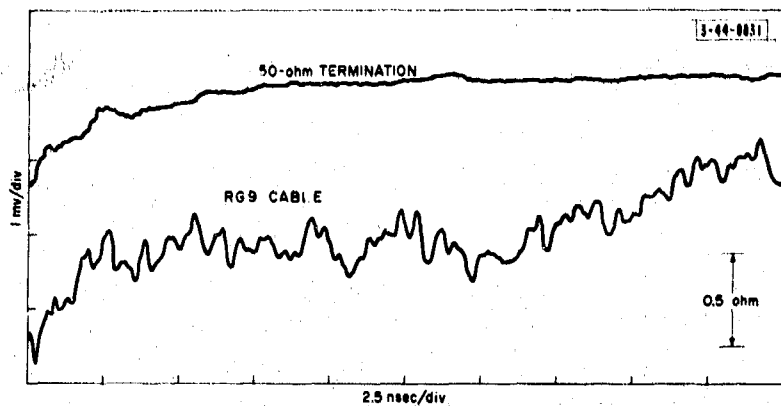


Fig. II-63. TDR record for RG9 cable.

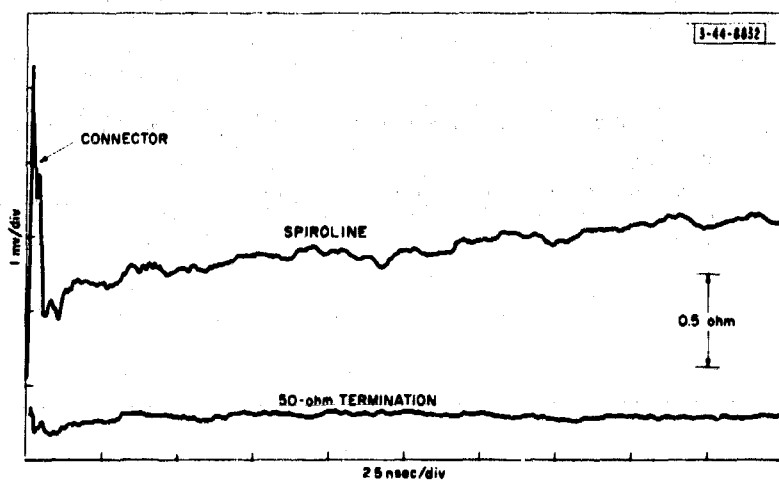


Fig. II-64. TDR record for Spirolite cable.

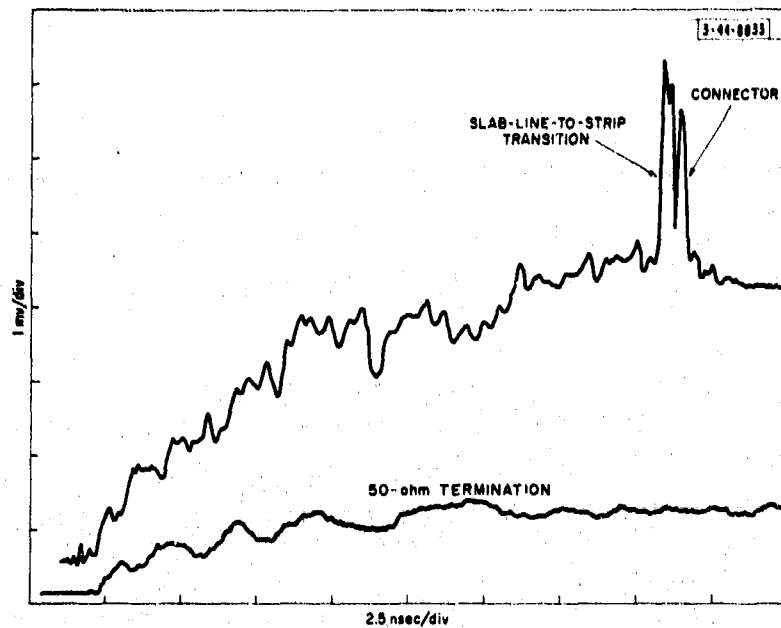


Fig. II-65. TDR record for strip transmission line.

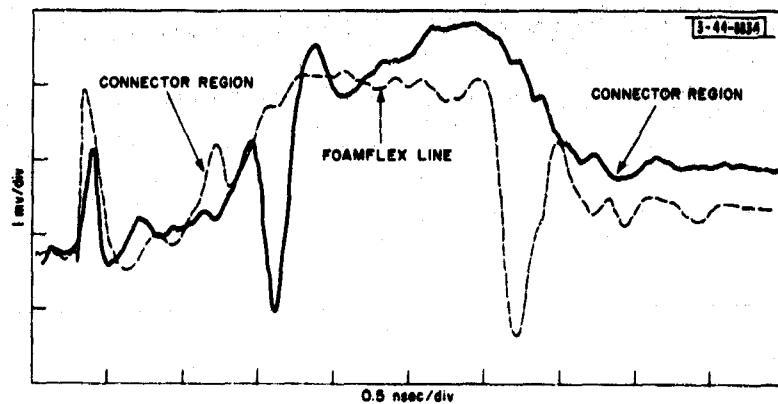


Fig. II-66. TDR record for Foamflex line with special connectors. Solid curve shows line as originally fitted to connectors; dashed curve shows cable turned end for end, connectors not moved.

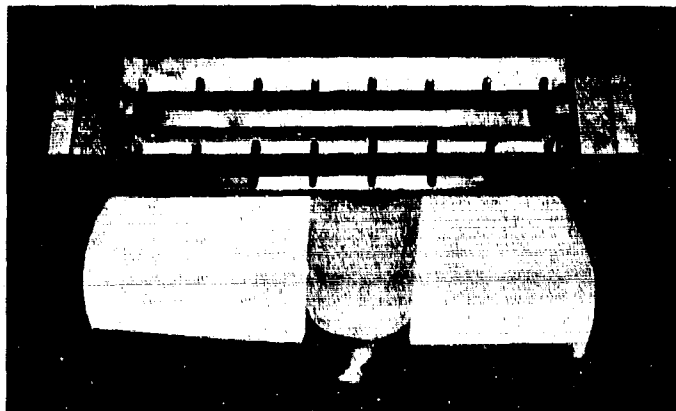


Fig. II-67. Strip-line test structure for "cleaning up" the reflections on TDR.

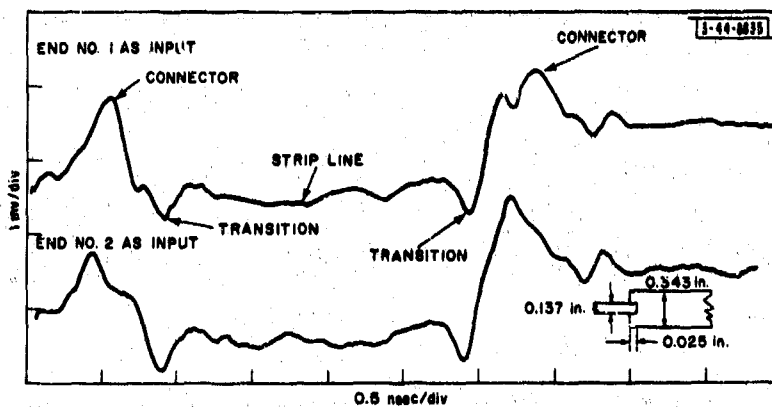


Fig. II-68. TDR record for test line as first assembled.

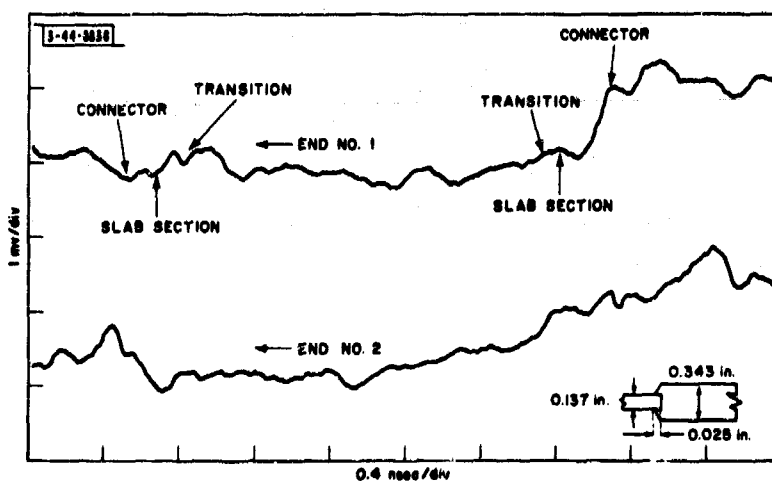
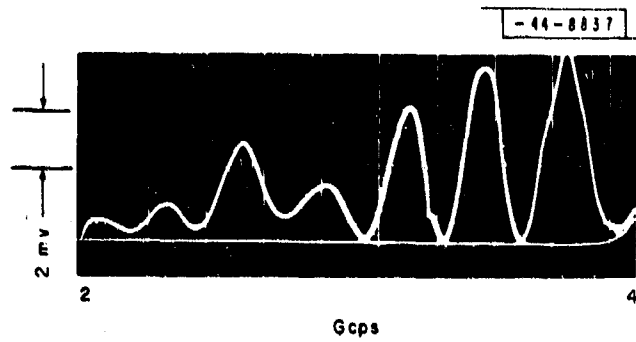
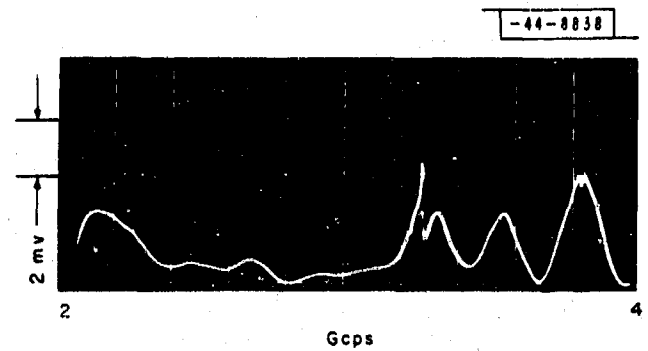


Fig. II-69. TDR record for test line after "fix-up" attempts.



(a) Test section, square transition, before "doctoring."  
3 divisions = 1.07 VSWR.



(b) Test section, new taper, after "doctoring."  
3 divisions = 1.07 VSWR.

Fig. II-70. FDR records for test line.

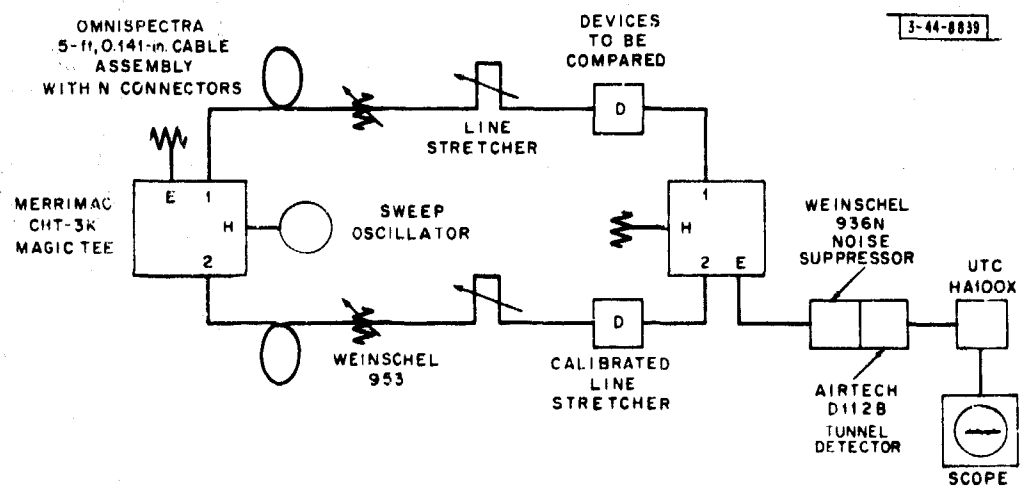


Fig. II-71. Transfer function comparison bridge.

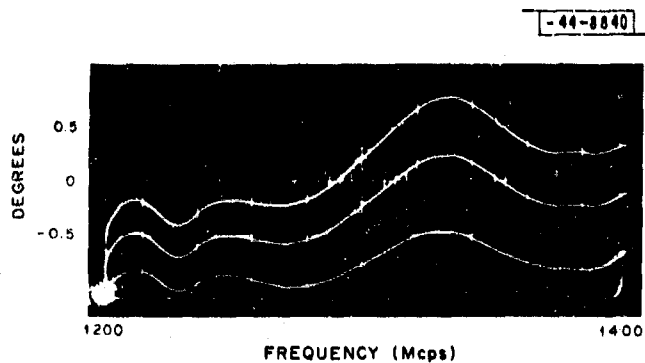


Fig. II-72. Oscilloscopic record of three unipolar unbalanced traces of bridge.

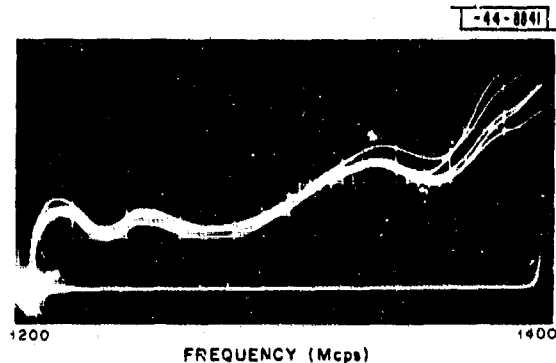


Fig. II-73. Cascaded coupler comparison.

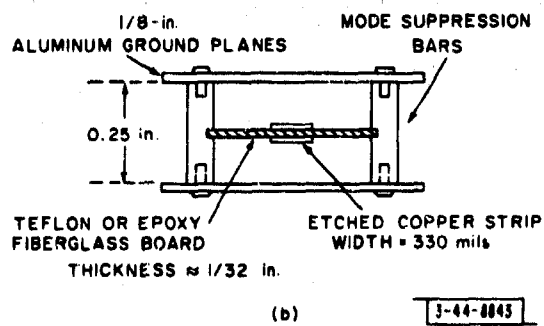
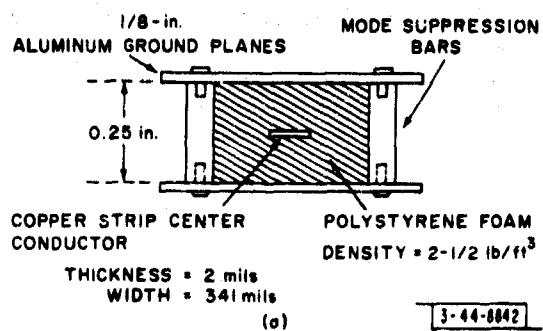


Fig. II-74. (a) Polyethylene dielectric foam-filled strip transmission line. (b) Air-filled strip transmission line with center conductor etched on thin dielectric sheet.

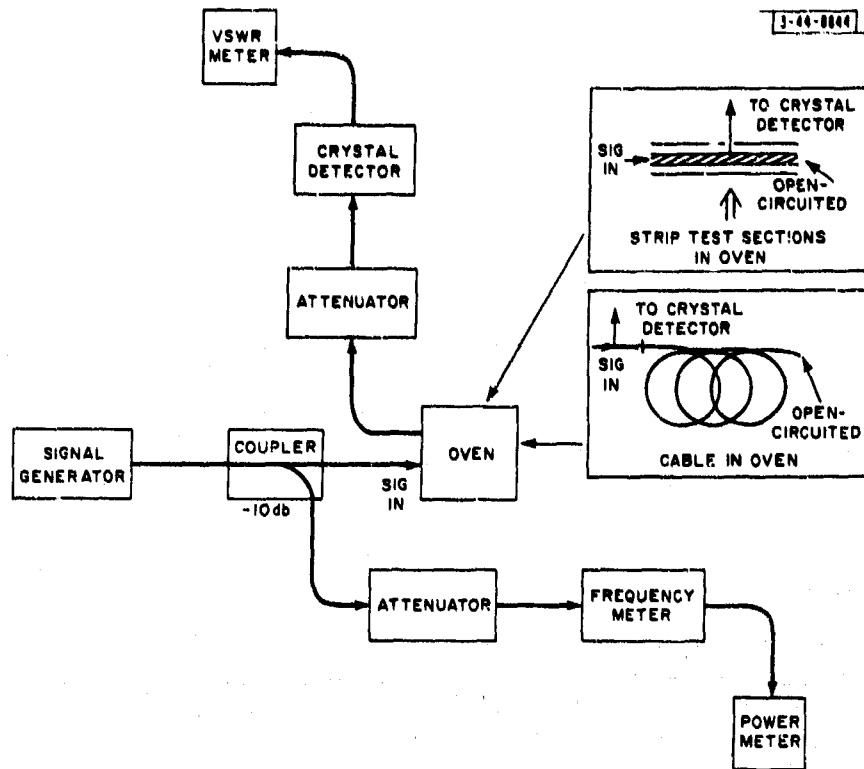


Fig. II-75. Temperature stability test circuit.

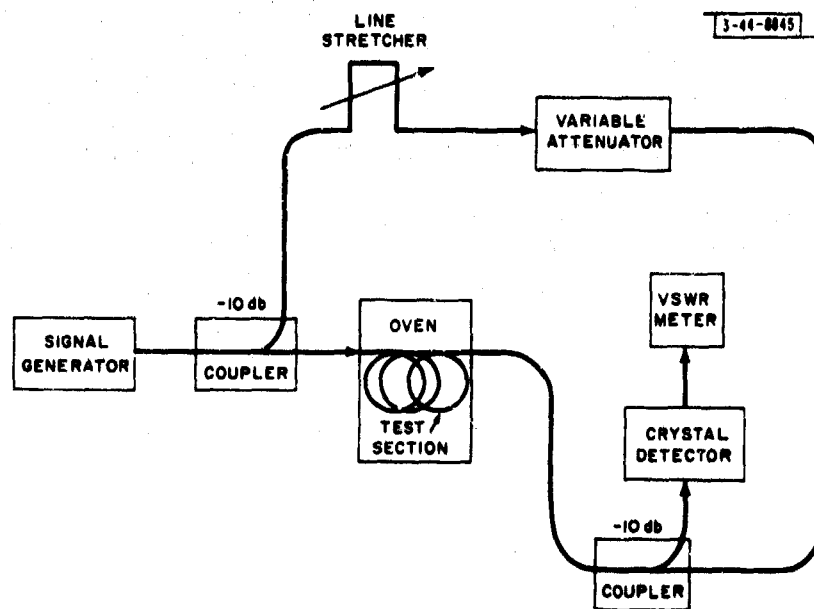


Fig. II-76. Temperature stability test circuit for lossy cables.



Fig. II-77(a). Hysteresis effect in irradiated polyethylene-filled strip transmission line.

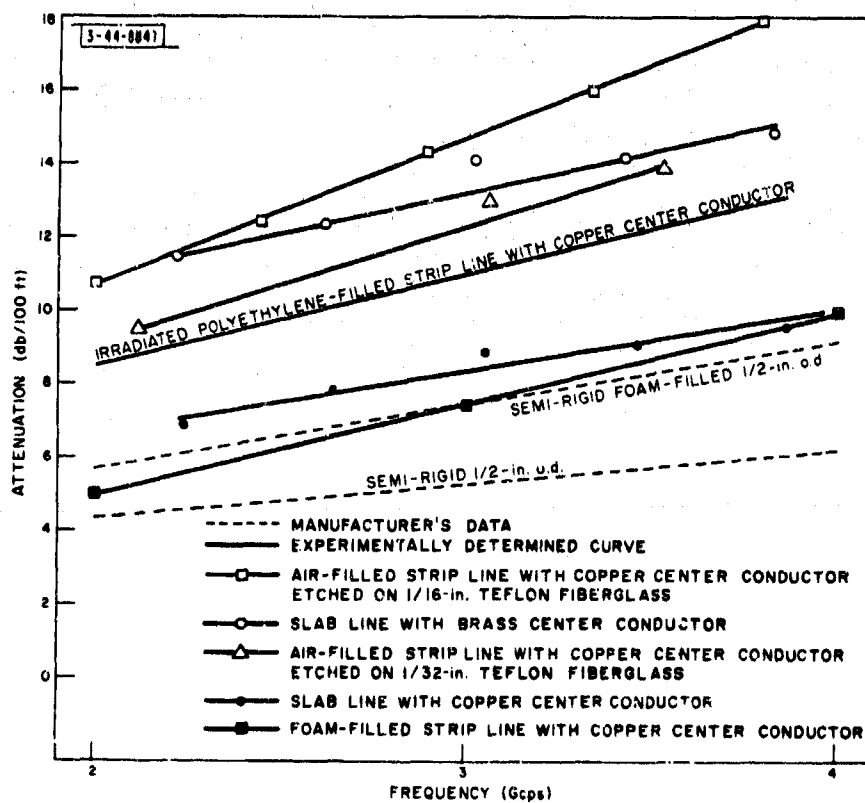
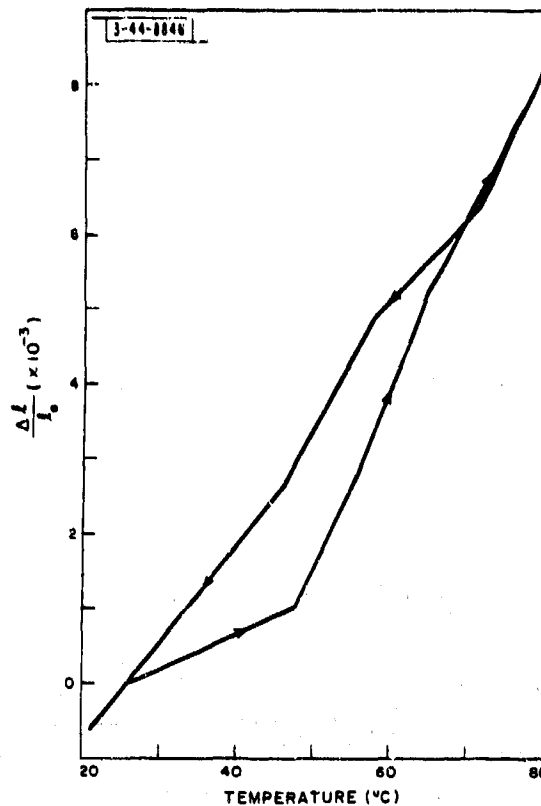


Fig. II-77(b). Attenuation characteristics of various transmission lines. All strip- and slab-line structures have aluminum ground planes, spaced 1/4 inch apart.

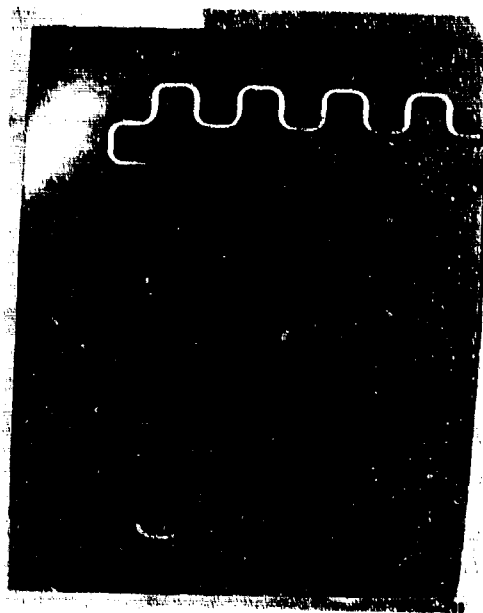


Fig. II-78. Center conductor of irradiated polyethylene "snake line" composed of 98 periodically spaced compensated turns.



P736-208

Fig. II-79. Center conductor of irradiated polyethylene "snake line" composed of 98 periodically spaced mitred turns.

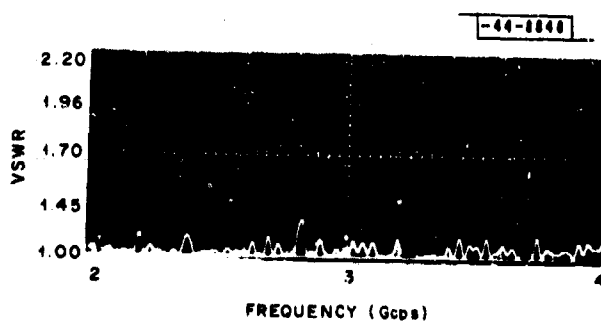


Fig. II-80. VSWR vs frequency for 98 periodically spaced mitred turns - S-band.

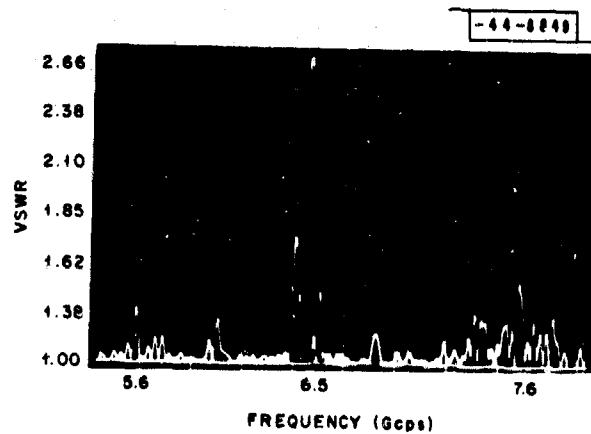


Fig. II-81. VSWR vs frequency for 98 periodically spaced mitred turns - X-band.

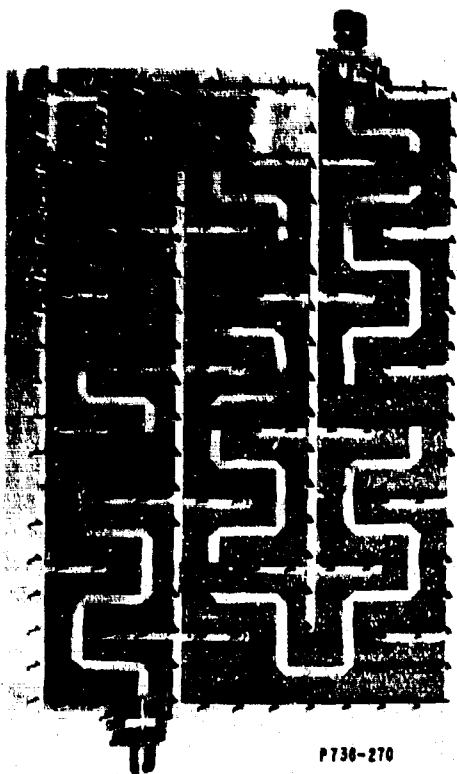


Fig. II-82. Center conductor of foam dielectric "snake line" composed of 50 periodically spaced mitred turns.

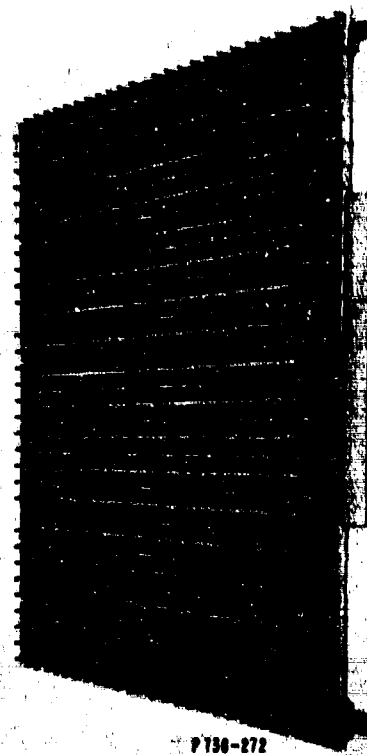


Fig. II-83. Center conductor of 100-wavelength S-band delay line using foam dielectric.

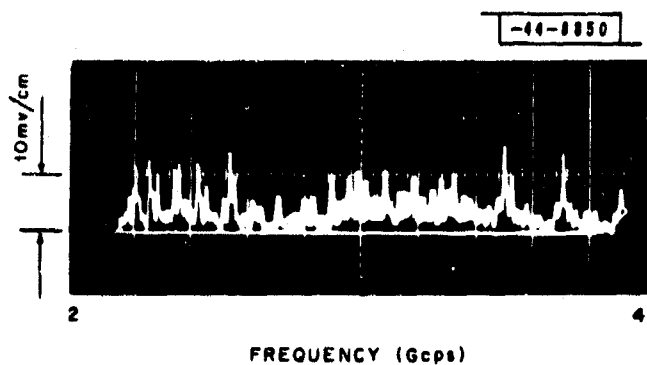


Fig. II-84. Standing-wave ratio vs frequency for 100-wavelength S-band delay line (1.5 mv = 1.1 VSWR).

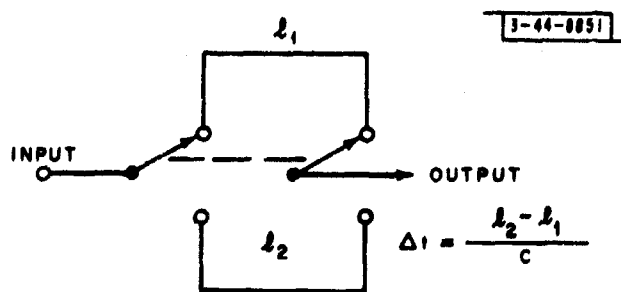


Fig. II-85. Basic time-delay configuration.

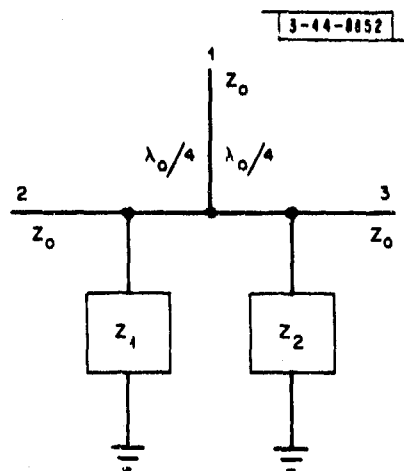


Fig. II-86. Single-pole double-throw switch.

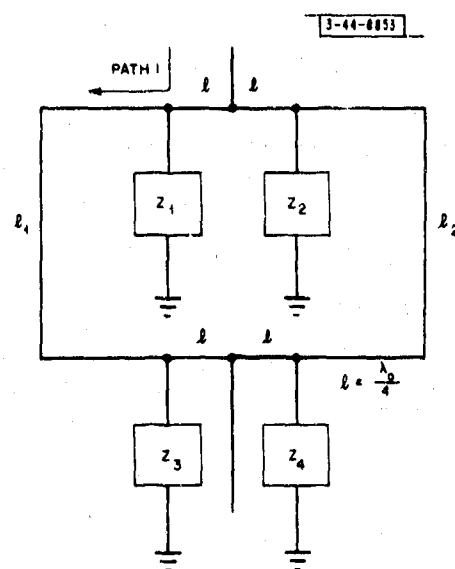


Fig. II-87. Four-diode delay unit.

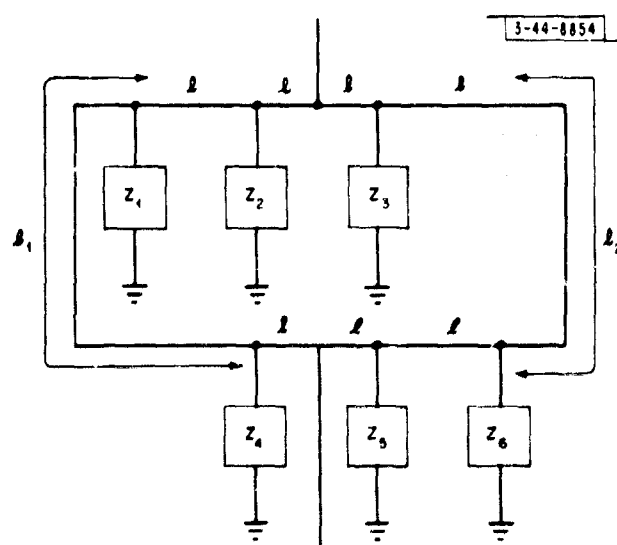


Fig. II-88. Six-diode delay unit.

Fig. II-89. Equivalent circuit for shunt switch in forward-biased case.

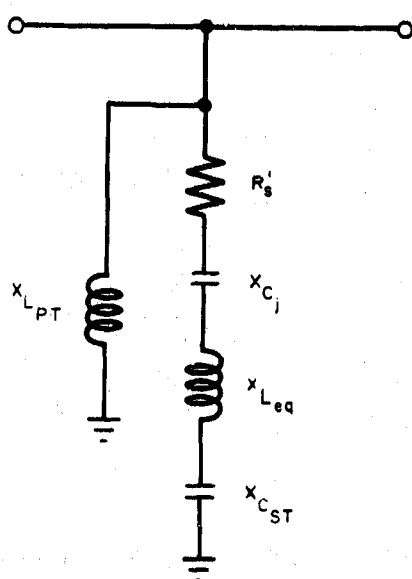
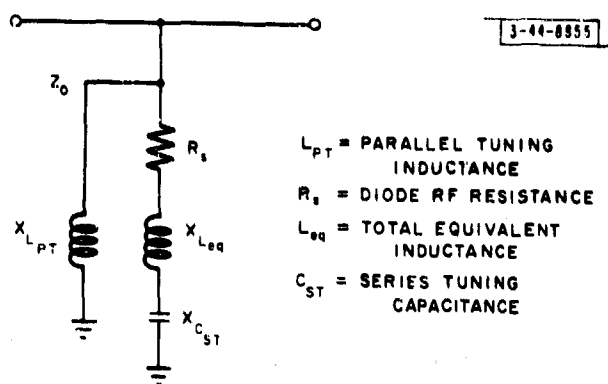
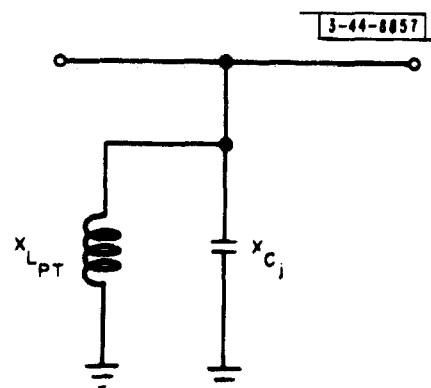


Fig. II-90. Equivalent circuit for shunt switch in reverse-biased case.

Fig. II-91. Simplified equivalent circuit for reverse-biased case.



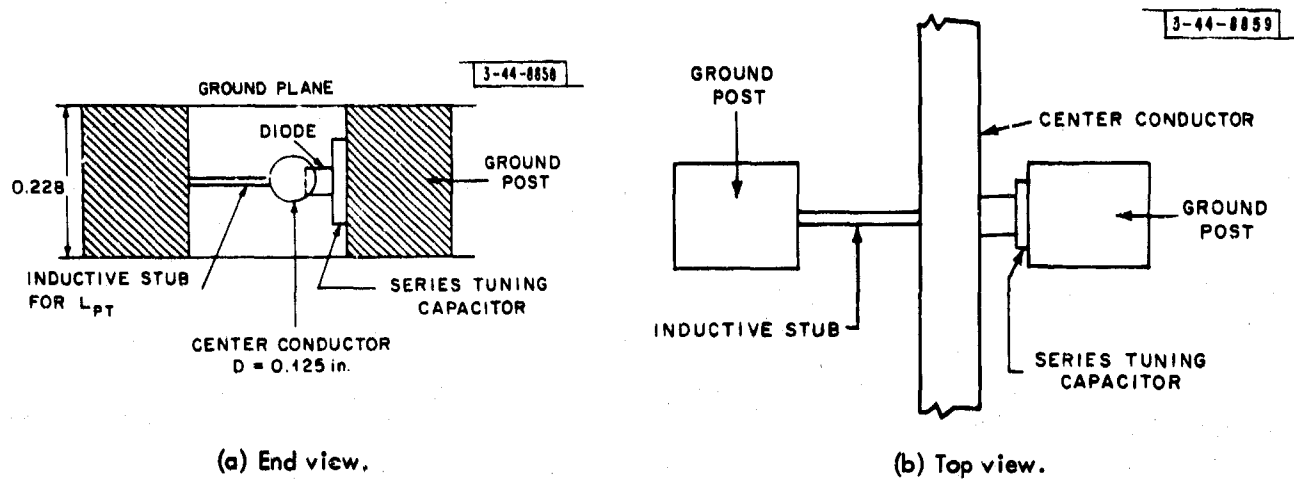


Fig. II-92. Slab-line diode mount.

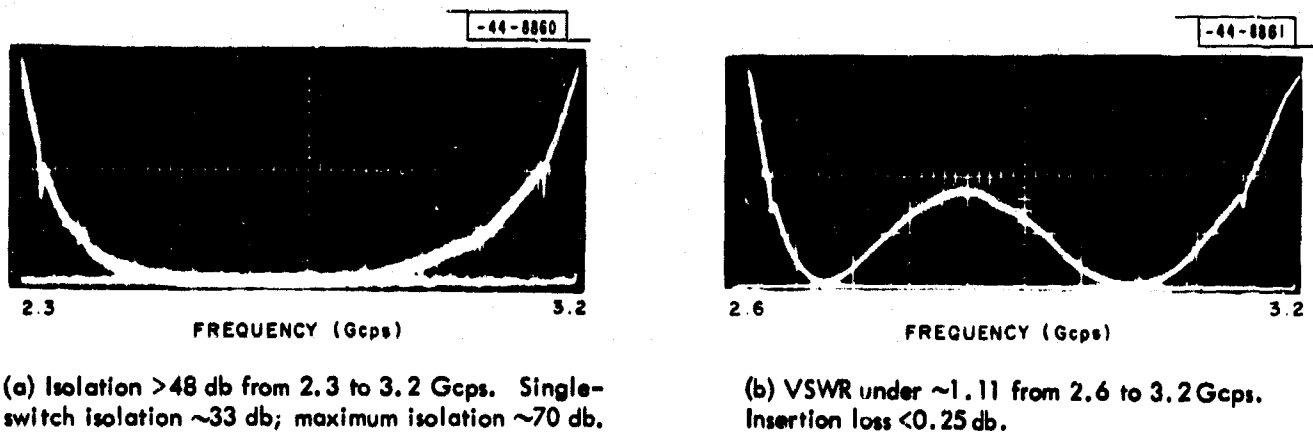


Fig. II-93. Performance of two-section slab-line switch using MA 4248's.

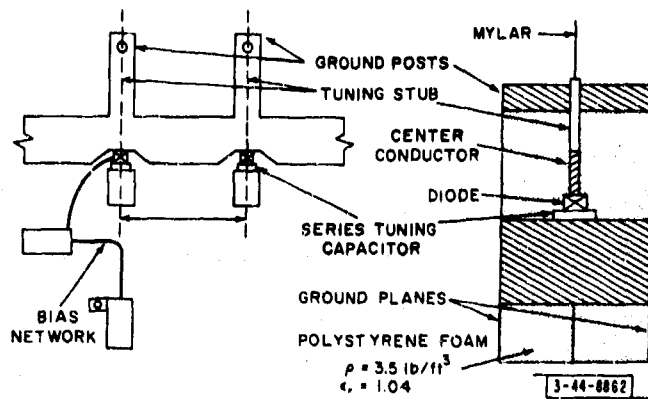


Fig. II-94(a). General layout of two-section strip-line switch with foam dielectric.

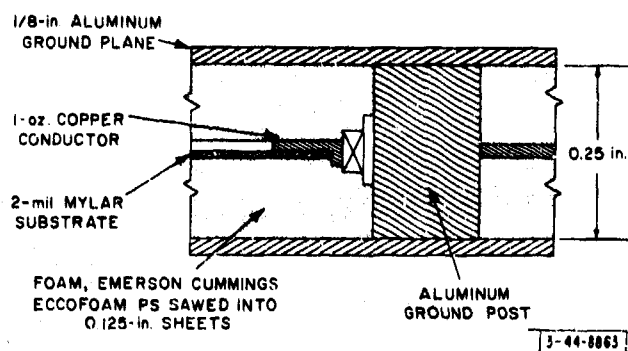


Fig. II-94(b). Details of switch construction.

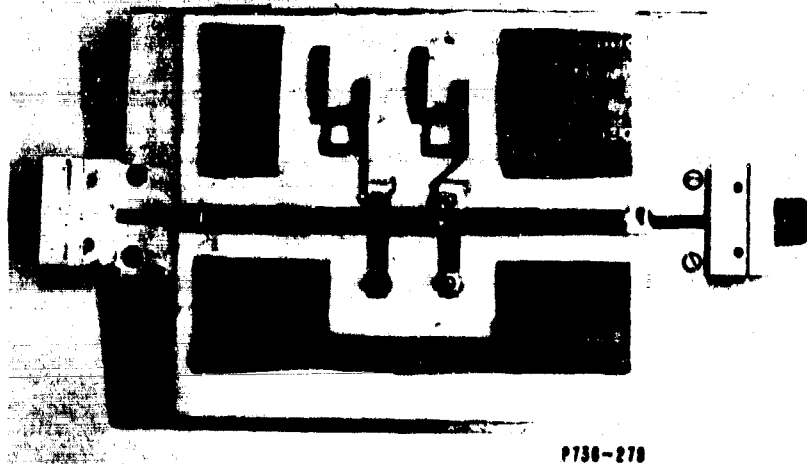


Fig. II-95. Foam dielectric strip-line switch.

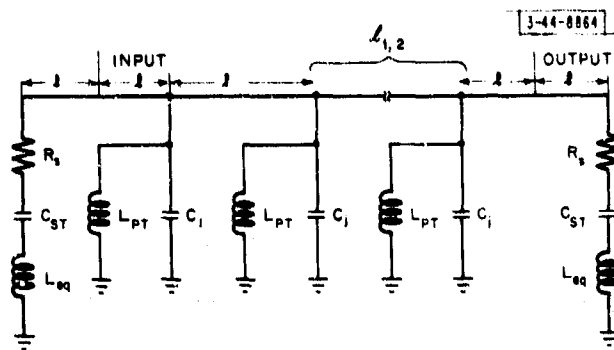
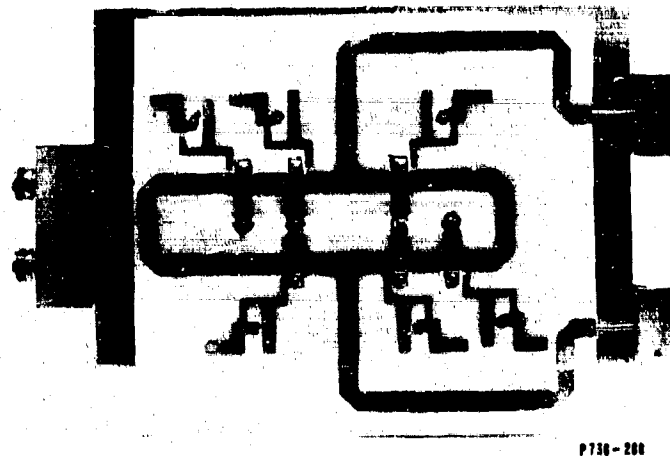


Fig. II-96. Equivalent circuit for path through time delay.

Fig. II-97. Six-switch time delay.



P730-200

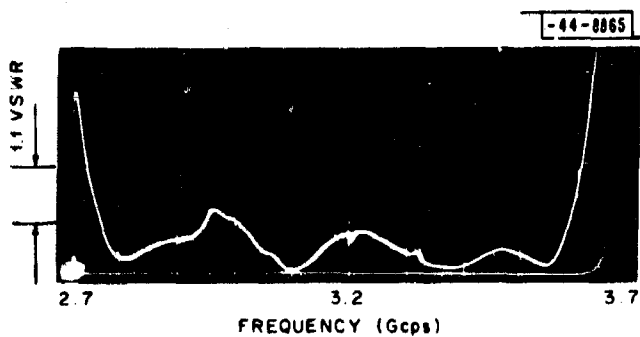


Fig. II-98. Time-delay reflection vs frequency. Transmission through reference path.



## CHAPTER 9 S-BAND SUBARRAY PATTERN RANGE

L. Cartledge

The S-band subarray will require a test bed capable of making antenna patterns at high peak and average power levels. Since the far-field distance ( $2d^2/\lambda$ ) of a single subarray is on the order of a meter, it was decided to build a small pattern range in which the subarray could be stationary. This pattern range with sixteen antenna elements installed is shown in Fig. II-99. The ground plane is 8 ft square, and the truss holding the horn is 12 ft long. The horn is rotated through a 180+ degree arc by a system of ropes and pulleys. Signals are transmitted to and from the moving horn through  $\frac{1}{4}$ -inch semi-rigid coaxial cable and a small coaxial rotary joint. A one-speed selsyn generates a position signal for the antenna pattern recorder.

As can be seen from the photograph (Fig. II-99), the pattern range is installed inside the 55-ft radome. At this writing, measurements are still being made in an attempt to find and eliminate the sources of significant pattern error. Figures II-100 and II-101 show representative patterns.

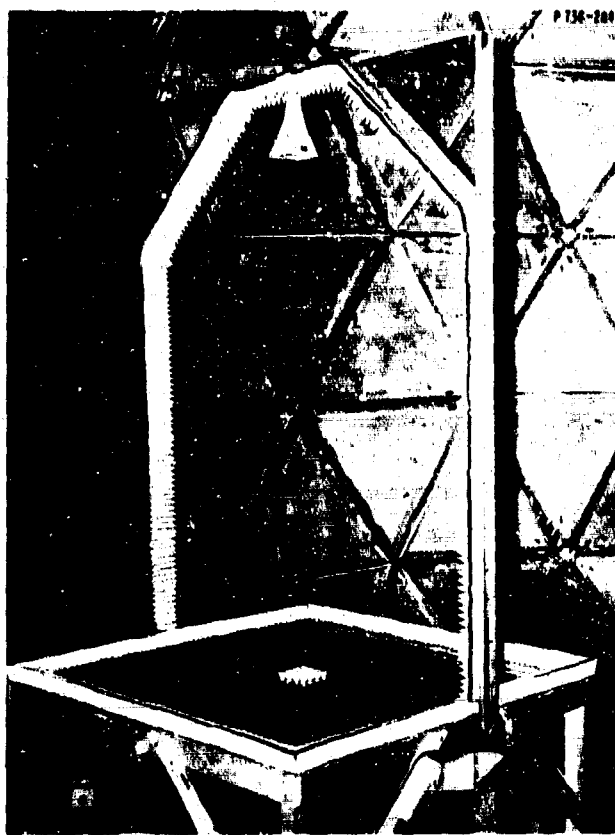


Fig. II-99. "Gallows" test range for S-band subarray with sixteen radiators installed.

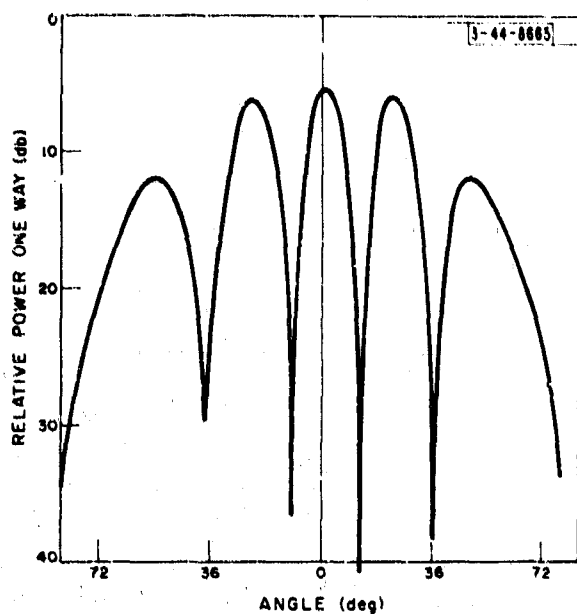
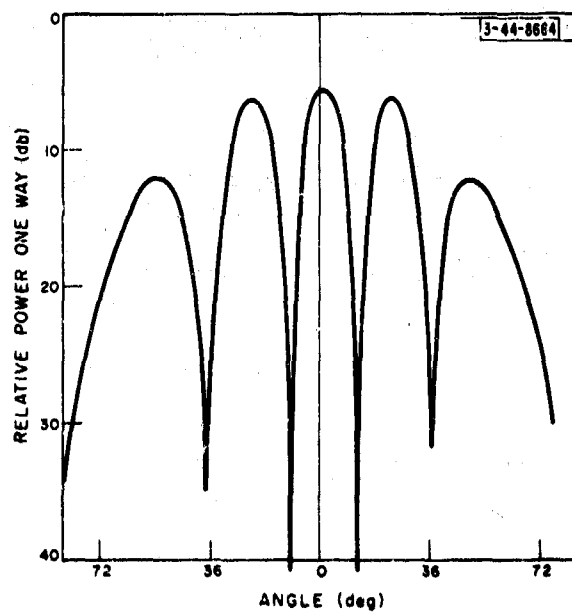


Fig. II-100. Interferometer pattern made on "gallows" test range using two S-band horns spaced 2.34 wavelengths.

Fig. II-101. Interferometer pattern same as in Fig. II-100 except that test fixture was rotated 90°.



## PART III ANTENNAS AND BEAM-FORMING STUDIES

### CHAPTER 1 RF BEAM-FORMING TECHNIQUES

D. M. Bernella  
H. J. Pratt

#### SUMMARY

Chapter 1 of Part III deals basically with the analysis of a series-fed RF multiple-beam-forming technique. It is shown that a beam-forming network can be designed using the above technique to have any efficiency (constant for all beams) up to 100 percent when orthogonal beams are formed. When high efficiencies are desired, the network must utilize the characteristic multiple path signals to form the required beams which thereby reduces the available bandwidth accordingly. The bandwidth is further limited by the number of elements across the array aperture (e.g., for a fixed high efficiency, the bandwidth is inversely proportional to the array width in wavelengths). There is, for any fixed array size, a three-way trade-off between design tolerances, efficiency, and array performance. Results of an investigation of the series-fed RF multiple beam former are given in the following sections. These results compare computed data from linear arrays of four to sixty-four elements.

Perhaps the most significant result is not that such a beam former can be designed, but rather that the performance of a particular design can be predicted exactly, for a minimal cost, using digital computer techniques.

#### A. INTRODUCTION

This chapter is concerned with the analysis of a series-fed simultaneous multiple beam former, which was originally conceived by Blass.<sup>†</sup> This study has been an extension of previous work on RF beam forming, at signal frequencies which included both a theoretical analysis and experimental verification of the performance of a parallel-fed simultaneous multiple beam former<sup>§</sup> (commonly called the Butler matrix).<sup>¶</sup> No attempt has been made in the present study to build any hardware for experimental work; instead, programs were written for the IBM 7094 computer to simulate the array performance. Although the basic concept involved with the series beam former is quite simple, underlying problems concerned with bandwidth, efficiency, practical coupler design, and pattern degradation have left much to the designer's speculation. Therefore, it has been the purpose of this study to find a more exacting method of analyzing the performance of the beam former without actually having to build the hardware first and then test it.

Section B of this chapter describes the basic configuration as originally presented by Blass and modified by Brigham.<sup>#</sup> The various problems associated with the concept are also discussed here.

<sup>†</sup> J. Blass, IRE Intl. Conv. Record, Vol. 8 Part 1, pp. 48-51 (1960).

<sup>§</sup> TR-236, pp. 19-48.

<sup>¶</sup> J. Butler and R. Lowe, Electronic Design 9, 170 (1961).

<sup>#</sup> E. Brigham, Sylvania Electric Products, Inc., private communication.

Section C describes a method of designing an "exact" one-dimensional matrix (e.g., linear array feed) for  $N$  elements to form exactly the  $N$  orthogonal beams possible for uniform drive to all antennas. This section deals only with the design frequency  $f_0$  and the maximum efficiency obtainable with a specific set of assumptions.

Section D of this chapter includes the results of an extensive computer program to actually compute the design of several beam formers and evaluate their performance as a function of various parameters, such as bandwidth, efficiency, nonexact component values, etc.

## B. BASIC CONFIGURATION

Figure III-1 is a schematic diagram of a series-fed beam former which will form one beam in space for an  $N$  element linear antenna array. A traveling wave is injected into the system at the feed point and fractions of the power are coupled into the vertical transmission lines via the directional couplers  $K_j$ . For a single-beam device, as shown in Fig. III-1, the  $K_j$ 's may be adjusted to couple all of the energy into the antennas and none into the load  $L_T$ . In this case, and for uniform illumination across the aperture, the values of the power coupling coefficients are given by

$$K_j = \frac{1}{N + 1 - j} \quad (1)$$

where  $N$  is the number of antennas and  $j$  is the coupler index, starting from the left as shown in the diagram. The phase of the radiation at each antenna, with respect to the input phase, is a function of the angle  $\alpha$  and the spacing between the vertical transmission lines.

$$\varphi_j = \psi_j + \frac{s}{\cos \alpha} [j - 1 + (N - j) \sin \alpha] \quad (2)$$

where

$\varphi_j$  = phase of radiated signal at the  $j^{\text{th}}$  antenna,

$s$  = spacing between adjacent vertical transmission lines in radians,

$\alpha$  = the angle of the feed bar measured counter-clockwise from the horizontal,

$\psi_j$  = the phase shift through a coupler.

This configuration has the advantage of being a true time delay system, in the sense that the beam pointing angle remains constant as a function of frequency. By varying  $\alpha$ , a beam may be formed in any desired direction in half-space, and by adjusting the values of  $K_j$ , the amplitude distribution across the aperture can be made to approximate almost any desired function.

Now if several feed bars are placed across the vertical transmission lines, as is shown in Fig. III-2, the basic series-fed simultaneous multiple beam former results. To illustrate the basic properties of this network, consider its operation in a transmitting sense.

A traveling wave is fed into the  $i^{\text{th}}$  feed bar and portions of the energy are coupled across and upward into the vertical transmission lines. Because of the properties of the directional couplers, part of the signals in the vertical arms are coupled back into those horizontal feed bars between the  $i^{\text{th}}$  bar and the antennas and hence into other vertical lines again. This gives the effect of a general migration of power into the upper right-hand corner of the matrix.

The amplitude and phase of the signal at a particular antenna port is the vector sum of all of the voltage components coupled from the  $i^{\text{th}}$  feed port to that antenna port. It will be shown later that under certain conditions these multiple path effects can be neglected, and when this is not possible a compensation technique can be applied to make the necessary corrections. For the moment, let us define what shall be called a "primary" or first-order path. This is the most direct path which the signal can travel in, going from port  $i$  to port  $j$ . In other words, energy will travel down the  $i^{\text{th}}$  bar to the  $K_{ij}^{\text{th}}$  coupler and then up the  $j^{\text{th}}$  transmission line to the  $j^{\text{th}}$  antenna.

Thus, it is seen that if only the primary paths are considered, a wave entering the  $i^{\text{th}}$  feed port will produce a wave front across the antenna ports with a linear phase gradient which is a function of the angle  $\alpha$  and the spacing  $s$ . With reference to Fig. III-2, the phase difference  $\Delta\phi$  between the  $j^{\text{th}}$  and  $j + 1^{\text{th}}$  antenna ports is given by

$$\Delta\phi = \frac{s}{\cos \alpha} (1 - \sin \alpha) \quad \text{radians} \quad (3)$$

and the relationship between the angle  $\alpha$  and the beam-pointing angle  $\Theta$  (measured from the normal to the array) is

$$\sin \Theta = \frac{1}{\cos \alpha} (1 - \sin \alpha) \quad (4)$$

where

$\Delta\phi$  = linear phase gradient between adjacent antenna ports,

$\Theta$  = far-field beam pointing angle referenced to the normal of the array.

It has been assumed here that the transmission line propagation constant is that of free space, and the phase shifts through all of the couplers are equal. This is not a necessary condition but is done merely to simplify the illustrative computations.

A modification of the beam former in Fig. III-2 is shown in Fig. III-3 and was originally suggested by Brigham. This technique merely bends the vertical antenna transmission lines into concentric circular arcs. For this configuration,

$$\Delta\phi_i = s(1 - \alpha_i) \quad \text{radians} \quad (5)$$

and

$$\sin \Theta_i = (1 - \alpha_i) \quad (6)$$

where the subscript  $i$  denotes a particular feed bar and its associated beam in space.

It should be re-emphasized here that the above elementary relations apply only to the primary paths, and therefore describe the operation of the network only if the interaction of the feed bars between the  $i^{\text{th}}$  feed and the antenna ports can be ignored, which is generally not the case.

The upper feed bar of the matrix in Fig. III-3 is shown in Fig. III-4.  $V_{ij}$  is considered to be the voltage appearing at the  $j^{\text{th}}$  antenna port when the  $i^{\text{th}}$  feed bar is energized. Similarly, the  $C_{ij}$ 's are the voltage coupling coefficients between the feed bars and the output transmission lines. As was stated earlier, the directional couplers have been assumed to have a constant

value of phase shift for all values of coupling,  $-\pi/2$  in the coupled direction and zero in the through path.

A set of simultaneous equations can be written describing the  $C_{m,n}$ 's:

$$\begin{aligned} V_{1,1} &= V_0 C_{1,1} \exp[-j \frac{\pi}{2}] \\ V_{1,2} &= V_0 (1 - C_{1,1}^2)^{1/2} C_{1,2} \exp[-j(\frac{\pi}{2} + s)] \\ &\vdots \\ V_{1,n} &= V_0 \left[ \prod_{k=1}^{n-1} (1 - C_{1,k}^2)^{1/2} \right] C_{1,n} \exp\{-j[\frac{\pi}{2} + (n-1)s]\} \end{aligned}$$

where  $V_0$  is the excitation voltage at the feed point. Define  $T_{i,n} = V_0/V_{i,n}$  as the voltage transfer coefficient. Then

$$T_{1,n} = \left[ \prod_{k=1}^{n-1} (1 - C_{1,k}^2)^{1/2} \right] C_{1,n} \exp\{-j[\frac{\pi}{2} + (n-1)s]\}$$

Now for the special case of equal amplitudes at each of the output ports,

$$\begin{aligned} |T_{1,1}| &= |T_{1,2}| = \dots, |T_{1,N}| \\ 1 &= \frac{|T_{1,k}|}{|T_{1,k+1}|} = \frac{C_{1,k}}{C_{1,k+1} (1 - C_{1,k}^2)^{1/2}} \end{aligned}$$

which results in the recursion relation

$$\frac{1}{C_{1,k}^2} - 1 = \frac{1}{C_{1,k+1}^2} \quad (7)$$

Set  $K_{i,j} = C_{i,j}^2$  = power coupling coefficient. Then the power coupling recursion relation is

$$\frac{1}{K_{1,k}} - 1 = \frac{1}{K_{1,k+1}} \quad (8)$$

From Eq. (1) it is seen that  $K_{1,k} < K_{1,k+1}$ , and therefore  $K_{1,N}$  will be the tightest coupler in the line. It remains then to determine the value of  $K_{1,N}$  and to compute the rest of the  $K$ 's or  $C$ 's in the line.

If only one beam is desired, the feed may be made 100 percent efficient with  $K_{1,N} = 1$ . However, if more than one feed is used and an attempt is made to use a unity coupler at the end of each line, the matrix degenerates into the triangular configuration shown in Fig. III-5. As one would expect, the configuration proved to be the limiting case of the series-fed beam former giving 100-percent efficiency and zero bandwidth. Because this is a unique case, it was felt a more general analysis would be obtained by using the general configuration where  $K_{1,N}$  had a

value different from unity. Thus, a 3-db coupler was chosen as a convenient maximum coupling coefficient for  $K_{1,N}$  ( $K_{1,N} = 1/2$ ,  $C_{1,N} = 1/\sqrt{2}$ ).

Substituting these values into Eqs. (7) and (8) gives the following set of values for equal excitation of each antenna element.

$$\begin{aligned} K_{1,1} &= \frac{1}{N+1} & C_{1,1} &= \frac{1}{\sqrt{N+1}} \\ K_{1,2} &= \frac{1}{N} & C_{1,2} &= \frac{1}{\sqrt{N}} \\ K_{1,3} &= \frac{1}{N-1} & C_{1,3} &= \frac{1}{\sqrt{N-1}} \\ &\vdots & & \vdots \\ &\vdots & & \vdots \\ K_{1,N} &= \frac{1}{2} & C_{1,N} &= \frac{1}{\sqrt{2}} \end{aligned}$$

Similar recursion formulas can be derived for other aperture voltage distributions.

The above set of values for the  $C_{1,j}$ 's in the first bar of a series matrix is exact, and if  $s = \pi$ , an end-fire beam would be produced when the feed point was energized. If the bar is placed at some other angle,  $\alpha$ , the beam points in the direction  $\Theta$ , according to the relation in Eq. (6).

In order to form simultaneous beams, several feed bars must be placed across the matrix at the appropriate angles  $\alpha_i$  and energized simultaneously. When this is done, and if high efficiencies are desired, the interaction between feeds must be considered. Figures III-6(a-b) and III-7(a-b) show the phase and amplitude across the apertures of four- and eight-element matrices when interaction is both considered and neglected. These matrices have the bars placed at angles  $\alpha_i$  such that the radiation beams are orthogonal; i.e., for uniform illumination the peak of each beam falls at the first null of the adjacent beam. It is readily seen from these plots that when high efficiencies are desired the result of neglecting the beam interaction in the design would be disastrous. It is also apparent that this effect becomes even more pronounced as the number of elements is increased.

To understand why this effect is so pronounced, consider the four-element matrix shown in Fig. III-8. From input port 1 to any antenna port, there is only one path through which energy can travel, this being the primary path defined earlier which only changes direction once. However, from input port 2, there are, in addition to its four primary paths, three other paths (one to each antenna  $j = 2, 3$ , and 4) where the signal changes direction three times. If we define these paths as second-order paths, then from input port 1 we have along with the primary paths, second-order, third-order, fourth-order paths, etc., down the input lines. These higher-order paths can be considered to be error voltages, arriving at the antenna ports along with the primary voltage. In Table III-1, the numbers of each type of path are given for the four-element matrix.

It is of interest to note in Table III-1 that the total number of paths for an  $N$  element array increases with increasing  $N$ , according to Pascal's triangle (Binomial Coefficients), a feature

TABLE III-1  
NUMBERS OF PATHS FOR FOUR-ELEMENT MATRIX

First-Order or "Primary" Paths					Second-Order Paths						
Input Ports		Output Ports				Input Ports		Output Ports			
	<u>i = 1</u>	<u>i = 2</u>	<u>i = 3</u>	<u>i = 4</u>		<u>i = 1</u>	<u>i = 2</u>	<u>i = 3</u>	<u>i = 4</u>		
i = 1	1	1	1	1	i = 1	0	0	0	0		
i = 2	1	1	1	1	i = 2	0	1	2	3		
i = 3	1	1	1	1	i = 3	0	2	4	6		
i = 4	1	1	1	1	i = 4	0	3	6	9		

Third-Order Paths					Fourth-Order Paths						
Input Ports		Output Ports				Input Ports		Output Ports			
	<u>i = 1</u>	<u>i = 2</u>	<u>i = 3</u>	<u>i = 4</u>		<u>i = 1</u>	<u>i = 2</u>	<u>i = 3</u>	<u>i = 4</u>		
i = 1	0	0	0	0	i = 1	0	0	0	0		
i = 2	0	0	0	0	i = 2	0	0	0	0		
i = 3	0	0	1	3	i = 3	0	0	0	0		
i = 4	0	0	3	9	i = 4	0	0	0	1		

Total Number of Paths					
Input Ports		Output Ports			
	<u>i = 1</u>	<u>i = 2</u>	<u>i = 3</u>	<u>i = 4</u>	
i = 1	1	1	1	1	
i = 2	1	2	3	4	
i = 3	1	3	6	10	
i = 4	1	4	10	20	



which is indicative of the geometric regularity of the network. Due to the number of times the higher-order terms are reduced by the coupling ratio, the resulting amplitude of each error voltage is less than the primary voltage at a particular port. However, when high efficiencies are desired, the error voltage magnitude is not reduced enough to compensate for the rapid increase in the number of these terms, with the result that the ensuing sum of error voltages at a port becomes a significant factor. Figures III-9 to III-12 show resulting computed far-field radiation patterns from a 16-element array of isotropic radiators for beams 6, 9, 12, and 15 when the error paths are ignored. Beam 9 is the boresight beam. In this case, coupler  $K_{1,N}$  is a 3-db coupler giving a bar efficiency of  $N/(N+1) = 16/17$ .

These error path effects can be reduced by decreasing the coupling coefficients  $K_{ij}$ , with a resulting decrease in efficiency, such that the multiple-coupling magnitudes are reduced faster than the number of paths are increased. The excess power is then dumped into the terminations at the ends of the input lines. Computed radiation patterns and output distributions illustrating this effect are given and discussed in Sec. D of this chapter.

A somewhat more tolerable solution to this problem would be to design a compensated matrix in such a way that all the error voltages plus the primary voltage give the proper amplitude and phase at each antenna port. The major drawback to this method is that the error paths are of different over-all length than their corresponding primary paths and the array is no longer exactly time delayed. This time-delay effect manifests itself in beam-pointing errors and aperture buildup time problems. We can consider this a bandwidth effect which can also be controlled by reducing the system efficiency. It will be shown that the degradation in efficiency necessary to give a desired performance is not nearly as severe as it would be for identical performance in the noncompensated design case.

During the study, it was found that rather than finding a compensation scheme to add to the basic matrix, it was necessary to design the couplers and connecting transmission lines specifically for the particular sized array and beam distribution desired. It is a formidable task to set up the simultaneous equations and to find a general form for the coupler and line length values for even the first few bars of an  $N$  element beam former. As an illustration, Eq. (9) gives the transfer coefficient for the third feed bar in an  $N$  element array.

$$\begin{aligned}
 T_{3,k} = & C_{1,k} \exp \{-j[5c + (k-1)s]\} \sum_{n=1}^{k-1} \exp[-j\varphi_{2,n}] C_{3,n} C_{2,n} \left[ \prod_{p=1}^{n-1} (1 - C_{3,p}^2)^{1/2} \right] \\
 & \cdot \left\{ \sum_{l=n+1}^{k-1} \exp[-j\varphi_{1,l}] C_{2,l} C_{1,l} \left[ \prod_{q=n+1}^{l-1} (1 - C_{2,q}^2)^{1/2} \right] \left[ \prod_{\omega=l+1}^{k-1} (1 - C_{1,\omega}^2)^{1/2} \right] \right\} \\
 & + C_{1,k} \exp \{-j[3c + (k-1)s]\} \left\{ \sum_{n=1}^{k-1} \exp[-j(\varphi_{2,n} + \varphi_{1,n})] C_{3,n} C_{1,n} (1 - C_{2,n}^2)^{1/2} \right. \\
 & \cdot \left[ \prod_{p=1}^{n-1} (1 - C_{3,p}^2)^{1/2} \right] \left[ \prod_{l=n+1}^{k-1} (1 - C_{1,l}^2)^{1/2} \right] \left. + C_{2,k} (1 - C_{1,k}^2)^{1/2} \right\} \\
 & \times \exp \{-j[3c + (k-1)s]\} \exp[-j\varphi_{1,k}] \left\{ \sum_{j=1}^{k-1} \exp[-j\varphi_{2,j}] C_{3,j} C_{2,j} \right.
 \end{aligned}$$

$$\begin{aligned}
& \cdot \left[ \prod_{p=1}^{n-1} (1 - C_{3,p}^2)^{1/2} \right] \left[ \prod_{\ell=n+1}^{k-1} (1 - C_{2,\ell}^2)^{1/2} \right] \left\{ + \exp \{-j [c + (k-1)s]\} \right. \\
& \times \exp [-j(\varphi_{2,k} + \varphi_{1,k})] \left[ \prod_{n=1}^{k-1} (1 - C_{3,n}^2)^{1/2} \right] C_{3,k} (1 - C_{2,k}^2)^{1/2} (1 - C_{1,k}^2)^{1/2} \left. \right\} \quad (9)
\end{aligned}$$

where

$c$  = phase shift through a coupler in the coupled direction (radians),

$s$  = spacing between antennas (radians),

$\varphi_{n,m}$  = the arc length between two horizontal bars (radians).

It is easily seen that this approach is totally hopeless and it was necessary to enlist the aid of our handy digital computer.

### C. MATRIX DESIGN PROCEDURE

One of the most desirable features of this beam former is its ability to form several beams simultaneously, each with the full gain of the array aperture. Then we have what we call "lossless" beams. Allen<sup>†</sup> has shown that in order to form lossless beams, beam space factors must be orthogonal in space, which implies that  $K \sum_{j=1}^N (V_{\ell,m}) \cdot (V_{m,n}^*) = \delta_{\ell,n}$  where  $\delta_{\ell,n}$  is the Kronecker delta,  $N$  is the number of elements in the array, the  $V_{\ell,m}$ 's represent the voltage distributions across the antennas  $j$  for each beam  $i$ , and  $K$  is the normalization constant. One such set of real orthogonal beams can be formed by using uniform power distribution across the aperture. The spacing of the beams in this class turns out to be such that the peak of one beam falls exactly at the first null of its adjacent beams. These beams, of the form  $\sin nx / \sin x$ , are said to be spaced one beamwidth apart, but here the beamwidth is not defined in the usual sense as being the  $-3$ -db points but rather as the  $-\pi/2$  or  $\approx -3.92$ -db points. It is possible to form exactly  $N$  (the number of regularly spaced antennas) unique orthogonal beams in half-space. If the elements are spaced farther apart than one-half wavelength, the  $N$  beams will not fill the total half-space, but more beams are formed which are grating lobes of the first  $N$ . For the purpose of illustrating the following design procedure, only uniform illumination beams will be considered. The method is of course valid for any spacing. Beam combining to form tapered aperture distributions will be discussed later.

Let us consider the design of a beam-forming matrix which will feed a four-element linear antenna array and form the four orthogonal  $\sin nx / \sin x$  beams possible in half-space. Further, we will assume the radiating elements to be spaced one-half wavelength apart, such that the four beams are positioned in space as shown in Fig. III-13. Figure III-13 also shows an arbitrary numbering of the beams which will be used throughout this chapter for all sizes of arrays; i.e., beam 1 will always be the leftmost beam, with the numbers increasing in a clockwise direction.

Once the array size and type of beams to be formed have been determined, each beam can be defined by a set of complex voltages at the antenna ports. The first step of the design

<sup>†</sup> J.L. Allen, Trans. IRE, PGAP AP-9, 530 (1961).

procedure is to find the component values (coupler coefficients and transmission line lengths) within the dashed lines shown in Fig. III-14. Before computing these values, we must choose a beam efficiency and decide which feed ports  $i$  we want to have correspond to the beam numbers  $l$ . As stated earlier, choosing 100-percent efficiency leads to the special case of the triangular matrix; therefore, something other than a unity coupler for  $K_{1,N}$  must be used for the general full matrix configuration. Using the convenient value of  $K_{1,N} = 1/2$  gives an efficiency of  $N/(N+1)$  or 80 percent in this case. We will choose beam  $l$  to match port  $i$  as shown in Fig. III-14. Thus, the top bar must be designed to couple (in the receive sense) the end-fire beam into port  $i = 1$ . In other words, because the network is reciprocal, the application of voltage to port  $i = 1$  must form an end-fire transmitting beam containing 80 percent of the injected power. Thus, the voltages at the antenna terminals will be

$$\begin{aligned} V_{11} &= \frac{1}{\sqrt{5}} e^{-j\Theta} \\ V_{12} &= \frac{1}{\sqrt{5}} e^{-j(\Theta+\pi)} \\ V_{13} &= \frac{1}{\sqrt{5}} e^{-j(\Theta+2\pi)} \\ V_{14} &= \frac{1}{\sqrt{5}} e^{-j(\Theta+3\pi)} \end{aligned}$$

where the subscripting  $V_{l,m}$  is defined such that  $l$  is the beam number and  $m$  is the antenna port. If the antenna spacing  $d$  (Fig. III-14) is chosen to be equal to one-half wavelength, and if we assume  $90^\circ$  of phase shift through the couplers in the coupled direction and zero degrees in the straight-through direction, then the values of the coefficients of the couplers  $C_{l,m}$  to give the above voltage distribution become  $C_{l,m} = 1/\sqrt{N+2-m}$  where the indices  $l, m$  are defined such that  $l$  is the input port number and  $m$  is the antenna port.

A scattering matrix  $\underline{S}$  can now be written for the first bar network ( $2N+2$  ports) using the coupling values just calculated. All ports are assumed to be matched and the network is lossless and reciprocal. Therefore, generalizing for the moment, the S-matrix can be written:

$$\underline{S} = \left[ \begin{array}{c|c} \underline{O}_{N+1, N+1} & \underline{s}_{N+1, N+1} \\ \hline \underline{s}_{N+1, N+1}^T & \underline{O}_{N+1, N+1} \end{array} \right] \quad (10)$$

where the following relationships hold

$$\begin{aligned} \underline{S}^\dagger \underline{S} &= \underline{I} \text{ (lossless condition)} \\ \underline{S}^T &= \underline{S} \text{ transpose} \\ \underline{S}^\dagger &= \underline{S} \text{ transpose-conjugate} \end{aligned} \quad (11)$$

The incident voltage distributions can be written as orthonormal column vectors of the form:

$$\underline{v}_m = \begin{bmatrix} a_1 \\ a_2 \\ a_3 \\ \vdots \\ a_i \\ \vdots \\ a_N \\ 0 \\ \vdots \\ 0_{N+1} \end{bmatrix} \quad (12)$$

where  $m$  is beam number. Hence, from our earlier definition of orthogonal beams, the inner product of the voltage distribution is

$$(\underline{v}_\ell, \underline{v}_m) = \underline{v}_\ell^\dagger \underline{v}_m = \delta_{\ell m} \quad (13)$$

The transformed voltage distribution  $\underline{v}'$  (voltages moving out from the network) can then be written

$$\underline{v}'_\ell = \underline{S} \underline{v}_\ell \quad (14)$$

The translation of the  $\underline{v}'_\ell$ 's along the curved paths of the beam former be expressed in terms of a diagonal matrix of the form

$$\underline{\psi} = \begin{bmatrix} e^{j\theta_1} & & & & & & \\ & e^{j\theta_2} & & & & & \\ & & e^{j\theta_7} & & & & \\ & & & 0 & & & \\ & & & & e^{j\theta_i} & & \\ & & & & & & \\ & & & & & & e^{j\theta_{2N+2}} \end{bmatrix} \quad (15)$$

For our particular case ( $\beta$ 's of Fig. III-14),  $\varphi$  can be reduced to:

$$\varphi = \begin{bmatrix} e^{j\beta_1} & & & & & & 0_{N+1, N+1} \\ & e^{j\beta_{N-1}} & & & & & \\ & & & & & & \\ & & & & & & \\ & & & & e^{j\beta_N} & & \\ 0_{N+1, N+1} & & & & & & I_{N+1, N+1} \end{bmatrix} \quad (16)$$

It can easily be shown that  $\varphi$  is unitary:

$$\varphi^\dagger \varphi = I \quad (17)$$

Hence the input distribution transformed through the first beam bar and along the matrix to the inputs of the second input bar  $v_l''$  can be written as

$$v_l'' = \varphi S \varphi v_l \quad (18)$$

The inner product of the  $v''$  distribution can then be formed

$$(v_l'', v_m'') = v_l''^\dagger v_m'' = v_l^\dagger \varphi^\dagger S^\dagger \varphi^\dagger \varphi S \varphi v_l \quad (19)$$

However, from Eqs. (11), (13), and (17), Eq. (19) is reduced to:

$$(v_l'', v_m'') = \delta_{lm} \begin{cases} 1 & l = m \\ 0 & l \neq m \end{cases}$$

Therefore, it can be concluded that the orthogonality of original input distributions have not been disturbed in translating them to the second beam bar. This argument can be iterated to show the same results for any number of input bars. It is recognized that the phase matrix, per se, could have been included directly in the  $S$  matrix and the length of the proof reduced; however, it was felt that the approach that was used better retains its physical relation to the problem considered.

Renumbering of the elements of the  $v_l''$  vectors, so they are in convenient form to be used as inputs to the following beam bar, can be accomplished by multiplication by a matrix of the form:

$$\begin{bmatrix} 0 & 1 & 0 & 0 & . & . & . & . & . & 0 & 0 \\ 0 & 0 & 1 & 0 & 0 & . & . & . & . & 0 & 0 \\ 0 & 0 & 0 & 1 & . & . & . & . & . & . & . \\ . & . & . & . & . & . & . & . & . & . & . \\ . & . & . & . & . & . & . & . & . & . & . \\ 0 & 0 & 0 & 0 & . & . & . & . & . & 0 & 1 \\ 1 & 0 & 0 & 0 & . & . & . & . & . & 0 & 0 \end{bmatrix}$$

with no effect on orthogonality.

The actual method of calculation used in the computer program is quite similar to the procedure described in the orthogonality proof. To reduce complexity, let us return to the consideration of the four-element matrix.

Distribution 1 (beam 1) is brought to the input ports (1, 2, 3, and 4) of bar 1. The magnitude of the largest coupler (and the efficiency) is then selected. In the case of an 80 percent efficient, equal amplitude four-element matrix,  $K_{1,4} = \frac{1}{2} = 3 \text{ db}$ . For a beam former of less efficiency, a smaller value of  $K_{1,4}$  is specified. To calculate the next coupler  $K_{1,3}$  the reciprocity of the network and the phase lengths between adjacent couplers in the same beam bar are utilized. If the input bar is energized, the couplers would have to be selected to give the same magnitude outputs, i.e.,  $|V_{10,3}| = |V_{10,4}|$ , for an equal amplitude illumination. Therefore, the input voltage at port 4 of Fig. III-15 translated to point A must be equal to the input to port 3 translated to the same reference point; i.e.,

$$V_{3,10}^A = V_{4,10}^A$$

From the above relation,  $K_{13}$  may be calculated. Similarly, at point B

$$V_{2,10}^B = V_{3,10}^B = V_{4,10}^C$$

and  $K_{12}$  is calculable. The same procedure may be applied to determining  $K_{11}$ .

Once these coupling values of the first bar have been found, the remaining input distributions (2, 3, and 4) can be translated to ports 6, 7, 8, and 9. The portion of distribution 1 which was not coupled to port 10 would also appear at ports 6, 7, 8, and 9, but is dropped at this point in the program to reduce computation time. It can be shown that this distribution will not couple to the other "orthogonal" horizontal bars and will be dissipated in the loads at bottom of the matrix (Fig. III-14).

As will be recalled from the earlier description of the Brigham form of the Blass matrix, the lengths of the curved paths ( $\beta$ 's) are arcs of concentric circles. The values of  $\beta$  are somewhat arbitrary in that it is necessary to pick one  $\beta$  ( $\beta$  should obviously be positive) before the others can be calculated. From the geometry, the recursion relation can be derived:

$$\beta_m = \beta_{m+1} + \left( \frac{2\pi d}{\lambda} \right) \phi \quad (\text{radians})$$

where  $d$  is defined in Fig. III-14, and  $\Theta$  is the angle between adjacent feed bars. In addition, the angle between the first feed bar and the  $(N/2) + 1$  feed is 1 radian; therefore, for a full matrix,

$$\Theta = \frac{2}{N} \quad (\text{radians})$$

and

$$\beta_m = \beta_{m+1} + \left(\frac{2\pi d}{\lambda}\right) \left(\frac{2}{N}\right)$$

As previously illustrated, these values of  $\beta$  must be compensated for by the  $\alpha$ 's in order to obtain the desired distribution in the presence of the error terms.

If now we proceed to the second input bar, the couplers for the second bar can be calculated. The magnitude of the voltage coupled from input 2 to line  $l$  (Fig. III-14) must be equal to the magnitude of the transformed voltage of distribution 2 in the same curved line.†  $K_{21}$  is now easily calculated. Similarly, the remainder of couplers in the second bar can be determined. The phase lengths  $\beta$  between curved bars have been determined; therefore, the phase corrections ( $\alpha_{ij}$  of Fig. III-14) can be calculated by applying reciprocity.

It is now possible to iterate the complete problem. Distributions 3 and 4 are brought through the second bar and translated in phase to the input points of the third bar. Bar 3 couplers are then determined, and finally the second set of phase corrections is calculated. Inductively, it can be seen that the process can be extended to a  $m \times n$  matrix with little difficulty.

The finished configuration has the unique property that the power lost due to the  $N/(N+1)$  efficiency factor is always dumped into the load at the end of each energized line in both the transmit and receive senses. In other words, when port  $m$  is fed to form a transmit beam,  $[N/(N+1)] \times P_m$  is dumped only in load  $L_m$ , while in the receive case,  $[N/(N+1)] \times$  power intercepted by the  $l^{\text{th}}$  antenna ends up in the  $L_l$  load.

Another property of the matrix when designed in the above manner is that it has some interesting symmetries. That is

$$C_{lm} = C_{(n+1-l), (n+1-m)} \quad (20)$$

and

$$\alpha_{lm} = -\alpha_{(n+2-l), (n+2-m)} \quad (21)$$

Therefore, when designing a compensated beam former, only the top half need be computed to obtain the complete design.

An inverse source program was also written to compute the beam radiation patterns for a linear array of isotropic radiators excited by the beam former when the values are specified for the couplers and phase compensations. The philosophy of this program is exactly the same as the design program except the inverse program starts with the lowest input bar ( $l = n$ ) in a transmit sense and transforms each set of voltages up through the bars, picking up the additional beams as it goes. The end result of the computation is a beam voltage matrix at the antenna aperture, which is used in a far-field subprogram to actually plot any or all of the desired beam radiation patterns. Problems such as efficiency, bandwidth, quantization of couplers and

---

† It is imperative that the power be normalized properly according to the particular configuration.

phase compensations, bar deletion, and several simultaneously excited bars (e.g.,  $\cos^n \theta$  illuminations) can then be readily examined.<sup>‡</sup>

#### D. COMPUTED RESULTS

The two computer programs described in the previous section were written to evaluate the performance of the series-fed beam former as completely as possible. The first program was designed to calculate the exact values of the directional coupling coefficients  $C_{ij}$  and the phase compensations  $\alpha_{ij}$  necessary to form perfectly, at one frequency, all the possible  $\sin nx / \sin x$  orthogonal beams commensurate with the number of elements in the linear antenna array. The second program was designed to compute the voltage amplitude and phase values as a function of frequency at each antenna port for all the input ports of a beam former when specific values of  $C_{ij}$  and  $\alpha_{ij}$  were used as inputs to the program. In addition to computing the antenna port voltages for all beams, a far-field antenna pattern plotting routine was included in the program in order to make evaluation of the data quicker and easier. It was felt that transforming the data into antenna patterns would give a more general figure-of-merit to the various configurations than would the raw voltage data at each antenna port. Most of the data presented in the following figures are given in antenna pattern form. A subroutine to sum adjacent beams to form aperture distributions of the form  $\cos^n \theta$  was also used.

All the computer programming was written in as general form as was convenient, with the number of elements, antenna spacing, frequency, and efficiency used as the major variables. As the program was originally written, the number of elements  $N$  was restricted to 75 due to core storage, but slight modifications can raise this number considerably. The bulk of the computing was done for a 16-element beam former as a compromise between computer time and significance of calculated data. A few runs were made for 4-, 8-, 25-, 32-, 50-, and 64-element arrays to check the validity of trends suggested by the 16-element results. The fact that an "exact" beam former could be designed to form ideal beams at a fixed or center frequency gave a point of reference for evaluating results when nonexact component values were used in the network, or when the frequency was changed to obtain bandwidth data.

As would be expected, due to the basic configuration, the lower numbered beams (e.g., the beams formed by bars near the top of the matrix) exhibited fewer error effects than those farther down the matrix. Beams 6, 9, and 15 were chosen as representative of the beam former performance and these are used throughout the remainder of this report for comparison purposes. Figure III-16(a-c) shows the three ideal beams which were calculated for a 16-element array using an efficiency of 16/17 and an element spacing one-half the normalized wavelength. The ordinate values are plotted in decibels and normalized to 100-percent efficiency. The abscissa is plotted in degrees from  $-90^\circ$  to  $+90^\circ$ . All the plots have the theoretical beam pointing position marked with a vertical dashed line and the actual maximum with a vertical solid line. The pointing error is indicated as  $\pm \Delta\theta$  to the nearest  $1/10^\circ$ . The horizontal dotted line represents the theoretical gain (efficiency), with the solid line representing the actual gain, and the loss indicated as  $\Delta G$  to the nearest  $1/8$  db.

The values of the couplers  $C_{ij}$  and phase increments  $\alpha_{ij}$  which were obtained from the ideal design computation are plotted in Figs. III-17 and III-18. Only the 8 uppermost bars are plotted

---

<sup>‡</sup>Copies of both source programs in Fortran II language are available upon request.



because the bottom bars have the reverse symmetry shown in Eqs. (20) and (21). The first effect to be studied was that of bandwidth in the case where  $K_{1,N} = \frac{1}{2}$  (a 3-db coupler). This is the tightest coupling used for the full rectangular matrix and will be referred to as maximum efficiency configuration. By using the values computed at  $f_0$  in the beam computation program, the normalized frequency was increased and decreased in steps, until definite beam degradation occurred. For the 16-element array, a change of  $\pm 5$  percent in frequency gave a beam pointing error at boresight of approximately  $0.5^\circ$ . The sidelobe nulls were also considerably filled in at this point. Figures III-19(a-c) and III-20(a-c) show the three reference beams at  $1.05 f_0$  and  $0.95 f_0$ , respectively. The only difference between the higher and lower frequencies was the direction of beam squint; therefore, no further computations were made at  $0.95 f_0$ .

The next effect investigated was the result of using nonexact values of  $C_{ij}$ 's and  $\alpha_{ij}$ 's. Figures III-17 and III-18 clearly show that both the couplers and phase shifts tend to bunch near the center of the matrix. Therefore, two sets of approximate  $C_{ij}$ 's and  $\alpha_{ij}$ 's were made up. The values were quantized into increments of 5 and 10 percent in the first and second sets, respectively. That is, a coupler of exact value 0.06 would be given the value of 0.05, and the exact value 0.09 would become 0.10. Figures III-21 and III-22 show the same beams for the 5-percent quantized values at  $f = f_0$  and at  $f = 1.05 f_0$ , respectively. It is apparent that although the  $f = f_0$  plots are quite satisfactory, the 5-percent change in frequency gives totally unacceptable results. Figures III-23(a-c) and III-24(a-c) show the same three beams for the 10-percent quantized values of  $C_{ij}$  and  $\alpha_{ij}$  which give the same sort of beam-pointing and gain errors as do the 5-percent quantized values but much more sidelobe deterioration. Two other nonexact configurations were also considered: (a) use of the correct values for  $C_{ij}$  and all  $\alpha_{ij}$ 's = 0 and (b) use of the same values of couplers in all the bars with no phase correction. In the latter case, the first bar was designed correctly with  $C_{ij} = 1/\sqrt{N+2-j}$  and all other bars used the same values. Figure III-25(a-c) shows the first case and Fig. III-26(a-c) the second case. Although the beam-pointing error is not excessive at  $f = f_0$ , the sidelobe structure has deteriorated sufficiently to classify the results as undesirable and no frequency change was investigated with the maximum efficiency.

The foregoing pattern results were all computed using the maximum efficiency criterion (16/17) and the multipath effects are quite pronounced under this condition. In the case of uniform illumination beams, the beam former does exhibit nominal bandwidth. However, were the matrix designed to give a strong amplitude taper across the aperture, the sidelobe degradation would be more severe with frequency change. In order to reduce the multipath problems and hence improve the array performance, it is necessary to reduce the coupling values to a point where the contributions from the error paths do not contribute significantly. To reduce the coupling values, it is necessary merely to scale them by a constant factor and keep the same  $\alpha_{ij}$ 's, which, of course, reduces the array efficiency. The remaining 16-element patterns show the effect of reducing the efficiency of the various configurations. Only beams 9 and 15 are shown since beam 9 shows an average error and beam 15 a near-maximum error.

Figures III-27(a-b) to III-30(a-b) show the correctly designed beam former at  $f = 1.05 f_0$  for 80-, 75-, 67-, and 50-percent efficiencies, respectively. Comparison of these figures with those of beams 9 and 15 in Fig. III-19(a-c) shows a rapid decrease in pattern degradation of 75-percent efficiency and virtually none at 50 percent. The next set of plots, Figs. III-31(a-b) and III-32(a-b) show the case of  $C_{ij} = 1/\sqrt{N+2-j}$ , all  $i, j$  for 50- and 10-percent efficiencies, respectively, and  $f = f_0$ . Figures III-33(a-b) and III-34(a-b) are the same with  $f = 1.05 f_0$ . By using these last

coupler and phase shift values, the bandwidth was investigated up to  $f = 1.5 f_0$ . Figures III-35(a-b) and III-36(a-b) are plots with 25-percent for  $f = 1.2 f_0$  and  $f = 1.33 f_0$ , respectively. Figure III-37(a-b) shows 10-percent efficiency and  $f = 1.5 f_0$ . It is quite obvious from Figs. III-27(a-b) to III-37(a-b) that the design of the beam former can be very loose if the efficiency is low enough.

The above effects in the 16-element configurations appear also in other length arrays. Figures III-38(a-b) through III-41(a-c) show representative beams for 4-, 8-, and 64-element beam formers. It should be noted that as  $N$  becomes large, the pattern degradation increases faster and for high efficiencies the available bandwidth is reduced. It appears that a beam former of this type has a constant bandwidth efficiency product similar to the gain bandwidth of an amplifier.

Beam combining computations were also carried out to form  $\cos^n$  type illuminations. These computations were performed only for maximum efficiency conditions. Figures III-42(a-b) and III-43(a-b) show some of the results.

Summarizing the results of the investigation, we find that a series-fed multiple beam-forming matrix can be designed to have any efficiency up to 100 percent when orthogonal beams are being formed. (For the case of 100-percent efficiency the normal rectangular network degenerates into the triangular form.) When high efficiencies are desired, the matrix must utilize the multiple path signals to form the required beams and as a consequence the beam former becomes frequency sensitive. Since it is no longer a true time delay device, the degree of frequency sensitivity increases with the number of elements for a fixed efficiency. There is a three-way trade-off between design tolerances, efficiency, and array performance. Perhaps the most significant result is not that such a beam former can be designed, but rather that the performance of a particular design can be predicted exactly for a minimal cost using the digital computer techniques outlined above. This type of beam former certainly should have a place in certain multiple-beam applications.

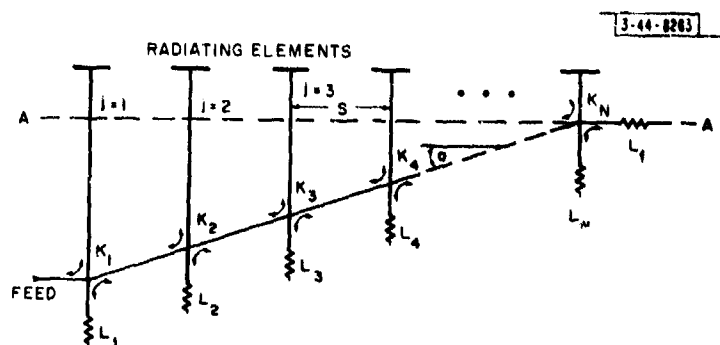


Fig. III-1. Single-beam series-fed beam former.

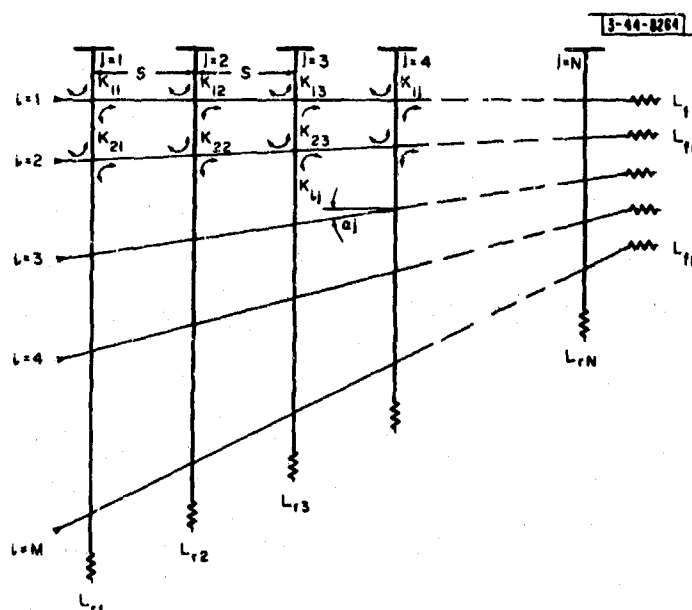


Fig. III-2. Multiple-beam series-fed beam former.

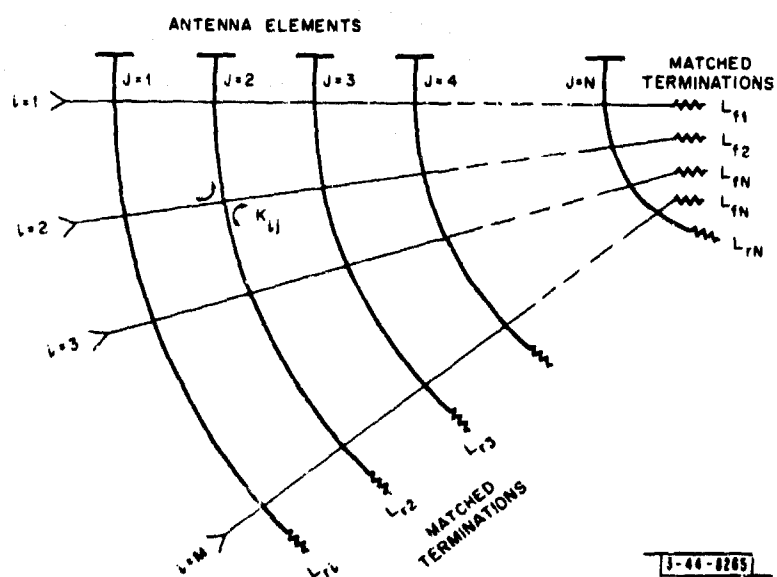


Fig. III-3. N element Brigham beam former.

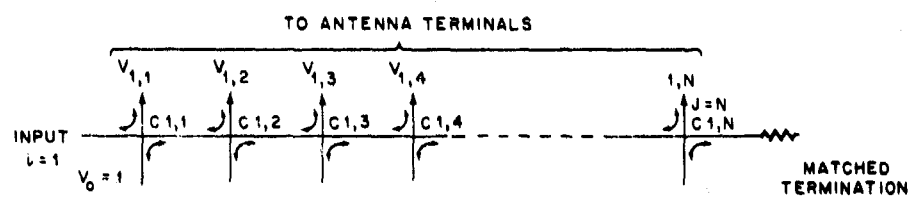


Fig. III-4. Uppermost feed bar of series-fed matrix.

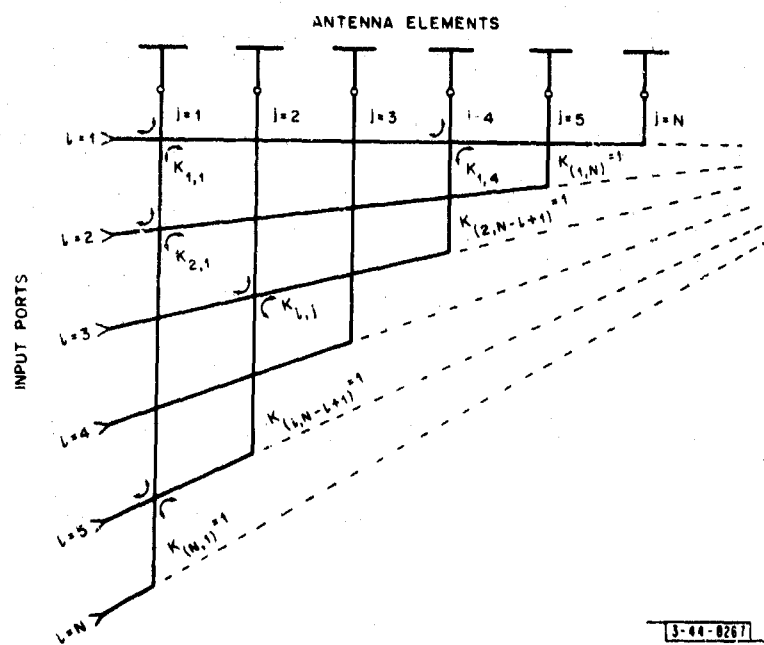
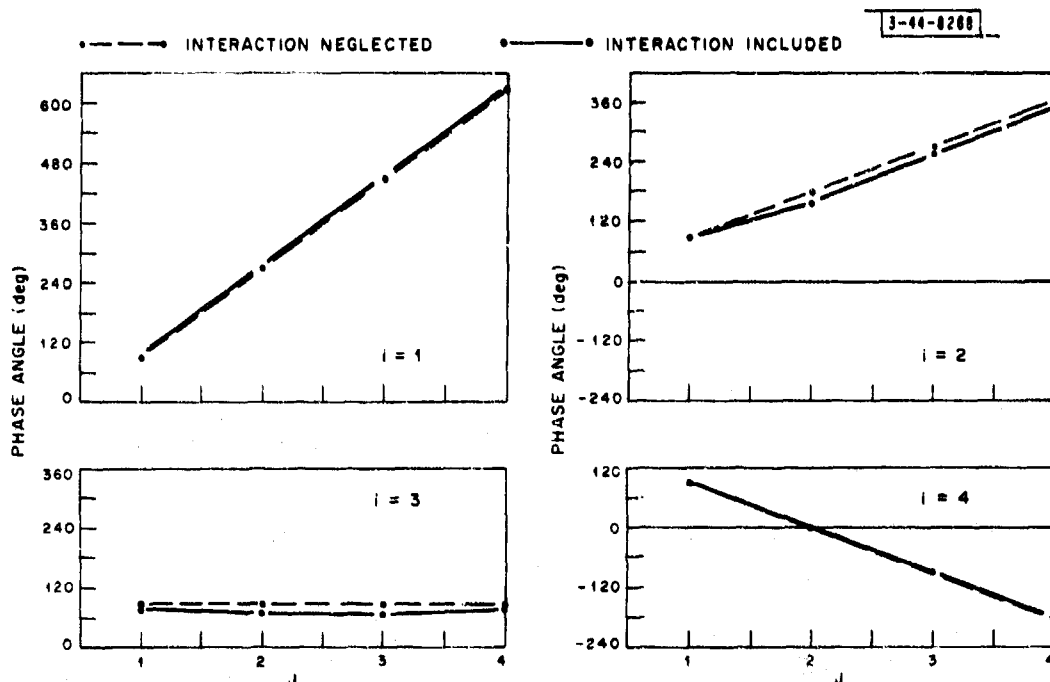
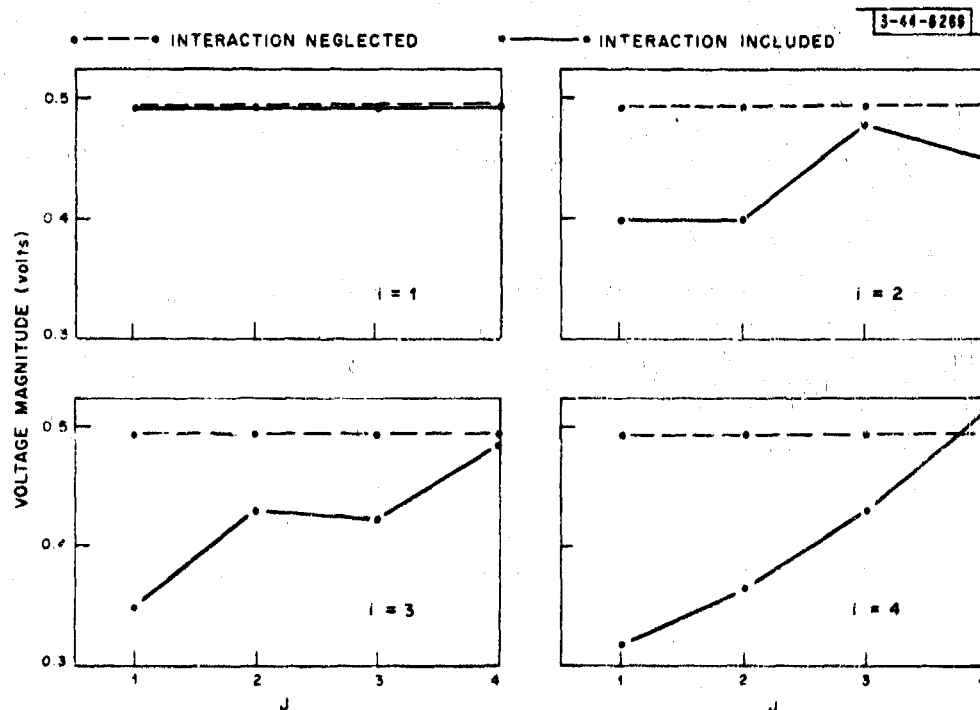


Fig. III-5. Triangular matrix beam former.

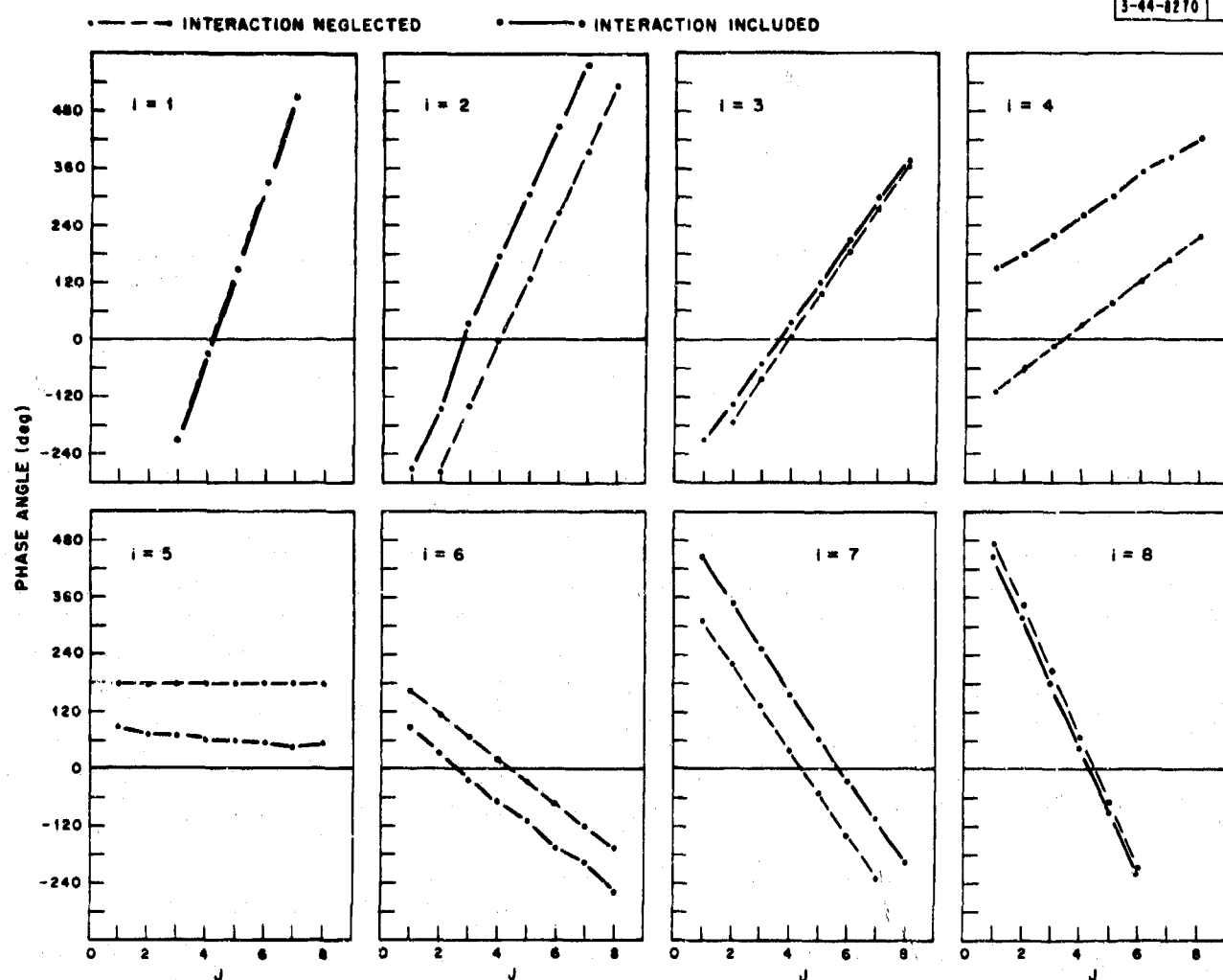


(a) Signal phase vs element position for 4-element orthogonal beam former with all feed bars designed alike using efficiency  $= 4/5$ .



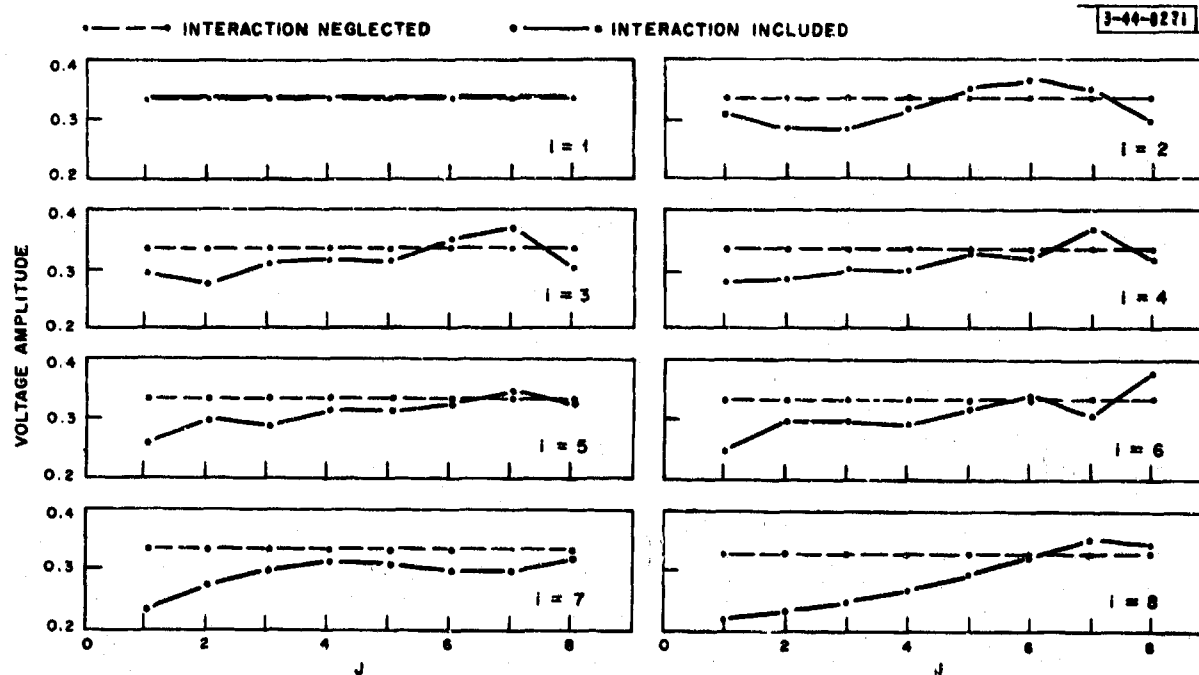
(b) Signal amplitude vs element position for 4-element orthogonal beam former with all feed bars designed alike using efficiency  $= 4/5$ .

Fig. III-6. Phase and amplitude response of 4-element matrix.



(a) Signal phase vs element position for 8-element orthogonal beam former with all feed bars designed alike and efficiency = 8/9.

Fig. III-7. Phase and amplitude response of 8-element matrix.



(b) Signal amplitude vs element position for 8-element orthogonal beam former with all feed bars designed alike and efficiency = 8/9.

Fig. III-7. Continued.

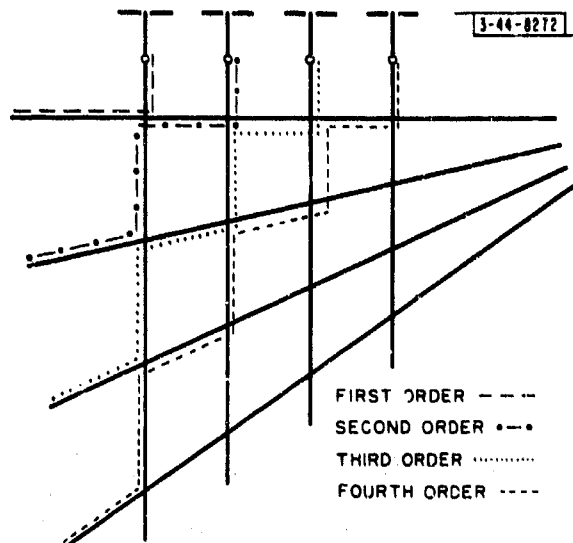


Fig. III-8. Multiple signal paths in 4-element matrix.

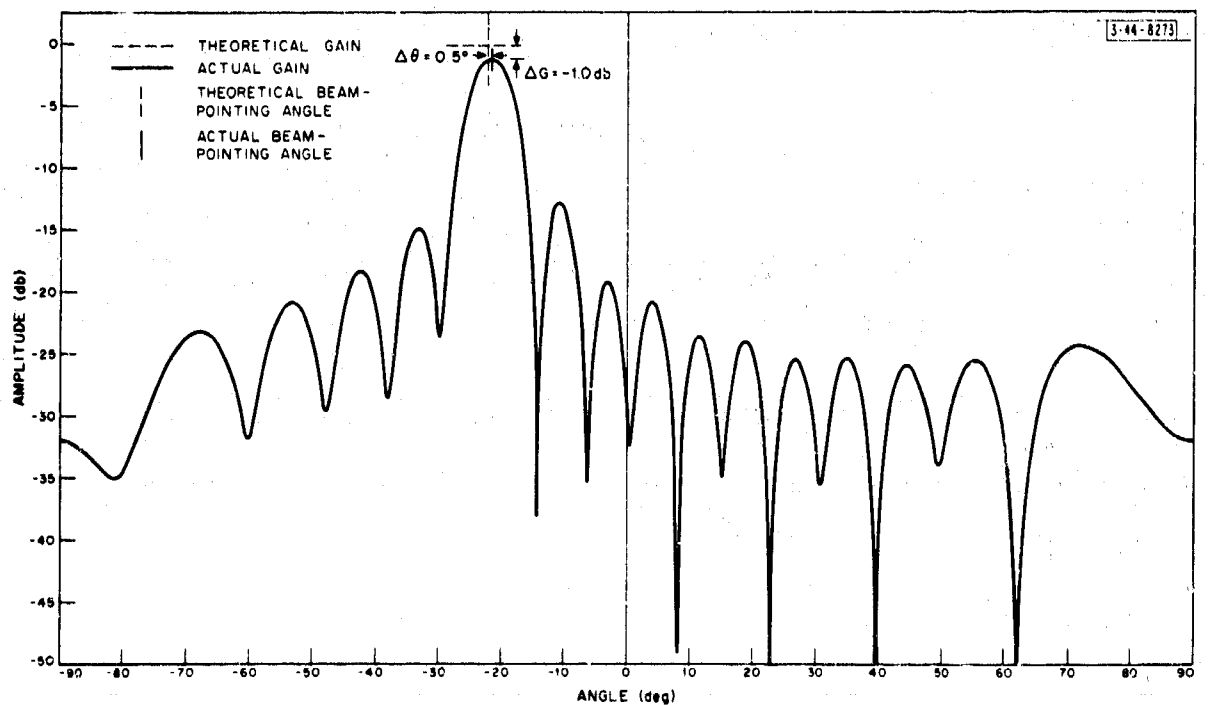


Fig. III-9. Beam 6 of uncorrected 16-element beam former.



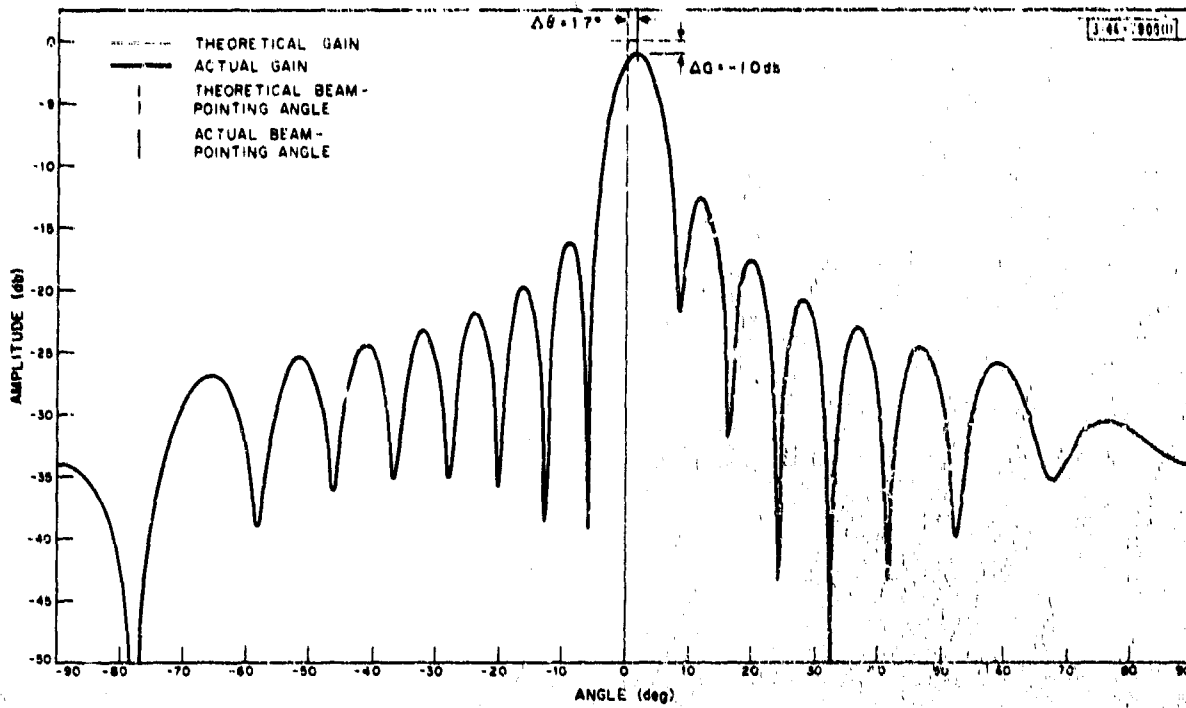


Fig. III-10. Beam 9 of uncorrected 16-element beam former.

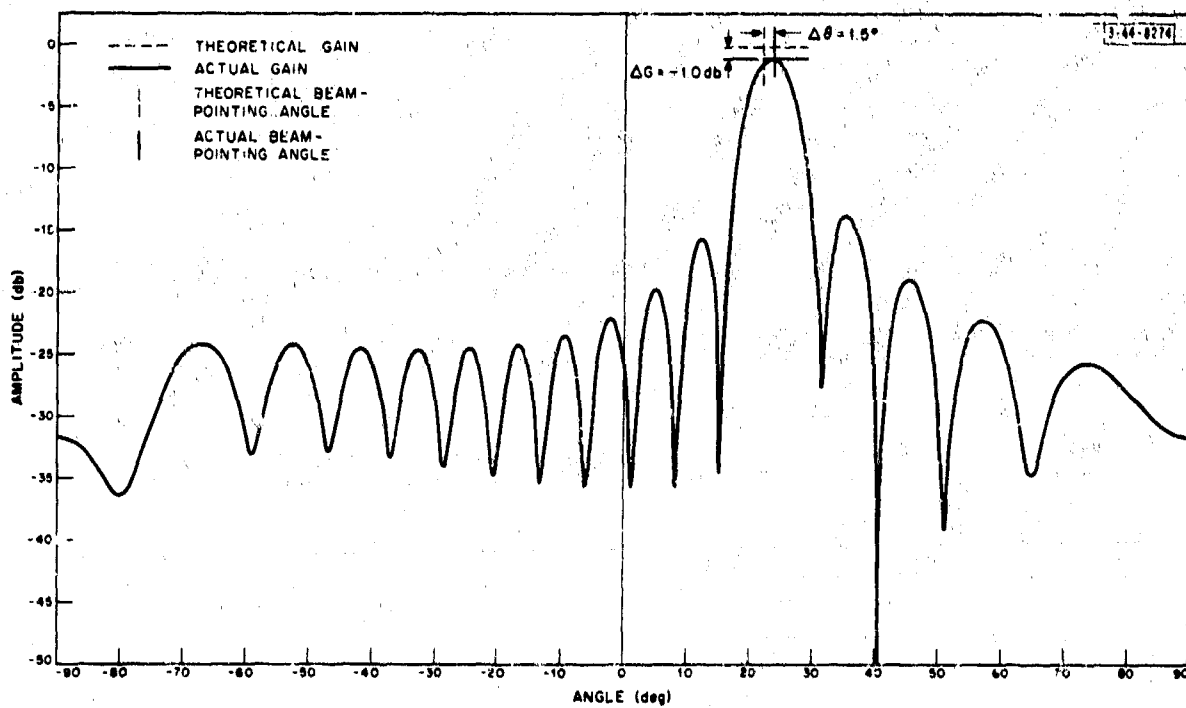


Fig. III-11. Beam 12 of uncorrected 16-element beam former.

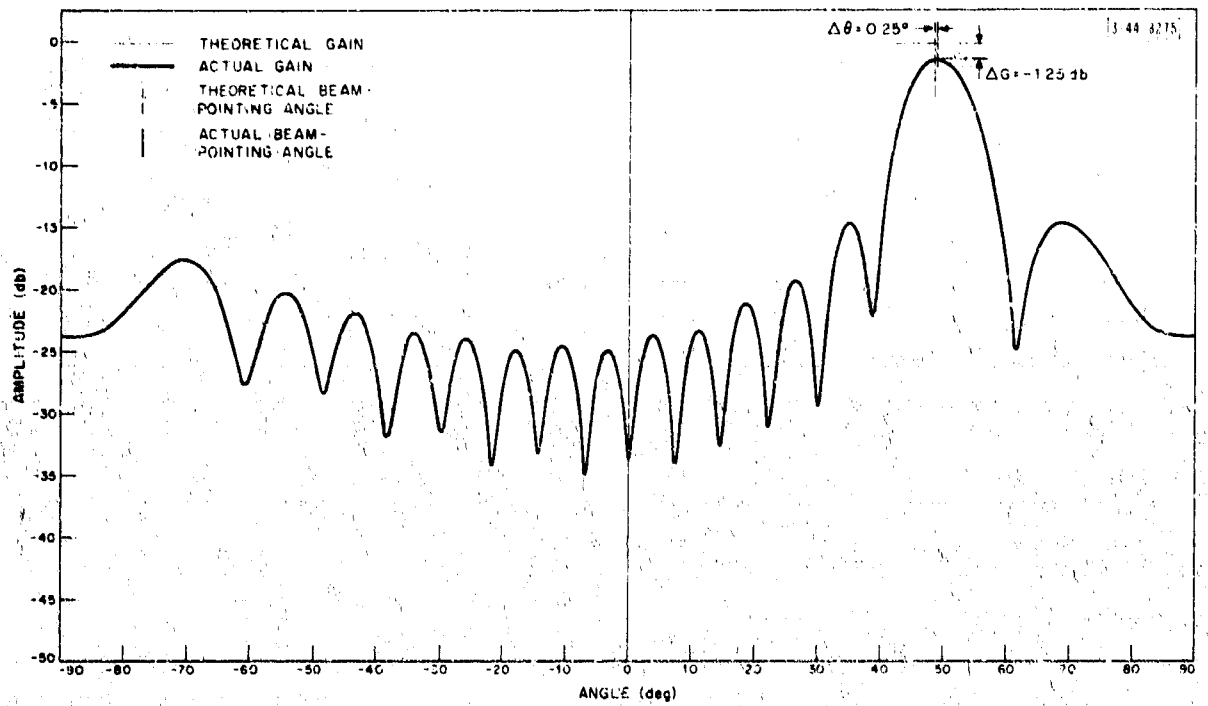


Fig. III-12. Beam 15 of uncorrected 16-element beam former.

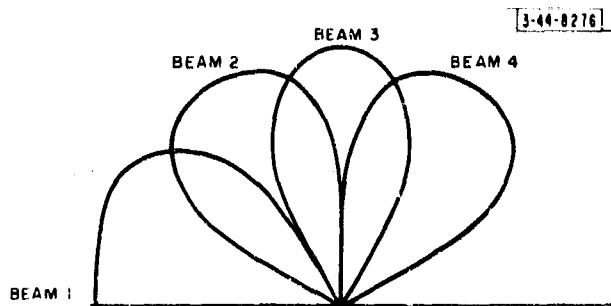


Fig. III-13. Beam identification for 4-element uniformly illuminated array.

Fig. III-14. Series-fed 4-element multiple beam former.

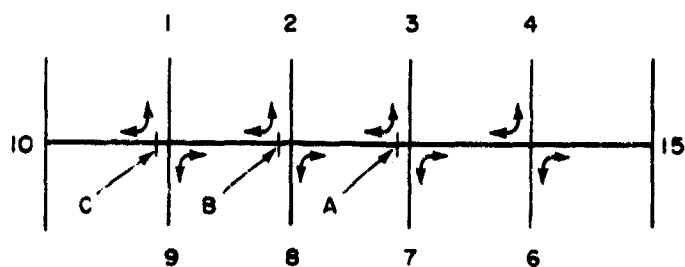
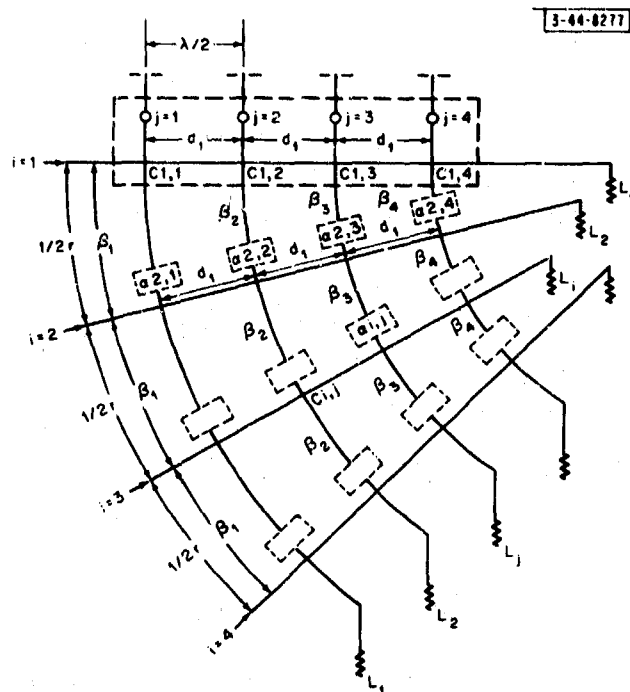
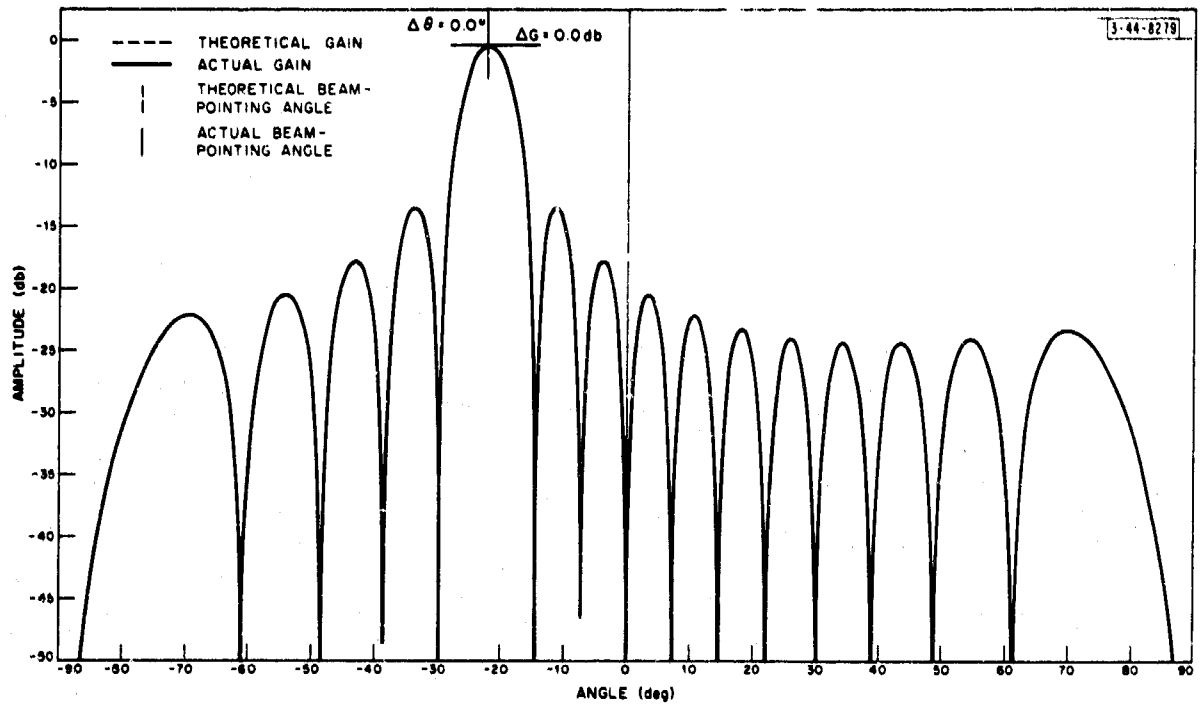
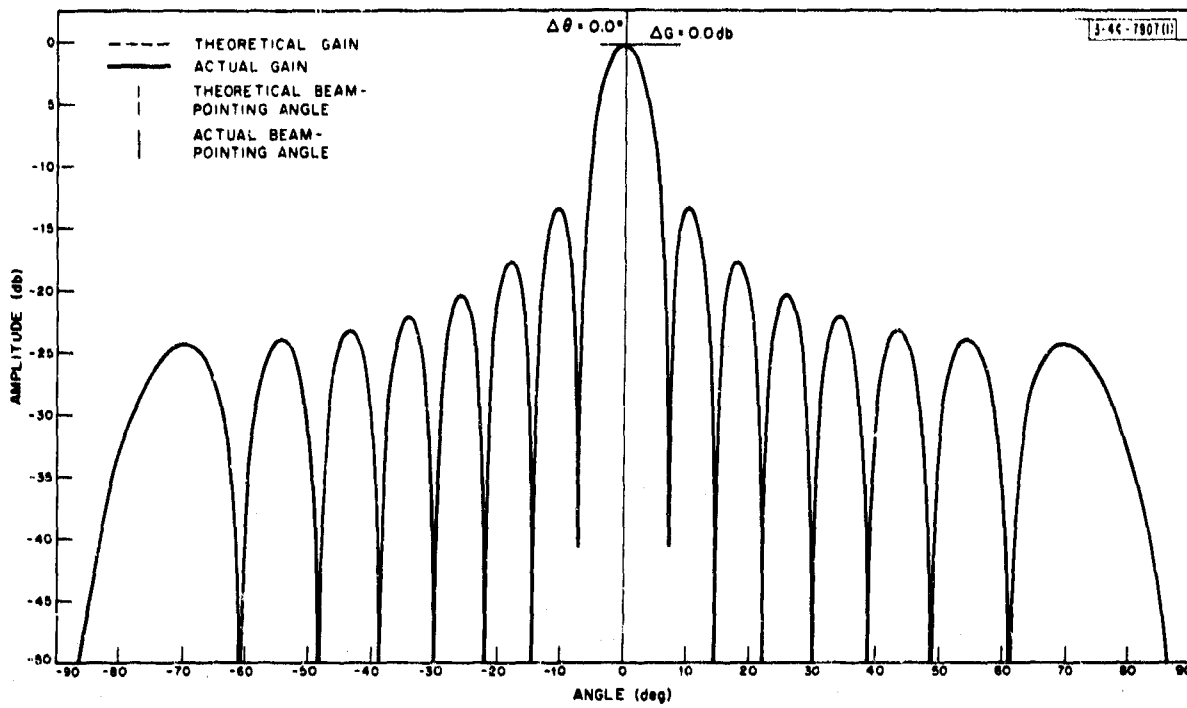


Fig. III-15. Schematic diagram of 4-element series-fed line.

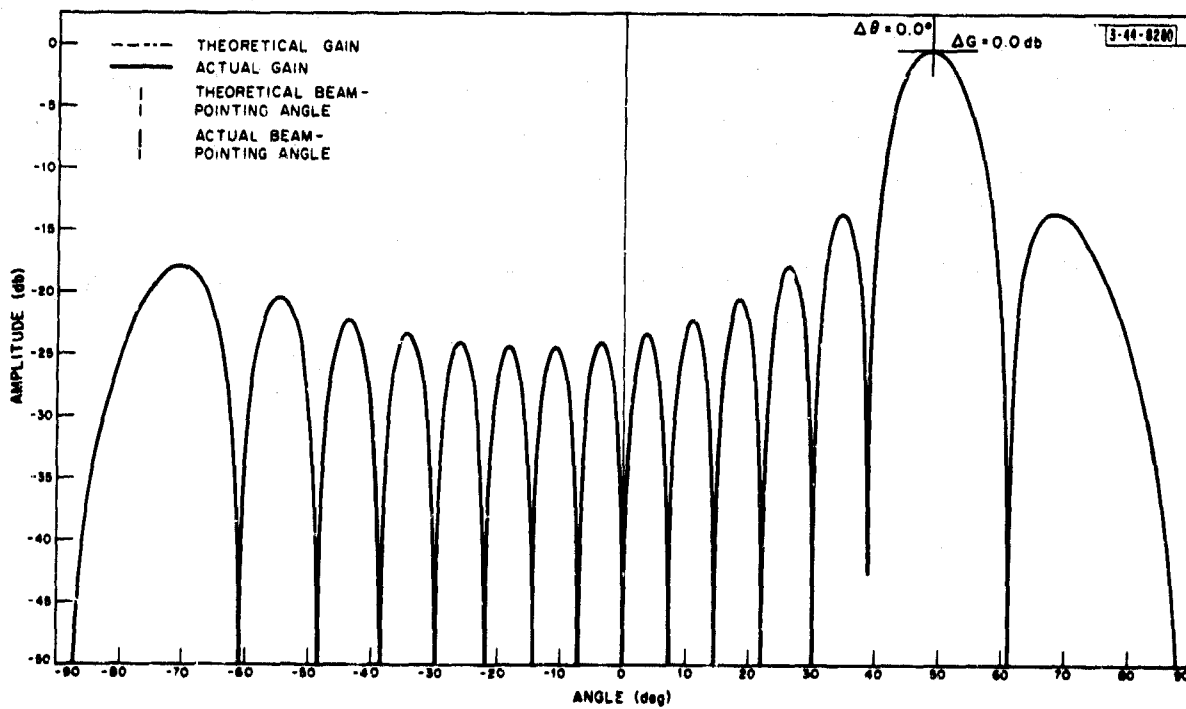


(a) Beam 6.

Fig. III-16. Beams 6, 9, and 15 for 16-element ideally designed linear beam former:  $f = f_0$ ,  $s = \pi$  radians, efficiency = 16/17.



(b) Beam 9 (boresight).



(c) Beam 15.

Fig. III-16. Continued.

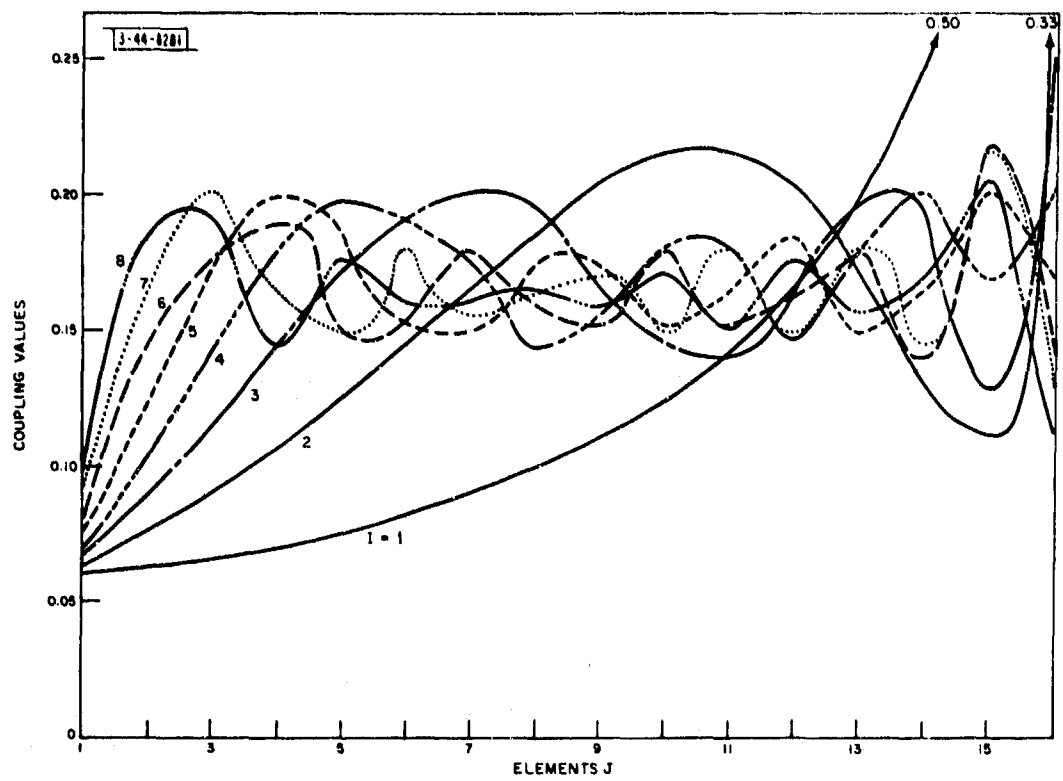


Fig. III-17. Plots of coupling values vs element number for bars  $l = 1$  through 8 ( $N = 16$ ).

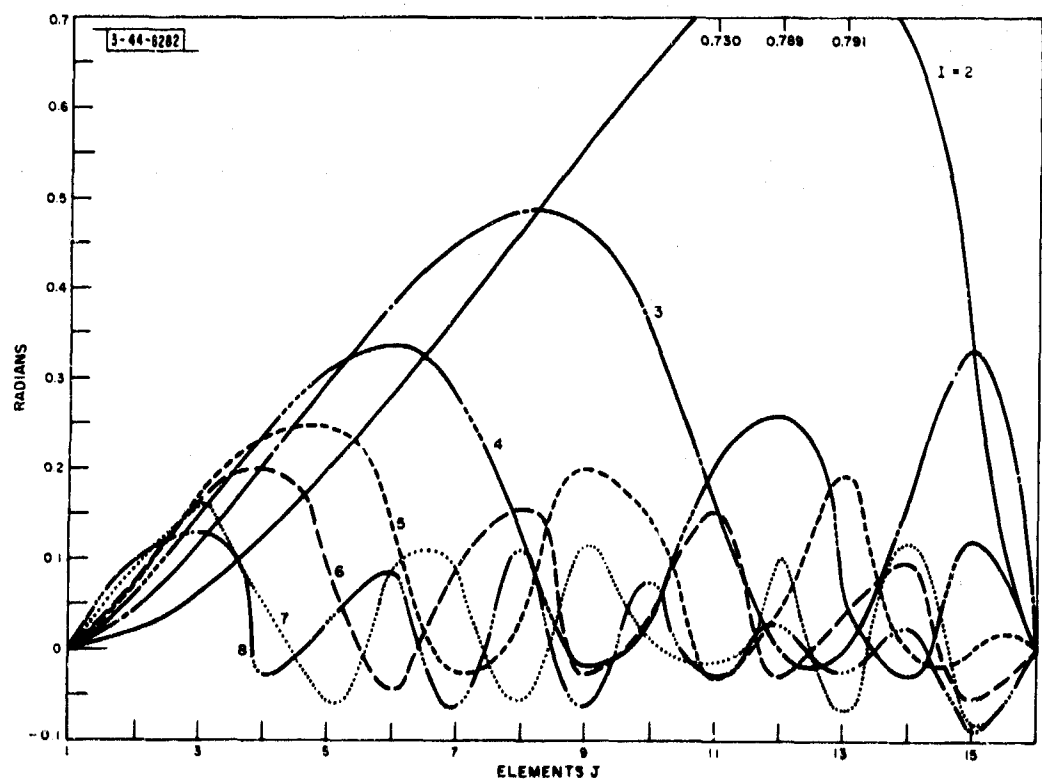
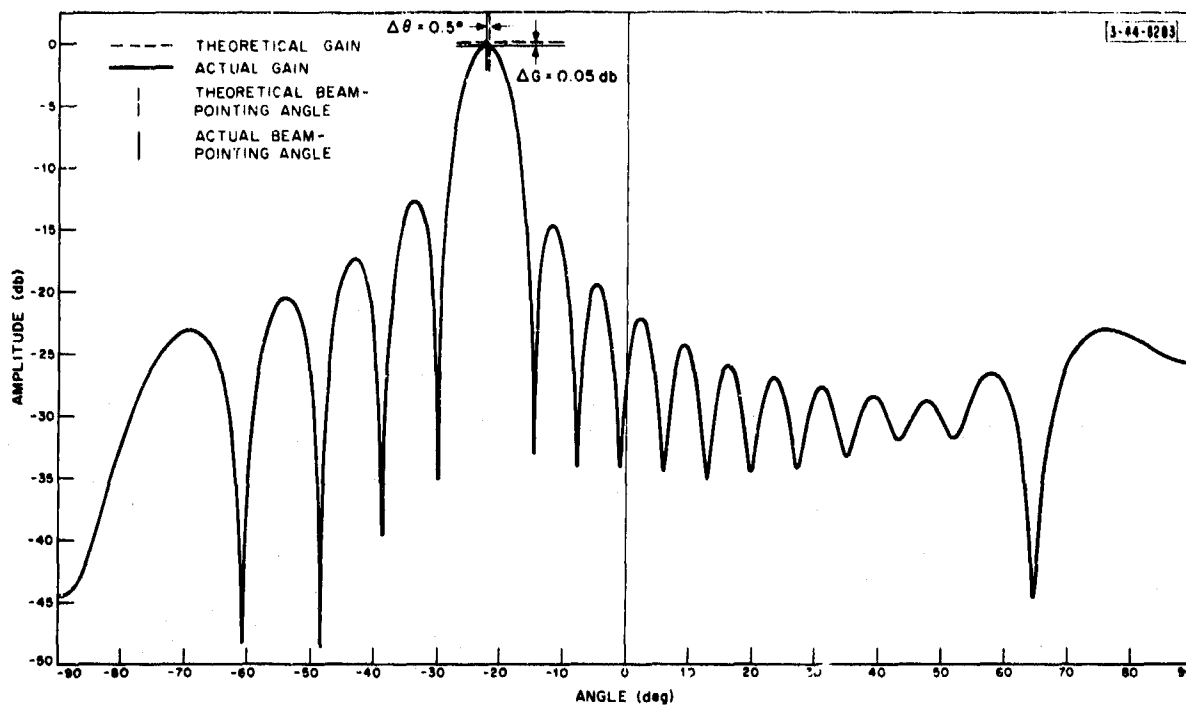
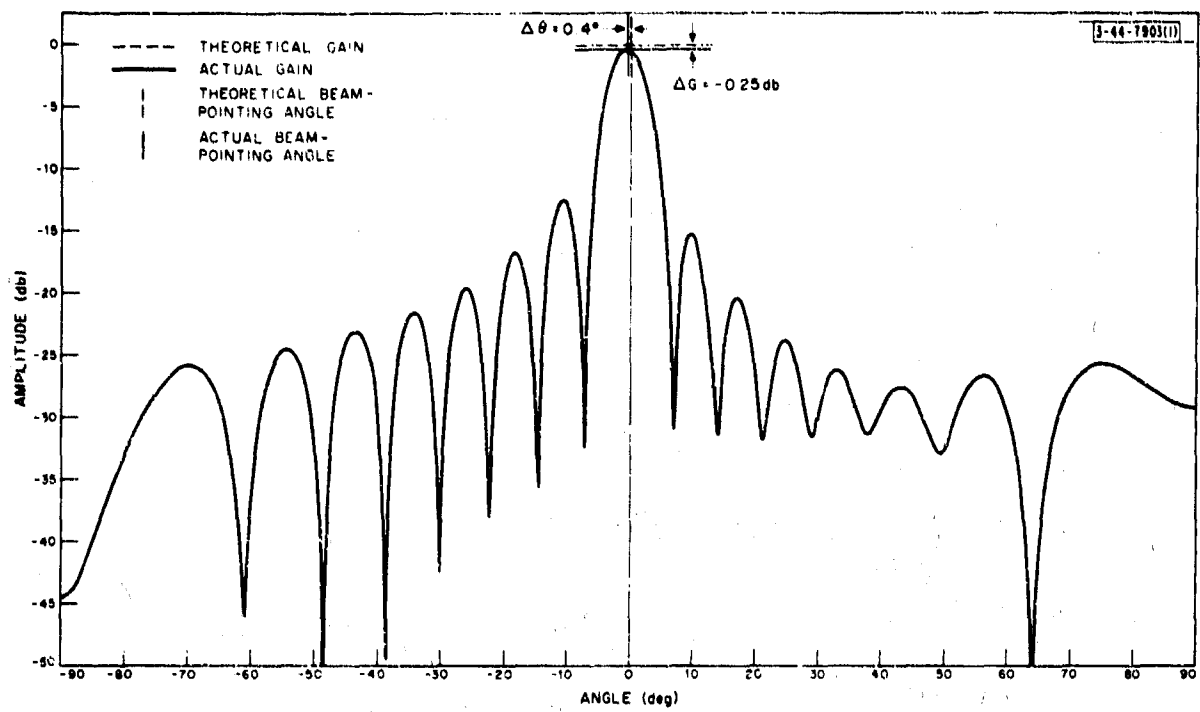


Fig. III-18. Plots of phase shift values vs element number for bars  $l = 1$  through 8 ( $N = 16$ ).

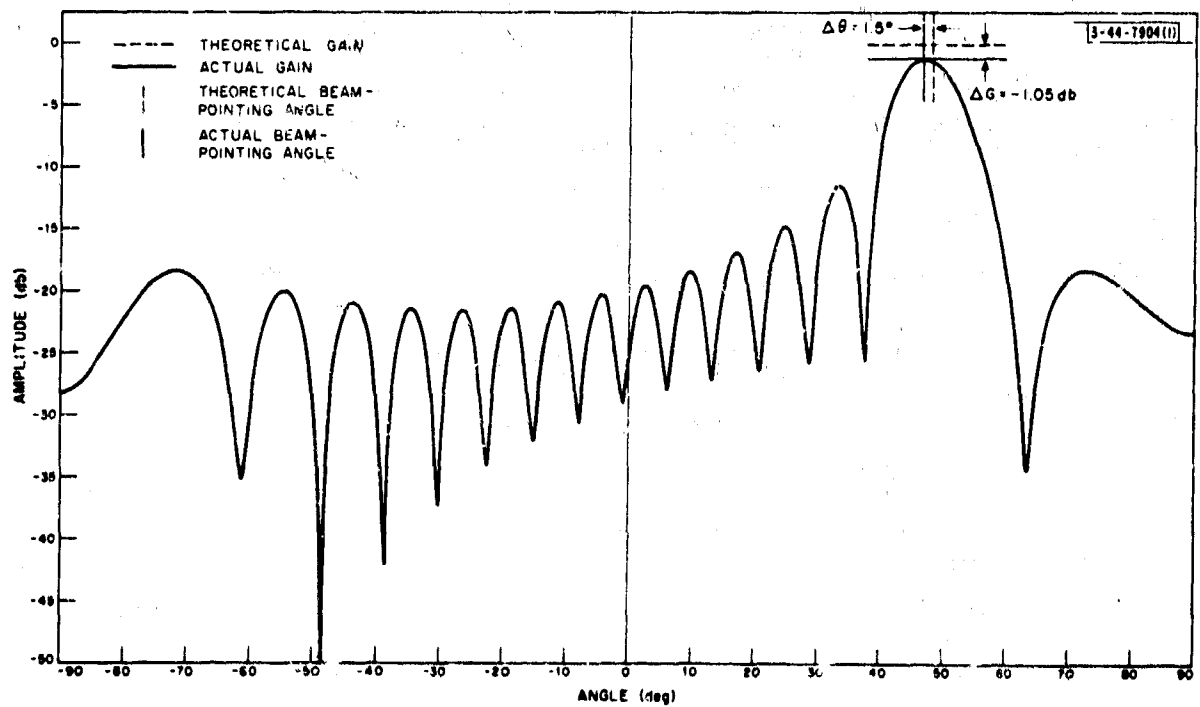


(a) Beam 6.

Fig. III-19. Beams 6, 9, and 15 for 16-element ideally designed linear beam former:  $f = 1.05 f_0$ ,  $s = \lambda_0/2$ , efficiency = 16/17.



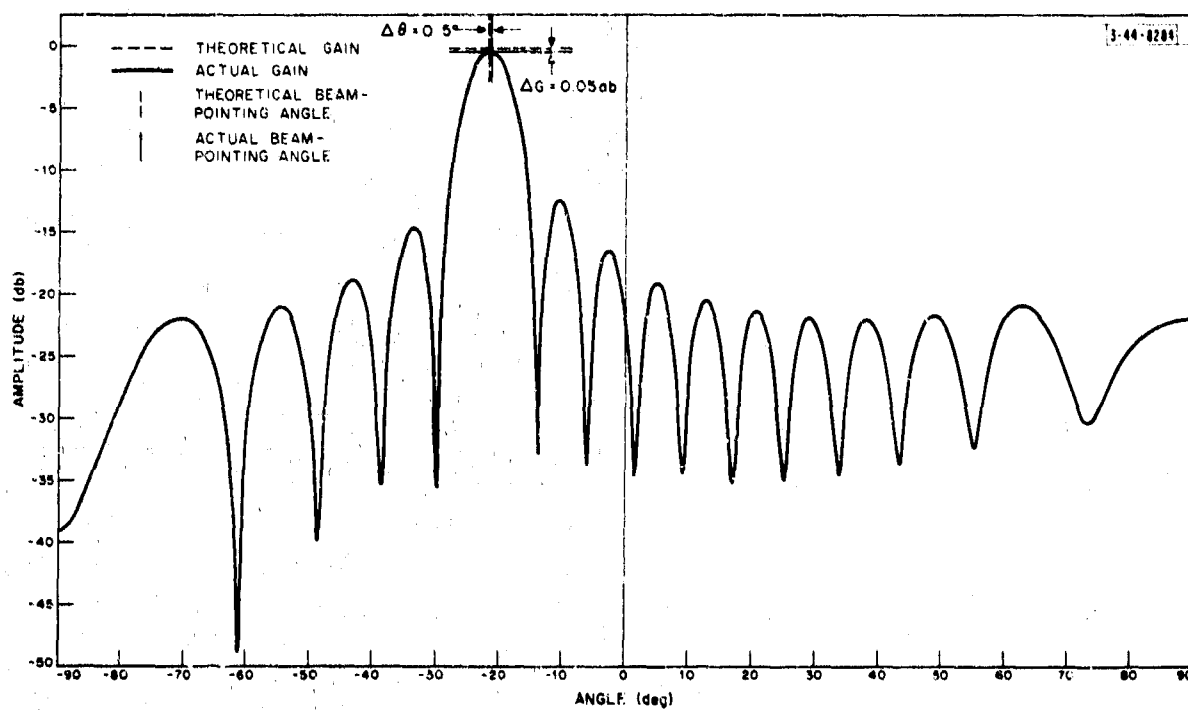
(b) Beam 9.



(c) Beam 15.

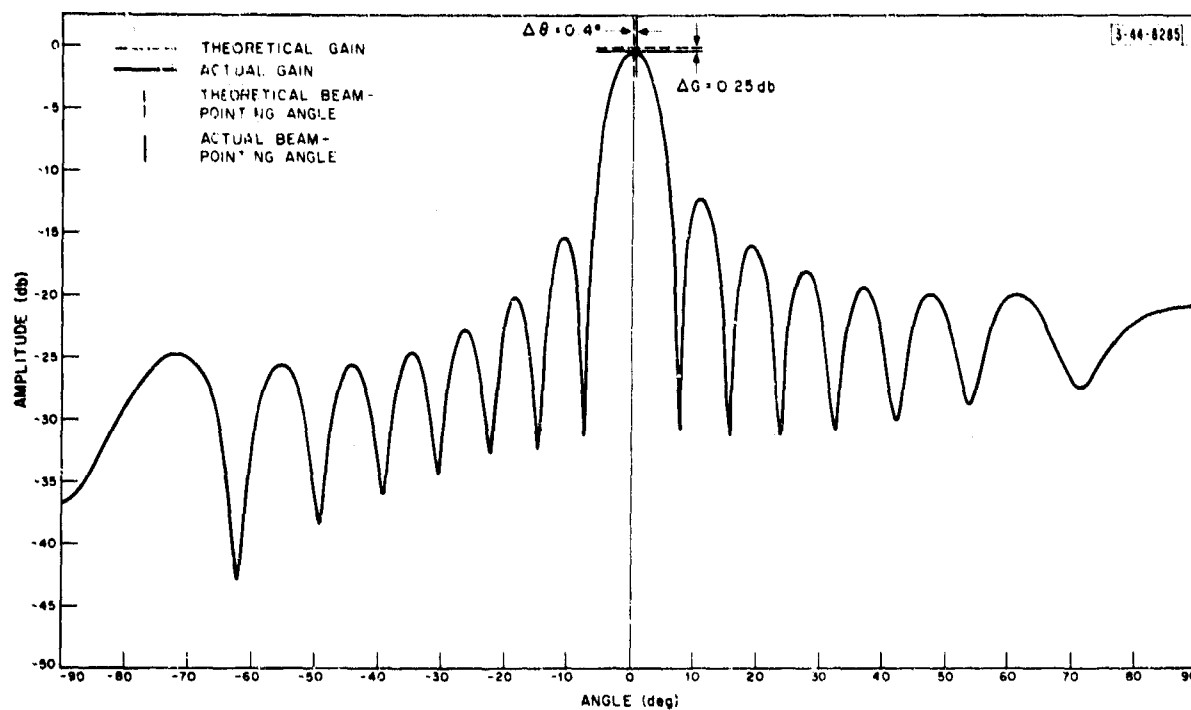
Fig. III-19. Continued.



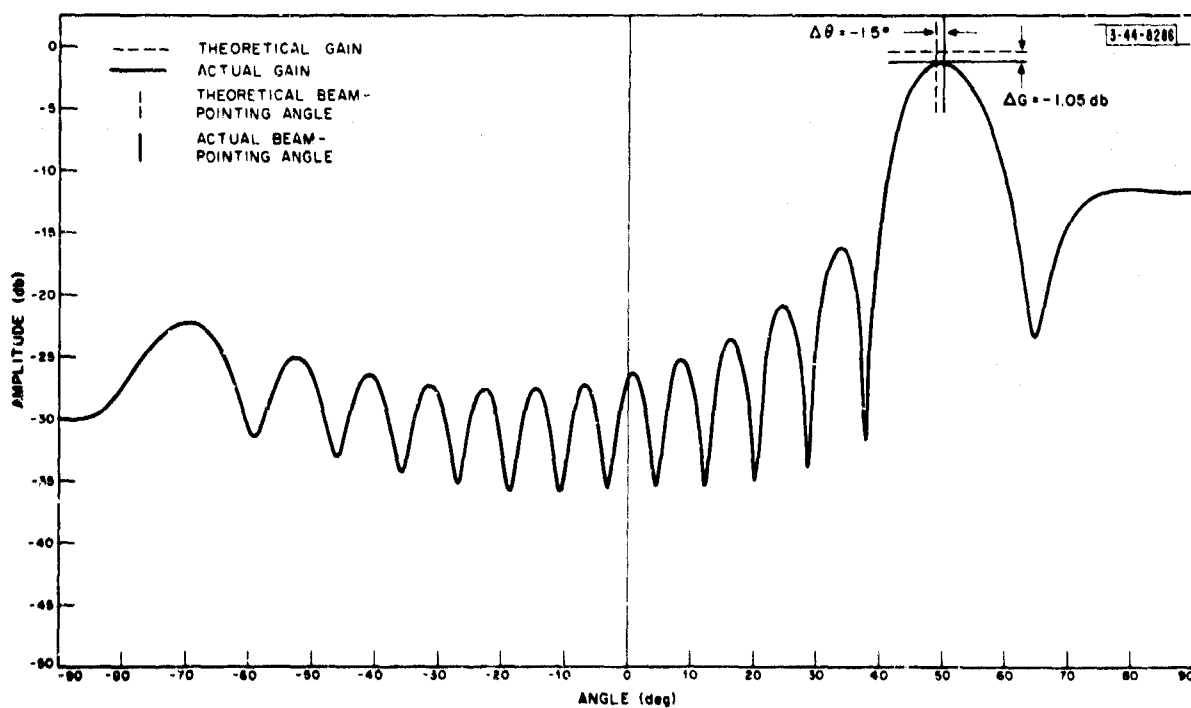


(a) Beam 6.

Fig. III-20. Beams 6, 9, and 15 for 16-element ideally designed linear beam former:  $f = 0.95 f_0$ ,  $s = \lambda_0/2$ , efficiency = 16/17.

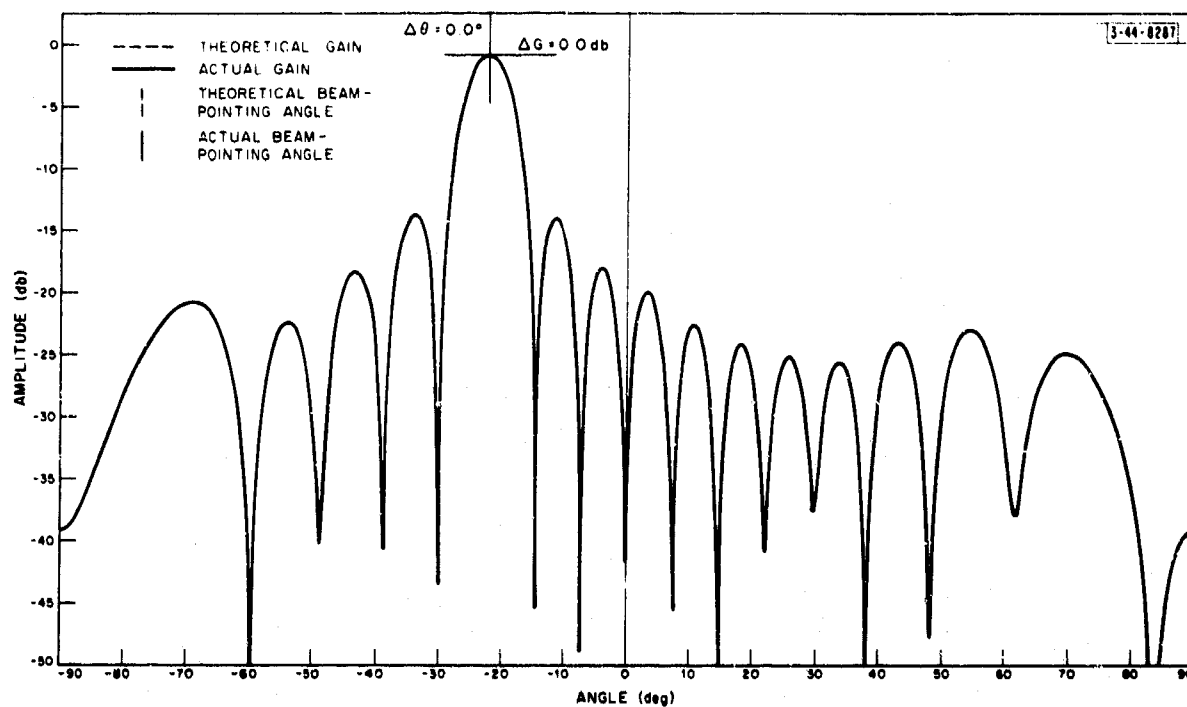


(b) Beam 9.



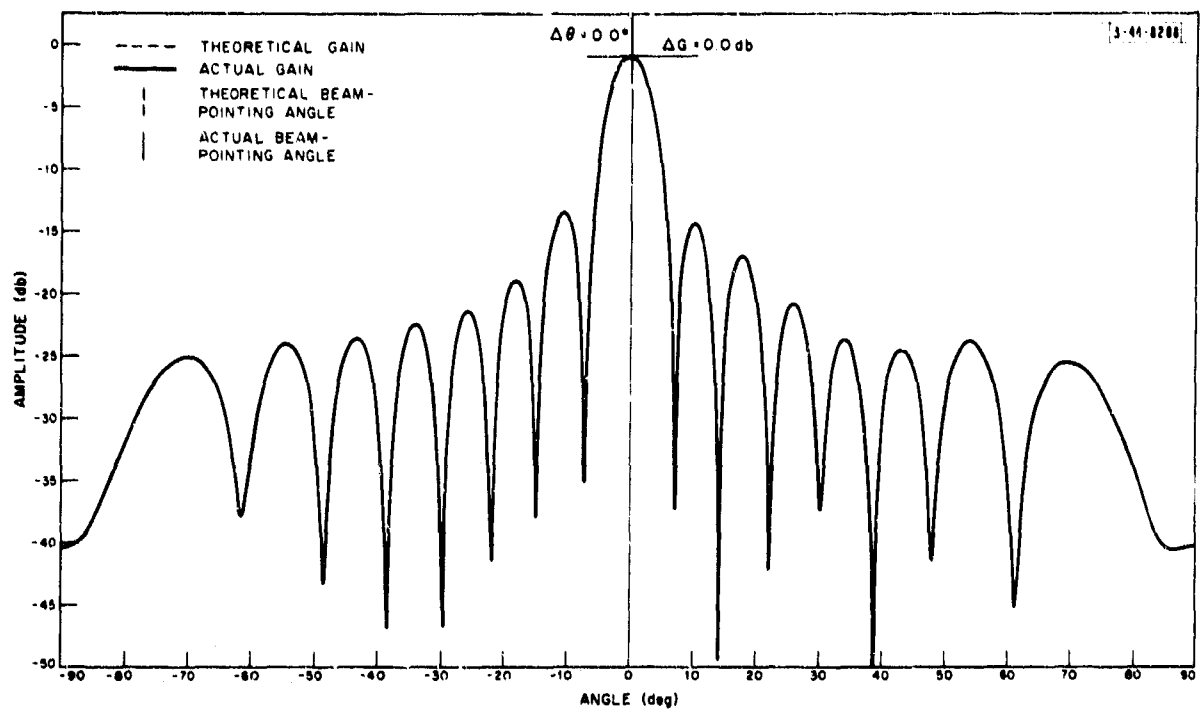
(c) Beam 15.

Fig. III-20. Continued.

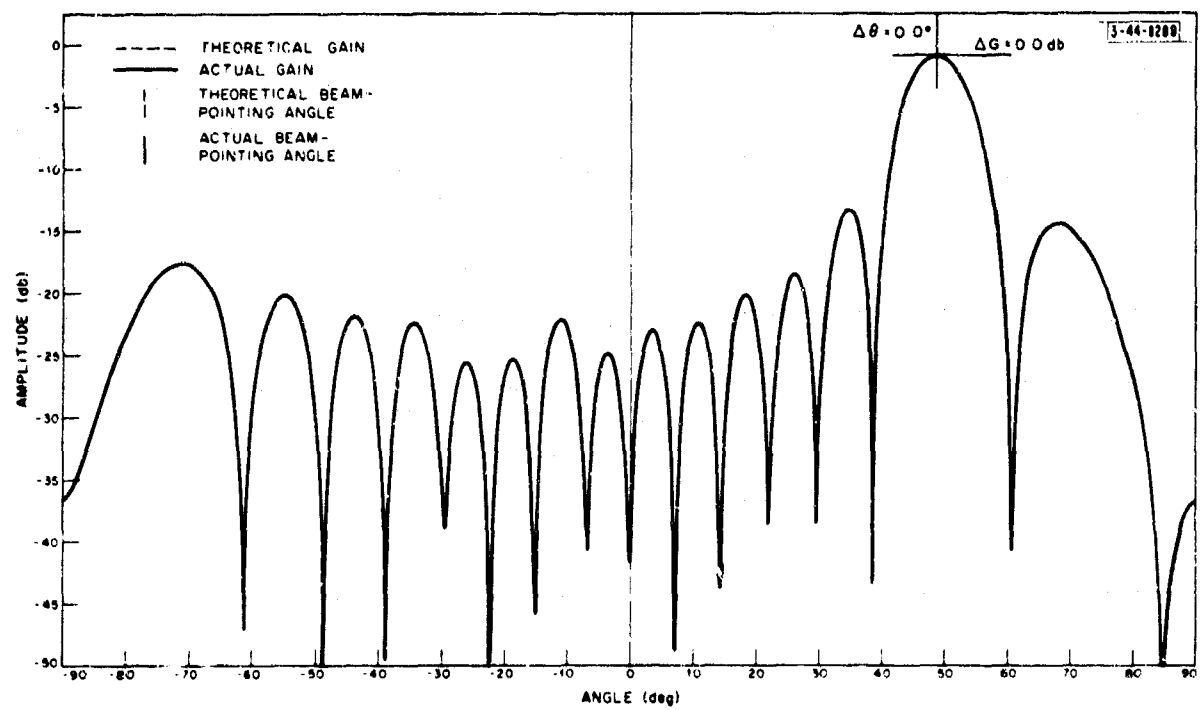


(a) Beam 6.

Fig. III-21. Beams 6, 9, and 15 for 16-element beam former using values  $C_{ij}$  and  $a_{ij}$  that have been quantized into 5-percent steps from the ideal values:  $f = f_0$ ,  $s = \lambda_0/2$ , efficiency = 16/17.

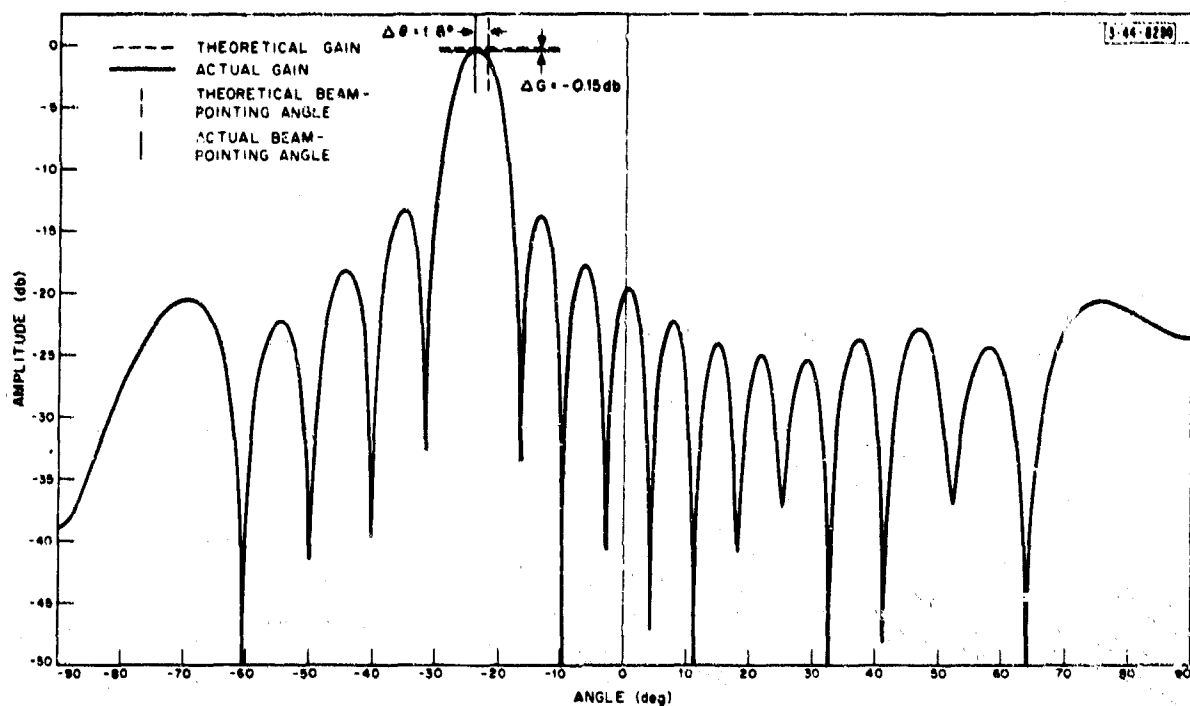


(b) Beam 9.



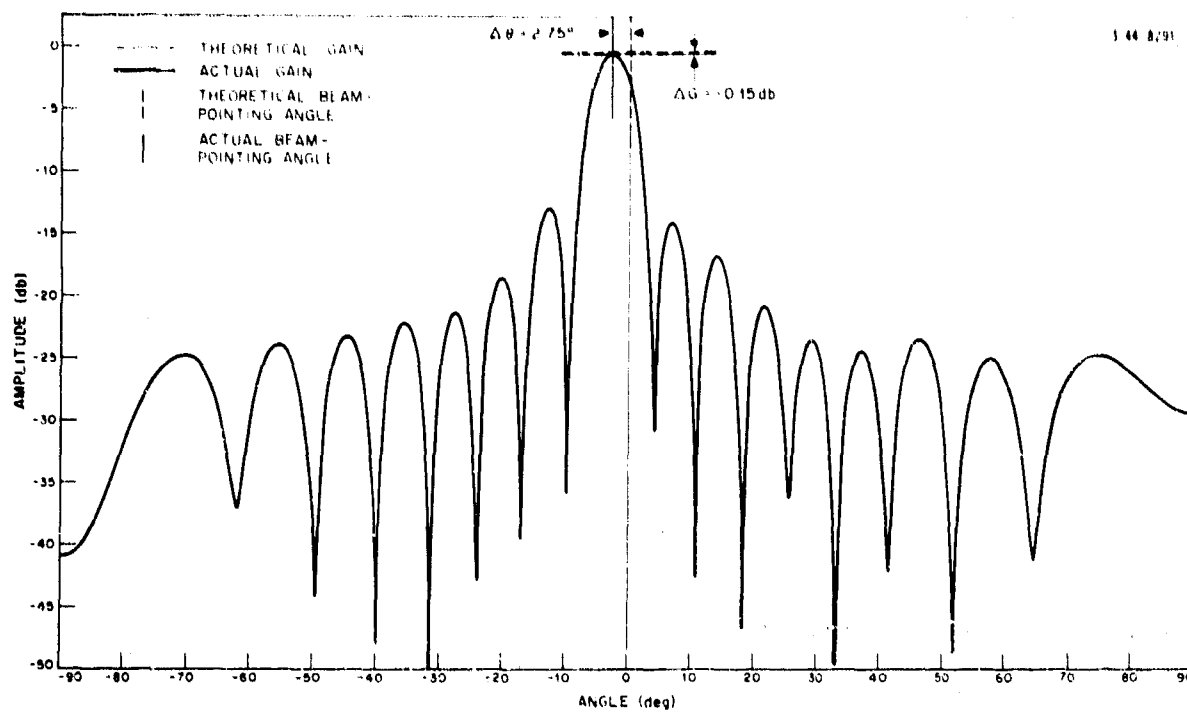
(c) Beam 15.

Fig. III-21. Continued.

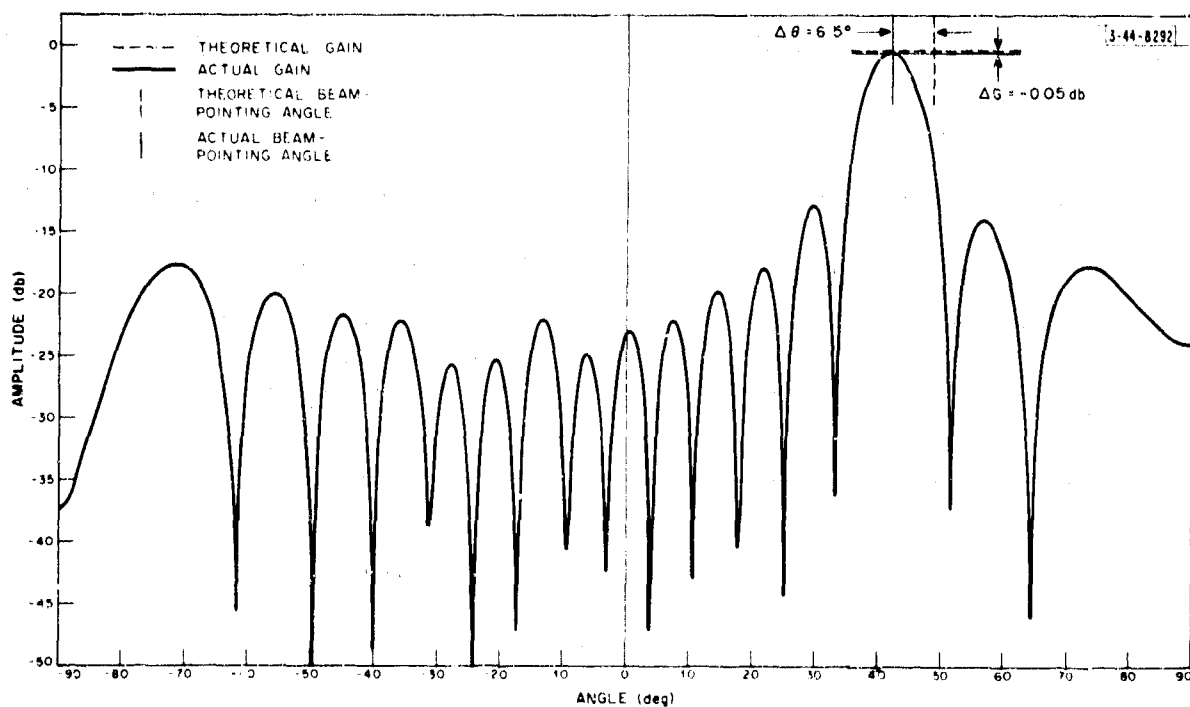


(a) Beam 6.

Fig. III-22. Beams 6, 9, and 15 for 16-element beam former using values of  $C_{ij}$  and  $a_{ij}$  that have been quantized into 5-percent steps from the ideal values:  $f = 1.05 f_0$ ,  $s = \lambda_0/2$ , efficiency  $= 16/17$ .

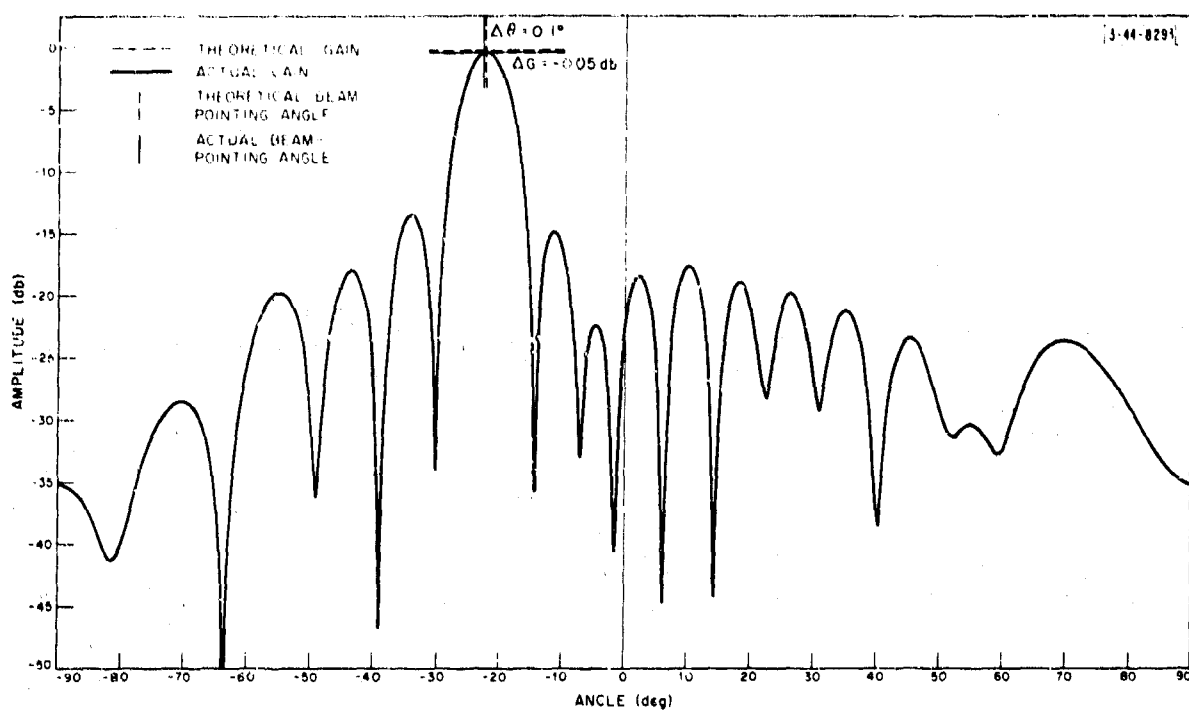


(b) Beam 9.



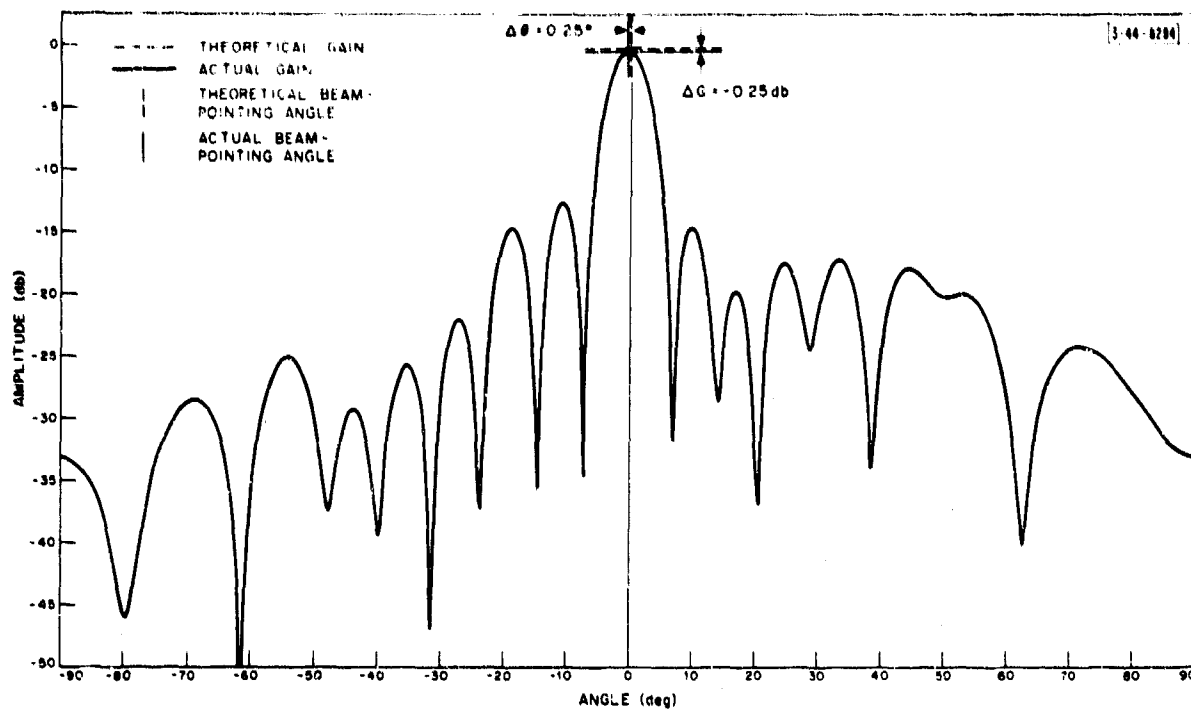
(c) Beam 15.

Fig. III-22. Continued.

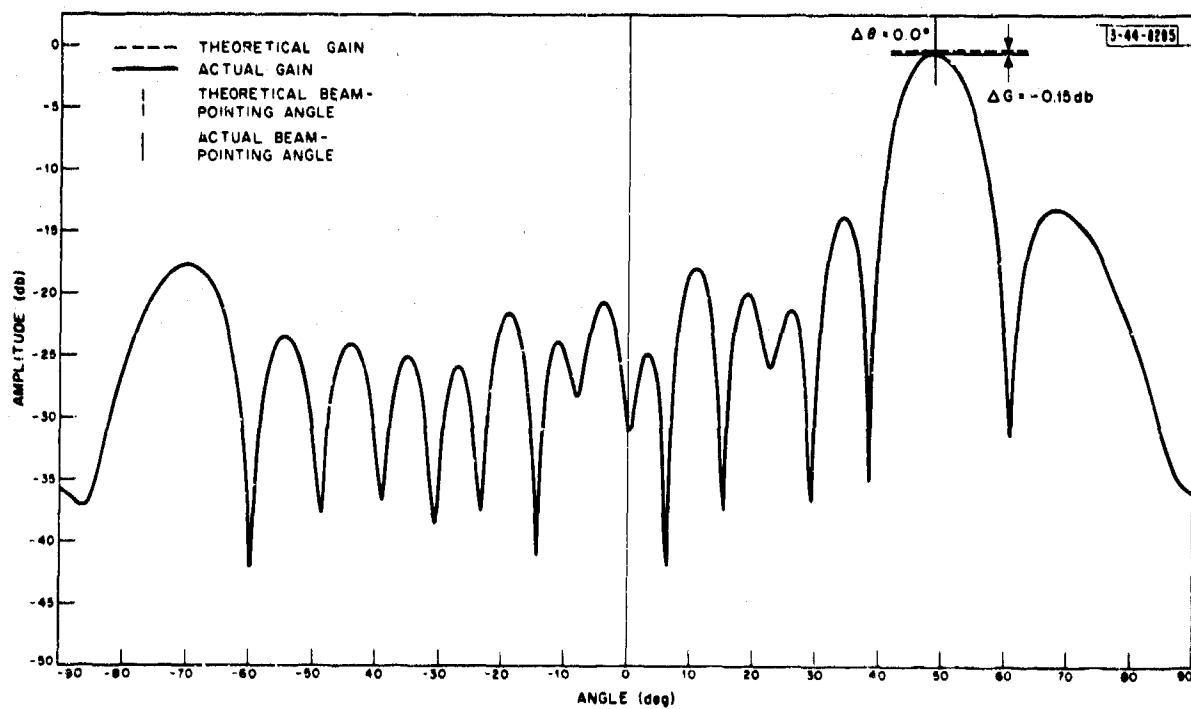


(a) Beam 6.

Fig. III-23. Beams 6, 9, and 15 for 16-element beam former using values of  $C_{ij}$  and  $a_{ij}$  that have been quantized into 10-percent steps from the ideal values:  $f = f_0$ ,  $s = \lambda_0/2$ , efficiency = 16/17.



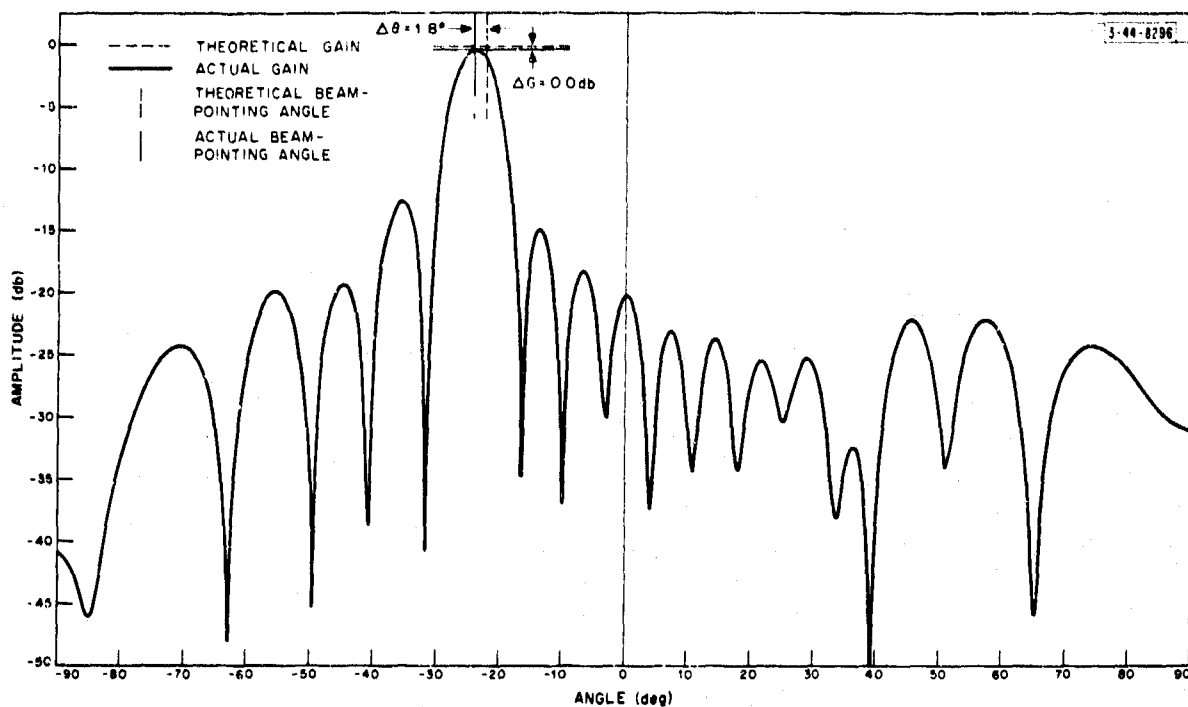
(b) Beam 9.



(c) Beam 15.

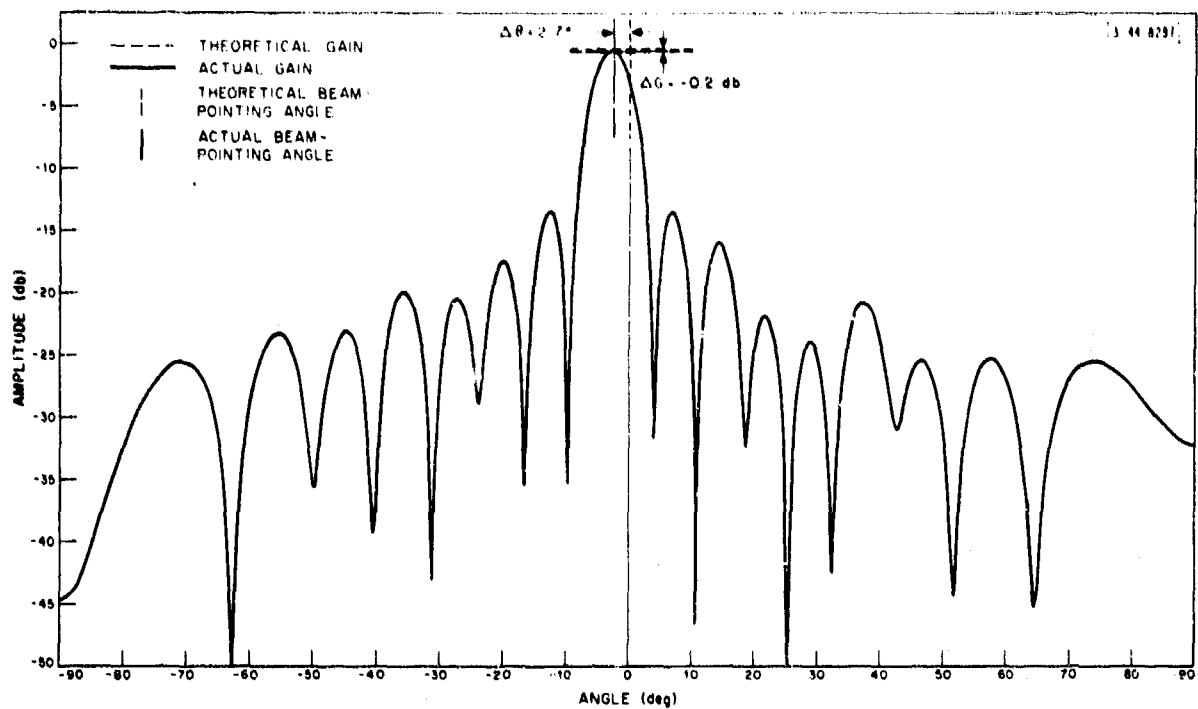
Fig. III-23. Continued.



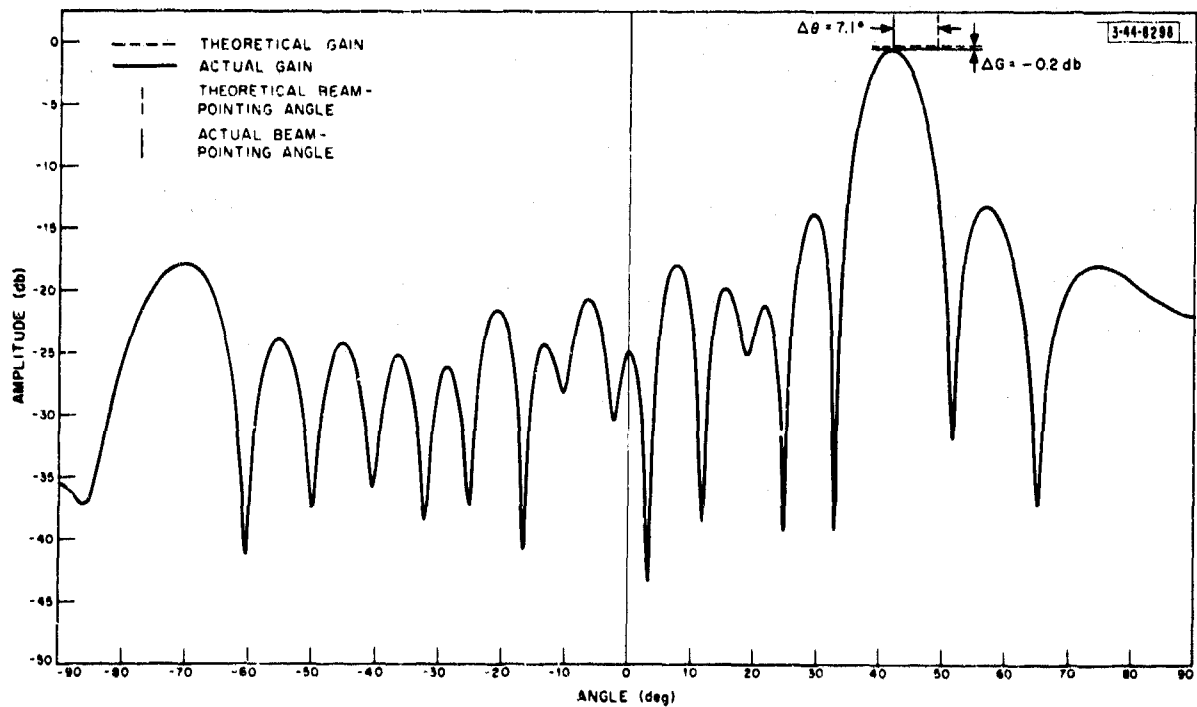


(a) Beam 6.

Fig. III-24. Beams 6, 9, and 15 for 16-element beam former using values of  $C_{ij}$  and  $a_{ij}$  that have been quantized into 10-percent steps from the ideal values:  $f = 1.05 f_0$ ,  $s = \lambda_0/2$ , efficiency = 16/17.

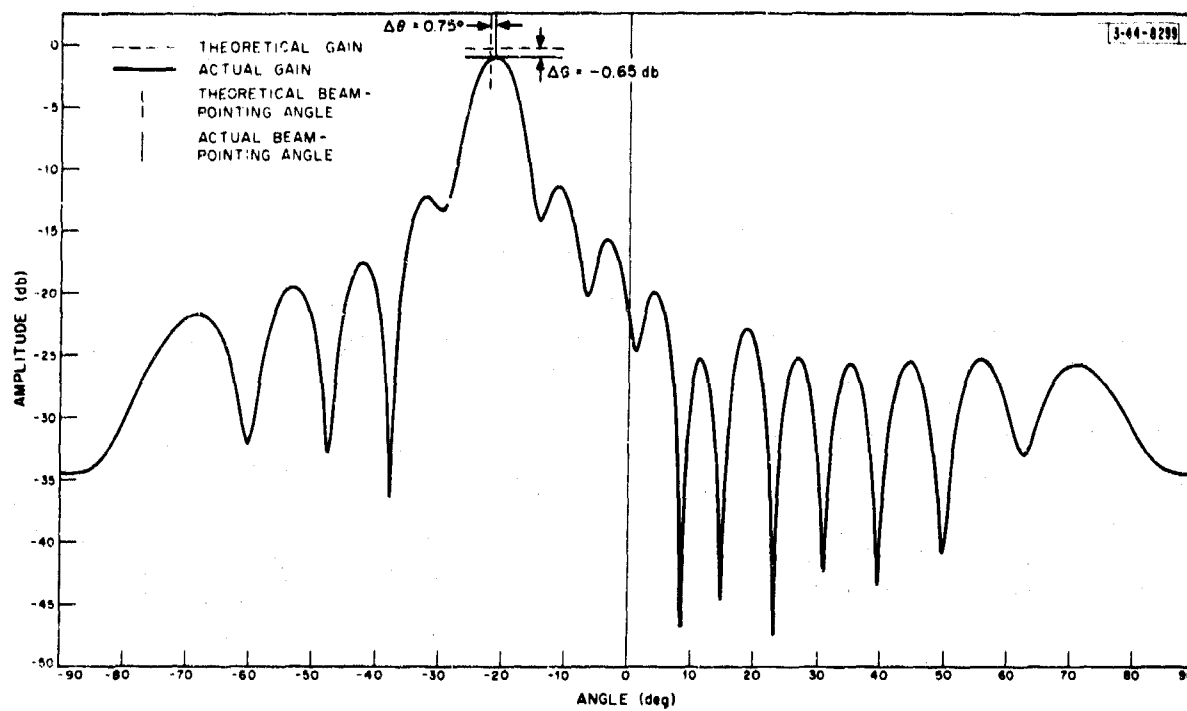


(b) Beam 9.



(c) Beam 15.

Fig. III-24. Continued.



(a) Beam 6.

Fig. III-25. Beams 6, 9, and 15 for 16-element beam former using correct values of  $C_{ij}$  and all  $a_{ij} = 0$ ,  $f = f_o$ ,  $s = \lambda_o/2$ , efficiency = 16/17.

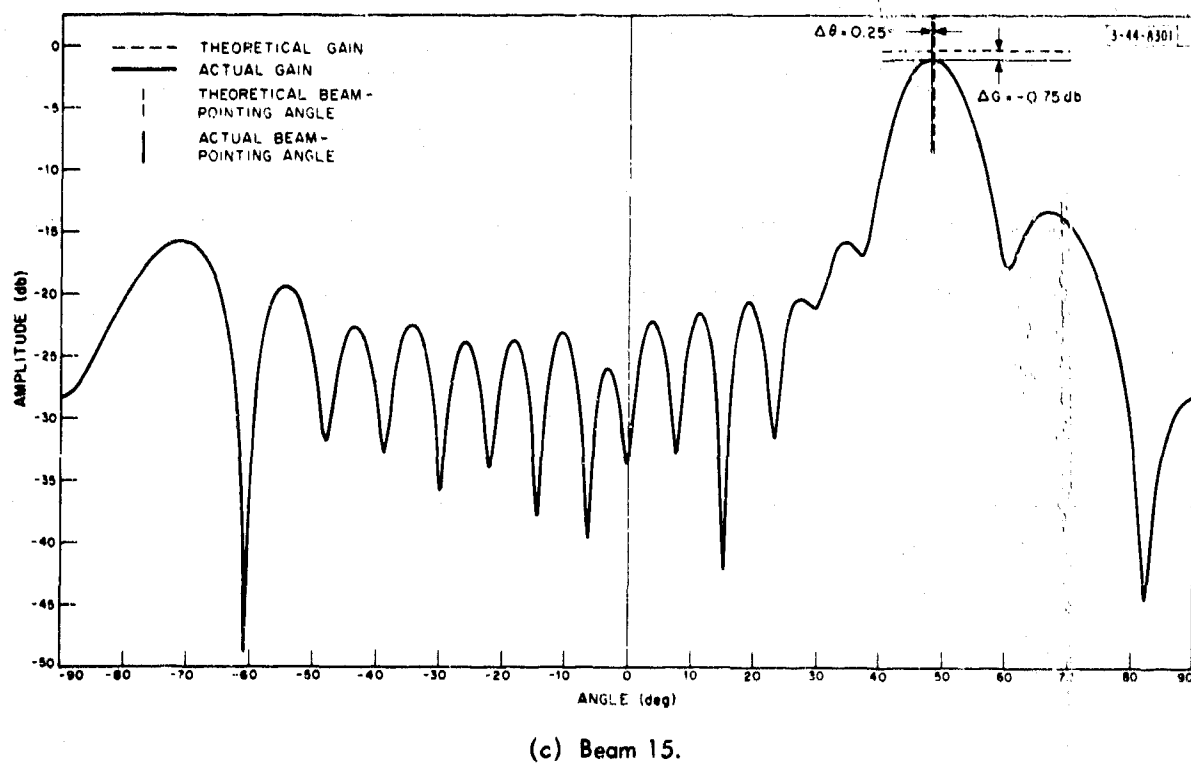
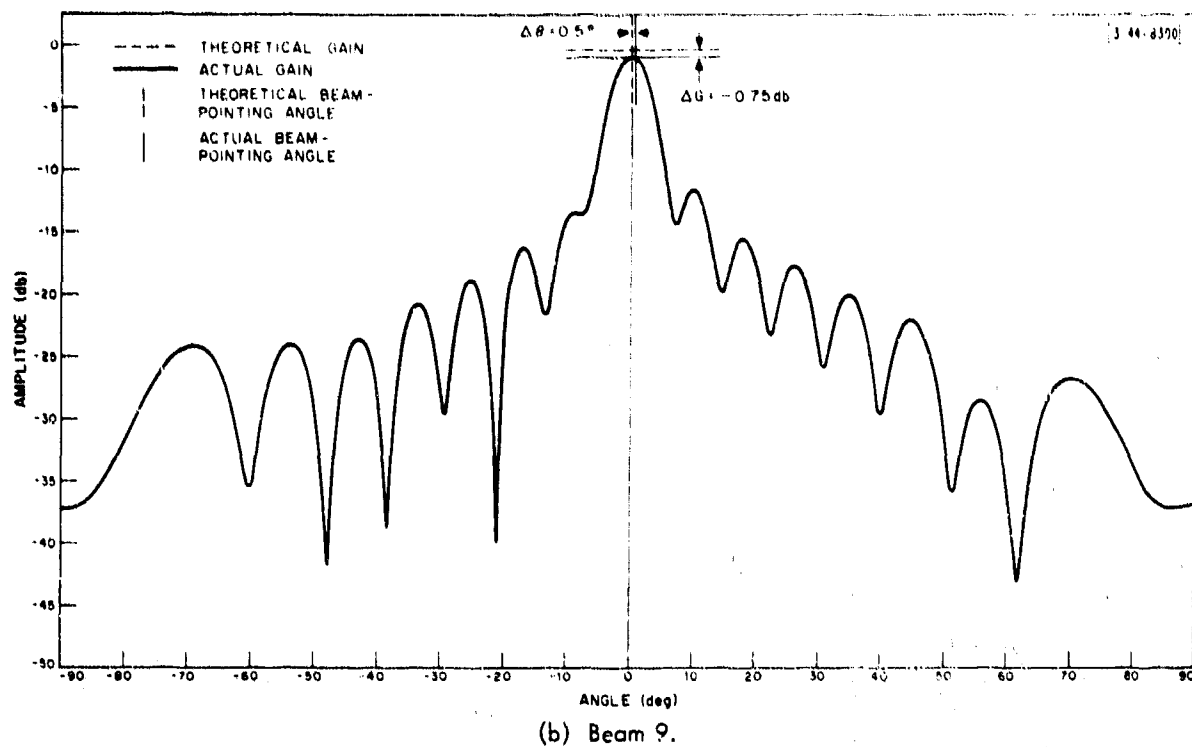
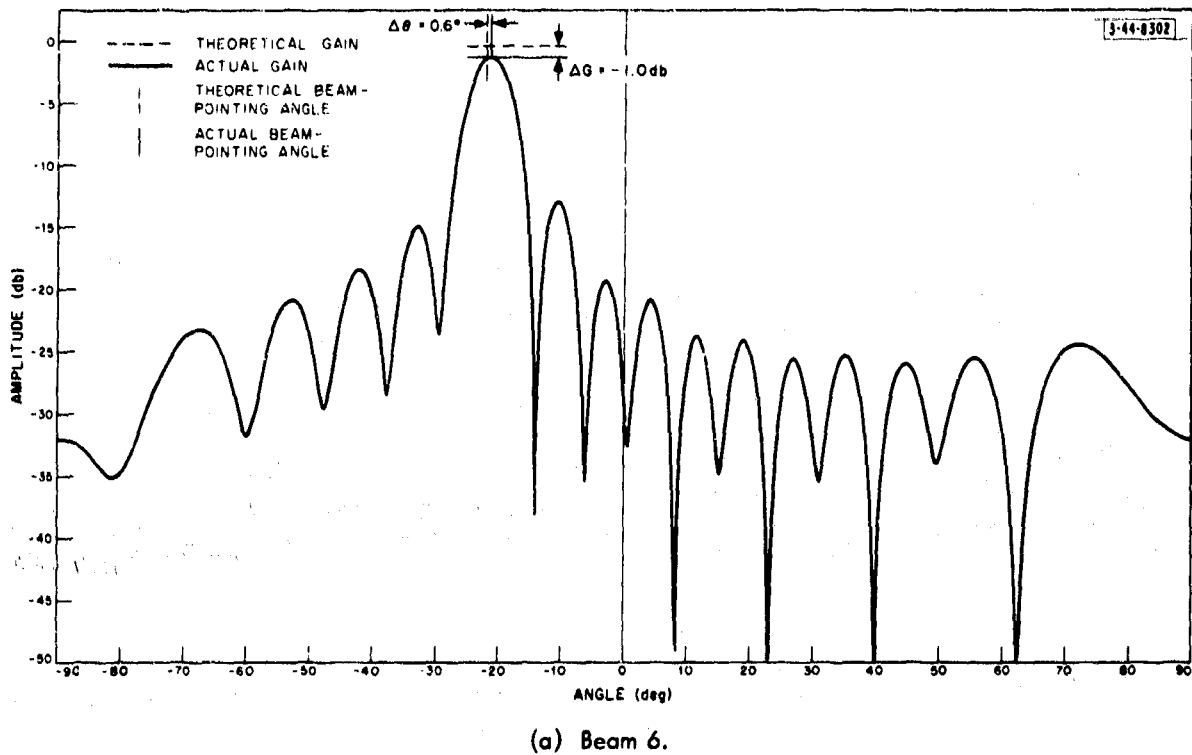
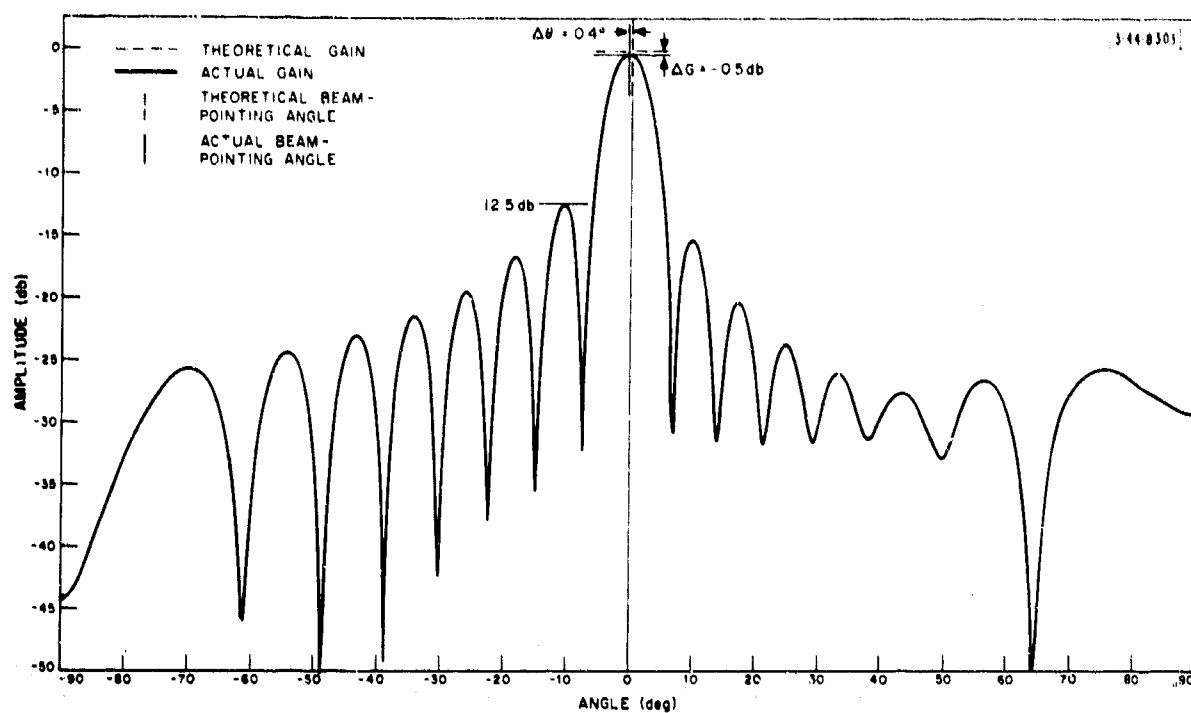


Fig. III-25. Continued.

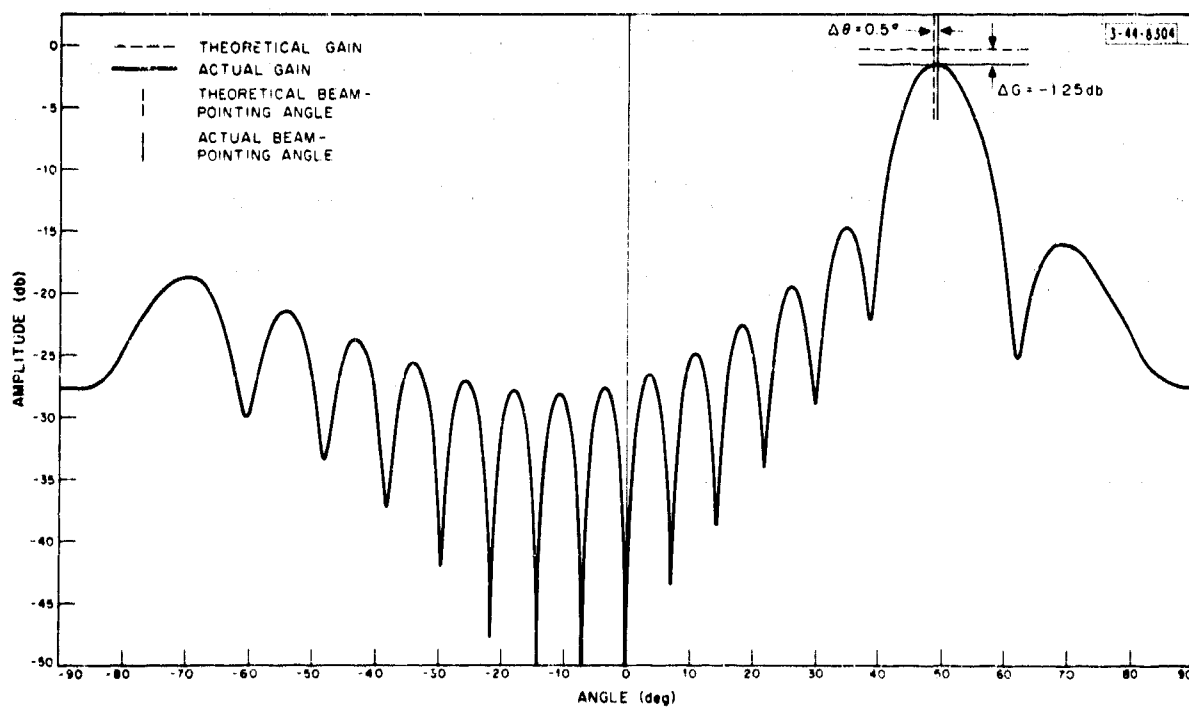


(a) Beam 6.

Fig. III-26. Beams 6, 9, and 15 for 16-element beam former using  $C_{ij} = 1/\sqrt{N+2-j}$  for all  $i$  and all  $a_{ij} = 0$ ,  $f = 1.05 f_o$ ,  $s = \lambda_o/2$ , efficiency = 16/17.

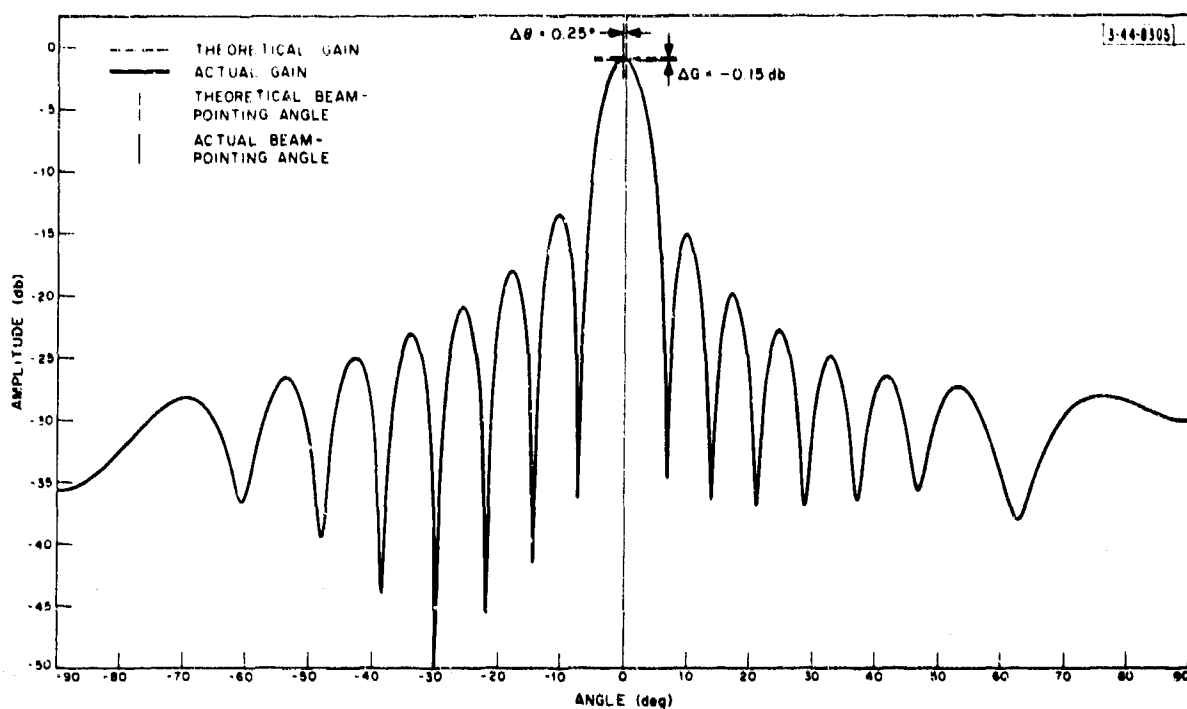


(b) Beam 9.

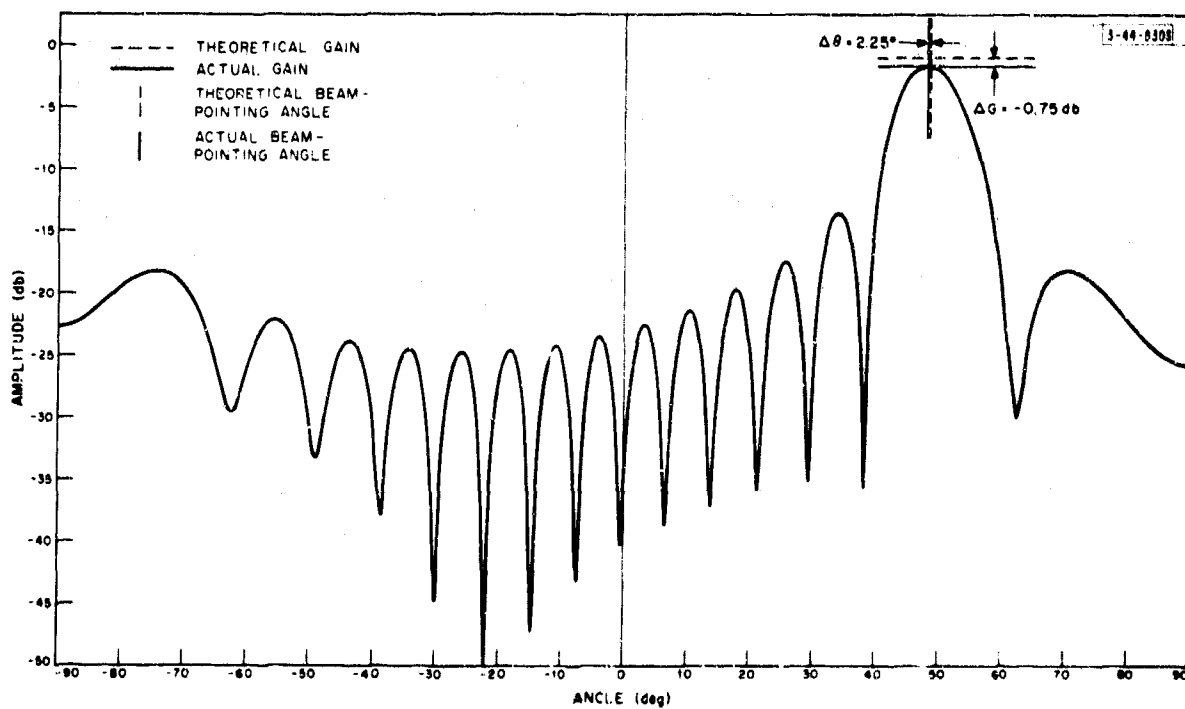


(c) Beam 15.

Fig. III-26. Continued.

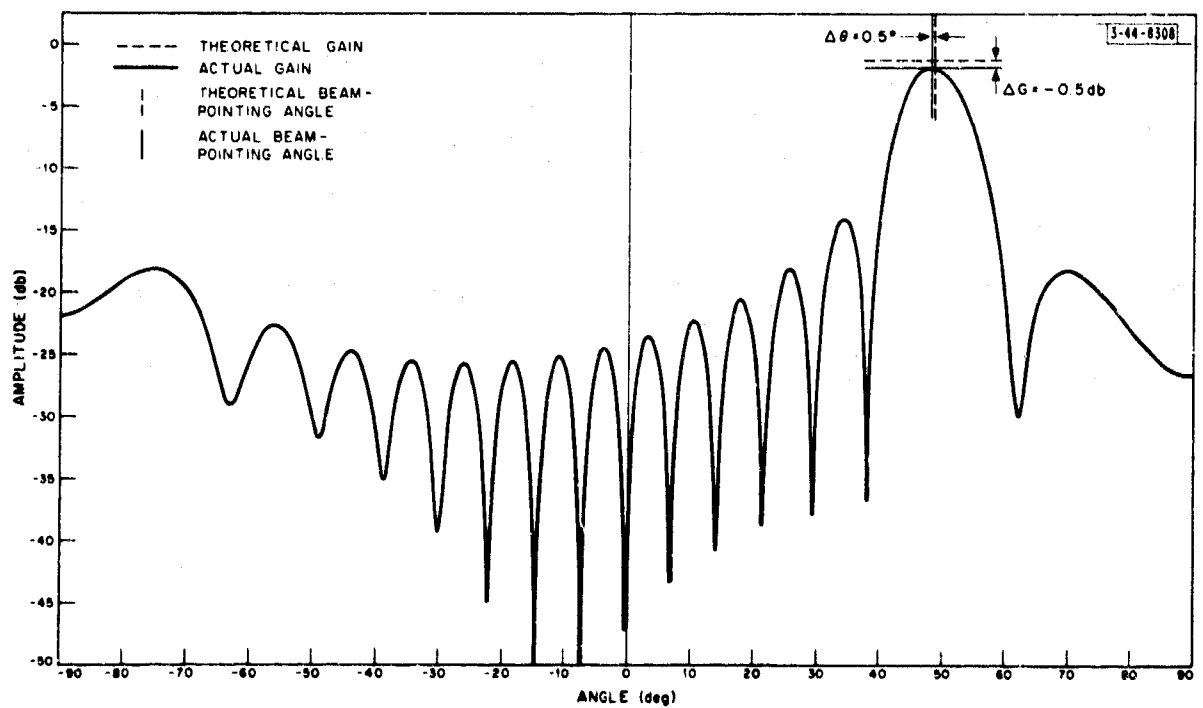
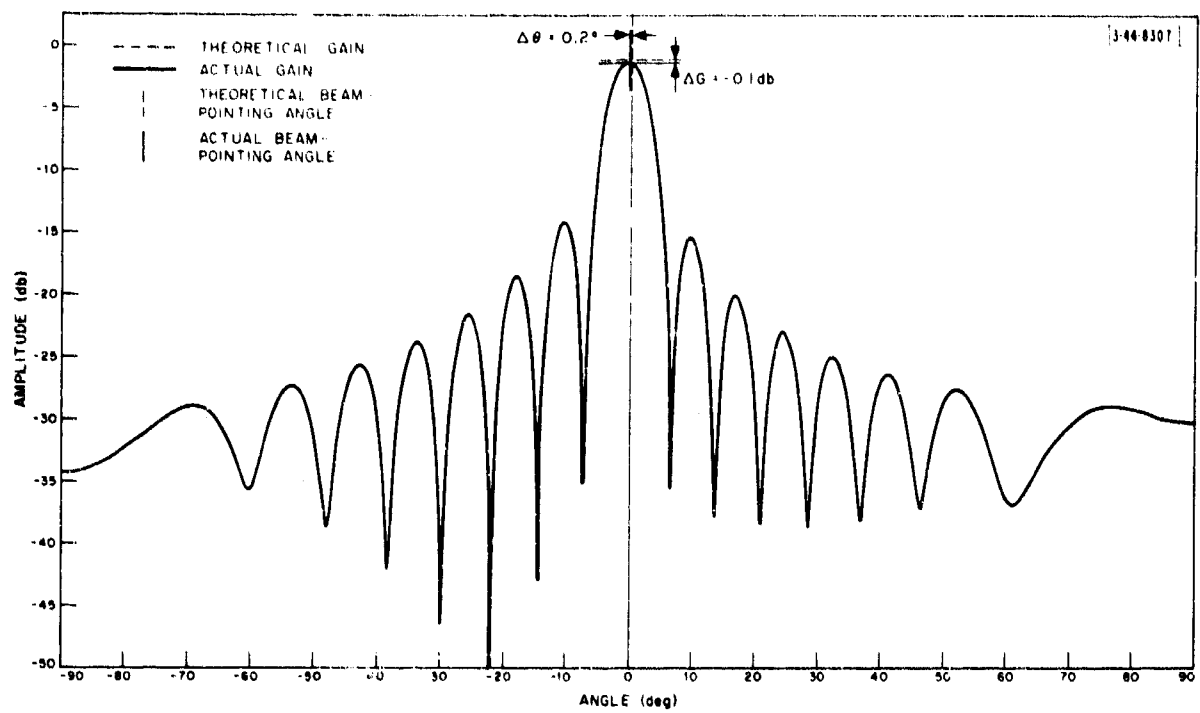


(a) Beam 9.



(b) Beam 15.

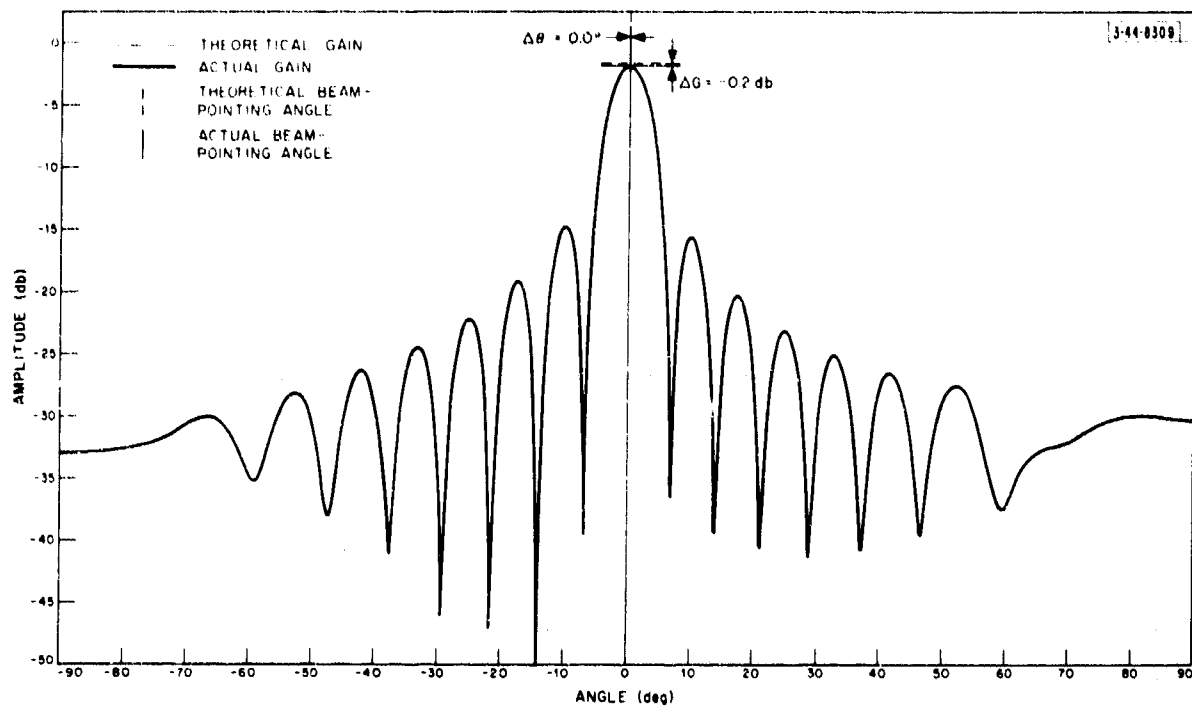
Fig. III-27. Beams 9 and 15 of 16-element beam former using correct values of  $C_{ij}$  and  $a_{ij}$  for 80-percent efficiency with  $f = 1.05 f_0$  and  $s = \lambda_0/2$ .



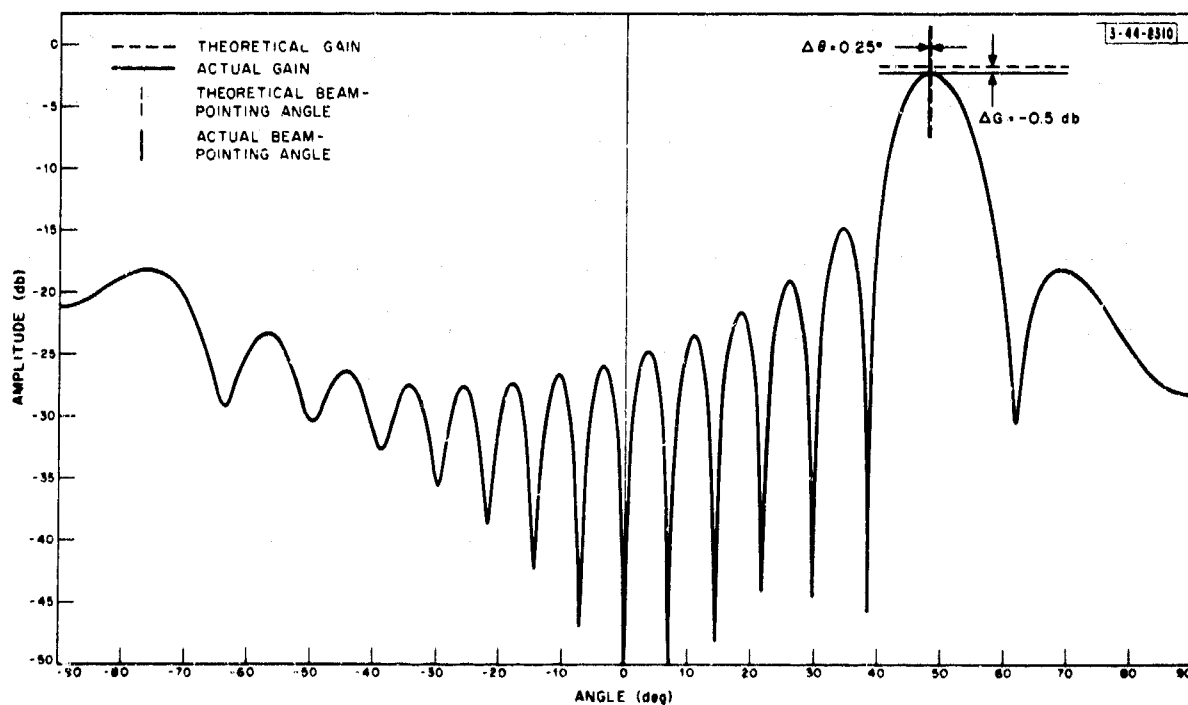
(b) Beam 15.

Fig. III-28. Beams 9 and 15 of 16-element beam former using correct values of  $C_{ij}$  and  $a_{ij}$  for 75-percent efficiency with  $f = 1.05 f_0$  and  $s = \lambda_0/2$ .



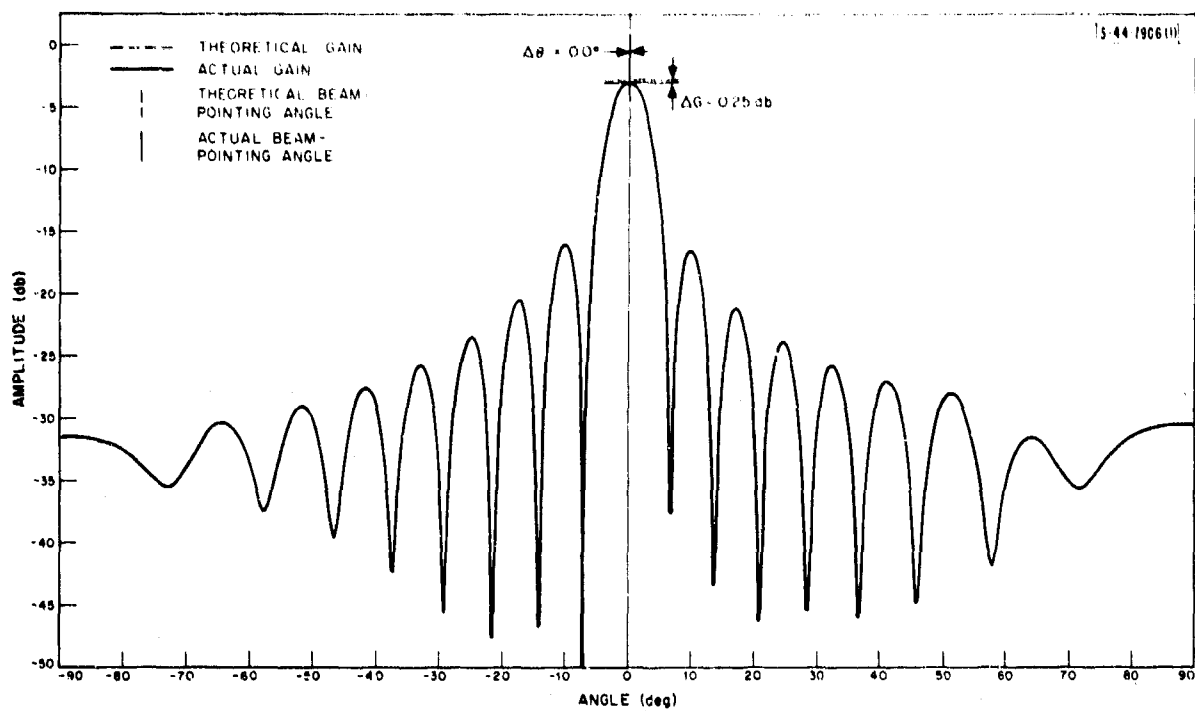


(a) Beam 9.

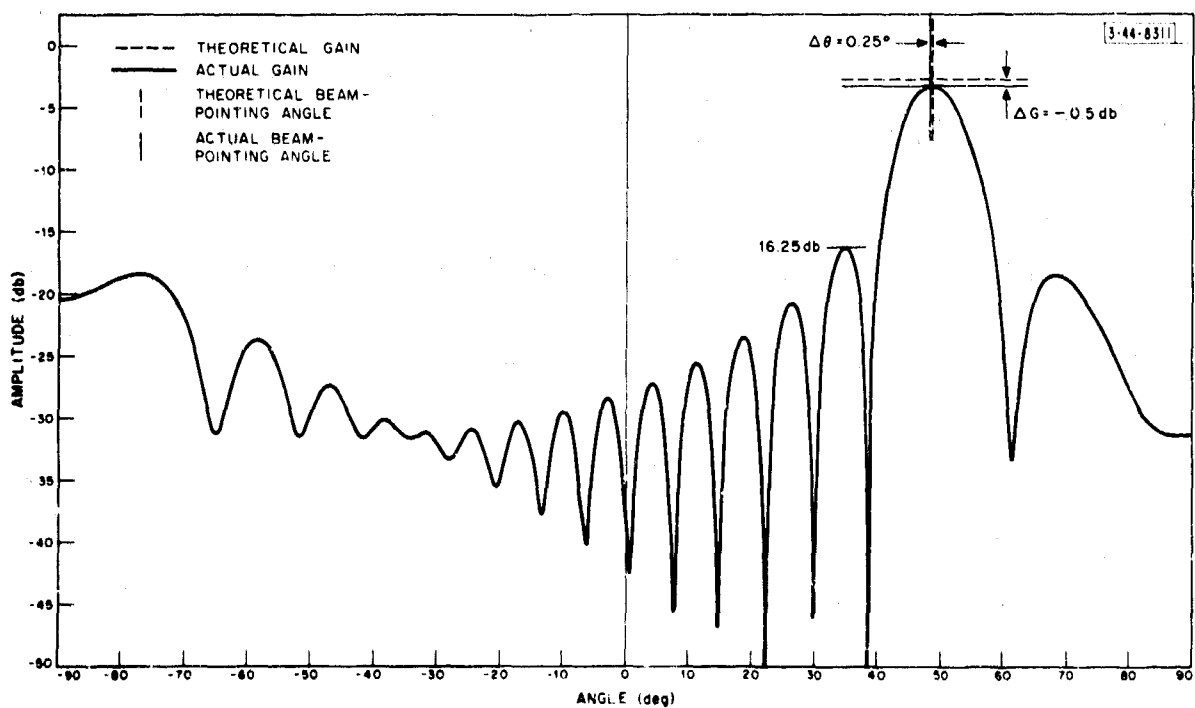


(b) Beam 15.

Fig. III-29. Beams 9 and 15 of 16-element beam former using correct values of  $C_{ij}$  and  $a_{ij}$  for 67-percent efficiency with  $f = 1.05 f_0$  and  $s = \lambda_0/2$ .

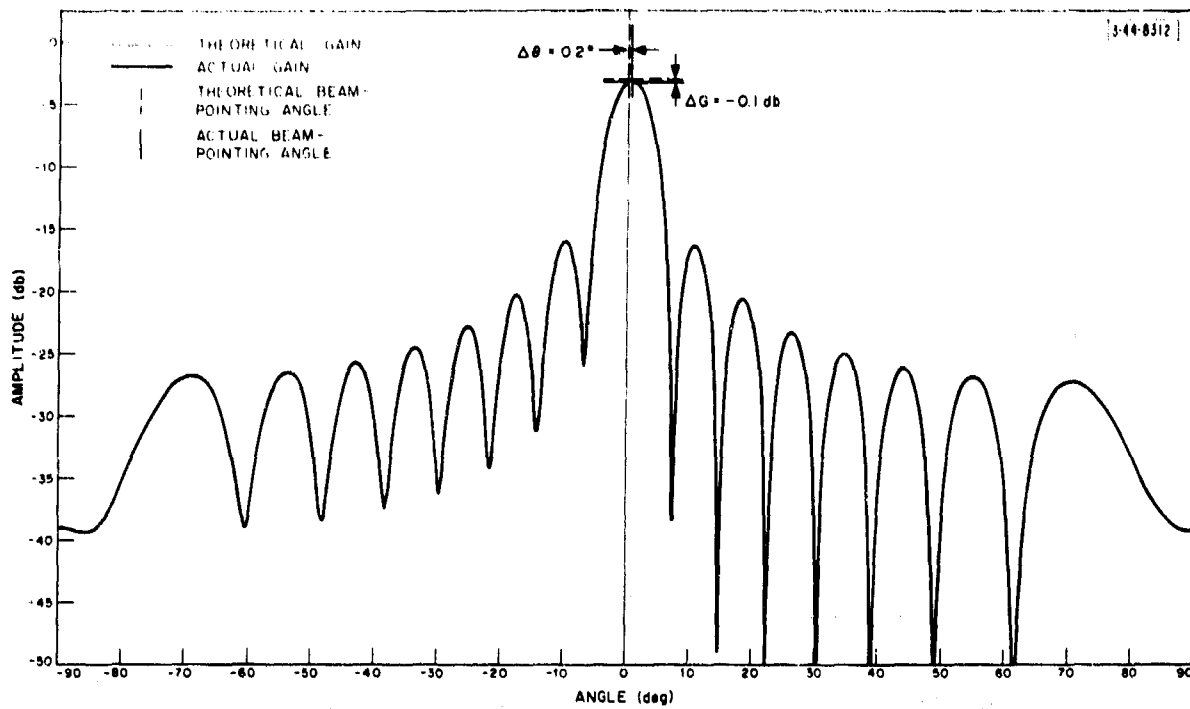


(a) Beam 9.

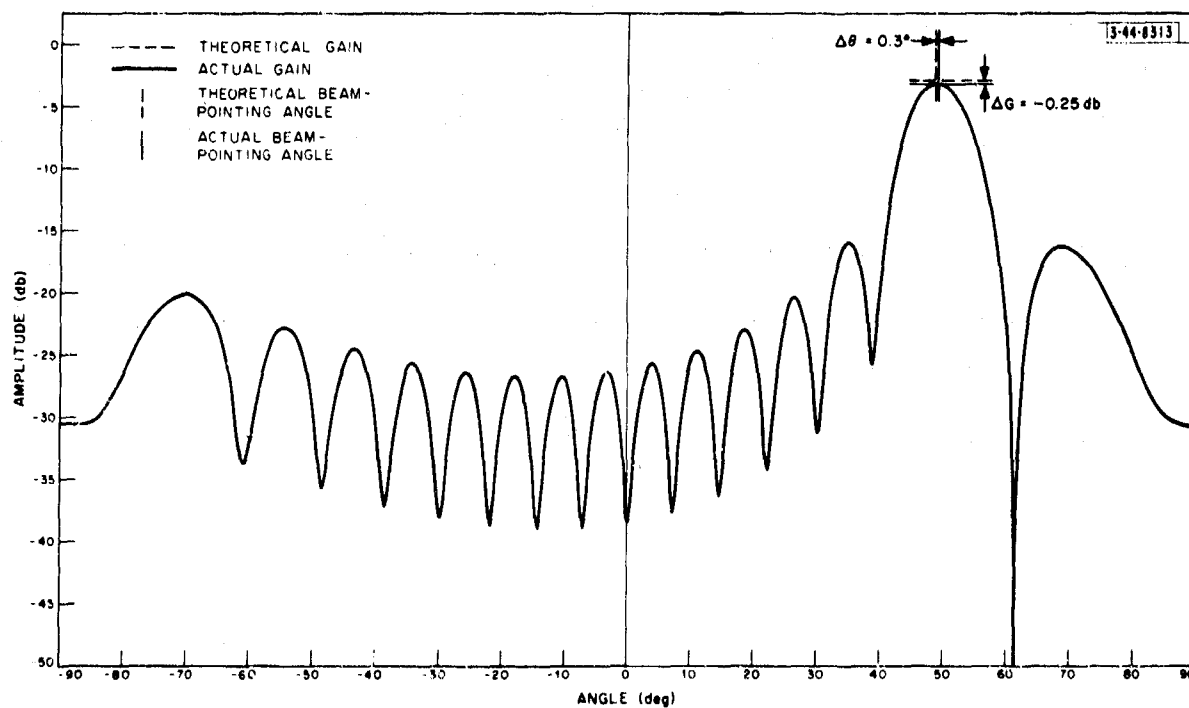


(b) Beam 15.

Fig. III-30. Beams 9 and 15 of 16-element beam former using correct values of  $C_{ij}$  and  $a_{ij}$  for 50-percent efficiency with  $f = 1.05 f_0$  and  $s = \lambda_0/2$ .

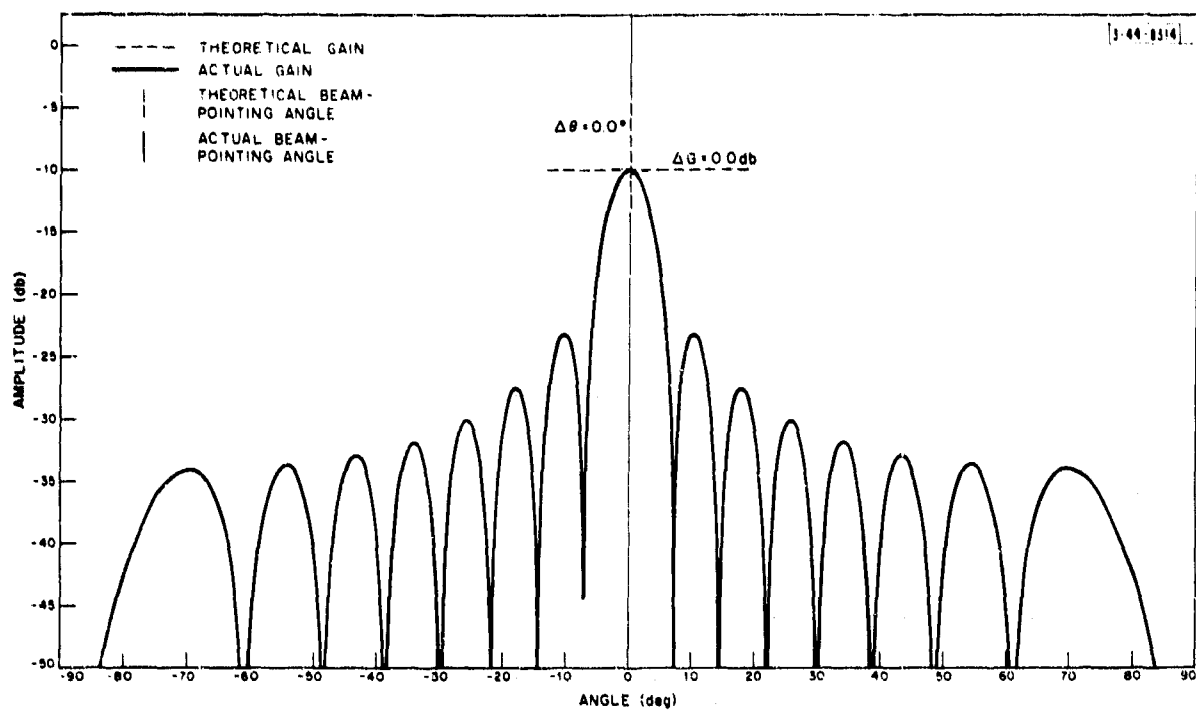


(a) Beam 9.

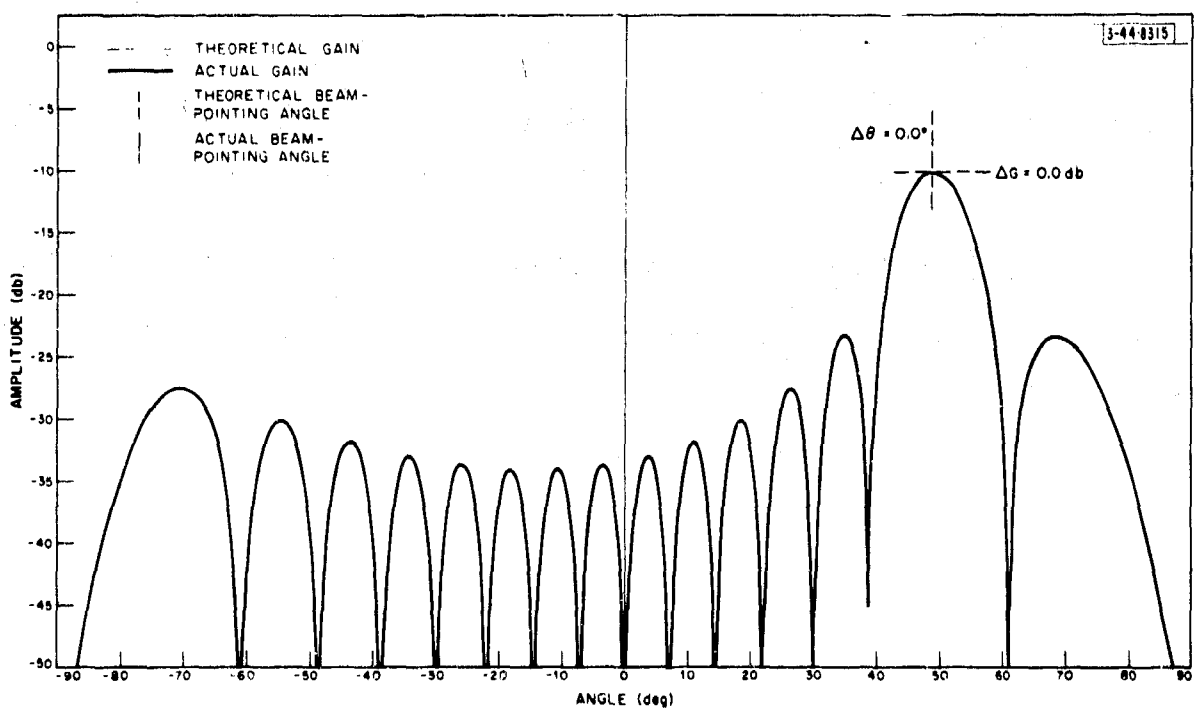


(b) Beam 15.

Fig. III-31. Beams 9 and 15 for 16-element beam former using  $C_{ij} = 1/\sqrt{N+2-j}$  and  $a_{ij} = 0$  for all  $i, j$  for 50-percent efficiency with  $f = f_0$  and  $s = \lambda_0/2$ .

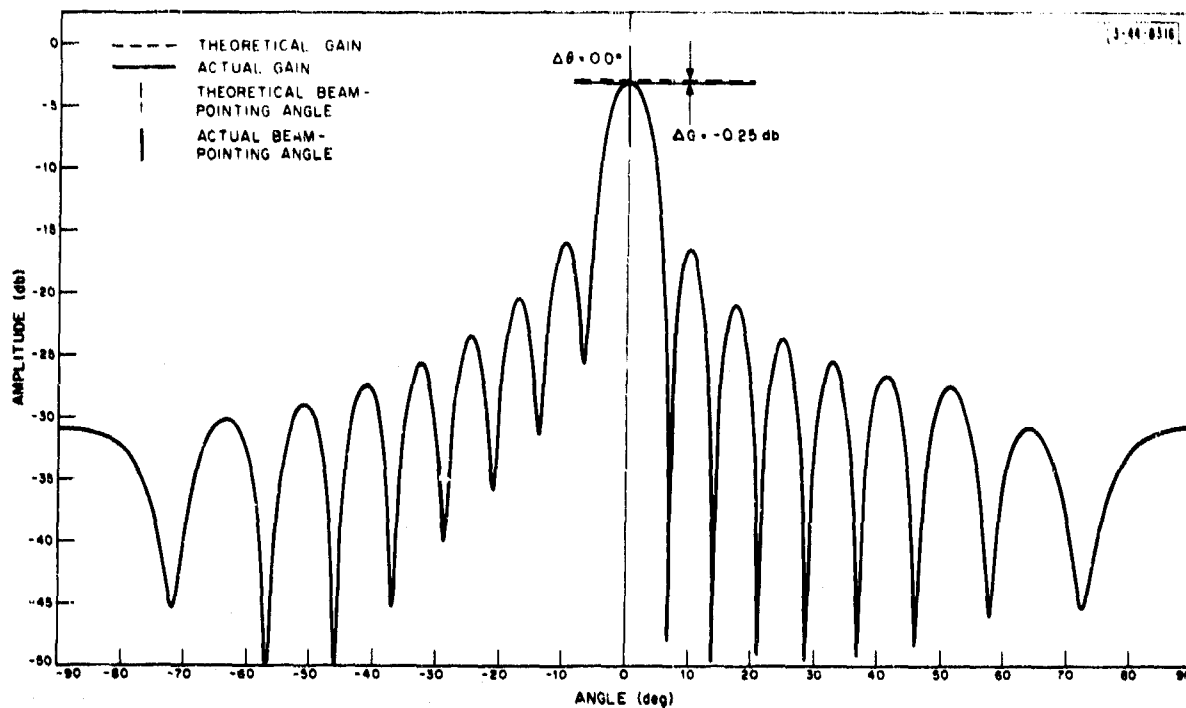


(a) Beam 9.

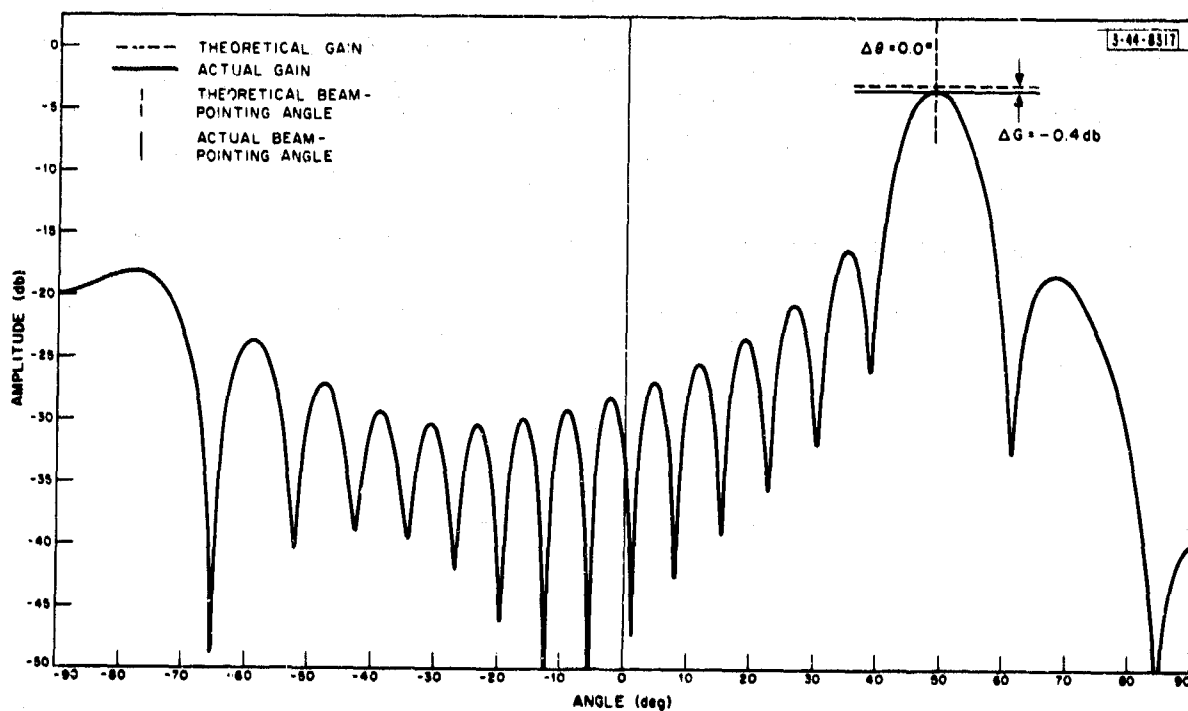


(b) Beam 15.

Fig. III-32. Beams 9 and 15 for 16-element beam former using  $C_{ij} = 1/\sqrt{N+2-j}$  and  $a_{ij} = 0$  for all  $i, j$  for 10-percent efficiency with  $f = f_0$  and  $s = \lambda_0/2$ .

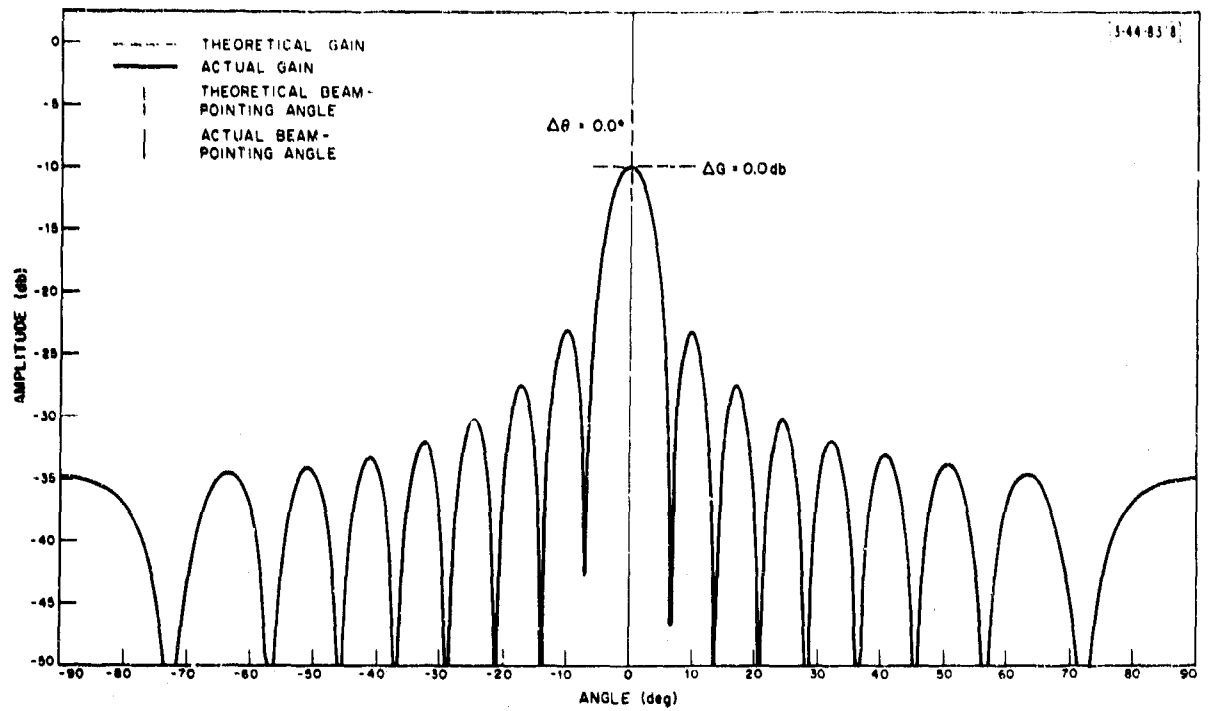


(a) Beam 9.

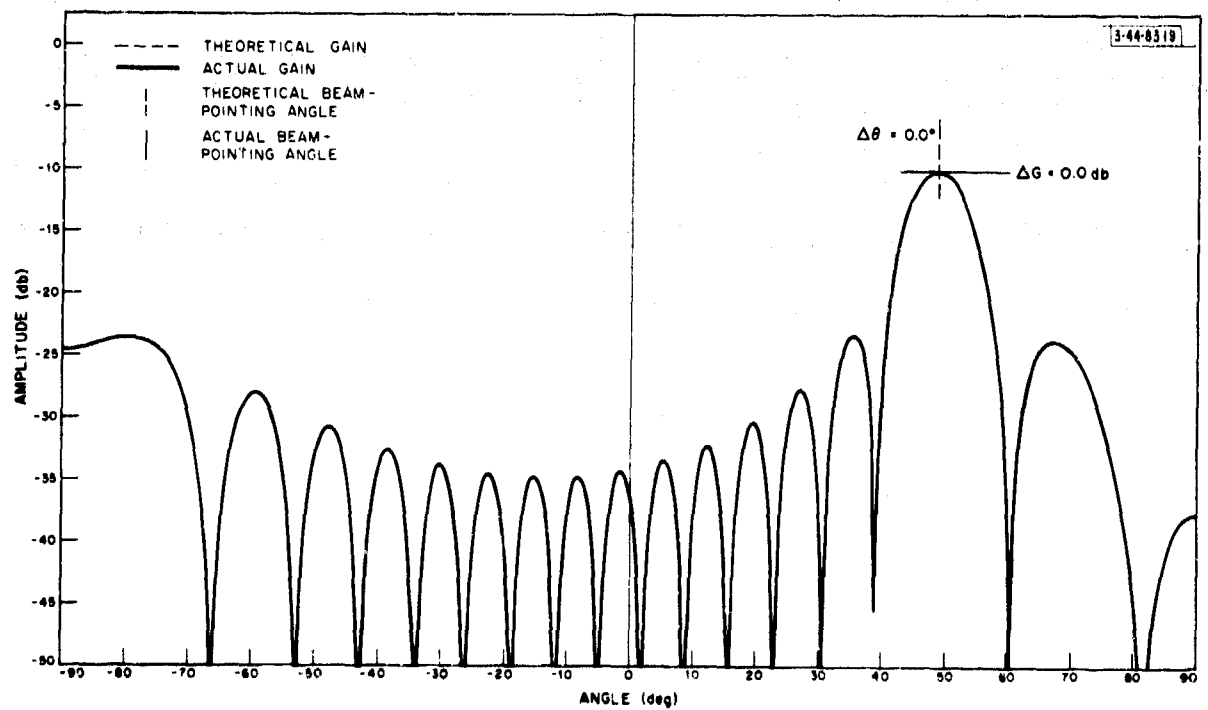


(b) Beam 15.

Fig. III-33. Beams 9 and 15 for 16-element beam former using  $C_{ij} = 1/\sqrt{N+2-i}$  and  $a_{ij} = 0$ , all  $ij$ , for 50-percent efficiency with  $f = 1.05 f_0$  and  $s = \lambda_0/2$ .

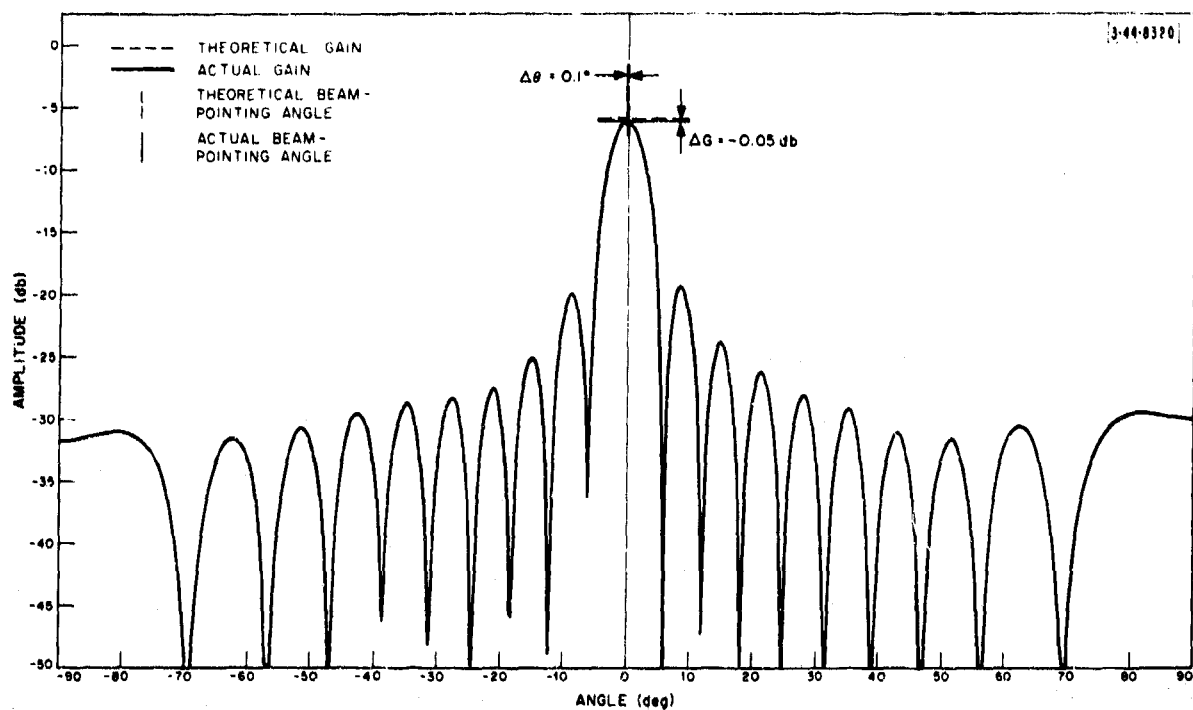


(a) Beam 9.

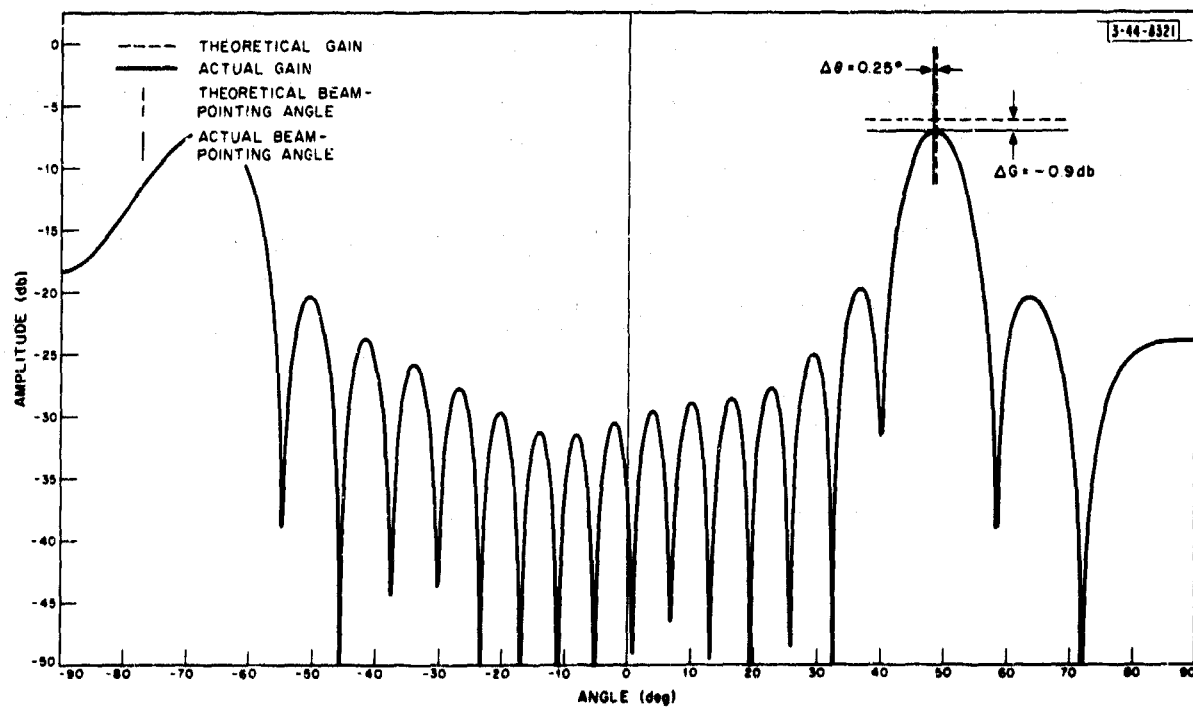


(b) Beam 15.

Fig. III-34. Beams 9 and 15 for 16-element beam former using  $C_{ij} = 1/\sqrt{N+2-j}$  and  $a_{ij} = 0$ , all  $i, j$ , for 10-percent efficiency with  $f = 1.05 f_0$  and  $s = \lambda_0/2$ .

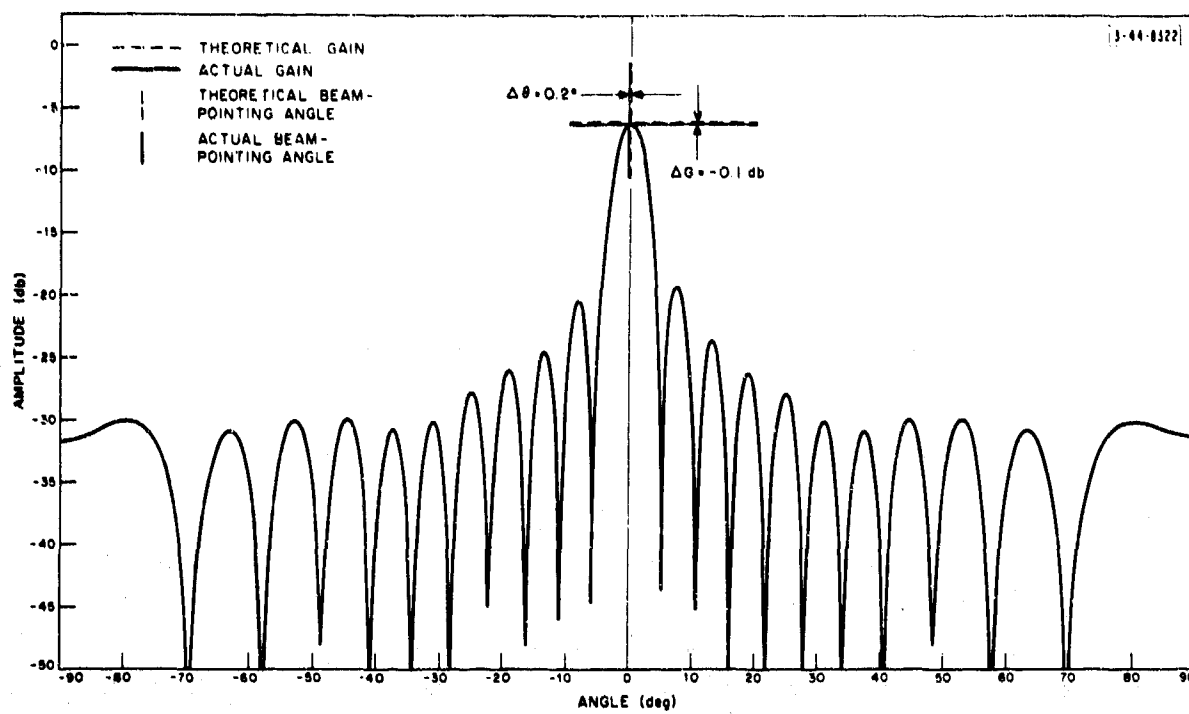


(a) Beam 9.

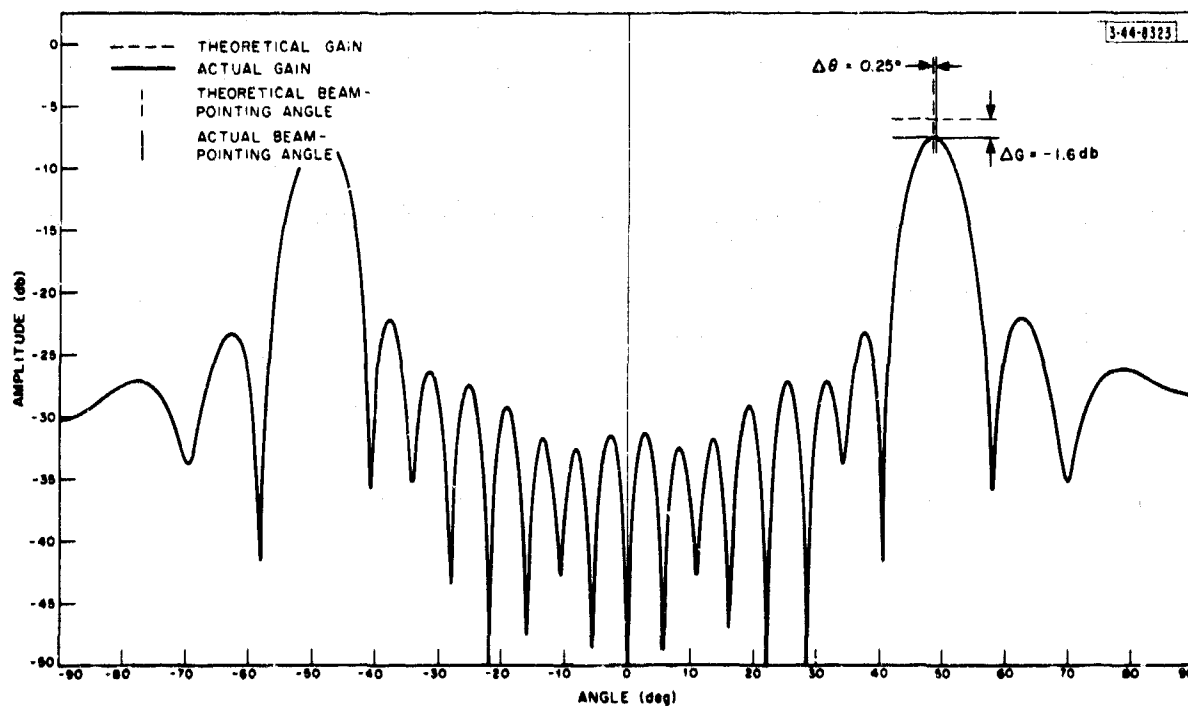


(b) Beam 15.

Fig. III-35. Beams 9 and 15 for 16-element beam former using  $C_{ij} = 1/\sqrt{N+2-j}$  and  $a_{ij} = 0$ , all  $ij$ , for 25-percent efficiency with  $f = 1.2 f_0$  and  $s = \lambda_0/2$ .



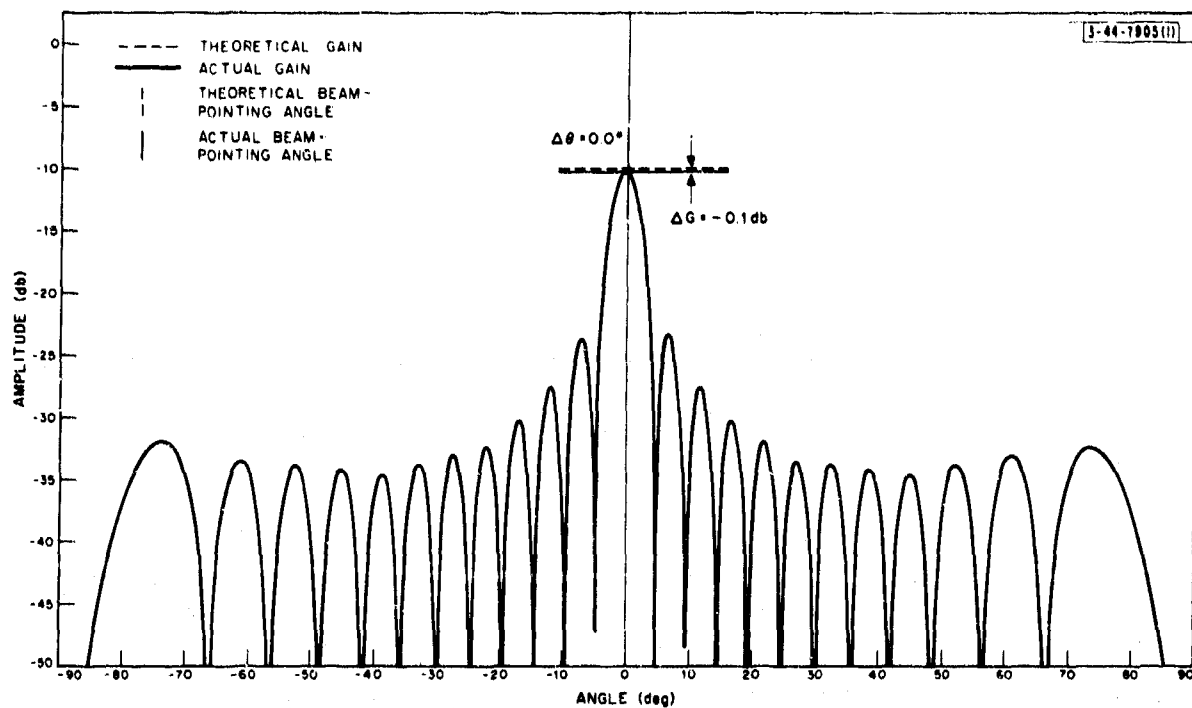
(a) Beam 9.



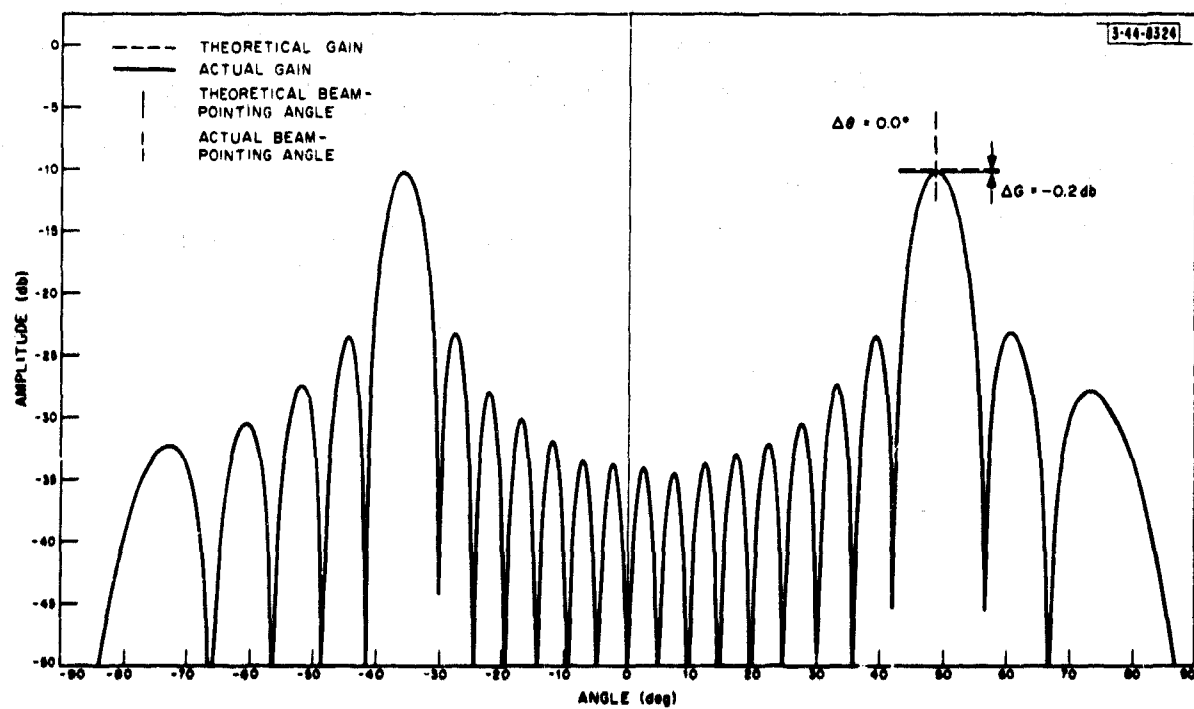
(b) Beam 15.

Fig. III-36. Beams 9 and 15 for 16-element beam former using  $C_{ij} = 1/\sqrt{N+2-j}$  and  $a_{ij} = 0$ , all  $ij$ , for 25-percent efficiency with  $f = 1.33 f_0$  and  $s = \lambda_0/2$ .



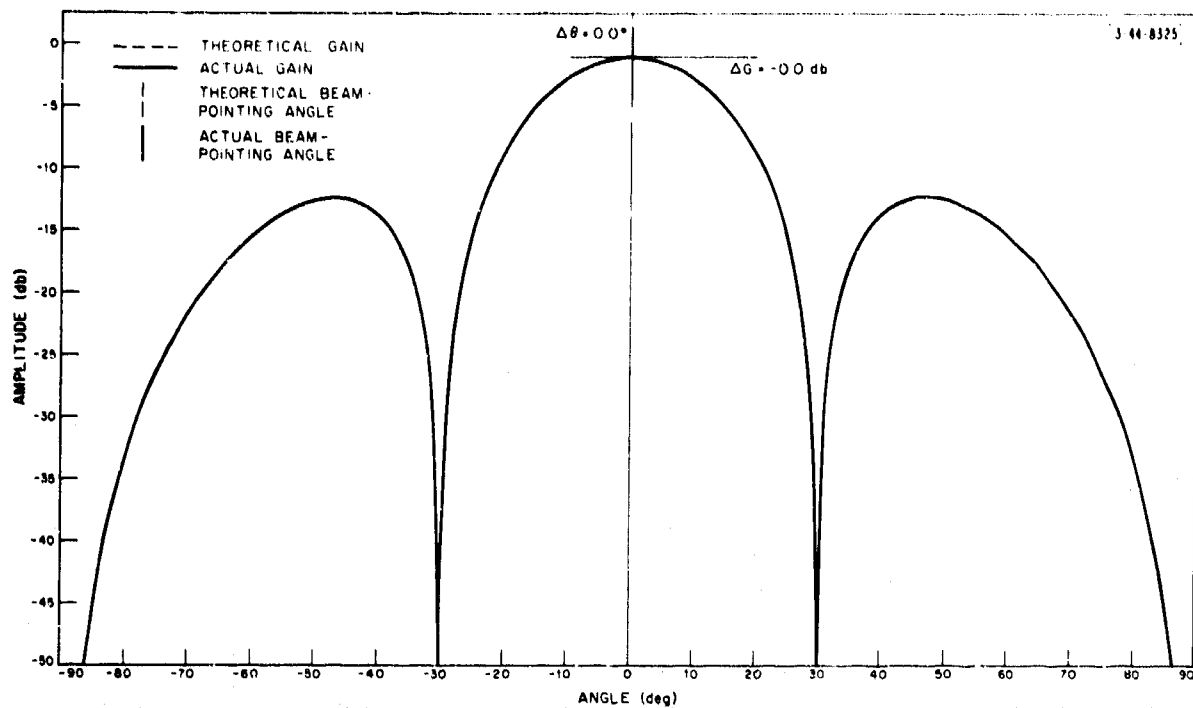


(a) Beam 9.

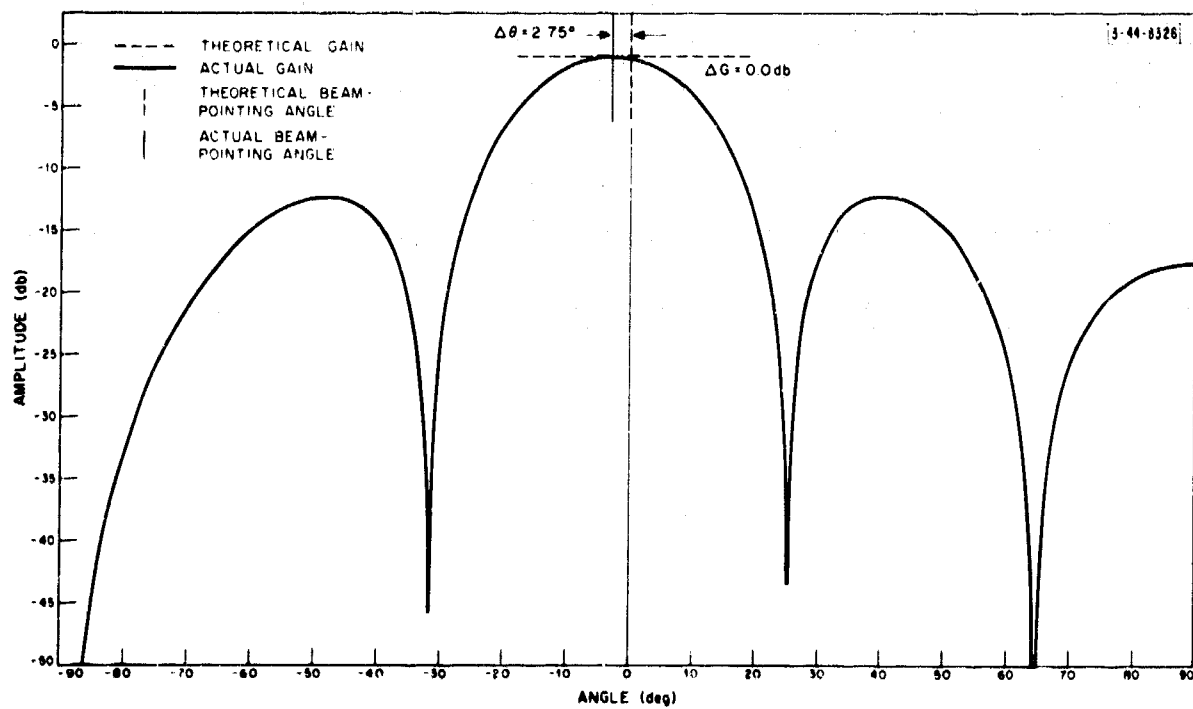


(b) Beam 15.

Fig. III-37. Beams 9 and 15 for 16-element beam former using  $C_{ij} = 1/\sqrt{N+2-i}$  and  $a_{ij} = 0$ , all  $i, j$ , for 10-percent efficiency with  $f = 1.5 f_0$  and  $s = \lambda_0/2$ .

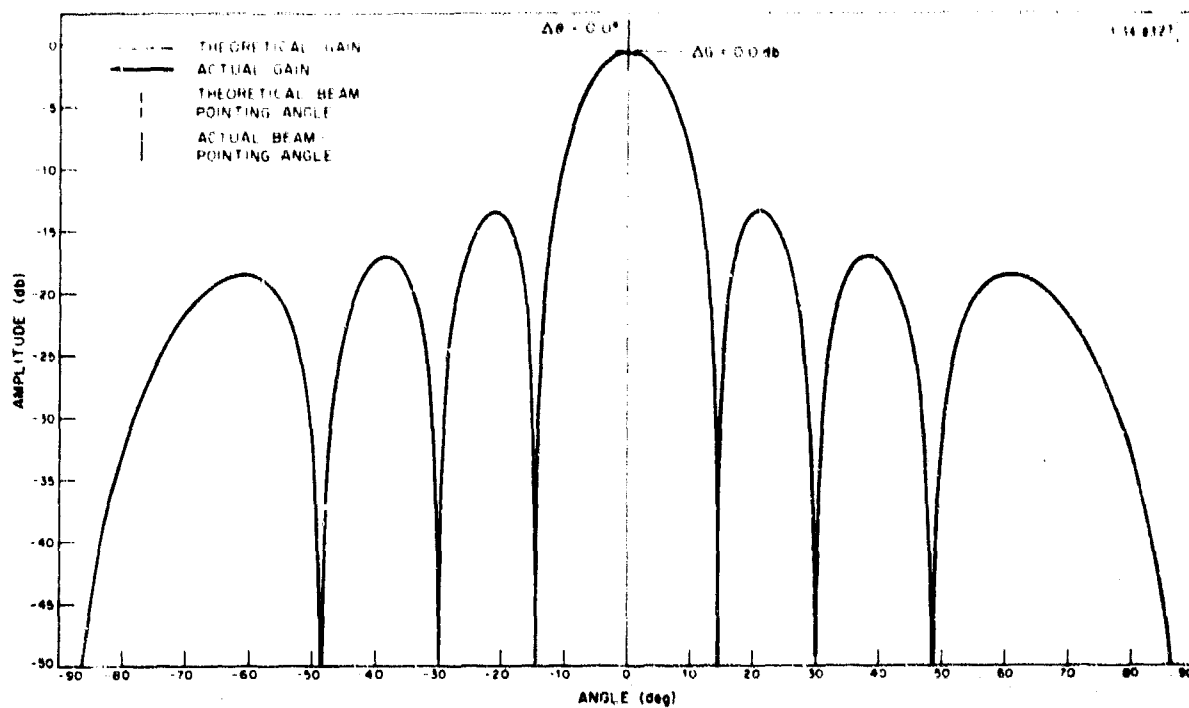


(a) Boresight beam,  $f = f_0$ .

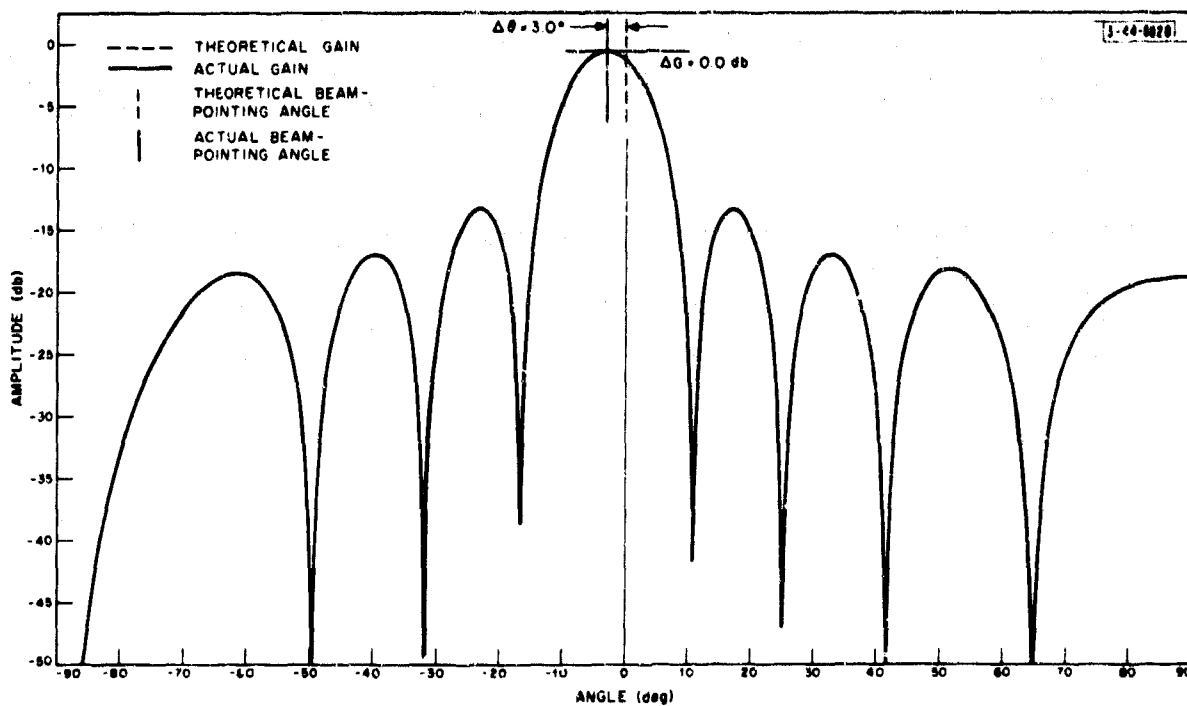


(b) Boresight beam,  $f = 1.05 f_0$ .

Fig. III-38. Boresight beams for 4-element beam former using exact  $C_{ij}$ 's and  $a_{ij}$ 's with  $s = \lambda_0/2$ .

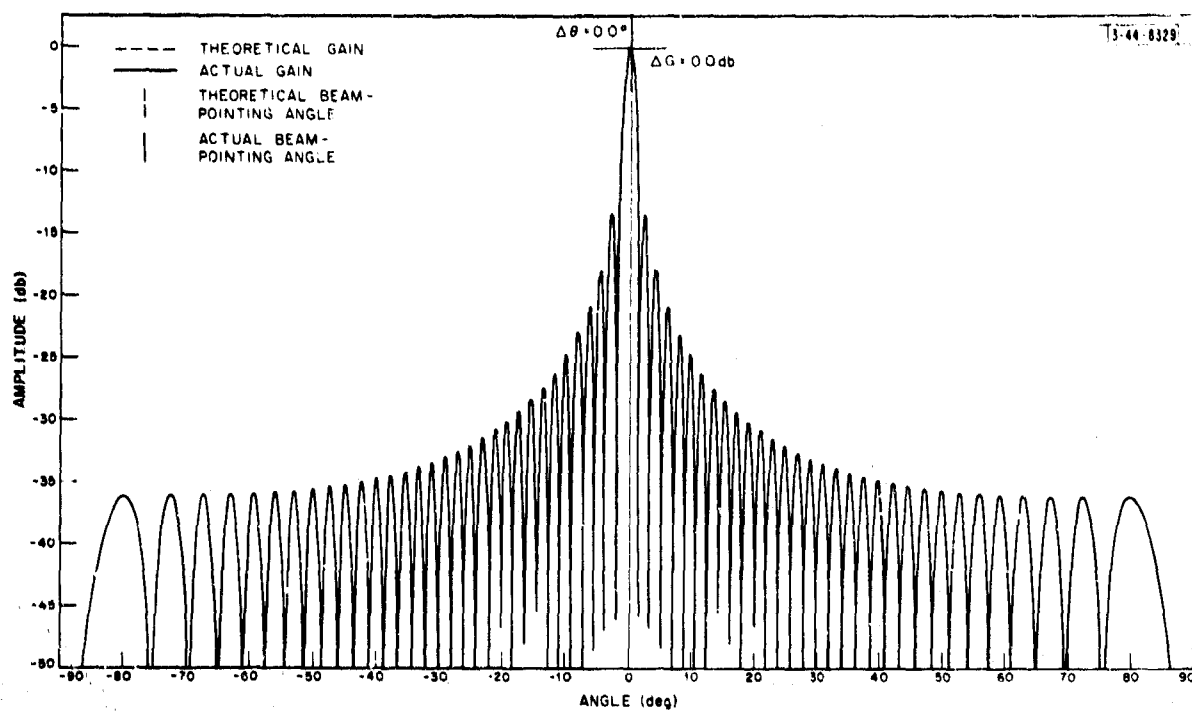


(a) Boresight beam,  $f = f_0$ .



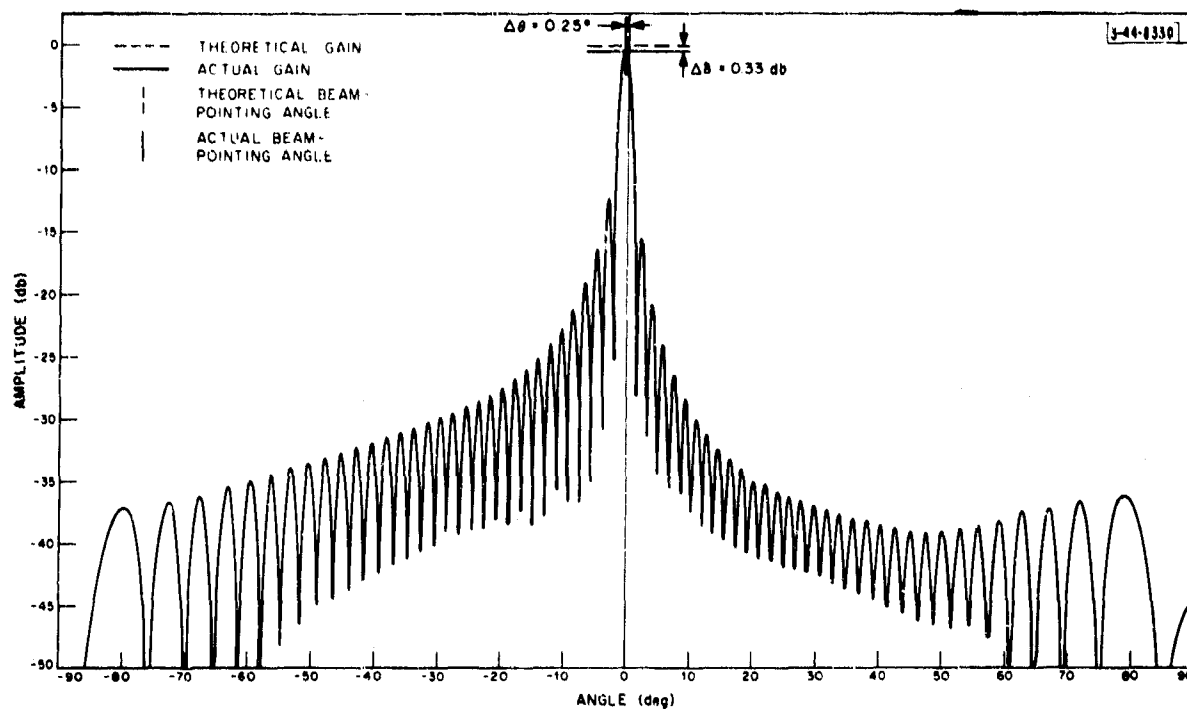
(b) Boresight beam,  $f = 1.05 f_0$ .

Fig. III-39. Boresight beams for 8-element beam former using exact  $C_{ij}$ 's and  $a_{ij}$ 's with  $s = \lambda_0/2$ .

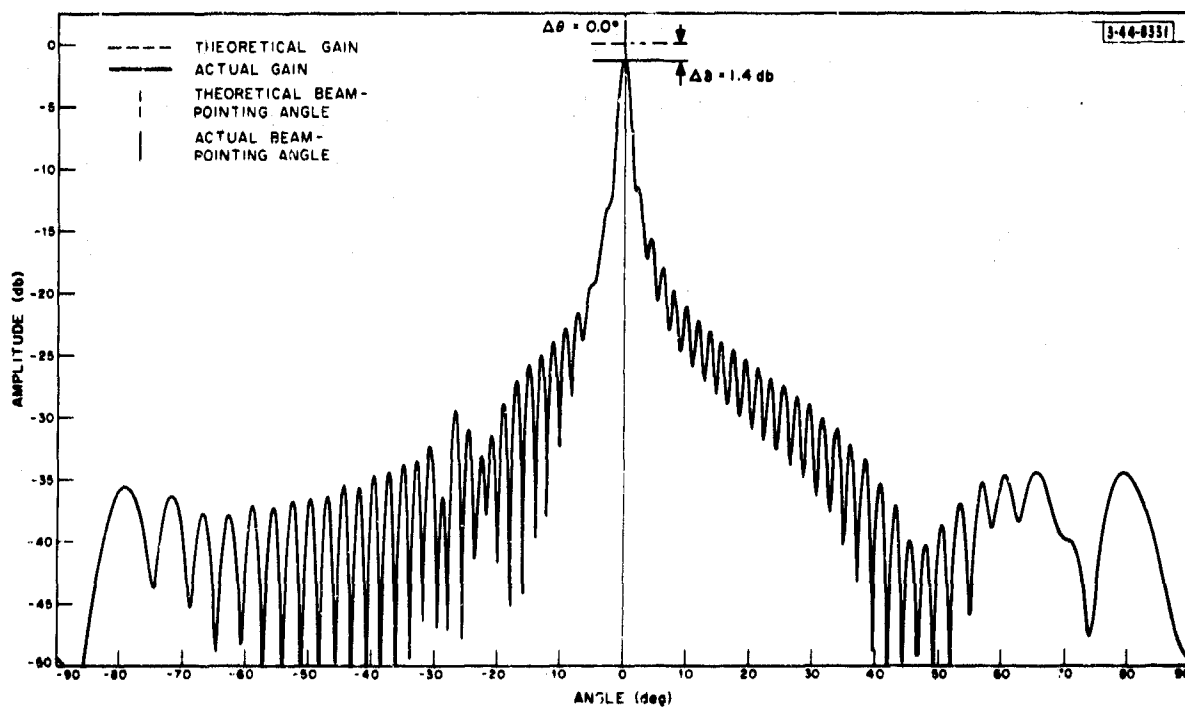


(a) Beam 33,  $f = f_0$ .

Fig. III-40. Boresight beams for 64-element ideally designed beam former,  $s = \lambda_0/2$ . Effect of frequency change is shown in (a) and (b). Effect of having all  $a_{ij} = 0$  is shown in (c).

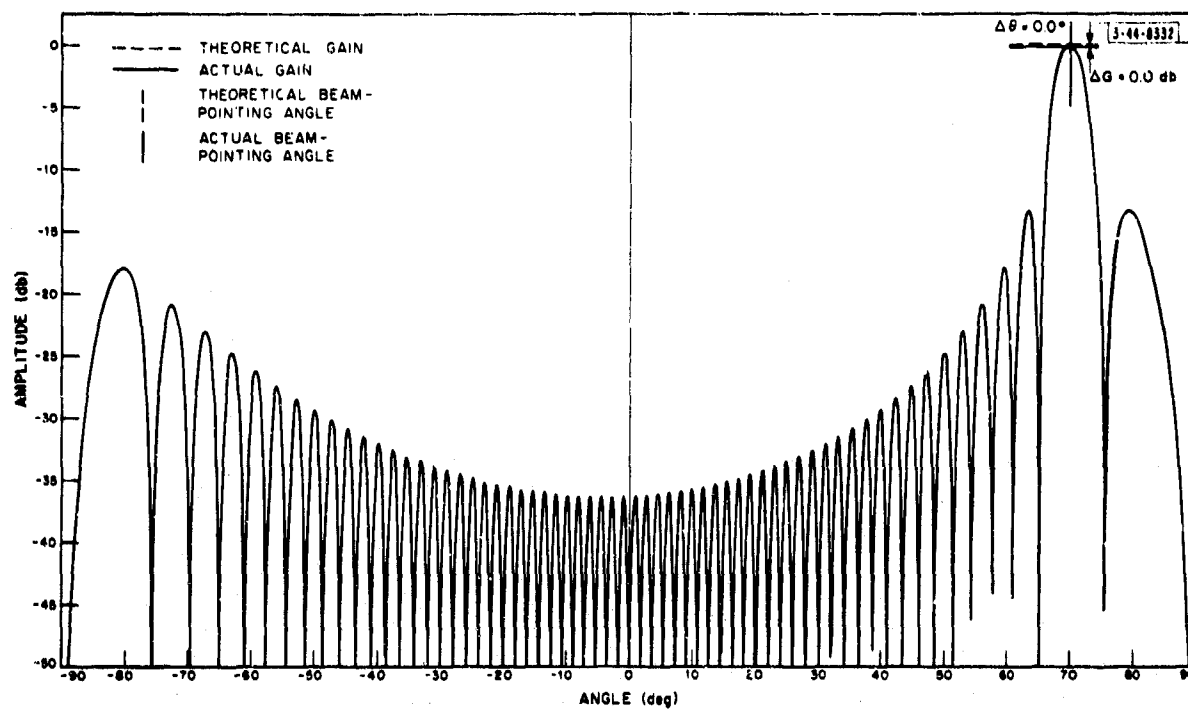


(b) Beam 33,  $f = 1.05 f_0$ .



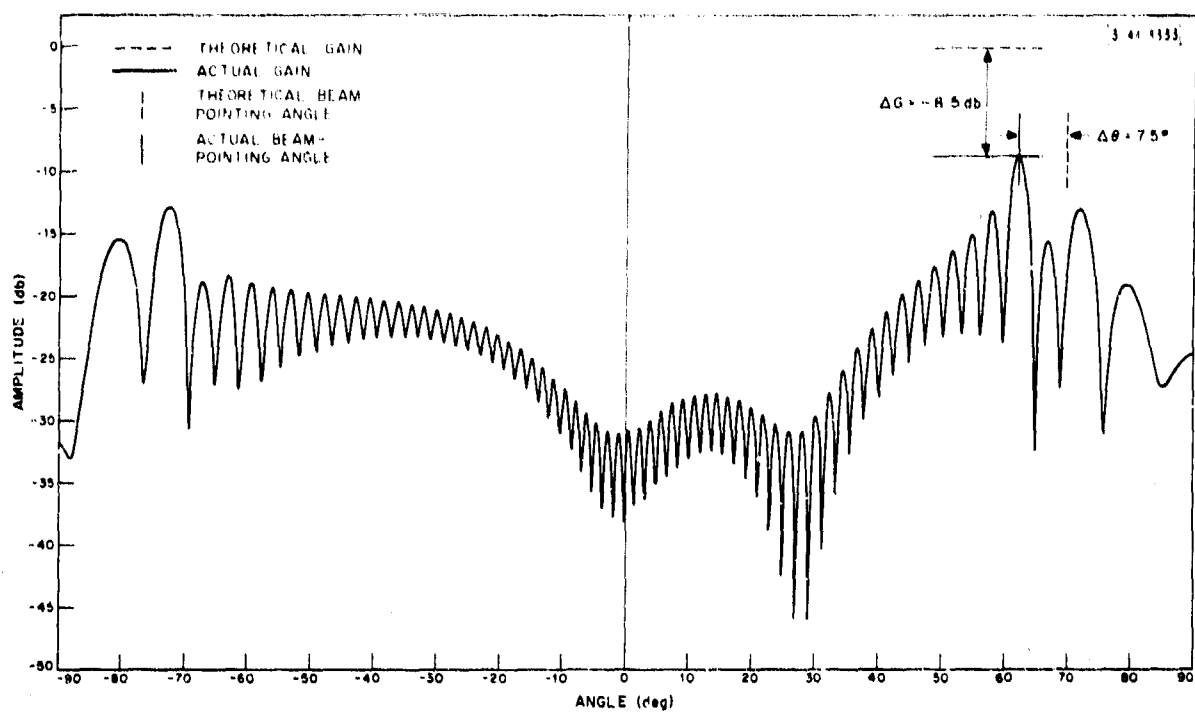
(c) Beam 33,  $f = f_0$  and all  $a_{ij} = 0$ .

Fig. III-40. Continued.

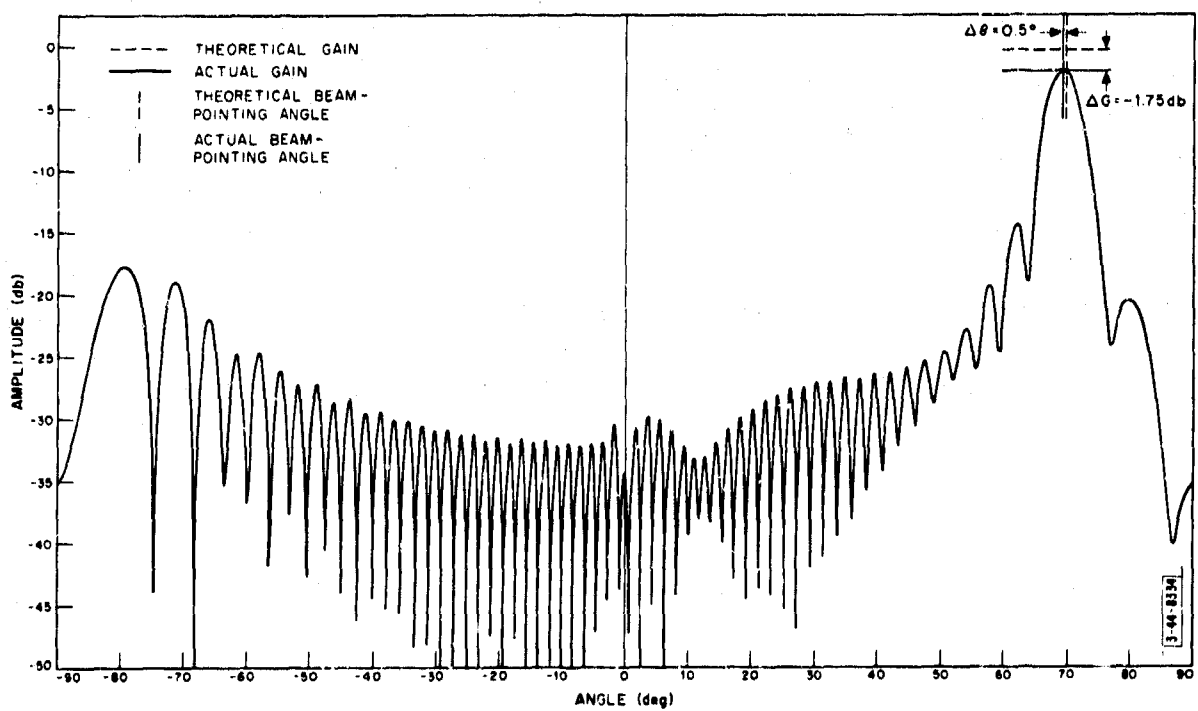


(a) Beam 63,  $f = f_0$ .

Fig. III-41. Beam 63 for 64-element ideally designed beam former  $s = \lambda_0/2$ . Effect of a frequency change is shown in (a) and (b). Effect of having all  $a_{ij} = 0$  is shown in (c).

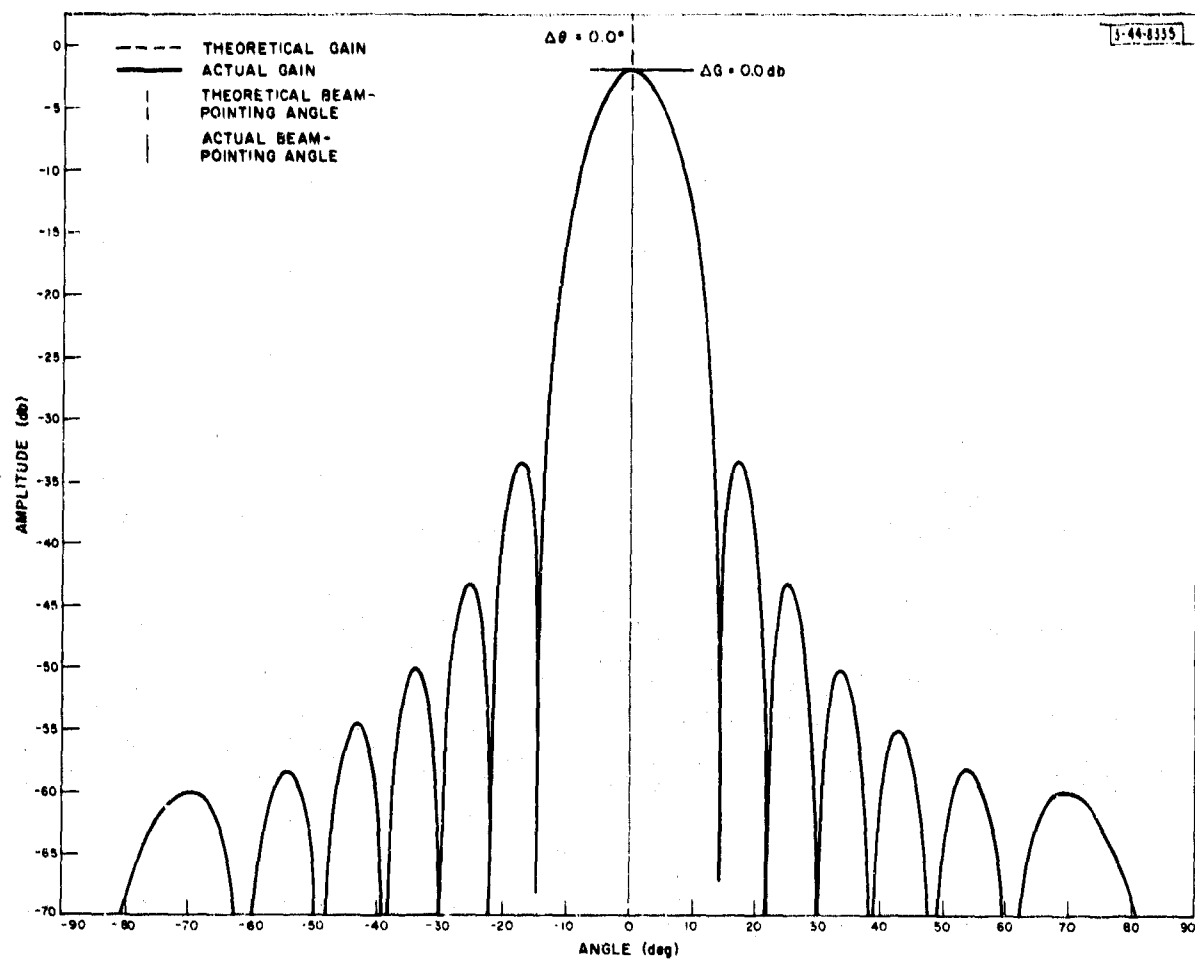


(b) Beam 63,  $f = 1.05 f_0$ .



(c) Beam 63,  $f = f_0$  and all  $a_{ij} = 0$ .

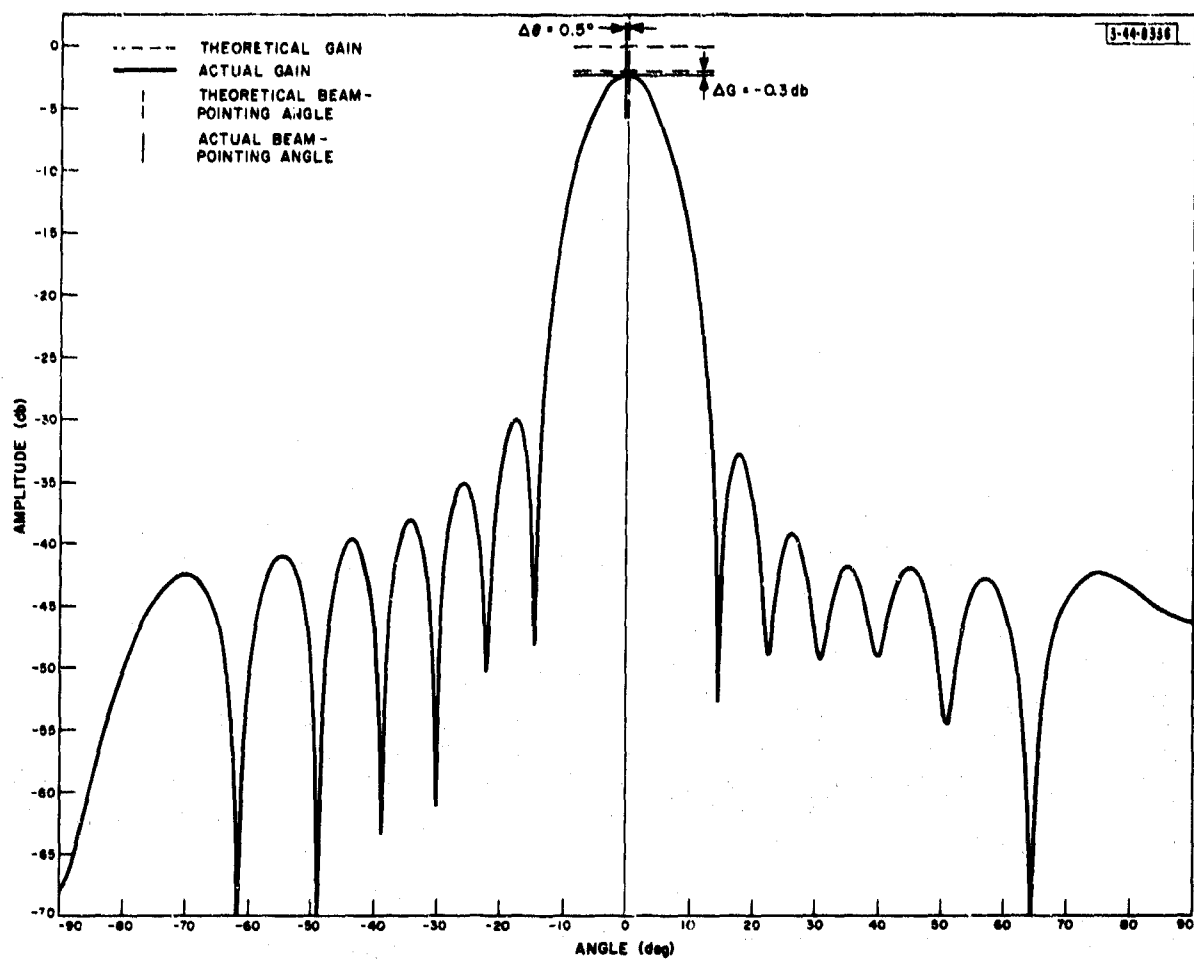
Fig. III-41. Continued.



(a) Boresight beam,  $f = f_0$ .

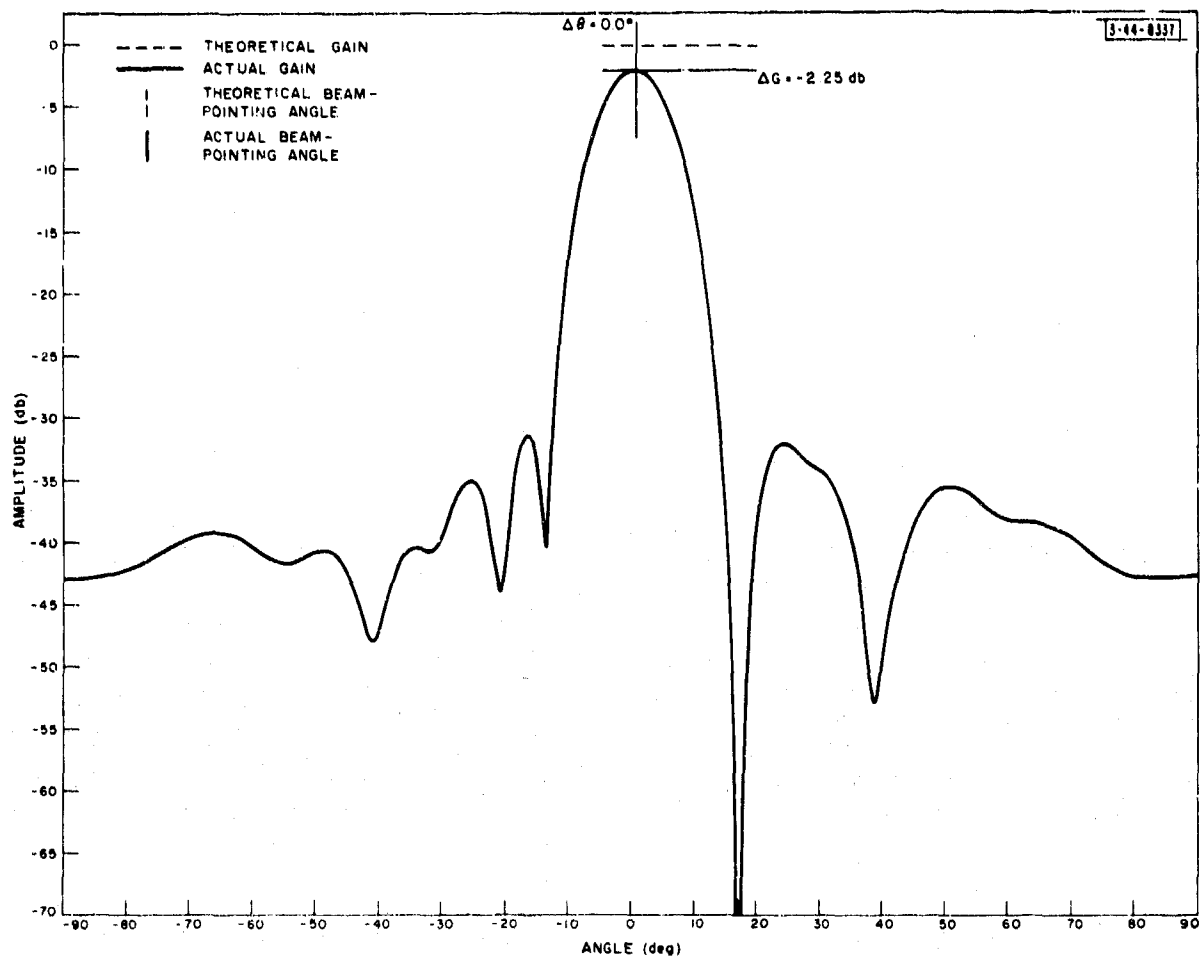
Fig. III-42. Boresight beams for 16-element beam former with cosine squared amplitude taper,  $s = \lambda_0/2$ .





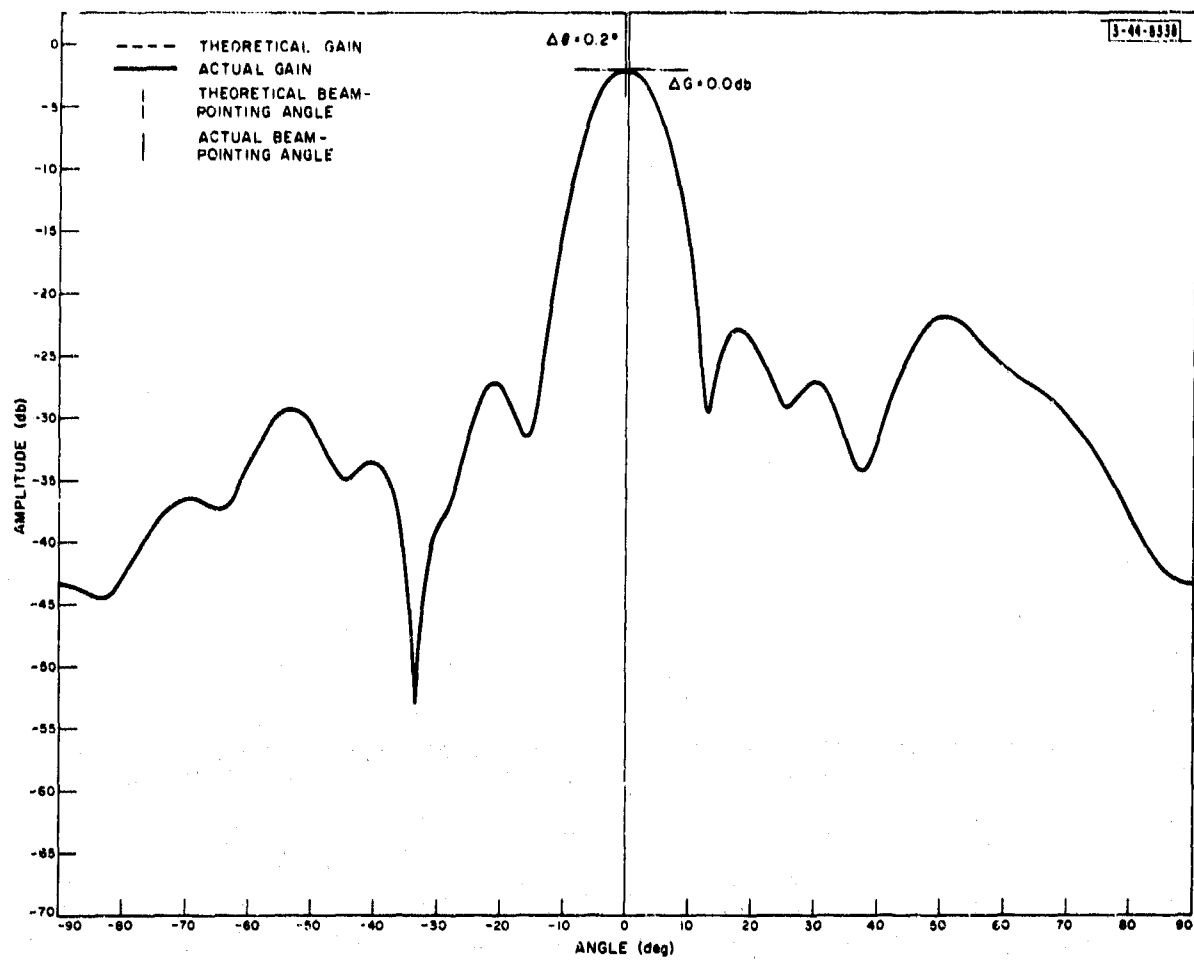
(b) Boresight beam,  $f = 1.05 f_0$ .

Fig. III-42. Continued.



(a) Boresight beam, 5-percent quantization of  $a_{ij}$ 's and  $C_{ij}$ 's.

Fig. III-43. Boresight beams for 16-element beam former with cosine squared amplitude taper,  $s = \lambda_0/2$  and  $f = f_0$ .



(b) Boresight beam, 10-percent quantization of  $a_{ij}$ 's and  $C_{ij}$ 's.

Fig. III-43. Continued.

## CHAPTER 2

### EFFECTS OF MUTUAL COUPLING ON PATTERNS OF MULTIPLE BEAM OPTICAL-TYPE ANTENNAS

J. L. Allen

#### SUMMARY

In this chapter, the effects of mutual coupling between feeds of an optical-type multiple beam forming antenna are examined. Specific attention is given to a Luneburg lens configuration, but the approach and results appear to be valid for other optical multibeam antennas, such as parabolic dishes and other types of lenses with multiple feeds.

It is proved that the shape of the "close-in" pattern (the main lobe and near-in sidelobe) is accurately predicted for an electrically large lens by applying the transformation from primary to secondary illumination appropriate for a single point source feed to the pattern of one feed excited in the presence of the other feeds, the latter terminated in their usual impedance. This is shown to be true despite the absence of a defined phase center for such a primary pattern, which is one of the usual criteria for invoking the simple geometrical optics transformation for such lenses.

It is pointed out that for electrically large lenses with many feeds, the shape of the equivalent primary pattern transformed by the lens is essentially the same shape as the "element gain function" of a similarly spaced flat array of the feeds used. Thus, the knowledge that has been obtained in shaping such element patterns by choice of feed element type, element spacing, choice of exciting and terminating impedances, and the use of additional interconnecting impedances can be applied directly to the multiple-feed design problem for optical beam formers. For example, it is shown that achievement of secondary illumination that is monotonically decreasing in intensity from the center requires the deliberate mismatching of the feed elements. Some indications of correspondence between coupling-induced gain limitations and the beam orthogonality requirement of multiple beam antennas are pointed out.

The Luneburg lens transformation is applied to several previously studied element gain functions with the dipoles above the ground plane and the results are indicated in terms of resulting secondary illumination.

#### A. INTRODUCTION

There are several techniques for the realization of simultaneous multiple beams from antennas, with perhaps the oldest being the use of multiple feeds in conjunction with a type of optical antenna, such as a reflector or a lens. For example, Fig. III-44 illustrates schematically a two-dimensional version of such an antenna: a Luneburg lens fed by multiple sources.

It has long been recognized that if excitation of any one feed element is attempted, the others are parasitically excited through mutual coupling and radiate as well. The frequent result is that the radiation pattern of such a lens with multiple feeds is inferior to the pattern of the same optical system with only a single feed of the same type. Although this problem has been recognized for some time, it has never been formally examined from a theoretical point of view, to the best of this writer's knowledge. This chapter will show that the multiple-feed problem has a precise counterpart in the theory of large arrays, and that the existing knowledge about the effect of coupling on the performance of large linear and planar arrays can be applied directly to this problem.

## B. ANALYSIS

As a starting point, we will analyze the two-dimensional (cylindrical) Luneburg lens system of Fig. III-44 (the figure is assumed to extend to  $|z| = \infty$ ). However, the results appear to be applicable to any multiple-feed optical system including three-dimensional systems (spherical lenses, spherical and parabolic reflectors with multiple feeds). (We will direct attention to the three-dimensional case later in the report.)

Let us initially consider the arrangement of Fig. III-45. The lens is fed by a single feed which produces an electric field per unit current per unit angle into the feed of  $e(\nu)$ , where  $\nu$  is the angle measured from the phase center of the feed (we assume it has one). The lens performs a linear transformation on  $e(\nu)$  to produce a secondary illumination  $E(y)$ .<sup>\*</sup> For example, if the cylindrical lens is designed for the feed phase centers to be on the lens surface, geometry will show that

$$E(y) = \frac{e(\nu)}{(\rho_0 \cos \nu)^{1/2}}, \quad y = \rho_0 \sin \nu \quad (1)$$

The far field at a range  $R$  is then determined to within a phase factor by<sup>†</sup>

$$E(\xi) = \frac{1}{R\lambda} \int_{-\rho_0}^{\rho_0} E(y) \exp[jky \sin \xi] dy \quad (2)$$

where  $k = 2\pi/\lambda$ .

The actual form of the transformation is of little consequence to our argument. For our purposes, it will suffice to use as a starting point the statement that energizing a single, isolated feed at a location corresponding to the  $n = 0$  position of Fig. III-44 produces an equiphase illumination along the aperture plane of  $E_0(y)$  per unit feed current.

If we now move the single feed to a new position – say the  $n^{\text{th}}$  of Fig. III-44 – the aperture plane moves around the lens through an angle  $nD/\rho_0$  in radians, as illustrated by Fig. III-46. Relative to the  $y$ -axis, the phase front is tilted by  $nD/\rho_0$  radians, and the phase center of the aperture plane has moved from  $x = R_0$ ,  $y = 0$ , to  $x = \rho_0 \cos nD/\rho_0$ ,  $y = \rho_0 \sin nD/\rho_0$ . Obviously, if  $nD/\rho_0 \ll 1$ , the displacement of the phase center in the  $x$ -direction becomes negligible, while the  $y$  displacement approaches  $nD$ . However, if  $\rho_0 \gg \lambda$ , as assumed, most of the pattern structure of interest will lie near  $\xi = 0$  of Fig. III-45, the  $y$ -offset of the phase center will have little effect on close-in sidelobe levels.

As a result of the foregoing approximations, we can assume that the change in the aperture illumination (on a line parallel to the  $y$ -axis) that results from moving the feed is simply a change in phase front slope.

$$E_n(y) = E_0(y) \exp[jkn(Dy/\rho_0)] \quad (3)$$

when viewed at small angles from broadside.<sup>‡</sup>

\* The dimensions on  $e(\nu)$  and  $E(y)$  differ so that squaring each and dividing by the intrinsic impedance of free space produces watts per unit solid angle and watts per unit surface area, respectively.

† S. Silver, Microwave Antenna Theory and Design, Radiation Laboratory Series, M. I. T. (McGraw-Hill, New York, 1949), Vol. 12, p. 173.

‡ A more rigorous derivation is given in Appendix III-A.

Returning, then, to the multiple-feed configuration of Fig. III-44, if we excite feed 0 with, for example, a voltage generator of open-circuit voltage  $V_0$  as in Fig. III-47(a), and terminate the other feeds as in Fig. III-47(b), then the current in the  $n^{\text{th}}$  feed is just

$$I_n = V_0 Y_{n0} \quad (4)$$

where  $Y_{n0}$  is the mutual admittance between feeds  $n$  and 0 (a function of the feed types, feed placements and  $Z_g$  and  $Z_t$  of Fig. III-47). The total illumination along a line parallel to the  $y$ -axis  $E_t(y)$  is then

$$E_t(y) = \sum_{n=-N}^N I_n E_n(y)$$

which, by Eqs. (3) and (4), gives\*

$$E_t(y) = E_0(y) \left[ V_0 \sum_{n=-N}^N Y_{n0} \exp[jknD(y/R_0)] \right] \quad (5)$$

Thus, the far field of a large ( $\rho_0 \gg \lambda$ ) optical system in the region near the main beam will be the Fourier transform of Eq. (5), where  $E_0(y)$  is the aperture illumination per unit current into the feed that would result from a single feed placed on the  $x$ -axis.

It will be useful to put Eq. (5) explicitly in the form of the primary feed illumination, which is easily done. The effect of the optical system on a single point source feed is to transform the feed primary pattern – say  $e_0(\nu)$ , where  $\nu$  is the angle from the  $x$ -axis as indicated in Fig. III-45 – into  $E_0(y)$  by some linear transformation, which we will denote as a operation  $L$ .

$$E(y) = L[e(\nu)] \quad (6)$$

For example, for a surface-focused Luneburg lens, the transformation is given by Eq. (1). The exact form of the transformation is not of immediate consequence here, only the fact that it is linear. This fact allows us to transform both sides of Eq. (5) to give

$$e_t(\nu) = e_0(\nu) V_0 \sum_{n=-N}^N Y_{n0} \exp[jknD \sin \nu] \quad (7)$$

where we have used  $y = \rho_0 \sin \nu$  in the exponent as appropriate to the Luneburg lens, since the phase slope in Eqs. (3) and (5) were derived for this configuration.

Now what physical interpretation can we give to  $e_t(\nu)$ ?

To answer this, consider a linear array of  $2N + 1$  elements (Fig. III-48), where each element is the same type as the feed antennas of the optical system, and they are similarly spaced. If we excite element 0 by a generator such as Fig. III-47(a), and terminate the others as in Fig. III-47(b), the radiation field of the ensemble is just

$$e(\nu) = \sum_{n=-N}^N e_0(\nu) I_n \exp[jknD \sin \nu]$$

\* The purist may object to the implicit assumption that the pattern which results from a feed being driven at its terminals and being parasitically excited is necessarily the same. This assumption, which used to simplify notation, is not really necessary to the argument.

by the principle of pattern multiplication, where the  $I_n$ 's are given by Eq. (4). Using Eq. (4) we write

$$e(u) = e_o(u) \left[ V_o \sum_{n=-N}^N Y_{nc} \exp[jknD \sin u] \right] \quad (8)$$

Note that  $e(u)$  as given in Eq. (8) is precisely  $e_t(u)$  of Eq. (7); but  $e(u)$  of Eq. (8) is the pattern of one element of a linear array taken in the presence of the remainder of the elements when they are passively terminated. This "element pattern" plays an important role in the theory of arrays. If there are enough feeds on either side of the one in question to assume an infinite number (say  $n > 3$ ), the pattern, when it is scaled, is the element gain function previously studied.\* Thus, the conclusion of the analysis is that a multiple feed for an optical system will radiate a pattern given by transforming the pattern of one feed in the presence of the others when they are terminated in the impedance normally used (the pattern will depend on the value of the impedance as elaborated upon later).

This conclusion is based upon the following approximations:

- (1)  $\rho_o \gg \lambda$ , and therefore geometrical optics hold.
- (2) The lens is large enough so that the feed assembly (or the extent of the feed over which elements couple appreciably) is small enough to neglect the curvature.†
- (3) The array is large enough so that the main-beam-and-sidelobe region of interest is of small angular extent, since for angles very far from the line through the excited feed (the x-axis of Fig. III-44 if feed 0 is excited), the difference in phase center locations of the aperture planes for the various feeds is not negligible in the direction of interest.

In substance, all the above restrictions amount to the restriction of very large (narrow beam) systems.

### C. GAIN AND DIRECTIVITY OF SYSTEM

A definition of antenna system gain (not directivity), consistent with its usage in the radar and radio equations (i.e., mismatch and dissipation losses are included), is

$$G_o = \frac{4\pi P_o}{P_a} \quad (9)$$

where  $G_o$  is the gain in the main beam direction,  $P_a$  is the power available from the transmitter into a matched load, and  $P_o$  is the power per unit solid angle in the main beam direction. In terms of Eq. (2),  $P_o$  is

$$P_o = R^2 \frac{|E(0)|^2}{\eta}$$

where  $\eta$  is the intrinsic impedance of free space.

\* J. L. Allen, Trans. IRE, PGAP AP-10, 566 (1962).

† This restriction is required only to permit the application of studies of  $e_t(u)$  on flat arrays; the statement of the proposition is valid with any curvature, subject to other restrictions.

From Eq. (2) it is seen that  $P_o$  is proportional to the square of the integrated field over the aperture plane. By way of specific example, let us consider a spherical Luneburg lens with an array of feeds as in Fig. III-49, then by analogy to Eq. (2), for aperture coordinates  $\rho$  and  $\varphi$  as indicated,

$$P_o = \frac{1}{\eta \lambda^2} \left| \int_0^{2\pi} \int_0^{\rho_o} E_t(\rho, \varphi) \rho d\rho d\varphi \right|^2 \quad (10)$$

For a spherical geometry, we can show that the lens transformation is

$$\left. \begin{aligned} E_t(\rho, \varphi) &= \frac{e_t(\varphi, \Theta)}{\rho_o \sqrt{\cos \Theta}} \\ \rho &= \rho_o \sin \Theta \end{aligned} \right\} \quad (11)$$

Substitution of Eq. (11) into Eq. (10) gives

$$P_o = \frac{\rho_o^2}{\eta \lambda^2} \left| \int_0^{2\pi} \int_0^{\pi/2} e_t(\varphi, \Theta) \sqrt{\cos \Theta} \sin \Theta d\Theta d\varphi \right|^2 \quad (12)$$

Now, note that if we were to remove the feed structure en masse and excite the feed exactly as before (same drive circuit), the gain of the feed structure  $g_o$  (one element directly excited, the others parasitically excited), would be just

$$g_o = \frac{4\pi}{\eta} \frac{|e_t(0, 0)|^2}{P_a} \quad (13)$$

Combining Eqs. (9), (12), and (13), we can write the gain of the lens system in the form

$$G_o = g_o \frac{\rho_o^2}{\lambda^2} \left| \int_0^{2\pi} \int_0^{\pi/2} \frac{e_t(\varphi, \Theta)}{e_t(0, 0)} \sqrt{\cos \Theta} \sin \Theta d\Theta d\varphi \right|^2 \quad (14)$$

We can go one step further and note that only  $e_t(\varphi, \Theta)$  depends upon  $\varphi$ . Consequently, integration on  $\varphi$  amounts to averaging  $e_t(\varphi, \Theta)$  with respect to  $\varphi$ . Let us therefore define a normalized, averaged (with respect to  $\varphi$ ) primary pattern  $e_n(\Theta)$  by

$$e_n(\Theta) = \frac{1}{2\pi} \int_0^{2\pi} \frac{e_t(\varphi, \Theta)}{e_t(0, 0)} d\varphi \quad (15)$$

which, when combined with Eq. (14) produces the final result\*

\* Note that for an arbitrary lens transformation  $E_t(\rho, \varphi) = L[a_t(\varphi, \theta)]$ ,  $\rho = f(\theta)$ , we can rederive Eq. (16) with the result that the gain is

$$G_o^2 = \frac{4\pi A}{\lambda^2} \left[ g_o \left| \int_0^{\theta_{\max}} L[e_n(\theta)] f(\theta) df(\theta) \right|^2 \right]$$

where  $\theta_{\max}$  is determined by  $f(\theta_{\max}) = \rho_o$ .



$$G_o = \frac{4\pi A}{\lambda^2} \left[ g_o \left| \int_0^{\pi/2} [e_n(\theta) \sqrt{\cos \theta}] \sin \theta \, d\theta \right|^2 \right] \quad (16)$$

where we have replaced  $\pi \rho_o^2$  by  $A$ , the projected lens area. The problem now is to make some physical sense of the term in brackets. First, however, let us derive an expression for the directivity  $U_o$  of the system from the definition

$$U_o = \frac{4\pi P_o}{P_{\text{rad}}}$$

where  $P_{\text{rad}}$  is the total power radiated. By the usual technique of determining  $P_{\text{rad}}$  by integrating the power density immediately in front of the aperture, we have

$$P_{\text{rad}} = \int_0^{2\pi} \int_0^{\pi/2} |E_t(\rho, \varphi)|^2 \rho \, d\rho \, d\varphi$$

assuming no spillover (i.e., the feeds radiate only into the half-space  $-\pi/2 < \theta < \pi/2$ ). In terms of the primary pattern, by use of Eq. (11),

$$P_{\text{rad}} = \int_0^{2\pi} \int_0^{\pi/2} |e_t(\varphi, \theta)|^2 \sin \theta \, d\theta \, d\varphi \quad (17)$$

Combination of Eq. (12) and (17) gives

$$U_o = \frac{4\pi}{\eta} \frac{\rho_o^2}{\lambda^2} \frac{\left| \int_0^{2\pi} \int_0^{\pi/2} e_t(\varphi, \theta) \sqrt{\cos \theta} \sin \theta \, d\theta \, d\varphi \right|^2}{\int_0^{2\pi} \int_0^{\pi/2} |e_t(\varphi, \theta)|^2 \sin \theta \, d\theta \, d\varphi} \quad (18)$$

Note that the directivity of the primary pattern is

$$u_o = \frac{4\pi}{\eta} \frac{|e_t(0, 0)|^2}{\int_0^{2\pi} \int_0^{\pi/2} |e_t(\varphi, \theta)|^2 \sin \theta \, d\theta \, d\varphi} \quad (19)$$

Combination of Eqs. (17), (18), and (19) gives

$$U_o = \frac{4\pi A}{\lambda^2} \left[ u_o \left| \int_0^{\pi/2} [e_n(\theta) \sqrt{\cos \theta}] \sin \theta \, d\theta \right|^2 \right] \quad (20)$$

Comparison with Eq. (16) shows that the ratio of the gain to directivity (a measure of any losses due to coupling to the terminated feeds and to mismatch in the active feed) is determined by the corresponding ratio of the gain to directivity of the single active feed in the presence of its terminated neighbors. There are some fundamental constraints on the ratio as a function of feed spacing<sup>\*†</sup> and there are also orthogonality constraints on feed spacing and pattern shape.<sup>‡</sup> The interrelationship of these two constraints has not been examined, but may be a fruitful direction for further inquiry.

\* TR-299.

† P. W. Hannon, Trans. IRE, PTGAP AP-12, 423 (1964).

‡ J. L. Allen, Trans. IRE, PGAP AP-9, 350 (1961).

There remains the question of the nature of the integral appearing in Eqs. (16) and (20) which we will denote as  $I$ :

$$I = \int_0^{\pi/2} |e_n(\theta) \sqrt{\cos \theta}| \sin \theta \, d\theta \quad (21)$$

Recalling that the lens illumination  $E(\rho, \varphi)$  is related to  $e(\varphi, \theta)$  by

$$E(\rho, \varphi) = \frac{e(\varphi, \theta)}{\rho_0 \sqrt{\cos \theta}}$$

and that  $e_n(\theta)$  is the normalized average (over  $\varphi$ ) value of  $e(\varphi, \theta)$ , it is apparent that for low sidelobes, we would like

$$e_n(\theta) \leq \sqrt{\cos \theta}$$

with equality at  $\theta = 0$ . Consequently, from Eq. (21)

$$I \leq \int_0^{\pi/2} \cos \theta \sin \theta \, d\theta$$

Integration gives

$$I \leq \frac{1}{2}$$

From the definition of  $u_0$ , if we have an antenna with a normalized pattern of  $\sqrt{\cos \theta}$  (voltage), it follows that

$$u_0 = 4$$

and

$$u_0 |I|^2 = 1$$

giving

$$U_0 = \frac{4\pi A}{\lambda^2}$$

as we would expect, since the primary pattern results in a uniform lens illumination. Note that as we "sharpen"  $e_n(\theta)$  by, for example, postulating a pattern

$$e_n(\theta) = \sqrt{\cos \theta [1 - |f(\theta)|^2]}$$

with the stipulation  $f(0) = 0$ , we increase the primary pattern directivity, but decrease the value of  $I$ . Since such a primary pattern leads to tapered aperture illumination, the system directivity obviously decreases; consequently, the value of  $|I|^2$  is more sensitive to tapering than is the value of  $u_0$ .

At this point, it is certainly not apparent that there is any great utility in the form chosen for Eqs. (16) and (20), in view of the conflicting behavior of the two factors inside the brackets. To show that there is a reason behind this representation, however, let us consider an analogy between the lens system and a planar array of similar elements, which we will refer to as the "reference array."

#### D. USE OF LENS FOR SIMULTANEOUS RECEPTION OF MULTIPLE BEAMS

Probably a primary reason for constructing an antenna with multiple feeds is the desire for simultaneous reception in multiple directions. Such an application forces a constraint on the configuration: all elements would have nominally identical circuits attached to their feeds. We can examine this situation from a transmitting point of view (one beam transmitting at a time), inferring the receiving situation by the combined use of reciprocity and superposition.

The assumption of identical feed circuitry on receive is then equivalent (when transmitting) to assuming that, in the nomenclature of Fig. III-47,  $Z_t = Z_g$ ; that is, the elements are passively terminated in the same impedance as that from which the driven element is excited. Henceforth, we will assume this to be the case for both the lens feed assembly and our reference array.

In order to determine  $e_t(\varphi, \theta)$ , we can conceptually remove the feed assembly from the lens, excite one feed (with the others terminated), and measure the pattern. If the feed assembly contains many feeds, the feed under consideration is not near the edge of the assembly, and the curvature of the feed assembly is slight, the pattern that we measure will be essentially the same as we would determine from our reference array by measuring the pattern of one element in the presence of the rest. This pattern is the so-called "element-gain function," which plays a major role in large array theory, and has been studied in this context.\*

The shape and the magnitude of the element-gain function depends not only upon the type of element used, but to an even greater extent upon the relative placements of the other elements and the impedances of the circuits of all the elements.

From planar-array theory, for elements spaced so that no grating lobes can be formed when the array is phased for broadside radiation (e.g., wavelength by wavelength spacing or smaller for a rectangular grid), we can write the element-gain function

$$g(\varphi_o, \theta_o) = \frac{4\pi a}{\lambda^2} \cos \theta_o [1 - |\Gamma(\varphi_o, \theta_o)|^2] \quad (22)$$

where  $a$  is the area allotted each element of the feed (if the elements are on a rectangular grid  $D_x$  by  $D_y$ ,  $a = D_x D_y$ ), and  $\Gamma$  is the reflection coefficient one would expect to see looking into the feed of such an element in the reference planar array when all elements are excited and the array is phased to point the beam in the  $\varphi_o, \theta_o$  direction. It is assumed that the element itself is lossless; that is, the array gain degradation is due to the mismatch factor  $1 - |\Gamma|^2$ .

From Eq. (22), it is apparent that the factor  $g_o$  of Eq. (16) has an upper bound of  $4\pi a/\lambda^2$ , achieved when the element generator and terminating impedances are the same as would be used in the reference array to maximize its gain (i.e., the impedance of the element under active conditions would be matched) when the array was phased for broadside radiation. It should be emphasized that choosing the impedance in this matter will result in a mismatch when only a single element is excited. (Although it may seem strange that this is a condition which maximizes  $g_o$ , it should be borne in mind that the element-gain function depends strongly on the radiation from the neighboring elements which is also dependent upon the impedances in which they are terminated. Thus, one should not be too surprised that the primary pattern gain can be increased by a deliberate mismatch of the element to the generator as it is used in the lens feed.)

\* J. L. Allen, Trans. IRE, PGAP AP-9, 350 (1961) and TR-236.

Assuming that one has chosen the circuit impedances such that the reflection coefficient would be zero in the planar array at broadside, it is apparent from Eq. (22) that the value of the gain function will fall off as fast or faster than  $\cos \theta$ . The lens transformation, as expressed by Eq. (11), then indicates\* that the resulting aperture distribution will be tapered by an amount depending upon the reflection coefficient that the element would have in the planar array.

Thus, we have added additional pattern synthesis parameters by surrounding the feed with other feeds. By adjusting the circuit impedance of the elements, the design parameters of the elements that influence their mutual coupling, and perhaps even by adding interconnections between elements,† we can shape the primary radiation pattern in such a manner, we hope, as to obtain a low sidelobe aperture illumination.

Let us return, then, to the question of the match (or lack of it) of the driving circuit to the element. Since we have pointed out that the driving impedance, which must be used to maximize  $g_o$ , represents a deliberate mismatch when a single element is excited, a logical question arises about what would happen if we ignored the other elements' presence completely and excited each feed with a driving impedance which would have properly matched that feed in free space. An indication of what may happen can be gained by reference to Eq. (22). We have chosen the circuit impedance to be a match in the reference array when only a single feed is used. If the elements are now placed in our reference array, they would appear mismatched when all elements of the array are excited and the array is phased for broadside radiation.  $\Gamma$  would not be zero at broadside, and

$$g_o < \frac{4\pi a}{\lambda^2}$$

In this case, however, studies‡ of the element-gain function show that there is some angle of scan in a planar array where the apparent impedance of the elements is essentially equal to the impedance of a single isolated element. At that angle,  $\Gamma$  of Eq. (22) vanishes. The resulting pattern is typically an element-gain function with a "saddle" shape as illustrated in Fig. III-50. When such a primary illumination is transformed, the resulting aperture illumination appears as in Fig. III-51. Although we have yet to actually calculate the far fields, it seems quite likely that the "hump" in the H-plane illumination will produce relatively high close-in sidelobes, and such an effect has been experimentally observed in multiple-feed optical systems.

By comparison, Fig. III-52 shows the aperture illumination derived for the case where the circuit impedance chosen was that which produced a broadside match in the active planar array. The curves were computed from Eqs. (22) and (11) taking values of  $\Gamma$  computed in TR-299 for elements placed on a regular  $\lambda/2 \times \lambda/2$  grid. The improvement over the illumination of Fig. III-51 is apparent.

\* Note that the gain function is related to  $e_i$  of Eq. (11) by

$$g(\phi_o, \theta_o) \propto |e_i(\phi_o, \theta_o)|^2$$

† P. W. Hannan, Trans. IRE, PTGAP AP-12, 423 (1964).

‡ J. L. Allen, Trans. IRE, PGAP AP-9, 350 (1961).

In fact, Fig. III-52 is even superior to what one would achieve feeding a lens with a single isolated dipole mounted a quarter-wavelength above a large ground plane as is evidenced from the transformed aperture illumination of Fig. III-53, although it may be possible to find a ground plane spacing which improves this result.

If the feed spacing is increased, the pattern of the excited feed in the presence of its neighbors tends to sharpen (become more directive). The aperture illumination is sharpened also, as indicated by comparison of Figs. III-54 and III-55 which illustrate the computed aperture illumination for  $\lambda/2$  dipoles above ground, spaced  $0.5\lambda$  and  $0.7\lambda$  on centers, respectively. The circuit impedances are nearly those\* which would give a broadside match in a reference planar array (comparison of Fig. III-54 with III-52 illustrates the effect of a slightly nonoptimum impedance choice). The spacing of the elements above a ground plane was one which minimized  $|\Gamma|$  at large angles for each spacing.

It is seen that the effects of the coupling to adjacent elements tend to sharpen the illumination and consequently broaden the far-field main lobe. Thus it appears that moving the feed elements further apart, which in turn increases the angular separation of the peaks of the main beams, also tends to broaden the beams and may<sup>†</sup> result in little change in crossover levels, but a significant change in sidelobe levels.

#### E. CONCLUSIONS AND SUGGESTIONS FOR FURTHER WORK

The results which have been presented have suggested that mutual coupling may actually be put to profitable use in multiple feeds for optical systems as a synthesis tool. It appears to be possible to improve the aperture illumination by suitable placement of the adjacent elements and proper choice of the driving impedances from which these elements are to be excited. Obviously, the foregoing remarks are largely qualitative, and an immediate starting point for further work would be to lend quantitative support to these observations.

---

\* The program, which computed the gain functions used to derive the aperture illumination of Figs. III-53 and III-54 used an approximation to the optimum  $Z$ , which was slightly in error.

† The statement is based on intuition.

Fig. III-44. Cylindrical lens geometry.

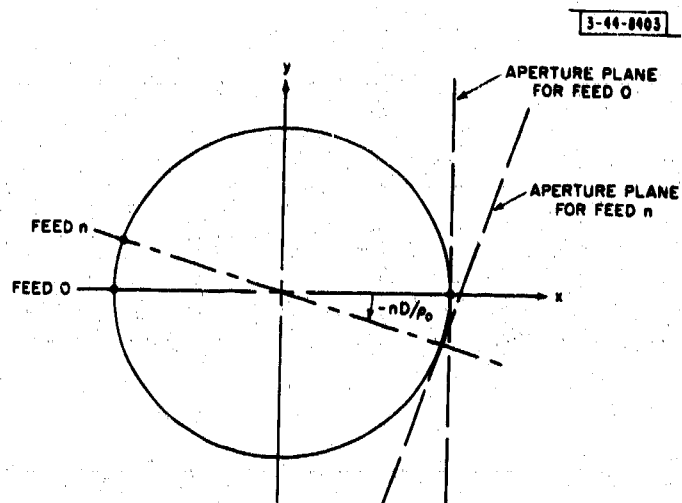
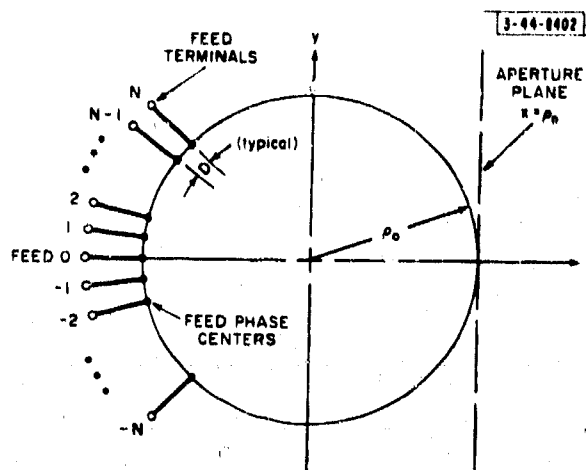
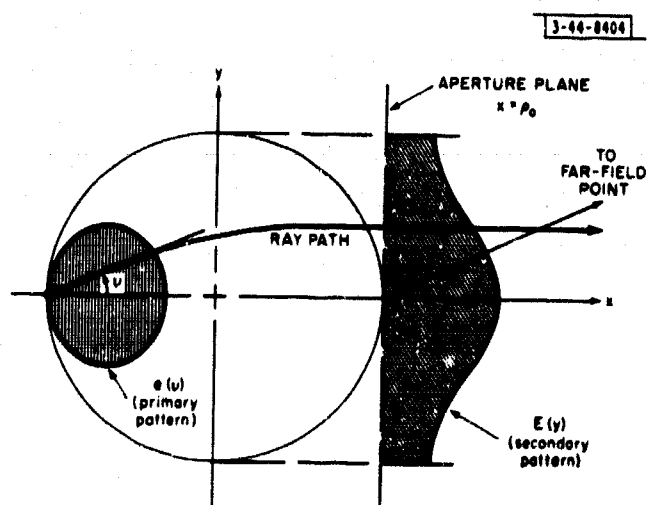


Fig. III-45. Change in geometry with field locations.

Fig. III-46. Pattern nomenclature.



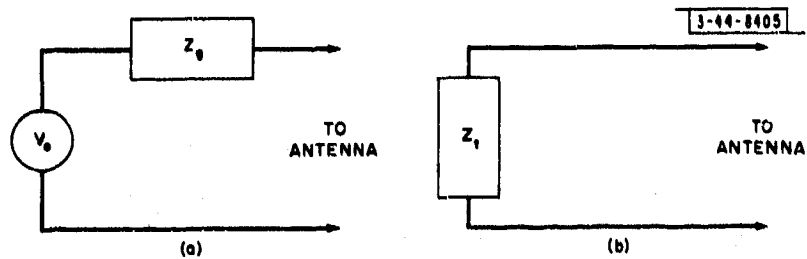


Fig. III-47. Assumed feed element circuit configurations. (a) Excited feed. (b) All other feeds.

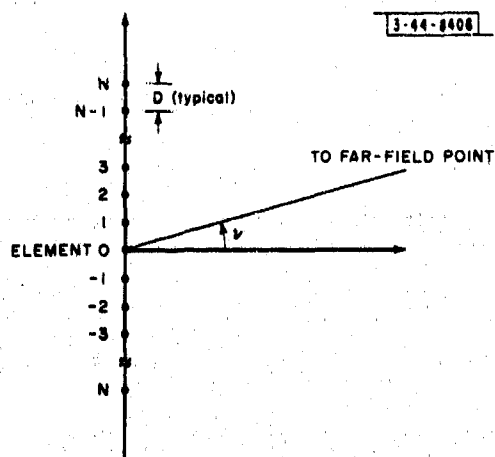


Fig. III-48. Equivalent linear array geometry.

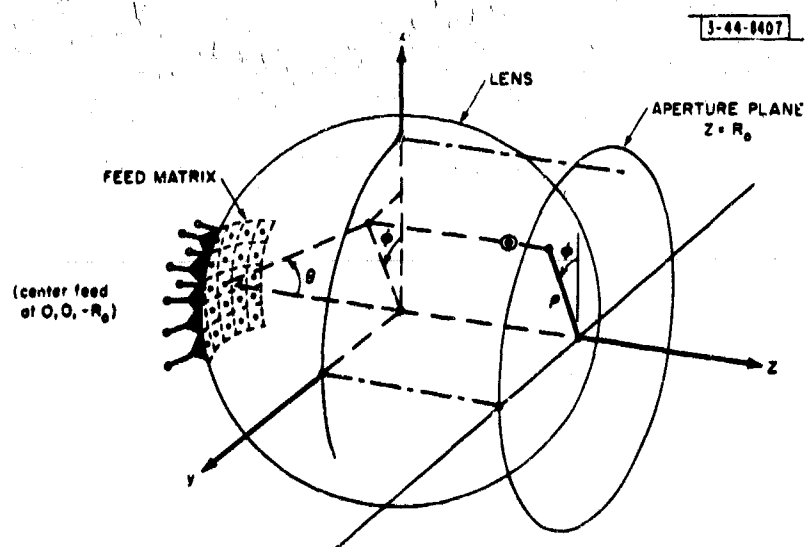


Fig. III-49. Spherical lens geometry.

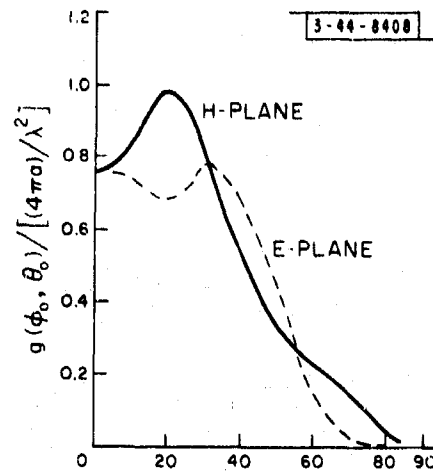


Fig. III-50. Measured gain function of  $\lambda/2$  dipole mounted  $\lambda/4$  above ground imbedded in array of similar dipoles equally spaced on  $0.6\lambda$  square grid. Circuit impedance was chosen to match single dipole above ground.  $Z_g = 86 - j72$ .

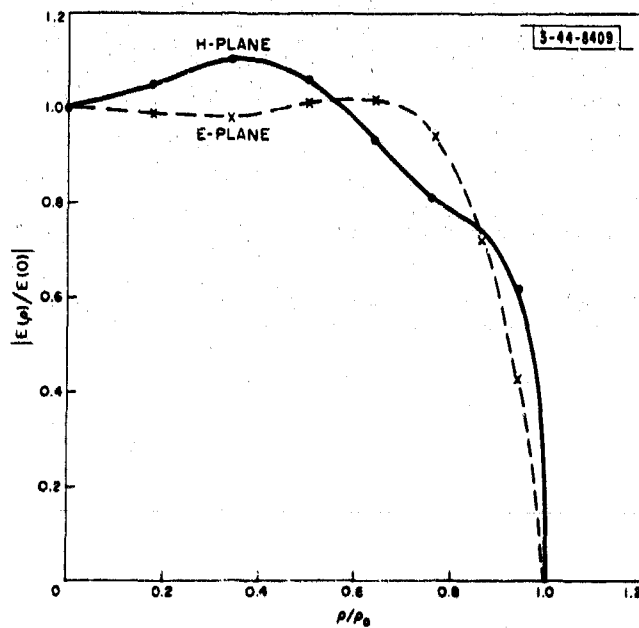


Fig. III-51. Lens illumination by  $\lambda/2$  dipole mounted  $\lambda/4$  above ground imbedded in array of similar dipoles spaced  $\lambda/2$  on centers.  $Z_g = 86 - j72$  (free space match) (geometrical optics).



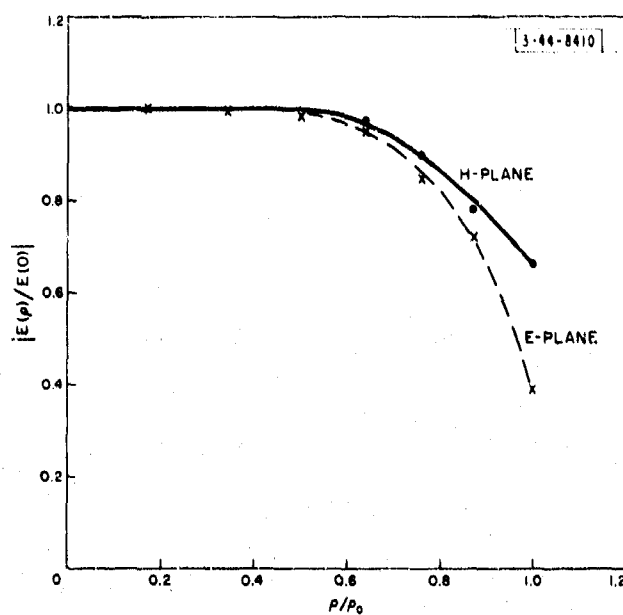


Fig. III-52. Lens illumination by  $\lambda/2$  dipole mounted  $\lambda/4$  above ground imbedded in array of similar dipoles spaced  $\lambda/2$  on centers.  $Z_g = 150 - j42$  (match in planar array).

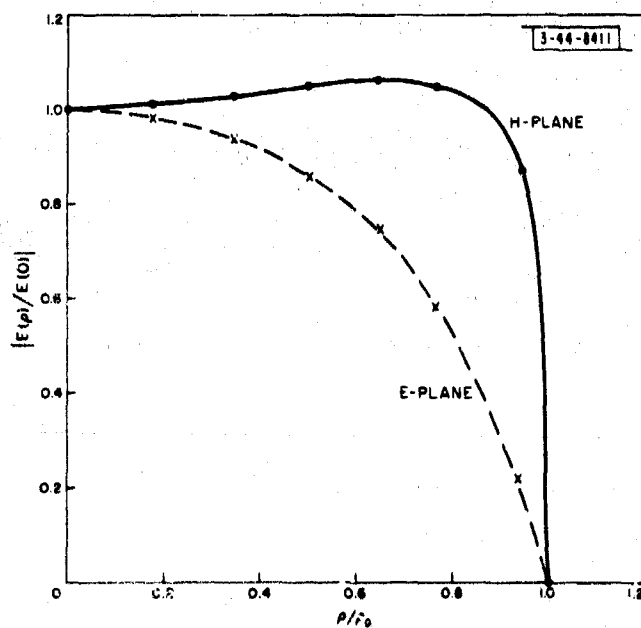


Fig. III-53. Lens illumination from single  $\lambda/2$  dipole mounted  $\lambda/4$  above ground (geometrical optics).

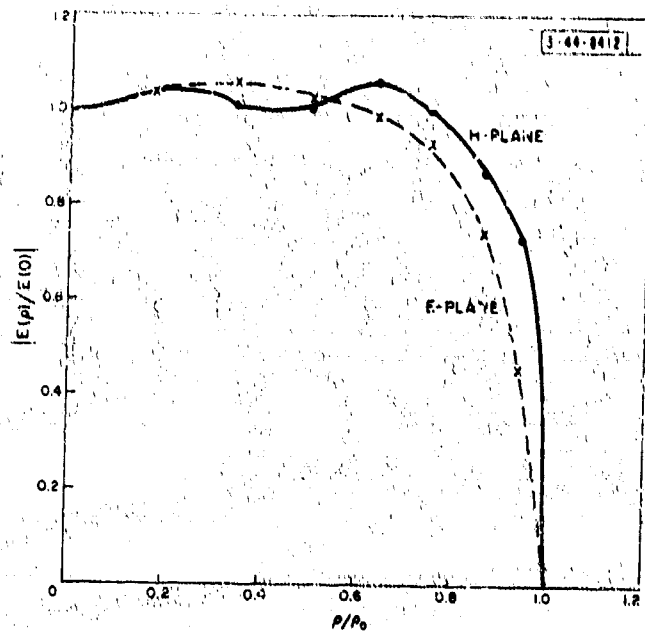


Fig. III-54. Lens illumination by  $\lambda/2$  dipole mounted  $\lambda/4$  above ground imbedded in array of similar dipoles spaced  $\lambda/2$  on centers ( $9 \times 7$  array gain function data),  $Z_g = 150 - j42$  (match in planar array) (geometrical optics).

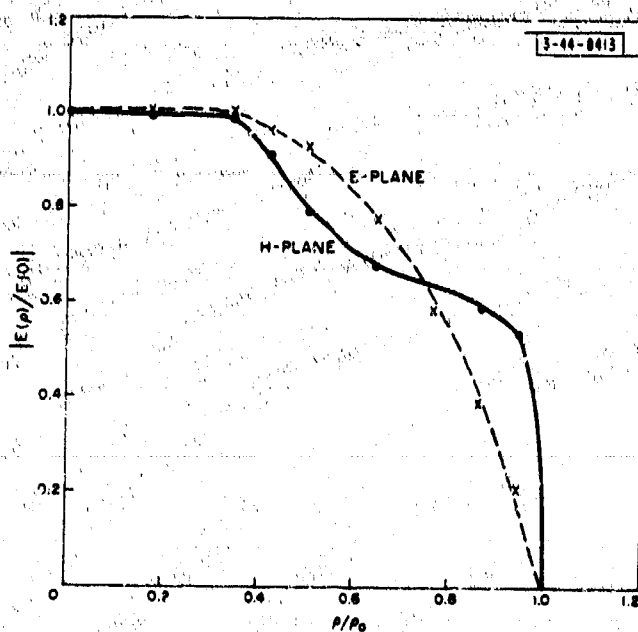


Fig. III-55. Lens illumination by  $\lambda/2$  dipole mounted  $\lambda/8$  above ground imbedded in array of similar dipoles spaced  $0.7\lambda$  on centers.  $Z_g = 37 - j59$  (match in planar array) (geometrical optics).

# CHAPTER 3

## THEORETICAL INVESTIGATION OF MUTUAL COUPLING EFFECTS

B. L. Diamond

### SUMMARY

This section is devoted to the results obtained during the past eighteen months from the continued investigation of the effects of mutual coupling in arrays. In a previous technical report (TR-236), an approach to the evaluation of mutual coupling effects through the use of the element gain function concept was outlined, and some results were given for small planar arrays of thin, half-wavelength dipoles. This concept is applicable (at least as an experimental tool) to arrays composed of any type of element. However, before attempting to obtain a better understanding of more "exotic" elements (such as log-periodics), it was felt that still further investigation of dipole arrays should be undertaken. For this reason, the previous studies have been extended to include arrays of electrically short dipoles and arrays without reflectors. The results of this investigation are reported in the following section.

The present study differs from previous investigations of arrays of thin dipoles mainly in the method of computing the array performance. Most of the previous work utilized infinite array approximations to compute the driving impedance of an element in the array (usually the center element), while in this investigation we solve for the current driving each element exactly by computing the inverse of the impedance matrix. In order to maximize the "insight content" of the results, wide ranges of element-to-element spacing and element-to-ground plane spacing were used.

Computations of gain and impedance variation with scan angle for arrays with 63 and 99 elements were performed to obtain an estimate of size effects. The comparison of these results with previous results and with infinite array results has demonstrated the validity and usefulness of the approach. In addition, the calculations have indicated the extent to which edge effects influence the performance of noncentral elements of an array.

The results of the previous study (TR-236) are confirmed and extended. For example, it is shown that the gain of the array as a function of scan angle depends primarily upon the element spacing and is quite insensitive not only to the height of the dipoles above the ground plane but also to the type of dipole element (short dipole or half-wavelength dipole). The gain variation of the array when the elements are fed from constant impedance sources is shown to be very nearly that predictable on a directivity basis from the well-known gain vs area relationship, modified to account for the grating lobe formation with scan. On the other hand, it is seen that the change in element impedance is considerably affected by parameters which have little effect on the array gain behavior, and possibilities for minimizing mismatch caused by scanning are pointed out making use of this result.

An investigation of edge effects in a  $9 \times 11$  array has shown that the performance of the outer 4 or 5 rows of elements in a large array will be considerably changed due to edge effects, when the array is above a ground plane. In the absence of a ground plane, edge effects influence the behavior of elements which are much further removed from the edge.

### A. INTRODUCTION

During the past few years there has been a growing interest in the effects of mutual coupling on the performance of phased array antennas. Experimental investigations of arrays of various

types of radiating elements have shown, qualitatively and quantitatively, the different kinds of effects which may be observed, e.g., gain and impedance variation with scan angle, depolarization, etc. Most types of array elements can only be evaluated by an experimental program because they are generally complicated mechanical and electrical structures. The exceptions are thin, linear antennas and their electromagnetic duals, narrow slots in a ground plane, which lend themselves to complete theoretical analysis. These simple types of elements are special cases, but it is found that a detailed study of array antennas using dipoles as radiating elements reveals some results which are generally applicable to all array antennas.

The primary purpose of the investigations reported here was to determine the exact performance (mainly, gain and impedance variations with scan angle) of small, regularly spaced, planar arrays of either thin, half-wavelength dipoles or electrically short dipoles. These performance characteristics of elements in an array are examined over a range of element-to-element spacings and element-to-ground plane spacings (including the no-ground-plane cases), in order to facilitate more enlightened design of scanning dipole arrays. Effect of array size on the performance of an element in the array was also investigated by computing two arrays of different sizes. Further insight into array performance was obtained by investigating the behavior of noncentral elements of the array.

There have been previous investigations of small arrays of thin half-wavelength dipoles mounted above ground planes, the most comprehensive being that of Allen.<sup>†</sup> The present study extends Allen's investigation to include arrays of electrically short dipoles and arrays without ground planes. Although the calculations which have been made during this reporting period have been limited to linearly polarized arrays, the theory section includes the relevant formulas for arrays of hybrid-fed, crossed-dipole-pair radiators. Most of the theory of linearly polarized arrays (as previously reported) is included for completeness and as a basis for comparison with the crossed-dipole case.

In the previous study, many of the results were obtained by applying the large array approximation to a planar array of  $\lambda/2$  dipoles above a ground plane having up to 63 radiating elements. In the present study, however, an exact solution is obtained for an array with up to 100 radiating elements by computing the inverse of the impedance matrix. The results obtained by these two methods for  $7 \times 9$  arrays of  $\lambda/2$  dipoles are compared for various values of element-to-element spacing and element-to-ground plane spacing. It was found that the approximate solution gives only a fair estimate of the actual performance of  $7 \times 9$  arrays.

It has been found from computations of  $7 \times 9$  arrays of short dipoles (and of  $\lambda/2$  dipoles) that the gain function of an element in the array is set completely by the array environment; that is, the amplitude and shape of the gain function depend only on the array geometry and not on element type (short or half-wavelength dipoles). This conclusion applies to arrays without ground planes as well as to arrays mounted above ground planes.

In order to have some way to assess the behavior of small arrays, a computer program was written to compute the approximate impedance variation of an infinite array by applying the infinite array approximation to a large (but finite) array. The results obtained for  $65 \times 149$  arrays above ground planes were found to agree very well with known results for infinite arrays. When the ground plane was removed, the infinite array approximation for a  $65 \times 149$  array gave relatively poor results (errors of the order of 5 percent).

---

<sup>†</sup>TR-236, pp. 199-242.

These studies have also shown that there is an optimum height above the ground plane for each element spacing at which the maximum mismatch incurred during scanning is minimum. The possibility of further decreasing the mismatch without substantially degrading the array gain by adjusting the generator impedance is pointed out.

An investigation of edge effects in a  $9 \times 11$  array has shown that the performance of the outer 4 or 5 rows of elements in a large array will be considerably changed due to edge effects, when the array is above a ground plane. In the absence of a ground plane, the small arrays of this study were completely dominated by edge effects which indicates that edge effects influence the behavior of elements far removed from the edge when there is no ground plane.

## B. MATHEMATICAL DESCRIPTION OF MUTUAL COUPLING EFFECTS

This section presents the theory of mutual coupling effects in linearly polarized and circularly polarized arrays of thin dipoles. Although the theory appears similar to that previously presented,<sup>†</sup> it has, in fact, a much wider range of applicability. The theory has been extended to include irregularly spaced arrays and the formulas developed apply to any element in the array (not just the center element). In addition, arrays of electrically short dipoles are investigated and the results compared with those obtained from arrays of half-wavelength dipoles. Arrays with and without ground planes are considered.

### 1. Basic Concepts and Definitions for Mutual Impedance

A well-known property of a dipole array is that the currents and voltages existing at the terminals of the elements can be expressed by circuit equations. Due to mutual coupling, the voltage at the terminals of an element in an array depends on the currents flowing in all elements of the array. The pertinent equations for the simple, two-dipole array shown in Fig. III-56 are of the form<sup>‡</sup>

$$\begin{aligned} V_m &= Z_{mm}I_m + Z_{mn}I_n \\ V_n &= Z_{nm}I_m + Z_{nn}I_n \end{aligned} \tag{1}$$

where the notation is indicated in the figure. Since this study is only concerned with planar arrays, the notation implies that dipoles  $m$  and  $n$  are located at the positions  $(x_m, y_m)$  and  $(x_n, y_n)$ , respectively, in the plane  $z = z_0$ . The quantities  $Z_{mm}$  and  $Z_{nn}$  are the self-impedances of the two dipoles, while  $Z_{mn}$  and  $Z_{nm}$  are the mutual impedances between the two dipoles. For reciprocal dipoles and media, which we assume throughout this section, the mutual impedances are equal. The self-impedances of the two dipoles will be the respective radiation impedances,  $Z_{r_m}$  and  $Z_{r_n}$ , when the antennas are completely isolated from all other antennas and reflecting surfaces.

As indicated in Fig. III-57, the mutual coupling between dipoles acts in the manner of a generator of open-circuit voltage  $v_m^i = Z_{mn}I_n$ . The current through the antenna may be either increased or decreased (with respect to the current in the absence of mutual coupling) depending

<sup>†</sup> TR-236, pp. 201-203.

<sup>‡</sup> Note that circuit equations can be written for arrays composed of any type of element; however, the self and mutual impedances can be interpreted as those of isolated elements only for thin, gap-fed dipoles.

upon the induced polarity. In the more general case of an array with many radiating elements, the induced voltage on the  $m^{\text{th}}$  antenna has contributions from all other elements ( $n \neq m$ ), that is

$$v_m' = \sum_{\substack{n \\ n \neq m}} Z_{mn} I_n \quad (2)$$

It then follows that the voltage at the terminals of the  $m^{\text{th}}$  dipole in an array is

$$V_m = Z_{r_m} I_m + v_m' \quad (3)$$

$$= Z_{r_m} I_m + \sum_{\substack{n \\ n \neq m}} Z_{mn} I_n \quad (4)$$

Note that the self and mutual impedances in Eq. (4) will be the same as those in Eq. (1) only when the radiating elements are nonscattering (assuming identical spacing between elements in both cases); open circuiting the terminals of an element is equivalent to removing it from the array. This will be true only for special types of elements such as thin dipoles and narrow slots in a ground plane.

To an observer looking into the terminals of the antenna, the presence of the generator leads to an alteration of the antenna impedance. This impedance will be referred to as the element driving impedance  $Z_D$  which depends on the relative current flowing in the dipoles. For the two-dipole case the driving impedance is

$$Z_{D_m} = \frac{V_m}{I_m} \quad (5)$$

$$= Z_{r_m} + Z_{mn} \frac{I_n}{I_m} \quad (6)$$

while for many dipoles, the pertinent equation is

$$Z_{D_m} = Z_{r_m} + \sum_{\substack{n \\ n \neq m}} Z_{mn} \frac{I_n}{I_m} \quad (7)$$

In this report, two types of thin dipoles will be considered: half-wavelength dipoles and electrically short dipoles ( $L \ll \lambda$ ). These elements may be located in "free-space" arrays or they may be placed in a planar array at height  $s$  above a perfectly conducting ground plane of effectively infinite extent (no ground plane edge effects).

Most of the formulas and tables of mutual impedance are stated in terms of impedance between isolated dipoles.<sup>†</sup> The formulas for "free-space" dipoles are readily adapted to dipoles above a ground plane by image theory. If a dipole with "free-space" radiation impedance  $Z_r$  is located at height  $s$  above a ground plane, as indicated in Fig. III-58, it can be readily verified that the self-impedance of such an element is

$$Z_{mm} = Z_{r_m} - Z_M(0, 0, 2s) \quad (8)$$

<sup>†</sup> J. D. Kraus, Antennas (McGraw-Hill, New York, 1950).

where  $Z_M(x, y, z)$  is the mutual impedance between two dipoles, one located at the origin and the other centered at the point  $(x, y, z)$ . In this study the dipoles are assumed to lie in a plane – the  $z = 0$  plane when there is no reflector and the  $z = s$  plane when there is a perfectly conducting ground plane at  $z = 0$ . The dipoles may be oriented in the parallel configuration shown in Fig. III-59 or they may be perpendicular to each other as shown in Fig. III-60. For either the parallel or the perpendicular orientation of the dipoles with no ground plane, the mutual impedance is simply

$$Z_{mn} = Z_M(x_o, y_o, 0) \quad (9)$$

where  $x_o = (x_m - x_n)$  and  $y_o = (y_m - y_n)$  are the x- and y-separations of the two dipoles. When there is a ground plane, the contribution to the mutual impedance by the image dipole must be included. This can be done by writing four equations in a manner similar to Eq. (1) for two dipoles plus two images. When this is done, the mutual impedance between two such basic elements  $Z_{mn}$  is seen to be the difference of the mutual impedance between the two dipoles of the same orientation in free space and the mutual impedance between one dipole and the image of the other in free space. In the geometry of Fig. III-61, one can write

$$Z_{mn} = Z_M(x_o, y_o, 0) - Z_M(x_o, y_o, z_o) \quad (10)$$

where, as above,  $x_o = (x_m - x_n)$  and  $y_o = (y_m - y_n)$ , and  $z_o = 2s$  are the separations of the two dipoles in each of the three Cartesian coordinates. By the use of Eqs. (8) and (10), mesh equations such as Eq. (1) can be written directly for an array above a ground plane considering an elemental radiator to be the combination of a dipole and the ground plane.

## 2. Fundamental Equations for Mutual Impedances

It is apparent that relationships such as Eq. (1) give only terminal information about the antenna currents. In order to apply the results of a study of mutual impedance to array pattern effects, some assumptions must be made regarding the distribution of the current on the radiating element. The usual assumption is that the mutually induced currents are distributed on the antenna in a form identical to that the current would assume on a single driven dipole in free space.<sup>†</sup> It is further assumed that the measurement of the terminal current gives a true indication of the magnitude of the current on the antenna.

For dipoles, there appears to be sufficient justification for the latter assumption if the coupling between feed lines carrying travelling waves, which may give rise to directional coupling, is negligible. The former assumption is generally conceded to be valid for very thin dipoles. If the dipoles are thick, both of the above assumptions may be very poor depending upon the length and the length-to-diameter ratio of the dipole.<sup>‡</sup> The current distribution on a thick dipole can vary considerably from that on a thin dipole when the total dipole length is near one wavelength. However, in this study the dipoles are either physically short dipoles or thin half-wavelength dipoles and it is found that the free-space current distribution on a half-wavelength dipole is relatively insensitive to diameter variation. Thus, one would expect reasonable correlation of

<sup>†</sup> This assumption was also used when we said that the self and mutual impedances of Eq. (4) were the same as those of Eq. (1).

<sup>‡</sup> J. D. Kraus, Antennas (McGraw-Hill, New York, 1950).

measured data for thick half-wavelength dipoles with computed data for thin half-wavelength dipoles.

The formulas for the mutual impedance between two thin half-wavelength dipoles, based on the above assumptions, are well known.<sup>†</sup> For this particular case, a sinusoidal current distribution on the  $m^{\text{th}}$  dipole is assumed:

$$I_m = I_1 \cos 2\pi(x - x_m) \quad , \quad |x - x_m| \leq \frac{1}{4} \quad (11)$$

for a dipole centered at the point  $(x_m, y_m, z_m)$  and aligned in the  $x$ -direction. Note that the dipole location is normalized by the free-space wavelength ( $x_m = X_m/\lambda$ ,  $y_m = Y_m/\lambda$ , and  $z = Z/\lambda$ ) which is convenient for our purposes because the product of the wave number  $k$  and the unnormalized distance  $R$  becomes simply  $2\pi r$  where  $r$  is now normalized. Throughout this section on mutual coupling, the element locations will be normalized by the wavelength.

Once the current distribution on the "transmitting" dipole is known [Eq. (11)], the electric field in all space for this dipole is determined. Then, the mutual impedance is computed from the formula

$$Z_{nm} = - \frac{1}{I_m(0) I_n(0)} \int_{\text{ant } n} I_n(u) \bar{E}_m(u) \cdot \bar{i}_u du \quad (12)$$

where  $\bar{i}_u$  is a unit vector in the direction of dipole  $n$ ,  $\bar{E}_m(u)$  is the vector electric field at the  $n^{\text{th}}$  dipole due to antenna  $m$ , and  $I_n(u)$  is the current distribution on the  $n^{\text{th}}$  dipole. The terminal currents of the two dipoles are  $I_m(0)$  and  $I_n(0)$ , respectively. If the  $n^{\text{th}}$  dipole, located at  $(x_n, y_n, z_n)$ , is parallel to the  $m^{\text{th}}$  dipole (that is, dipole  $n$  is also  $x$ -directed), then the assumed current distribution is

$$I_n = I_2 \cos 2\pi(x - x_n) \quad , \quad |x - x_n| \leq \frac{1}{4} \quad (13)$$

and the unit vector  $\bar{i}_u$  becomes  $\bar{i}_x$ , the  $x$ -directed unit vector. Thus, Eq. (12) can be written as

$$Z_{nm}^{(xx)} = - \frac{1}{I_1} \int_{x_n - 1/4}^{x_n + 1/4} (E_m)_x \cos 2\pi(x - x_n) dy \quad (14)$$

where the superscripts indicate that dipoles  $m$  and  $n$  are both  $x$ -aligned. The notation  $(E_m)_x$  implies that only the  $x$ -component of the electric field is used in the equation.

If, on the other hand, the  $n^{\text{th}}$  dipole is oriented perpendicular to the  $m^{\text{th}}$  dipole, then the unit vector  $\bar{i}_u$  becomes the  $y$ -directed unit vector  $\bar{i}_y$  and  $du = dy$ . Only the radial component (cylindrical coordinates) of the electric field  $(E_m)_\rho$  acts on the dipole in this case. Thus,

$$Z_{nm}^{(yx)} = - \frac{1}{I_1} \int_{y_n - 1/4}^{y_n + 1/4} \frac{(y - y_m)}{\rho} (E_m)_\rho \cos 2\pi(y - y_n) dy \quad (15)$$

where  $\rho$  is the radius in a cylindrical coordinate system centered at  $(x_m, y_m, z_m)$  and has the value  $\sqrt{(y - y_m)^2 + (z_n - z_m)^2}$ . Also, we have used the relation  $\bar{i}_y \cdot \bar{i}_\rho = (y - y_m)/\rho$ , and the assumed sinusoidal current distribution on the  $n^{\text{th}}$  dipole is

$$I_n = I_2 \cos 2\pi(y - y_n) \quad , \quad |y - y_n| < \frac{1}{4} \quad (16)$$

<sup>†</sup> J.D. Kraus, Antennas (McGraw-Hill, New York, 1950).



Equations (14) and (15) have been evaluated for dipoles in free space and for dipoles located parallel to and at height  $s$  above a perfectly conducting ground plane. The appropriate formulas are tabulated in Table III-2. Also given in the table are the asymptotic limits,  $r = \sqrt{r_n^2 - r_m^2} \gg 1$ , for the mutual impedance of collinear dipoles (the E-plane limit where  $y_n = y_m$  and  $z_n = z_m$ ) and of parallel dipoles (the H-plane limit where  $x_n = x_m$  and  $z_n = z_m$ ). Some of the formulas in Table III-2 can be written in terms of tabulated functions, but for computational purposes it is more convenient to retain the integral forms.

A similar development can be performed for electrically short dipoles. In this case, the formulas are considerably simplified because an accurate approximation is that the electric field at the  $n^{\text{th}}$  dipole due to the  $m^{\text{th}}$  dipole is uniform and can, therefore, be taken outside the integral. The appropriate formulas, normalized with respect to the free-space radiation resistance  $R_r$  of an isolated dipole of equal length, are tabulated in Table III-3. The previously defined E- and H-plane asymptotic limits are also given in the table.

### 3. Matrix Formulation of Mutual Impedance Effects

The relationship of Eq. (4) gives the voltage on the  $m^{\text{th}}$  antenna in terms of the currents flowing on all antennas in the array. Similar equations can be written for all other elements in the array. For large arrays it is convenient to use matrix notation for this system of equations:

$$V = [Z] \cdot I \quad (17)$$

where  $V$  and  $I$  are column matrices and  $[Z]$  is a square, symmetrical matrix. The diagonal elements of the impedance matrix  $Z_{mm}$  are the self-impedances of the various antennas in the array.

An additional requirement for the straightforward applications of Eq. (17) is that one set of variables, the terminal voltages (or currents), be constrained by taking a sufficient description of the driving network into the equation. For a linearly polarized array (a single,  $x$ -aligned dipole at each location is assumed in the present study), the dipoles are assumed to be fed by independent constant voltage generators, with independently adjustable open-circuit voltages  $v_m$  and with generator impedances  $Z_{gm}$ . Schematically, the circuit of each dipole is of the form shown in Fig. III-62 and the relationship for the  $m^{\text{th}}$  source becomes

$$V_m = v_m - Z_{gm} I_m \quad (18)$$

For simplicity, and since it is the usual case for large arrays, all generator impedances are considered equal with the value  $Z_g$ . It is also assumed that all element self-impedances are identical ( $Z_{mm} = Z_a$ , all  $m$ ); that is, all elements are assumed to be identical and the ground plane (if any) is assumed to be sufficiently larger than the array so that ground plane edge effects are negligible. All matching impedances are assumed to be included in  $Z_g$ .

For this type of drive, Eq. (17) can be rewritten in terms of the drive voltages  $v_m$  as

$$v = \{[Z] + Z_g [U]\} \cdot I \quad (19)$$

where  $[U]$  is the unit matrix. Equation (19) can be simply written as

$$v = [Z] I \quad (20)$$

where the diagonal elements of the impedance matrix now include the generator impedances ( $Z_{mm} = Z_a + Z_g$ , all  $m$ ).

TABLE III-2  
MUTUAL IMPEDANCE FORMULAS FOR THIN HALF-WAVELENGTH DIPOLES

Mutual Impedance Formula	E-Plane Limit	H-Plane Limit
Dipoles in Free Space (No Ground Plane)		
$Z_{21}^{(xx)}(r_o) = j30 \int_{x_o - 1/4}^{x_o + 1/4} \left[ \frac{\exp[-j2\pi r_1]}{r_1} + \frac{\exp[-j2\pi r_2]}{r_2} \right] \cos 2\pi(x - x_o) dx$	$\frac{-j15}{4} \frac{\exp[-j2\pi x_o]}{x_o^2}$	$-j \frac{60}{\pi} \frac{\exp[-j2\pi y_o]}{y_o}$
$Z_{21}^{(xy)}(r_o) = -j30 \int_{y_o - 1/4}^{y_o + 1/4} \left[ \left(x_o - \frac{1}{4}\right) \frac{\exp[-j2\pi r_1]}{r_1} + \left(x_o + \frac{1}{4}\right) \frac{\exp[-j2\pi r_2]}{r_2} \right] \frac{\cos 2\pi(y - y_o)}{y} dy$	0	0
Dipoles at Height $s$ Above Ground		
$Z_{21}^{(xx)}(r_o) = j30 \int_{x_o - 1/4}^{x_o + 1/4} \left[ \frac{\exp[-j2\pi r_1]}{r_1} - \frac{\exp[-j2\pi(r_1^2 + 4s^2)^{1/2}]}{(r_1^2 + 4s^2)^{1/2}} + \frac{\exp[-j2\pi r_2]}{r_2} - \frac{\exp[-j2\pi(r_2^2 + 4s^2)^{1/2}]}{(r_2^2 + 4s^2)^{1/2}} \right] \cos 2\pi(x - x_o) dx$	$-j15\pi^2 \frac{\exp[-j2\pi x_o]}{x_o^3}$	$-240s^2 \frac{\exp[-j2\pi y_o]}{y_o^2}$
$Z_{21}^{(xy)}(r_o) = -j30 \int_{y_o - 1/4}^{y_o + 1/4} \left( \left(x_o - \frac{1}{4}\right) \left[ \frac{\exp[-j2\pi r_1]}{r_1 y} - \frac{y \cdot \exp[-j2\pi(r_1^2 + 4s^2)^{1/2}]}{\rho^2(r_1^2 + 4s^2)^{1/2}} \right] + \left(x_o + \frac{1}{4}\right) \left[ \frac{\exp[-j2\pi r_2]}{r_2 y} - \frac{y \cdot \exp[-j2\pi(r_2^2 + 4s^2)^{1/2}]}{\rho^2(r_2^2 + 4s^2)^{1/2}} \right] \right) \cos 2\pi(y - y_o) dy$	0	0
$r_o = (x_o^2 + y_o^2)^{1/2} \qquad r_1 = \left[(x - \frac{1}{4})^2 + y^2\right]^{1/2}$ $\rho = (y^2 + 4s^2)^{1/2} \qquad r_2 = \left[(x + \frac{1}{4})^2 + y^2\right]^{1/2}$		

TABLE III-3  
MUTUAL IMPEDANCE FORMULAS FOR SHORT DIPOLES ( $L \ll \lambda$ )

Mutual Impedance Formulas	E-Plane Limit	H-Plane Limit
Dipoles in Free Space (No Ground Plane)		
$\frac{Z_{21}^{(xx)}(r_o)}{R_r} = i \frac{3}{4\pi} \left[ \frac{\exp[-j2\pi r_o]}{r_o} \left( \frac{y_o}{r_o} \right)^2 + \left( \frac{j}{2\pi r_o} + \frac{1}{4\pi^2 r_o^2} \right) \frac{2x_o^2 - y_o^2}{r_o^2} \right]$	$- \frac{3}{4\pi^2} \frac{\exp[-j2\pi x_o]}{x_o^2}$	$i \frac{3}{4\pi} \frac{\exp[-j2\pi y_o]}{y_o}$
$\frac{Z_{21}^{(xy)}(r_o)}{R_r} = -i \frac{3}{4\pi} \frac{\exp[-j2\pi r_o]}{r_o} \cdot \frac{x_o y_o}{r_o^2} \left[ 1 - 3 \left( \frac{j}{2\pi r_o} + \frac{1}{4\pi^2 r_o^2} \right) \right]$	0	0
Dipoles at Height $s$ Above Ground		
$\frac{Z_{21}^{(xx)}(r_o)}{R_r} = i \frac{3}{4\pi} \frac{\exp[-j2\pi r_o]}{r_o} \left[ \left( \frac{y_o}{r_o} \right)^2 + \frac{1}{2\pi r_o} \left( i + \frac{1}{2\pi r_o} \right) \frac{2x_o^2 - y_o^2}{r_o^2} \right]$ $- i \frac{3}{4\pi} \frac{\exp[-j2\pi r_1]}{r_1} \left[ \frac{y_o^2 + 4s^2}{r_1^2} + \frac{1}{2\pi r_1} \left( i + \frac{1}{2\pi r_1} \right) \frac{2x_o^2 - y_o^2 - 4s^2}{r_1^2} \right]$	$- i \frac{3}{\pi} s^2 \frac{\exp[-j2\pi x_o]}{x_o^3}$	$- 3s^2 \frac{\exp[-j2\pi y_o]}{y_o^2}$
$\frac{Z_{21}^{(xy)}(r_o)}{R_r} = -i \frac{3}{4\pi} \frac{\exp[-j2\pi r_o]}{r_o} \cdot \frac{x_o y_o}{r_o^2} \left[ 1 - \frac{3}{2\pi r_o} \left( i + \frac{1}{2\pi r_o} \right) \right]$ $+ i \frac{3}{4\pi} \frac{\exp[-j2\pi r_1]}{r_1} \cdot \frac{x_o y_o}{r_1^2} \left[ 1 - \frac{3}{2\pi r_1} \left( i + \frac{1}{2\pi r_1} \right) \right] \cdot \sqrt{1 + \frac{2s^2}{y_o^2}}$	0	0
$r_o = \sqrt{x_o^2 + y_o^2}$ $r_1 = \sqrt{x_o^2 + y_o^2 + 4s^2}$	$R_r = \frac{2\pi}{3} \left( \frac{L}{\lambda} \right)^2 \sqrt{\frac{\mu}{\epsilon}}$ $L_o = \frac{1}{I(0)} \int_{-L/2}^{L/2} I(z) dz$	

For an array designed to transmit a circularly polarized electromagnetic wave (crossed dipoles at each location in the array), the above formulation is inadequate.<sup>†</sup> First of all, the relation of Eq. (17) must be expanded to include the coupling between dipoles that are perpendicular to each other:

$$\begin{bmatrix} V^{(x)} \\ V^{(y)} \end{bmatrix} = \begin{bmatrix} Z^{(xx)} & Z^{(xy)} \\ Z^{(yx)} & Z^{(yy)} \end{bmatrix} \begin{bmatrix} I^{(x)} \\ I^{(y)} \end{bmatrix} \quad (21)$$

where  $V^{(x)}$  and  $I^{(x)}$  are column matrices of the voltages and currents on the x-aligned dipoles, and  $V^{(y)}$  and  $I^{(y)}$  are the corresponding matrices for the y-aligned dipoles. The submatrices of the impedance matrix are square, symmetrical matrices relating the terminal voltages and currents of the elements according to the superscripts. For example,  $Z^{(xy)}$  is the matrix relating the open-circuit voltages induced on the x-aligned dipoles due to currents flowing on the y-aligned dipoles.

In much the same manner as for the linearly polarized array, a suitable description of the network which drives the dipoles must be included in Eq. (21). A common type of feed circuit for obtaining circularly polarized waves from crossed dipoles is a 3-db coupler, as indicated in Fig. III-63. Port 1 of the coupler is fed by a voltage generator, with the independently adjustable open-circuit voltage,  $V_m$  and with generator impedance  $Z_g$  (for the  $m^{\text{th}}$  dipole pair), while port 2 is passively terminated with an impedance of value  $Z_t$ . The x-aligned dipole and the y-aligned dipole are connected to ports 3 and 4, respectively.

For the following analysis, a perfect 3-db coupler with characteristic impedance  $R_o + j0$  is assumed to drive each dipole pair as indicated in the equivalent circuit of Fig. III-64 (the characteristic impedance must be real because of the lossless condition). The effect of the dipoles is represented in the figure by the driving impedances  $Z_{D_m}^x$  and  $Z_{D_m}^y$  for the  $m^{\text{th}}$  x-aligned and y-aligned dipoles, respectively. In the following analysis, it is convenient to include the matching reactance  $jX_T$  with the element driving impedances to obtain the equivalent load impedances  $Z_m^x$  and  $Z_m^y$  at ports 3 and 4, respectively. Both  $Z_m^x$  and  $Z_m^y$  will depend on the scan angle  $(\phi_o, \theta_o)$ .

The behavior of the coupler is most easily described in terms of the scattering variables  $a_n$  and  $b_n$  at each port as defined by

$$\left. \begin{aligned} a_n &= \frac{V_n + R_o I_n}{2\sqrt{R_o}} \\ b_n &= \frac{V_n - R_o I_n}{2\sqrt{R_o}} \end{aligned} \right\}, \quad n = 1, 2, 3, 4 \quad (22)$$

The  $a_n$ 's and  $b_n$ 's are related by the equation

$$b = [S] \cdot a \quad (23)$$

where  $[S]$  is the unitary scattering matrix:

<sup>†</sup> An equivalent, but somewhat different, derivation of the relationships for hybrid-fed, crossed-dipole pair arrays has been made by J. L. Allen in private communications.

$$\frac{1}{\sqrt{2}} \begin{bmatrix} 0 & 0 & j & 1 \\ 0 & 0 & 1 & j \\ j & 1 & 0 & 0 \\ 1 & j & 0 & 0 \end{bmatrix}$$

The source applied to port 1 and the terminations on the other three ports give the following constraint relations between the  $a_n$ 's and  $b_n$ 's:

$$\left. \begin{aligned} a_1 &= \Gamma_g b_1 + \frac{\sqrt{R_o}}{Z_g + R_o} v_m \\ a_2 &= \Gamma_t b_2 \\ a_3 &= \Gamma_m^x b_3 \\ a_4 &= \Gamma_m^y b_4 \end{aligned} \right\} \quad (24)$$

where

$$\Gamma_i = \frac{Z_i - R_o}{Z_i + R_o}$$

The constraint relations given in Eq. (24) can be written in matrix form as

$$a] = [\Gamma] \cdot b] + a_s] \quad (25)$$

where  $[\Gamma]$  is a diagonal matrix with the reflection coefficients as elements, and  $a_s]$  is a column matrix representing the source:

$$a_s] = \begin{bmatrix} a_{in} \\ 0 \\ 0 \\ 0 \end{bmatrix}, \quad a_{in} = \frac{\sqrt{R_o}}{Z_g + R_o} v_m \quad (26)$$

When Eq. (25) is used in Eq. (23), a matrix equation for the four unknown  $b_n$ 's is obtained:

$$\{[U] - [S] \cdot [\Gamma]\} \cdot b] = [S] \cdot a_s] \quad (27)$$

The coefficient matrix in Eq. (27),  $\{[U] - [S] \cdot [\Gamma]\}$ , is

$$\frac{1}{\sqrt{2}} \begin{bmatrix} \sqrt{2} & 0 & j\Gamma_m^x & \Gamma_m^y \\ 0 & \sqrt{2} & \Gamma_m^x & j\Gamma_m^y \\ j\Gamma_g & \Gamma_t & \sqrt{2} & 0 \\ \Gamma_g & j\Gamma_t & 0 & \sqrt{2} \end{bmatrix}$$

while the source matrix  $[S] = a_s$  is

$$\begin{bmatrix} 0 \\ 0 \\ -ja_{in}/\sqrt{2} \\ -a_{in}/\sqrt{2} \end{bmatrix}$$

When Eq. (27) is solved for the  $b_n$ 's, the following results are found

$$\left. \begin{aligned} b_1 &= -\frac{a_{in}}{2} \left( \frac{\Gamma_m^x - \Gamma_m^y + 2\Gamma_m^y \Gamma_t}{D} \right) \\ b_2 &= j \frac{a_{in}}{2} \left( \frac{\Gamma_m^x + \Gamma_m^y}{D} \right) \\ b_3 &= -j \frac{a_{in}}{\sqrt{2}} \left( \frac{1 + \Gamma_m^y \Gamma_t}{D} \right) \\ b_4 &= -\frac{a_{in}}{\sqrt{2}} \left( \frac{1 - \Gamma_m^x \Gamma_t}{D} \right) \end{aligned} \right\} \quad (28)$$

where

$$D = 1 + \Gamma_m^x \Gamma_m^y \Gamma_g \Gamma_t + \frac{1}{2} (\Gamma_m^x - \Gamma_m^y) (\Gamma_g - \Gamma_t)$$

In practice, one would normally choose  $Z_g$  and  $Z_t$  to be the same; furthermore, they would usually be made equal to  $R_0 + j0$ , the characteristic impedance of the coupler, which eliminates the problems of multiple reflections due to mismatches. The characteristic impedance of the coupler will (in a later section) be chosen equal to the geometric mean of the real parts of  $Z_D^x(0, 0)$  and  $Z_D^y(0, 0)$  which maximizes the array gain when the array is phased to point a beam at broadside. In the meantime, we shall assume a matched source and a matched orthogonal port termination which results in the following simple expressions for the  $b_n$ 's

$$\left. \begin{aligned} b_1 &= -\frac{a_{in}}{2} (\Gamma_m^x - \Gamma_m^y) \\ b_2 &= j \frac{a_{in}}{2} (\Gamma_m^x + \Gamma_m^y) \\ b_3 &= -j \frac{a_{in}}{\sqrt{2}} \\ b_4 &= -\frac{a_{in}}{\sqrt{2}} \end{aligned} \right\} \quad , \quad a_{in} = \frac{v_m}{2\sqrt{R_0}} \quad (29)$$

Equations (24) and (29) give complete terminal information for the couplers, which is required for relating the dipole currents to the source voltage. To proceed, we note that the current into the  $m^{\text{th}}$  x-aligned dipole is just the current out of port 3 of the  $m^{\text{th}}$  coupler, while the terminal voltage is related to the voltage at port 3 by

$$V_m^{(x)} = V_{3m} - jX_T I_m^{(x)} \quad (30)$$

where

$$\begin{aligned} V_{3m} &= \sqrt{R_o} (a_3 + b_3) \\ &= -j \frac{V_m}{2\sqrt{2}} (1 + \Gamma_m^x) \end{aligned}$$

If the  $m^{\text{th}}$  x-aligned dipole is removed, an open-circuit voltage of value  $-jV_m/\sqrt{2}$  appears at port 3. Thus, to the antenna, the coupler appears as a voltage source with open-circuit voltage  $-jV_m/\sqrt{2}$  and with generator impedance  $R_o$ . Equation (30) can therefore be written as

$$V_m^{(x)} = -j \frac{V_m}{\sqrt{2}} - (R_o + jX_T) I_m^{(x)} \quad (31)$$

A similar development for the y-aligned dipole gives

$$V_m^{(y)} = -\frac{V_m}{\sqrt{2}} - (R_o + jX_T) I_m^{(y)} \quad (32)$$

The use of Eqs. (31) and (32) in Eq. (21) gives the result:

$$\begin{bmatrix} jV \\ V \end{bmatrix} = -\sqrt{2} \begin{bmatrix} Z^{(xx)} & Z^{(xy)} \\ Z^{(yx)} & Z^{(yy)} \end{bmatrix} \begin{bmatrix} I^{(x)} \\ I^{(y)} \end{bmatrix} \quad (33)$$

where now  $Z_{mm} = R_o + Z_a + jX_T$ , for all  $m$ .

The matrix equations, given by Eq. (20) for linearly polarized arrays and by Eq. (33) for circularly polarized arrays, relate the terminal currents of the antennas to the open-circuit voltages of the sources. Since the computation of the element-driving impedances and of the array far-field pattern requires a knowledge of the currents flowing on the various dipoles, it is necessary to solve the above equations for the antenna currents. This amounts to finding the admittance matrix  $[Y]$  such that  $[Y]$  is the inverse of  $[Z]$  for the particular array. For a linearly polarized array a typical element current is given by

$$I_m = \sum_n Y_{mn} V_n$$

and by

$$I_m^{(x)} = -\frac{1}{\sqrt{2}} \sum_n \{jY_{mn}^{(xx)} + Y_{mn}^{(xy)}\} V_n$$

for a circularly polarized array.

Up to this point, the open-circuit source voltages were allowed to have arbitrary amplitude and phase. Now it is convenient to assume that the voltages are amplitude tapered and progressively phased so that the drive voltages are related to the desired pointing angle by

$$V_m(\tau_o, \mu_o) = a_m \exp[-j2\pi(x_m \tau_o + y_m \mu_o)] \quad (34)$$

where the  $a_m$  are the real amplitude taper coefficients, and  $(\phi_o, \theta_o)$  defines the angle at which it is desired to point the beam (in the geometry of Fig. III-65) through the equivalences

$$\left. \begin{aligned} \tau_o &= \sin \Theta_o \cos \phi_o \\ \mu_o &= \sin \Theta_o \sin \phi_o \end{aligned} \right\} \quad (35)$$

It is now a straightforward problem to determine the element-driving impedance as a function of the desired pointing angle  $(\phi_o, \Theta_o)$ :

$$\begin{aligned} Z_{D_m}(\tau_o, \mu_o) &= \frac{V_m}{I_m} - Z_g \\ &= \left( \sum_n \frac{a_n}{a_m} Y_{mn} \exp \{-j2\pi [(x_n - x_m) \tau_o + (y_n - y_m) \mu_o]\} \right)^{-1} - Z_g \end{aligned} \quad (36)$$

for linearly polarized arrays, and

$$\begin{aligned} Z_{D_m}^x(\tau_o, \mu_o) &= \left( \sum_n \frac{a_n}{a_m} [(Y_{mn}^{(xx)} - jY_{mn}^{(xy)})] \right. \\ &\quad \times \exp \{-j2\pi [(x_n - x_m) \tau_o + (y_n - y_m) \mu_o]\} \Big)^{-1} - R_o - jX_T \\ Z_{D_m}^y(\tau_o, \mu_o) &= \left( \sum_n \frac{a_n}{a_m} [Y_{mn}^{(yy)} + jY_{mn}^{(yx)}] \right. \\ &\quad \times \exp \{-j2\pi [(x_n - x_m) \tau_o + (y_n - y_m) \mu_o]\} \Big)^{-1} - R_o - jX_T \end{aligned} \quad (37)$$

for circularly polarized arrays.

There are two other quantities of interest for a circularly polarized array: the input impedance at port 1  $Z_{1_m}$  and the power lost in the terminated port. Both of these quantities are functions of scan angle and are given by

$$\begin{aligned} Z_{1_m}(\tau_o, \mu_o) &= \frac{V_1}{I_1} = R_o \left( \frac{a_1 + b_1}{a_1 - b_1} \right) \\ &= R_o \left\{ \frac{1 - \frac{1}{2} [\Gamma_m^x(\tau_o, \mu_o) - \Gamma_m^y(\tau_o, \mu_o)]}{1 + \frac{1}{2} [\Gamma_m^x(\tau_o, \mu_o) - \Gamma_m^y(\tau_o, \mu_o)]} \right\} \end{aligned} \quad (38)$$

and

$$\begin{aligned} \frac{P_{D_m}}{P_{avail}}(\tau_o, \mu_o) &= \left| \frac{b_2}{a_{in}} \right|^2 \\ &= \frac{1}{4} |\Gamma_m^x(\tau_o, \mu_o) + \Gamma_m^y(\tau_o, \mu_o)|^2 \end{aligned} \quad (39)$$

for

$$Z_g = Z_t = R_o + j0$$

The above development is designed to give an exact solution for the currents in a finite array (within the bounds set by the assumptions which have been made). Due to the complexity and time



consumption involved in inverting large matrices, the size of an array, which can be solved exactly is severely restricted (to the order of 100 elements). Exact solutions for even the small arrays of this study are, however, quite illuminating as will be seen.

#### 4. "Element Gain Function" Concept

As discussed in a previous report,<sup>†</sup> the gain function concept has considerable practical utility because the gain of a "large" array is completely specified by the element gain function  $g(\tau_o, \mu_o, \bar{e}_p)$  of a typical element in the array (assuming a regularly spaced array):

$$G(\tau_o, \mu_o, \bar{e}_p) = \eta_a N_T g(\tau_o, \mu_o, \bar{e}_p) \quad (40)$$

where  $\eta_a$  is the efficiency of the amplitude taper,  $N_T$  is the total number of elements in the array, and  $\bar{e}_p$  is a unit polarization vector. The array gain formula of Eq. (40) is an approximation which is only accurate when the array is large enough so that almost all elements have essentially identical gain functions.

Only the gain of a typical element is required in Eq. (40), so attention can be confined to the element gain function of the center element in an array that is just large enough so that the gain is essentially unchanged by an enlargement of the array. The element gain function found in this manner (experimentally or analytically) will be nearly identical to that of a typical element in a large array. Therefore, much can be learned about large arrays while attention is confined to relatively small arrays.

The element gain functions for elements not in the center of a small array are also of considerable interest, since they give a quantitative measure of the effect of asymmetry and edge effect.

The gain of an array is defined as the ratio of the main beam peak power density to the total power available to the array from its generators. In a similar manner, the element gain function of the  $m^{\text{th}}$  element in the array is defined as the gain of the array when only the  $m^{\text{th}}$  element is driven, while all other elements are terminated in their normal generator impedances. It follows directly from this definition that, relative to a sampling polarization specified by the unit vector  $\bar{e}_p$ , the gain function of the  $m^{\text{th}}$  element is

$$g_m(\tau_o, \mu_o, \bar{e}_p) = 4\pi \frac{\left| \bar{e}_p \cdot \frac{r}{\sqrt{\eta}} \bar{E}_m^t(\tau_o, \mu_o) \right|^2}{\frac{|v_m|^2}{4R_g}} \quad (41)$$

where  $\bar{E}_m^t(\tau, \mu)$  is the total field strength at some radius  $r = R/\lambda \gg 2D^2/\lambda^2$  (far-field condition) when the antenna in question is excited by a generator with open-circuit voltage  $a_m \exp[-j2\pi(x_m \tau + y_m \mu)]$ , and with generator impedance  $Z_g = R_g + jX_g$ . All other elements are terminated with impedance  $Z_g$ . The quantity  $\eta$  is the intrinsic impedance of free space.

For the general case of crossed radiators, it follows that

$$\begin{aligned} \bar{E}_m^t(\tau, \mu) = & \sum_n [\bar{e}_x E_n^{(x)}(\tau, \mu) I_n^{(x)} + \bar{e}_y E_n^{(y)}(\tau, \mu) I_n^{(y)}] \\ & \times \exp\{j2\pi[(x_r - x_m)\tau + (y_n - y_m)\mu]\} \end{aligned}$$

<sup>†</sup> TR-236, p. 208.

where  $\bar{e}_x$  and  $\bar{e}_y$  denote the unit polarization vectors of x- and y-aligned dipoles as a function of  $(\varphi, \Theta)$ , and  $E_n^{(x)}(\tau, \mu)$  and  $E_n^{(y)}(\tau, \mu)$  are the scalar E-fields of the  $n^{\text{th}}$  x- and y-aligned dipoles (including image effects if a ground plane is used) per unit exciting current. Since the pattern for an x-aligned dipole,  $f_i^x(\tau, \mu)$ , is related to the E-field of the dipole by the relation

$$f_i^x(\tau, \mu) = \frac{r}{\sqrt{\eta}} E^{(x)}(\tau, \mu)$$

(and similarly for a y-aligned dipole), Eq. (41) can be written as

$$\begin{aligned} g_m(\tau_o, \mu_o, \bar{e}_p) = & 16\pi R_g \left| (\bar{e}_p \cdot \bar{e}_x) f_i^x(\tau_o, \mu_o) \sum_n \frac{I_n^{(x)}}{a_m} \right. \\ & \times \exp \{ j2\pi [(x_n - x_m) \tau_o + (y_n - y_m) \mu_o] \} \\ & + (\bar{e}_p \cdot \bar{e}_y) f_i^y(\tau_o, \mu_o) \sum_n \frac{I_n^{(y)}}{a_m} \\ & \left. \times \exp \{ j2\pi [(x_n - x_m) \tau_o + (y_n - y_m) \mu_o] \} \right|^2 \end{aligned} \quad (42)$$

A significant simplification of the gain expression results when it is noted that the current on the  $n^{\text{th}}$  x-aligned dipole due to a voltage applied to the  $m^{\text{th}}$  coupler is

$$I_n^{(x)} = \frac{-j}{\sqrt{2}} a_m [Y_{nm}^{(xx)} - jY_{nm}^{(xy)}]$$

and therefore by Eq. (37)

$$\begin{aligned} \sum_n \frac{I_n^{(x)}}{a_m} \exp \{ j2\pi [(x_n - x_m) \tau_o + (y_n - y_m) \mu_o] \} = & -\frac{j}{\sqrt{2}} \\ & \times \frac{1}{Z_{D_m}^x(-\tau_o, -\mu_o) + R_o + jX_T} \end{aligned}$$

where we have assumed no amplitude tapering ( $a_m = a$ , all  $m$ ). We have also made use of the fact that the submatrices of the  $[Y]$  matrix are symmetrical. The notation for the scan angles  $(-\tau_o, -\mu_o)$  implies that  $\varphi_o$  is replaced by  $\varphi_o + \pi$  in Eq. (35) which amounts to scan from broadside in the opposite direction in the vertical scan plane specified by  $\varphi = \varphi_o$ . A similar development shows that the second sum in Eq. (42) is just

$$-\frac{1}{\sqrt{2}} \cdot \frac{1}{Z_{D_m}^y(-\tau_o, -\mu_o) + R_o + jX_T}$$

Therefore, the element gain function for the  $m^{\text{th}}$  crossed-dipole pair in the array is

$$g_m(\tau_o, \mu_o, \bar{e}_p) = 8\pi R_g \left| \frac{(\bar{e}_p \cdot \bar{e}_x) f_i^x(\tau_o, \mu_o)}{Z_m^x(-\tau_o, -\mu_o) + R_o} - j \frac{(\bar{e}_p \cdot \bar{e}_y) f_i^y(\tau_o, \mu_o)}{Z_m^y(-\tau_o, -\mu_o) + R_o} \right|^2 \quad (43)$$

where the element driving impedances  $Z_m^x(-\tau_o, -\mu_o)$  and  $Z_m^y(-\tau_o, -\mu_o)$  include the matching reactances  $jX_T$ . The reflection coefficient at port 3 of the  $m^{\text{th}}$  coupler was defined in Sec. B-3 of this chapter as

$$\Gamma_m^x = \frac{Z_m^x - R_o}{Z_m^x + R_o}$$

so

$$\frac{1}{Z_m^x(-\tau_o, -\mu_o) + R_o} = \frac{1 - \Gamma_m^x(-\tau_o, -\mu_o)}{2R_o}$$

and similarly for the y-aligned dipole. Thus, Eq. (43) can be written in the alternate form

$$g_m(\tau_o, \mu_o, \bar{e}_p) = 2\pi \frac{R_g}{R_o^2} |(\bar{e}_p \cdot \bar{e}_x) f_i^x(\tau_o, \mu_o) [1 - \Gamma_m^x(-\tau_o, -\mu_o)] - j(\bar{e}_p \cdot \bar{e}_y) f_i^y(\tau_o, \mu_o) [1 - \Gamma_m^y(-\tau_o, -\mu_o)]|^2 \quad (44)$$

A similar development for an array composed of x-aligned dipoles (linearly polarized array) leads to the following result

$$g_m(\tau_o, \mu_o, \bar{e}_p) = 16\pi R_g \left| (\bar{e}_p \cdot \bar{e}_x) \frac{f_i^x(\tau_o, \mu_o)}{Z_{D_m}(-\tau_o, -\mu_o) + Z_g} \right|^2$$

which can be written as

$$g_m(\tau_o, \mu_o, \bar{e}_p) = 4R_a R_g \left| \frac{\bar{e}_p \cdot \bar{e}_x}{Z_{D_m}(-\tau_o, -\mu_o) + Z_g} \right|^2 g_{i_{\max}}(\tau_o, \mu_o) \quad (45)$$

when it is observed that the maximum matched gain obtainable from an isolated dipole (including image effects if a ground plane is used) is

$$g_{i_{\max}}(\tau_o, \mu_o) = \frac{4\pi}{R_a} |f_i(\tau_o, \mu_o)|^2$$

If the voltage reflection coefficient is defined such that the generator reactance  $jX_g$  is included in the antenna driving impedance

$$\begin{aligned} \Gamma_m(\tau_o, \mu_o) &= \frac{|Z_{D_m}(\tau_o, \mu_o) + jX_g] - R_g}{[Z_{D_m}(\tau_o, \mu_o) + jX_g] + R_g} \\ &= \frac{Z_{D_m}(\tau_o, \mu_o) - Z_g^*}{Z_{D_m}(\tau_o, \mu_o) + Z_g} \end{aligned} \quad (46)$$

then the gain expression of Eq. (45) takes the simple form

$$g_m(\tau_o, \mu_o) = \frac{R_a}{R_g} |\bar{e}_p \cdot \bar{e}_x|^2 |1 - \Gamma_m(-\tau_o, -\mu_o)|^2 g_{i_{\max}}(\tau_o, \mu_o) \quad (47)$$

The formulation given above concisely demonstrates the close connection between the element gain function and the element driving impedance for a dipole (or crossed dipole pair) in the array environment, and therefore has many practical uses. First, it is easily established that to maximize the ratio of the gain of the  $m^{\text{th}}$  element at a particular angle to the gain of the isolated element, one should choose (for the linearly polarized array)

$$Z_g = Z_{D_m}^* (-\tau_1, -\mu_1) \quad (48)$$

where  $(\tau_1, \mu_1)$  represents the angle at which it is desired to maximize the ratio. In a small array (or an irregularly spaced array), this choice will only be optimum for the  $m^{\text{th}}$  element; however, in a large regularly spaced array, the array gain will be maximized at the angle in question because the  $m^{\text{th}}$  element is just a typical element in the array. One possible choice for  $Z_g$  (not necessarily optimum) in a small regularly spaced array is the value of  $Z_g$  which matches the center element when the array is phased for broadside (this is the choice made for most of the arrays investigated in this study).

For the  $m^{\text{th}}$  crossed dipole pair in a regularly spaced, circularly polarized array, the gain function can be shown to be nearly maximum at the angle  $(\tau_1, \mu_1)$  when  $R_o$  and  $X_T$  are chosen such that

$$\left. \begin{aligned} R_o &= \sqrt{R_{D_m}^x(-\tau_1, -\mu_1) \cdot R_{D_m}^y(-\tau_1, -\mu_1)} \\ X_T &= -\frac{1}{2} \left[ X_{D_m}^x(-\tau_1, -\mu_1) + X_{D_m}^y(-\tau_1, -\mu_1) \right] \end{aligned} \right\} \quad (49)$$

In a large array, the choices for  $R_o$  and  $X_T$  given in Eq. (49) will be nearly optimum for maximizing the array gain when the array is phased to point a beam at the angle  $(\tau_1, \mu_1)$ . The above expressions for  $R_o$  and  $X_T$  are somewhat simpler in the case of an infinite array with the dipole pairs placed in a square grid when the array is phased for broadside; that is

$$\left. \begin{aligned} R_o &= R_{D_m}^x(0, 0) \\ X_T &= -X_{D_m}^x(0, 0) \end{aligned} \right\} \quad (50)$$

because  $Z_{D_m}^y(0, 0) = Z_{D_m}^x(0, 0)$  for an infinite array. Since there is complete symmetry for the center dipole pair in a small array with  $2N + 1$  dipole pairs in both dimensions, the relations of Eq. (50) will also apply.

The gain functions for isolated elements (with or without a ground plane) are well known.<sup>†</sup> However, for convenience, they are tabulated in Table III-4 for an x-aligned dipole (for a y-aligned dipole  $\tau$  is replaced by  $\mu$ ).

It is also convenient to tabulate the expressions for the polarization vector  $\vec{e}_p$  for some common types of polarization. These are given in Table III-5 in terms of the previously defined parameters  $(\tau, \mu)$  which are related to the spherical coordinates  $(\varphi, \theta)$  by the equivalences of Eq. (35).

<sup>†</sup>J. D. Kraus, Antennas (McGraw-Hill, New York, 1950).

TABLE III-4 GAIN FUNCTION FORMULAS FOR ISOLATED, x-ALIGNED DIPOLES WITH AND WITHOUT GROUND PLANE	
Type of Element	Gain Function $g_{\max}(\tau, \mu)$
$\lambda/2$ dipole No ground plane	$1.641 \frac{\cos^2(\frac{\pi}{2}\tau)}{1-\tau^2}$
$\lambda/2$ dipole Height $s$ above ground	$\frac{480}{R_a} \frac{\cos^2(\frac{\pi}{2}\tau)}{1-\tau^2} \sin^2(2\pi s \cos \theta)$
Short dipole No ground plane	$1.5(1-\tau^2)$
Short dipole Height $s$ above ground	$6 \frac{R_r}{R_a} (1-\tau^2) \sin^2(2\pi s \cos \theta)$

TABLE III-5 POLARIZATION VECTOR FORMULAS FOR SOME COMMON TYPES OF POLARIZATION	
Type of Polarization	Polarization Vector $\bar{e}_p$
x-directed linear $\bar{e}_p = \bar{e}_x$	$-\sqrt{1-\tau^2} \bar{i}_x + \frac{\tau}{\sqrt{1-\tau^2}} (\mu \bar{i}_y + \cos \theta \bar{i}_z)$
y-directed linear $\bar{e}_p = \bar{e}_y$	$\frac{\mu}{\sqrt{1-\mu^2}} (\tau \bar{i}_x + \cos \theta \bar{i}_z) - \sqrt{1-\mu^2} \bar{i}_y$
Right circular	$\frac{1}{\sqrt{2} \sin \theta} [(\tau \cos \theta -  \mu ) \bar{i}_x + (\mu \cos \theta +  \tau ) \bar{i}_y]$ $-\frac{\sin \theta}{\sqrt{2}} \bar{i}_z$
Left circular	$\frac{1}{\sqrt{2} \sin \theta} [(\tau \cos \theta +  \mu ) \bar{i}_x + (\mu \cos \theta -  \tau ) \bar{i}_y]$ $-\frac{\sin \theta}{\sqrt{2}} \bar{i}_z$
Vectors $\bar{i}_x$ , $\bar{i}_y$ , and $\bar{i}_z$ are Cartesian unit vectors.	

## 5. Some Large Array Approximations

In the previous sections, the formulas developed were quite general, being applicable to thin-dipole arrays of any size with arbitrary element spacing (in a plane) and amplitude tapering. This section, however, will be more specific because the study will be restricted to large arrays with no amplitude tapering and with regularly spaced radiators (rectangular-grid and triangular-grid arrays, for example). When these special conditions are used, the expressions for element current, element-driving impedance, and gain function are simplified.

When we speak of a large array, we imply that the array is large enough so that a negligible fraction of the total number of elements suffer from "edge effects"; that is, most of the elements see an environment which is arbitrarily close to that an element would see in an infinite array. A moderately sized array is sufficient to satisfy these conditions if the array is mounted above a ground plane. However, if the array is in free space (no ground plane), it will have to be quite large, because the rate of decrease of mutual coupling is lower in this case.

If the array is regularly spaced and essentially infinite with no measurable amplitude tapering, all elements will have identical gain functions and driving impedances, and we can confine our attention to the center element. Furthermore, with these assumptions, all drive voltages will have the form

$$v_m = v_o \exp[-j2\pi(x_m\tau_o + y_m\mu_o)]$$

for a beam pointing in the direction  $(\tau_o, \mu_o)$ . Since all element driving impedances are identical, all currents will now bear the same relation to their drive voltages

$$I_m = I_o \exp[-j2\pi(x_m\tau_o + y_m\mu_o)] \quad (51)$$

for a linearly polarized array (in a circularly polarized array  $I_o^{(x)}$  and  $I_o^{(y)}$  will generally be different for a beam not pointed at broadside). In this case Eq. (4) becomes

$$v_o = I_o \sum_m Z_{om} \exp[-j2\pi(x_m\tau_o + y_m\mu_o)]$$

and Eq. (7) becomes

$$Z_D(\tau_o, \mu_o) = Z_a + \sum_{m \neq 0} Z_{om} \exp[-j2\pi(x_m\tau_o + y_m\mu_o)] \quad (52)$$

for the element driving impedance of the center element (or any other element) in a linearly polarized array. It should be noted that the element driving impedance for a large array as given by Eq. (52) does not depend on the generator impedance in contrast to the situation for a small array. Furthermore, the symmetry of the array about the center element (any element of an infinite array) implies that

$$Z_D(-\tau_o, -\mu_o) = Z_D(\tau_o, \mu_o)$$

and, therefore, the gain function is

$$\frac{g_o(\tau_o, \mu_o, \bar{e}_p)}{g_{i_{\max}}(\tau_o, \mu_o)} = \frac{R_a}{R_g} |\bar{e}_p \cdot \bar{e}_x|^2 |1 - \Gamma(\tau_o, \mu_o)|^2 \quad (53)$$

Note that in a large, regularly spaced array the element gain function at the pointing angle  $(\phi_o, \theta_o)$  depends on the impedance at the angle  $(\phi_o, \theta_o)$  in contrast to Eq. (47) where the gain function at the pointing angle  $(\phi_o, \theta_o)$  depends on the impedance at the angle  $(\phi_o + \pi, \theta_o)$ . It is quite clear that the gain function formulas for a circularly polarized array will be similarly modified as the array becomes large.

If the polarization vector  $\bar{e}_p$  equals  $\bar{e}_x$ , then we can obtain an expression for the broadside element gain function as given in a previous report, by using the first formula in Table III-4 in Eq. (53):

$$g_o(0, 0, \bar{e}_x) = \frac{480}{R_D(0, 0)} \sin^2 2\pi s \quad (54)$$

for a large array with regularly spaced, thin, half-wavelength dipoles matched at broadside,  $Z_g = Z_D^*(0, 0)$ , and mounted at height  $s$  above a perfectly conducting ground plane. A formula for the broadside resistance of an element in a rectangular-grid, infinite array has been derived by Stark:<sup>†</sup>

$$R_D(0, 0) = \frac{120}{\pi} \cdot \frac{\sin^2 2\pi s}{D_x D_y} \quad (55)$$

Thus

$$g_o(0, 0, \bar{e}_x) = 4\pi D_x D_y \quad (56)$$

where  $D_x$  and  $D_y$  are the normalized element spacings (with respect to a wavelength) in the  $x$ - and  $y$ -coordinates.

A completely analogous development for a rectangular-grid array without a ground plane ("free-space" array) leads to the result

$$g_o(0, 0, \bar{e}_x) = 2\pi D_x D_y \quad (57)$$

Finally, Eq. (56) can be used in Eq. (40) to obtain the familiar expression for the gain of a large array matched for the beam pointing at broadside

$$G(0, 0, \bar{e}_x) = 4\pi A \eta_a$$

since  $N_T D_x D_y$  is the total normalized array area.

Formulas (56) and (57) can also be shown to be applicable to arrays composed of electrically short dipoles.

The analysis of infinite, rectangular-grid arrays with thin  $x$ -aligned dipoles at each location leads to the following formula (in the notation used above)

$$R_D(\tau_o, \mu_o) = \frac{120}{\pi} \frac{\sin^2 2\pi s}{D_x D_y} \cdot \left[ \frac{\cos^2(\pi \tau_o/2)}{1 - \tau^2} \right] \cdot \left[ \frac{\sin^2 2\pi s \cos \theta_o}{\sin^2 2\pi s} \right] \cdot \frac{1}{\cos \theta_o} \quad (58)$$

for the element driving resistance variation as a function of scan angle  $(\tau_o, \mu_o)$ , for arrays of half-wavelength dipoles above a ground plane. A straightforward extension of Stark's analysis

<sup>†</sup> L. Stark, "Radiation Impedance of a Dipole in an Infinite Array," Formel Technical Document FL60-230, Hughes Aircraft Company (1 May 1960).

can be made to obtain similar formulas for electrically short dipoles and for "free-space" arrays (no ground plane). Table III-6 presents the formulas which are relevant to the arrays investigated in this study. These formulas are very useful for evaluating "edge effects" in small arrays; that is, deviations of the element-driving resistance in a small array relative to the infinite array driving resistance give a measure of "edge effect." Note also that these formulas only apply for scan angles where no grating lobes appear in visible space.

It should be noted that all of the formulas in Table III-6 are the product of the broadside resistance and the scanning factor. The variation of the resistance with scan angle is given by the scanning factor which is unity at broadside. Furthermore, it is easily seen that the scanning factor is just the normalized gain function of an isolated element divided by the aperture factor  $\cos \theta_o$ .

The situation is complicated when the radiators are crossed dipoles, because it is no longer possible to write the element gain function as the product of the gain of an isolated element and an impedance factor. However, one can still obtain expressions for the broadside resistance and element gain for large, crossed-dipole arrays on regularly spaced grids by making use of a property of the mutual impedance between orthogonal dipoles:

$$Z_{21}^{(xy)}(-x_o, y_o, z_o) = -Z_{21}^{(xy)}(x_o, y_o, z_o) \quad (59)$$

and similarly

$$\left. \begin{aligned} Z_{21}^{(xy)}(x_o, -y_o, z_o) &= -Z_{21}^{(xy)}(x_o, y_o, z_o) \\ Z_{21}^{(xy)}(-x_o, -y_o, z_o) &= Z_{21}^{(xy)}(x_o, y_o, z_o) \end{aligned} \right\} \quad (60)$$

TABLE III-6 INFINITE ARRAY DRIVING RESISTANCE FORMULAS AS FUNCTION OF SCAN ANGLE	
Type of Element	Driving Resistance $R_D(\tau_o, \mu_o)$
$\lambda/2$ dipole No ground plane	$\frac{60}{\pi} \cdot \frac{1}{D_x D_y} \left[ \frac{\cos^2(\pi \tau_o/2)}{1 - \tau_o^2} \right] \cdot \frac{1}{\cos \theta_o}$
$\lambda/2$ dipole Height $s$ above ground	$\frac{120}{\pi} \cdot \frac{\sin^2 2\pi s}{D_x D_y} \left[ \frac{\cos^2(\pi \tau_o/2)}{1 - \tau_o^2} \right] \cdot \left[ \frac{\sin^2(2\pi s \cos \theta_o)}{\sin^2(2\pi s)} \right] \cdot \frac{1}{\cos \theta_o}$
Short dipole No ground plane	$\frac{3}{4\pi} \frac{1}{D_x D_y} \cdot \left[ \frac{1 - \tau_o^2}{\cos \theta_o} \right]$
Short dipole Height $s$ above ground	$\frac{3}{2\pi} \frac{\sin^2 2\pi s}{D_x D_y} [1 - \tau_o^2] \cdot \left[ \frac{\sin^2(2\pi s \cos \theta_o)}{\sin^2(2\pi s)} \right] \cdot \frac{1}{\cos \theta_o}$



From the relationships of Eqs. (59) and (60) and the symmetry of a regularly spaced array, it is seen that the effect of the y-aligned dipoles on a typical x-aligned dipole is zero when the array is phased for pointing a beam at broadside. In other words, an x-aligned dipole will "see" only the other x-aligned dipoles. Thus, the broadside resistance for either an x-aligned dipole or a y-aligned dipole will be just that of a dipole in a linearly polarized array (as given by Eq. (55) for half-wavelength dipoles in a rectangular-grid array, for example). In general, the broadside reactances of the y-aligned dipoles will be different from that of the x-aligned dipoles in a regularly spaced array. An exception is the square-grid array ( $D_x = D_y = D$ ) which we will now consider. If the array is matched at broadside,  $R_g = R_o = R_D(0, 0)$  and  $X_T = -X_D(0, 0)$ , then from Eq. (44) the broadside element gain function can be written as

$$g_o(0, 0, \bar{e}_p) = \frac{R_a}{2R_D(0, 0)} g_{i_{\max}}(0, 0) |\bar{e}_p(\varphi_o, 0) \cdot (\bar{i}_x - j\bar{i}_y)|^2$$

since  $\Gamma_1^y(0, 0) = \Gamma_1^x(0, 0)$  and  $\Gamma_o^x(0, 0) = \Gamma_o^y(0, 0) = 0$ . This expression is maximum when the sampling polarization vector is right circular

$$\bar{e}_p(\varphi_o, 0) = \bar{e}_R(\varphi_o, 0) = \frac{1}{\sqrt{2}}(\cos \varphi_o - j \sin \varphi_o)(\bar{i}_x + j\bar{i}_y)$$

Thus

$$g_o(0, 0, \bar{e}_R) = \frac{R_a}{R_D(0, 0)} g_{i_{\max}}(0, 0)$$

which is identical to Eq. (53) for linearly polarized arrays with  $\bar{e}_p = \bar{e}_x$ ,  $\tau_o = \mu_o = 0$ ,  $R_g = R_D(0, 0)$ , and  $\Gamma(0, 0) = 0$ . That is, we have demonstrated that Eqs. (56) and (57) also apply to crossed-dipole arrays with a square grid and either half-wavelength dipoles or electrically short dipoles.

By the use of the relationships developed above, it is possible to compute gain functions and driving point impedances, given expressions for the self and mutual impedances between dipoles (half-wavelength or electrically short) in free space. Even for a relatively small planar array, the calculations rapidly become overwhelming for the exact solution if attempted by hand. For a large array, the calculations require special techniques in programming for a large digital computer when an exact solution is attempted. Fortunately, the approximations of this section allow one to obtain results for arrays with  $10^4$  to  $10^5$  elements with no particular difficulty. Furthermore, the gain function concept offers the possibility of obtaining meaningful results for large arrays on a smaller array; consequently, such computations (exact solutions) can be managed in a straightforward manner with a computer.

### C. COMPUTATIONAL PROGRAMS

Programs have been written for the IBM 7094 computer to calculate gain functions and driving impedances using the formulas of Sec. B of this chapter. One program computes exact numerical values for small planar arrays, while the other utilizes the large array approximations of Sec. B-5 to compute gain and impedance functions for the center element in a rectangular-grid array with a large number of elements. In the following subsections, a brief description of each program will be given. This will be followed by a summary of the particular arrays which have been computed.

## 1. Program to Compute Exact Performance of Small Planar Arrays

This program is used to compute the element driving impedance and element gain function for any element in a small planar array. Array size has been restricted to a total of 100 radiating elements (50 crossed-dipole pairs) in order to avoid the use of auxiliary storage when the computations are performed. This is also a practical limit set by the computation time required.

A block diagram of the operations involved in the computation of the performance of a small array is given in Fig. III-66. As indicated in the figure, the program is broken into 6 subprograms which are controlled by a main program. The operations performed by the various subprograms and the main program will now be discussed.

The first operation (performed by the main program) is that of reading the input data which specifies the parameters of the array to be computed. These data are:

- (a) Array dimensions – element spacings, height above the ground plane, number of elements in the x-direction and in the y-direction, dipole type, and array type (linear or circular polarization);
- (b) Integers to instruct the program to print the required information in the desired form;
- (c) Location numbers of the elements for which impedance and gain computations are to be performed;
- (d) Type of sampling polarization;
- (e) Values for  $\phi_1$  (3 cuts),  $\Delta\theta (\geq 1^\circ)$ , and  $N(N\Delta\theta \leq 90^\circ)$ .†

There are also some optional inputs such as amplitude taper coefficients and specific generator impedances.

Once the array has been specified, it is a straightforward computation to generate the impedance matrix  $[Z]$ . The self and mutual impedances are computed using the formulas in Tables III-2 and III-3 and then arranged in the proper order to form the impedance matrix. If the array is regularly spaced, it is only necessary to compute a small number of the mutual impedances (of the order of the total number of elements) with the remainder being found by re-ordering the computed values according to the geometry of the array. The symmetry of the impedance matrix is also used to reduce the computation time.

The self and mutual impedances for the electrically short dipoles are found by direct numerical evaluation of the formulas in Table III-3. For the half-wavelength thin dipoles, however, numerical integration is required. A five-point Gauss-Legendre numerical integration method‡ was found to be very efficient and, in addition, resulted in very accurate values for the impedances.

The next step is to add a suitable generator impedance  $Z_g$  to each of the diagonal elements of the impedance matrix. Any value could be assigned to the generator impedance and the array performance computed for this value. This is done for certain special cases; however, in the usual case, the generator impedance is chosen such that the array will be optimized in some sense. One possible choice is to match all elements when they are isolated; i.e.,  $Z_g = Z_a^*$  (this is a built-in option of the subprogram). Another possibility is to match the center element when the

†The element gain function and driving impedance are computed in three scan planes defined by the array normal and the polar angle  $\phi_1$ . In each scan plane, the beam-pointing angle  $\theta$  is varied in discrete increments  $\Delta\theta$  from broadside to a maximum value equal to or less than  $90^\circ$  (endfire). The number of angles at which computations are performed is  $N$  where  $N \leq 90^\circ/\Delta\theta$ .

‡F. B. Hildebrand, Introduction to Numerical Analysis (McGraw-Hill, New York, 1956).

array is phased to point a beam at broadside. This requires successive iterations (as indicated in Fig. III-66) because the element driving impedance in an array is initially unknown and, in addition, it varies as a function of the generator impedance for a small array. A suitable first approximation for  $Z_g$  is afforded by the infinite array formula of Eq. (52):

$$Z_g = Z_{D_N}^* = Z_a^* + \sum_{\substack{m=1 \\ m \neq N}}^{N_T} Z_{Nm}^* \quad (64)$$

where  $N_T$  is the total number of elements and  $N$  is the location number of a central element of the array (a similar relation applies for a crossed-dipole array). After about four iterations,  $Z_g$  differs from  $Z_{D_N}^*$  by considerably less than one percent in both real and imaginary parts.

Once the generator impedance is chosen, the complete impedance matrix must be inverted to determine the array performance for that particular  $Z_g$ . This step is very critical because (even at best) most of the computation time is used in this operation. For this reason a special subprogram was written using a modified Gauss-Jordan matrix inversion process which takes advantage of various properties of the impedance matrix:

$$\left. \begin{aligned} |Z_{mm}| &> 0 \\ |Z_{mm}| &> |Z_{nm}|, \quad \text{all } n \neq m \\ Z_{mn} &= Z_{nm} \text{ (symmetry)} \end{aligned} \right\}$$

The first two properties eliminate the need to interchange rows (or columns) to get the largest element (magnitude) of a row (or column) on the diagonal (this step is usually required in a Gauss-Jordan inversion to obtain reasonable accuracy). The third property allows us to reduce the impedance matrix to diagonal form by premultiplying  $[Z]$  by a triangular matrix  $[A]$  and postmultiplying by the transpose of  $[A]$ ,  $[A]^T$ :

$$[A] \cdot [Z] \cdot [A]^T = [D] \quad (62)$$

where  $[D]$  is a diagonal matrix ( $D_{mn} = 0, n \neq m$ ) and the matrix  $[A]$  has nonzero elements only on and below the main diagonal ( $A_{mn} = 0, n > m$ ). Thus

$$[Z] = [A]^{-1} \cdot [D] \cdot ([A]^T)^{-1}$$

or

$$[Y] = [Z]^{-1} = [A]^T \cdot [D]^{-1} \cdot [A] \quad (63)$$

where the diagonal elements of  $[D]^{-1}$  are just the reciprocals of the corresponding elements of  $[D]$ . The diagonal elements of  $[A]$  are all real with unit value while the other nonzero elements are just those required by the Gauss-Jordan reduction to reduce the impedance matrix to diagonal form; for example, premultiplication of  $[Z]$  by  $[A_1]$ ,

$$[A_1] = \begin{bmatrix} 1 & 0 & \dots & 0 \\ -\frac{Z_{21}}{Z_{11}} & 1 & \dots & 0 \\ \vdots & \vdots & \ddots & \vdots \\ -\frac{Z_{N_T 1}}{Z_{11}} & 0 & \dots & 1 \end{bmatrix}$$

and postmultiplication by  $[A_1]^T$  leaves the product

$$[A_1] \cdot [Z] \cdot [A_1]^T = \begin{bmatrix} Z_{11} & 0 & \dots & 0 \\ 0 & Z'_{22} & \dots & Z'_{2N_T} \\ \vdots & \vdots & \ddots & \vdots \\ 0 & Z'_{N_T 2} & \dots & Z'_{N_T N_T} \end{bmatrix} \quad (64)$$

where

$$Z'_{mn} = Z_{mn} - Z_{1n} \left( \frac{Z_{m1}}{Z_{11}} \right), \quad n \leq m$$

and

$$Z'_{nm} = Z'_{mn}$$

That is, all elements of the impedance matrix are modified and symmetry still applies. This process is continued until  $[Z]$  is reduced to diagonal form. When this is done, the transformation matrix is

$$[A] = [A_{N_T-1}] \cdot [A_{N_T-2}] \cdot \dots \cdot [A_2] \cdot [A_1]$$

Finally, the admittance matrix is formed by the matrix multiplication indicated in Eq. (63).

Since the matrix inversion process discussed above reduces successive rows and columns of  $[Z]$  to zero (except the diagonal elements), the successive columns of  $[A]$  can be stored in the space previously occupied by the corresponding column of  $[Z]$ . This permits the solution of a larger array in the computer because the  $[Z]$  and  $[Y]$  matrices are not simultaneously contained in core storage. Since the impedance matrix is destroyed in the inversion process, it is necessary to store the impedance matrix on an auxiliary tape when successive iterations are performed (as indicated in Fig. III-66).

After the admittance matrix  $[Y]$  has been found, the broadside impedance for a central element is computed from

$$Z_{D_N}(0,0) = \frac{1}{N_T \sum_{n=1}^N \frac{a_n}{a_N} Y_{Nn}} - Z_g$$

for linearly polarized arrays, and

$$\left. \begin{aligned} Z_{D_N}^x(0,0) &= \frac{1}{N_T \sum_{n=1}^N \frac{a_n}{a_N} [Y_{Nn}^{(xx)} - jY_{Nn}^{(xy)}]} - R_o - jX_T \\ Z_{D_N}^y(0,0) &= \frac{1}{N_T \sum_{n=1}^N \frac{a_n}{a_N} [Y_{Nn}^{(yy)} + jY_{Nn}^{(yx)}]} - R_o - jX_T \end{aligned} \right\}$$

for crossed-dipole arrays. Then the computed driving impedance is compared with the conjugate of the generator impedance (or  $R_o - jX_T$  for crossed dipoles) to determine the source mismatch. If the mismatch is small enough, the program proceeds with the calculation of element driving impedances and gain functions. When a considerable mismatch still exists, the generator impedance  $Z_g$  is set equal to the conjugate of the driving impedance of the central element, the impedance matrix is read from the auxiliary tape and stored in the computer memory, and the computations repeated. Note that the iterations are skipped when a specific generator impedance is part of the input data.

Once the admittance matrix has been determined for the "optimum" (or specified) generator impedance, it is then a straightforward computation to obtain the element driving impedance and element gain function for any element in the array using the formulas of Secs. B-3 and B-4 of this chapter. These quantities are computed as a function of the angle from broadside  $\Theta$  for various planes defined by the array normal and the polar angle  $\phi$ . Typically, the E-plane ( $\phi = 0^\circ$ ), the H-plane ( $\phi = 90^\circ$ ), and the diagonal plane ( $\phi = 45^\circ$ ) are used in these calculations. The array cannot be scanned into invisible space with the present program, so the maximum scan angle  $N\Delta\Theta$  is restricted to  $90^\circ$ .

As shown in Fig. III-66, there are various computer printouts for information of interest. The element driving impedances and gain functions are written as functions of the scan angle  $\Theta$ . Printout of the impedance and/or admittance matrices is optional.

## 2. Large Array Program

This program is used to compute the element driving impedance and element gain function for the center element in a large, rectangular-grid array with an odd number of elements. At present, this program computes only arrays with single, x-aligned dipoles at each position. The limit on array size is 250,000 total elements (a  $249 \times 999$  array, for example).

Since the large array approximation does not require an inversion of the impedance matrix, it is possible to handle quite large arrays without exceeding the limitations of the computer because only the center row of the impedance matrix needs to be calculated and stored. In addition, the computation time remains within reasonable bounds.

A block diagram of the operations involved in the large array program is shown in Fig. III-67. Note that the program is much the same as the small array program except that there are fewer different operations involved. The three subroutines are much the same as those described previously for the small array program; only the formula for the element driving impedance is

changed. For the large array program, the array illumination is uniform, and only the behavior of the center element is considered; otherwise, the data input is the same as described above for the small array program.

### 3. Summary of Array Computations

The computations performed up to the present are restricted to element driving impedances and gain functions for  $\lambda/2$  and short dipoles arranged in planar, linearly polarized, square-grid arrays. All calculations reported are for arrays with an odd number of total elements, specifically,  $7 \times 9$  (7 elements in the collinear direction and 9 elements in the parallel direction) and  $9 \times 11$  arrays. Figure III-68 shows the array geometry and element numbering system used by the program.

Extensive computations have been performed for  $7 \times 9$  arrays of both  $\lambda/2$  and short dipoles. Interelement spacings ( $D_x = D_y = D$ ) of  $0.5\lambda$ ,  $0.6\lambda$ ,  $0.7\lambda$ , and  $0.8\lambda$  and ground plane heights ( $s/\lambda$ ) of 0 (no ground plane)<sup>†</sup>  $1/16$ ,  $1/8$ ,  $3/16$ ,  $1/4$ ,  $5/16$ , and  $3/8$  were used to investigate the effects of element spacing and of height above the ground plane. A few  $9 \times 11$  arrays of  $\lambda/2$  dipoles were also computed to determine the effect of increasing the size of the array. Element gain functions and driving impedances were computed for E-plane ( $\phi = 0^\circ$ ), D-plane ( $\phi = 45^\circ$ ), and H-plane ( $\phi = 90^\circ$ ) cuts for the center element of all arrays. In addition, some gain functions and driving impedances were computed for some noncenter elements of  $9 \times 11$  arrays to determine the effects of asymmetry.

Several arrays with up to 65 elements in the E-plane and 149 elements in the H-plane were computed with the large array program. The main purpose for these calculations was to obtain a reasonably good approximation to an infinite array so that the performance of small arrays could be properly assessed. This also allows us to determine the degree of precision with which we can predict the performance of large arrays by restricting attention to smaller arrays.

For the small arrays, four iterations were used so that the final results were obtained with the generator impedance chosen such that the center element was matched at broadside:

$$Z_g = Z_{D_N}^* (0, 0)$$

The computed gain functions were normalized by dividing by  $4\pi D^2/\lambda^2$  for arrays above a ground plane or by  $2\pi D^2/\lambda^2$  for arrays without a reflector. As discussed in Sec. B-5 of this chapter, the value of the normalized gain function at broadside ( $\phi = \theta = 0$ ) gives a measure of the sufficiency of array size for making projections to large arrays. This value should be unity when the array is large enough [see Sec. B-5] because the generator impedance was chosen such that the broadside gain of the center element would be maximized.

### D. COMPARISON OF COMPUTED RESULTS WITH KNOWN RESULTS FOR INFINITE ARRAYS

The calculations of small arrays using the exact method of solution are of importance by themselves, since actual array measurements are often performed on smaller arrays (see Part III, Chapter 4, for example). However, a more important application of finite array calculations (exact or approximate) is, perhaps, the extrapolation of the results to large arrays; that

<sup>†</sup> Technically, the no ground plane case is given by  $s/\lambda = \infty$ ; however, for computational convenience this case was defined by  $s/\lambda = 0$ .

is, we would like to deduce with reasonable accuracy the performance of large arrays from our calculations of small arrays. A further use of small array calculations is to determine the effects of size on array performance. Except for the first case, it is important to have some measure with which we can assess our ability to predict the performance of large, finite arrays. Since there are no known theoretical results for large, finite arrays, we must make use of known results for infinite arrays to obtain a limiting case. The degree of correlation between the small array results and the corresponding infinite array results gives us an estimate of the confidence with which we can extrapolate the small array results to larger arrays. There are two known results for infinite arrays which can be used to evaluate the results of small array calculations. First, as pointed out above, the normalized broadside gain function should approach a value of unity for an infinite array when the generator circuit is matched to the broadside driving impedance of the elements. Second, by virtue of Stark's<sup>†</sup> results, we have a useful prediction of the value of  $R_D(\phi, \theta)$ . Since the calculated values of driving impedance were used to select the generator circuit impedance, we will first examine the correlation of the calculated impedances and the theoretical, infinite array impedances.

### 1. Accuracy of Small Array Estimation of Driving Impedance of Large Array

Comparison of the calculated values of  $Z_D$  for the small arrays discussed in this report with known expressions for infinite arrays appears to represent a meaningful test of the effect of array size on element driving impedance. In addition, we can use this test to measure the degree of convergence of the results of the large array program. Stark's result for an infinite array of dipoles gives the element driving impedance as an infinite series. The resistive part of the driving impedance consists of only as many terms as there are grating lobes in visible space for the particular element spacing and scan angle, while the reactive part is always an infinite series. The reactive part is of little help for evaluating the performance of small arrays. The real part, however, is easy to evaluate and proves to be quite useful in assessing the performance of small arrays.

Stark's expressions were used to construct the curves of Fig. III-69 for  $\lambda/2$  dipoles and Fig. III-70 for electrically short dipoles. These figures give the driving resistance of the center element of the array (any element of an infinite array) with the array phased to point the beam at broadside. In Fig. III-70 we compare the values of  $R_D(0, 0)$  for  $7 \times 9$  arrays computed by the exact method and by the use of the infinite array approximation as previously reported.<sup>‡</sup> It is seen that the exact solution gives a better estimate of  $R_D(0, 0)$  for an infinite array than the approximate solution except for  $D/\lambda = 0.5$ . The difference between  $R_D(0, 0)$  for the infinite array and for the exact solution of the  $7 \times 9$  array is never more than 10 percent and for most values of  $D/\lambda$  and  $s/\lambda$  is considerably less. This contrasts with the nearly 30-percent error which can result when the approximate solution of the  $7 \times 9$  array is used. Note also that corresponding agreement with an infinite array (10 percent or less) is also obtained when the radiating elements of the  $7 \times 9$  array are short dipoles (see Fig. III-70). In addition, the numerical values for  $R_D(0, 0)$  obtained from the large array program for 65 element (collinear) by 149 element (parallel) arrays agree very closely with Stark's results (errors less than 0.1 percent).

From Table III-6 we note that the broadside resistance formula for  $\lambda/2$  dipoles in an infinite array differs from the formula for short dipoles only by a factor of 80; that is, if Fig. III-69

<sup>†</sup> L. Stark, "Radiation Impedance of a Dipole in an Infinite Array," Formal Technical Document FL60-230, Hughes Aircraft Company (1 May 1960).

<sup>‡</sup> TR-236, pp. 199-242.

were suitably scaled and then superimposed on Fig. III-70, the curves for the infinite array broadside impedance would exactly coincide. This fact gives us a useful way to compare the relative performance of similar  $\lambda/2$  and short dipole arrays. Figure III-71 shows that a  $7 \times 9$  array of short dipoles has nearly the same normalized broadside resistance as does the  $7 \times 9$  array of  $\lambda/2$  dipoles; the difference is very small (less than 2 percent) except for  $D/\lambda = 0.5$  where the "error" can be as large as 6 percent.

It is also informative to compare the driving resistance of the center element of a small array with that of an infinite array when the array is phased to point a beam at various angles off broadside. In Fig. III-72 we show a typical plot of the driving resistance vs scan angle from broadside for three different planes of scan [ $E(\varphi = 0^\circ)$ ,  $D(\varphi = 45^\circ)$ , and  $H(\varphi = 90^\circ)$ ] for  $\lambda/2$  dipole arrays. Note that the approximate solution for the  $65 \times 149$  array agrees very closely with the infinite array expressions for scan angles as large as  $85^\circ$ . The small array resistance values (which were computed exactly) oscillate around those for the infinite array with differences as large as 15 percent for the  $7 \times 9$  array and 10 percent for the larger  $9 \times 11$  array for scan angles less than  $60^\circ$ . A similar set of curves is shown in Fig. III-73 for a short dipole array. Again we find nearly complete agreement between the  $65 \times 149$  array and the infinite array, while the  $7 \times 9$  array resistance values oscillate around those for the infinite array with deviations of approximately 10 percent for scan angles up to  $60^\circ$ .

It is readily evident from Figs. III-72 and III-73 that the short dipole array resistance and the  $\lambda/2$  dipole array resistance have much the same behavior as a function of scan angle. In fact, for infinite arrays the normalized resistance varies with scan angle as shown in Fig. III-74. The curves fall in much the same way for both types of elements (with complete agreement for H-plane scan). For small arrays, the correlation of short and  $\lambda/2$  dipole array resistance values is still quite good as evidenced by Fig. III-75.

Up to now we have been concerned with the very practical case of a dipole array mounted above a perfectly conducting ground plane. When the ground plane is removed, the dipole array is probably not practical, but its electromagnetic dual, narrow slots in a ground plane, is very practical so we turn now to dipole arrays without ground planes. In this case, the coupling between elements increases and, consequently, the correlation between a small array and an infinite array deteriorates. For example, Fig. III-76 indicates that even though short and  $\lambda/2$  dipole arrays have nearly identical normalized broadside resistances, they still differ by as much as 20 percent from the infinite array. The situation is even worse when the arrays are phased to point the beams at some angle off broadside. Figure III-77 for  $\lambda/2$  dipole arrays and Fig. III-78 for short dipole arrays illustrate the convergence problems which are involved when the ground plane is removed. Differences between the small arrays and the infinite arrays become as large as 50 percent as the array is scanned from  $0^\circ$  to  $60^\circ$ . Figure III-77 also indicates that increasing the array size from  $7 \times 9$  to  $9 \times 11$  does little toward decreasing the magnitude of the difference between the small array and infinite array resistances.

Again, similar to the case of arrays above a ground plane, we note that the short dipole and  $\lambda/2$  dipole arrays have driving resistances which behave in much the same way as a function of scan angle. For infinite arrays, the comparative resistance variation with scan angle for  $\lambda/2$  dipole and short dipole radiators is as shown in Fig. III-79. As above, we see that the resistance variations for the two types of elements are quite similar and, in fact, agree completely for H-plane scan. From Fig. III-80 it is evident that there is reasonably good correlation between a  $7 \times 9$  array of  $\lambda/2$  dipoles and a  $7 \times 9$  array of short dipoles.



## 2. Accuracy of Small Array Estimate of Broadside Gain of Large Array

As previously mentioned, the results of Wheeler<sup>†</sup> indicate that the value of the normalized element gain function should be unity when the array is phased to point a beam at broadside if the generator circuit impedance is matched to the broadside driving impedance. When the above conditions are met in a small array, it is generally found that the normalized gain function at broadside does not have unit value. Figure III-81 for  $7 \times 9$  arrays of  $\lambda/2$  dipoles and Fig. III-82 for  $7 \times 9$  arrays of short dipoles illustrate this fact for various values of  $D/\lambda$  and  $s/\lambda$ . Note that the results for these small arrays are only in error by 6.5 percent for all cases except when  $D/\lambda = 0.5$  and  $s/\lambda > 0.25$  for  $\lambda/2$  dipole arrays.

When the ground plane is removed, the tighter coupling between elements manifests itself in much larger errors in the normalized gain function at broadside, as shown in Fig. III-83. The difference between the normalized gain function of the center element at broadside,  $g_c(0, 0)/(2\pi D^2/\lambda^2)$ , and unity oscillates between  $\pm 15$  percent as the element spacing is increased from 0.5 to 0.8 for both  $\lambda/2$  dipole and short dipole arrays.

In a previous report<sup>‡</sup> the fact that the normalized gain function at broadside did not have a value of unity was attributed to a mismatched generator impedance. The findings of the present study, on the other hand, indicate that the effect is due entirely to the small size of the arrays. Since Eqs. (56) and (57) were derived for an infinite array which was matched at broadside, we would expect differences for small arrays except in the unlikely instance where the small array driving resistance were very nearly equal to that of an infinite array having the same element spacings. From Figs. III-69, III-70, and III-76, we see that for most values of  $D/\lambda$  and  $s/\lambda$  the broadside driving impedance for the  $7 \times 9$  arrays is different by several percent from that of the corresponding infinite array.

In most of the cases where the normalized gain function at broadside is less than unity, the gain function has its maximum value at some beam pointing angle different from broadside which is just another manifestation of array size effects. A typical plot of an element gain function which exhibits this behavior is shown in Fig. III-84. Note the close correlation between the  $\lambda/2$ -dipole array and the short dipole array gain functions and also the way in which the array dominates the shape of the element gain function.

## 3. Conclusions

From the above results we see that the large array program, which uses the infinite array approximation to compute the element driving impedance, can be successfully used to compute the performance of a typical element in a very large array with a high degree of accuracy, when the array is mounted above a ground plane. The same degree of accuracy is not obtained when the ground plane is removed; that is, a considerably larger array (much larger than  $65 \times 149$ ) is required to obtain results for  $Z_D$  which are within 1 percent of the infinite array results.<sup>§</sup>

The exact solutions obtained by use of the small array program also agree reasonably well with the expressions for an infinite array. Thus, we would anticipate reasonable success in

---

<sup>†</sup> H. A. Wheeler, Proc. IRE 36, 478 (1948).

<sup>‡</sup> TR-236, p. 217.

<sup>§</sup> The  $65 \times 149$  array results, without a ground plane, agree with the infinite array results to about 5 percent (except for beam pointing angles near endfire) which is certainly sufficient for experimental work.

extrapolating the results to large arrays. It should be noted that the small array program gives an exact solution for the particular array under consideration, while the large array program is mainly used to approximate an infinite array and therefore exact array size has little meaning. Further, the exact solution allows the evaluation of asymmetry and edge effects by the computation of the performance of noncentral elements.

## E. SUMMARY AND DISCUSSION OF COMPUTED RESULTS<sup>†</sup>

In this section, the various results which have been found during this study will be summarized and discussed. In particular, the variation of impedance with scan angle for selected values of  $D/\lambda$  and  $s/\lambda$  will be presented for some  $7 \times 9$  and  $9 \times 11$  arrays. This will be followed by a discussion of gain functions with particular emphasis on the effect of mutual coupling on the scan angle in the two principal planes at which the gain is decreased by 3 db when the elements are matched at broadside. Following this, the maximum VSWR incurred when the array is scanned to the angle at which grating lobes form will be given for scan in the principal planes (an arbitrary value of  $50^\circ$  is assigned when  $D/\lambda = 0.5$ ). Finally, the gain and impedance variations with scan angle will be given for various noncentral elements of a  $9 \times 11$  array.

### 1. Variation of Impedance with Scan Angle

As previously discussed, the element driving impedance varies when the array is phased to point beams in directions different from broadside. In this section, several rectangular plots of  $Z_D$  for scan in the  $E(\varphi = 0^\circ)$ ,  $D(\varphi = 45^\circ)$ , and  $H(\varphi = 90^\circ)$  planes will be given. (In Appendix A, several Smith Chart plots of  $Z_D$  are presented.) These plots are compared with the large array impedance variations of  $65 \times 149$  arrays, which should represent good approximations to infinite arrays. Furthermore, the  $65 \times 149$  array impedance variation with scan angle agrees quite closely with the results given by Carter<sup>‡</sup> for the driving impedance of the center element of a 61-element (parallel direction) planar array, infinite in extent in the collinear direction. The only case which Carter considered was  $D = 0.5\lambda$  and  $s = 0.25\lambda$  for an array composed of  $\lambda/2$  dipole radiators.

Figure III-85 shows the impedance variations with scan angle for  $7 \times 9$  arrays of  $\lambda/2$  dipole radiators with element spacings of one-half wavelength and a quarter wavelength above ground (Carter's case). One set of curves gives the results for the exact solution while another gives the results for the approximate solution. Both sets of curves are then compared with the large array impedance variation with scan angle. It is evident that the  $7 \times 9$  array results (both exact and approximate) agree reasonably well with the large array results in all three scan planes (the difference in the magnitudes of the  $7 \times 9$  array impedance and the large array impedance at a particular scan angle is less than 14 percent). Near broadside the small array impedances exhibit rather unusual behavior, while at larger scan angles they tend to oscillate around the values for a large array.

When the array size (for the exact solution) is increased from  $7 \times 9$  to  $9 \times 11$  the results shown in Fig. III-86 are obtained. From this figure, it is seen that the  $9 \times 11$  array gives an

<sup>†</sup> Some of the computed gain functions and impedance plots from which these data were extracted are presented in Appendix A.

<sup>‡</sup> P. S. Carter, Jr., Trans. IRE, PGAP AP-8, 276 (1960).

improved estimate of the large array impedance even though there is still several percent error in the magnitudes of the impedances. It is also worth noting that the oscillatory behavior still exists for the  $9 \times 11$  array impedances. If the array size were further increased, the oscillations of the impedances about the large array values would continue to exist with smaller amplitude and period because we are trying to approximate a curve with a finite Fourier series and the results are typical of the manner in which Fourier series converge.

From our knowledge of Fourier series, we know that convergence to the correct function occurs in an rms sense. Thus, it would be expected that a still better approximation to the infinite array impedance could be obtained by taking the geometric mean of the  $7 \times 9$  and  $9 \times 11$  array impedances at each of the sample points (scan angles). This has been done for the case  $D = 0.5\lambda$  and  $s = 0.25\lambda$  (see Fig. III-86) with the result shown in Fig. III-87. It is evident from this figure that the agreement with the large array is now very good for all scan angles (within 2 or 3 percent for most scan angles). This operation is probably equivalent to doubling the array size in both dimensions (for example, a  $19 \times 23$  array).

If the radiating elements are changed from  $\lambda/2$  dipoles to short dipoles while  $D/\lambda$  and  $s/\lambda$  remain the same ( $D = 0.5\lambda$  and  $s = 0.25\lambda$ ), the results shown in Fig. III-88 are obtained. It is readily evident that the behavior of the small array impedance relative to the large array impedance is about the same (qualitatively) when the radiating elements are changed. The errors in the magnitudes of the impedances are slightly smaller and the differences among the polar angles of the impedances  $[(Z_D - Z_g^*) = |Z_D - Z_g^*| e^{j\alpha}]$  for the three planes of scan are reduced when the radiating elements are short dipoles rather than  $\lambda/2$  dipoles.

When the element spacing is increased from  $0.5\lambda$  to  $0.6\lambda$  with  $s$  remaining at  $0.25\lambda$  for arrays of  $\lambda/2$  dipoles, the impedance variation with scan angle is as shown in Fig. III-89. The agreement with the large array ( $65 \times 149$ ) is seen to be better in this case which is probably due to the fact that  $\lambda/2$  dipoles placed in a square-grid array with  $\lambda/2$  element spacing is a special case [the ends of the dipoles are infinitely close (touching) and therefore anomalous behavior is to be expected]. In other respects, the impedance variations are qualitatively the same as they were for the  $\lambda/2$  element spacing. Note that the E-plane plots go to  $55^\circ$  which is the approximate scan angle where the main beam and the grating lobe have the same amplitude (the grating lobe first appears in visible space when the main beam is scanned to  $42^\circ$  in the E-plane).

A more severe effect occurs when the ground plane is removed as evidenced by Fig. III-90 where a  $7 \times 9$  array and a  $9 \times 11$  array are compared. It is clear from the very poor correlation between the two arrays that small arrays without a reflector are not very useful for predicting the performance of large arrays. In addition, it has been found that even a  $65 \times 149$  array solved by the approximate method gives a rather poor approximation to an infinite array (a much larger array would be required to obtain good results).

## 2. Effects of Coupling on Element Gain Functions

In the absence of mutual coupling the gain function for any element in the array would be just that of an isolated element (and its image when a ground plane is used). When mutual coupling is included, the element gain function is set almost completely by the array geometry; that is, the shape of the gain function for any element in the array bears very little resemblance to that of an isolated element for the array configurations considered here (see Fig. III-84 as an example).

Figure III-91 for  $s = 0$  (no ground plane) and Fig. III-92 for  $s = \lambda/4$  show the shapes of the H-plane gain functions for the center elements of  $7 \times 9$  arrays with  $\lambda/2$  dipole radiators as the element spacing is varied from  $0.5\lambda$  to  $0.8\lambda$ . The general effect of the array environment is to peak the gain function and narrow its beamwidth. As the element spacing is increased the beamwidth decreases while the broadside gain increases [ $g_c(0, 0)$  can become considerably larger than that of an isolated element for the larger element spacings]. The large amplitude ripples seen in Fig. III-91 and to a lesser extent in Fig. III-92 are just further manifestations of the effects of array size on the array performance.

### 3. Effects of Coupling on Scan Angle Corresponding to 3-db Decrease in Gain

The gain function 3-db points describe the solid angle over which the beam of an array can be scanned with less than 3-db decrease in array gain. It is evident from the results of Sec. B-4 of this chapter that the shape of the gain function (and, hence, its beamwidth) is dependent on the value of the generator impedance [see Eq. (47)]. In this section we present results only for the case where the center element of the array is matched at broadside by the generator impedance. The possibility of "tailoring" the gain function by properly choosing the generator impedance has not been investigated.

As pointed out in a previous report,<sup>†</sup> the 3-db beamwidth of an isolated dipole depends on how one defines beamwidth for large values of  $s$  ( $s > \lambda/4$ ), as can be seen from Fig. III-84, which illustrates the H-plane gain function of a dipole ( $\lambda/2$  or short)  $3\lambda/8$  above ground. The curves of 3-db beamwidth of isolated dipoles as a function of  $s$  shown in Fig. III-93 can be generated, dependent on whether the beamwidth is taken 3 db down from the broadside gain, or from the angle of maximum gain. In either case, it is evident that the beamwidth is quite a sensitive function of  $s$ .

As previously mentioned (and illustrated by Figs. III-84, III-91, and III-92), the environment takes over almost completely when the dipole is placed in an array. Figure III-94 for dipole arrays without ground planes and Figs. III-95 and III-96 for arrays above ground planes give the 3-db H- and E-plane beamwidths for  $7 \times 9$  arrays of  $\lambda/2$  dipoles and short dipoles. The gain function beamwidth is relatively insensitive to  $s$  and corresponds roughly to the included angle  $2\theta_{\max}$  over which an infinite array can be scanned without grating lobe formation for  $D > 0.5\lambda$ , given by

$$D/\lambda = \frac{1}{1 + \sin |\theta_{\max}|}$$

For H-plane scan, the angle of 3-db gain decrease and the angle of grating lobe formation occur almost simultaneously for most cases. The maximum usable scan angle in the E-plane, on the other hand, will usually be the angle of grating lobe formation.

Note that there is good correlation between  $\lambda/2$  dipole arrays and short dipole arrays for all element spacings, except  $D = 0.5\lambda$ , and for all ground plane spacings. The exception,  $D = 0.5\lambda$ , is presumably due to the fact that the  $\lambda/2$  dipoles have touching ends when the element spacing is one-half wavelength.

<sup>†</sup> TR-236, p. 221.

#### 4. Maximum VSWR Incurred During Scan

The maximum VSWR that would be incurred in scanning to the grating lobe formation angle  $\Theta_{\max}$  was computed from the computed data from  $7 \times 9$  arrays. All the results were obtained with the generator impedance matched to the broadside impedance of the center element. No attempt was made to reduce the maximum mismatch by properly choosing the generator impedance. A value of  $50^\circ$  was arbitrarily assigned to  $\Theta_{\max}$  for the case where  $D = 0.5\lambda$ , since no grating lobes occur for any scan angle. The value of  $\Theta_{\max}$  for other spacings are not exact. These spacings are merely the multiple of  $5^\circ$  closest to  $\Theta_{\max}$ .

The resulting VSWR plots for scan in the two principal planes are shown in Fig. III-97 for both  $\lambda/2$  dipole arrays and short dipole arrays mounted above a ground plane (the no ground plane case was not included because the lack of reasonable convergence of the solution would invalidate any conclusions which might be reached). Except for  $D = 0.5\lambda$  for  $\lambda/2$  dipole arrays, the maximum VSWR for scan in the E-plane is relatively insensitive to  $s$ , while for H-plane scan the VSWR increases with  $s$ . Again we note that there is relatively good agreement between  $\lambda/2$  dipole arrays and short dipole arrays, except when  $D = 0.5\lambda$ . The behavior of the VSWR for scan in the two principal planes indicates that for a given element spacing there is an optimum height above the ground plane for which the maximum VSWR incurred (as the beam is scanned) is a minimum. The optimum values for  $s$  are indicated in Fig. III-97 for scanning to  $\Theta_{\max}$  in both principal planes. It is evident that for all cases the maximum VSWR can be held to 3.5:1, and for many cases to 2:1.

#### 5. Asymmetry and Edge Effects in Small Arrays

All elements in an infinite array have identical gain functions and identical driving impedance variation with scan angle. In a small array, however, almost every element will have a different gain function and a different impedance variation with scan angle. The location of an element relative to the center element of the array and the size of the array determine the manner in which the gain and impedance of the element will vary as the beam is scanned over the desired volume of space; that is, elements near the edge of an array will exhibit considerably more asymmetry in their gain functions than will the elements near the center.

The element gain functions for 5 elements in a  $9 \times 11$  array of  $\lambda/2$  dipoles with  $D = 0.5\lambda$  and  $s = 0.25\lambda$  are given in Figs. III-98 to III-100 for E-, D-, and H-plane cuts, respectively. (The array geometry and element numbering system are indicated in Fig. III-68.) The E-plane gain functions do not exhibit very much asymmetry even for the corner element (element 1) and the edge elements (elements 5 and 46); most of the effect appears in the amplitude. For D- and H-plane cuts, however, the asymmetries of the gain functions for edge elements (elements 1, 5, and 46) become rather severe. Even the element adjacent to the center element (element 40) has a gain function which exhibits some asymmetry effects.

The close relationship between gain and impedance variations for arrays indicates that there will be considerable differences in the magnitudes and phases of the impedances of noncentral elements at each scan angle, as well as significant asymmetry effects. This behavior is illustrated graphically in Figs. III-101 to III-105 for 5 elements in the  $9 \times 11$  array. In each figure, the impedance variations with scan angle from broadside for 3 planes of scan are given [scan in one direction from broadside is represented by  $Z_{D_m}(\varphi_i, \Theta)$  and in the other by  $Z_{D_m}(\varphi_i + \pi, \Theta)$ ]. Note that the results of Figs. III-102 to III-105 also apply to elements which are symmetrically located with respect to the center element by merely replacing  $\varphi_i$  by  $\varphi_i + \pi$ .

As previously discussed, the impedance variation (magnitude) with scan angle for the center element (element 50) agrees within about 10 percent with the values for an infinite array (see Fig. III-101). For the impedance variation with scan angle of an interior, noncenter element (element 40), it is found that there is still reasonably good agreement with an infinite array even though there is substantial asymmetry in a given scan plane [ $Z_{D_{40}}(\varphi_i + \pi, \theta) \neq Z_{D_{40}}(\varphi_i, \theta)$ ], as shown in Fig. III-102.

The situation is considerably worse when the elements are on the edges of the array as shown in Fig. III-103 for the element in the middle of the edge where the dipoles are parallel, in Fig. III-104 for the element in the middle of the edge where the dipoles are collinear, and in Fig. III-105 for the corner element. In these three figures, it is observed that the correlation of the impedance variation with that for an infinite array is very poor. In addition, there is considerable asymmetry effect as evidenced by the fact that  $Z_{D_m}(\varphi_i + \pi, \theta)$  differs substantially (magnitude and phase) from  $Z_{D_m}(\varphi_i, \theta)$ . Note that the array is symmetrical about element 46 for H-plane scan and therefore no asymmetry is observed in the H-plane impedance variation with scan angle, as shown in Fig. III-103 (similarly, the array is symmetrical about element 5 for E-plane scan).

From the above results, we are led to conclude that for a  $9 \times 11$  array above a ground plane there is no typical element; that is, every element has a different impedance variation with scan angle and a different gain function. The two central elements (elements 40 and 50), which were considered, have driving impedances that differ by as much as 15 percent (magnitude) at some scan angles. From an experimental standpoint this is probably not a very important difference; however, it does indicate that edge effects amounting to approximately 10 percent in impedance variation (compared to the center element of a large array) will be observed in the outer 4 or 5 rows of elements in a large array.

## F. CONCLUSIONS AND OBSERVATIONS

The foregoing results have shown that the array environment completely dominates the performance of an element in the array. In particular, the gain, beamwidth, and impedance of an element in the array have values which are nearly independent of the values which an isolated element would have. If the center element is matched by the generator impedance when the array is phased to point a beam at broadside, the following general results have been found for the center element:

- (1) The maximum (matched) broadside gain of an element in the array is equal to  $4\pi D_x D_y / \lambda^2$  ( $2\pi D_x D_y / \lambda^2$  in the absence of a ground plane) independent of the broadside gain of the element when it is isolated.
- (2) The 3-db beamwidth of the element gain function is rendered essentially independent of the beamwidth of an isolated element.

These two properties of elements in an array have been obtained at the expense of an impedance variation with scan angle. It has been demonstrated that this impedance variation can result in a maximum VSWR of 3.5:1 at the maximum scan angle for some cases but is more usually about 2:1. Judicious choice of the generator impedance makes it quite probable that the maximum mismatch incurred as the beam is scanned over the required volume could be reduced substantially.

An investigation of edge elements in a  $9 \times 11$  array above a ground plane has indicated that edge effects of the order of 10 percent or more will be observed in at least the outer 4 or 5 rows of elements of an array. Since the coupling between elements is much tighter when the ground plane is removed, edge effects will be observed much further into the interior of the array (at least 10 to 20 rows of elements).

The large array program which uses the infinite array approximation for driving impedance calculations gives an excellent approximation to the driving impedance of an infinite array except near endfire, when the array is mounted above a ground plane. When the large array approximation is applied to a  $65 \times 149$  array without a ground plane, the results deviate by approximately 5 percent (except near endfire) from the infinite array values which is sufficient for experimental purposes.

If thin dipoles of any length are used as the radiating elements of the array, the above conclusions would also be expected to apply. That is, the results for  $\lambda/2$  dipole arrays and for short dipole arrays should represent "upper" and "lower" bounds on the expected array performance. The detailed variation of impedance with scan angle and the magnitude and phase of the impedance at a particular scan angle will be functions of dipole length (but apparently not very strong ones), but the gain functions and beamwidths will be essentially the same for any dipole length.

There are still several problems which are of considerable practical interest. These are:

- (1) The effect of the generator impedance on the gain function, beamwidth, and maximum mismatch.
- (2) Gain and impedance properties of arrays having geometries other than rectangular grid (for example, triangular- and hexagonal-grid arrays).
- (3) Effect of mutual coupling on space- and amplitude-tapered arrays (see TR-299).
- (4) Mutual impedance effects in hybrid driven, crossed-dipole arrays (gain, impedance variation, power lost in the terminated port, and depolarization).
- (5) Broad bandwidth effects in both linearly polarized and circularly polarized arrays. (These effects are probably best investigated in short dipole arrays where the mutual impedances are normalized by the free-space radiation resistance of a typical element of the array.)

These problems (which are currently being investigated) will be discussed in detail in a future report.

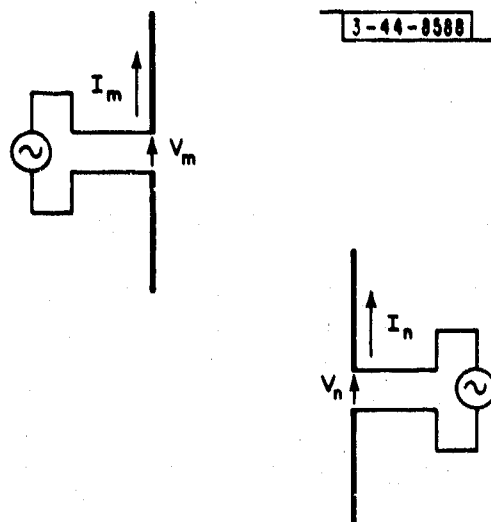


Fig. III-56. Dipoles and notation.

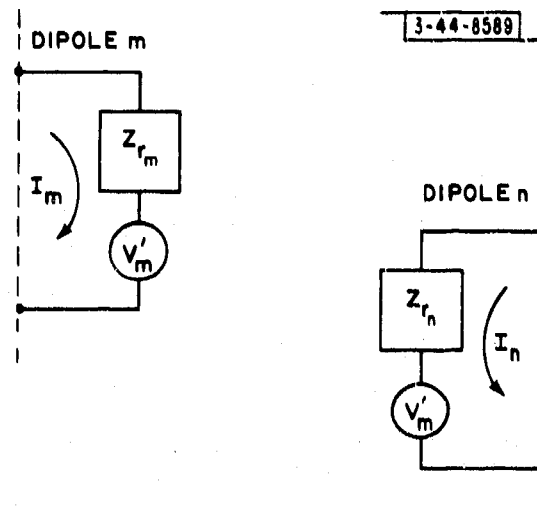


Fig. III-57. Equivalent circuit of Fig. III-56 dipoles.

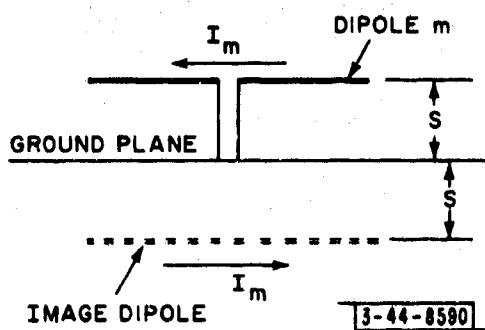


Fig. III-58. Dipole above ground plane and its image.

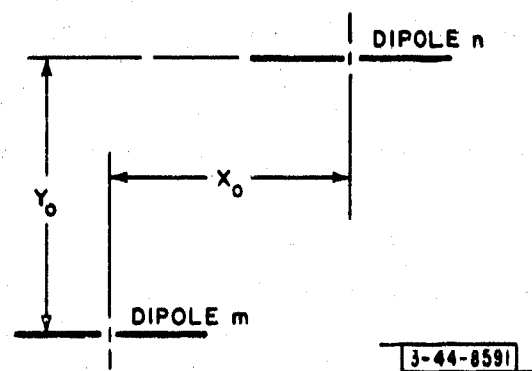


Fig. III-59. Parallel dipole configuration and spacing nomenclature.



Fig. III-60. Perpendicular dipole configuration and spacing nomenclature.

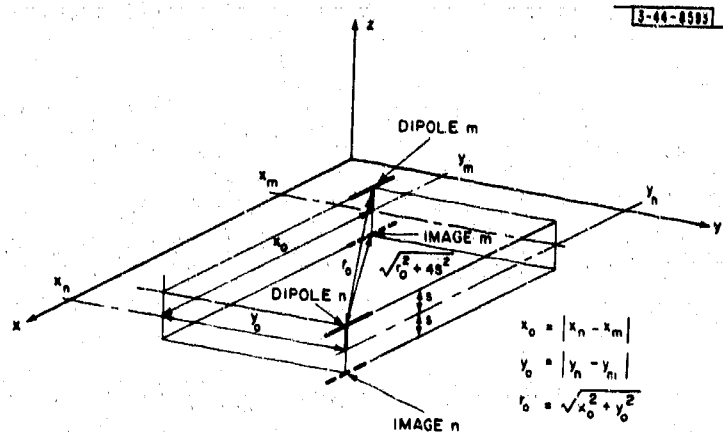
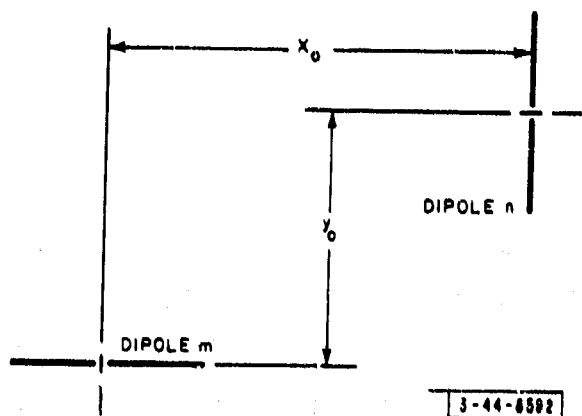
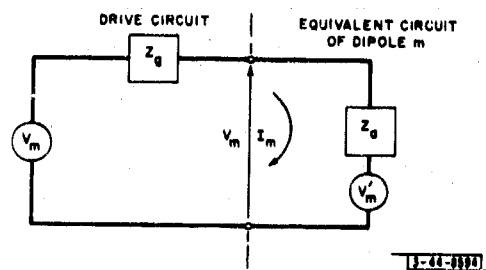


Fig. III-61. Geometry of dipoles above ground plane ( $Z = 0$  is ground plane). Dipole n may be parallel or perpendicular to dipole m.

Fig. III-62. Equivalent circuit of dipole and drive circuit for linearly polarized array.



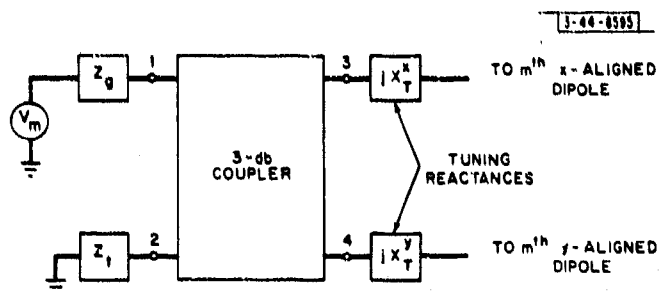


Fig. III-63. Drive circuit for obtaining circularly polarized waves from crossed dipoles.

Fig. III-64. Equivalent circuit for dipoles and drive circuit for crossed dipoles in array environment.

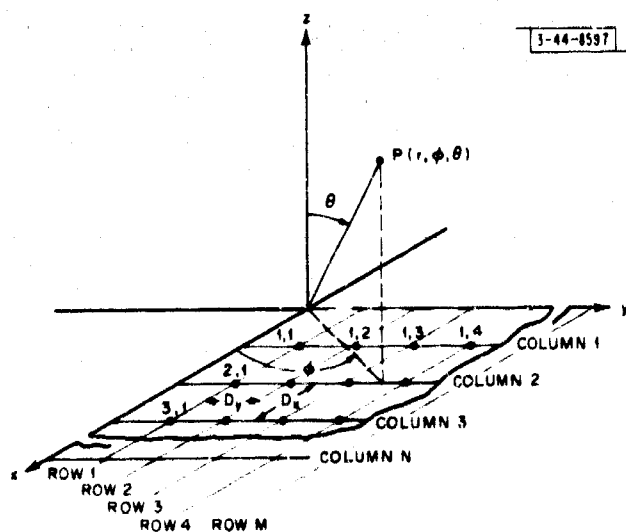
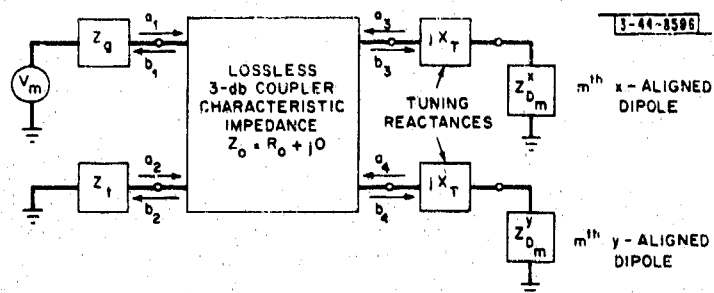


Fig. III-65. Generalized planar array geometry. Spherical coordinates are indicated and a rectangular-grid array is shown as an example.

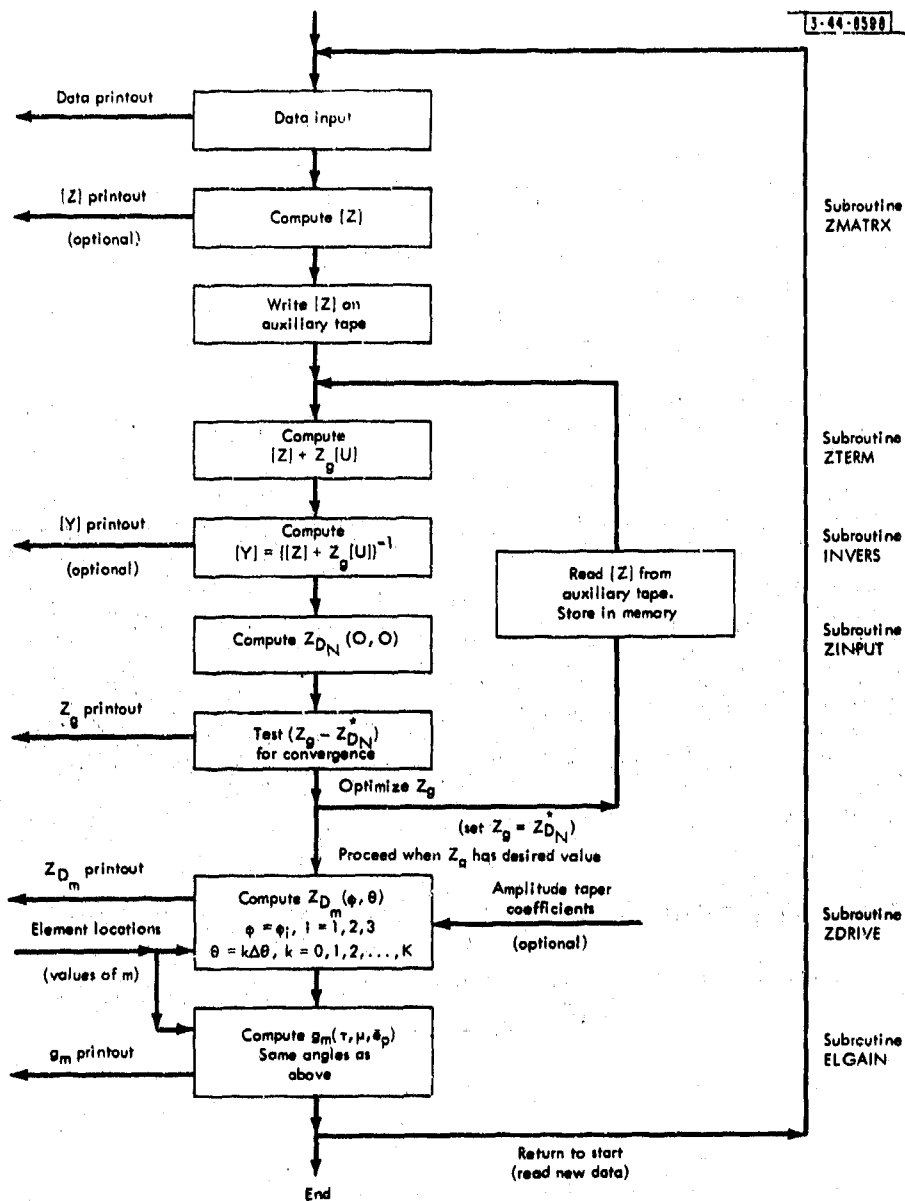


Fig. III-66. Block diagram of operations performed in small array program.  $N$  is the location number of a central element and  $K$  is chosen so that  $K\Delta\theta \leq 90^\circ$ .

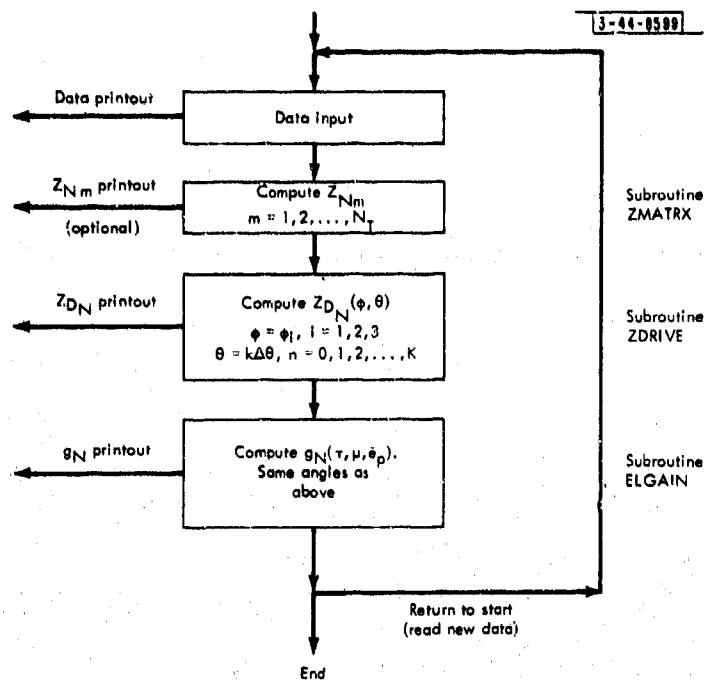


Fig. III-67. Block diagram of operations performed in large array program.  $N$  is the location number of the center element,  $N_T$  is the total number of elements and  $K$  is chosen so that  $K\Delta\theta \leq 90^\circ$ .

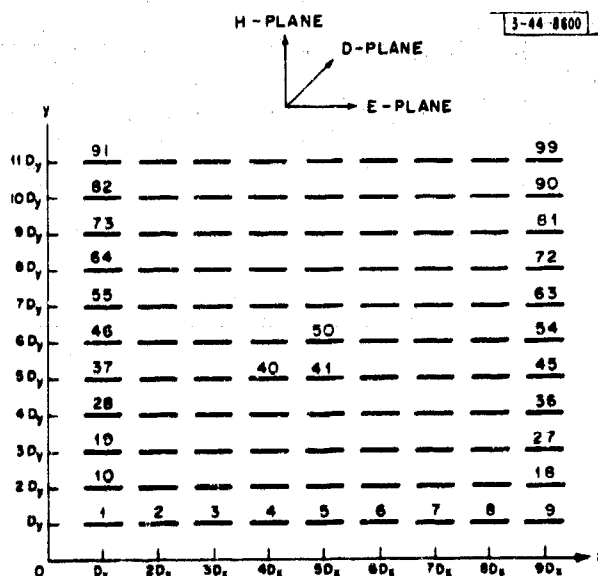


Fig. III-68.  $9 \times 11$  element array configuration. Element numbering system is indicated. (Element 50 is center element.)

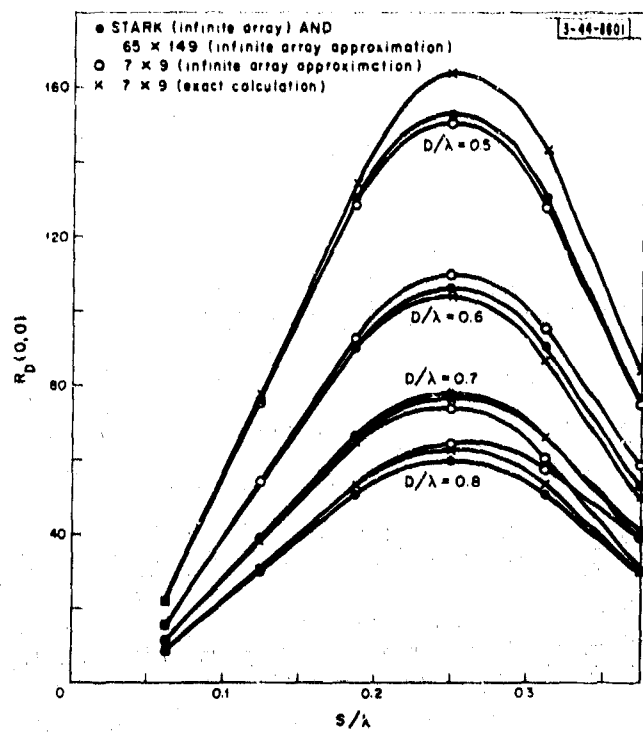


Fig. III-69. Comparison of broadside driving resistance calculations for  $\lambda/2$  dipole arrays.

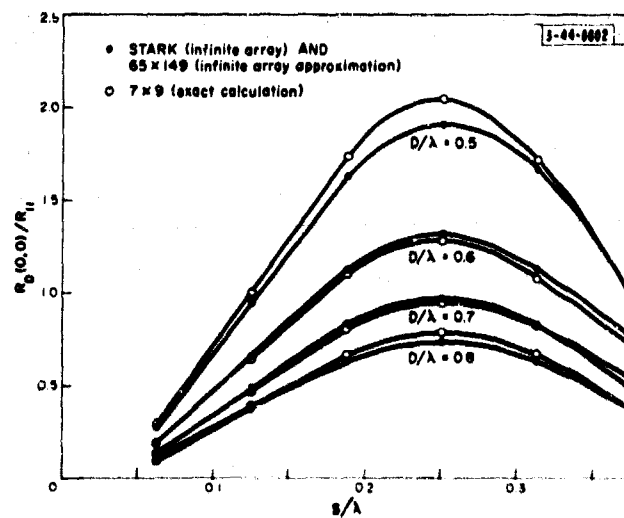


Fig. III-70. Comparison of normalized broadside driving resistance calculations for short dipole arrays.

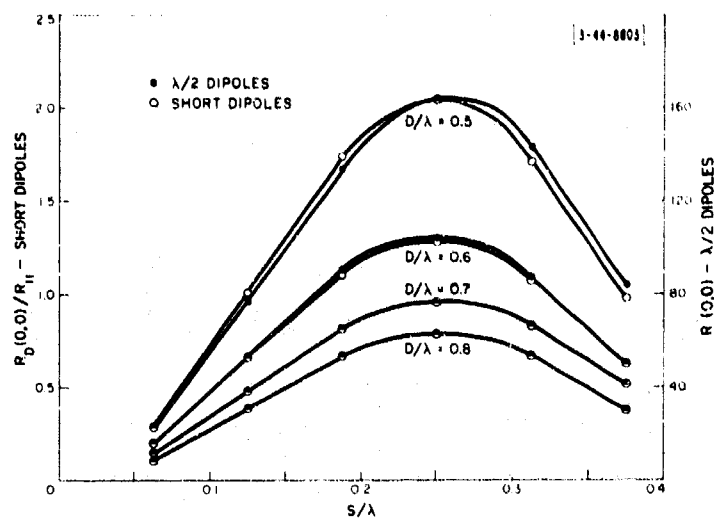


Fig. III-71. Comparison of broadside driving resistance of  $\lambda/2$  dipole arrays and short dipole arrays. Array size is  $7 \times 9$ .

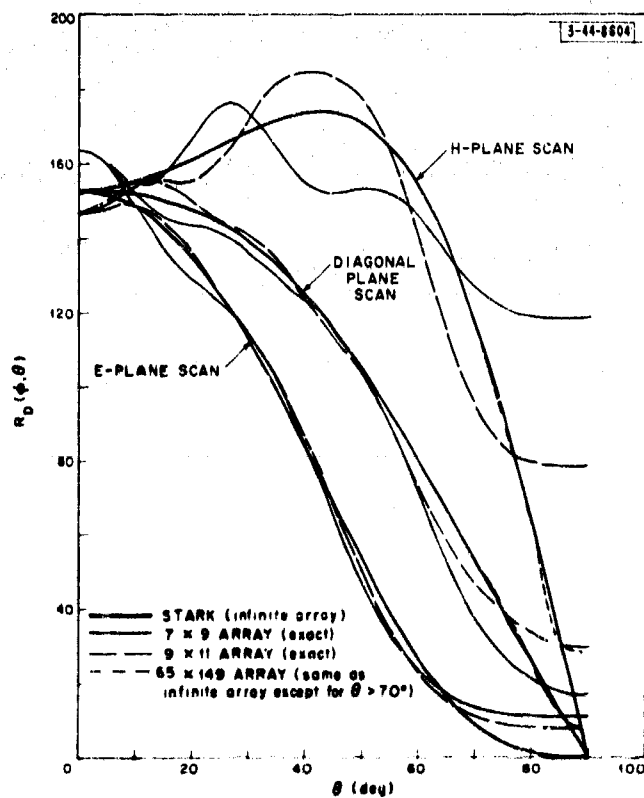


Fig. III-72. Comparison of driving resistance with scan angle for  $\lambda/2$  dipole arrays with  $D = 0.5\lambda$  and  $s = 0.25\lambda$ .

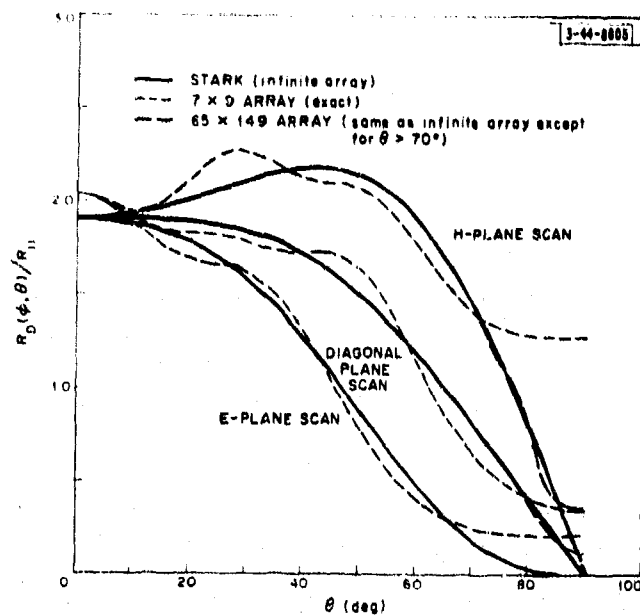


Fig. III-73. Comparison of driving resistance with scan angle for short dipole arrays with  $D = 0.5\lambda$  and  $s = 0.25\lambda$ .

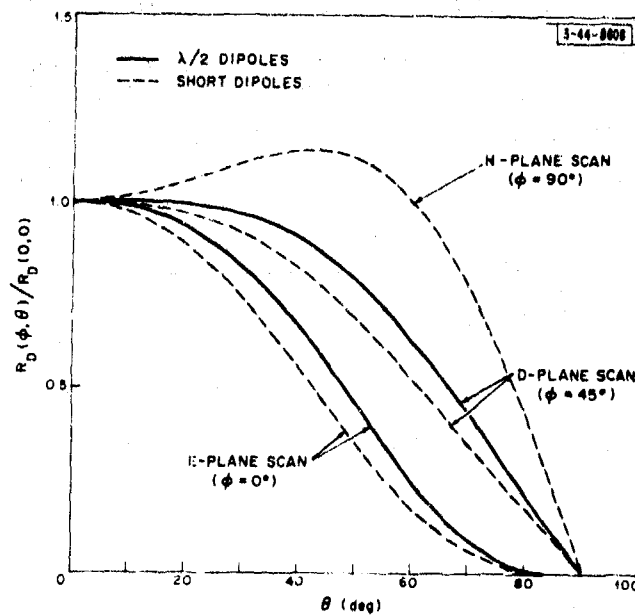


Fig. III-74. Comparison of infinite array driving resistance with scan angle for  $\lambda/2$  dipole array and short dipole array each with  $D = 0.5\lambda$  and  $s = 0.25\lambda$ .

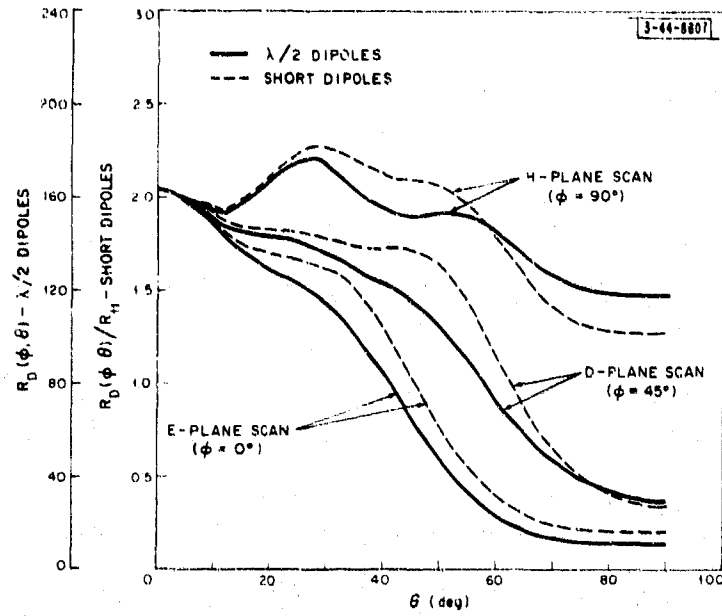


Fig. III-75. Comparison of driving resistances with scan angle for  $\lambda/2$  dipole array and short dipole array each with  $D = 0.5\lambda$  and  $s = 0.25\lambda$ . Array size is  $7 \times 9$ .

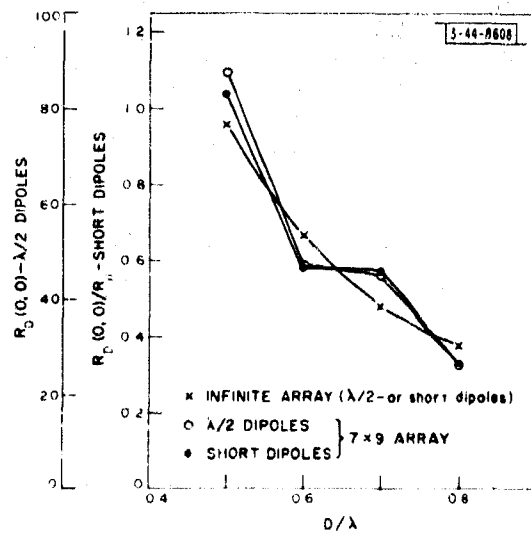


Fig. III-76. Comparison of broadside driving resistance calculations for arrays without ground planes.



Fig. III-77. Comparison of driving resistance with scan angle for  $\lambda/2$  dipole arrays without ground plane;  $D = 0.5\lambda$ .

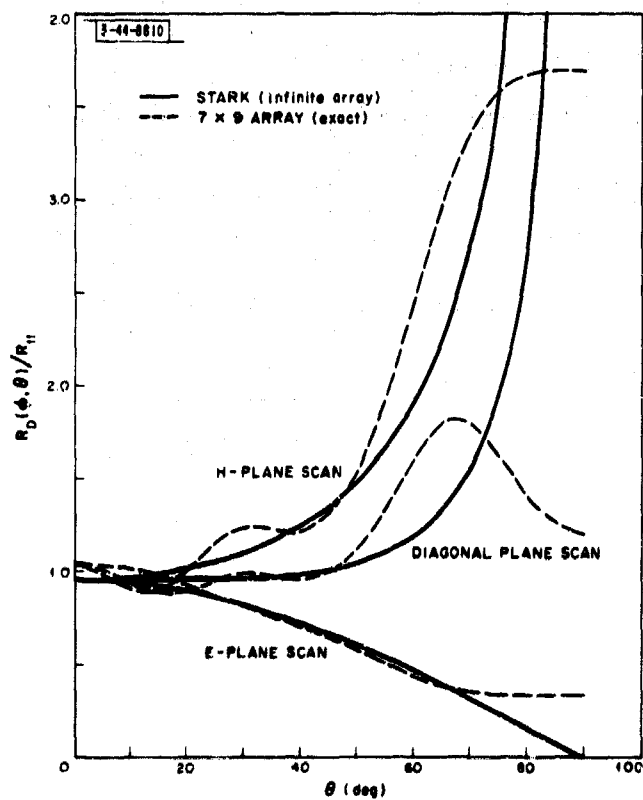
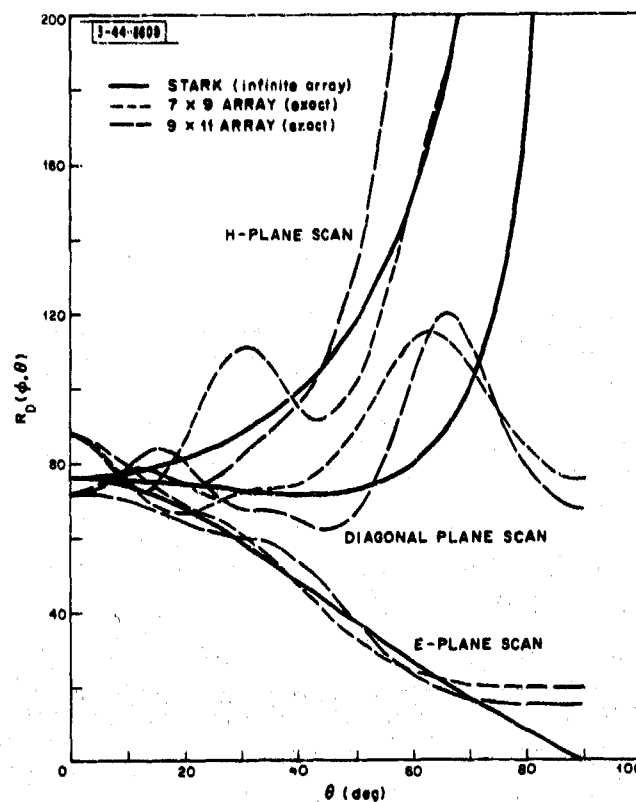


Fig. III-78. Comparison of driving resistance with scan angle for short dipole arrays without ground plane;  $D = 0.5\lambda$ .

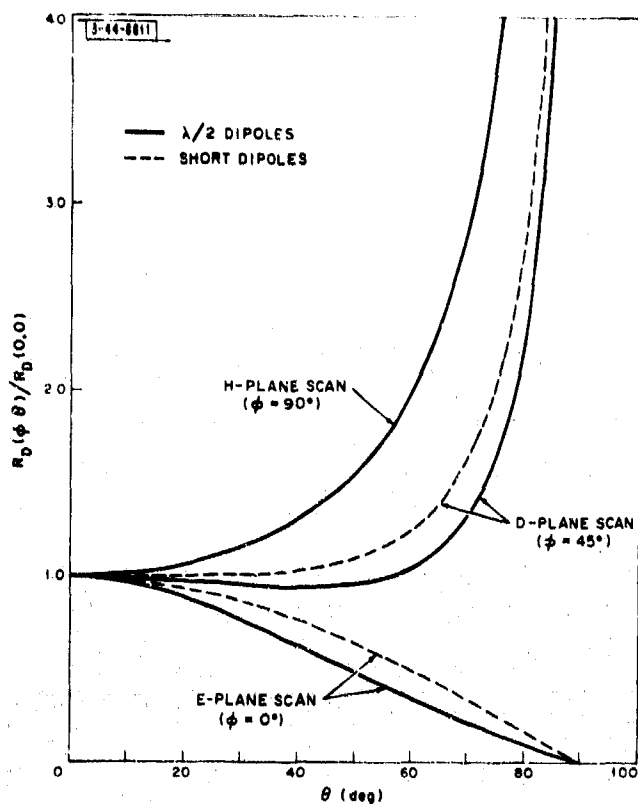


Fig. III-79. Comparison of infinite array driving resistance with scan angle for  $\lambda/2$  dipole array and short dipole array each without a ground plane;  $D = 0.5\lambda$ .

Fig. III-80. Comparison of driving resistance with scan angle for  $\lambda/2$  dipole array and short dipole array each without ground plane;  $D = 0.5\lambda$ . Array size is  $7 \times 9$ .

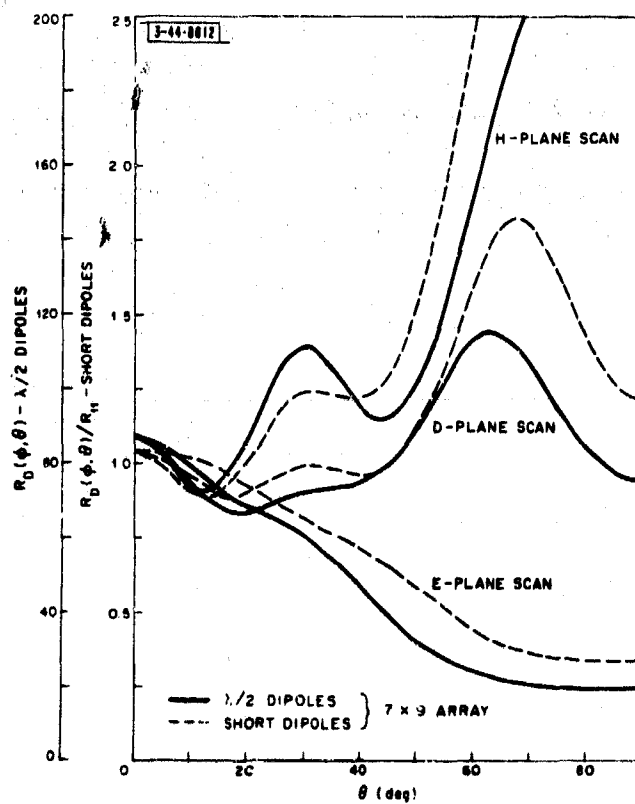


Fig. III-81. Computed values of normalized broad-side element gain function for  $7 \times 9$  arrays of  $\lambda/2$  dipoles.

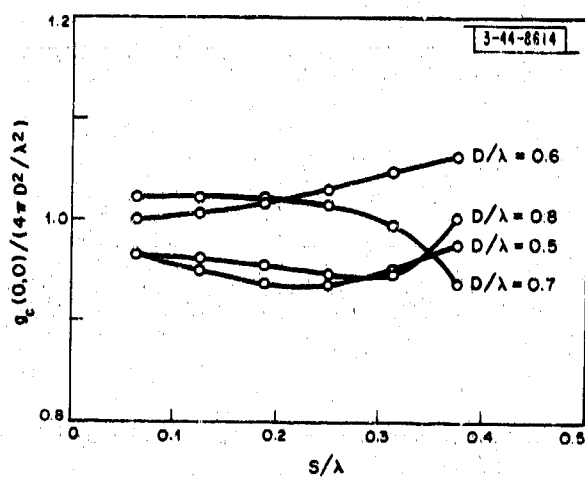
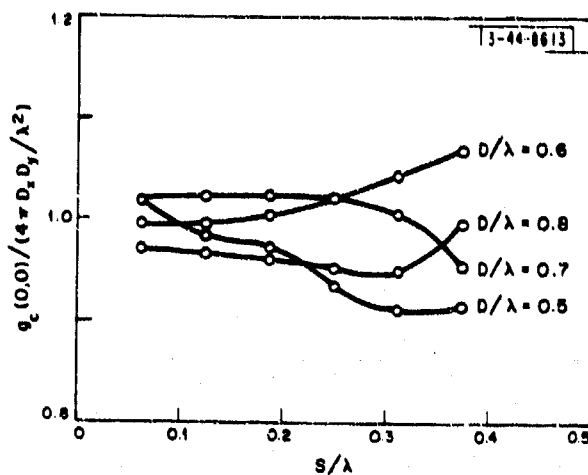
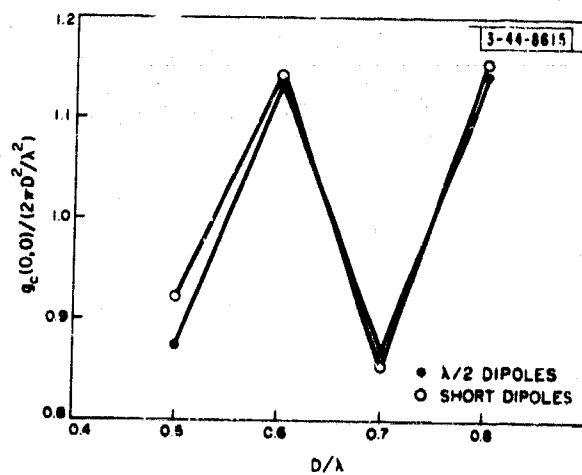


Fig. III-82. Computed values of normalized broad-side element gain function for  $7 \times 9$  arrays of short dipoles.

Fig. III-83. Computed values of normalized broad-side element gain function for  $\lambda/2$  dipole arrays and short dipole arrays without ground planes. Array size is  $7 \times 9$ .



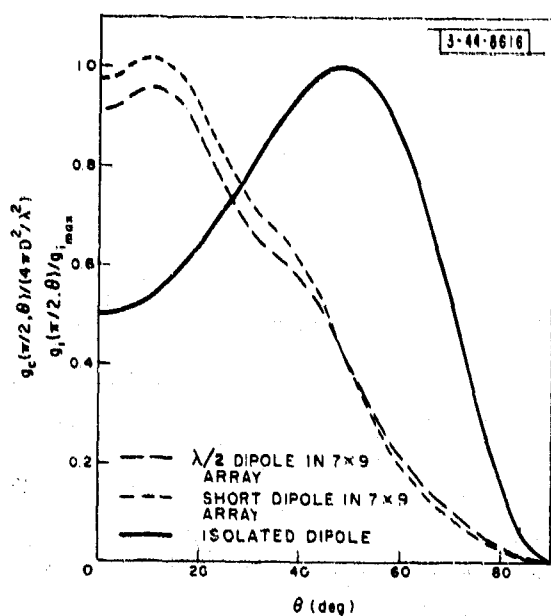


Fig. III-84. Normalized H-plane gain functions for isolated dipoles (short or  $\lambda/2$ ) and for the center elements of  $7 \times 9$  arrays ( $\lambda/2$  dipole or short dipole radiators). Ground plane spacing is  $3\lambda/8$ .

Fig. III-85. Comparison of  $Z_D(\phi, \theta)$  for  $7 \times 9$  arrays of  $\lambda/2$  dipoles with large array results;  $D = 0.5\lambda$ ,  $s = 0.25\lambda$ .

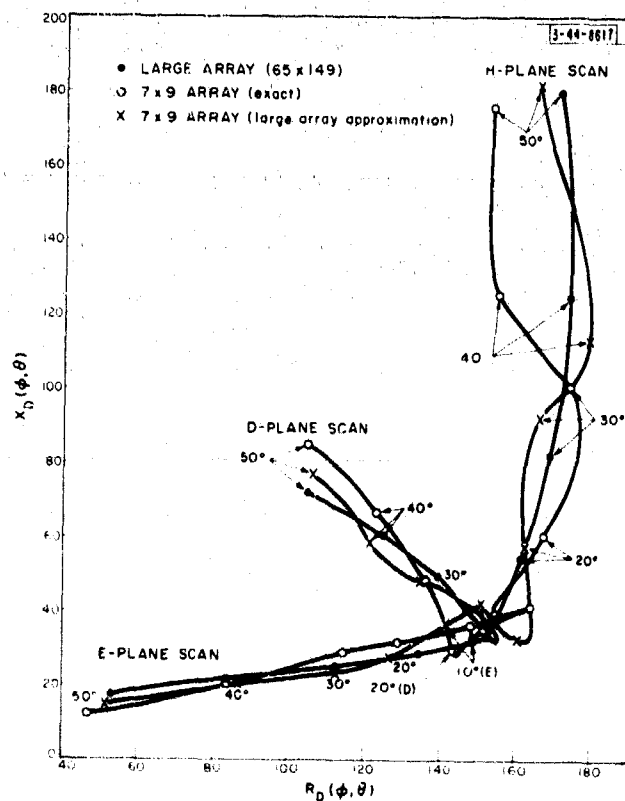


Fig. III-86. Comparison of  $Z_D(\phi, \theta)$  for  $7 \times 9$  and  $9 \times 11$  arrays of  $\lambda/2$  dipoles with large array results;  $D = 0.5\lambda$ ,  $s = 0.25\lambda$ .

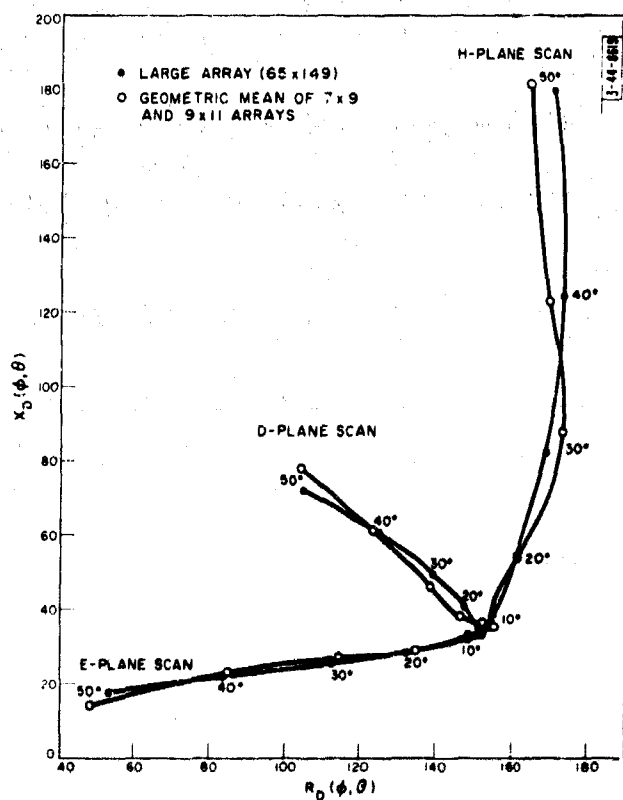
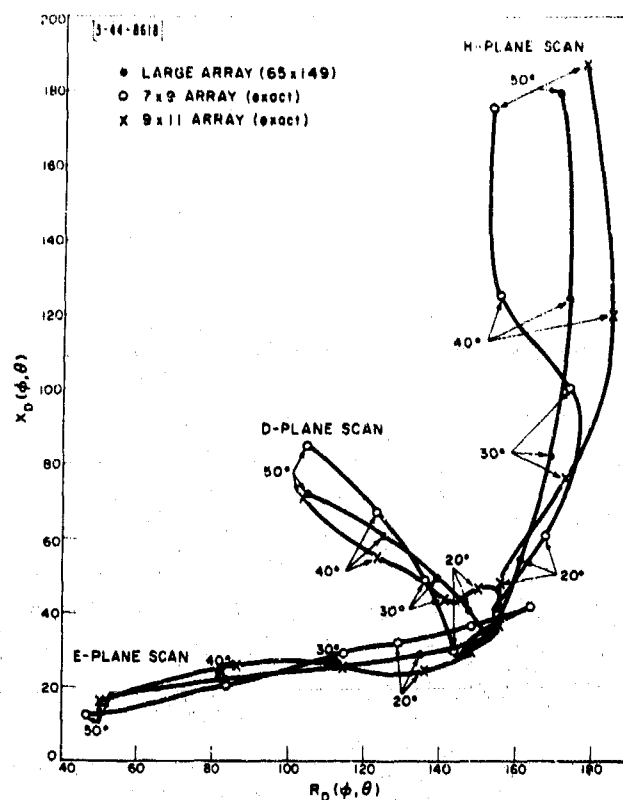


Fig. III-87. Comparison of geometric mean of  $Z_D(\phi, \theta)$  for  $7 \times 9$  and  $9 \times 11$  arrays of  $\lambda/2$  dipoles with large array results;  $D = 0.5\lambda$ ,  $s = 0.25\lambda$ .

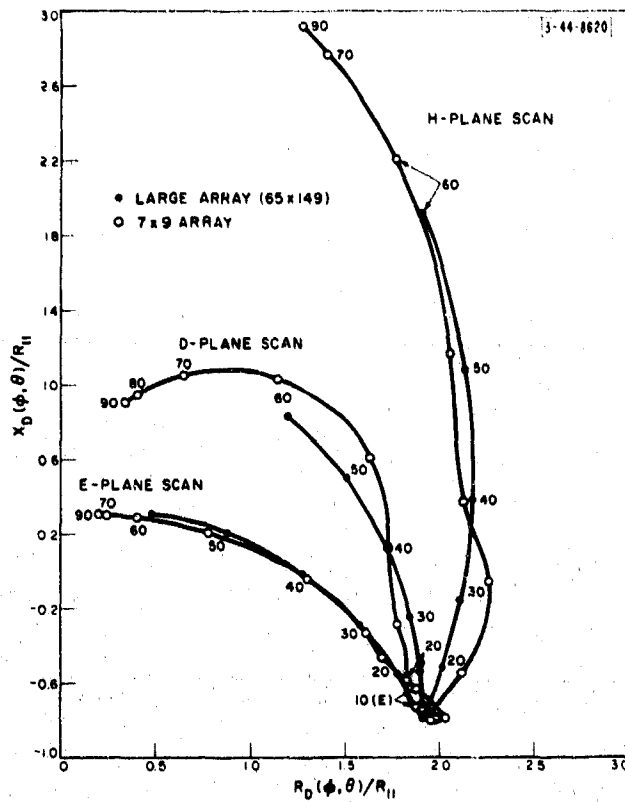


Fig. III-88. Comparison of  $Z_D(\phi, \theta)/R_{11}$  for  $7 \times 9$  array of short dipoles with large array results;  $D = 0.5\lambda$ ,  $s = 0.25\lambda$ .

Fig. III-89. Comparison of  $Z_D(\phi, \theta)$  for  $7 \times 9$  and  $9 \times 11$  arrays of  $\lambda/2$  dipoles with large array results;  $D = 0.6\lambda$ ,  $s = 0.25\lambda$ .

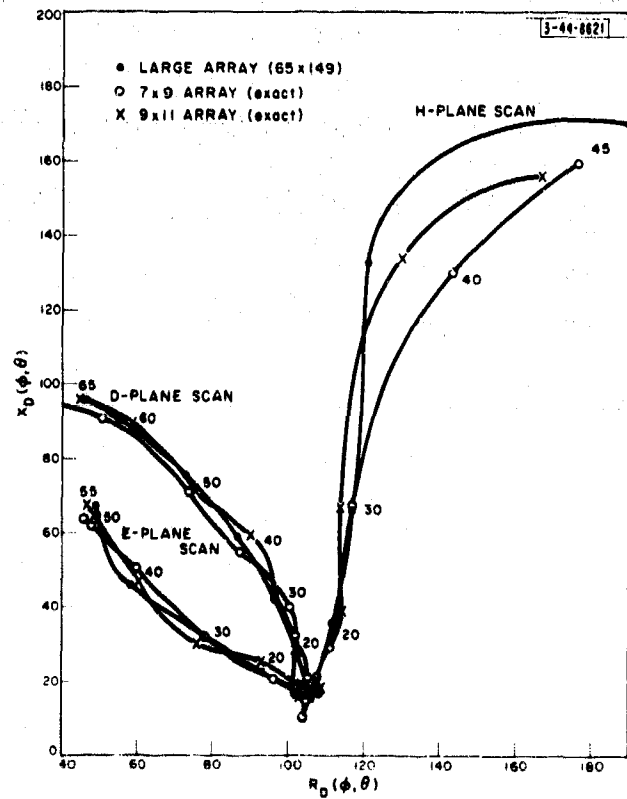


Fig. III-90. Comparison of  $Z_D(\phi, \theta)$  of  $7 \times 9$  and  $9 \times 11$  arrays of  $\lambda/2$  dipoles without ground plane;  $D = 0.5\lambda$ .

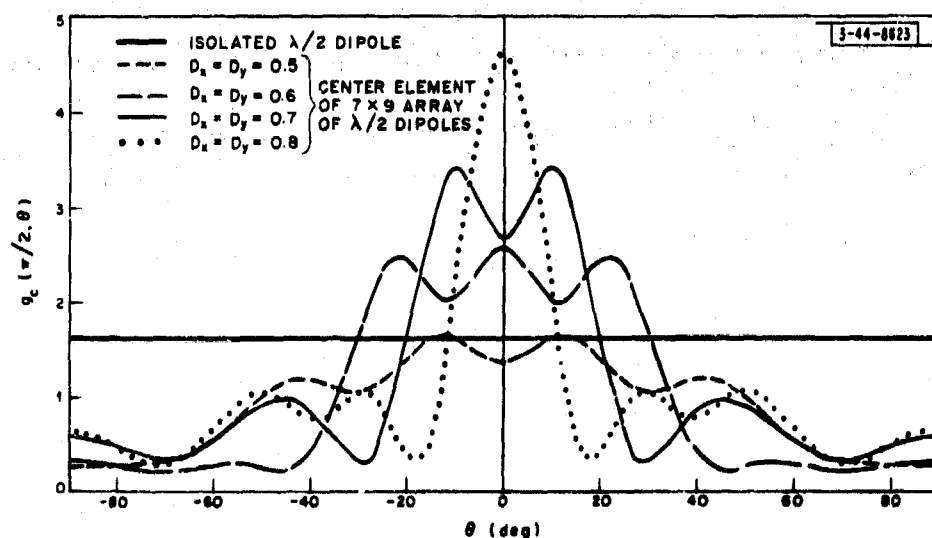
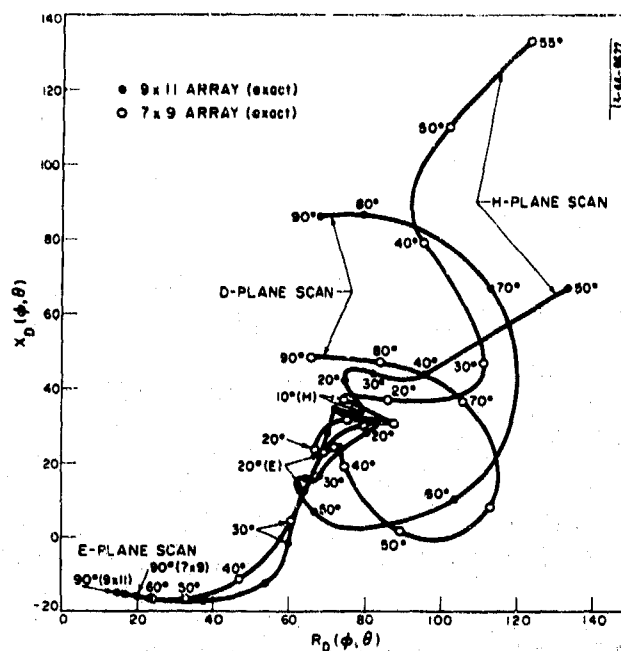


Fig. III-91. H-plane element gain functions for center elements of  $7 \times 9$  arrays of  $\lambda/2$  dipoles; no ground plane.

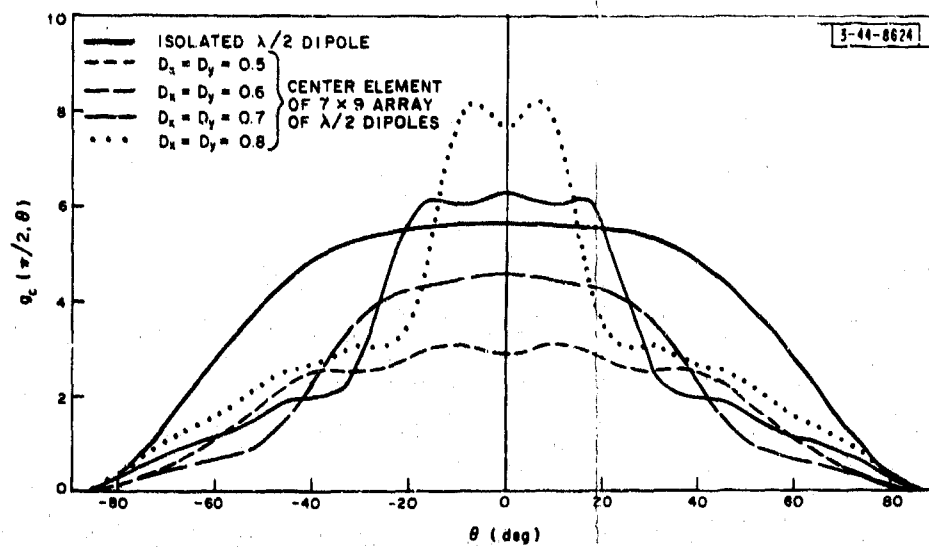


Fig. III-92. H-plane element gain functions for center elements of  $7 \times 9$  arrays of  $\lambda/2$  dipoles;  $s = 0.25\lambda$ .

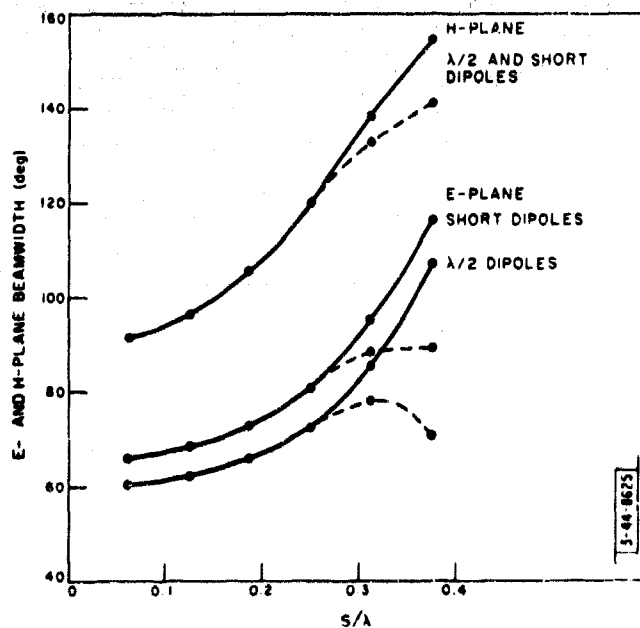


Fig. III-93. Half-power beamwidth of single dipole vs height  $s$  above ground. (Solid curve is half power relative to broadside; dashed curve is relative to angle of maximum gain.)



Fig. III-94. Half-power E- and H-plane beamwidths of gain function for  $7 \times 9$  array without ground plane; short dipole and  $\lambda/2$  dipole radiators.

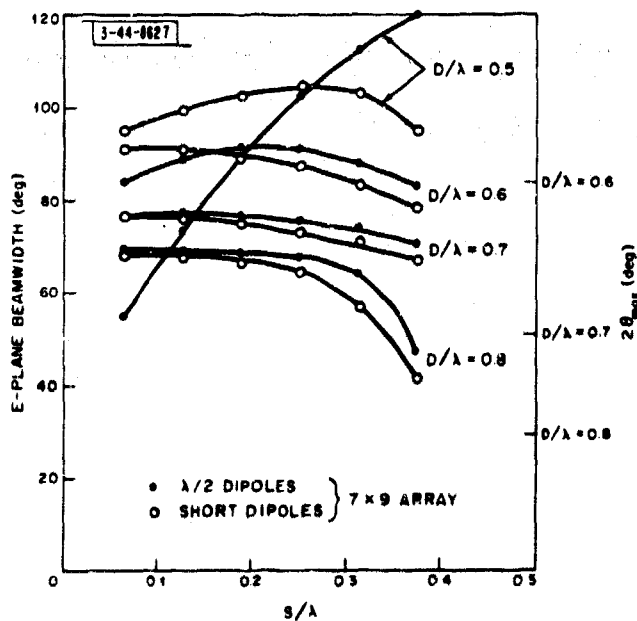
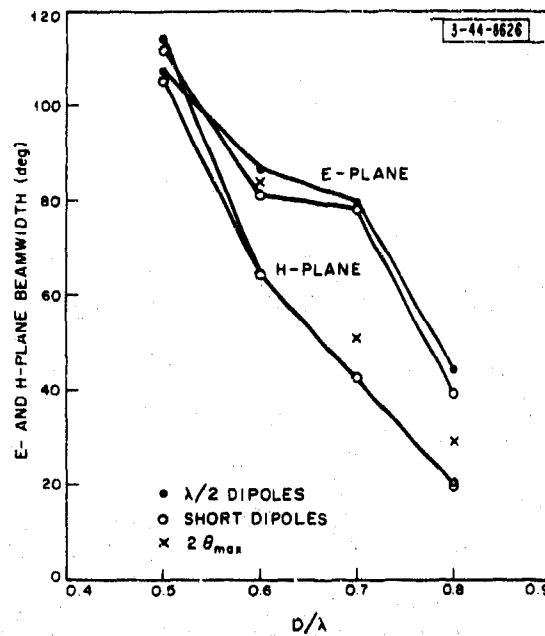


Fig. III-95. Half-power E-plane beamwidth of gain function for broadside match vs  $D/\lambda$  and  $s/\lambda$ ;  $7 \times 9$  arrays,  $\lambda/2$  dipole radiators or short dipole radiators.

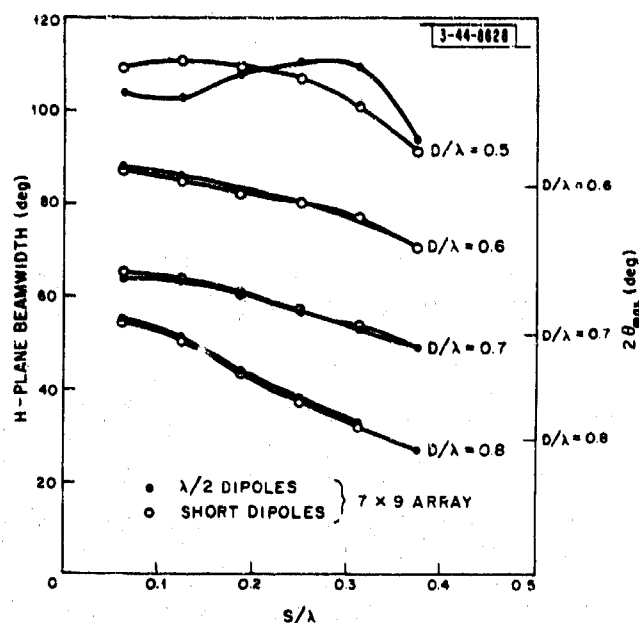


Fig. III-96. Half-power H-plane beamwidth of gain function for broadside match vs  $D/\lambda$  and  $s/\lambda$ ;  $7 \times 9$  arrays,  $\lambda/2$  dipole radiators or short dipole radiators.

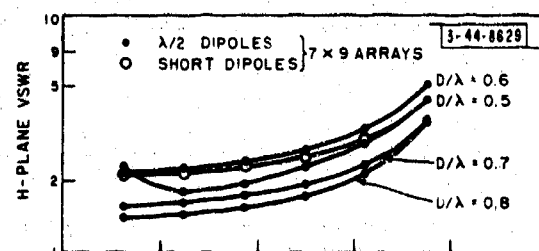
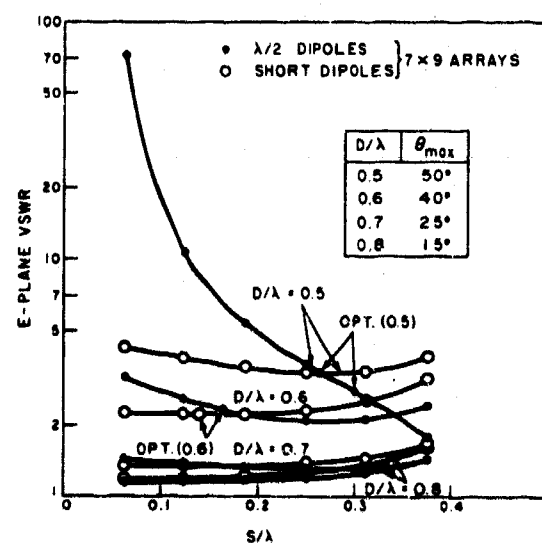


Fig. III-97. Maximum VSWR to scan to  $\theta_{\max}$  (match at  $\theta = 0$ );  $7 \times 9$  arrays,  $\lambda/2$  dipole radiators or short dipole radiators.



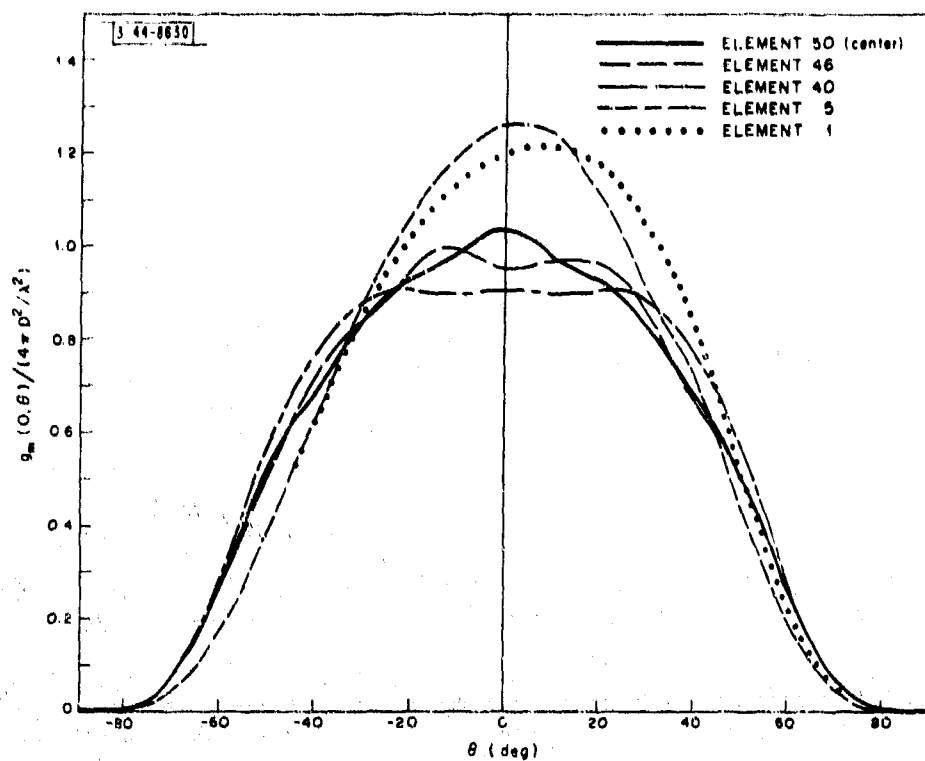


Fig. III-98. E-plane gain functions for 5 elements in  $9 \times 11$  array of  $\lambda/2$  dipoles;  $D = 0.5\lambda$ ,  $s = 0.25\lambda$ .

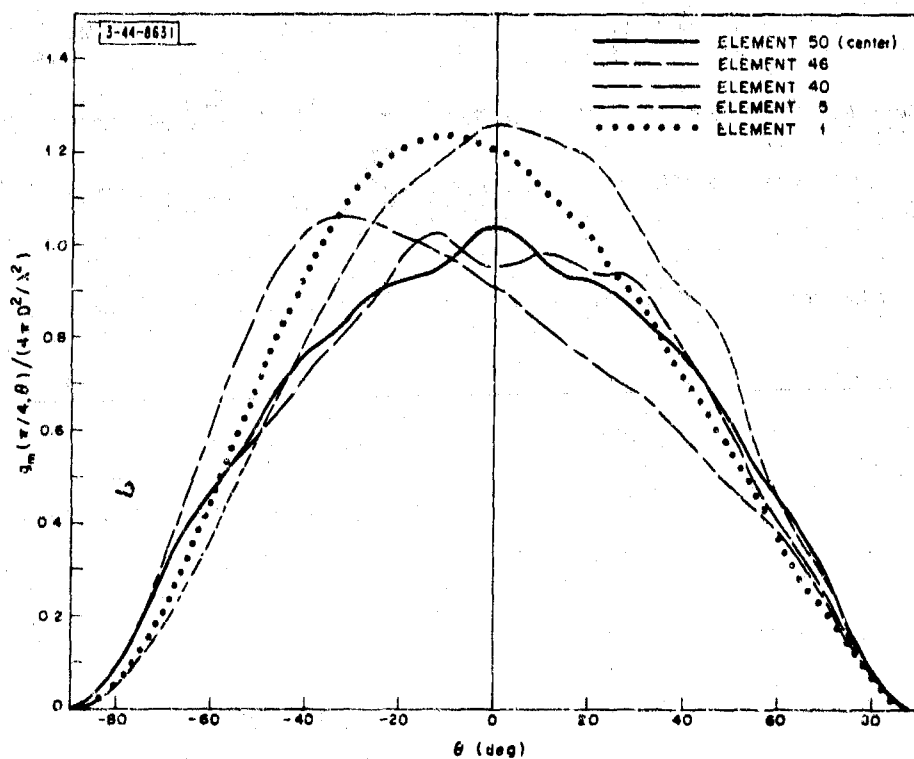


Fig. III-99. D-plane gain functions for 5 elements in  $9 \times 11$  array of  $\lambda/2$  dipoles;  $D = 0.5\lambda$ ,  $s = 0.25\lambda$ .

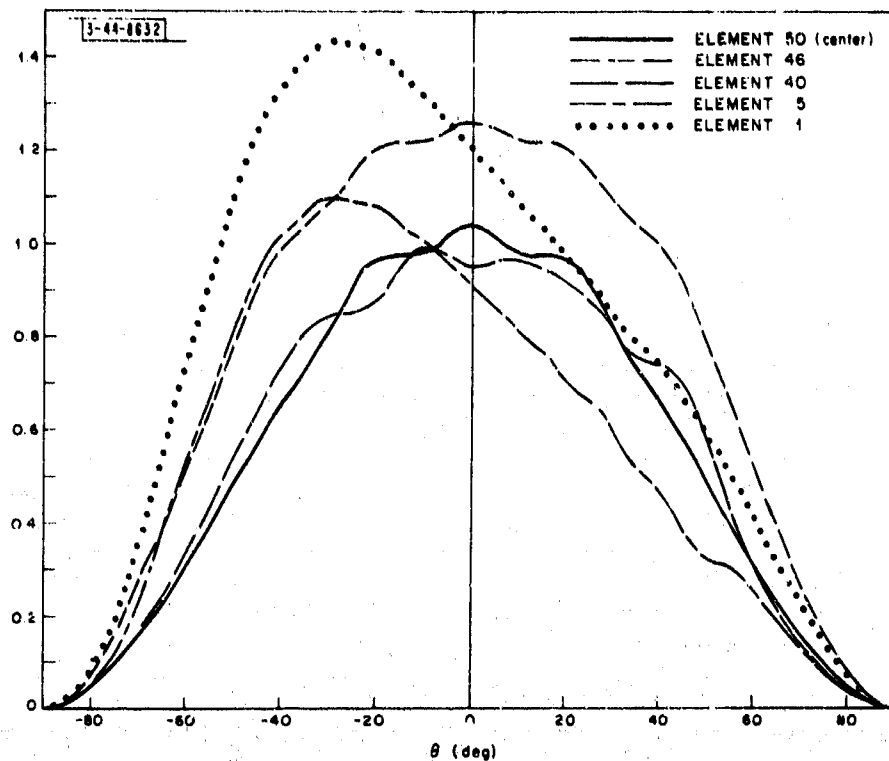


Fig. III-100. H-plane gain functions for 5 elements in  $9 \times 11$  array of  $\lambda/2$  dipoles;  $D = 0.5\lambda$ ,  $s = 0.25\lambda$ .

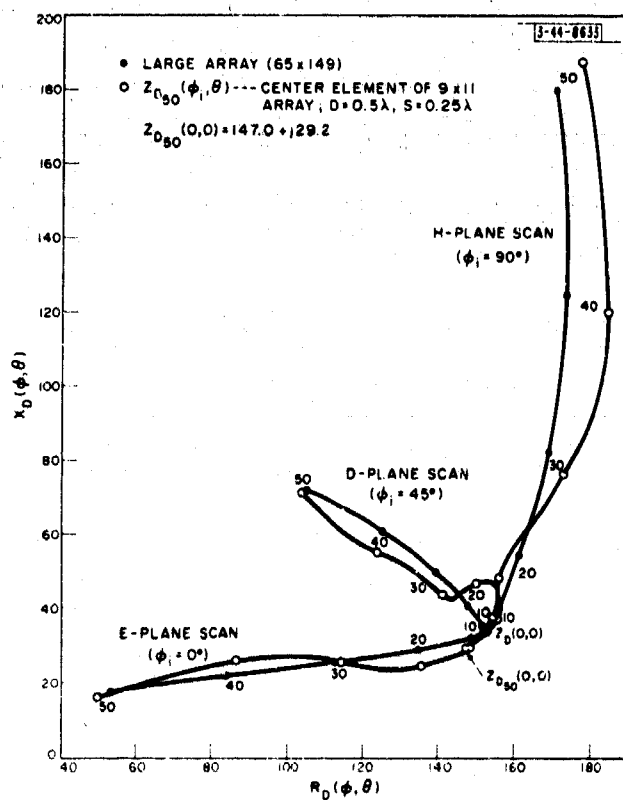


Fig. III-101. Variation of driving impedance with scan angle for center element of  $9 \times 11$  array of  $\lambda/2$  dipoles;  $D = 0.5\lambda$ ,  $s = 0.25\lambda$ .

Fig. III-102. Variation of driving impedance with scan angle for interior, noncenter element of  $9 \times 11$  array of  $\lambda/2$  dipoles;  $D = 0.5\lambda$ ,  $s = 0.25\lambda$ .

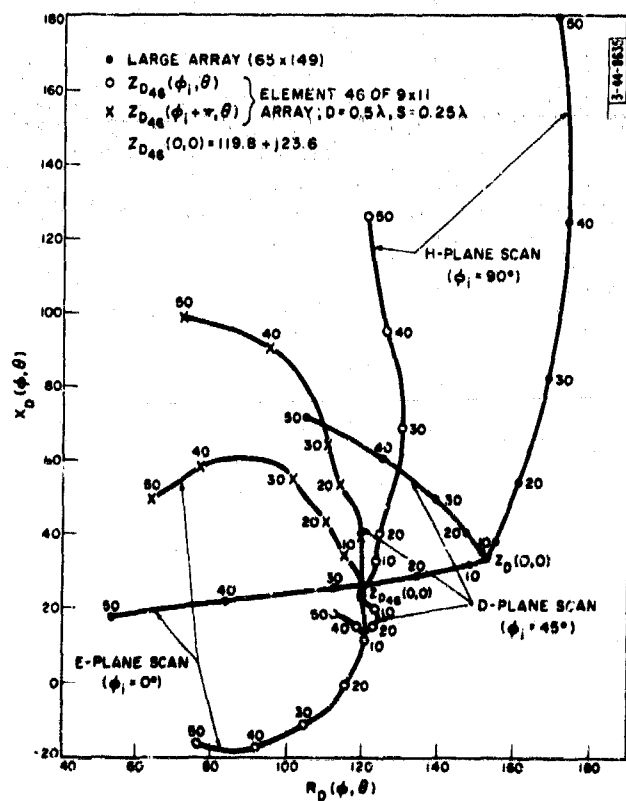
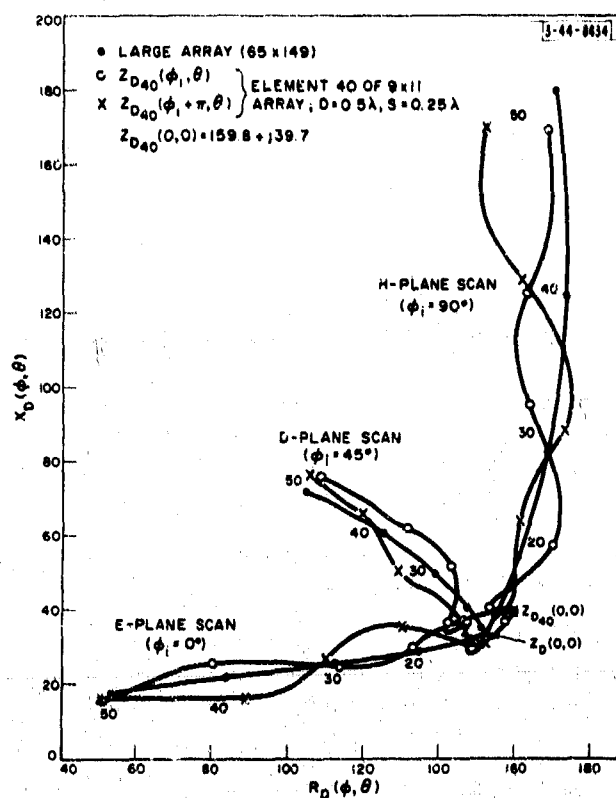


Fig. III-103. Variation of driving impedance with scan angle for element in center of parallel-dipole edge of  $9 \times 11$  array of  $\lambda/2$  dipoles;  $D = 0.5\lambda$ ,  $s = 0.25\lambda$ .

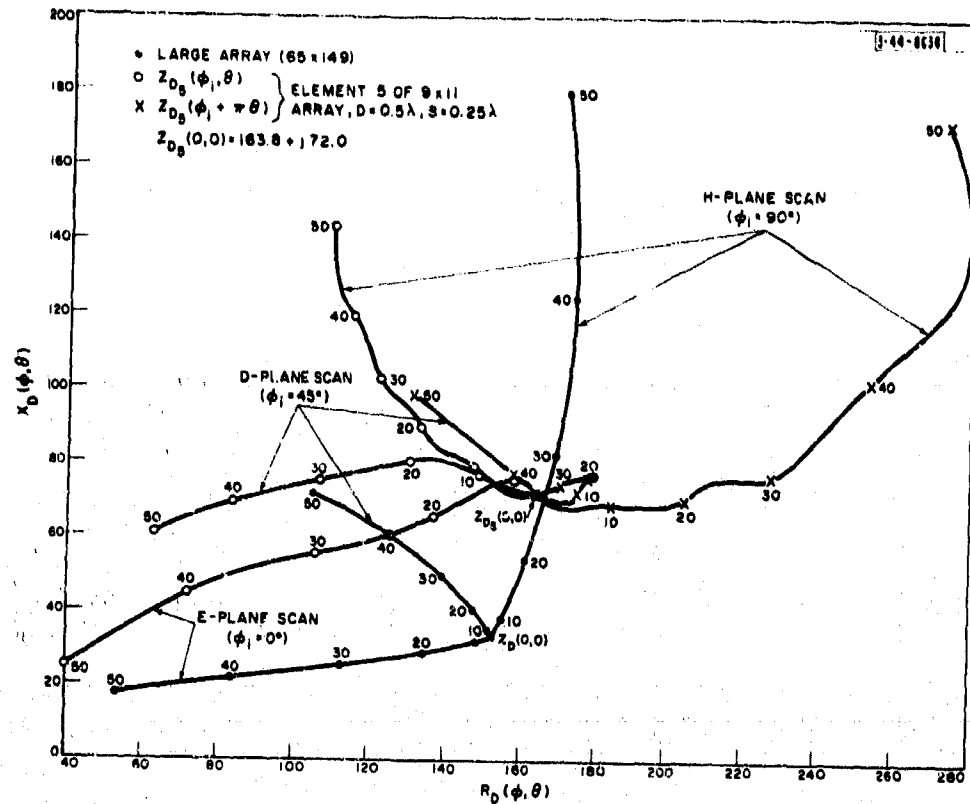


Fig. III-104. Variation of driving impedance with scan angle for element in center of collinear-dipole edge of  $9 \times 11$  array of  $\lambda/2$  dipoles;  $D = 0.5\lambda$ ,  $s = 0.25\lambda$ .

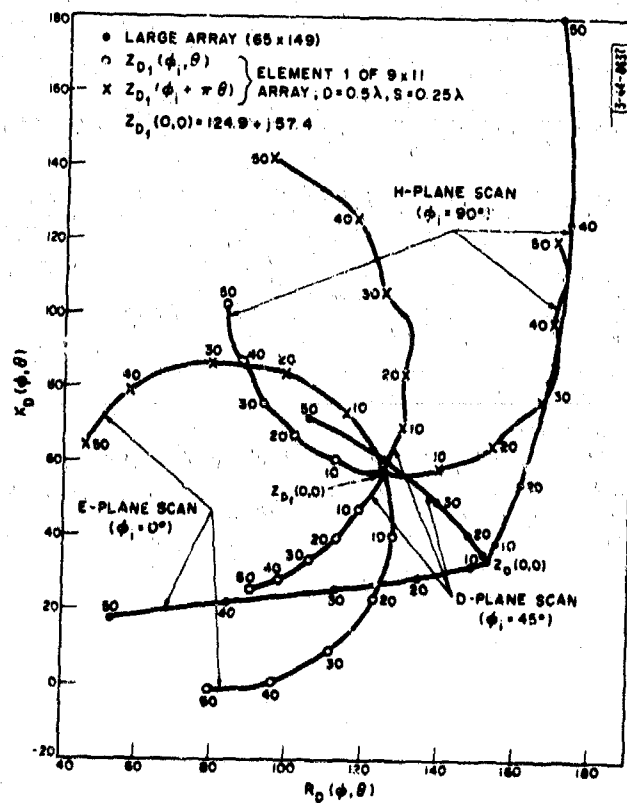


Fig. III-105. Variation of driving impedance with scan angle for corner element of  $9 \times 11$  array of  $\lambda/2$  dipoles;  $D = 0.5\lambda$ ,  $s = 0.25\lambda$ .

## CHAPTER 4

### EXPERIMENTAL MUTUAL COUPLING PROGRAM

T. B. Lewis  
J. L. Allen

#### SUMMARY

In this chapter the experimental mutual coupling program recently begun is described and the first results are reported. There are a great many methods of determining the variation of impedance of an antenna in an array, e.g., mutual impedance matrix, scattering coefficients, simulation techniques, and model arrays have all been utilized. Although each method has its disadvantages, the most direct method, building a small array and feed network and actually measuring the impedance of an element, was chosen. Consequently, a  $10 \times 10$  dipole array was built and it was excited by an  $8 \times 8$  Butler matrix at a frequency of 1.3 Gcps.

Because dipole arrays are readily amenable to mathematical analyses, the experimental program using dipoles was used primarily for verification. When the theoretical and experimental data were compared, it was found that agreement was well within the expected limits. Because the computed impedance was available only for  $\lambda/2$  dipoles scanned along the principal E-, H- and D-planes, it seemed that comparing the experimental data for  $3/8\lambda$  dipoles scanned by a Butler matrix might be ridiculous. However, the close agreement of the data pointed out that the size of the dipoles mounted above a ground plane is not an important parameter in the variation of impedance as a function of scan.

#### A. INTRODUCTION

##### 1. Survey of Element Impedance Measurement Techniques

In the quest for a unified understanding of the effects of mutual coupling of the performance of arrays, there is an obvious need for experimental measurements. If the effects of coupling in all antenna types of interest were amenable to mathematical analyses, a measurements program would only be necessary for verification of the analyses; since the number of types of antennas which can be mathematically analyzed is severely limited, the necessity for an experimental program is enhanced.

Measurement of coupling effects is no easy task. For some time, workers often took the "easy out" of basing an estimate of the coupling difficulties to be expected with a particular type of antenna on a measurement of the magnitude of the coupling between two isolated antennas as a function of separation. Recent results\* have shown that such measurements can be completely misleading. Consequently, we are forced to do a more thorough experimental job and actually determine the impedance or reflection coefficient variation of an element of an array as the array is scanned.

There are still a number of techniques by which one might arrive at this goal. These have varying degrees of applicability, accuracy, and convenience. The principal techniques are:

- (1) The variation of the classical complex mutual impedance between two antennas is determined (as a function of relative position) experimentally, and from the measured data the mutual impedance matrix is determined. By suitably factoring the drive circuits into this matrix and

---

\* J. L. Allen, Trans. IEEE, PTGAP (Correspondence), AP-12, 371 (1964).

then performing a matrix inversion, a matrix relating the source excitation of each antenna to the current that flows in that antenna can be computed. From this matrix the driving impedance and pattern data can be obtained.

- (2) One can measure directly the complex value of the signal coupled into an antenna by each of the other antennas being excited one at a time (with all others terminated). The total coupled energy when the array is operating is the vector sum of these individual contributions. This is a so-called "scattering coefficient" or mutual admittance approach.
- (3) One can measure directly the impedance variation of the center element of a model array as the array is scanned. This could be done either by building an array large enough so that the central element sees negligible edge effect or by simulating an element of an infinite array by imaging techniques.\* The impedance measurement is a direct one, in either case.

Each of these techniques has its advantages and disadvantages. The first is relatively easy<sup>†</sup> but is of questionable generality: the assumption that the mutual impedance between two isolated antennas can be operated upon to produce the variation of impedance of an entire array depends for its validity on the antennas being geometrically simple so that open circuiting an antenna is precisely equivalent to removing it from the array. This technique is probably applicable only to the same kinds of antennas that can be mathematically analyzed: thin dipoles and thin slots. The second technique involves the actual construction of at least an array large enough to render edge effects negligible. It also depends for the accuracy of the result on the ability to measure accurately the amplitude and phase of very small scattering coefficients. Thus, there is a question of accuracy of the resulting answers. Finally, if one is willing to build an array to perform experiments, it is a comparatively easy and "one-shot" extension to build a feed network so that the entire array can be excited and the element impedance variation with scan angle measured directly. As an alternative method of direct measurement, it has recently been pointed out<sup>‡</sup> that a number of waveguide structures can be constructed to simulate the various scan angles in an array.

It appears to us that method 3 is the best choice. The choice between waveguide simulation and the construction and exciting of a small array is not an obvious one. The waveguide approach is hard to adapt to some antennas (notably those that are not simple apertures of some sort) and involves a substantial amount of careful machining. On the other hand, it does tend to eliminate the question of edge effects which must always be coped with if one wants to build only a small array to determine the essentially infinite array effects. We have chosen to pursue the direct measurement of mutual impedance on a small array. The choice of this technique rather than the simulation technique was mitigated by the overriding consideration that we were not aware of the simulation approach at the time that the decision was made; even had we known, a strong factor in our choice would have been our desire to check our previous calculated results on dipoles. Consequently, we favor a technique which makes this possible.

## 2. Design Considerations of Experimental Array Feed

Having decided on a technique, the next consideration was the design of a general purpose planar array feed which could be attached to a variety of such array elements for measuring

\* P. W. Hannan, P. J. Meier, and M. A. Balfour, *Trans. IEEE, PTGAP AP-11*, 715 (1963).

† W. P. Rupp, *Microwave J.*, **5**, 95 (1962).

‡ P. W. Hannan, *et al.*, *Trans. IEEE, PTGAP AP-11* (1963).



the impedance of the central (or near central) element. The first efforts were directed toward finding a phasing technique that could be used with an array of many tens of elements. The obvious choice was between an array using analog phase shifting techniques (such as trombone line stretchers) and an array using multiple-beam-forming techniques. The latter appeared to offer advantages insofar as experimental setup time and agonies were concerned, and it was chosen.

The next consideration was the size of the array to be used. Our early computational program results<sup>\*</sup> indicated that for elements like dipoles above a ground plane an absolute minimum size would be on the order of  $5 \times 5$  elements and something larger would be preferable (later results have indicated that elements with wider primary radiation patterns (Part III, Chapter 3) or tendencies towards setting up surface waves<sup>†</sup> may demand a much larger array for accurate impedance determination; however, even such a small array can provide rough data on difficult elements and give warnings of impending problems). Furthermore, since the simplest multiple beam matrix assembly available appeared to be the Butler matrix, it was desirable to restrict the size of the array to either an 8- or a 16-element dimension in the two principal planes. We also anticipated the loan of small arrays that existed at other organizations, and these tended to run in sizes of about  $8 \times 8$  or  $10 \times 10$  elements. Thus it was decided that the beam forming matrix would be an  $8 \times 8$  planar array of Butler matrices. Finally, since most of our available hardware was in the region near L-band, the decision was also made to implement the measurement setup at 1300 Mcps.

### 3. Experimental Plan

In order to have a cross-check on both the validity of the experimental procedure and previous computations, the initial phase of the experimental program was directed towards arrays of dipoles above a ground plane, making use of a  $10 \times 10$  array of dipoles (the height of which can be adjusted) loaned to us by the Sperry Gyroscope Division of the Sperry Rand Corporation. Some data on this array are reported below.

We then plan to proceed for practical reasons to an array of open-ended waveguide, since such an element appears to have significant advantages from a mechanical configuration point of view, and significant questions from an electrical standpoint.

This we propose to follow with experiments on an  $8 \times 8$  log-periodic array which has been offered on loan by Rome Air Development Center and the Bendix Corporation. This would give us a chance to examine a complex radiator above a ground plane which some experiments have shown may have peculiar and poorly understood coupling properties. As a complement to this complex antenna above the ground plane, we plan to make measurements on a small array of open-ended circular ridged-guide radiators of the type developed by Hughes Aircraft Company and outlined in Part II of this report under the S-band subarray. These radiators will also allow us to do experiments with dual polarization.

### B. DESCRIPTION OF EXPERIMENTAL SYSTEM

As stated above, the initial phase of the experimental mutual coupling program used a  $10 \times 10$  array of dipoles arranged on a square grid above an aluminum ground plane. Figure III-106

---

<sup>\*</sup> J. L. Allen, Trans. IEEE, PGAP AP-10, 566 (1962) and TR-236.

<sup>†</sup> R. H. T. Bates, "Mode Theory Approach to Arrays," IEEE Trans. on Antennas and Propagation, to be published in March 1965.

shows the array. The dipoles in Fig. III-106 are spaced  $0.6\lambda$  apart and are  $1/8\lambda$  above the ground plane. Their height above the ground plane is easily changed, and spacings of  $1/4\lambda$  and  $3/8\lambda$  have also been used. Figure III-107 shows a single dipole, which is slot-fed with an open-ended termination. The wings of the dipole are nearly  $3/8\lambda$  at the frequency used throughout the measurements, 1.3 Gcps. Figure III-108 shows the impedance variation of a typical single element above an infinite ground plane (actually  $4 \times 4$  feet) as a function of height above the ground plane. The average VSWR of all elements when placed  $1/4\lambda$  above a ground plane was found to be 1.44 with a maximum VSWR of 1.74.

The center  $8 \times 8$  array of dipoles is excited through an  $8 \times 8$  Butler beam-forming matrix, fabricated by the Advanced Development Laboratories. The other dipoles not driven by the Butler matrix are terminated in 50 ohms. Figure III-109 shows a block diagram of the beam-forming matrix and a photograph of the actual beam former within the experimental system appears in Fig. III-110. A typical matrix has the following characteristics:

Average VSWR	
Beam ports *	1.10 (1.24 max)
Antenna ports	1.11 (1.19 max)
rms phase error	$1.8^\circ$
rms amplitude error	0.18 db
Average isolation between	
Beam ports	44 db (27.5 db min)
Antenna ports	36 db (29.0 db min)

The beam can be easily pointed in any of 64 different directions by changing the input port of matrix m-0 and by changing the cables from matrix m-0 to matrices m-1 through m-8. Thus the combination of the beam-forming matrix and the  $10 \times 10$  array of dipoles provides a convenient setup for studying the variation of element impedance as a function of beam pointing angles.

In order to measure the impedance, a cable from one of the antenna ports of the matrix to an array element was replaced by a slotted line. The slotted line had the identical electrical characteristics of the cable it replaced. Figure III-111 is a block diagram of the apparatus used to find the VSWR of the element in question. Figure III-110 shows the display.

### C. RESULTS AND COMPARISON OF DATA WITH COMPUTED DATA

In order to identify the various beam positions, a system of describing the elevation and azimuth phasing is employed. The elevation phasing is termed  $\alpha_i$  with values from  $\pm\alpha_1$  to  $\pm\alpha_4$ . These values of  $\alpha$  correspond to the eight different phasings produced by a Butler matrix. The azimuth phasing is termed  $\beta_k$  with eight different values also available. The choice of sign can readily be made from the diagram in Fig. III-112. The element numbering system is shown there also. The beam position will therefore be designated by specifying  $\alpha_i$  and  $\beta_k$ .

Figures III-113(a-d) to III-115(a-c) show the measured impedances of element 56 for various beam positions and for spacings above the ground of  $\lambda/4$ ,  $3\lambda/8$  and  $\lambda/8$ , respectively. In each of the 16 Smith Charts,  $\alpha_i$  is held constant while  $\beta_k$  is changed. Figure III-116(a-d) displays the impedance plots for element 82 as an example of the impedance variation of an edge element. The height above the ground plane for these measurements is  $1/4\lambda$ , and the same beam positions of Figs. III-113(a-d) to III-115(a-d) are used.

\* See Fig. III-109 to differentiate between beam ports and antenna ports.

Because the main objective of these experimental measurements was to verify the theoretical computer computations as described in Part III, Chapter 3, the experimental results were compared with the Smith Chart plots of the computed data. The computer program currently can calculate the impedance of a  $\lambda/2$  dipole only as the beam is scanned along the principal E- and H-planes and also along a diagonal scan. The beam former using the Butler matrices cannot scan the principal E- and H-planes, but it can scan quite closely to the H-plane scan by holding the elevation phasing at  $\pm\alpha_1$  and the E-plane scan can be approximated by  $\pm\beta_1$ . The diagonal plane can be scanned exactly by the beam former.

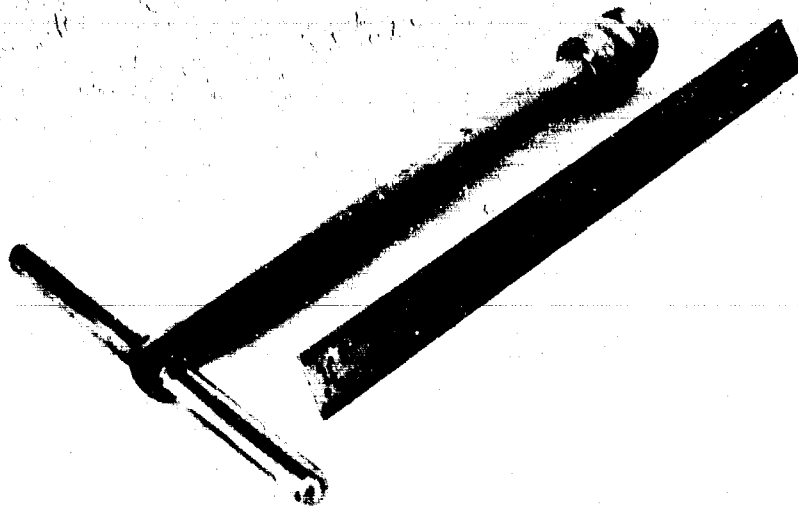
In order to make a comparison of the computed impedance for elements matched at broadside with experimental data of the dipoles which are approximately matched when placed individually above a ground plane, the experimental data were matched at broadside by an arbitrary network. This network was chosen such to match one group of experimental data with the corresponding computed data. In this case the experimental data in Fig. III-117(a-b) were given the "optimum" match. This same network was then used to transform all other experimental data. Although it is not entirely correct to compare the computed data which were computed from dipoles matched at broadside to the experimental results, which used dipoles not matched at broadside, the error introduced surely does not contribute nearly as much error as the difference in the Butler scans and the computer scans.

In Fig. III-117(a-b) the Smith Chart plots of the computed data for the H-plane scan for  $1/4\lambda$  height above the ground plane are shown with the experimental data appearing as nonconnected points. The agreement between the data is quite good especially considering that the beam former did not scan the principal planes. The same agreement is evident in Fig. III-118(a-b) which shows the comparison for the E-plane scan. The diagonal scan data are displayed in Fig. III-119.

In conclusion, the agreement between the computed impedances and the transformed measured impedances seems to point up that the impedance variation as a function of scan angle does not depend a great deal on the size of the dipole. That is, the experimental  $3/8\lambda$  dipole data agree quite well with the computed  $1/2\lambda$  data. When comparing purely theoretical data, the impedance of short dipoles and  $\lambda/2$  dipoles above a ground plane also are not greatly different. More importantly, the theoretical results have been confirmed experimentally even with errors in scan angle, generator impedance and size of dipole.



Fig. III-106. Experimental  $10 \times 10$  array of dipoles mounted above aluminum ground plane. Height of element above ground plane is  $1/8\lambda$  and spacing between elements is  $0.6\lambda$ .



P 7-6-201

Fig. III-107. Typical dipole used in  $10 \times 10$  experimental array. Wings of this slot-fed, open-ended terminated dipole are  $3/8\lambda$  at frequency of operation, 1.3 Gcps.

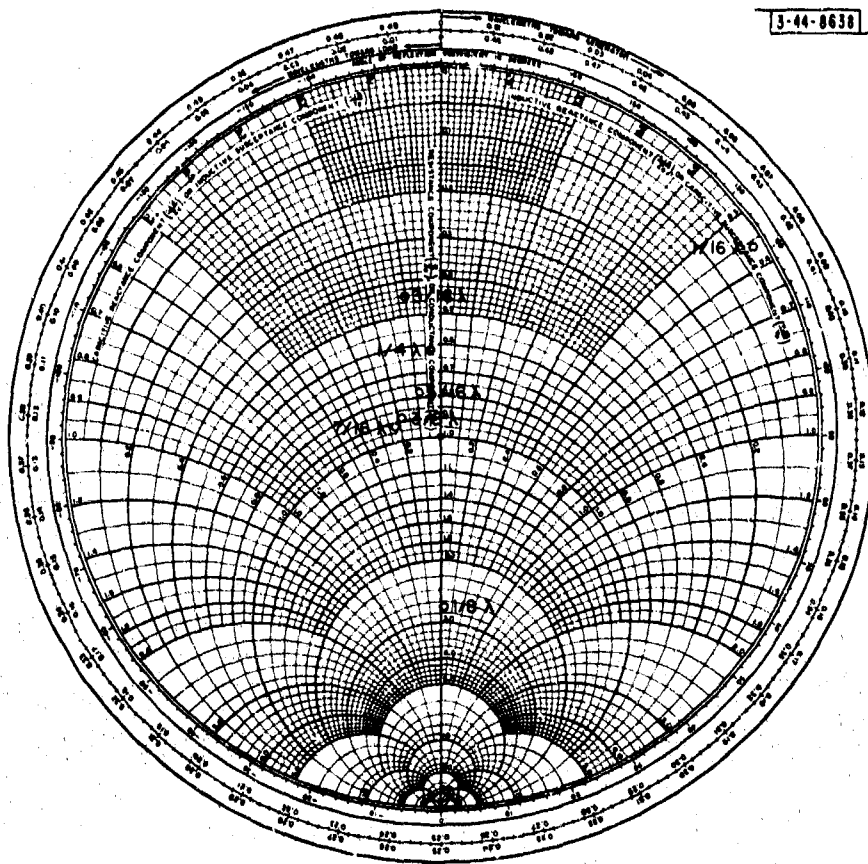


Fig. III-108. Plot of impedance of a typical dipole as height above ground plane is changed.

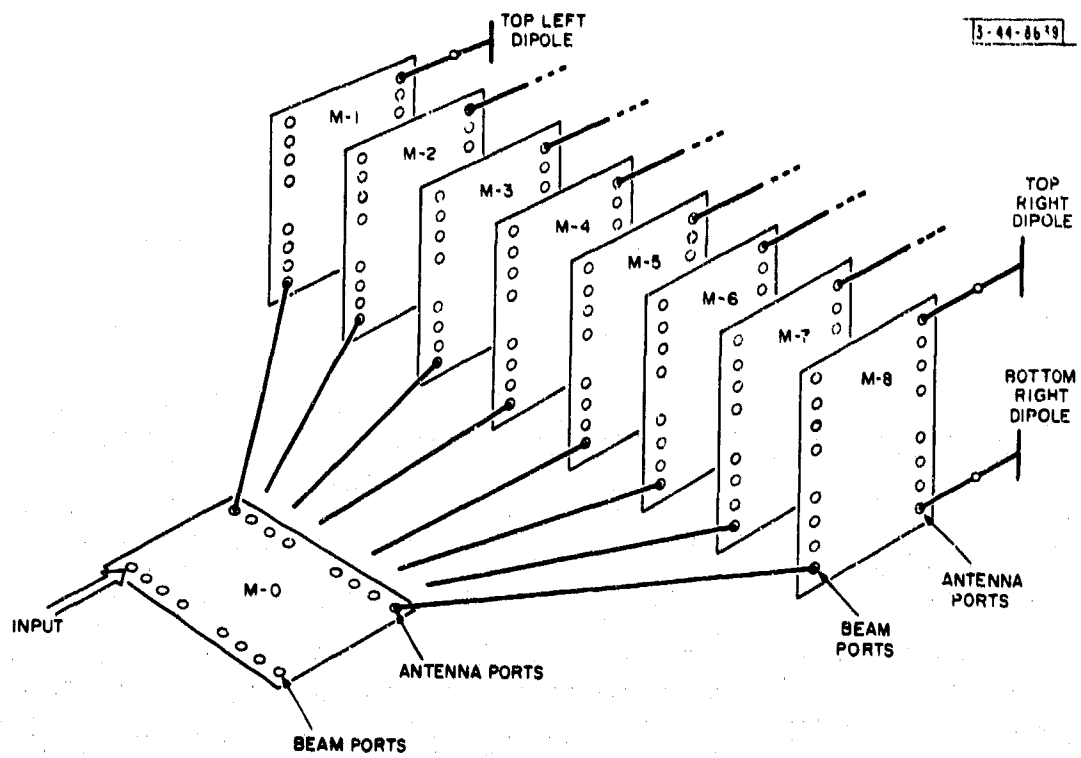


Fig. III-109. Block diagram of multiple beam-forming matrix using 9 Butler matrices.

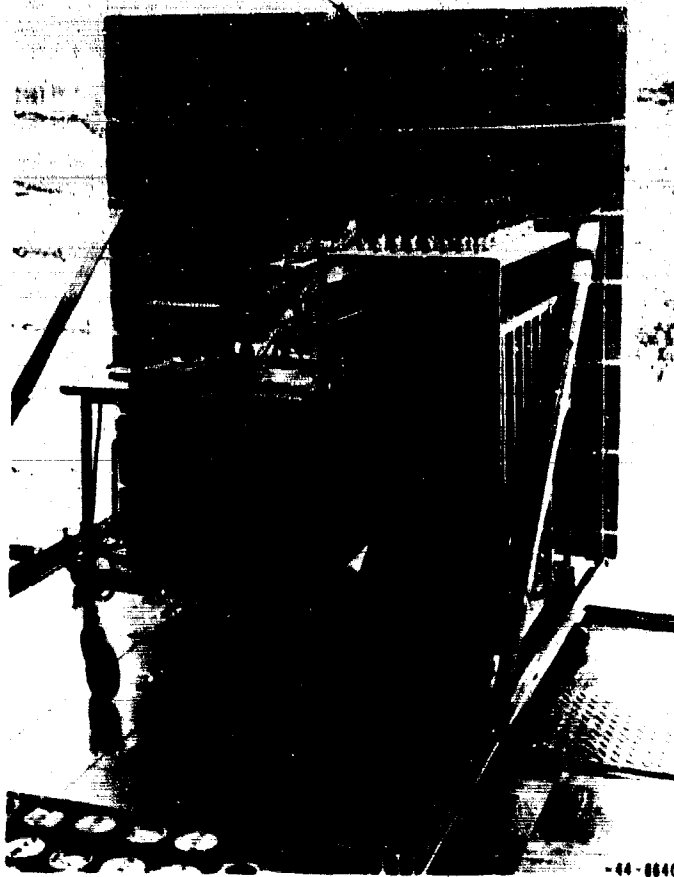


Fig. III-110. Experimental  $10 \times 10$  dipole array (from behind) and measuring apparatus used to determine impedance of various elements.

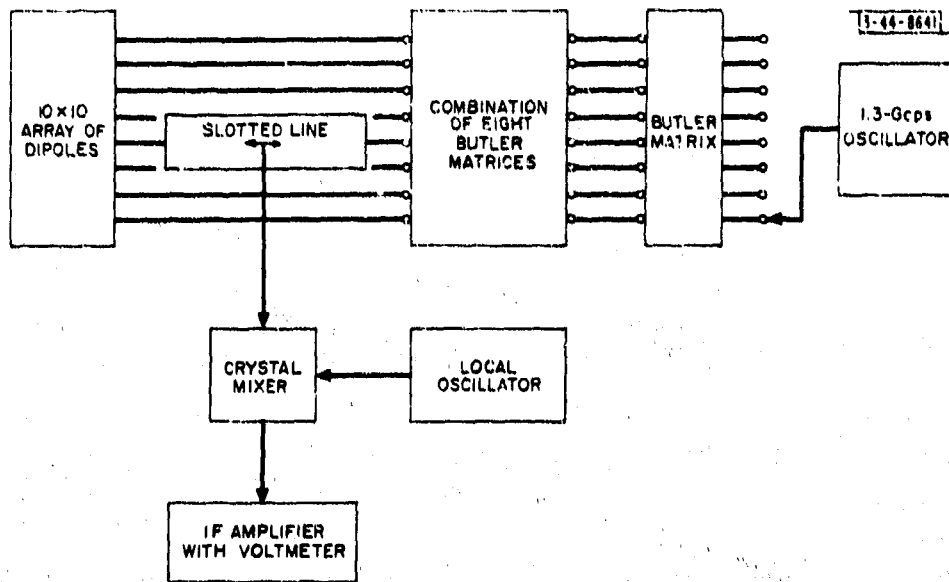


Fig. III-111. Block diagram of apparatus used to measure impedance of dipole in array as beam position is changed.

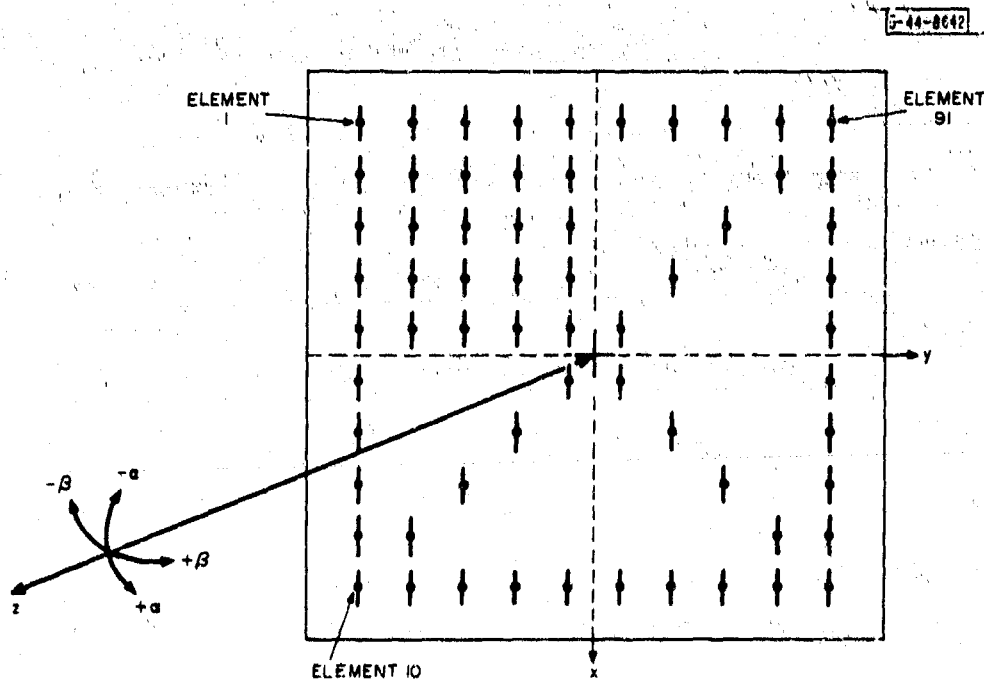
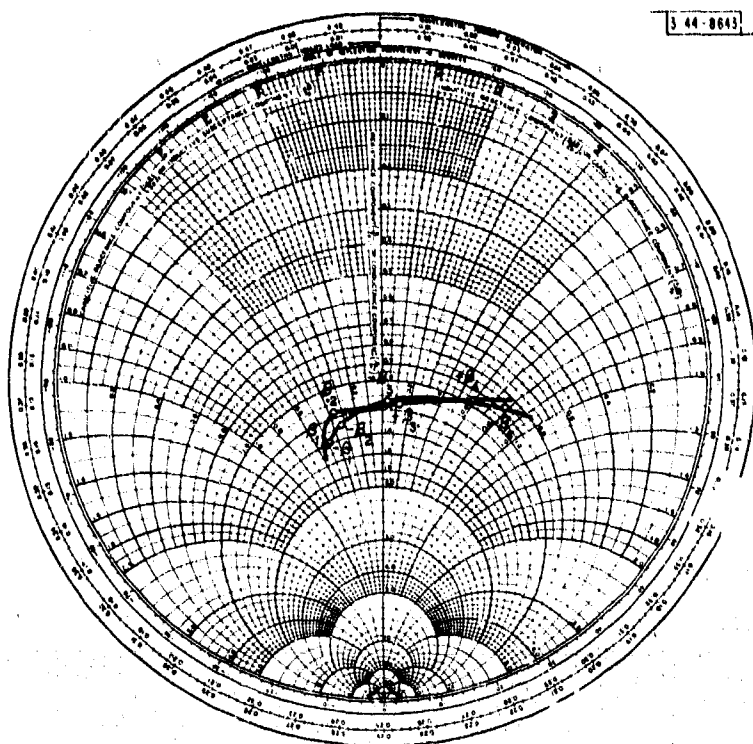
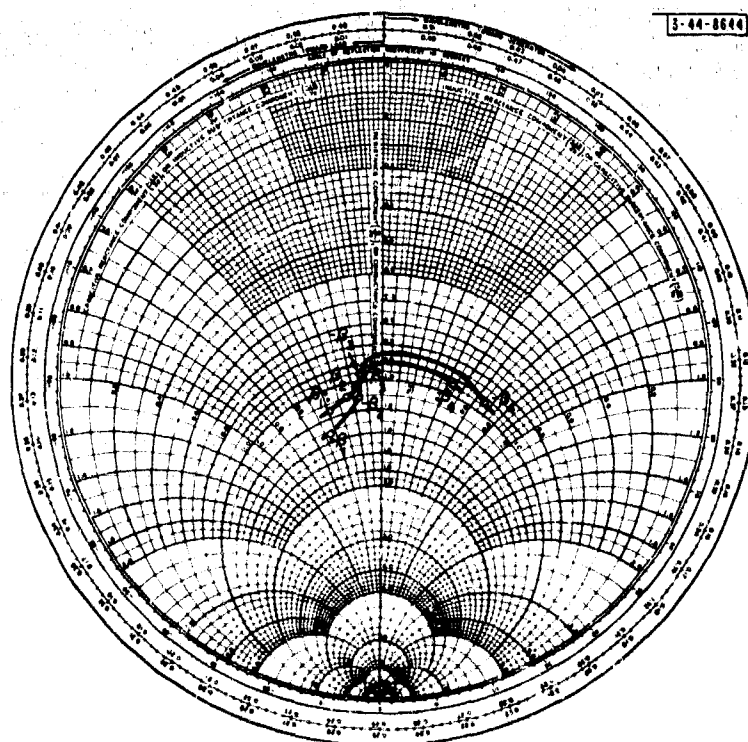


Fig. III-112. Diagram of 10x10 dipole array showing beam pointing nomenclature and element numbering system.



(a) Elevation phasing  $-a_1$ .

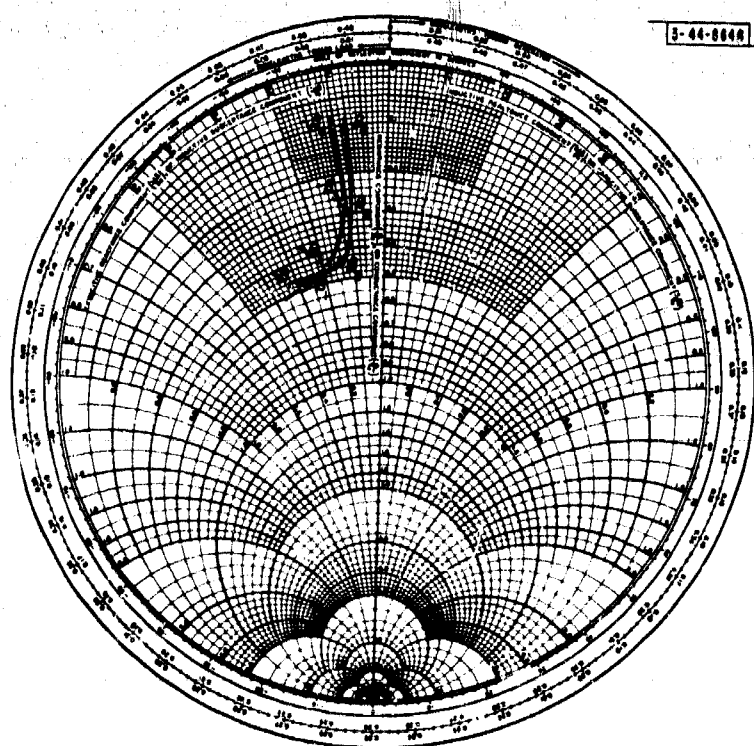
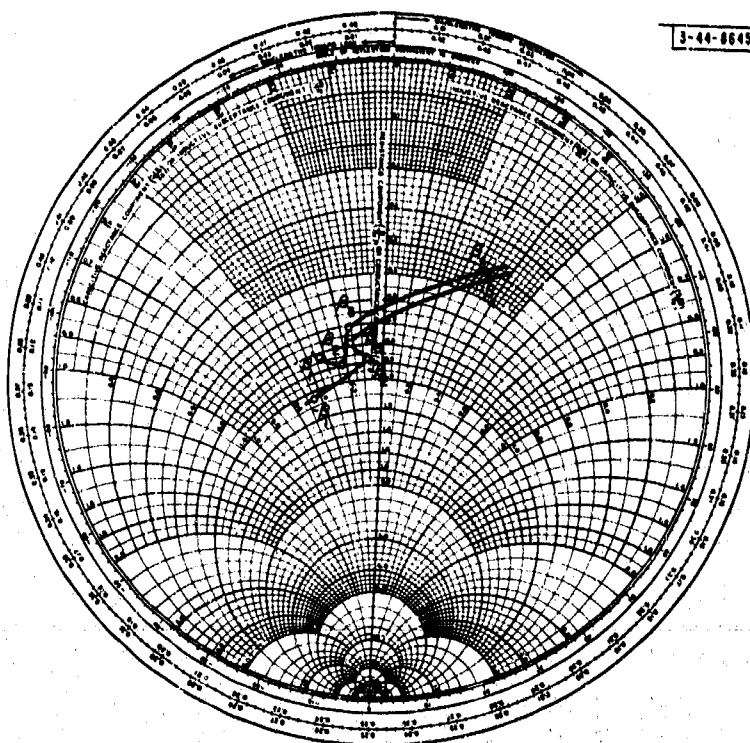


(b) Elevation phasing  $-a_2$ .

Fig. III-113. Impedance of dipole 56 as beam is scanned in azimuth, and as elevation phasing  $a_1$  is constant. Height above ground plane is  $1/4\lambda$ .

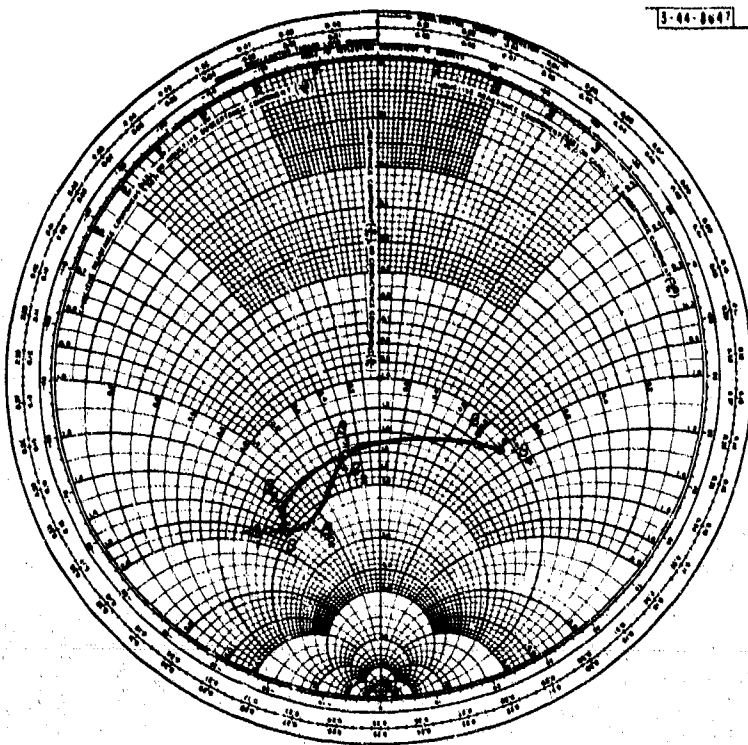


(c) Elevation phasing  $-\alpha_3$ .

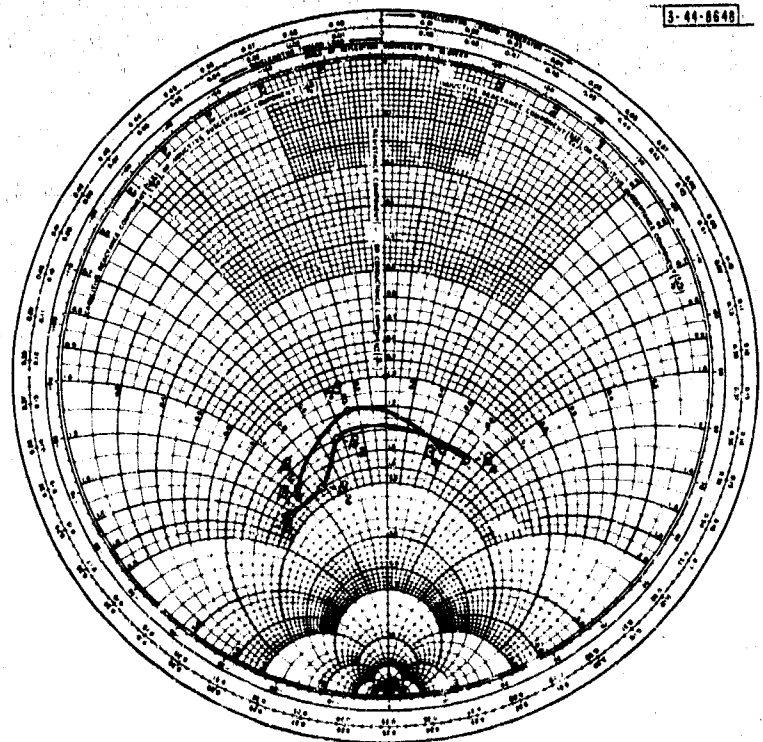


(d) Elevation phasing  $-\alpha_4$ .

Fig. III-113. Continued.



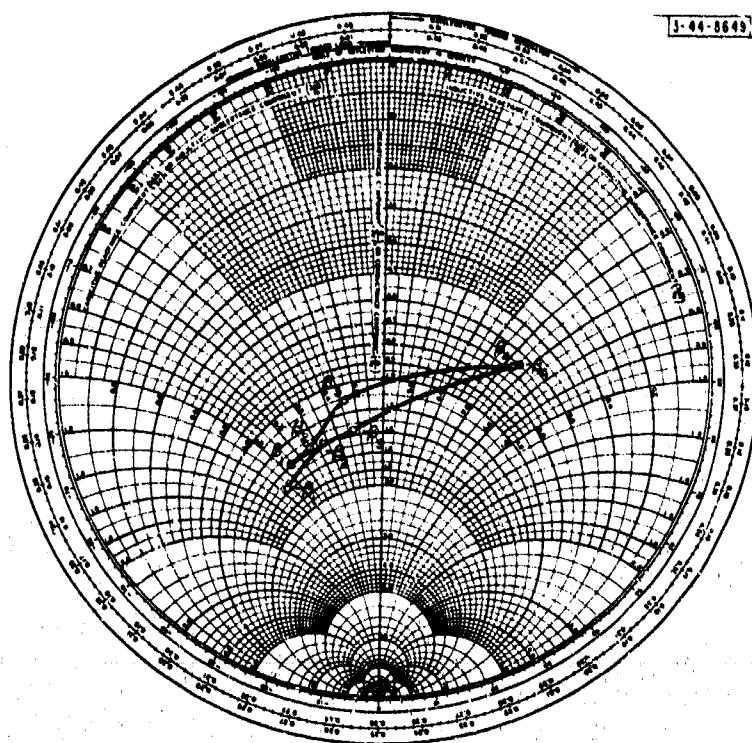
(a) Elevation phasing  $-a_1$ .



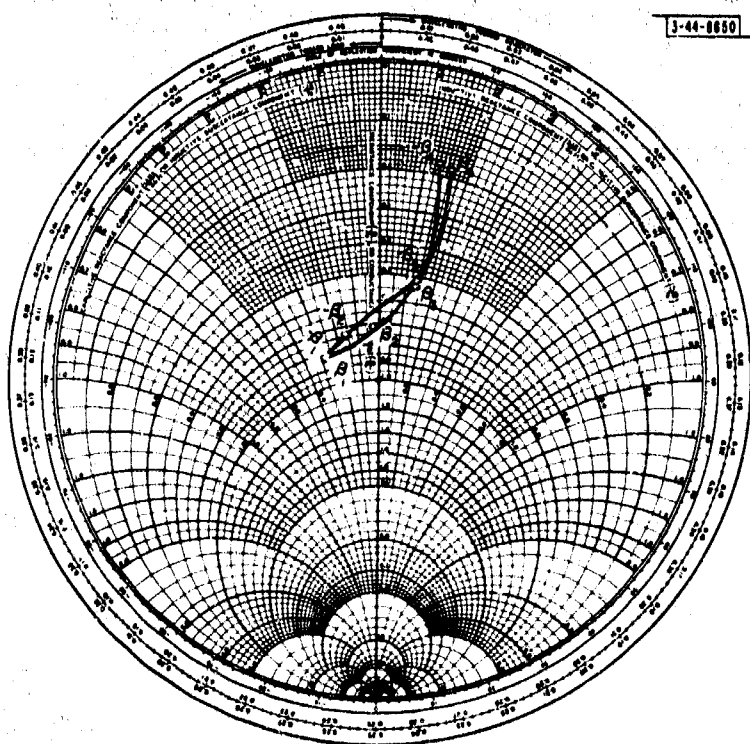
(b) Elevation phasing  $-a_2$ .

Fig. III-114. Impedance of dipole 56 as beam is scanned in azimuth and elevation phasing  $a_1$  is constant. Height above ground plane is  $3/8\lambda$ .

(c) Elevation phasing  $-\alpha_3$ .

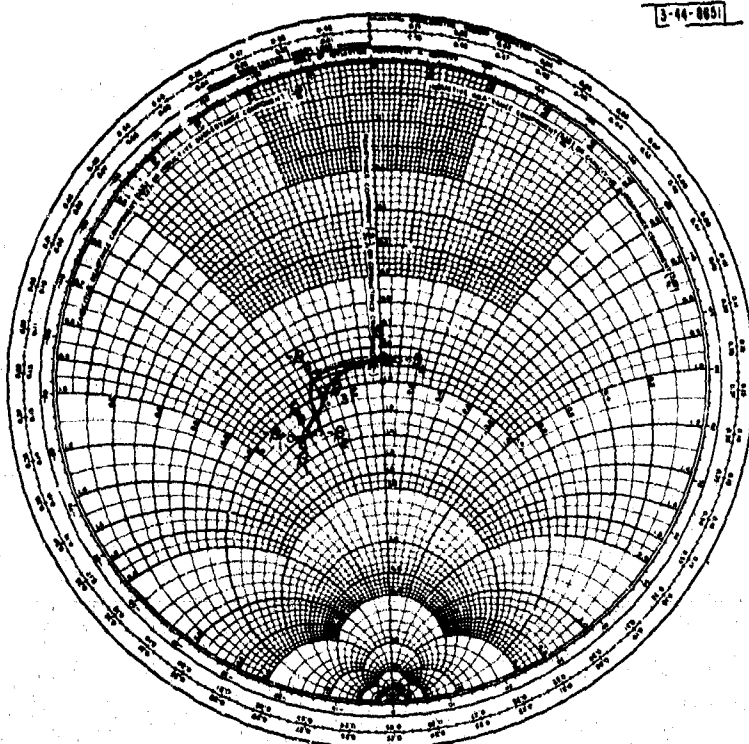


3-44-8650

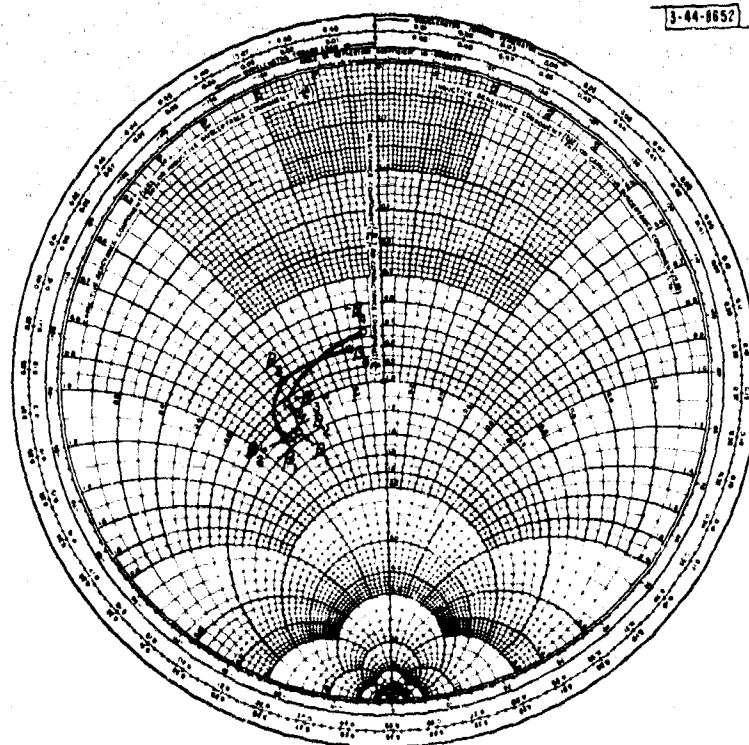


(d) Elevation phasing  $-\alpha_4$ .

Fig. III-114. Continued.



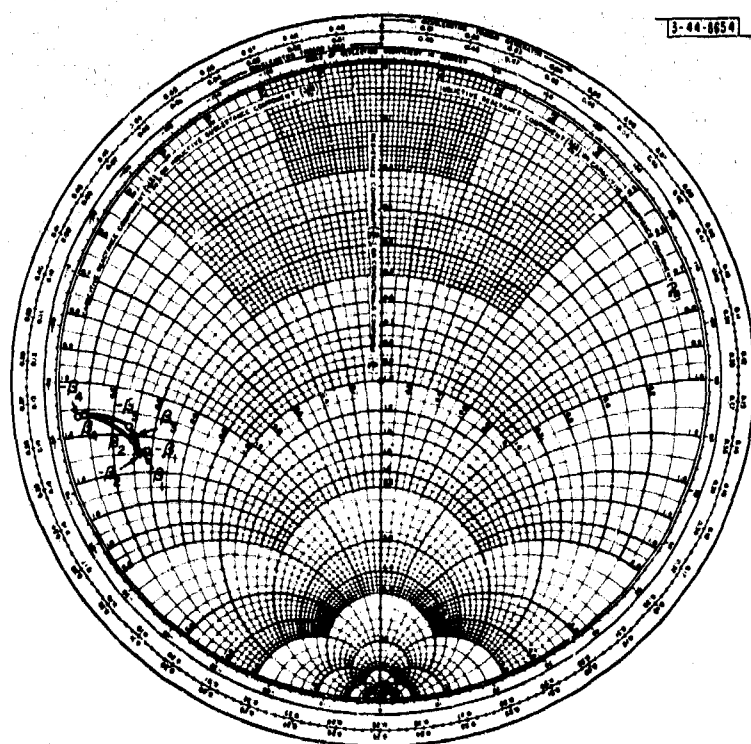
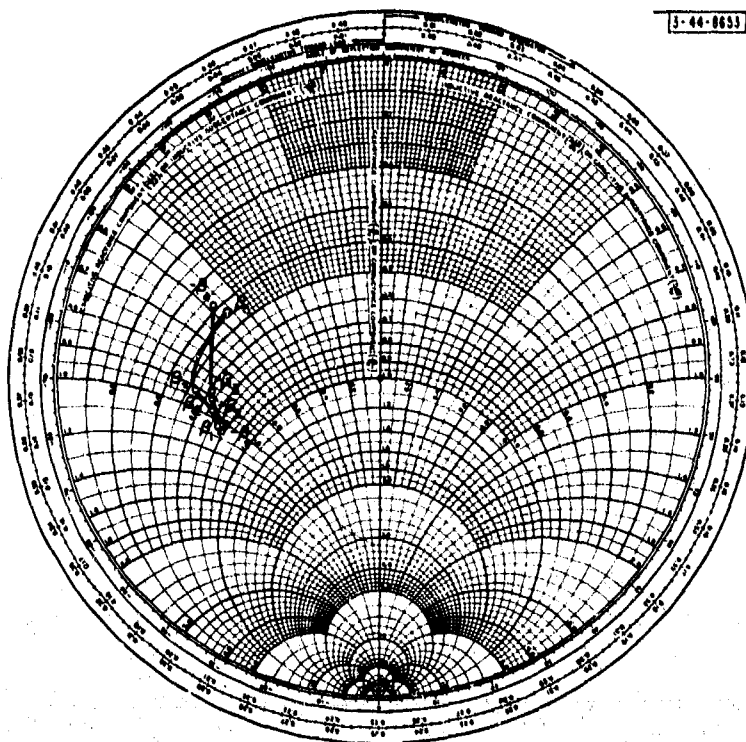
(a) Elevation phasing  $-a_1$ .



(b) Elevation phasing  $-a_2$ .

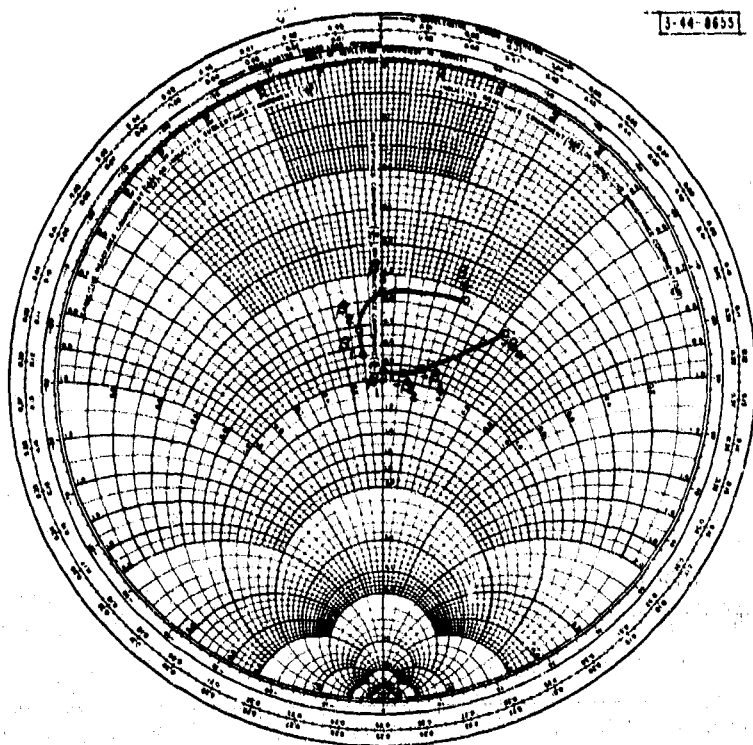
Fig. III-115. Impedance of dipole 56 as beam is scanned in azimuth and elevation phasing  $a_1$  is constant. Height above ground plane is  $1/8\lambda$ .

(c) Elevation phasing  $-\alpha_3$ .



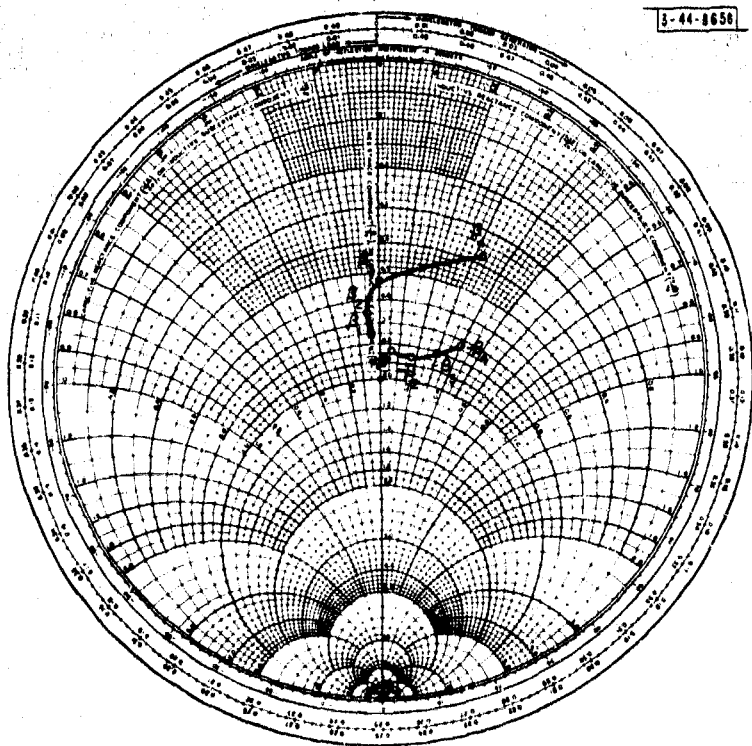
(d) Elevation phasing  $-\alpha_4$ .

Fig. III-115. Continued.



3-44-8653

(a) Elevation phasing  $-a_1$ .

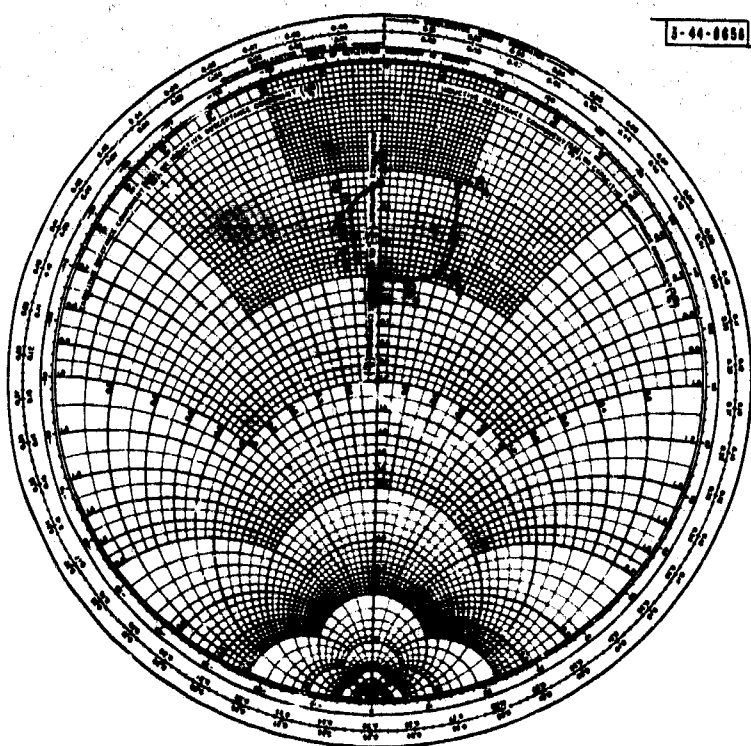
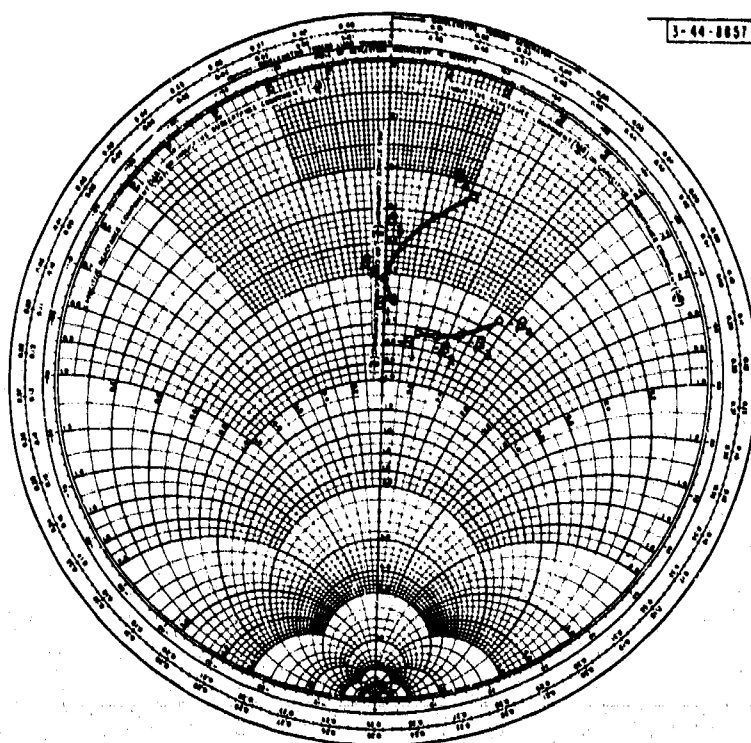


3-44-8658

(b) Elevation phasing  $-a_2$ .

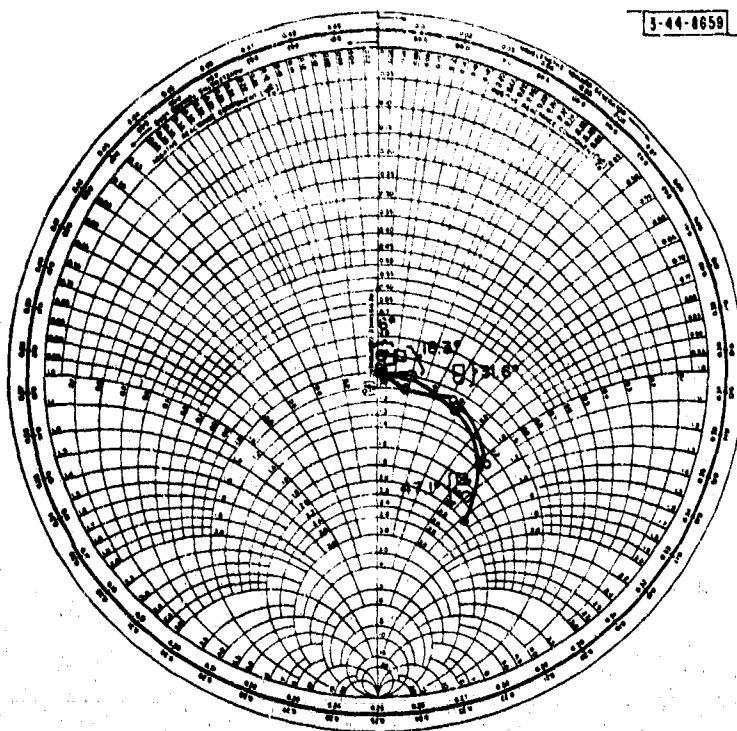
Fig. III-116. Impedance of dipole 82 as beam is scanned in azimuth and elevation phasing  $a_1$  is constant. Height above ground plane is  $1/4\lambda$ .

(c) Elevation phasing  $-a_3$ .

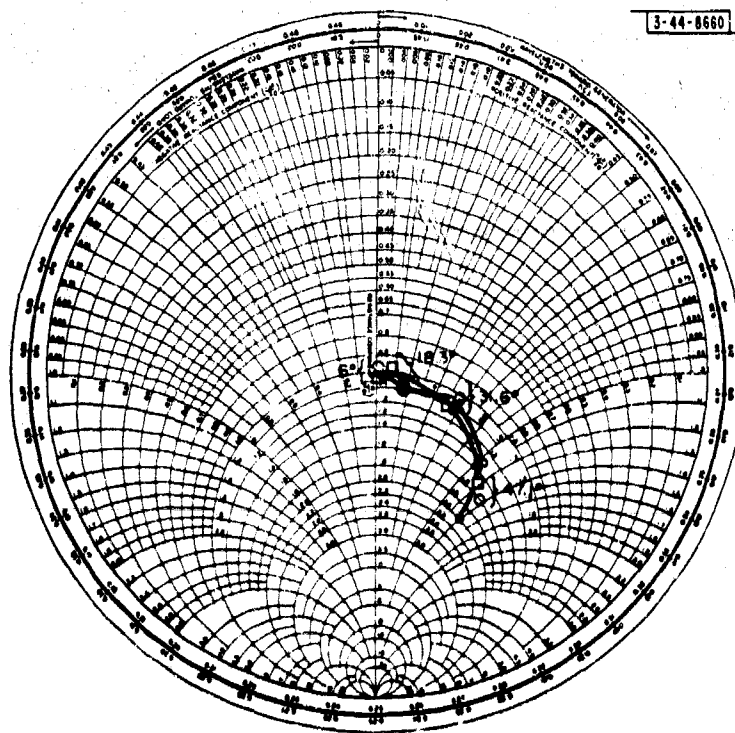


(d) Elevation phasing  $-a_4$ .

Fig. III-116. Continued.



(a) Elevation phasing  $+\alpha_1$ .

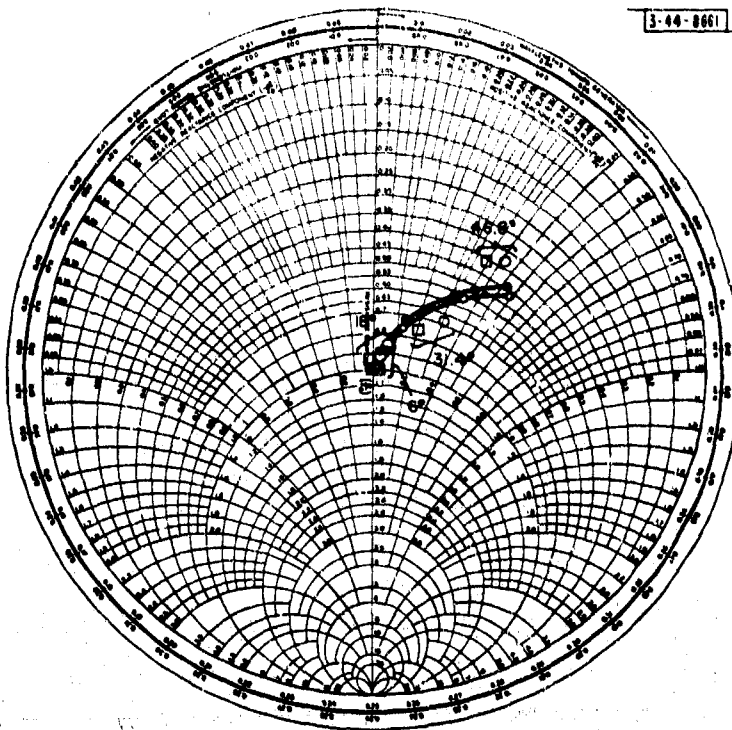


(b) Elevation phasing  $-\alpha_1$ .

Fig. III-117. Smith Chart plots of theoretical impedance of  $\lambda/2$  dipole, number 45, as H-plane is scanned in  $10^\circ$  steps, and plots of actual impedance of  $3/8\lambda$  dipole, number 45, when elevation phasing is  $\pm\alpha_1$  and azimuth phasing is varied from  $\pm\beta_1$  to  $\pm\beta_4$ .



(a) Elevation phasing  $+a_1$ .



(b) Elevation phasing  $-a_1$ .

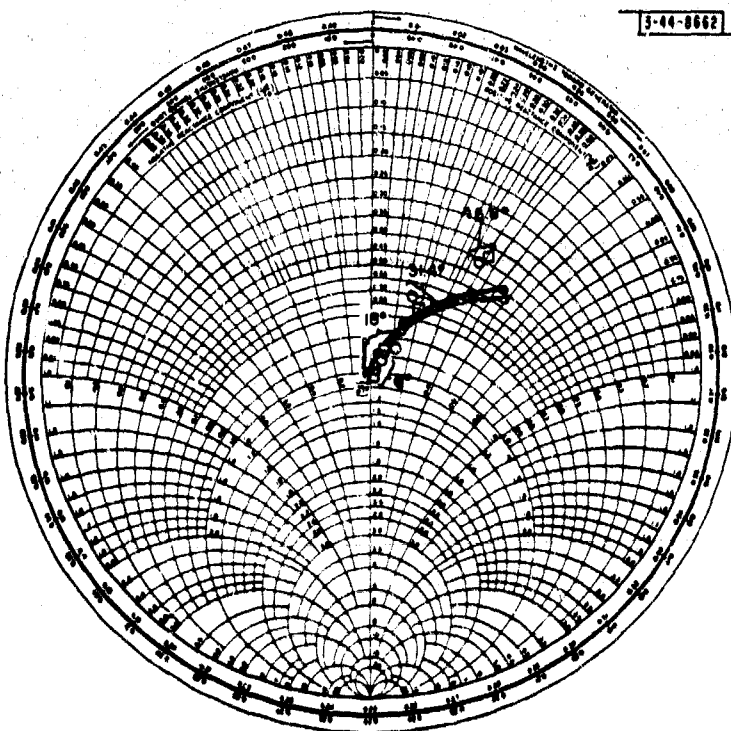


Fig. III-118. Smith Chart plots of theoretical impedance of  $\lambda/2$  dipole, number 45, as E-plane is scanned in  $10^\circ$  steps, and plots of actual impedance of  $3/8\lambda$  dipole, number 45, when azimuth phasing is  $\pm\beta_1$  and elevation phasing is varied from  $\pm a_1$  to  $\pm a_4$ .

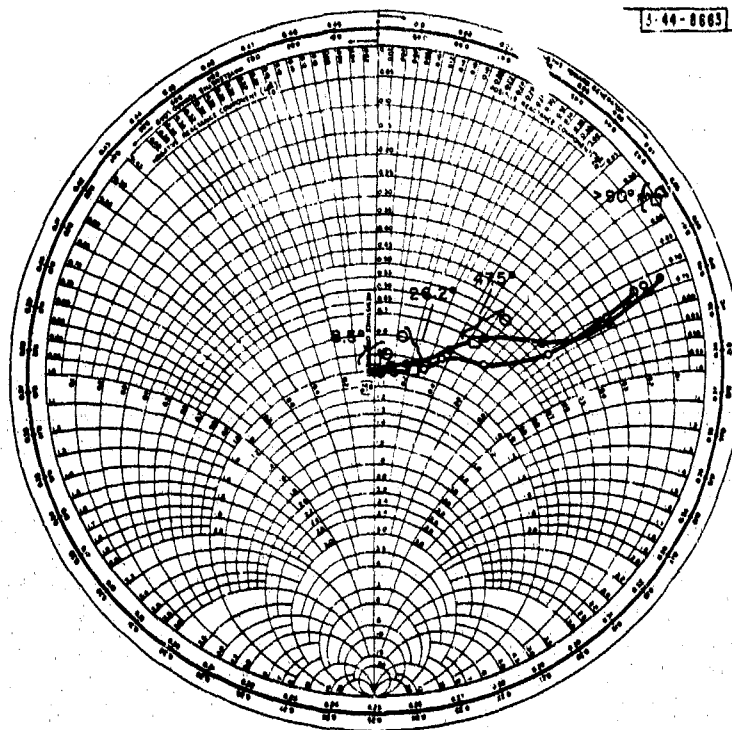


Fig. III-119. Smith Chart plots of theoretical impedance of  $\lambda/2$  dipole, number 45, as diagonal plane is scanned in  $10^\circ$  steps, and plots of actual impedance of  $3/8\lambda$  dipole, number 45, when phasing is  $-\alpha_i$ ,  $-\beta_k$  or  $\alpha_i$ ,  $\beta_k$ ,  $i = k$ .

## APPENDIX A

### RIGOROUS DERIVATION OF APERTURE ILLUMINATION RELATIONSHIP

In the geometry of Fig. III-A-1, the far field due to feed O can be expressed in the unprimed coordinate system as\*

$$E(R, \xi) = \frac{e^{-jkR}}{\lambda R} \int_{-\rho_0}^{\rho_0} E_0(y) \exp[jky \sin \xi] dy \quad (A-1)$$

where  $E_0(y)$  is the illumination along the line  $x = \rho_0$ . Similarly, the far field due to feed n is given in the primed coordinates by

$$E(R', \xi + nD/\rho_0) = \frac{e^{-jkR'}}{\lambda R'} \int_{-\rho_0}^{\rho_0} E_n(y') \exp[jky' \sin(\xi + nD/\rho_0)] dy' \quad (A-2)$$

where  $E_n(y')$  is the illumination along the  $x' = \rho_0$  due to feed n.

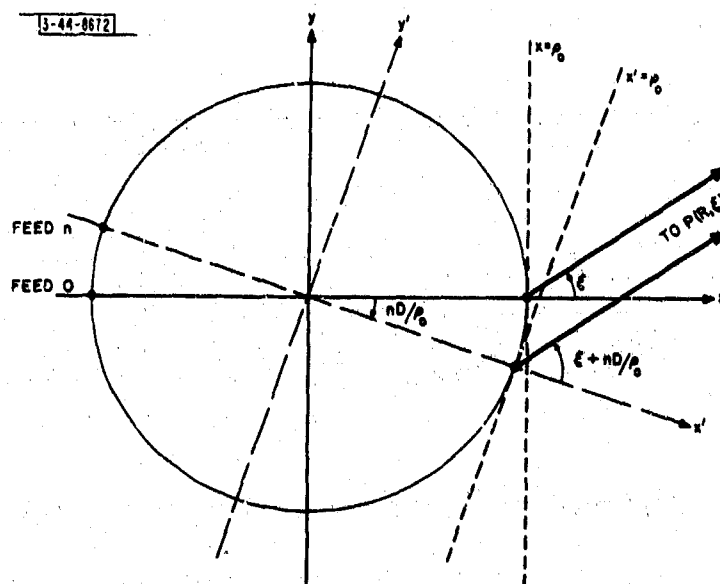


Fig. III-A-1. Lens coordinate systems.

The transformations between systems are

$$\begin{aligned} x' &= x \cos nD/\rho_0 - y \sin nD/\rho_0 \\ y' &= x \sin nD/\rho_0 + y \cos nD/\rho_0 \end{aligned} \quad (A-3)$$

If we let  $R_0$  be the distance between the origin and the far-field point (the same in both systems), we can express  $R$  in the form

$$(R)^2 = R_0^2 - \rho_0^2 - 2\rho_0 R \cos \xi$$

and  $R'$  as

\* The validity of determining the field on an imaginary aperture is assumed from geometrical optics, then physical optics is used to determine the far field.

$$(R')^2 = R_0^2 - \rho_0^2 - 2\rho_0 R' \cos(\xi + nD/\rho_0)$$

In the far field,  $R_0 \gg \rho_0$ , so we can write with vanishingly small error

$$R = R_0 - \rho_0 \cos \xi \quad (A-4)$$

$$R' = R_0 - \rho_0 \cos(\xi + nD/\rho_0) \quad (A-5)$$

Consequently, we can re-write Eqs. (A-1) and (A-2), replacing  $R$  and  $R'$  in the exponents by Eqs. (A-4) and (A-5), respectively (and ignoring a common term  $e^{-jkR_0}$ ), and replacing  $R$  and  $R'$  in the denominator by  $R_0$ :

$$E(R, \xi) = \frac{\exp[jk\rho_0 \cos \xi]}{\lambda R_0} \int_{-\rho_0}^{\rho_0} E_0(y) \exp[jky \sin \xi] dy \quad (A-6)$$

$$E(R', \xi + nD/\rho_0) = \frac{\exp[jk\rho_0 \cos(\xi + nD/\rho_0)]}{\lambda R_0} \int_{-\rho_0}^{\rho_0} E_n(y') \times \exp[jky' \sin(\xi + nD/\rho_0)] dy' \quad (A-7)$$

Turning attention to the integral portion of Eq. (A-7), note that along the line  $x' = \rho_0$ , we have, from Eq. (A-3), that

$$\rho_0 = x \cos nD/\rho_0 - y \sin nD/\rho_0$$

or

$$x = \frac{\rho_0 + y \sin nD/\rho_0}{\cos nD/\rho_0} \quad (A-8)$$

Consequently, along this line, substituting for  $x$  in the second of the set (A-3) and using a few identities gives

$$y' = \rho_0 \tan nD/\rho_0 + \frac{y}{\cos nD/\rho_0} \quad (A-9)$$

The integral of Eq. (A-7) thus becomes

$$I = \int_{-\rho_0}^{\rho_0} E_n(y') \exp[jky' \sin(\xi + nD/\rho_0)] dy' = \frac{\exp[jk\rho_0 \tan nD/\rho_0 \sin(\xi + nD/\rho_0)]}{\cos nD/\rho_0} \times \int_{-\rho_0(\cos nD/\rho_0 - \sin nD/\rho_0)}^{\rho_0(\cos nD/\rho_0 + \sin nD/\rho_0)} E_n \left[ \rho_0 \tan nD/\rho_0 + \frac{y}{\cos nD/\rho_0} \right] \times \exp \left[ jky \frac{\sin(\xi + nD/\rho_0)}{\cos nD/\rho_0} \right] dy \quad (A-10)$$

Since we are primarily interested in the large lens case ( $\rho_0 \gg \lambda$ ) and the close-in pattern structure, let us assume  $nD/\rho_0 \ll 1$ . Then we can approximate

$$\cos nD/\rho_0 = 1$$

$$\sin nD/\rho_0 = \tan nD/\rho_0 = nD/\rho_0$$

Then we can simplify Eq. (A-10) to

$$I \approx \exp[jknD \sin(\xi + nD/\rho_0)] \int_{-\rho_0}^{\rho_0 - nD} E_n[y + nD] \exp[jky \sin(\xi + nD/\rho_0)] dy$$

Making the substitution  $y_1 = y + nD$ ,

$$I = \int_{-\rho_0}^{\rho_0} E_n(y_1) \exp[jky_1 \sin(\xi + nD/\rho_0)] dy_1 \quad (A-11)$$

Finally, writing

$$\cos(\xi + nD/\rho_0) \approx \cos \xi - nD/\rho_0 \sin \xi$$

$$\sin(\xi + nD/\rho_0) \approx \sin \xi + nD/\rho_0 \cos \xi$$

we can write Eq. (A-7) as

$$E(R', \xi + nD/\rho_0) = \frac{\exp[jk\rho_0 \cos \xi]}{\lambda R_0} \exp[-jknD \sin \xi] \int_{-\rho_0}^{\rho_0} E_n(y) \times \exp[jky(\sin \xi + nD/\rho_0 \cos \xi)] dy \quad (A-12)$$

We can now combine the two fields directly to arrive at a total field,  $E_t(R_0, \xi)$ , which can be written (ignoring the common  $\exp[jk\rho_0 \cos \xi]$  as

$$E_t(R_0, \xi) = \frac{1}{\lambda R_0} \int_{-\rho_0}^{\rho_0} \left( E_0(y) + \{E_n(y) \exp[-jknD \sin \xi] \exp[jknD \frac{y}{\rho_0} \cos \xi]\} \right) \times \exp[jky \sin \xi] dy \quad (A-13)$$

If the feeds are the same,  $E_0(y)$  and  $E_n(y)$  will differ by only a complex scale factor related to the current exciting each feed  $I_n$ . Thus, in summary, we can write the total aperture illumination for a multiple feed structure (identical elements, regularly spaced, edge effects ignored) as

$$E_t(y) = E_0(y) \sum_n I_n \exp[-jknD \sin \xi] \exp[jknD \frac{y}{\rho_0} \cos \xi] \quad (A-14)$$

The factor  $\exp[-jknD \sin \xi]$  is due to the  $y$ -displacement of the phase center of the radiation from the  $n^{\text{th}}$  feed. For small angles, it is negligible, as is the  $\cos \xi$  factor in the second term (which is an aperture foreshortening factor); neglecting both gives terms of the simple form of Eq. (3) of the main text.

## APPENDIX B

Figures III-B-1 through III-B-24 present many of the computed gain functions and Smith Chart plots of the driving impedance of the center element in a  $7 \times 9$  array of  $\lambda/2$ -dipoles. The driving impedance is normalized by the generator impedance; that is, we plot

$$Z(\tau_o, \mu_o) = \frac{Z_D(\tau_o, \mu_o) + jX_g}{R_g}$$

which has the value  $1 + j0$  when the center element is matched at broadside. Corresponding plots for  $7 \times 9$  arrays of short dipoles are given in Figs. III-B-25 through III-B-28. The plots are given for three ground plane spacings;  $s = 0$  (no ground plane),  $s = \lambda/8$ , and  $s = \lambda/4$ , and for element spacings of  $0.5$ ,  $0.6$ ,  $0.7$  and  $0.8\lambda$ .

The gain functions and Smith Charts are presented for E-, H- and D-plane scans, with the numerical values representing the angle  $\theta$  measured from broadside (Fig. III-65). The Smith Charts also indicate the impedance of a single dipole above ground, normalized, and the gain function plots indicate the angle over which the beam of the array can be scanned with less than 3-db loss in one-way gain.

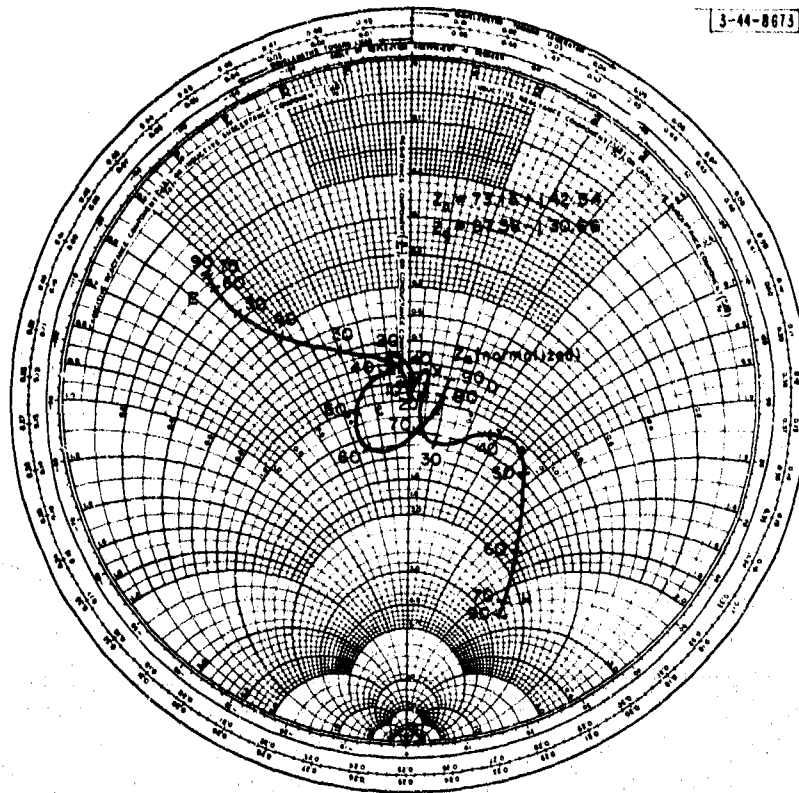


Fig. III-B-1. Variation in normalized driving impedance with scan angle for center element of  $9 \times 7$  array of  $\lambda/2$  dipoles for element spacing  $D = 0.5 \lambda$  and element height above ground plane  $s = 0$  (no ground plane). Impedance of an isolated element  $Z_G$  and generator impedance  $Z_G$  are also given. Normalized value of  $Z_G$  is indicated on chart.

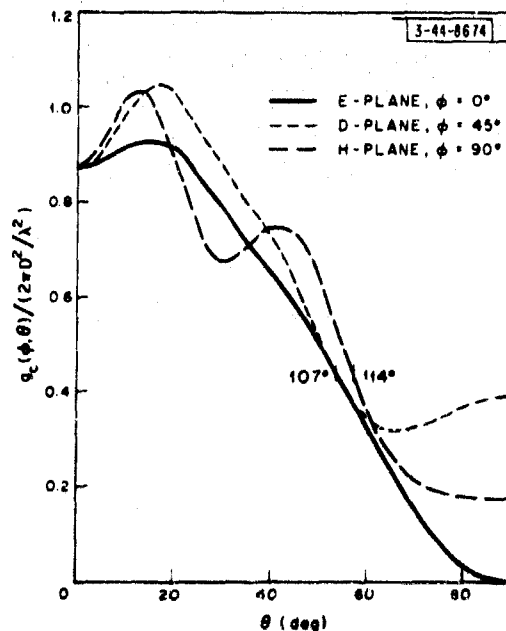


Fig. III-B-2. Normalized gain function for center element of  $9 \times 7$  array of  $\lambda/2$  dipoles for element spacing  $D = 0.5 \lambda$  and element height above ground plane  $s = 0$  (no ground plane). Also indicated is included angle over which array may be scanned in each plane with less than 3-db loss in gain.

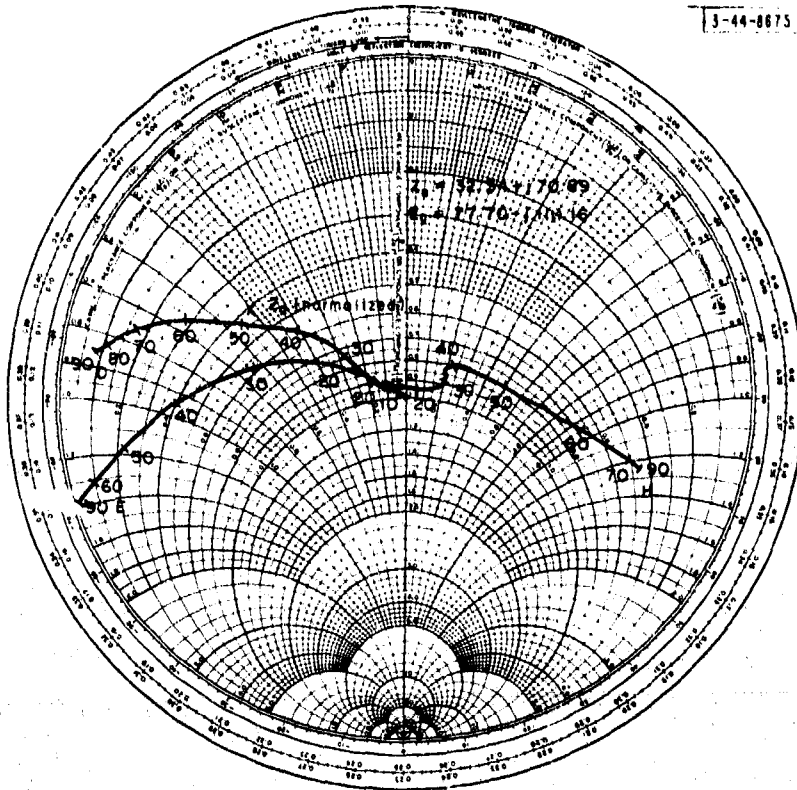


Fig. III-B-3. Variation in normalized driving impedance with scan angle for center element of  $9 \times 7$  array of  $\lambda/2$  dipoles for element spacing  $D = 0.5 \lambda$  and element height above ground plane  $s = \lambda/8$ . Impedance of an isolated element  $Z_0$  and generator impedance  $Z_g$  are also given. Normalized value of  $Z_0$  is indicated on chart.

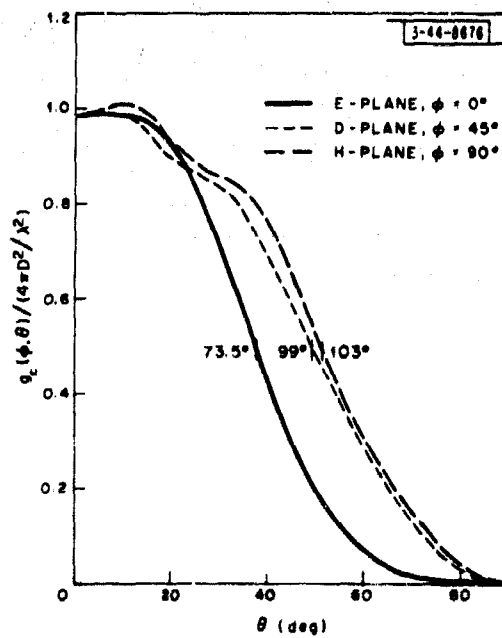


Fig. III-B-4. Normalized gain function for center element of  $9 \times 7$  array of  $\lambda/2$  dipoles for element spacing  $D = 0.5 \lambda$  and element height above ground plane  $s = \lambda/8$ . Also indicated is included angle over which array may be scanned in each plane with less than 3-db loss in gain.



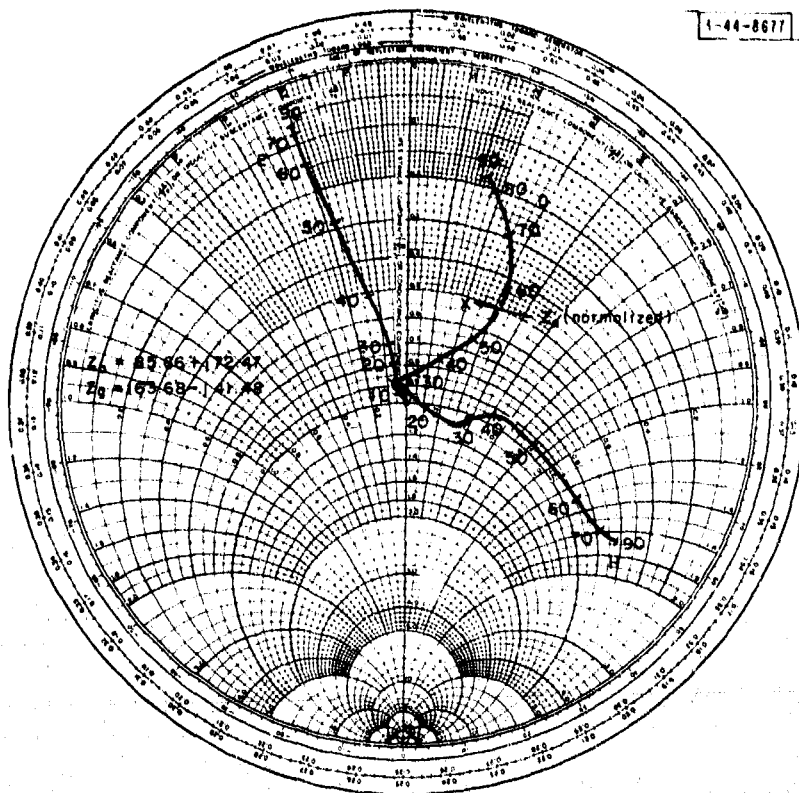


Fig. III-B-5. Variation in normalized driving impedance with scan angle for center element of  $9 \times 7$  array of  $\lambda/2$  dipoles for element spacing  $D = 0.5 \lambda$  and element height above ground plane  $s = \lambda/4$ . Impedance of an isolated element  $Z_0$  and generator impedance  $Z_g$  are also given. Normalized value of  $Z_0$  is indicated on chart.

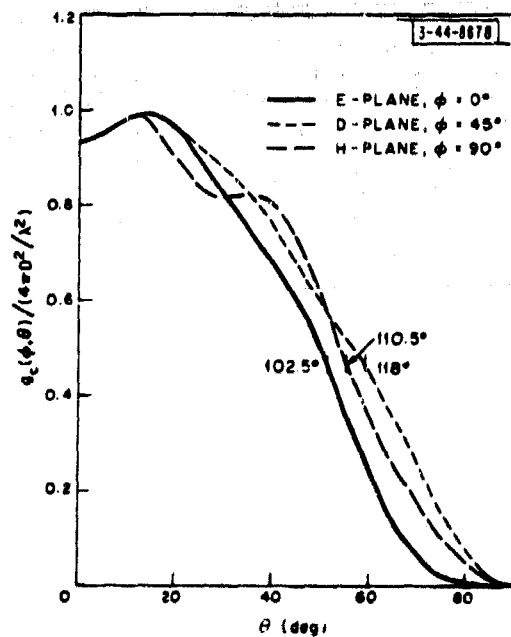


Fig. III-B-6. Normalized gain function for center element of  $9 \times 7$  array of  $\lambda/2$  dipoles for element spacing  $D = 0.5 \lambda$  and element height above ground plane  $s = \lambda/4$ . Also indicated is included angle over which array may be scanned in each plane with less than 3-db loss in gain.

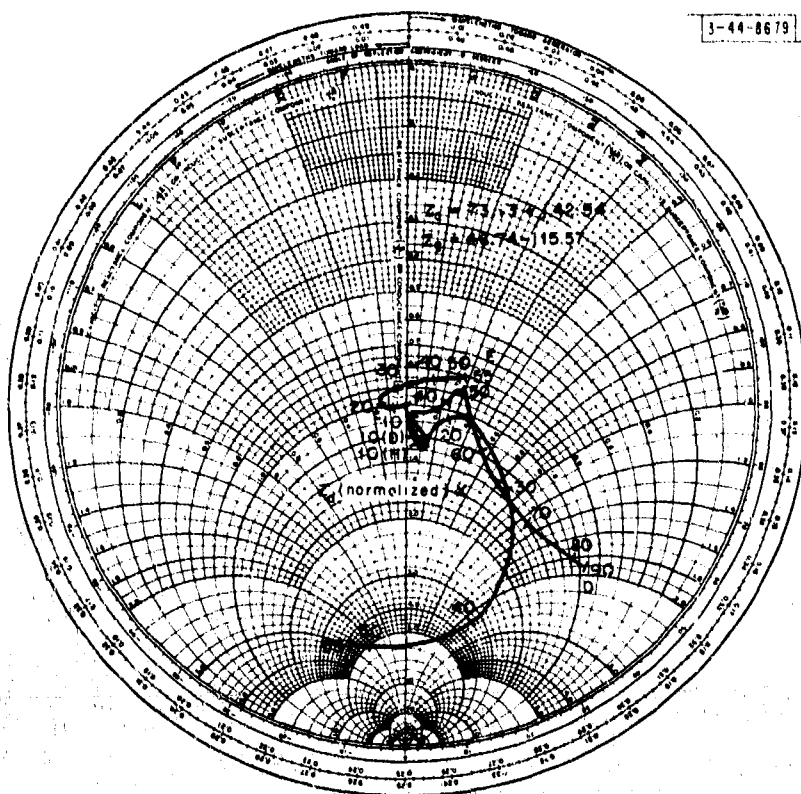
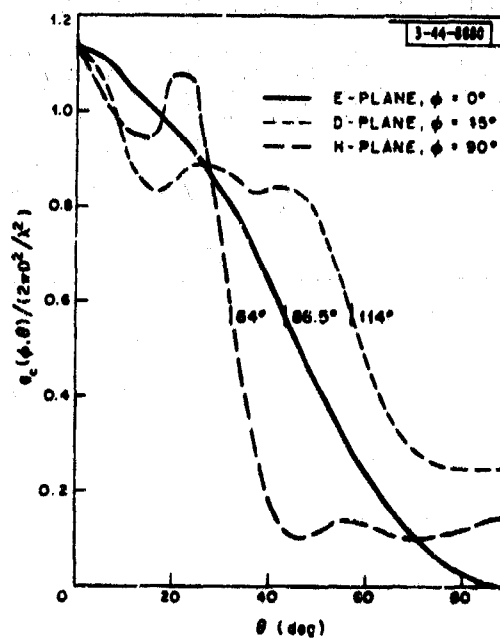


Fig. III-8-7. Variation in normalized driving impedance with scan angle for center element of  $9 \times 7$  array of  $\lambda/2$  dipoles for element spacing  $D = 0.6 \lambda$  and element height above ground plane  $s = 0$  (no ground plane). Impedance of an isolated element  $Z_0$  and generator impedance  $Z_g$  are also given. Normalized value of  $Z_0$  is indicated on chart.

Fig. III-8-8. Normalized gain function for center element of  $9 \times 7$  array of  $\lambda/2$  dipoles for element spacing  $D = 0.6 \lambda$  and element height above ground plane  $s = 0$  (no ground plane). Also indicated is included angle over which array may be scanned in each plane with less than 3-db loss in gain.



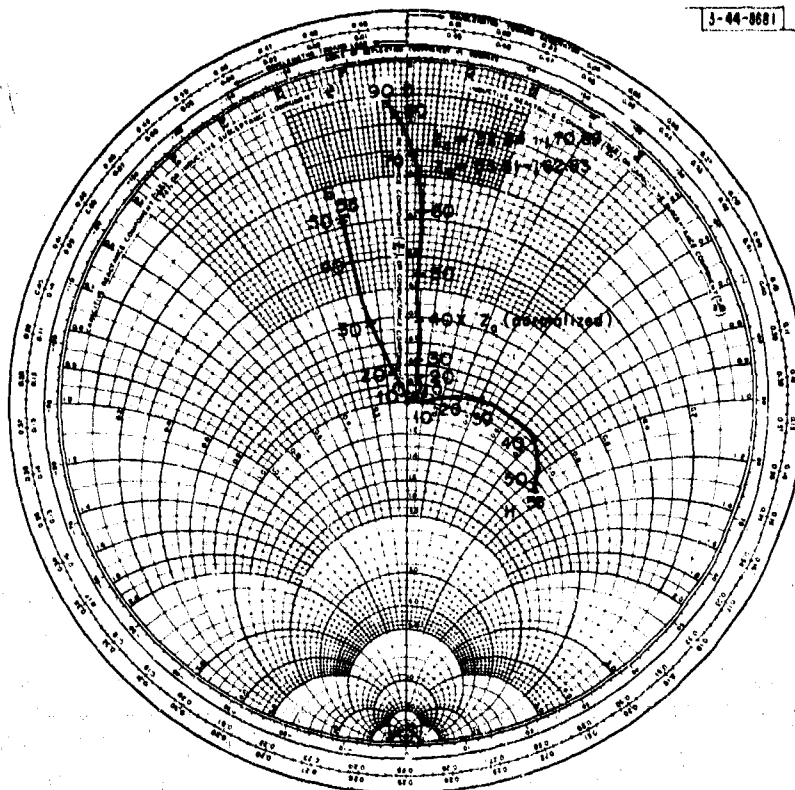


Fig. III-B-9. Variation in normalized driving impedance with scan angle for center element of  $9 \times 7$  array of  $\lambda/2$  dipoles for element spacing  $D = 0.6 \lambda$  and element height above ground plane  $s = \lambda/8$ . Impedance of an isolated element  $Z_0$  and generator impedance  $Z_g$  are also given. Normalized value of  $Z_0$  is indicated on chart.

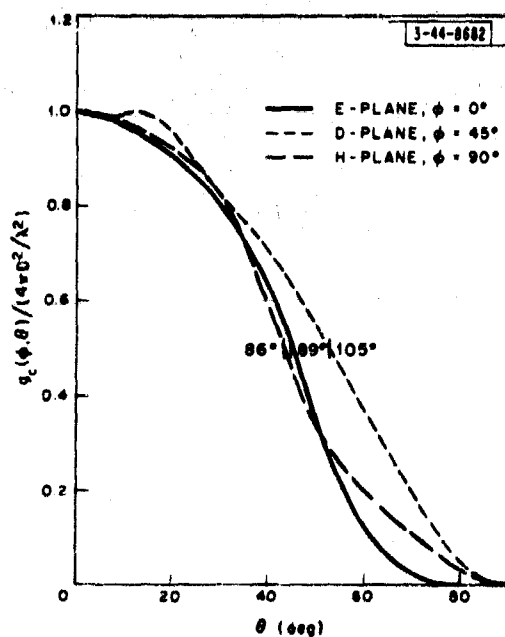


Fig. III-B-10. Normalized gain function for center element of  $9 \times 7$  array of  $\lambda/2$  dipoles for element spacing  $D = 0.6 \lambda$  and element height above ground plane  $s = \lambda/8$ . Also indicated is included angle over which array may be scanned in each plane with less than 3-db loss in gain.

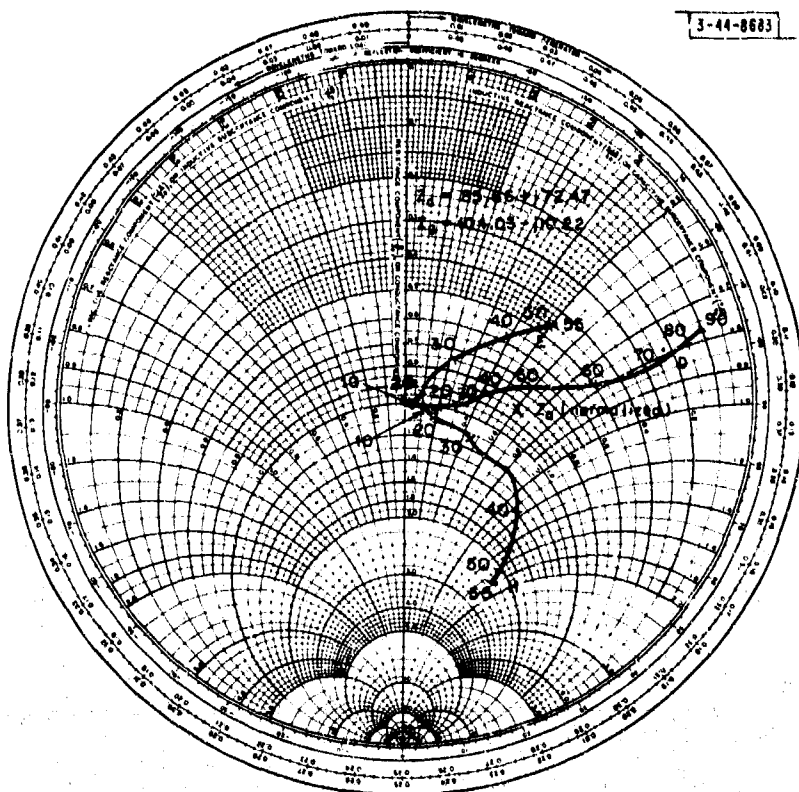


Fig. III-B-11. Variation in normalized driving impedance with scan angle for center element of  $9 \times 7$  array of  $\lambda/2$  dipoles for element spacing  $D = 0.6 \lambda$  and element height above ground plane  $s = \lambda/4$ . Impedance of an isolated element  $Z_a$  and generator impedance  $Z_g$  are also given. Normalized value of  $Z_a$  is indicated on chart.

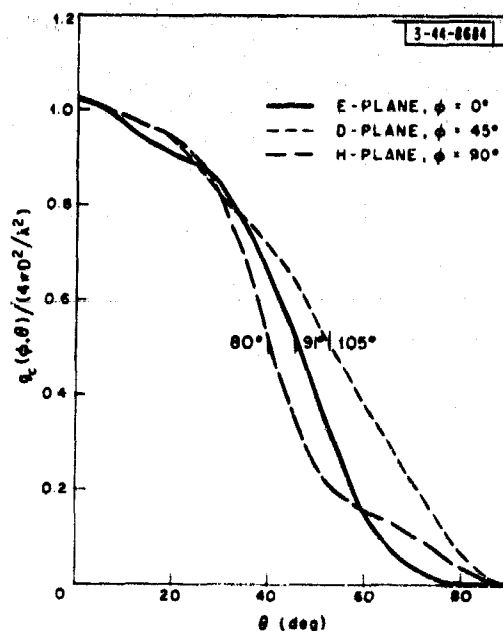


Fig. III-B-12. Normalized gain function for center element of  $9 \times 7$  array of  $\lambda/2$  dipoles for element spacing  $D = 0.6 \lambda$  and element height above ground plane  $s = \lambda/4$ . Also indicated is included angle over which array may be scanned in each plane with less than 3-db loss in gain.

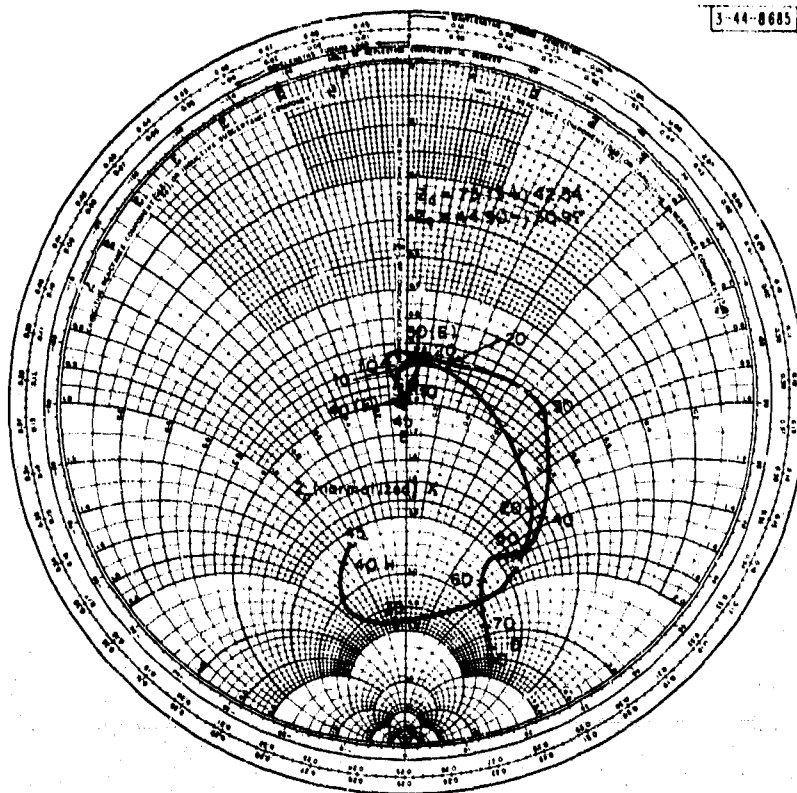


Fig. III-B-13. Variation in normalized driving impedance with scan angle for center element of  $9 \times 7$  array of  $\lambda/2$  dipoles for element spacing  $D = 0.7 \lambda$  and element height above ground plane  $s = 0$  (no ground plane). Impedance of an isolated element  $Z_0$  and generator impedance  $Z_g$  are also given. Normalized value of  $Z_0$  is indicated on chart.

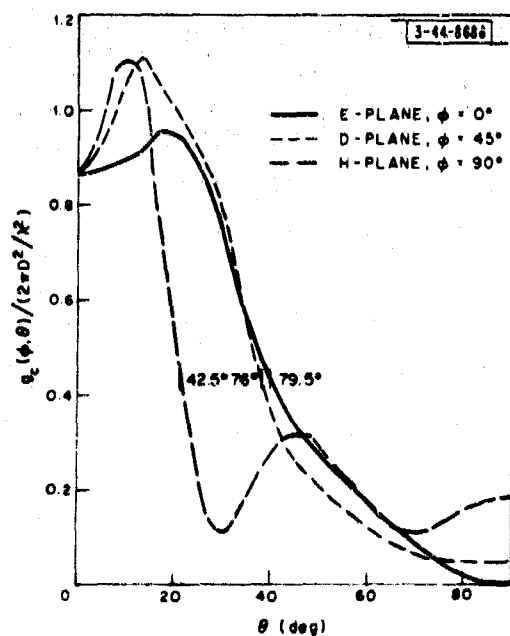


Fig. III-B-14. Normalized gain function for center element of  $9 \times 7$  array of  $\lambda/2$  dipoles for element spacing  $D = 0.7 \lambda$  and element height above ground plane  $s = 0$  (no ground plane). Also indicated is included angle over which array may be scanned in each plane with less than 3-db loss in gain.

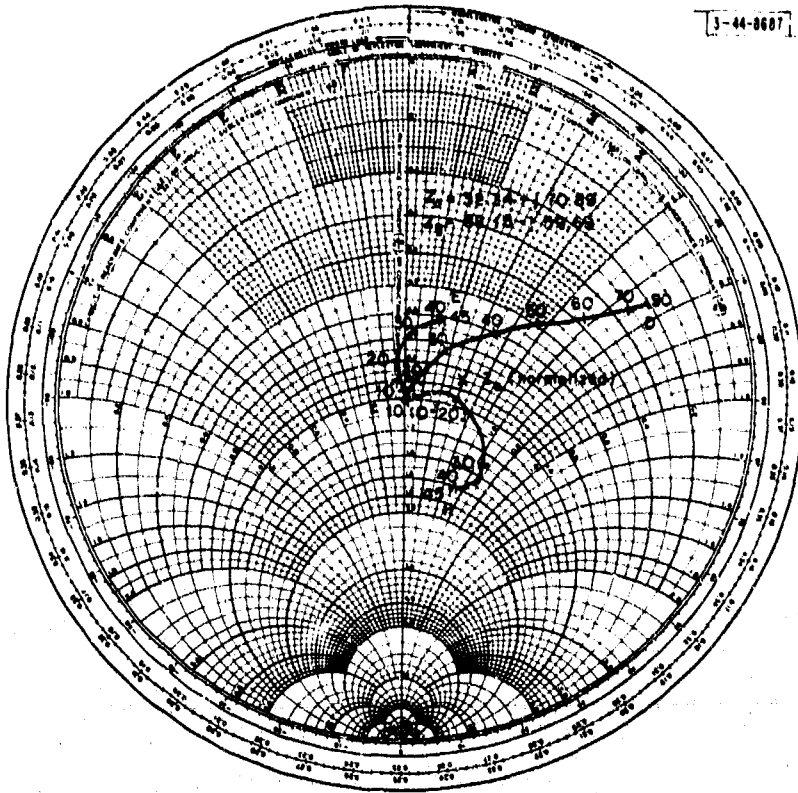


Fig. III-B-15. Variation in normalized driving impedance with scan angle for center element of  $9 \times 7$  array of  $\lambda/2$  dipoles for element spacing  $D = 0.7 \lambda$  and element height above ground plane  $s = \lambda/8$ . Impedance of an isolated element  $Z_0$  and generator impedance  $Z_g$  are also given. Normalized value of  $Z_0$  is indicated on chart.

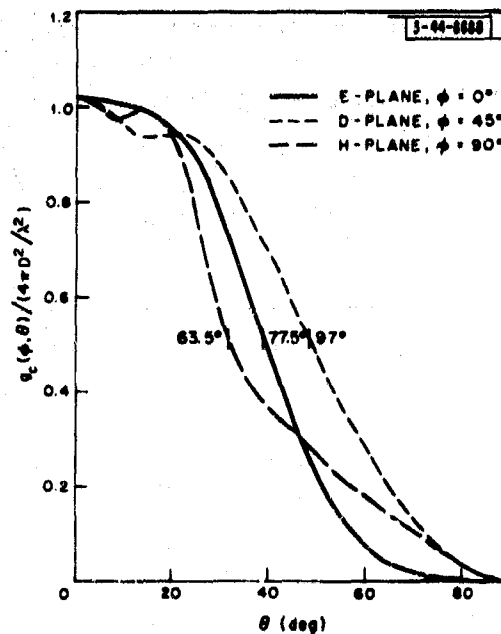


Fig. III-B-16. Normalized gain function for center element of  $9 \times 7$  array of  $\lambda/2$  dipoles for element spacing  $D = 0.7 \lambda$  and element height above ground plane  $s = \lambda/8$ . Also indicated is included angle over which array may be scanned in each plane with less than 3-db loss in gain.

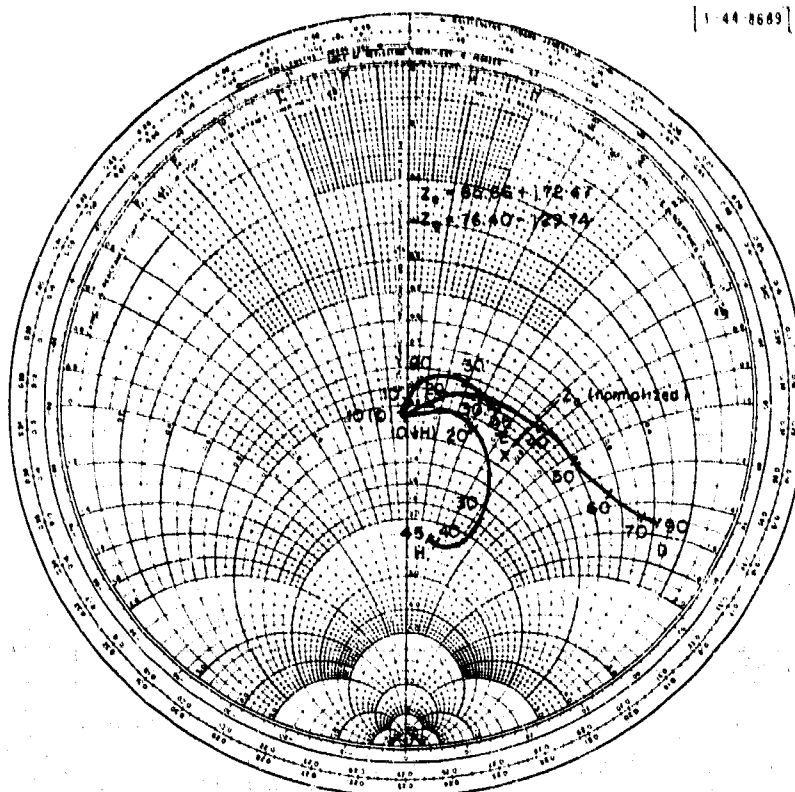


Fig. III-B-17. Variation in normalized driving impedance with scan angle for center element of  $9 \times 7$  array of  $\lambda/2$  dipoles for element spacing  $D = 0.7 \lambda$  and element height above ground plane  $s = \lambda/4$ . Impedance of an isolated element  $Z_0$  and generator impedance  $Z_g$  are also given. Normalized value of  $Z_0$  is indicated on chart.

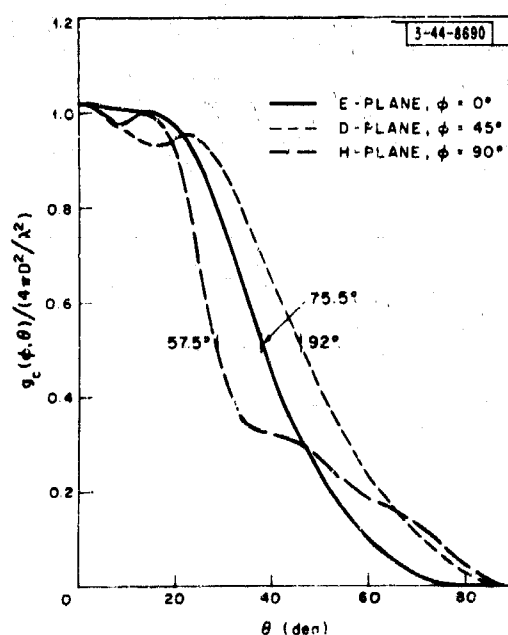


Fig. III-B-18. Normalized gain function for center element of  $9 \times 7$  array of  $\lambda/2$  dipoles for element spacing  $D = 0.7 \lambda$  and element height above ground plane  $s = \lambda/4$ . Also indicated is included angle over which array may be scanned in each plane with less than 3-db loss in gain.

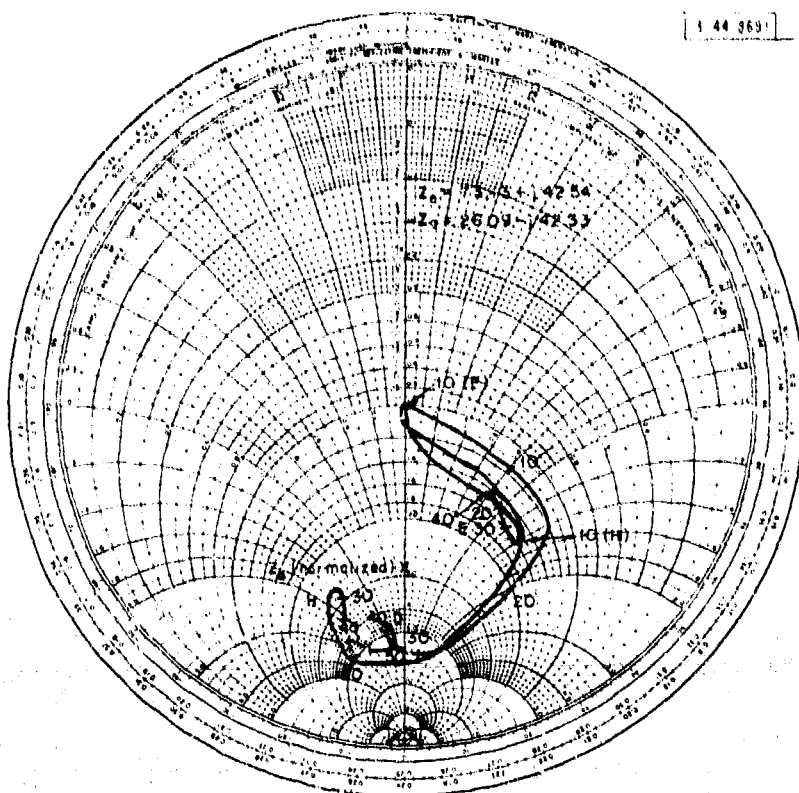


Fig. III-B-19. Variation in normalized driving impedance with scan angle for center element of  $9 \times 7$  array of  $\lambda/2$  dipoles for element spacing  $D = 0.8 \lambda$  and element height above ground plane  $s = 0$  (no ground plane). Impedance of an isolated element  $Z_a$  and generator impedance  $Z_g$  are also given. Normalized value of  $Z_a$  is indicated on chart.

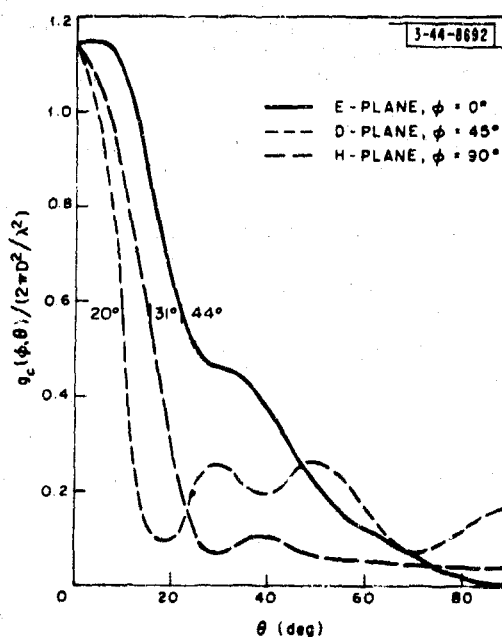


Fig. III-B-20. Normalized gain function for center element of  $9 \times 7$  array of  $\lambda/2$  dipoles for element spacing  $D = 0.8 \lambda$  and element height above ground plane  $s = 0$  (no ground plane). Also indicated is included angle over which array may be scanned in each plane with less than 3-db loss in gain.



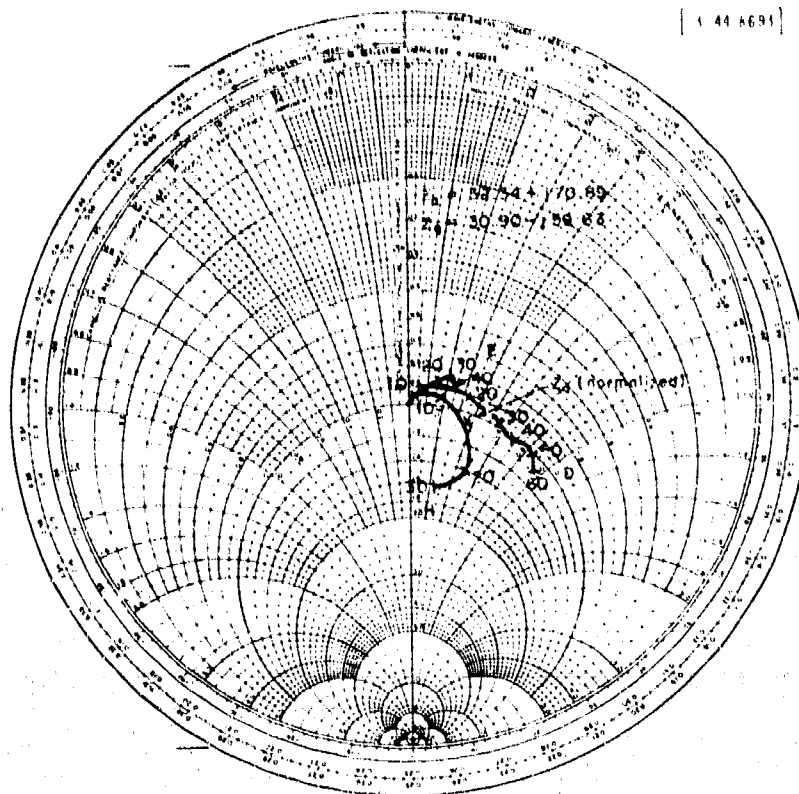


Fig. III-B-21. Variation in normalized driving impedance with scan angle for center element of  $9 \times 7$  array of  $\lambda/2$  dipoles for element spacing  $D = 0.8 \lambda$  and element height above ground plane  $s = \lambda/8$ . Impedance of an isolated element  $Z_0$  and generator impedance  $Z_g$  are also given. Normalized value of  $Z_0$  is indicated on chart.

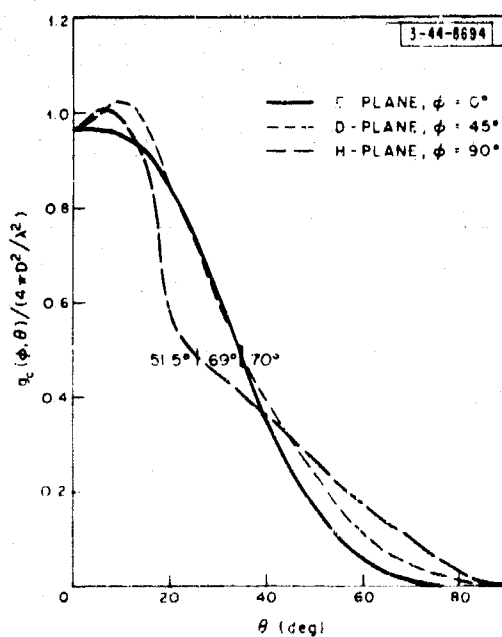


Fig. III-B-22. Normalized gain function for center element of  $9 \times 7$  array of  $\lambda/2$  dipoles for element spacing  $D = 0.8 \lambda$  and element height above ground plane  $s = \lambda/8$ . Also indicated is included angle over which array may be scanned in each plane with less than 3-db loss in gain.

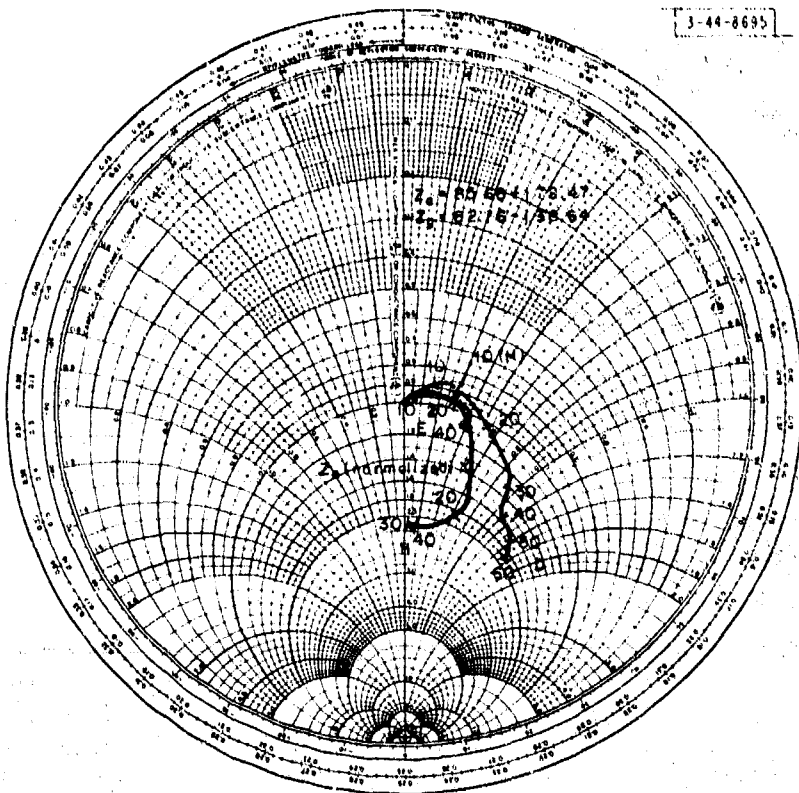


Fig. III-B-23. Variation in normalized driving impedance with scan angle for center element of  $9 \times 7$  array of  $\lambda/2$  dipoles for element spacing  $D = 0.8 \lambda$  and element height above ground plane  $s = \lambda/4$ . Impedance of an isolated element  $Z_a$  and generator impedance  $Z_g$  are also given. Normalized value of  $Z_a$  is indicated on chart.

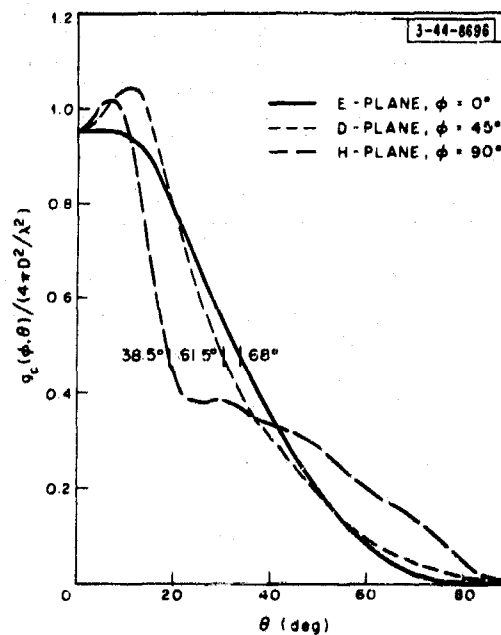


Fig. III-B-24. Normalized gain function for center element of  $9 \times 7$  array of  $\lambda/2$  dipoles for element spacing  $D = 0.8 \lambda$  and element height above ground plane  $s = \lambda/4$ . Also indicated is included angle over which array may be scanned in each plane with less than 3-db loss in gain.

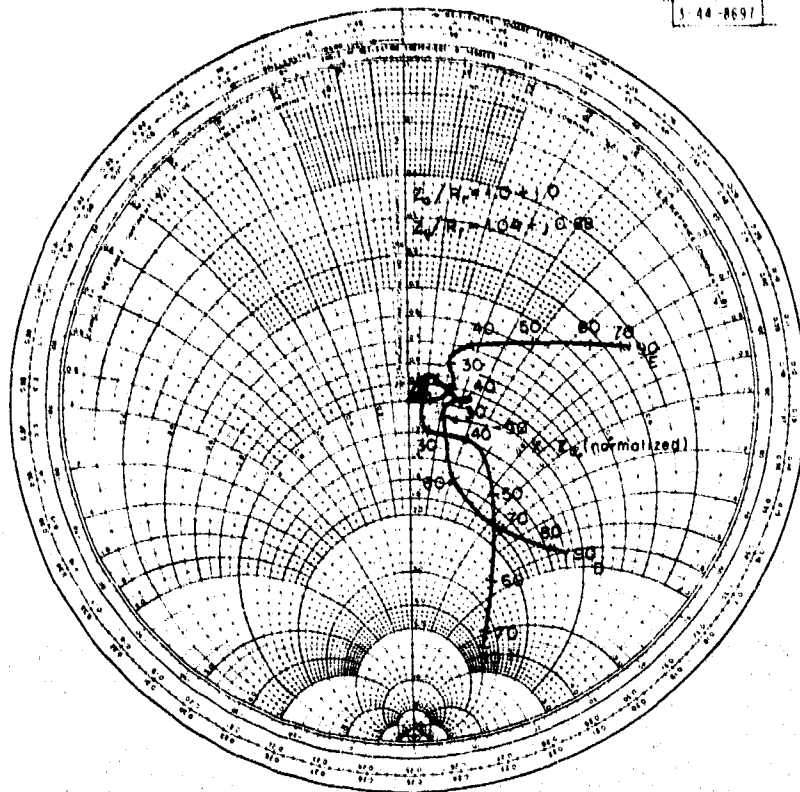


Fig. III-B-25. Variation in normalized driving impedance with scan angle for center element of  $9 \times 7$  array of short dipoles for element spacing  $D = 0.5 \lambda$  and element height above ground plane  $s = 0$  (no ground plane). Impedance of an isolated element  $Z_0$  and generator impedance  $Z_g$  are also given. Normalized value of  $Z_0$  is indicated on chart.

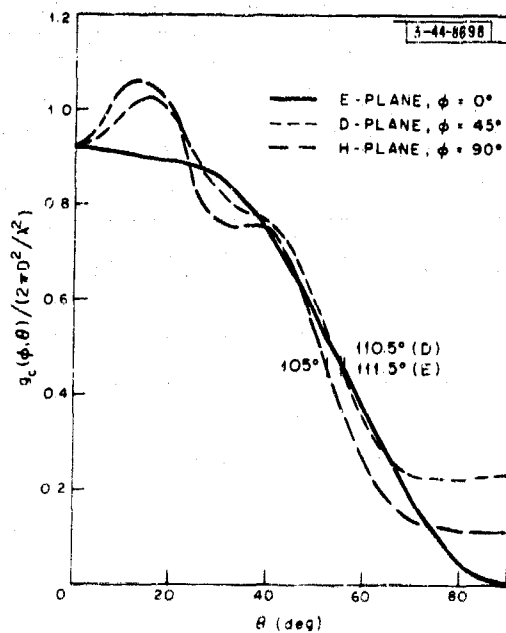


Fig. III-B-26. Normalized gain function for center element of  $9 \times 7$  array of short dipoles for element spacing  $D = 0.5 \lambda$  and element height above ground plane  $s = 0$  (no ground plane). Also indicated is included angle over which array may be scanned in each plane with less than 3-db loss in gain.

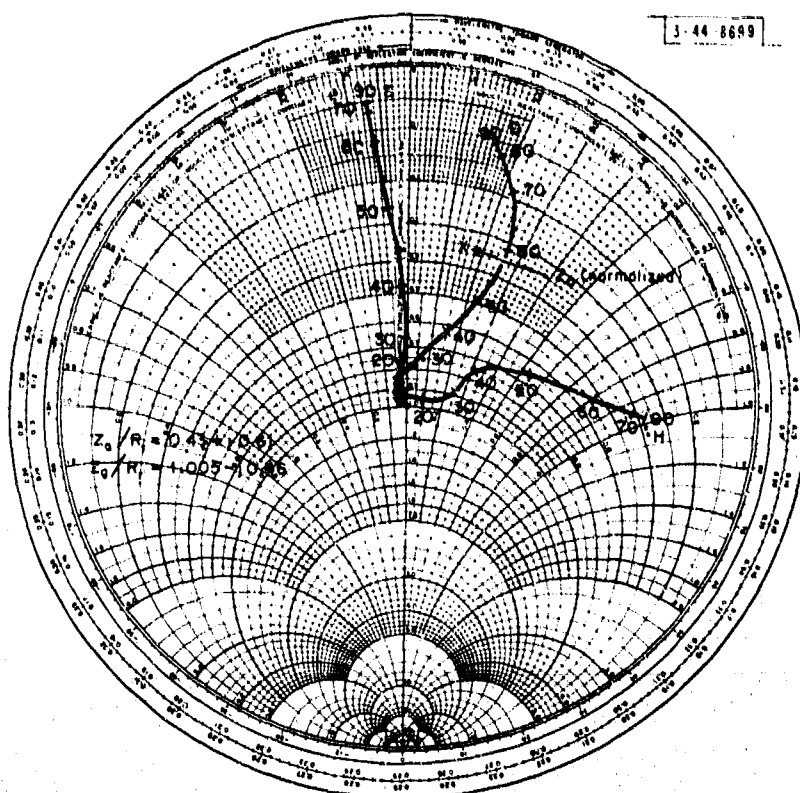


Fig. III-B-27. Variation in normalized driving impedance with scan angle for center element of  $9 \times 7$  array of short dipoles for element spacing  $D = 0.5 \lambda$  and element height above ground plane  $s = \lambda/8$ . Impedance of an isolated element  $Z_0$  and generator impedance  $Z_g$  are also given. Normalized value of  $Z_0$  is indicated on chart.

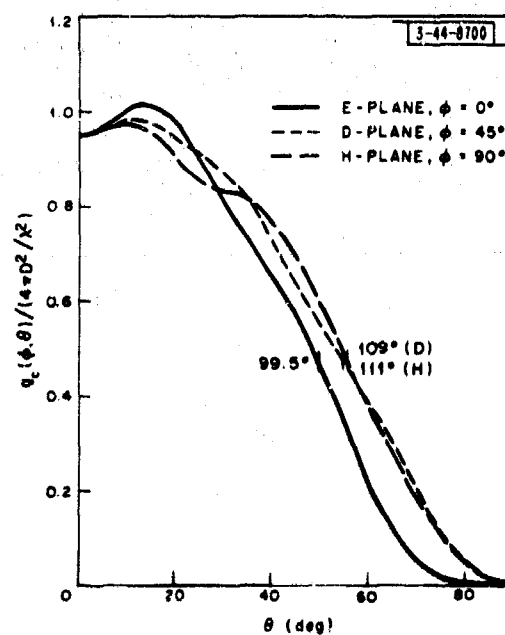
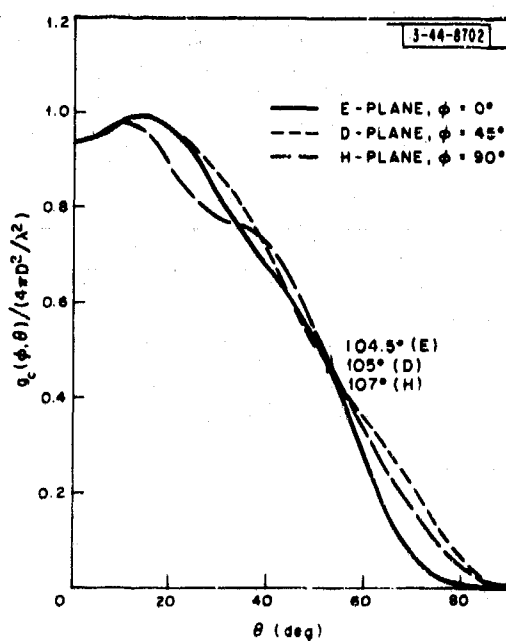
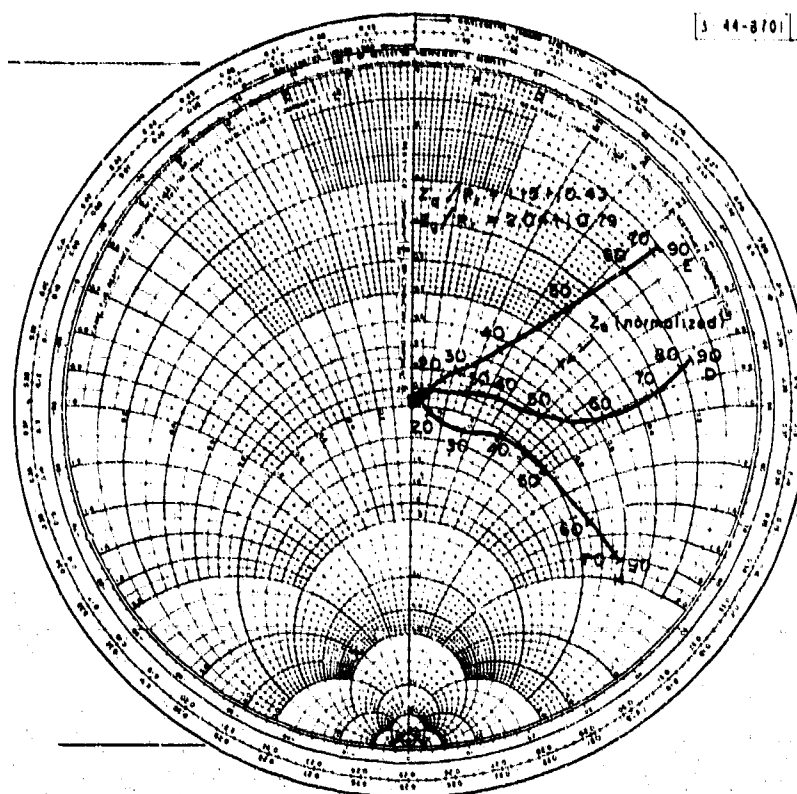


Fig. III-B-28. Normalized gain function for center element of  $9 \times 7$  array of short dipoles for element spacing  $D = 0.5 \lambda$  and element height above ground plane  $s = \lambda/8$ . Also indicated is included angle over which array may be scanned in each plane with less than 3-db loss in gain.



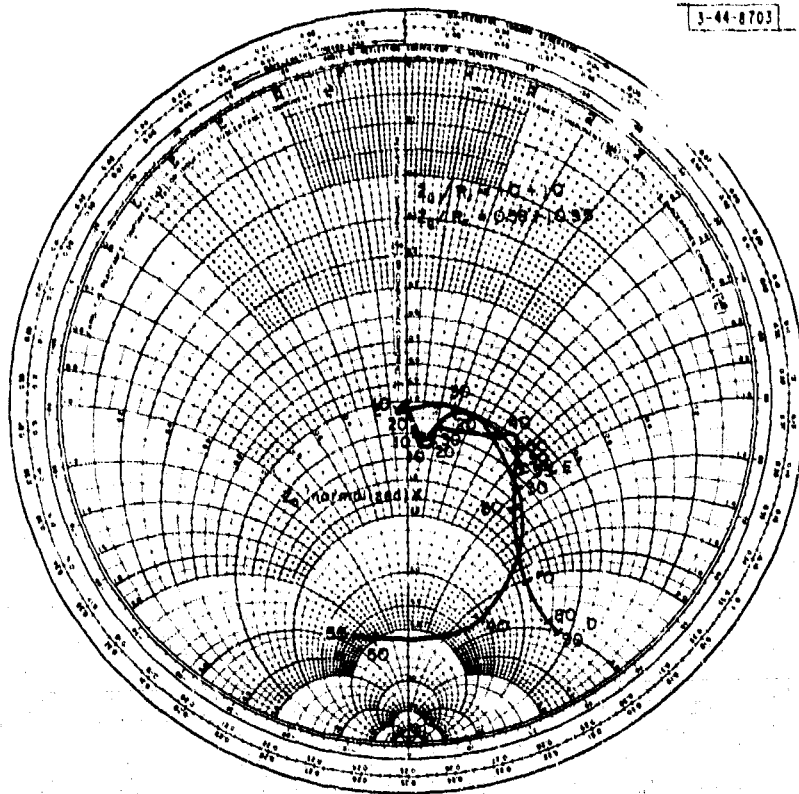
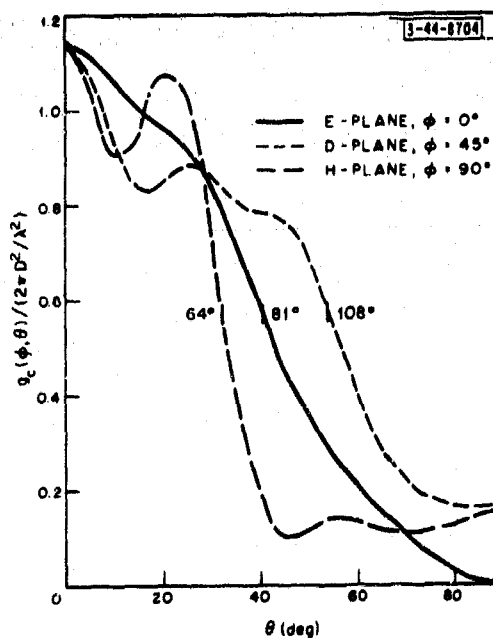


Fig. III-B-31. Variation in normalized driving impedance with scan angle for center element of  $9 \times 7$  array of short dipoles for element spacing  $D = 0.6 \lambda$  and element height above ground plane  $s = 0$  (no ground plane). Impedance of an isolated element  $Z_0$  and generator impedance  $Z_g$  are also given. Normalized value of  $Z_0$  is indicated on chart.

Fig. III-B-32. Normalized gain function for center element of  $9 \times 7$  array of short dipoles for element spacing  $D = 0.6 \lambda$  and element height above ground plane  $s = 0$  (no ground plane). Also indicated is included angle over which array may be scanned in each plane with less than 3-db loss in gain.



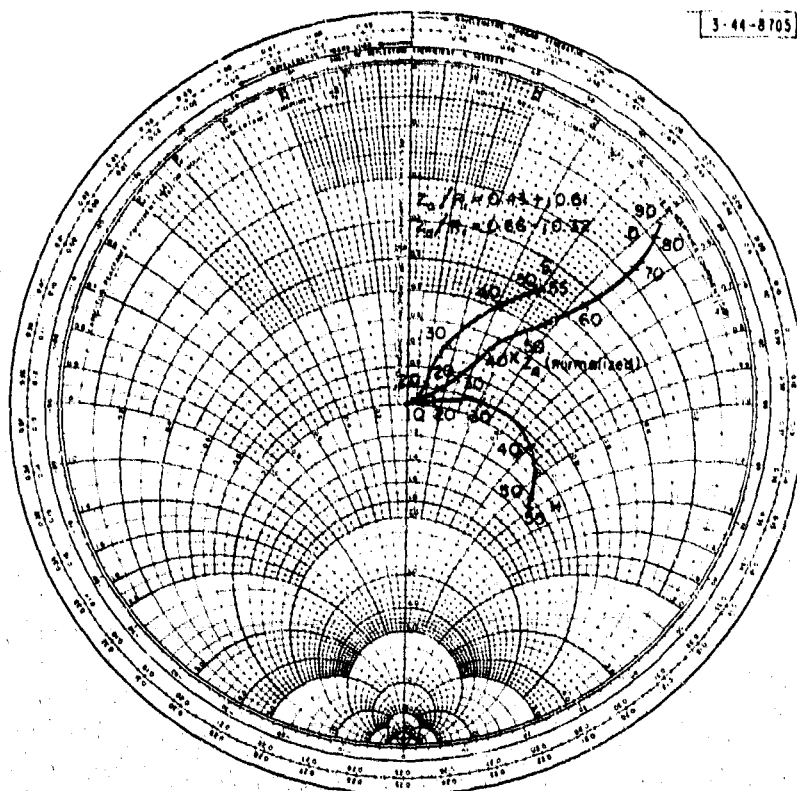


Fig. III-B-33. Variation in normalized driving impedance with scan angle for center element of  $9 \times 7$  array of short dipoles for element spacing  $D = 0.6 \lambda$  and element height above ground plane  $s = \lambda/8$ . Impedance of an isolated element  $Z_0$  and generator impedance  $Z_g$  are also given. Normalized value of  $Z_0$  is indicated on chart.

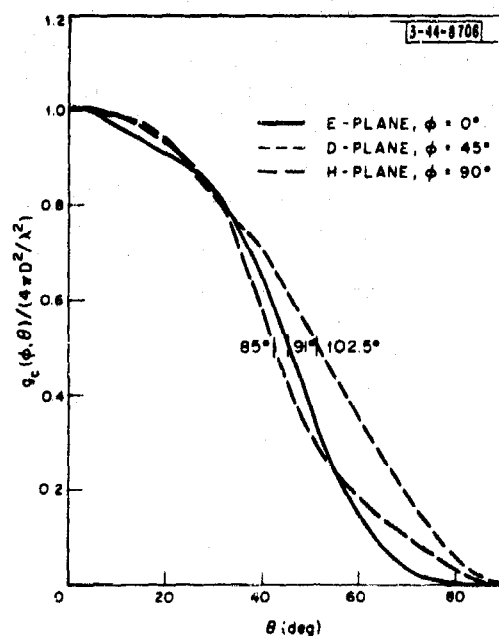


Fig. III-B-34. Normalized gain function for center element of  $9 \times 7$  array of short dipoles for element spacing  $D = 0.6 \lambda$  and element height above ground plane  $s = \lambda/8$ . Also indicated is included angle over which array may be scanned in each plane with less than 3-dB loss in gain.

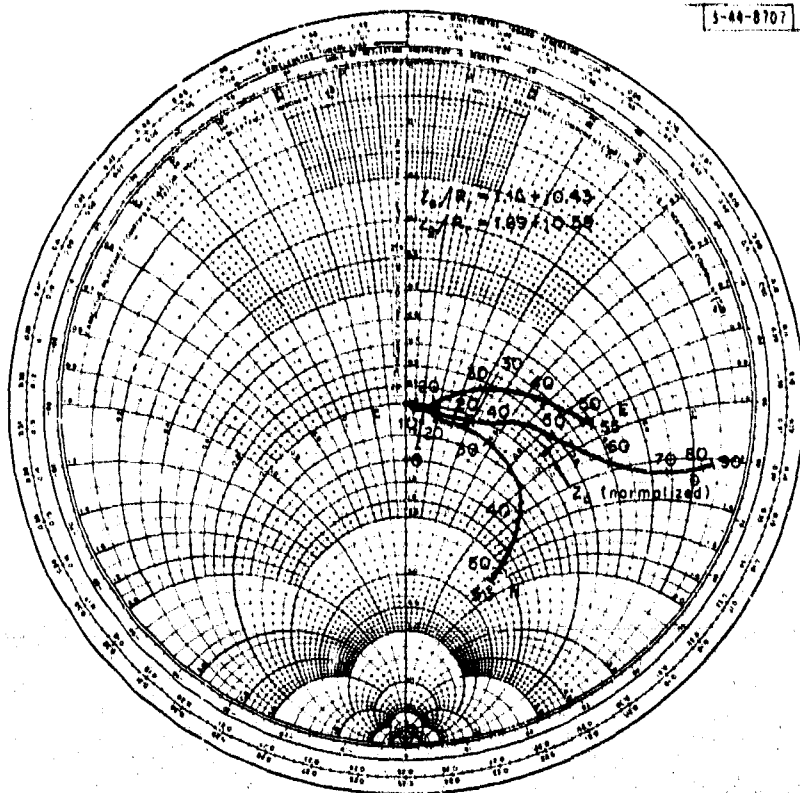


Fig. III-B-35. Variation in normalized driving impedance with scan angle for center element of  $9 \times 7$  array of short dipoles for element spacing  $D = 0.6 \lambda$  and element height above ground plane  $s = \lambda/4$ . Impedance of an isolated element  $Z_0$  and generator impedance  $Z_g$  are also given. Normalized value of  $Z_0$  is indicated on chart.

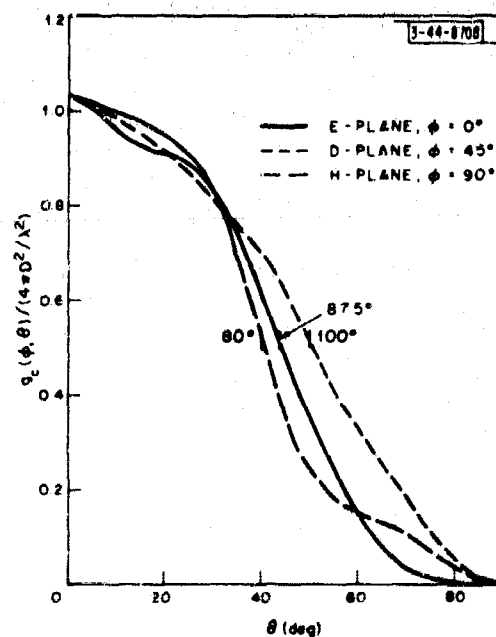


Fig. III-B-36. Normalized gain function for center element of  $9 \times 7$  array of short dipoles for element spacing  $D = 0.6 \lambda$  and element height above ground plane  $s = \lambda/4$ . Also indicated is included angle over which array may be scanned in each plane with less than 3-db loss in gain.



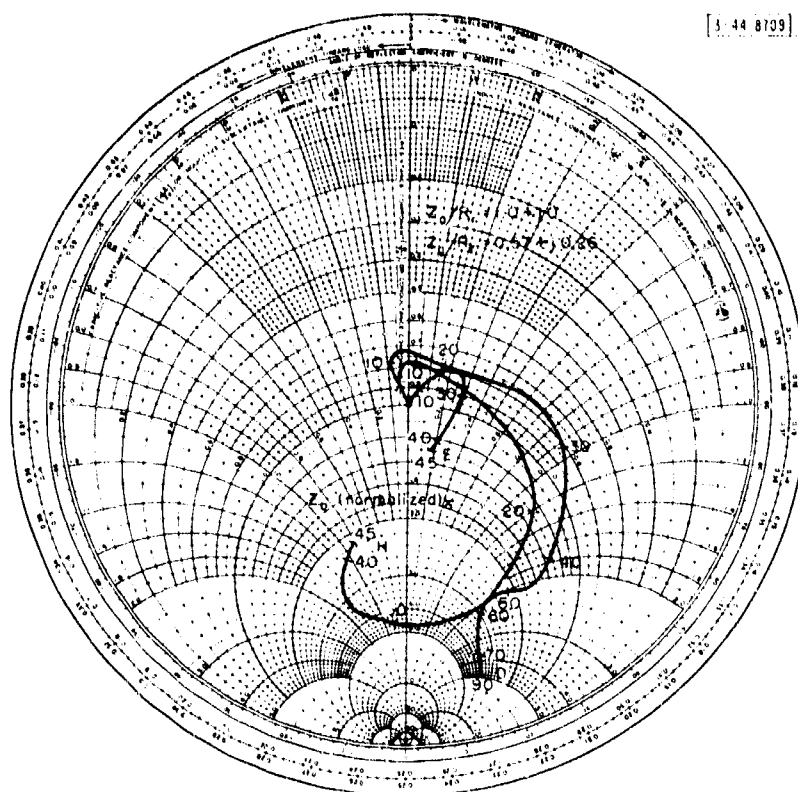


Fig. III-B-37. Variation in normalized driving impedance with scan angle for center element of  $9 \times 7$  array of short dipoles for element spacing  $D = 0.7 \lambda$  and element height above ground plane  $s = 0$  (no ground plane). Impedance of an isolated element  $Z_0$  and generator impedance  $Z_g$  are also given. Normalized value of  $Z_0$  is indicated on chart.

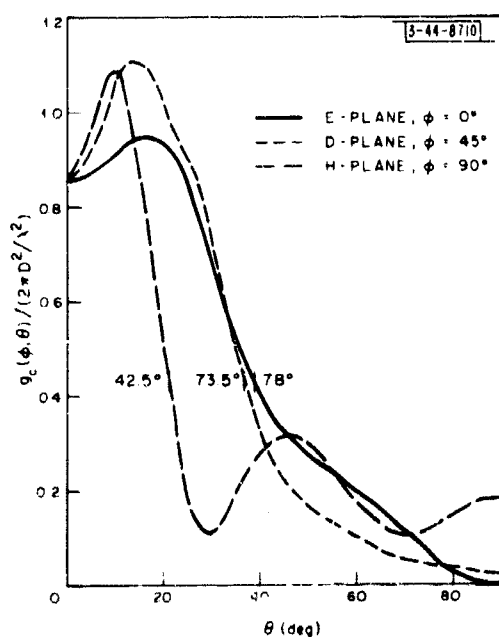


Fig. III-B-38. Normalized gain function for center element of  $9 \times 7$  array of short dipoles for element spacing  $D = 0.7 \lambda$  and element height above ground plane  $s = 0$  (no ground plane). Also indicated is included angle over which array may be scanned in each plane with less than 3-db loss in gain.

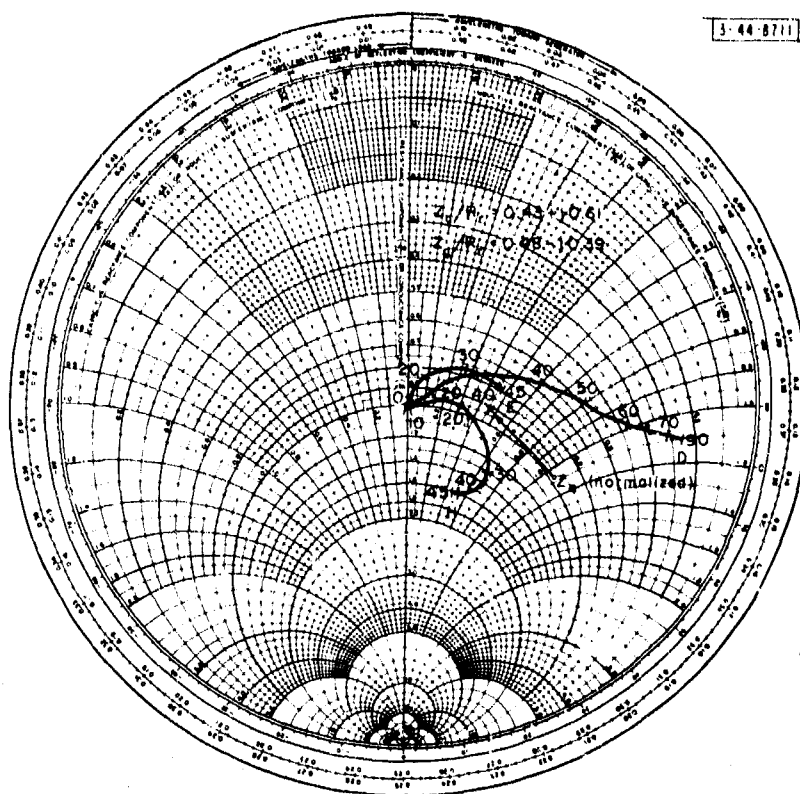


Fig. III-B-39. Variation in normalized driving impedance with scan angle for center element of  $9 \times 7$  array of short dipoles for element spacing  $D = 0.7 \lambda$  and element height above ground plane  $s = \lambda/8$ . Impedance of an isolated element  $Z_0$  and generator impedance  $Z_g$  are also given. Normalized value of  $Z_0$  is indicated on chart.

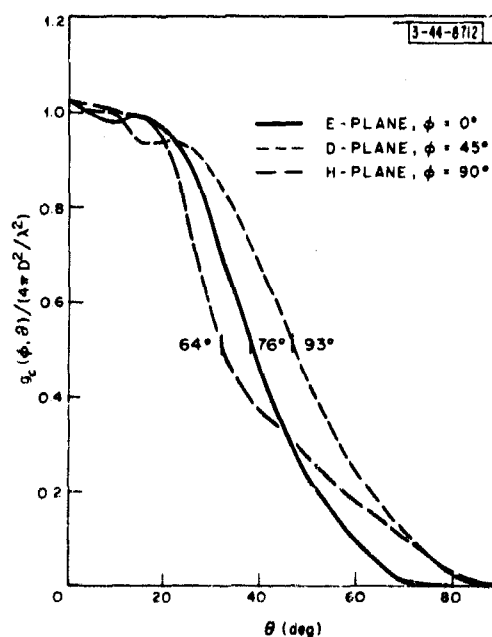


Fig. III-B-40. Normalized gain function for center element of  $9 \times 7$  array of short dipoles for element spacing  $D = 0.7 \lambda$  and element height above ground plane  $s = \lambda/8$ . Also indicated is included angle over which array may be scanned in each plane with less than 3-db loss in gain.

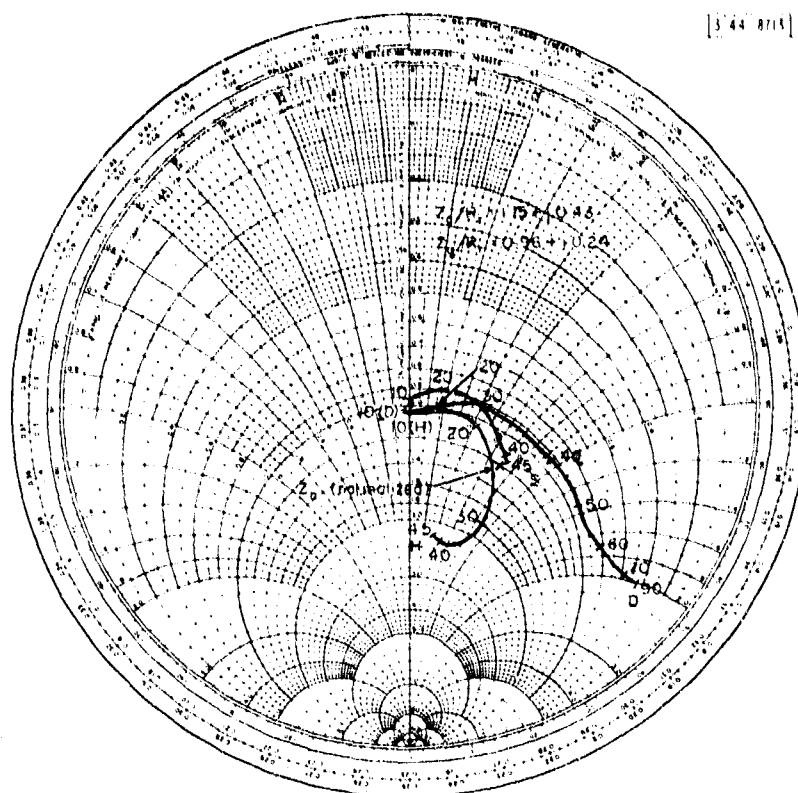


Fig. III-B-41. Variation in normalized driving impedance with scan angle for center element of  $9 \times 7$  array of short dipoles for element spacing  $D = 0.7 \lambda$  and element height above ground plane  $s = \lambda/4$ . Impedance of an isolated element  $Z_0$  and generator impedance  $Z_g$  are also given. Normalized value of  $Z_0$  is indicated on chart.

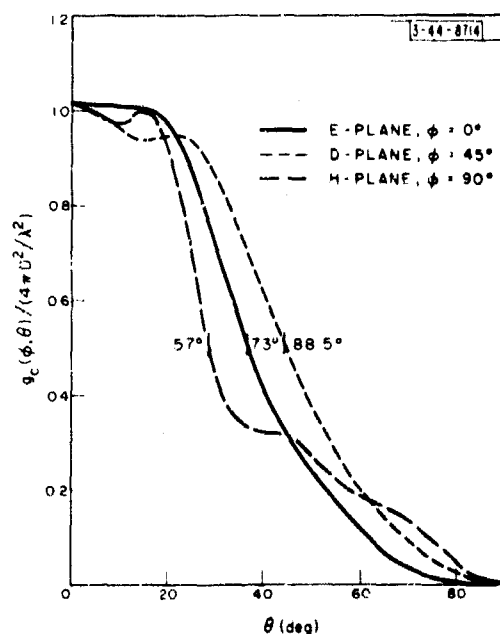


Fig. III-B-42. Normalized gain function for center element of  $9 \times 7$  array of short dipoles for element spacing  $D = 0.7 \lambda$  and element height above ground plane  $s = \lambda/4$ . Also indicated is included angle over which array may be scanned in each plane with less than 3-db loss in gain.

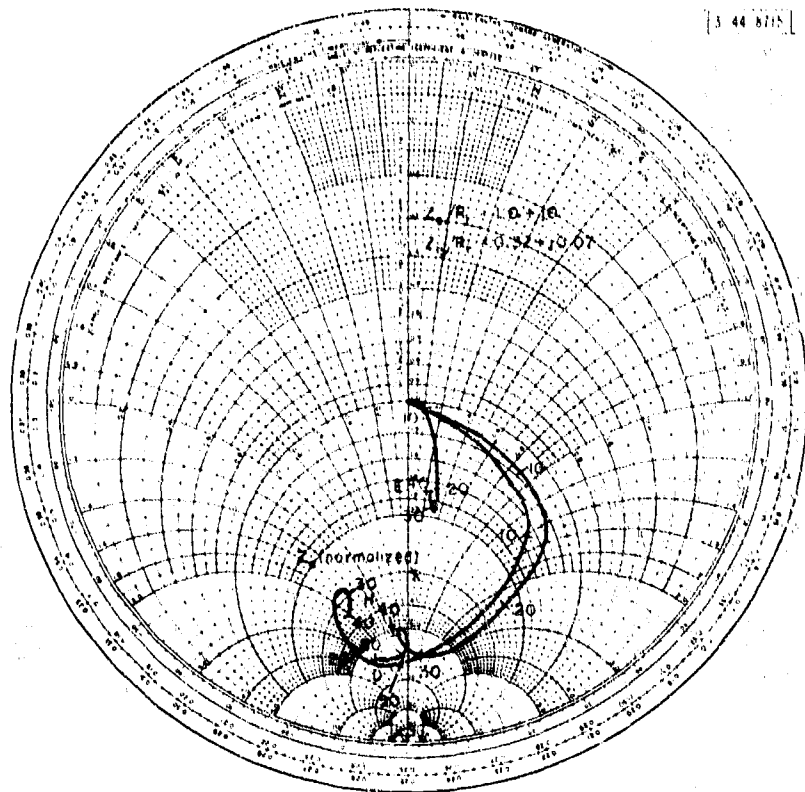


Fig. III-B-43. Variation in normalized driving impedance with scan angle for center element of  $9 \times 7$  array of short dipoles for element spacing  $D = 0.8 \lambda$  and element height above ground plane  $s = 0$  (no ground plane). Impedance of an isolated element  $Z_0$  and generator impedance  $Z_g$  are also given. Normalized value of  $Z_0$  is indicated on chart.

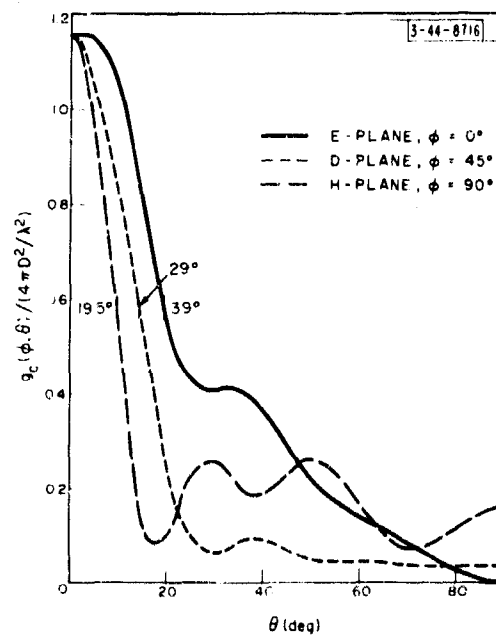


Fig. III-B-44. Normalized gain function for center element of  $9 \times 7$  array of short dipoles for element spacing  $D = 0.8 \lambda$  and element height above ground plane  $s = 0$  (no ground plane). Also indicated is included angle over which array may be scanned in each plane with less than 3-db loss in gain.

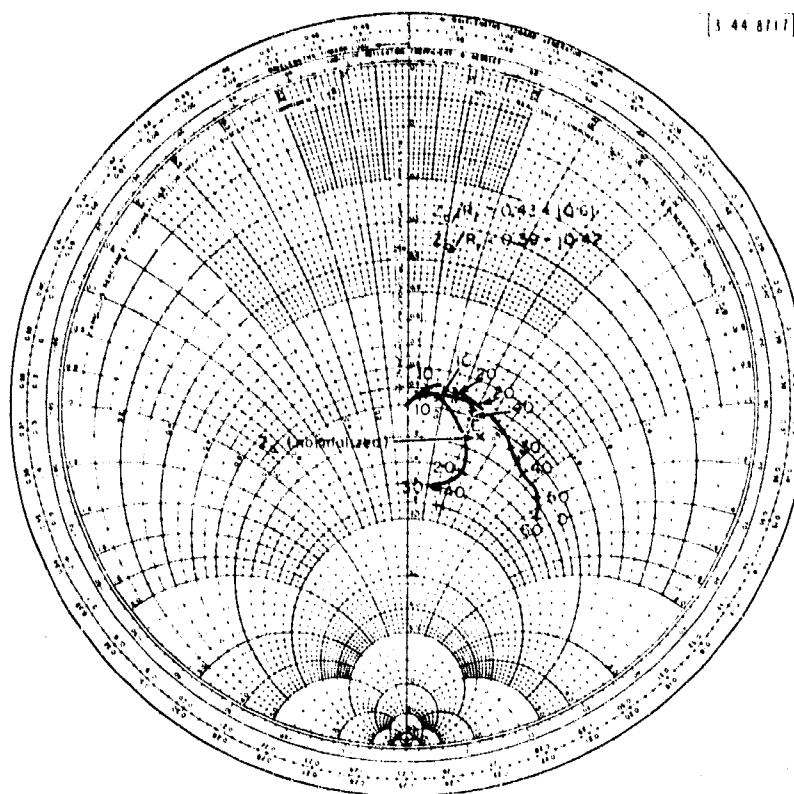


Fig. III-B-45. Variation in normalized driving impedance with scan angle for center element of  $9 \times 7$  array of short dipoles for element spacing  $D = 0.8 \lambda$  and element height above ground plane  $s = \lambda/8$ . Impedance of an isolated element  $Z_0$  and generator impedance  $Z_g$  are also given. Normalized value of  $Z_0$  is indicated on chart.

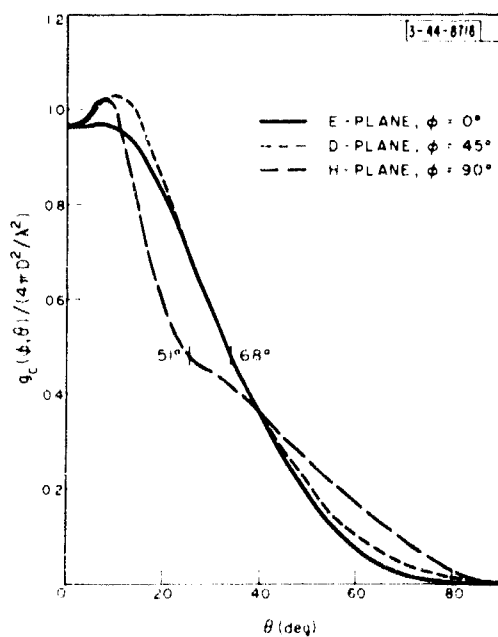


Fig. III-B-46. Normalized gain function for center element of  $9 \times 7$  array of short dipoles for element spacing  $D = 0.8 \lambda$  and element height above ground plane  $s = \lambda/8$ . Also indicated is included angle over which array may be scanned in each plane with less than 3-dB loss in gain.

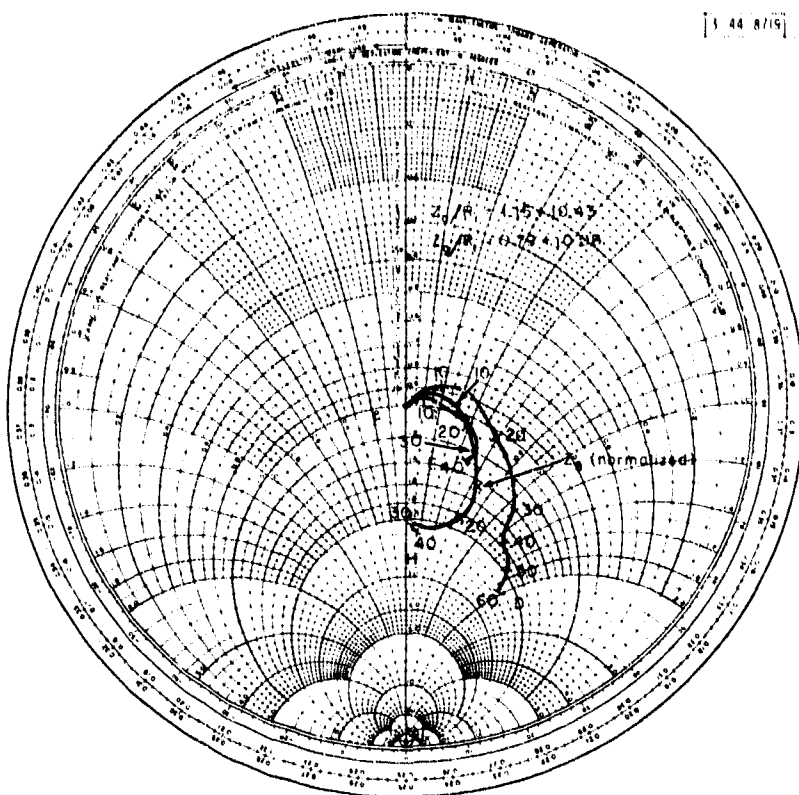


Fig. III-B-47. Variation in normalized driving impedance with scan angle for center element of  $9 \times 7$  array of short dipoles for element spacing  $D = 0.8 \lambda$  and element height above ground plane  $s = \lambda/4$ . Impedance of an isolated element  $Z_0$  and generator impedance  $Z_g$  are also given. Normalized value of  $Z_0$  is indicated on chart.

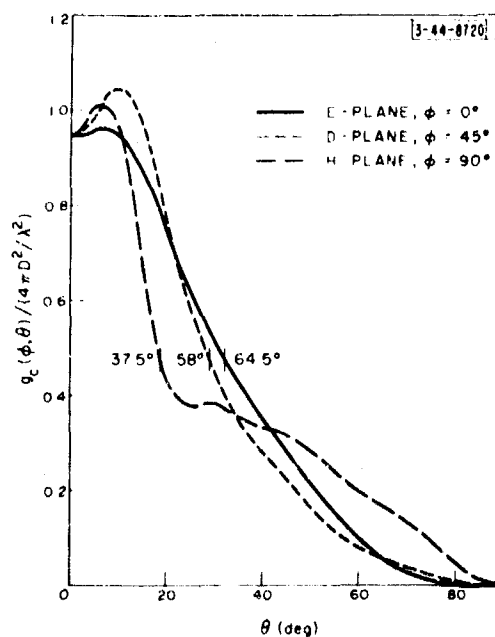


Fig. III-B-48. Normalized gain function for center element of  $9 \times 7$  array of short dipoles for element spacing  $D = 0.8 \lambda$  and element height above ground plane  $s = \lambda/4$ . Also indicated is included angle over which array may be scanned in each plane with less than 3-db loss in gain.

UNCLASSIFIED  
Security Classification

DOCUMENT CONTROL DATA - R&D		
(Security classification of title, body of abstract and indexing annotation must be entered when the overall report is classified)		
1. ORIGINATING ACTIVITY (Corporate author)  Lincoln Laboratory, M.I.T.	2a. REPORT SECURITY CLASSIFICATION Unclassified	
	2b. GROUP None	
3. REPORT TITLE  Phased Array Radar Studies - 1 January 1963 to 1 July 1964		
4. DESCRIPTIVE NOTES (Type of report and inclusive dates) Technical Report - 1 January 1963 to 1 July 1964		
5. AUTHOR(S) (Last name, first name, initial)  Allen, John L., et al.		
6. REPORT DATE 31 March 1965	7a. TOTAL NO. OF PAGES 354	7b. NO. OF REFS. 72
8a. CONTRACT OR GRANT NO. AF 19(628)-500	9a. ORIGINATOR'S REPORT NUMBER(S) Technical Report 381	
b. PROJECT NO. 649L	9b. OTHER REPORT NO(S) (Any other numbers that may be assigned this report) ESD-TDR-65-66	
c.		
d.		
10. AVAILABILITY/LIMITATION NOTICES  None		
11. SUPPLEMENTARY NOTES  None	12. SPONSORING MILITARY ACTIVITY  Air Force Systems Command, USAF	
13. ABSTRACT  This is the fourth in the series of reports describing the work of a general research nature carried out by the Lincoln Laboratory Array Radars Group.  The effort reported is directed toward an investigation of components, techniques, and fundamental theoretical limitations of arrays, primarily for high-power radar applications. The emphasis is on those applications which place the most stringent demands on the radar for resolution of very small targets from backgrounds of extensive and relatively large clutter (arrays with capability for high power, broad bandwidth, and narrow beamwidth).  Part I deals with the concluding activities on the 900-Mcps test array, emphasizing the configuration of the transmitting array and our experiences with it.  Part II is devoted to work on an S-band subarray transmitter configured around the use of high-power helical phase shifters.  Part III deals with theoretical and experimental studies in multiple-beam-forming systems and studies in mutual-coupling effects.		
14. KEY WORDS  phased array radars                      radar transmitters                      mutual coupling high-power radar                      radar beam forming                      amplifiers phase shifters                      array antennas		